ENGINEERING SEISMOLOGICAL STUDIES AND SEISMIC DESIGN CRITERIA FOR THE BULLER REGION, SOUTH ISLAND, NEW ZEALAND

A THESIS
SUBMITTED TO THE UNIVERSITY OF CANTERBURY
IN PARTIAL FULFILMENT OF THE REQUIREMENTS
FOR THE DEGREE OF
DOCTOR OF PHILOSOPHY

By
Peter James Stafford
February 2006

Department of Civil Engineering
College of Engineering
University of Canterbury
Christchurch, New Zealand

Thesis Abstract

This thesis addresses two fundamental topics in Engineering Seismology; the application of Probabilistic Seismic Hazard Analysis (PSHA) methodology, and the estimation of measures of Strong Ground Motion. These two topics, while being related, are presented as separate sections.

In the first section, state-of-the-art PSHA methodologies are applied to various sites in the Buller Region, South Island, New Zealand. These sites are deemed critical to the maintenance of economic stability in the region. A fault-source based seismicity model is developed for the region that is consistent with the governing tectonic loading, and seismic moment release of the region. In attempting to ensure this consistency the apparent anomaly between the rates of activity dictated by deformation throughout the Quaternary, and rates of activity dictated by observed seismicity is addressed. Individual fault source activity is determined following the application of a Bayesian Inference procedure in which observed earthquake events are attributed to causative faults in the study region. The activity of fault sources, in general, is assumed to be governed by bounded power law behaviour. An exception is made for the Alpine Fault which is modelled as a purely characteristic source. The calculation of rates of exceedance of various ground motion indices is made using a combination of Poissonian and time-dependent earthquake occurrence models. The various ground motion indices for which rates of exceedance are determined include peak ground acceleration, ordinates of 5% damped Spectral Acceleration, and Arias Intensity. The total hazard determined for each of these ground motion measures is decomposed using a four dimensional disaggregation procedure. From this disaggregation procedure, design earthquake scenarios are specified for the sites that are considered.

The second part of the thesis is concerned with the estimation of ground motion measures that are more informative than the existing scalar measures that are available for use in New Zealand. Models are developed for the prediction of Fourier Amplitude Spectra (FAS) as well as Arias Intensity for use in the New Zealand environment. The FAS model can be used to generate ground motion time histories for use in structural and geotechnical analyses. Arias Intensity has been shown to be an important strong motion measure due to its positive correlation with damage in short period structures as well as its utility in

predicting the onset of liquefaction and landslides. The models are based upon the analysis of a dataset of New Zealand Strong Motion records as well as supplementary near field records from major overseas events. While the two measures of ground motion intensity are strongly related, different methods have been adopted in order to develop the models. As part of the methodology used for the FAS model, Monte Carlo simulation coupled with a simple ray tracing procedure is employed to estimate source spectra from various New Zealand earthquakes and, consequently, a magnitude – corner-frequency relationship is obtained. In general, the parameters of the predictive equations are determined using the most state-of-the-art mixed effects regression procedures.

Acknowledgements

I would firstly like to express my sincere gratitude to my supervisors, Dr. John B. Berrill, and Dr. Jarg R. Pettinga. I cannot express just how much I value the freedom that you have allowed me in conducting this research. The leadership that you have both provided me has always come at exactly the right time, as has your encouragement. I think that walking the path of a PhD would have been a lot more difficult had I not had you behind me to push me up the hills just when I needed it. Thank you both.

Additionally, I would like to thank John firstly for making me aware of this research position. Accepting this position has enabled me to experience some of the most enjoyable years of my life. I suspect that you knew far better than I did that I would ultimately enjoy the challenge of a research position. I have been conscious for some time now that I would be your last graduate student, and at times I put myself under a lot of pressure, not just because of my own motivations, but because I wanted this thesis to be a reflection of the incredible impact that your teachings have had on not only me, but hundreds of other students over the time you have spent in academia. The University of Canterbury will suffer a great loss upon your retirement; not only because of your ability to instruct students in matters relating to Geomechanics and Earthquake Engineering, but because of your ability to instruct students in matters relating to life. I would like to think that I will still share many of your outlooks on life when I come to retire myself.

To Jarg, thank you firstly for the significant contribution that you have made with respect to helping me come to grips with the geology involved in this research. There is no question that geology is not my strong suit so knowing that I have had access to such a tremendous resource has been a continual source of comfort to me over the past four years. What I would most like to thank you for though is not so much your assistance with research but with your assistance in helping me to see the rules of the game that must be played if one wants to be successful in academia. I hope that in the years to come I am able to draw on your vast knowledge and professionalism to an even greater degree than I have done over the past four years.

I would also like to acknowledge the significant financial support for this project that was provided by Solid Energy New Zealand Ltd. Without their support this project simply would not have taken place and I would not have had the chance to experience what I have over the past four years; for this I am extremely greatful. Particular thanks must be given to Richard Mould and Steve Bell who have acted as representatives of Solid Energy with respect to this project. The freedom to conduct the research in the manner that we felt was most appropriate has, I think, ultimately lead to the best result for both of us.

Lastly I would also like to acknowledge my family; Mum, Dad, Shannon, and Matthew. You know all too well how much effort I have put into this work over the last four years. What you may not appreciate though is that I am continually encouraged to achieve the things that I have achieved, and to believe the things that I believe, in large part due to an overwhelming desire to make you feel proud of me. There is little else that I can do to repay you for everything that you have given me over my entire life. The love and support that I have always been aware of is the main reason why I am the person I am today, and therefore, without you, this thesis would not exist.

Having now completed this thesis I am finally in a position to view the process of writing a PhD thesis in its entirity. People that have never been through this process can never know what its like. But now that I have, I realise that it is much like M. C. Escher's "Drawing Hands". While I have ultimately created this work, the process of doing so has also had a signifcant impact in defining who I am. I would finally like to once again thank all those people that have influenced me throughout the course of writing this thesis.

Table of Contents

Table of Figures

List of Tables

List of Symbols

Arabic Symbols

$\mathbf{1}_{n_i}$	Unit matrix of size $n_i \times n_i$
$\mathbf{A}^{FP}, \mathbf{A}^{FS}$	Far field radiation pattern terms for both pressure and shear waves in terms of a co-ordinate system at the seismic source
$\mathbf{A}^{IP}, \mathbf{A}^{IS}$	Intermediate field radiation pattern terms for both pressure and shear waves in terms of a co-ordinate system at the seismic source
$\mathbf{A}^{N}$	Near field radiation pattern term in terms of a co-ordinate system at the seismic source
A	Total number of events in an aftershock sequence above some magnitude level (Omori Law)
A	Fault rupture area
A	Generic expression for an ordinate of the Fourier Amplitude Spectrum of Acceleration
A_i	Area of the i^{th} fault
$A(f)$	Fourier Amplitude Spectrum; generic expression used in Parseval's theorem
$A_{k,ij}$	Ordinate of the Fourier Amplitude Spectrum of acceleration at the k^{th} frequency and for the j^{th} recording of the i^{th} earthquake
$A(c, p)$	Function used in the Maximum Likelihood Estimation formulae of Ogata (1983)
a	Rate of earthquake occurrence above a given magnitude level (daily rate when used in aftershock formulae, annual rate when used in magnitude – frequency formulae)
a	Radius of a circular rupture surface
a_{f_c}	Regression coefficient for the corner frequency – moment magnitude relationship
a_L, a_W	Coefficients for the finite fault scaling relation for length and width respectively

$a(t)$	Acceleration time history; generic expression used in Parseval's theorem
$a_x(t)$	Acceleration time history in the x direction
b	Gutenberg – Richter 'b - value'
b_{AS}	Gutenberg – Richter 'b - value' for an aftershock sequence
$\hat{b}_{GR,MLE}$	Maximum likelihood estimate of the Gutenberg – Richter 'b - value'
b_L, b_W	Coefficients for the finite fault scaling relation for length and width respectively
$\mathbf{C}, c_{ij}$	Correlation coefficients in both matrix form and indicial form
$\mathbb{C}$	Coefficient term of the FAS model encapsulating various physical constants
$C_{a_L,a_L}, C_{a_L,a_W}, \ldots$	Correlation coefficients between the scaling of source lengths and widths considering finite fault scaling effects for the Monte Carlo simulation procedure
C_{f_c}	Coefficient representing various factors in the determination of the corner frequency – moment magnitude relationship
C_{source}	Correlation coefficient matrix for the finite source scaling effects used in the Monte Carlo simulation procedure
c	Temporal shift parameter in the Modified Omori Law; related to the completeness level of the sequence
c	Coefficient of the Hanks and Kanamori (1979) moment magnitude expression
$c_1, c_2, c_3, \ldots$	Regression coefficients
$\hat{c}$	Maximum likelihood estimate of c
c_{ijpq}	Elastic Tensor
c_Q	Seismic velocity used for the determination of the anelastic attenuation parameter
D	Duration of strong ground motion
d	Coefficient of the Hanks and Kanamori (1979) moment magnitude expression
E	Eastings, in NZMG co-ordinates
$E_{(t_1,t_2)}$	Expectation of a future earthquake occurrence between t_1 and t_2
E_i, E_{i+1}	End points of a fault segment in NZMG Eastings
F	Free surface amplification factor
f	Natural, or oscillator, frequency
$\overline{f}$	Normalised frequency; used in integrations for the theoretical Arias Intensity model
f_1, f_2	High and Low pass filter limits
$f_c, f_c(\mathbf{M})$	Corner frequency, and its magnitude dependent designation
$f_{c,i}$	Corner frequency of the i^{th} earthquake in the strong motion dataset
$f_{c,ij}$	Corner frequency determined from the j^{th} component of the i^{th} earthquake in the strong motion dataset
f_k	The k^{th} frequency for which the regression procedure is performed

F_i	The i^{th} fault source
$F^i(f)$	The i^{th} component of the Fourier Amplitude Spectrum in terms of natural frequency
$F^i(\omega)$	The i^{th} component of the Fourier Amplitude Spectrum in terms of angular frequency
$F_M(m)$	Cumulative distribution function of the doubly bounded Gutenberg – Richter magnitude – frequency distribution
F_N, F_R	Generic dummy parameters for normal and reverse faulting source mechanisms in the final model for the FAS of acceleration
$F_{N,i}, F_{R,i}$	Dummy regression parameters for normal and reverse faulting source mechanisms respectively for the i^{th} earthquake
$F_T(t)$	Cumulative distribution function of the time dependent probability distributions for earthquake occurrence (Poisson, Lognormal, and Brownian Passage Time)
$F_T(t \mid \mathbf{x})$	Cumulative distribution function of a time dependent probability distribution, conditioned upon a given dataset, $\mathbf{x}$
$f(\boldsymbol{\xi}_u, \boldsymbol{\theta})$	Functional form of a nonlinear regression model evaluated for a given set of predictor variables and parameter values
$f(M_{W,i}, r_{ij}, \boldsymbol{\theta})$	Functional form of a regression model
$f(r_{ij}, \boldsymbol{\theta})$	Functional form of a regression model with the magnitude scaling removed
f_u^0	Evaluation of the functional form of a regression model for its initial parameters
$f_\varepsilon(\varepsilon)$	Probability density function of the parameter epsilon
$f_M(m)$	Probability density function of the doubly bounded Gutenberg - Richter magnitude – frequency distribution (or of magnitude in general when used in PSHA methodology)
$f_{M_0}(M_0)$	Probability density function of the doubly bounded Gutenberg - Richter Seismic Moment – frequency distribution
$f_{M,R}(m,r)$	Joint Probability Density Function in m and r
$f_{M,R,\varepsilon}(m,r,\varepsilon)$	Joint Probability Density Function in m, r, ε
$f_R(r)$	Probability density function of distance
$f_R(r \mid m, r_{hyp}, \boldsymbol{\theta})$	Probability density function of a distance measure incorporating finite fault effects conditional upon magnitude, hypocentral distance, and various properties of the fault source
$f_R(r \mid m, \mathbf{x}_{hyp}, \boldsymbol{\theta}_i)$	Probability density function of a distance measure incorporating finite fault effects conditional upon magnitude, hypocentral position, and various properties of the i^{th} fault source

$f_{R_{hyp}}\left(r_{hyp}\right)$	Probability density function of hypocentral distance
$f_T\left(t\right)$	Probability density function of the time to the next earthquake occurrence (applies to all three occurrence models considered, Poisson, Lognormal, and Brownian Passage Time)
$f_T\left(t \mid \mathbf{x}\right)$	Recurrence time probability density function determined given a set of data, $\mathbf{x}$
$f_T\left(t \mid \boldsymbol{\theta}, \mathbf{x}\right)$	Recurrence time probability density function determined given both a set of data, $\mathbf{x}$, and a set of parameters, $\boldsymbol{\theta}$
$f_X\left(\mathbf{x}\right)$	Probability density function of a particular dataset of recurrence intervals, $\mathbf{x}$
$f_{\mathbf{X}_{hyp}}\left(\mathbf{x}_{hyp}\right)$	Probability density function of a hypocentral position in Cartesian space
$G_M\left(m\right)$	Cumulative complementary distribution function of the doubly bounded Gutenberg – Richter distribution function
$G_{np}\left(\mathbf{x},t;\boldsymbol{\xi},\tau\right)$	Green's function giving the motion in the n^{th} direction at location $\mathbf{x}$ and time t caused by a point force acting in the p direction at location $\boldsymbol{\xi}$ and time τ
g	Acceleration due to gravity at the Earth's surface $\left(\sim 9.81\ \mathrm{m/s^2}\right)$
$g\left(M,R,\boldsymbol{\theta}\right)$	Functional form of a predictive equation for a strong ground motion measure
$g\left(\boldsymbol{\theta} \mid \mathbf{x}\right)$	Conditional probability density function of the parameters, $\boldsymbol{\theta}$, given a set of data, $\mathbf{x}$
H_k	The k^{th} cell (in the context of the Bayesian Inference procedure)
$h\left(t\right)$	Hazard rate function
$h\left(t \mid \mathbf{x}\right)$	Hazard rate function conditioned upon a particular dataset, $\mathbf{x}$
$h_{T,\mathrm{BPT}}$	Hazard rate for the Brownian Passage Time
$h_{T,\mathrm{LGN}}$	Hazard rate for the lognormal distribution
$\mathbf{I}_N$	Identity matrix of dimension N
$I\left[S_a > S_a^* \mid m,r,\varepsilon\right]$	Binary indicator function; one if the condition $S_a > S_a^*$ is true given the set m,r,ε; zero otherwise
I_a, I_{aa}	Arias Intensity
I_a^*, I_{aa}^*	Design, or target, Arias Intensity
I_{xx}, I_{yy}, I_{zz}	Arias Intensity in the xx, yy, and zz directions respectively
$I_{xx}\left(\xi\right)$	Arias Intensity for a given value of viscous damping
i_ξ	Take-off angle
i_1, i_2	Angle of incidence, and transmission, respectively of a pressure wave in two adjoining crustal layers
J	Integral of the power spectrum

j_1, j_2	Angle of incidence, and transmission, respectively of a shear wave in two adjoining crustal layers
$J(\boldsymbol{\theta}; S, T)$	Fisher Information Matrix (conditional upon a given completeness interval)
K	Total number of events in an aftershock sequence above some magnitude level (Modified Omori Law)
$\hat{K}$	Maximum likelihood estimate of K
k	Cell index
k	Total number of recurrence intervals used in the time dependent probability calculations for the Alpine Fault
L	Length of a rectangular rupture
L	Likelihood expression
L_i	Length of the i^{th} fault segment
$L(\boldsymbol{\theta})$	Likelihood value for a given set of parameters
L_{sub}	Subsurface rupture length
$\mathbf{l}$	Pressure wave direction vector
M, m	Magnitude (general expression; but typically implies moment magnitude)
M	Total number of earthquake in regression dataset
$M*$	Modal value of magnitude, M
$\mathbf{M}, M_W$	Moment Magnitude
$M_{W,i}$	Moment Magnitude of the i^{th} earthquake in the strong motion dataset
$\hat{M}_{W,i}$	Mean moment magnitude of the i^{th} earthquake in the strong motion dataset
$\bar{m}$	Mean magnitude value
M_0	Seismic Moment
$M_0\left(t-\frac{r}{\alpha}\right)$	Time dependent Seismic Moment, adjusted for pressure wave velocity travel time
$M_0\left(t-\frac{r}{\beta}\right)$	Time dependent Seismic Moment, adjusted for shear wave velocity travel time
$M_{0,\max}$	Maximum Seismic Moment
$M_{0,\min}$	Minimum Seismic Moment
$M_{0,rate}$	Seismic Moment release rate
$\dot{M}_0$	Seismic Moment release rate
$\dot{M}_0\left(t-\frac{r}{\alpha}\right)$	Time dependent Seismic Moment release rate, adjusted for pressure wave travel time
$\dot{M}_0\left(t-\frac{r}{\beta}\right)$	Time dependent Seismic Moment release rate, adjusted for shear wave travel time
$m_{AS}^{\max}$	Maximum magnitude in an aftershock sequence (excluding the mainshock)

m_b	Body Wave Magnitude
M_D	Duration Magnitude
m_i, m_j	Central magnitude value of the i^{th} or j^{th} magnitude bin
M_L	Local Magnitude
$M_{\max}$	Maximum magnitude assigned to a given seismic source
$M_{\max,i}$	Maximum magnitude assigned to a given seismic source for the i^{th} branch of a logic tree
$M_{\min}, m_{\min}$	Minimum magnitude of engineering interest considered in a PSHA
$m_{\max}$	Maximum magnitude level of an aftershock sequence
$m_{\min}$	Minimum magnitude level of an aftershock sequence
m_{MS}	Magnitude of the mainshock in an aftershock sequence
m_n	Minimum possible magnitude value in a seismicity catalogue (including the special case of an aftershock sequence); related to $m_{\min}$ via $m_n = m_{\min} - \delta/2$
M_S	Surface Wave Magnitude
m_x	Maximum possible magnitude value in a seismicity catalogue (including the special case of an aftershock sequence); related to $m_{\max}$ via $m_x = m_{\max} + \delta/2$
N, N1	SPT blow count, and its corrected value
N	Northings (in the NZMG convention)
N	Total number of fault sources in the fault model
N	Total number of events at all completeness levels in a given seismicity catalogue
N	Total number of records in the regression dataset
$N*$	Modal value of the Northings co-ordinate
N_{cells}	Total number of cells used in the Bayesian Inference procedure
N_i, N_{i+1}	End points of a fault segment in NZMG Northings
$N_{i,50}$	Median number of events associated with the i^{th} seismic source
$N_{i,\max}$	Maximum number of events associated with the i^{th} seismic source
$N_{i,\text{mean}}$	Mean number of events associated with the i^{th} seismic source
$N_{i,\min}$	Minimum number of events associated with the i^{th} seismic source
$N(m)$	Total number of events of magnitude equal to or greater than a given magnitude
n_i	Number of events in the i^{th} magnitude bin
n_i	Number of records from the i^{th} earthquake
$n(t)$	Rate of aftershock occurrence
$n(t;\boldsymbol{\theta})$	Conditional rate of aftershock occurrence (conditioned upon a given parameter set)
O	Observations (in the context of Bayesian Inference)

P	Probability
P	Designation for the pressure wave components of ground motion
$\hat{P}, \breve{P}$	Upwards, and downwards, travelling pressure wave
P_i^{SH}, P_i^{SV}	Relative magnitude of the i^{th} ray after effects associated with scattering and partitioning of energy due to interactions with material interfaces have been accounted for; for SH and SV waves (rays)
$P\left[E_{(t_1,t_2)}\right]$	Probability of an earthquake occurring in the future interval (t_1, t_2)
$P(B)$	Prior probability that an event occurs in the background source
$P(F_i)$	Prior probability of an event occurring on the i^{th} fault
$P(F_i \mid H_k)$	Conditional probability of an event occurring on the i^{th} fault source given that it occurs in cell H_k
$P(F_i \mid O)$	Conditional probability of an event occurring on the i^{th} fault source given the observations, O
$P(H_k)$	Prior probability of an event occurring in cell H_k
$P(H_k \mid B)$	Conditional probability of an event being located in cell H_k given that it occurs in the background source
$P(H_k \mid F_i)$	Conditional probability of an event being located in cell H_k given that it is generated by the i^{th} fault source
$P(H_k \mid O)$	Conditional probability that an event occurs in cell H_k given the observations, O
p	Time exponent in both Omori's Law and the Modified Omori Law for aftershock occurrence
p	Ray parameter (horizontal slowness)
$\hat{\mathbf{p}}$	SV wave direction unit vector
$\hat{p}$	Maximum likelihood estimate of p
p_i	Incremental probability (dependent upon the period of catalogue completeness) in the MLE procedure of Weichert (1980)
$p(r)$	Probability density of an event occurring at a certain distance from a fault plane
$p(\mathbf{x})$	Three dimensional spatial probability density function
$p_X(x)$	Probability density function for the Poisson distribution
$\mathbf{Q}, q_{ii}, q_{jj}, q_{ij}$	Components of the correlation coefficient matrix (non-normalised expressions)
$Q(f)$	Frequency dependent anelastic attenuation function
Q_0	Frequency independent anelastic attenuation factor
R, r	Distance from a fault plane
R_0	Reference distance

r	Source radius of a circular rupture
r_i	Distance travelled by the i^{th} ray during the ray tracing procedure
$\hat{\mathbf{r}}$	Unit vector in the radial direction (spherical co-ordinates)
$R*$	Modal value of R
R_{epi}	Epicentral distance
R_{fact}	Spatial scaling factor for aftershock interactions in the Reasenberg (1985) algorithm
R_{hyp}, r_{hyp}	Hypocentral distance
R_{jb}, r_{jb}	Joyner – Boore distance; closest distance to the horizontal projection of the rupture surface
$r_{\max}$	Maximum distance used in the PSHA calculations
R_{rup}, r_{rup}	Closest distance to rupture surface
$r_{rup,ij}$	Closest distance to the rupture surface for the j^{th} record from the i^{th} earthquake
R_{seis}, r_{seis}	Closest distance to the seismogenic part of the rupture surface
$\mathbb{R}_{\phi\theta}$	Generic radiation pattern expression
$\mathbb{R}^P$	Far field pressure wave radiation pattern
$\mathbb{R}^{SH}$	Far field radiation pattern for the horizontal component of shear waves
$\mathbb{R}_i^{SH}$	Far field radiation pattern for the horizontal component of shear waves for the i^{th} ray traced during the ray tracing procedure
$\mathbb{R}_i^{SV}$	Far field radiation pattern for the horizontal component of shear waves for the i^{th} ray traced during the ray tracing procedure
$\mathbb{R}^{SV}$	Far field radiation pattern for the vertical component of shear waves
$\overline{\mathbb{R}}^{SH}$	Characteristic SH wave radiation pattern from Monte Carlo simulation
$\overline{\mathbb{R}}^{SV}$	Characteristic SV wave radiation pattern from Monte Carlo simulation
$\mathfrak{R}^i(\mathbf{x},\boldsymbol{\xi})$	Generic geometric spreading function for any wave type
$\mathfrak{R}^P(\mathbf{x},\boldsymbol{\xi})$	Geometric spreading function for pressure waves
$\mathfrak{R}^S(\mathbf{x},\boldsymbol{\xi})$	Geometric spreading function for shear waves
S	Initial time of completeness for an aftershock sequence at some magnitude level
S	Designation for the shear wave components of ground motion
$\hat{S}, \breve{S}$	Upwards, and downwards, travelling shear wave
S_i	Site class term for the i^{th} site category
$S(f)$	Frequency dependent site response
S_a	Response Spectral Acceleration
$S_{a,predicted}$	Predicted response spectral acceleration
$S_{a,recorded}$	Recorded response spectral acceleration

S_a^*	Design, or target, response spectral acceleration
S_B, S_C	Generic dummy parameters for site classes B and C respectively for the final model for the FAS of acceleration
$S_{B,ij}, S_{C,ij}$	Dummy regression parameters for site classes B and C respectively for the j^{th} record from the i^{th} earthquake
s_i	Standard Deviation of the magnitude distribution for the i^{th} earthquake
T	Final time of completeness for an aftershock sequence at some magnitude level
T	Period
T	Time to the first occurrence of an earthquake (random variable in probability calculations)
T	Return Period
T_{ave}	Average time between the occurrence of earthquakes (used in time dependent probability calculations)
T_d	Duration of ground motion signal used in the Fourier Transform
T^P, T^S	Retarded, or travel, time for pressure and shear waves respectively
t	Time
τ	Time after the initiation of rupture
t_i	Time of the i^{th} event in an aftershock sequence
t_i, t_j	Period of observation for the i^{th} or j^{th} completeness level in a seismicity catalogue
$u(t)$	Time dependent displacement pulse at the source of an earthquake
$u(\infty)$	Final static displacement at the source of an earthquake
$\mathbf{u}(\mathbf{x},t)$	Displacement vector of ground motion at position $\mathbf{x}$ and at time t
$\mathbf{u}^{FS}(\mathbf{x},t)$	Far field shear wave component of the displacement vector at position $\mathbf{x}$ and at time t
$\mathbf{u}^{P}(\mathbf{x},t)$	Far field pressure wave displacement field
$\mathbf{u}^{S}(\mathbf{x},t), \mathbf{u}^{S}$	Far field shear wave displacement field (and its abbreviated version)
$\mathbf{u}^{SH}(\mathbf{x},t)$	Horizontal component of the far field shear wave displacement field
$\mathbf{u}^{SV}(\mathbf{x},t)$	Vertical component of the far field shear wave displacement field
$\overline{\mathbf{u}}$	Slip vector on a rupture surface
$\overline{u}$	Average slip over a rupture surface
$\dot{\overline{\mathbf{u}}}$	Slip velocity vector on a rupture surface
$\dot{\overline{\mathbf{u}}}(t-T^S)$	Time dependent slip velocity for time retarded shear waves
$[u_i(\boldsymbol{\xi},\tau)]$	Spatio-temporal slip distribution across a rupture surface (relative slip)
$u_i^+(\boldsymbol{\xi},\tau), u_i^-(\boldsymbol{\xi},\tau)$	Spatio-temporal slip distribution on a particular side of a rupture (dislocation)

$u_n(\mathbf{x},t)$	The n^{th} component of displacement of the ground at some arbitrary location $\mathbf{x}$ and at some time t
$\ddot{u}_g^i(t)$	Ground motion acceleration time history for the i^{th} orthogonal component
$\ddot{u}_g^\theta(t)$	Ground motion acceleration time history for the transverse cylindrical component
$\ddot{u}_g^r(t)$	Ground motion acceleration time history for the radial cylindrical component
$\ddot{u}_g^x(t)$	Ground motion acceleration time history for the x, horizontal, Cartesian component
$\ddot{u}_g^y(t)$	Ground motion acceleration time history for the y, horizontal, Cartesian component
$\ddot{u}_g^z(t)$	Ground motion acceleration time history for the z, vertical component (applicable in both Cartesian and cylindrical co-ordinate systems)
$\mathbf{U}^i(\mathbf{x}, f)$	The i^{th} component of the Fourier Amplitude Spectrum of displacement in the natural frequency domain
$\dot{\mathbf{U}}^i(\mathbf{x}, f)$	The i^{th} component of the Fourier Amplitude Spectrum of velocity in the natural frequency domain
$\ddot{\mathbf{U}}^i(\mathbf{x}, f)$	The i^{th} component of the Fourier Amplitude Spectrum of acceleration in the natural frequency domain
$\mathbf{U}^{SV}(\mathbf{x}, f)$	SV component of the Fourier Amplitude Spectrum of displacement in the natural frequency domain
$\mathbf{U}^{SV}(\mathbf{x},\boldsymbol{\xi}, f, \mathbf{M}, \boldsymbol{\theta})$	Complete description of the FAS of displacement, including its dependecies
$\mathbf{V}$	Variance – Covariance matrix for regression procedures
V	Factor for the partitioning of energy into two horizontal components
$V(f)$	Fourier Amplitude Spectrum of velocity
$V_{background}$	Volume of the total background source (neglecting fault sources) used in ensuring compatibility between seismicity analyses and PSHA
$V_{S_{30}}$	Shear wave velocity averaged over the upper 30m of a site
v_i	Wave velocity, either pressure of shear wave depending upon the context
W	Width of a rectangular rupture
W_i	Weight assigned to the i^{th} branch of a logic tree
X	Random variable
$X(f)$	Signal representation in the frequency domain (part of a Fourier Transform pair)
$\mathbf{x}$	Position vector in Cartesian co-ordinates
x	Random variable (discrete in the case of the Poisson distribution, i.e. number of earthquake events)
$\hat{\mathbf{x}}$	Unit vector in the $\mathbf{x}$ direction in Cartesian co-ordinates
$x(t)$	Signal representation in the time domain (part of a Fourier Transform pair)

x_i	Spatial position in the i^{th} co-ordinate direction
x_i^k, x_{ki}	Spatial position of the centre of the k^{th} cell in the i^{th} co-ordinate direction
$\mathbf{Y} - \mathbf{f^0}$	Modified response vector for the regression procedure, after the Taylor series expansion
$\mathbf{Y} - \mathbf{f}^j$	Modified response vector evaluated after the j^{th} iteration
$\overline{Y_i}$	Average (mean) observed response for the i^{th} earthquake
$\mathbf{y}$	Vector of observed responses in a regression model
y	Peak Ground Acceleration
$\hat{\mathbf{y}}$	Unit vector in the $\mathbf{y}$ direction in Cartesian co-ordinates
$y*$	Design, or target, peak ground acceleration
y_{ij}	Observed response from the j^{th} recording from the i^{th} earthquake
$y_{k,ij}$	Modified Fourier spectral amplitude at the k^{th} frequency for the j^{th} recording from the i^{th} earthquake
y_{1j}, y_{2j}	Individual components of response for the j^{th} strong motion record
$\mathbf{Z_0}$	Matrix form of the Taylor series gradient expression in the nonlinear regression procedure
$\mathbf{Z}_j$	Gradient matrix for the Taylor series expansion evaluated at the j^{th} iteration
Z	Depth (as a random variable)
Z_{iu}^0	Initial evaluation of the gradient matrix (partial derivatives of the functional form of the regression model with respect to the parameters of the model)
z	Focal depth
z_i	Thickness of the i^{th} layer in the Monte Carlo simulation procedure
$\hat{\mathbf{z}}$	Unit vector in the $\mathbf{z}$ direction in Cartesian co-ordinates
Z_{seis}, z_{seis}	Depth to the base of the seismogenic layer
z_{src}	Focal depth used in the Monte Carlo simulation procedure

Greek Symbols

α	Aperiodicity parameter (equivalent to the coefficient of variance) for BPT model
α	Pressure wave velocity
α_1, α_2	Pressure wave velocities in two adjoining crustal layers
$\alpha(\boldsymbol{\xi}), \alpha(\mathbf{x})$	Pressure wave velocity at the source and at a point in space respectively
α_i	Normalizing expression for the probability of events occurring about the i^{th} fault plane

α_i	Pressure wave velocity of the i^{th} crustal layer in the Monte Carlo simulation procedure
α_s	Aperiodicity parameter drawn randomly from a uniform distribution
$\boldsymbol{\beta}_0$	Vector of the initial transformed parameter estimates for the regression procedure
$\hat{\boldsymbol{\beta}}_0$	Initial parameter optimal estimate following the regression procedure
β	Parameter directly related to the Gutenberg – Richter '$b-$value', via $\beta = \ln(10)b$
β	Shear wave velocity
β_1, β_2	Shear wave velocities in two adjoining crustal layers
$\overline{\beta}$	Composite shear wave velocity
$\beta(\boldsymbol{\xi}), \beta(\mathbf{x})$	Shear wave velocity at the source and at a point in space respectively
$\overline{\beta}(\mathbf{x}, \boldsymbol{\xi})$	Composite shear wave velocity; made of component of both the source and a point in space
β_i	Shear wave velocity of the i^{th} crustal layer in the Monte Carlo simulation procedure
β_i^0	Initial estimate of the i^{th} transformed parameter in the nonlinear regression model
Δm	Difference between a mainshock and the largest aftershock in the associated aftershock sequence
$\Delta\sigma$	Stress Drop (or Stress Parameter); applies either for static or dynamic case
$\Delta\mathbf{x}$	Differential position vector
Δx_i	Half – width of a cell in the i^{th} co-ordinate direction
Δz	Crustal layer thickness
δ	Fault Dip Angle
δ	Residuals of strong ground motion predictive models
δ_i	Dip of the i^{th} fault segment
δ_i	Difference between the observed moment magnitude and the mean moment magnitude for the i^{th} earthquake in a strong motion dataset
δ	Bin size of magnitude values (related to the rounding accuracy of a seismicity catalogue)
$\boldsymbol{\varepsilon}$	Vector of fixed error components in the standard regression model
ε	Epsilon; deviation of the logarithm of a ground motion measure about its mean in units of $\sigma_{\ln S_a}$
ε_{ij}	Fixed Effect, of intra event error component, for the j^{th} component from the i^{th} earthquake
ε^*	Modal value of epsilon, ε
$\varepsilon_{\max}$	Maximum value of epsilon allowed in the PSHA calculations
$\Phi(x^*)$	Cumulative distribution function of the standard normal distribution evaluated at x^*

$\Phi^i(\omega)$	The i^{th} component of the Fourier Phase Spectrum in terms of angular frequency
$\hat{\boldsymbol{\varphi}}$	Unit vector for the direction of declination in spherical co-ordinates
$\hat{\boldsymbol{\varphi}}$	SH wave direction vector
$\boldsymbol{\gamma}$	Unit vector defining the direction of take-off for a ray departing a seismic source
γ	Related directly to the coefficient of the Hanks and Kanamori (1979) moment magnitude expression via $\gamma = \ln(10)c$
η_i	Random Effect, or inter event error component, for the i^{th} earthquake
$\tilde{\eta}_i$	Conditional maximum likelihood estimate of the random effects components of the regression model accounting for individual magnitude uncertainties
κ_0	Site diminution factor
κ_Q	Anelastic scaling parameter
Λ	Solution to the integral required for the theoretical derivation of an expression for Arias Intensity
λ	Rake Angle
λ	The Lamé constant
λ	Average rate of earthquake occurrence in the Poisson model
λ	Product of corner frequency and anelastic scaling parameter used in the integrations for the theoretical Arias Intensity expression
λ_y^*	Design frequency (or rate) of ground motion exceedance
$\lambda_{I_a > I_a^*}, \lambda_{I_{aa} > I_{aa}^*}$	Mean annual frequency (rate) of exceedance of the target Arias Intensity, I_a^* or I_{aa}^*
$\lambda_{S_a > S_a^*}$	Mean annual frequency (rate) of exceedance of the target spectral acceleration, S_a^*
$\lambda_{y>y^*}$	Mean annual frequency (rate) of exceedance of the target peak ground acceleration, y^*
$\boldsymbol{\mu}$	Vector of modelled responses in a regression model
μ	Shear Modulus
μ	General expression for the mean (applicable in various contexts)
$\mu(\boldsymbol{\xi})$	Shear modulus at the source
$\overline{\mu}_i$	Average (mean) modelled response for the i^{th} earthquake
μ_i	Mean spatial position in the i^{th} Cartesian co-ordinate direction
μ_{ij}	Modelled response for the j^{th} record from the i^{th} earthquake
μ_s	Mean recurrence interval for a particular sample, drawn from an assumed prior distribution when performing time dependent probability calculations
$\boldsymbol{\nu}$	Fault normal vector
ν	Poisson's Ratio

ν_i	Annual number of events greater than or equal to some minimum magnitude level for the i^{th} seismic source
ν_j	The j^{th} component of the fault normal vector (vector normal to the rupture surface)
ν_{m_n}	Annual number of events greater than or equal to the minimum possible magnitude in the seismicity catalogue (accounting for binning of magnitude values)
$\nu_{m,\min}$	Annual number of events greater than or equal to $m_{\min}$
$\boldsymbol{\theta}$	Vector of parameters; specific parameters depend upon the context in which the symbol is used
$\boldsymbol{\theta}_j, \boldsymbol{\theta}_{j+1}$	Vector of parameters in a regression model for particular iterations (j and $j+1$)
$\hat{\boldsymbol{\theta}}$	Maximum Likelihood Estimate vector of values for a particular parameter set
$\hat{\boldsymbol{\theta}}$	Unit vector for the azimuthal direction in spherical co-ordinates
$\boldsymbol{\theta}_0$	"True" vector of parameter values for a particular parameter set
$\boldsymbol{\theta}_0$	Initial parameter estimates for the regression procedures
θ	Fault Strike Angle
θ	Angle of rotation (in terms of bearing) for co-ordinate transformation
θ_i	Value of the i^{th} parameter in a set of parameters
θ_{i0}	Initial estimate of the i^{th} parameter in a set of parameters
ρ	Crustal Density
$\overline{\rho}$	Composite crustal density
$\rho(\boldsymbol{\xi}), \rho(\mathbf{x})$	Crustal Density at the source and at a point in space respectively
$\overline{\rho}(\mathbf{x}, \boldsymbol{\xi})$	Composite crustal density; made of components of both the source and a point in space
$\rho_{\boldsymbol{\alpha},\boldsymbol{\beta}}$	Correlation coefficients for the crustal velocities used in the Monte Carlo simulation
Σ	Symbolic designation of the rupture surface
σ	Standard Deviation (applicable in various contexts)
σ	Standard Deviation of the intra-event (fixed effects) error components
σ_1	Standard Deviation of the intra event error components found from a regression on geometric (average) components of ground motions
$\sigma_{\boldsymbol{\alpha}}$	Standard Deviation of the pressure wave velocities used in the Monte Carlo simulation
$\sigma_{\boldsymbol{\alpha},\boldsymbol{\beta}}$	Covariance matrix for crustal velocities used in the Monte Carlo simulation
$\sigma_{\%i}$	Standard Deviation of the percentage of events associated with the i^{th} seismic source
$\sigma_{\boldsymbol{\beta}}$	Standard Deviation of the shear wave velocities used in the Monte Carlo simulation
σ_β	Standard Deviation of the parameter β in the Weichert (1980) method

σ_c	Standard Deviation of the between component error terms for arbitrary to average error conversions
σ_D	Standard Deviation of the inter event recurrence interval (lognormal distribution)
σ_f	Standard Deviation of the positions of events distributed about a given fault plane
σ_i	Standard Deviation of position in the i^{th} Cartesian spatial direction
$\sigma_{\ln S_a}$	Standard Deviation of the natural logarithm of response spectral acceleration
$\sigma_{\ln I}$	Total standard deviation for an unspecified component of Arias Intensity (usually the average component is assumed)
$\sigma_{\ln I,arb}$	Total standard deviation for the arbitrary components of Arias Intensity
$\sigma_{\ln I,ave}$	Total standard deviation for the average components of Arias Intensity
$\sigma_{\ln Y}$	Total standard deviation for an unspecified component of ground motion (usually the average component is assumed)
$\sigma_{\ln Y,arb}$	Total standard deviation for the arbitrary components of ground motion
$\sigma_{\ln Y,ave}$	Total standard deviation for the average components of ground motion
σ_M	Standard Deviation of magnitude
$\sigma_{M,foreign}$	Standard Deviation of magnitude for foreign strong motion records
$\sigma_{\nu_{m,\min}}$	Standard Deviation of the annual number of events with magnitudes greater than or equal to $m_{\min}$
σ_{Ni}	Standard Deviation of the number of events assigned to the i^{th} seismic source
$\sigma_{\boldsymbol{\theta}}$	Vector of marginal errors for a particular parameter set
σ_T	Total Standard Deviation of a mixed effects regression model
τ	Time interval (when used in the Poisson model for aftershock occurrence)
τ	Standard Deviation of the inter-event (random effects) error components
Ω_0	Zero frequency source spectral amplitude
$\Omega_0^{SV}(\mathbf{x},\boldsymbol{\xi},\mathbf{M},\boldsymbol{\theta})$	Zero frequency source spectral amplitude for SV waves including all dependencies
Ω_0^{SV}	Zero frequency source spectral amplitude for SV waves
$\Omega(f)$	Source spectrum in terms of natural frequency
$\Omega(\omega)$	Modulus of the Fourier transform of displacement in terms of angular frequency (in this context it is equivalent to the source spectrum in angular frequency)
ω	Angular frequency
ω_c	Angular corner frequency
$\boldsymbol{\xi}$	Spatial position on a rupture surface
$\boldsymbol{\xi}_u$	Vector of predictor variables for the regression models, i.e. magnitude, distance, etc.
ξ	Viscous damping factor

ξ_i	Random effect for the i^{th} earthquake, allowing for individual magnitude uncertainties
$\tilde{\xi}_i$	Conditional maximum likelihood estimate of ξ_i
Ψ	Component of the integral solution in the derivation of a theoretical model for Arias Intensity (include sine and cosine integrals)
ζ	Exponent for the rate of geometric spreading

Mathematical Functions/Operators and Constants

$\lvert x \rvert$	Absolute value operator
arccos	Arc-Cosine function
Ci	Cosine Integral function (particular version of it)
cos	Cosine function
Cov	Covariance matrix
δ_{ij}	Kronecker delta function
E	Expected value
e	Natural base of logarithms
erf	Error function
exp	Exponential function
γ	Euler's constant
i	Imaginary unit; equal to the square root of negative one
ln	Natural logarithm
$\log_{10}$	Logarithm to base 10
$\prod$	Product operator
π	Ratio of the circumference of a circle to its diameter
$\sum$	Discrete summation operator
$\sum^{+}$	Direct summation operator
$\int dx$	Indefinite integral
$\int_{x_1}^{x_2} dx$	Definite integral
$\iiint_{\mathbf{x}} d\mathbf{x}$	Triple integral in Cartesian space
Si	Sine Integral function (particular version of it)
sin	Sine function
$\sqrt{x}$	Square Root operator

$\tan^{-1}$	Inverse Tangent function
tanh	Hyperbolic Tangent function
tr	Trace of a matrix
var	Variance matrix expression
$\mathbf{X}^T$	Matrix Transpose
$\mathbf{X}^{-1}$	Matrix Inverse
$x!$	Factorial operator

Miscellaneous Symbols

$\in$	Is an element of…
∞	Infinity
$\therefore$	Therefore
$\%_{i,50}$	Median percentage of events associated with the i^{th} seismic source with respect to the total number of events in a given seismicity catalogue
$\%_{i,\max}$	Maximum percentage of events associated with the i^{th} seismic source with respect to the total number of events in a given seismicity catalogue
$\%_{i,\text{mean}}$	Mean percentage of events associated with the i^{th} seismic source with respect to the total number of events in a given seismicity catalogue
$\%_{i,\min}$	Minimum percentage of events associated with the i^{th} seismic source with respect to the total number of events in a given seismicity catalogue

Abbreviations

AD, A.D.	anno Domini (Latin)
AIC	Akaike Information Criteria
AS97	Abrahamson and Silva, 1997
AY92	Abrahamson and Youngs, 1992
BC, B.C.	Before Christ
BJF97	Boore, Joyner, and Fumal, 1997
BPT	Brownian Passage Time
BSSC	Building Seismic Safety Council
CB03	Campbell and Bozorgnia, 2003
CDF	Cumulative Distribution Function
CCDF	Cumulative Complementary Distribution Function
CMT	Centroid Moment Tensor
CWB	Central Weather Bureau

CZP99	Cousins, Zhao, and Perrin, 1999
DSHA	Deterministic Seismic Hazard Analysis
ΔCFS	Change in secular Coulomb stress
EEPAS	Every Earthquake a Precursor According to Scale
ETAS	Epidemic - Type Aftershock Sequence
FAS	Fourier Amplitude Spectrum
GPS	Global Positioning System
GR	Gutenberg – Richter
IAS	Inangahua Aftershock Sequence
JMA	Japanese Meteorological Agency
LSQ	Least Squares
MFZ	Marlborough Fault Zone
MLE	Maximum Likelihood Estimation
MMI	Modified Mercalli Intensity
MZAS00	McVerry, Zhao, Abrahamson, and Somerville, 2000
NEHRP	National Earthquake Hazard Reduction Program
NEIC	National Earthquake Information Centre
NNSN	New Zealand National Seismic Network
NZ	New Zealand
NZMG	New Zealand Map Grid
NZS	New Zealand Standard
PDF	Probability Density Function
PEER	Pacific Earthquake Engineering Research Centre
PSHA	Probabilistic Seismic Hazard Analysis
R97	Rhoades, 1997
RVT	Random Vibration Theory
SCEMY97	Sadigh, Chang, Egan, Makdisi, and Youngs, 1997
SDOF	Single Degree Of Freedom
SOC	Self – Organised Criticality
SPT	Standard Penetration Test
ULLN	Upper Limit Lognormal
US, U.S.A.	United States, United States of America
USGS	United States Geological Survey
USSR	United Soviet Socialists Republic
VPSHA	Vector-Valued Probabilistic Seismic Hazard Analysis
WGCEP	Working Group for Californian Earthquake Probabilities

SECTION A

PROBABILISTIC SEISMIC HAZARD ANALYSIS (PSHA) FOR THE BULLER REGION, SOUTH ISLAND, NEW ZEALAND

A.1. General Introduction to Section A

Since time immemorial philosophers have grappled with concept of causality. Giants of the philosophical world such as Aristotle, Hume, and Russell were all perplexed to varying extents by this notion and the philosophical implications that the existence of such a notion might have. In more recent times, Engineering Seismologists have also been enticed by the concept of causality, albeit in a far less esoteric sense. The lure that entices practitioners and researchers from the independent fields of geotechnical, or structural, engineering, and seismology into the somewhat cross-disciplinary field of engineering seismology and earthquake engineering is the hope that the nature of the relationship between the cause of seismic waves and their subsequent effects upon the engineered environment might be understood. If the nature of any causal relationships can be understood, then as a society we are fundamentally better placed to deal with the infrequent, yet devastating, seismic episodes that have been known to cause great physical, emotional, financial, and general social, trauma to large numbers of people in many areas of the world.

The primary framework within which engineering seismologists attempt to relate causes and effects associated with earthquakes is Probabilistic Seismic Hazard Analysis (PSHA) (Cornell 1968), and Probabilistic Seismic Demand Analysis (PSDA) (Bazzurro 1998). Both frameworks, as their names suggest are probabilistically based. This is a necessary requirement when trying to develop generally applicable models for phenomena that are notoriously variable, such as the occurrence of earthquakes, and the nature of strong ground motions. Every possible model of a physical process is to some extent an approximation, by definition. Every approximation carries with it some associated error and the most convenient way to deal with such errors when conducting an analysis of a physical system is to represent these errors as known distributions and to apply probability theory to try and take into account the approximations that are necessarily made. PSHA considers a huge number of causes and effects pertaining to earthquakes and seismic waves from the fields of geology, geophysics, seismology, probability theory, and both geotechnical and structural engineering; all of these are uncertain to some degree. Upon considering all these sources of information, a hazard analyst may arrive at a representation of the seismic hazard for a given position that can be used for the engineering design of infrastructure. PSDA takes the probabilistically framed outputs of a PSHA and couples these with some model of the probable response of a structure in order to estimate the most likely demands imposed upon a structure as a result of the estimated hazard. Section A of this thesis is concerned with undertaking a comprehensive modern PSHA for specific sites within the Buller region, in the South Island of New Zealand. Many studies of this nature have been performed throughout

the world, but relatively few have been performed in New Zealand using state-of-the-art techniques. Given New Zealand's global location astride a major tectonic boundary, this is somewhat surprising. However a thorough PSHA is a significant and costly undertaking that must draw from a huge number and variety of resources and scientific fields. In New Zealand there are relatively few situations for which such an analysis is regarded as being warranted by those funding engineering projects.

The underlying framework of PSHA has essentially remained intact since its inception (Cornell 1968). In a very general manner, this underlying framework can be summarised by the following steps:

- Identify the locations, and define the geometry of all seismic sources within some distance of a site;
- Quantify the rate at which earthquakes are generated within each of these sources;
- Select from the existing literature, or derive, a model that relates the source strength of an earthquake to a ground motion level at some other distant point, including an estimate of the error in the model;
- Combine the previous two points in order to calculate the rate at which a ground motion level is exceeded;
- Combine the calculated rates from all the seismic sources identified in order to obtain an estimate of the total rate at which a particular ground motion level is exceeded at a particular site;
- Using these computed rates, suggest appropriate design levels so that engineers can ensure that structures can withstand the ground motion level in question.

Each of these steps is relatively simple to define, in a qualitative sense, and the procedure therefore presents itself as a simple, logical, recipe for obtaining estimates of seismic hazard. The quantitative formulation associated with these steps is a series of mathematical abstractions with their basis in probability theory. However, the essence of these abstractions is equally as simple as the qualitatively defined steps presented above. Although the governing equations may appear formidable upon first sight, their actual application is made simple through the necessary requirement that expressions within the governing equations must be evaluated numerically in almost all realistic cases.

The basic steps outlined above, as well as splitting the overall task up into discrete elements, also suggest a logical structure for Section A of this thesis. Of the chapters that follow, Chapter A.2 is concerned with identifying the seismic sources within the Buller – NW Nelson region that are most applicable to the estimation of hazard for sites within the region. Chapter A.3 is concerned with estimating the rate of earthquake occurrence associated with each of the seismic sources that are identified. Chapter A.4 discusses the selection of the most appropriate predictive models for the measures of strong ground motion that are considered in this PSHA. Chapter A.5 presents the details of the methodology required to marry the findings of the previous three chapters regarding spatio-temporal earthquake occurrence and consequent ground motion intensities. Finally, Chapter A.6 presents the results of the application of the proposed methodology to a series of specific sites within the Buller region. Chapter A.7 then goes on to

summarise these findings, highlighting the main conclusions drawn from each section of work; before suggesting potential areas for future research.

The simple procedure outlined above is indeed that which remains at the heart of modern probabilistic seismic hazard analyses. However, engineering seismologists, as was previously suggested, do not remain idle; rather, they continue to question the nature of causality in their chosen field and, in doing so, have developed a series of critical modifications to the original methodology of Cornell (Cornell 1968). The main developments that have taken place with respect to this original methodology include (along with some representative, or summarising, references):

- Improved models for the magnitude - frequency characteristics of seismic sources (Schwartz and Coppersmith 1984; Utsu 1999);
- A general increase in the level of sophistication of predictive models for strong ground motion measures (Idriss 1978; Douglas 2001);
- The consideration of time dependent probability models of earthquake occurrence (Nishenko and Buland 1987; Cornell and Winterstein 1988; Matthews et al. 2002);
- Development of a framework for accounting for epistemic uncertainties (Kulkarni et al. 1984); and
- The introduction of methods for obtaining earthquake scenarios and visualising the results of PSHA (National Research Council (NRC) 1988; McGuire 1995; Bazzurro and Cornell 1999).

There are of course many additional developments that have importance in their own right, but that have not been included here. Many of these are of a more technical nature and will be frequently discussed throughout the remainder of this section. Given the governing goal of applying state-of-the-art PSHA techniques where possible; all of the above elaborations to the original formulation are incorporated into the methodology that is employed in this thesis.

Obviously, a thorough understanding of the mathematical framework underpinning probabilistic seismic hazard analysis methodology must be possessed by the analyst if the full power of the methodology is to be exploited. However, it is one thing to become proficient at performing the mathematical calculations required as part of the PSHA methodology; it is another thing entirely to develop the skills and knowledge base required to apply these techniques to real world problems. Each tectonic region of the world, while often sharing some similarities with other regions, is essentially a special case for which various adjustments to the underlying PSHA framework must be made. This statement of fact is very evident when consulting the available literature on PSHA. While the general methodology has been in place for close to 40 years now, it is quite difficult to find examples of applications of PSHA where the exact same method has been adopted. This is again the case for the present work, where the applied methods represent many slight deviations from other previous analyses, as well as some original contributions. The methods that are finally adopted for use in making estimates of hazard at particular sites in the Buller region are governed by various factors such as the theoretical strength of the assumptions inherent in the potential methods, the availability of data for which the methods can be applied, financial and time constraints, as well as limited

manpower. Recent foreign hazard assessments such as the most recent WGCEP (Working Group for California Earthquake Probabilities 2003) assessment of seismic hazard for the San Francisco Bay region draw on the experience and findings of a huge number of researchers. While the methods used in a study like this represent the state-of-the-art in seismic hazard analysis, the potential to apply these modern methods is limited for other regions of the world as the data required in order to apply the methods simply does not exist. This is most certainly the case for the present study. Consequently, the methodologies that are adopted throughout the work strongly reflect the availability of relevant data for the desired purpose. In cases where less than ideal methods must be employed, these are highlighted as being potential areas for further research.

The Buller region represents a very interesting case for which modern probabilistic seismic hazard methods may be applied. However, no such attempts have previously been made for this region. Although estimates of hazard for the region have been made indirectly as a consequence of larger projects, such as the development of the probabilistic seismic hazard maps for New Zealand (Stirling, Wesnousky et al. 1998; Stirling et al. 2000; Stirling et al. 2002), or partially through the development of national seismicity models (Stock 2001), no specific regional hazard assessments for the Buller region have been made (at least in as far as publicly available analyses are concerned). This is most likely due to the recognition that while the Buller region may represent a region of high seismic hazard, it simultaneously represents a region of relatively low seismic risk as the population density, and associated economic activity is relatively sparse. However, what does and does not represent high risk is very much a matter of perspective. Risk considerations aside; the problem of quantifying the seismic hazard in the region remains an interesting, and challenging, one.

Throughout the past 150 years or so, the Buller region has been one of the most seismically active regions in New Zealand. However, until relatively recently, the general consensus found from the existing literature suggests that the observed rates of seismic activity for the region are significantly over-represented throughout the period of European occupation of New Zealand. Reconciling this paradox will prove to be one of the major challenges of this project. The existence of contrasting opinions regarding how seismically active the Buller region is means that great care must be made in obtaining constraints with which to measure the validity of the devised hazard models. It is eventually found that there are very few constraints with which to qualify the findings of the PSHA conducted as part of this thesis. This is not simply a problem associated with the present study. Very rarely are there external constraints that can be used to test the validity of the results obtained from PSHA. It must, after all, be continually appreciated that the predictions made for common design return periods such as 475, or 1000, years, while seeming like an eternity to mankind, are but the most fleeting of instants in geologic time. So, while the old adage 'time will tell' most certainly applies to the results of PSHA; the measure of success of these predictions will be left for the generations to follow to judge.

Throughout both sections of this thesis many engineering seismological considerations are discussed. The reasonably generic nature of the title of this thesis reflects this to some extent. While the thesis is partitioned into two reasonably self contained sections for practical reasons, some aspects of the two

sections are quite strongly related and in some isolated cases reference is made between them. This internal referencing is minimised, were possible, so that the two sections may be regarded as being relatively self contained.

The combined result of the two individual sections of this thesis represents a significant advancement of the current understanding of the likely seismic hazard expected in the Buller region in both the near future and in the long-term. While the results of the first section of work are presented with respect to specific examples, the methodology that is employed throughout the thesis is kept as general as possible so that the methods employed may be readily transferable to other probabilistic hazard analyses conducted for other regions, or to future revised estimates of seismic hazard for the Buller region itself.

A.2. Geological Setting of the Buller Region

A.2.1. Introduction

The starting point of any seismic hazard analysis, be it probabilistic or deterministic, is an investigation of the regional geology. This investigation must be undertaken to provide the analyst with information regarding the spatial locations and state of activity of the various seismic sources within the study region. The primary outcome of such an investigation should be a fault model, or source model, that is consistent with the governing tectonic deformation of the region. These fault (or source) models consist of a suite of individual seismic sources that are usually assumed to act in an internally consistent manner, i.e. seismic activity within the source is assumed to be uniformly distributed and equally probable. The definition of a particular seismic source generally requires the analyst to make simplifying assumptions regarding the geometry of the source as well as assumptions regarding the spatial definition of source boundaries.

While this stage of the Probabilistic Seismic Hazard Analysis (PSHA) procedure is of fundamental importance, it is also the stage of the procedure that is most subjective. The degree of subjectivity involved in developing fault models is contingent upon the amount, and nature, of geological information that is available to the analyst. There is a famous Buddhist parable[†] relating the tale of several blind men who, upon being positioned around various parts of an elephant, and asked to describe this elephant, all return vastly different descriptions. While the description of each man is internally consistent with his observations, a true description of the elephant cannot be made until the independent observations are integrated into a global description of the elephant. Continuing this analogy, this stage of the PSHA is very much our 'elephant'. There are many types of geological data that can be gathered for a particular region. Most of this information can be related to earthquake activity in some way or another. The goal of this chapter is to consider the various types of geological data that are available for the Buller region and, from the integration of this information, select a suite of seismic sources that can be regarded as adequately

[†] Jainism and Buddhism: Tipitaka → Sutta Pitaka → Khuddaka Nikaya → Udana 68-69: Parable of the Blind Men and the Elephant.

portraying the spatial distribution of seismic activity in the region. In this way, it is hoped that the mistake of reaching premature conclusions based upon limited perspective, similar to those of the blind men in the parable above, may be avoided.

Examples of the types of geological information that are available for the region include:

- Spatial positions of active faulting structures from topographic and structural geology considerations;
- Estimates of fault source properties such as strike and dip angles from field investigations;
- Orientations of faults at depth from seismic reflection lines;
- Timing of prehistoric earthquakes from paleoseismic investigations;
- Timing of prehistoric earthquakes from tree-ring analysis;
- Constraint on Seismic Moment release rates from both long term plate motion modelling and Geodetic information;
- Constraints on long-term rates of regional deformation from geologic markers;
- Constraint on the probable orientation of the regional stress field from field based structural observations, long-term plate motion modelling and Geodetic information;
- Information regarding the correlations of spatial and temporal earthquake occurrence from static coulomb stress changes, stress triggering etc;
- Information regarding recent earthquake activity from observed earthquake data (seismicity datasets); and
- Constraint of the probable orientation of the regional velocity and stress field from finite element modelling.

Each of these potential sources of information, or constraint, are examined in the remainder of this chapter, before the selection of the preferred final fault model for the PSHA.

A.2.2. Regional Geological Setting

New Zealand straddles the boundary between the Pacific and Australian plates, which are currently converging obliquely (DeMets et al. 1990; 1994). There are three primary and distinct tectonic regions that relate to this boundary. To the east of the North Island, the oceanic Pacific plate subducts beneath the continental Australian plate creating the Hikurangi margin (Lewis 1980; Lewis and Pettinga 1994). Conversely, to the southwest of the South Island, including Fiordland, the oceanic Australian plate subducts beneath the continental Pacific plate forming the Puysegur margin(Lamarche and Lebrun 2000; Eberhart-Phillips and Reyners 2001). Connecting these two subduction zones is a transform boundary resulting from the oblique collision of continental crust of both the Pacific and Australian plates. This

collision is responsible for the creation of the Southern Alps mountain range and is characterised primarily by the Alpine Fault. This tectonic setting is shown in Figure A.2.1.

In Figure A.2.1 the study region considered in this analysis, the Buller region (also referred to as the Buller –NW Nelson) coincides with the label 'northwest Nelson reverse faults'; this region is also marked in the figure as being the study region. This region covers the north western part of the South Island and is primarily bounded by the Alpine Fault along its eastern/south eastern boundary.

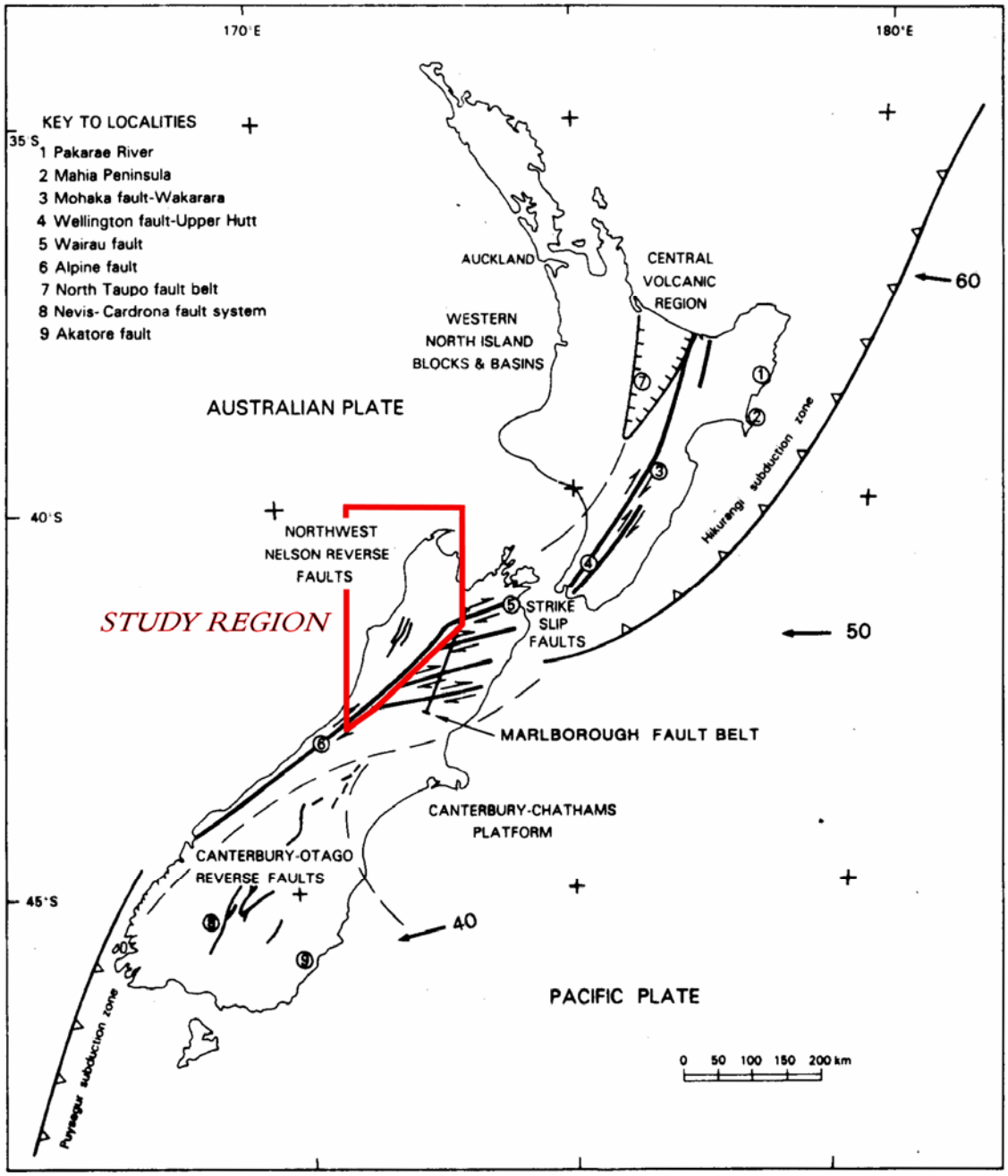

Figure A.2.1: Tectonic setting of New Zealand. Relative plate motions in mm a^{-1} are from Walcott (1981). Tectonic provinces, shown by dashed boundaries, are based on faulting style (Berryman and Beanland 1991). The study region is indicated by the box in the northwest of the South Island.

The Alpine fault is a remarkably linear feature that has experienced a total of approximately 470km dextral displacement (Berryman et al. 1992). The central section of the fault last ruptured in 1717 AD over a length of approximately 375 km spanning the southern and central sections of the fault (Yetton 2000). In the same region, the penultimate event is placed at 1620 AD and included rupture of the northern portions of the fault (Yetton 2002). Given that the recurrence interval for this fault is about 200 years (varying from 100 to at least 280 years) logic would suggest an imminent rupture of this fault in the foreseeable future (Yetton et al. 1998). It should be noted, however, that there is currently some ambiguity regarding the state of activity of the Alpine Fault. For quite some time it was thought that very little seismic activity is associated with the Alpine Fault (Anderson and Webb 1994); more recent evidence suggests that this may not be the case and that the apparent low level of seismicity could be related to the sparsity of recording instruments in this area (Leitner et al. 2001). Given also the proximity of the Alpine Fault to the Buller region, the Alpine Fault is likely to significantly contribute to the seismic hazard in the Buller region. The extent of this contribution will be quantified in subsequent chapters. However, it can be stated from the outset that the Alpine Fault is one of the key seismic sources that will be included in the fault model for the Buller region.

In order to select the remaining fault sources to be included in the PSHA it is first necessary to outline and assess the nature of the potential sources in the region. This is done in the following section.

A.2.3. Faulting Structures in the Buller – NW Nelson Region

The reverse faulting structures in the Buller – NW Nelson region are predominantly N-S to NNE-SSW trending and have steep near-surface dips (Ghisetti and Sibson 2006). The major faults in the region and their associated dips are shown diagrammatically in Figure A.2.2. It can be seen from the histogram in panel (b) of this figure that the number of steeply dipping faults $(60-90°)$ far outweighs the number of shallow dipping faults (at a ratio of approximately 2:1).

Ideally, compressional tectonic regimes would develop faults that dip at much lower angles than those observed in the near surface throughout the Buller region. This statement follows from simple mechanistic principles (Davis and Reynolds 1996). In fact, there is reasonable evidence to suggest that such steep faults should not be able to accommodate the governing regional contraction (Sibson 1995; Sibson and Xie 1998). The reason that the present day reverse faults act in this state is because the current suite of reverse faults are reactivated normal faults (Anderson et al. 1993; Anderson et al. 1994; Ghisetti and Sibson 2006). A possible mechanism for this reactivation was presented by Anderson et al. (1993) and has been hypothesised as being the same mechanism responsible for the development of the bend in the Alpine Fault (Walcott 1978). This inversion process is interpreted to have commenced during the Neogene period. The initial extension was oriented WNW-ESE, while the subsequent shortening currently occurs along the same axis (Bishop and Buchanan 1995). An initial estimate of the degree of shortening was placed at *c.* 3-4%, while the prior extension was of the order of *c.* 5% (Bishop and Buchanan 1995).

These strain magnitudes are related to a general cross section for the West Coast of the South Island and are representative of areas to the south of the present study region, but are regarded as being also representative of the Buller region. However, a recent study by Ghisetti and Sibson (2006) has predicted much higher amounts of shortening in this northern region, forming the focus of this study. A summary of these new findings are presented in Figure A.2.3.

In addition to these two studies, Saul (1994) presents estimates of shortening for a crustal block immediately north east of Westport including the Kongahu fault zone and its northward extension offshore (Figure A.2.2). Average rates of shortening are predicted as being 0.73 mm/yr for the Kongahu fault, although this rate of shortening also includes the contribution of a blind, east dipping unnamed thrust fault to the west of the Kongahu fault. The total estimate of shortening between the Kongahu fault and the Cape Foulwind fault is given as 10%. This figure is in much closer agreement to the estimates of Ghisetti and Sibson (2006) than are those of Bishop and Buchanan (1995).

While the two figures (Figure A.2.2 and Figure A.2.3) indicate the approximate surface expression of the faulting structures in the region, the subsurface conditions are far more complex. Because the faults are generally reactivated normal faults the observed near surface dips do not necessarily correspond to the structure of these faults at depth. An example if this is shown by a hypothesised crustal cross section presented by Ghisetti and Sibson (2006). This cross section is repeated here as and relates to the line denoted by 'Figure 6' in Figure A.2.3. The cross section shown here is quite speculative in many aspects but does act to portray the degree of complexity, the uncertainty, and the extent of assumption, that is associated with approximating fault sources by planes in three-space.

In this figure it can be seen that the near surface expressions of the fault structures relate well to their original orientations consistent with the period of extension across the region. However, there is a significant departure of these faults from their observed near surface dips at depth. Near the base of the seismogenic crust the orientation of the faults is much more optimally aligned with the present day compressional environment. Given the curved nature of the faults between these extremities it can be appreciated that shortening occurring near the base of the seismogenic crust may not necessarily relate directly to shortening deformation occurring at the surface. In order to maintain a consistent average displacement over the entire rupture surface horizontal components of motion existing at depth would need to be converted to vertical components near the surface. This process of conversion would also expend a degree of the energy associated with the rupture and cause the displacements that are observed at the surface to be smaller than those at depth. A possible example of such an effect may be given by the relatively small surface displacements associated with the Inangahua Earthquake. This event, as well as other significant events to have occurred within the study region, is discussed next. Because the faults are not oriented optimally to accommodate the shortening being driven at depth via slipping on their respective faults planes, it is highly likely that a significant amount of folding will occur in this region. This is seen to be the case, and more will be said on this topic later.

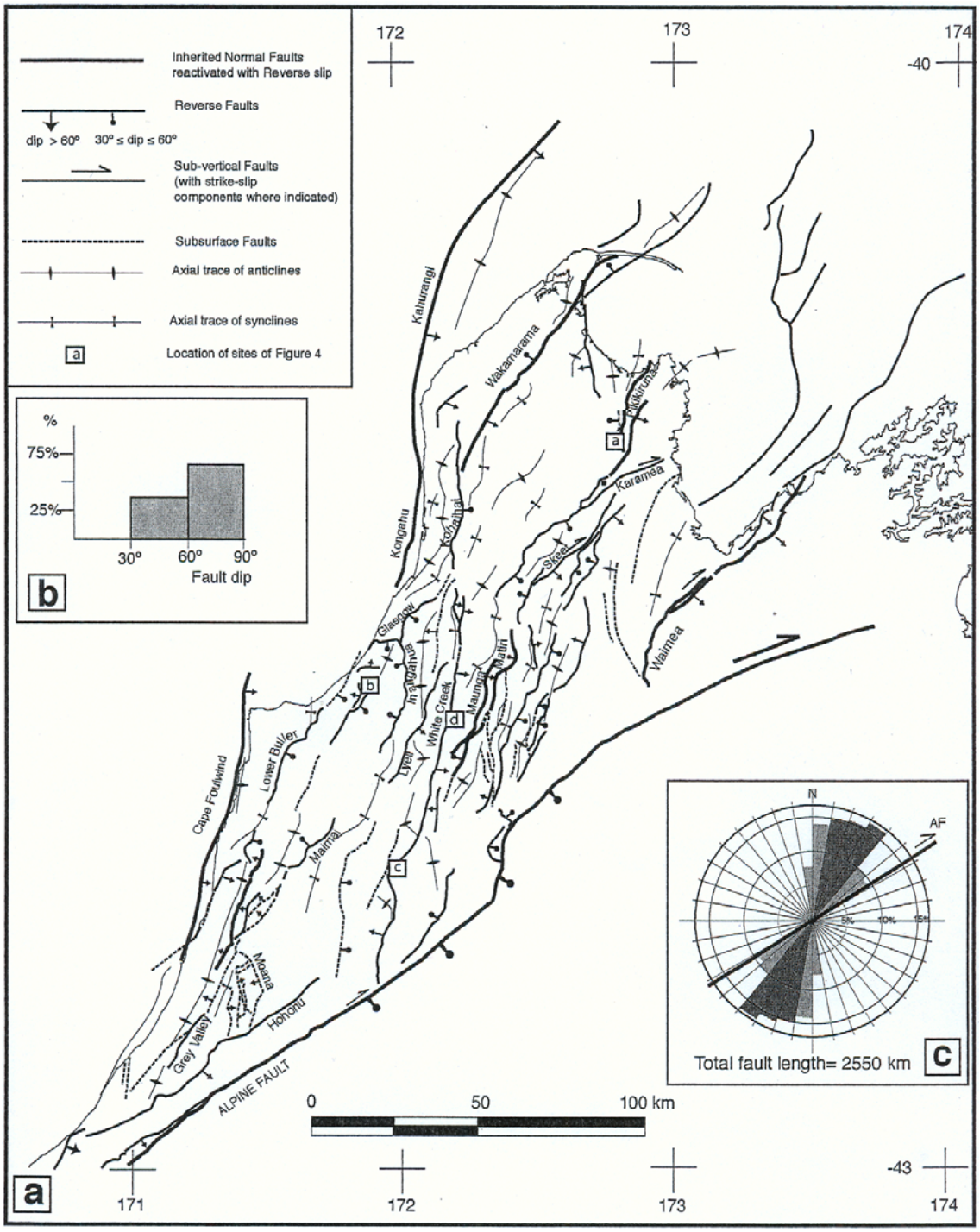

Figure A.2.2: Major faults in the Buller-NW Nelson region and approximate classification of their dip angles (from Ghisetti and Sibson, 2006). Panel (a) shows the mapping of faults as well as their dip directions. Panel (b) shows the relative number of events in two broad ranges of dip values, and Panel (c) shows the orientation and distribution of fault lengths in the region.

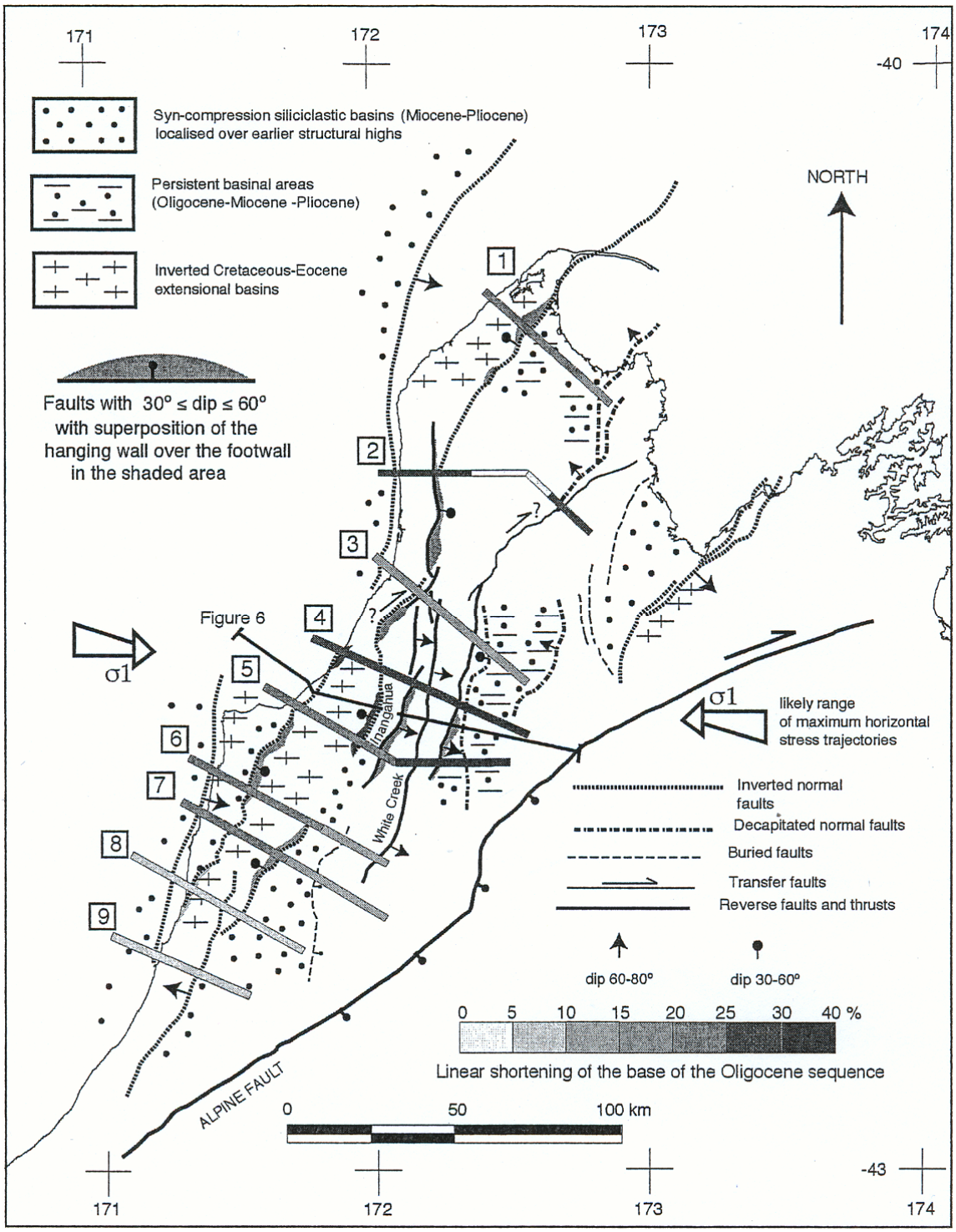

Figure A.2.3: Spatial variation of compression at the base of the Oligocene sequence (from Ghisetti and Sibson, 2006). Thick lines represent the typical degree of shortening over a given cross section; the shading of each line corresponds to a particular degree of shortening.

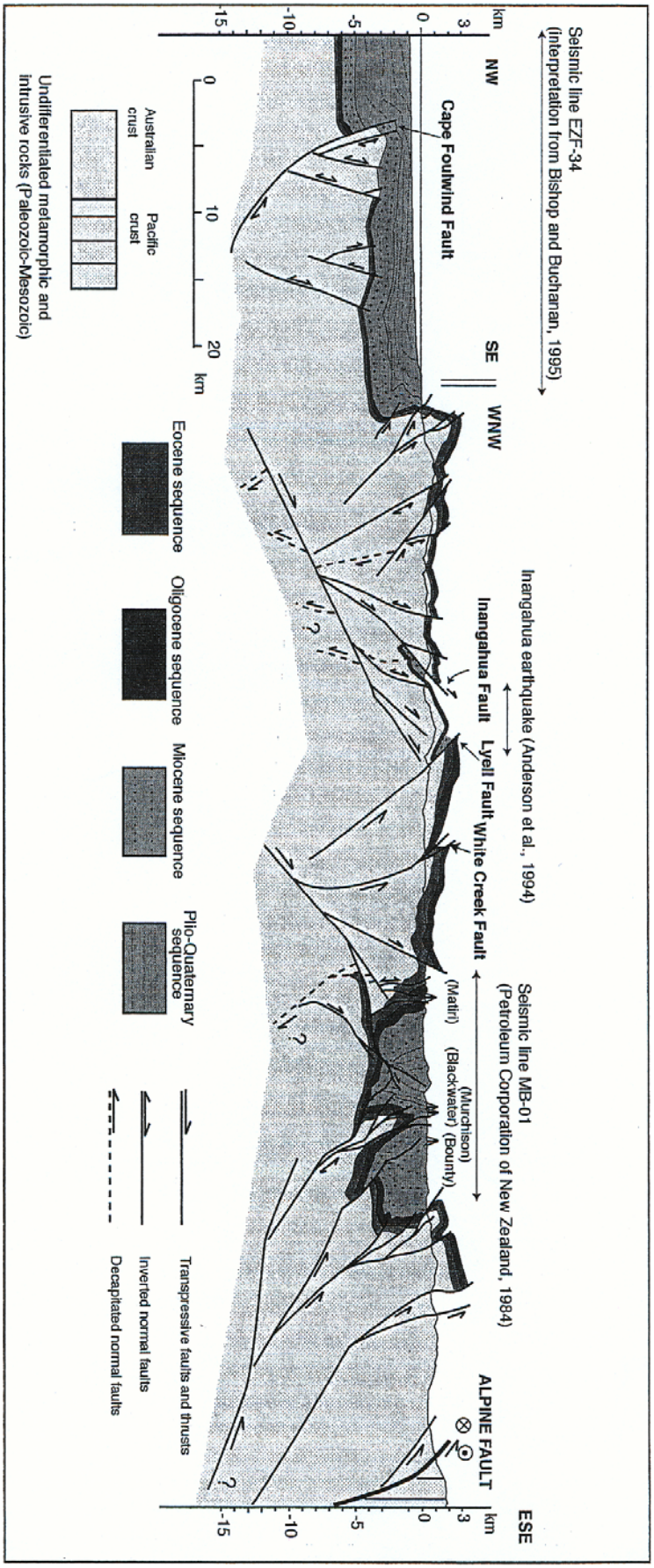

Figure A.2.4: Hypothesised fault structure at depth for the cross section indicated in Figure A.2.3 by 'Figure 6' (image reproduced from Ghisetti and Sibson, 2006)

A.2.4. Historic Seismicity in the Buller Region

The length of the historic record of earthquake occurrence in New Zealand is usually taken to coincide with the duration of European settlement[†]. Specifically, the catalogue is deemed to be complete for earthquake events having magnitudes in excess of 6.5 from 1850 onwards. During this period the Buller region has been one of the most seismically active regions of New Zealand. The most significant events to have occurred throughout this period are described below. Accompanying these brief descriptions are isoseismal maps taken from Downes (1995). The isoseismal contours presented in these figures (except for the Buller event) relate to the Modified Mercalli Intensity (MMI) scale adapted for New Zealand by Eiby (1966). This version of the MMI scale is given in Appendix One. Also in Appendix One is the updated version of this intensity scale (Study Group of the New Zealand National Society for Earthquake Engineering 1992) which is used for the isoseismal map for the 1929 Buller Earthquake. The main reason for a revised intensity scale being devised was simply to correlate the descriptions of felt effects and the influence of ground shaking upon model building stock. The building methods employed in New Zealand, as well as the quality of building materials, have improved since 1966 and consequently the typical types of damage associated with a given level of shaking intensity may not correspond to the effects that were aligned with such shaking intensities in the original scale. The nature of the effects have also been defined more rigorously in terms of those related to the natural physical environment, those relating to building stock, and those relating to animals and people.

A.2.4.1. Cape Farewell Earthquake, 19 October 1868

The location and magnitude of this early event are quite uncertain. The position, initially thought to be north-east of the currently reported position, is slightly north of the region considered in the present study. However, there is an anecdotal suggestion that the rupture may be related to activity on the Wakamarama fault (Anderson et al. 1994) which does lie in the region being considered in the present work.

The inclusion of this event here is deemed prudent as it demonstrates the relative uniformity of the high seismic activity throughout the Buller-NW Nelson region over the period of European occupation. The estimate of the magnitude between M7.0-7.5 is based upon the spatial distribution of felt effects (Figure A.2.5). The reports of the earthquake were fairly widespread, as were reports of strong aftershocks related to this event. Reports of 10 aftershocks that have estimated magnitudes in excess of M6 have been attributed to the event based upon the distant locations at which these aftershocks were felt. Given the size of the mainshock, as well as the strength and number of the subsequent aftershocks, this event rates as one of the strongest observed in New Zealand and would have been responsible for a significant amount of strain energy release.

[†] While the term 'European Settlement' is commonly used, it is not entirely accurate. The first European settlers arrived in New Zealand before the close of the 18th Century. In addition, the Treaty of Waitangi was even signed in 1840; ten years prior to the apparent level of completeness.

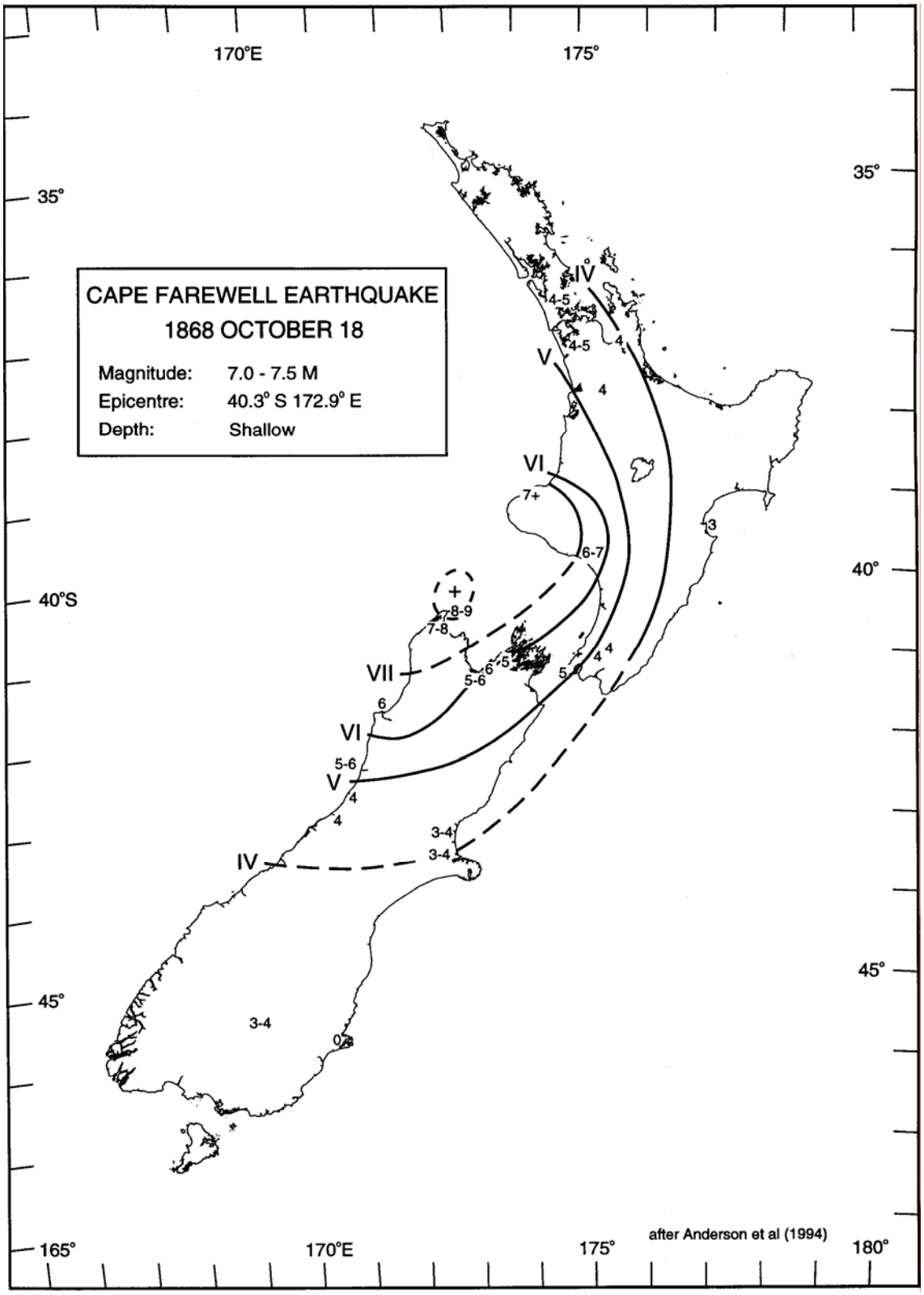

Figure A.2.5: Isoseismal Map for the 18 October 1868, Cape Farewell Earthquake. The epicentral position that is marked by the 'plus' sign should be regarded as being very uncertain. Initial estimates placed this centre to the NE of this position (from Downes, 1995).

A.1.1.1. Buller Earthquake, 16 June 1929

The Buller Earthquake (also referred to by some authors as the Murchison Earthquake) to this day remains the largest observed earthquake to have occurred in the South Island. The event was recorded by seismographs throughout the world, and only a few worldwide events prior to the Buller event had been felt over such a large spatial region (Bastings 1933). The mainshock has been assigned a surface wave magnitude of $M_S 7.8$ (Dowrick and Smith 1990). Estimates of the value of the moment magnitude are more variable and range from $M_W 7.3$ (Doser et al. 1999) to $M_W 7.7$ (Dowrick and Rhoades 1998). Doser et al. (1999) however, state that it is possible that they have not modelled all of the moment release or source complexity in their estimation and that the limited bandwidth of the recording instruments of the time may have prevented the inclusion of significant low frequency components that contribute strongly to seismic moment estimates. Consequently, the value of Dowrick and Rhoades (1998) has been adopted for the present work. Other recent research has also adopted this value for the Buller event (e.g. Hincapie et al., 2005).

Surface faulting of at least 8 km occurred along the east dipping White Creek fault (Henderson 1937). The Buller event was primarily a reverse event having a maximum vertical displacement at the surface of 4.9 m as well as a maximum sinistral component of 2.5 m (Berryman 1980). The focal mechanism for the event has been determined by Doser et al. (1999) to have the following properties; a strike of $\theta = 358 \pm 30°$, a dip of $\delta = 46 \pm 13°$, a rake of $\lambda = 69 \pm 16°$, and a focal depth of $z = 9 \pm 3$ m. The slip vector for the event occurred at a bearing of 295°, 40° clockwise of the principle direction of contraction in the region as estimated from the NUVEL-1 plate motion model (DeMets et al. 1990).

The isoseismal map for this event, shown in Figure A.2.6, makes use of the updated MMI scale for New Zealand. This MMI scale is presented in Appendix One. Given the high MMI values shown in Figure A.2.6, it is not surprising that extensive damage was caused by the event; a summary of this damage can be found in Dowrick (1994). A comprehensive assessment of the occurrence of landslides and other ground damage during the Buller event has been presented by Hancox et al. (2002). In this work a regional isoseismal map is given that overlays the positions of significant landslide events as well as reported instances of liquefaction induced sand boils and lateral spreading. This figure is repeated here as Figure A.2.7 as it shows well the distribution of ground shaking intensities throughout the region. More recently, Carr (2004) has summarised reports of liquefaction that occurred during the event and the references therein are a good source for further information regarding the damage caused by the Buller event.

Unfortunately, from an engineering seismologist's viewpoint, the Buller event occurred prior to the deployment of strong motion recording instruments in New Zealand. Consequently, the event did not contribute to the New Zealand (or international) strong motion database.

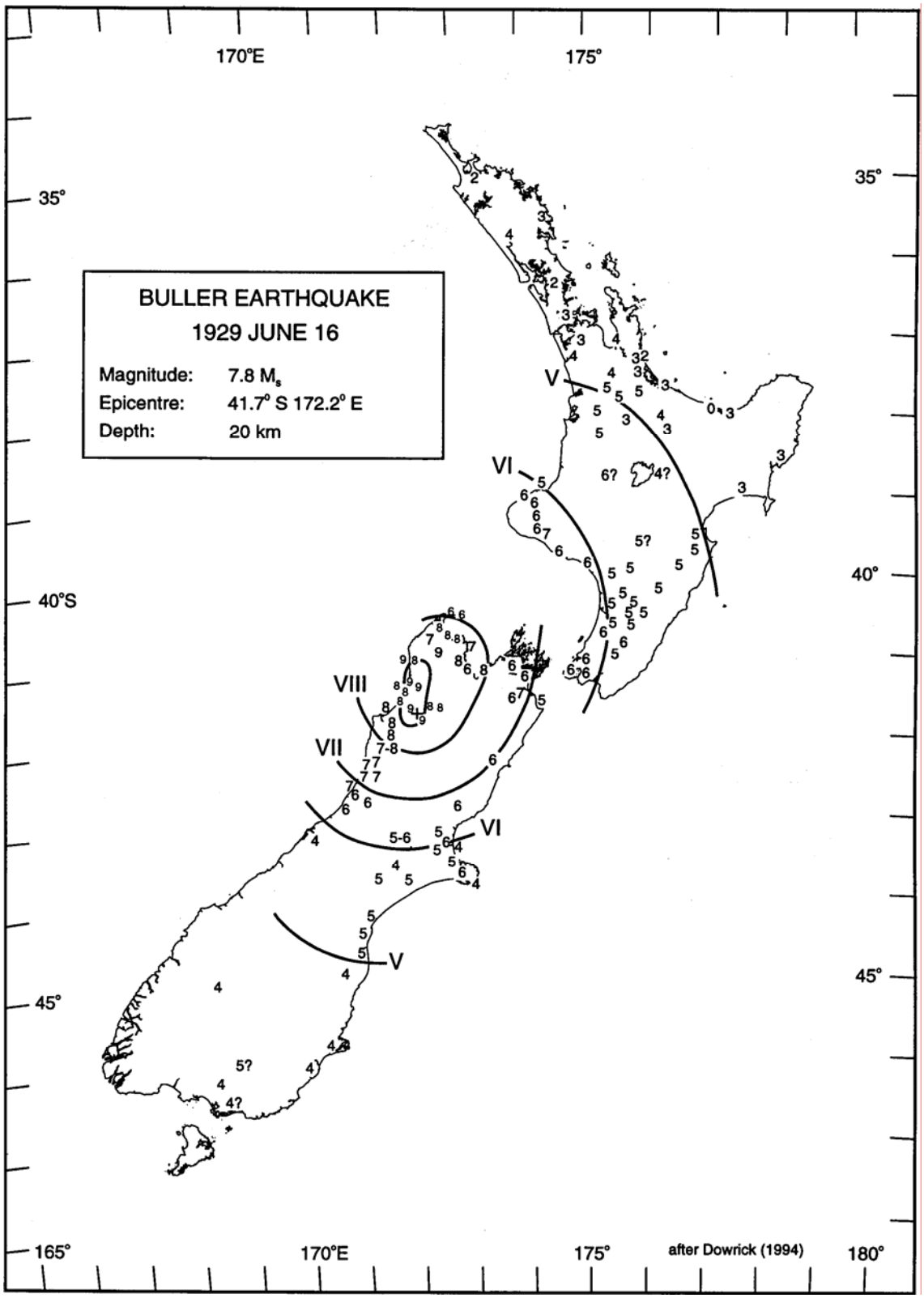

Figure A.2.6: Isoseismal map for the 1929 Buller Earthquake. Isoseismals for this event are given in terms of the revised MMI scale for New Zealand (refer Appendix One). The depth given for the event in this figure differs from the best estimate of 9 km as mentioned in the text (from Downes, 1995).

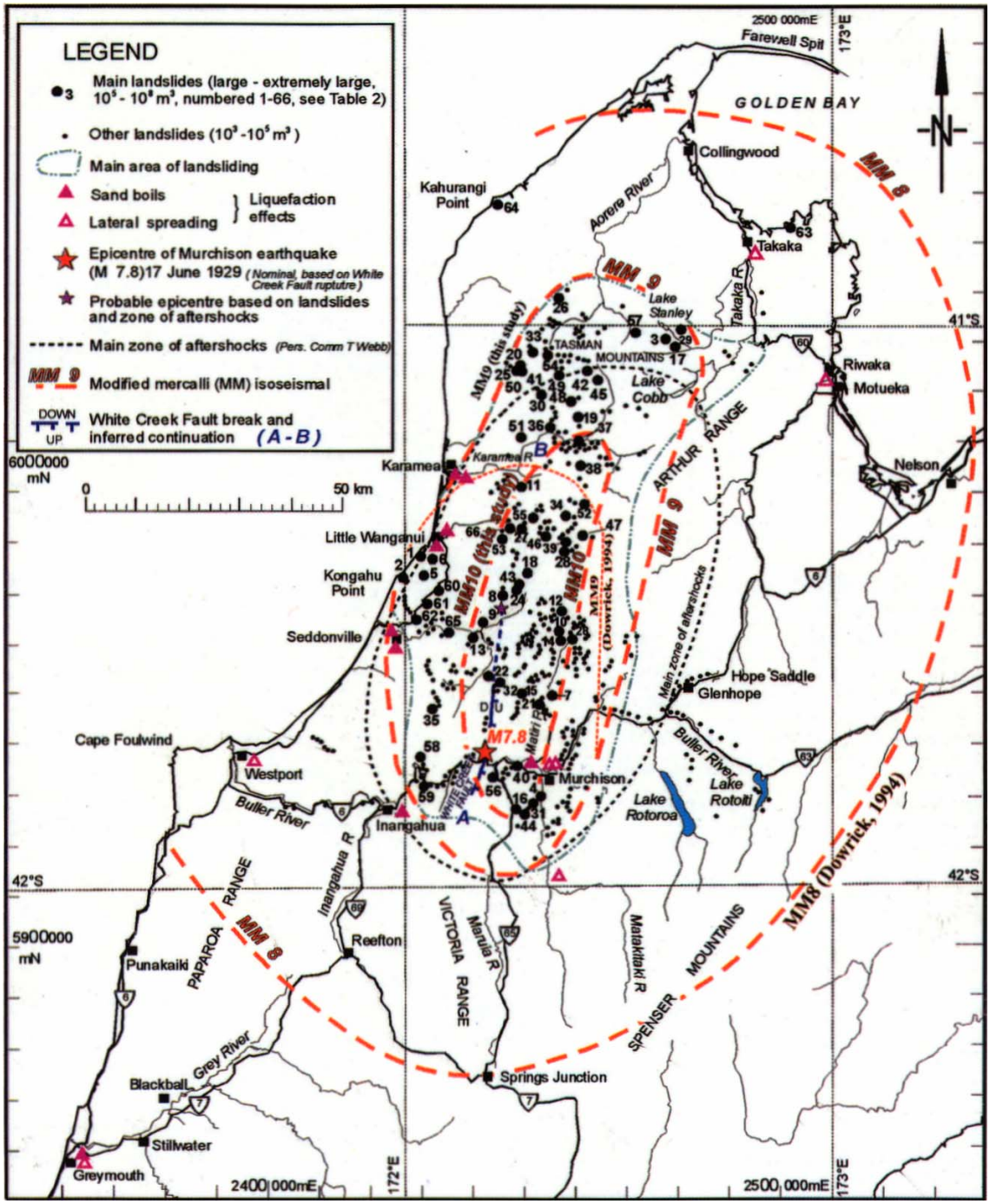

Figure A.2.7: Regional isoseismal map for the 1929 Buller earthquake showing the spatial distribution of large landslides and reported site of liquefaction (from Hancox et al. 2002)

A.1.1.2. Westport Earthquakes, May 1962

In mid May of 1962 a sequence of over 80 earthquakes occurred off the coast near Westport. The first and largest shock took place on May 10 and had a moment magnitude of $M_W 5.9$ (Dowrick and Rhoades 1998). The second, and next largest, shock occurred on May 17 and had a local magnitude of $M_L 5.6$ (Adams and Le Fort 1963). The sequence of earthquakes caused a significant amount of damage to structures in Westport and the surrounding area due to their close proximity and shallow focal depths. Felt intensities as high as VII were reported in and around Westport. The events were located offshore and can be attributed seismic activity on the Cape Foulwind fault.

While the events of this sequence are only moderate in terms of magnitude, they are very useful for helping to place limits on the level of magnitude that can be regarded as being of engineering significance in the PSHA. These events also help to show the effect that repeated events can have in terms of inflicting damage. It is likely that the first shock acted to weaken the regional infrastructure and that this event would have consequently accentuated the effects of the second shock.

The isoseismal map for the first shock of the Westport sequence is shown in Figure A.2.8. The isoseismal map for the second shock is not provided but the mechanism is similar to that of the first shock (Adams and Le Fort 1963). Whereas the first shock generated felt intensities of MM VII in Westport, the second shock generated felt intensities of MM VI in the same locations.

Evison (1977; 1978) has identified the Westport sequence as being part of a long-term seismic precursor to the 1968 Inangahua Earthquake. The relatively low number of events that have been used in support of this hypothesis, as well as the highly variable nature of seismic swarms and precursory seismicity patterns means that the conclusions drawn have only a weak degree of statistical significance. Regardless of whether or not the Westport sequence is linked to the Inangahua event, it is prudent to include an offshore fault source in the final fault model for the PSHA.

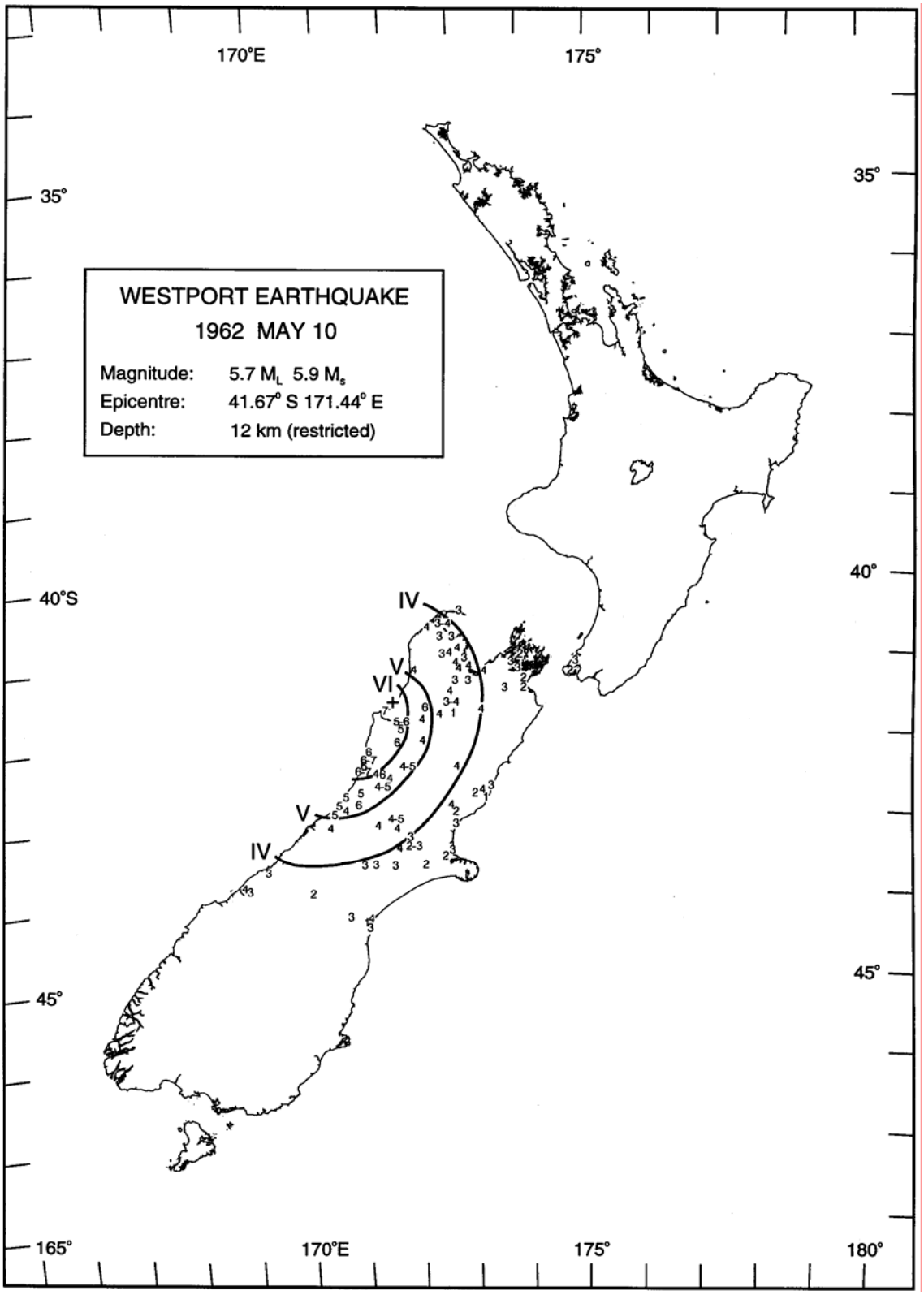

Figure A.2.8: Isoseismal map for the first Westport mainshock of May 10, 1962. Note that the value given for the local magnitude is the revised estimate and differs from the original reported value of Adams and le Fort (1963) (from Downes, 1995)

A.1.1.3. Inangahua Earthquake, 23 May 1968

On May 23, 1968, the third large earthquake to have occurred in the region during the period of European occupation occurred. The Inangahua Earthquake had a surface wave magnitude of $M_S 7.4$ (Dowrick and Smith 1990) and a moment magnitude of $M_W 7.2$ (Dowrick and Rhoades 1998). The Inangahua event was significant at the time because it generated strong peak ground accelerations, the largest of which was 0.61g recorded at Reefton (Cousins 1993). As Dowrick and Sritharan (1993a) point out, "the accelerations recorded at Reefton were the strongest recorded in the world at that time, and would have been considered with some surprise and some disbelief had they been firmly established and proclaimed in 1968." The reason that the levels of ground motions were not firmly established at the time were mainly to do with inconsistencies in the acceleration levels obtained from scratch plate acceleroscopes. For some time the large accelerations were reported as being much lower, in accordance with a misjudgement of the scale of the acceleroscopes.

Obviously, a reasonable degree of damage was associated with such strong ground motions (Suggate and Wood 1979; Dowrick et al. 2003), although the damage was not as significant as might be expected from an event of this size (Anderson et al. 1994). The isoseismal map presented in Figure A.2.9 shows that Modified Mercalli Intensities of X were reported in the vicinity of the epicentre as well as intensities of between VIII and IX in Westport. Fortunately the area in the vicinity of the mainshock is sparsely populated; otherwise the death toll would have significantly exceeded the three deaths that were caused as a result of the event. Comprehensive reports on the effects of the Inangahua event were compiled shortly after its occurrence (Adams et al. 1968; Boyes 1969; Adams et al. 1971).

More recently multidisciplinary interpretations, including geological, geodetic, and seismological aspects of the Inangahua event have been integrated (Anderson et al. 1994; Beanland et al. 1994; Suggate 1994). The seismological considerations are based upon the study of Anderson et al. (1993) in which a focal mechanism solution for the Inangahua event is presented. This focal mechanism is similar to that reported for the Buller earthquake having the following characteristic descriptors; a strike of $\theta = 232+3/-12°$, a dip of $\delta = 51 \pm 7°$; a rake of $\lambda = 103 \pm 15°$, and a focal depth of $z = 10+5/-4$ km. The slip vector for this motion was calculated as acting at a bearing of $291+9/-11°$, which is rotated 36° clockwise from the direction of maximum compression predicted by the NUVEL-1 plate motion model. Anderson et al. (1993) also find from the minimum misfit solution for the focal mechanism that the Inangahua Earthquake was a complex event consisting of a 'small' initial subevent of $M_W 6.5$, followed by a much larger episode of moment release corresponding to a moment magnitude of $M_W 7.0$. It was not possible to determine the spatial separation of these two events, or any difference in focal mechanism.

In many ways the Inangahua event was a very complex earthquake event. In addition to the complications of moment release determined from the focal mechanism estimation, there is significant controversy

regarding the orientation of the fault plane, and indeed even the causative fault for the event (Anderson et al. 1994; Beanland et al. 1994; Suggate 1994; Yeats 2000). The observed surface deformation resulting from the earthquake is complicated (Lensen and Suggate 1968; Boyes 1969; Lensen and Otway 1971) with several spatially distributed surface breaks of varying nature. The most commonly reported surface break was over a length of approximately 1 km and had an uplift of 0.4 m (uplifted on the east side). This scarp closely matched the position of a previous scarp that formed the basis of Berryman's (1980) conclusion that at least one, maybe two, events of similar nature have occurred over the past 18,000 years. However, other scarps, such as those defining the Rotokohu trace and those at Rough Creek complicate the interpretation of the event (Anderson et al. 1994; Yeats 2000). The selection of a westerly dipping fault has been favoured primarily due to the position of the epicentre with respect to the surface breaks. Spatial distributions of aftershocks have also been used as supporting evidence for this orientation of the fault plane, although the validity of this evidence has been questioned (Suggate 1994). Later, in the next chapter, the events of the aftershock sequence are shown to be normally distributed about the westerly dipping fault plane that is adopted in the final fault model. This selection of the fault plane is furthermore consistent with the structural cross section proposed by Ghisetti and Sibson (2006), (refer Figure 2.4).

The degree of uncertainty regarding the position and orientation of the causative fault plane should be kept in mind when making assumptions to do with the geometry of this source in the fault model for the PSHA. The analysis of Berryman (1980) that suggests a recurrence interval for this seismic source of the order of 6,000 years is made on the basis that repeatable events occur on specific faults in the Inangahua area. However, given the complexity of the source mechanism and the surface deformation, any conclusions regarding the characteristic nature[†] of this fault source would have to be regarded as being very tenuous.

The Inangahua event also had a pronounced aftershock sequence (Adams and Lowry 1971; Adams et al. 1971; Robinson et al. 1975) that included at least 800 events above a magnitude of 3.1. The influence of this aftershock sequence on the average rate of activity in the Buller region is significant to the estimation of Poissonian earthquake activity for the region. This issue is discussed more fully in the next chapter where the aftershock sequence is reanalysed in order to most appropriately decluster the seismicity catalogues for use in the PSHA.

[†] Here, by 'characteristic', inference is made to the Characteristic fault model, i.e. Schwartz and Coppersmith (1984), rather than to some generic description.

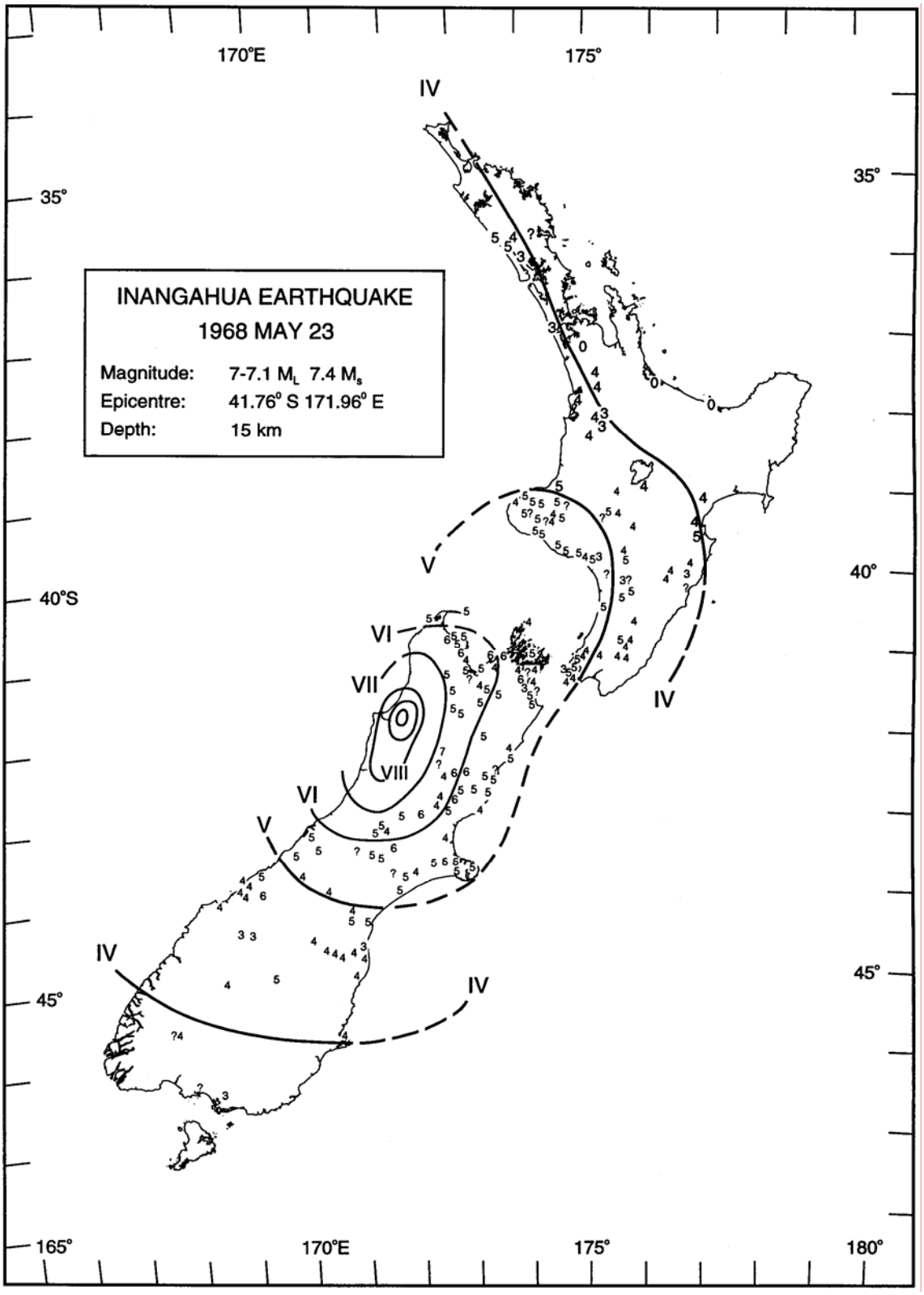

Figure A.2.9: Isoseismal map of the felt intensities from the 1968 Inangahua event (from Downes, 1995). Downes (1995) also provides a near field isoseismal map that more accurately details the MM IX and MM X contours.

A.1.1.4. Hawks Crag Earthquakes, January 1991

On January 28, 1991 the region in and around Westport was shaken again, this time by two moderate sized events separated by approximately five hours. These two initial shocks were followed by another event of slightly lesser magnitude on February 15 of the same year. The events were centred near Hawks Crag in the Buller Gorge, hence their name. The three main shocks, the Hawks Crag 1, 2, and 3 events, had moment magnitudes of $M_W 5.79$, $M_W 5.93$, and $M_W 5.42$ respectively (Dowrick and Rhoades 1998). Modified Mercalli Intensities of around MM VI were reported in Westport with felt reports received from as far away as Christchurch (Smith 1992). Strong ground motion records that were recorded during this sequence of events have been reported and include some significant levels of ground motion acceleration (Cousins et al. 1991). The event was primarily recorded by strong motion instruments in the Buller/West Coast region but records were also obtained as far away as Wellington.

Focal mechanism solutions for the two main Hawks Crag events have been obtained (Anderson et al. 1993). The relevant parameters describing these mechanisms are again similar to both the Buller and Inangahua earthquakes in that their slip vectors are rotated significantly clockwise of the direction corresponding to maximum contraction through the region. The focal mechanism solution for the Hawks Crag 1 event are; a strike of $\theta = 042 + 20/-10°$, a dip of $\delta = 30 + 10/-5°$, a rake of $\lambda = 99 \pm 10°$, and a focal depth of $z = 10 + 3/-2$ km. The slip vector for the event was oriented at a bearing of $302 \pm 5°$, corresponding to a clockwise rotation of 47° from the direction of shortening inferred from plate motion models. The Hawks Crag 2 event was described by the following parameters; a strike of $\theta = 008 \pm 10°$, a dip of $\delta = 48 \pm 5°$, a rake of $\lambda = 77 + 10/-5°$, and a focal depth of $z = 11 + 4/-3$ km. In this case, the slip vector was oriented at a bearing of $297 \pm 10°$, a clockwise rotation of 42° from the direction of shortening inferred from plate motion models.

The author is not aware of any isoseismal map that has been generated for these events, although Smith (1992) alluded to ongoing research related to the events. Intensities that were reported for the Hawks Crag sequence have not been utilised in the development of recent attenuation models for Modified Mercalli Intensity for New Zealand (Dowrick and Rhoades 1999; Smith 2002).

A.1.1.5. A Note on the Observed Focal Mechanism Solutions for the Region

The focal mechanisms of all the major events that have been observed in the Buller region (with the exception of the 1868 event (which has no solution and lies to the north of this region) share the similar property that their slip vectors are rotated approximately 40° clockwise from the plate motion vector. This discrepancy is in excess of the typical errors associated with the determination of slip vectors from focal mechanism solutions and must therefore represent some real effect. To the east of the Alpine Fault, in the Marlborough fault zone, the slip vectors are systematically rotated counter-clockwise with respect to the

direction of principle compression as governed by plate motion (DeMets et al. 1990; 1994). In this region the discrepancy is of the order of the error in the estimate of the slip vector, but all errors associated with these estimates are biased in the same sense suggesting some underlying departure from the direction of the plate motion vector (Anderson et al. 1993). Anderson et al. (1993) point out that while the above pattern emerges from their determination of focal mechanisms, the *P*-axes of the solutions are remarkably constant. The *P*-axis (pressure axis) of a focal mechanism represents the principal axis of the Moment Tensor, and in the case where the plane of dislocation coincides with the plane of maximum shear, the *P*-axis corresponds to the principal stress direction (Aki and Richards 1980). For the Buller region, the fault planes are not optimally oriented shear planes, in large part due to their being inherited fault structures[†]. Therefore, the *P*-axes do not necessarily correspond to the principal stress directions. However, in the case that is considered for the northern South Island, the orientation of the *P*-axes corresponds well with direction of principal shortening across the northern South Island which suggest that the strain is uniform across the region, despite the slip rates being markedly different either side of the Alpine Fault (Anderson et al. 1993). This finding suggests that the accommodation of deformation caused by plate motion convergence across the northern South Island may be partitioned between the Buller and Marlborough regions. This concept of partitioning is discussed in detail in the next section.

A.2.5. Partitioning of Strain Energy Release between the Buller and Marlborough Regions

In the north of the South Island, while the Hope and Alpine Faults are primarily responsible for relieving tectonically induced strain, the accommodation of deformation is also partitioned across the entire Island. To the east of the Alpine Fault, a network of predominantly strike slip faults splay from just south of the bend in the Alpine fault towards the east coast and beyond. This network of faults constitutes the Marlborough Fault Zone. To the northwest of the Alpine Fault, on the Australian plate, deformation is accommodated by a network of predominantly reverse faults and related folds. This latter network of faults is the environment characterising basin and range topography of the Buller-NW Nelson region (Nicol and Nathan 2001). The degree to which the total regional deformation is partitioned between the Marlborough and Buller fault zones is a fundamental piece of information that can help to constrain the seismicity rates of the two regions. If one had a long period of observation of earthquake activity to consider, the estimate of the degree of partitioning of seismic moment release between these two regions would be straight forward. In this sense, a long period would need to be long with respect to the average recurrence intervals of the faults in the regions themselves. Given these conditions, one would simply calculate the average moment release rates for the two regions and partition estimates of future moment release accordingly. Unfortunately this ideal is far removed from reality. In addition to the period of earthquake observation being small in relation to the average return periods of many of the faults in the two regions, the period of observation has included the occurrence of two large events in the Buller

[†] More will be said about this inheritance of fault structures in a subsequent section.

region, the June 17, 1929 Buller Earthquake of $M_W 7.7$ (Dowrick and Rhoades 1998), and the May 23, 1968 Inangahua Earthquake of $M_W 7.2$ (Dowrick and Rhoades 1998). These two events, as well as the earlier 1868 event, which have already been briefly described, represent the majority of strain energy release across the northern South Island over the past 150 years (Holt and Haines 1995). Consequently, if the method briefly mentioned above of simply averaging the moment release rates across the two regions was employed for the current environment the contribution to moment release from the Buller region would significantly outweigh that from the Marlborough region. However, comparisons of estimated slip rates of faults in the Marlborough (Bourne et al. 1998) and Buller (Berryman 1980) regions suggest that this dominance of regional strain energy release from the Buller region is not consistent with longer term behaviour. The average slip rates on faults throughout the Marlborough region is significantly larger than those in the Buller region and consequently, the Marlborough region should be responsible for the majority of strain energy release across the northern South Island (excluding the contribution from the Alpine Fault).

This anomaly proves to be a significant problem when trying to calculate future estimates of seismic hazard. The general consensus in the research community is that the observed activity in the Buller region reflects a period of temporal clustering (Berryman and Beanland 1991). Berryman and Beanland (1991) go further to state that evidence for long term periods of fault quiescence followed by episodic bursts of activity, as well as evidence of equal increments of fault slip, suggest an intermittently characteristic fault behaviour. This comment is made with respect to both the Central Otago and Northwest Nelson reverse fault zones, with the comment regarding the evidence of equal increments of fault slip primarily referring to the Central Otago region. Berryman and Beanland (1991) conclude that none of the fault rupture models that they consider display such a pattern of activity. The fault rupture models that are considered in their work include the variable slip model, the uniform slip model, the characteristic earthquake model, the overlap model and the coupled model. For descriptions of these models see (Shimazaki and Nakata 1980; Schwartz and Coppersmith 1984; Scholz 2002).

Yeats and Berryman (1987) state that earthquake recurrence intervals on individual reverse faults in the Buller-NW Nelson region are so long that fault segments are characterised by short bursts of seismicity separated by long periods of quiescence. They also express an opinion that the historical and instrumental seismicity is a poor indicator of the potential of faults to rupture or of the future occurrence of large magnitude earthquakes. Rather, the Late Quaternary fault history is a much more reliable guide to future fault activity and is particularly valuable when evaluating sites for critical facilities with long lifetimes. A critical qualifier of this statement, however, is the application to long-term probability forecasts, i.e. for the design of critical structures or facilities with long lifetimes. In such cases the PSHA methodology should tend towards a deterministic approach (DSHA) as is vehemently, and repeatedly, expressed by Krinitzsky (1993; 1995; 1995a; 1998; 2002; 2002a; 2003). Even if a purely PSHA methodology is used for such long design periods the time dependence of the PSHA is essentially removed as the hazard is controlled by the

same events that would govern a DSHA[†]. However, in the far more common case, where shorter design return periods are required, the PSHA method relies significantly on estimates of activity of moderate sized events. The estimates of this type of earthquake activity can not usually be gleaned from geological evidence such as the Late Quaternary faulting history (paleoseismic history).

A.2.6. Models of the Deformation Across the Northern South Island

Various studies have modelled the deformation across the northern South Island. The methods employed to do so are varied and have yielded differing results. One of the most comprehensive investigations was that of Holt and Haines (1995). In this study, the regional deformation is modelled by a continuous velocity field. This model is consistent with the established belief that long-wavelength distributed deformation of the continental lithosphere is described more appropriately by a continuous velocity field than by the relative motion of rigid blocks (Haines et al. 1998). The model that is implemented takes estimates of Quaternary fault slip rates from across the northern South Island to define shear strain rates across the region. This procedure is therefore very much inline with the recommendations of Yeats and Berryman (1987). The estimated shear strain rates are then used to define the velocity gradient field over the region. Using this methodology, and altering various other model parameters, such as rates of erosion, Holt and Haines (1995) are able to determine a velocity field with directions that are indistinguishable from that predicted by the NUVEL-1A plate motion model of DeMets et al. (1994), but with velocity magnitudes differing by approximately 10-15%. They conclude that the major strike slip structures in the Marlborough fault zone are accommodating 80-100% of the total plate motion between the Pacific and Australian plates in the northern South Island. As a corollary of this conclusion, they find that the earthquake moment release rate over the last 150 years in the Buller-NW Nelson region is at least half an order of magnitude higher than the predicted long term rate of moment release.

From their strain rate solutions, Holt and Haines (1995) are able to calculate moment release rates for their models. What they find is that for the models that most accurately match the velocity field predicted by the NUVEL-1A plate motion model, seismic moment release rates in the Marlborough region are approximately an order of magnitude larger than those in the Buller-NW Nelson region. However, calculations of the observed moment rates show that over the period of observation, the seismic moment release from the Buller region is approximately twice that of the Marlborough region. In order to try and address this significant discrepancy Holt and Haines (1995) implement a model that replaces the geologic strain rates, based on the Quaternary slip rates, with strain rates estimated from the moment tensors of the major recorded events in the Buller region. The velocity field that they subsequently obtain shows a mismatch of both direction and magnitudes of the velocity field with respect to that predicted by long term plate motion models. These findings are the primary basis for their conclusion that the Marlborough

[†] Provided that the PSHA seismic source model is composed of fault sources. In the case where areal sources are employed the two methods may produce disparate hazard estimates.

fault zone must accommodate 80-100% of the regional deformation. In their optimal model the total moment release rate across the entire northern South Island was $\dot{M}_0 = 6.60 \times 10^{18}$ Nm/yr, of which 0.35×10^{18} Nm/yr can be attributed to the Buller-NW Nelson region. However, it should be noted that when constructing the model in which the geologic strain rates are replaced by those reflecting the seismicity, the assumed geologic strain rates are maintained in the Marlborough region. Therefore the mismatch between the plate motion model and the velocity field calculated in this analysis does not consistently model the observed seismicity across the entire northern South Island. What effect implementing a model of this nature would have on the solution is not known.

Prior to the study of Holt and Haines (1995), Pearson (1993) performed a more approximate analysis of a somewhat similar nature. Rather than inverting the geologic strain rates, Pearson (1993) estimated moment tensors for major earthquakes to have occurred in the northern South Island and from these estimated the associated strain tensors. From the total determined strain tensor, the directions of the principal strain axes can be inferred. Of the earthquakes that were considered in the Pearson (1993) study, only one focal mechanism solution was available. Consequently the moment tensors of the various earthquakes had to be estimated from geological descriptions. Obviously there is a considerable degree of uncertainty associated with this process. For example, the dip of the White Creek fault was initially assumed, based upon geological investigations of the surface rupture, to be 70°, however, the focal mechanism solution of Doser et al. (1999) gives an estimate of approximately 50° for the event. Such discrepancies between source parameters estimated from focal mechanism solutions and from geologic observations are common; for example Molnar and Chen (1982) suggest that a lower limit to the error estimates of focal mechanism solutions is $\pm 10°$. The estimate of the orientation of the rupture plane, particularly near the focal depth, based upon surface evidence is likely to have error estimates of at least a similar magnitude. The significance of the errors associated with the methodology used by Pearson (1993) were recognised and were addressed where possible. In particular, the Buller Earthquake, which contributed the majority of the strain release for the upper South Island, was given particular attention in terms of considering possible configurations of the source mechanism parameters.

Pearson (1993) finds a reasonable agreement between the estimates of coseismic strain release calculated from the historical seismicity and plate motion models (NUVEL-1). Coseismic energy release is estimated to accommodate approximately 70% of the plate motion. Pearson also estimates that 75% of the coseismic strain release from the observed seismicity was accommodated by the Buller-NW Nelson region whereas the geological data suggest that approximately 60% should have been accommodated by the Marlborough faults. It is also found that the direction of the principal axis of contraction is significantly different than that predicted by the NUVEL-1 plate motion model. This is proposed to be an artefact of the overrepresentation of the seismic activity in the Buller-NW Nelson region. When the principal direction of contraction was estimated excluding the Buller events the directions between the moment tensor solutions and the plate motion model agrees well. The results of Pearson (1993) shed some light on the misfit that might be expected for the hypothetical Holt and Haines (1995) model based purely on observed seismicity.

A.2.7. Reconciling Late Quaternary Slip Rates and Observed Seismic Activity

Given the findings of the existing literature, it appears clear that the observed seismicity in the Buller region is not particularly indicative of the long-term energy release associated with the region. However, simply recognising this is not overly useful when it comes to assigning activity rates for seismic sources in the region. It may be reasonable to adopt the activity rates based upon seismicity as being a conservative estimate, or as an upper bound on the rates of activity for the region. What is most desired though is an estimate of the long-term moment release rate for the region. An estimate of this value is given by Holt and Haines (1995), as previously stated. It is worthwhile considering how appropriate this estimate is. Recall that their estimate of $\dot{M}_0 = 0.35 \times 10^{18}$ Nm/yr was based upon the inversion of Quaternary slip rates on active faults in the region, and that Pearson (1993) suggests that 70% of deformation is manifested in coseismic energy release. If this partitioning between aseismic and coseismic energy release is uniform across the northern South Island then the moment release rate may be quite reasonable. If however, the contribution of aseismic deformation in the Buller – NW Nelson region is relatively higher than that in the Marlborough region then the model may underestimate the contribution to the accommodation of deformation made by the Buller – NW Nelson region. Both Yeats (2000) and Nicol & Nathan (2001) indicate that a significant amount of folding occurs in the Buller –NW Nelson region. Yeats (2000) states that if active folding as an expression of blind reverse faults is taken into account then the shortening rate across the Buller-NW Nelson region may be considerably higher than previously believed. Nicol and Nathan (2001) highlight that in parts of the Buller region reverse faults do not break the surface and therefore deformation is manifest by folding. In addition, Berryman (1980), in the process of reporting very low slip rates on the structures responsible for the Buller and Inangahua earthquakes, offers an alternative model to the notion that the seismicity in the area is anomalously high. He states that it may be that the level of observed seismicity is normal and that there are many structures, including faults and folds that accommodate the deformation. Berryman (1980) also notes that the surface breaks of both the Buller and Inangahua events were relatively small in comparison to the smaller 1888 Amuri event in the Marlborough region. While any inferences drawn from this would carry very low statistical significance, it may be that large events in the Buller region, occurring on faults not optimally oriented to accommodate the applied deformation, do not cause large surface displacements. If this is the case then the slip rates determined from geological investigation may underestimate the amount of deformation accommodated by the region. The fact that the reverse and thrust faulting is occurring on inherited structures would logically suggest that the mechanism by which the faults accommodate deformation should be different from faults that are optimally oriented to accommodate contraction.

Beavan and Haines (2001) performed an analogous analysis to that of Holt and Haines (1995) for the whole of New Zealand. Rather than using Quaternary slip rates as the initial input into determining the velocity model, the input for this more recent analysis was GPS data. The methodology implemented in this analysis is very accurate in recovering the continuous strain and velocity fields from the recorded GPS measurements (Haines et al. 1998). The GPS data used in the compilation of the velocity model comes from a 29 station GPS network distributed throughout the county as well as an additional 333 stations that

are deployed in regional networks throughout the country. One of these regional networks is positioned over the northern South Island, and is primarily concerned with monitoring the deformation through the Marlborough Fault Zone. However, in order to allow relative deformation to be observed this network also extends across the island and into the Buller region. This specific regional network includes 29 GPS stations. Deformation associated with GPS measurements from this regional network has been analysed and presented previously by Bourne et al. (1998). The Bourne et al. (1998) study, however, focussed almost exclusively on the deformation in the Marlborough Fault Zone and made only scant reference to deformation in the Buller region. The Beavan and Haines (2001) analysis, on the other hand, focussed on the entire Pacific-Australian plate interface throughout New Zealand. An important finding of the Beavan and Haines (2001) paper was that, contrary to the conclusions of Holt and Haines (1995), the present day strain field shows a small, but significant, shortening throughout the Buller-NW Nelson area. They note that while this finding does not resolve the issue of whether or not this state is rare in a long-term sense, the current ENE-WSW contraction throughout this region is continuing and that consequently further thrust/reverse earthquakes in this region can be expected.

Another deformation analysis on a national scale was conducted by Liu and Bird (2002) and employed finite element modelling. In this model Liu and Bird (2002) were able to take into account the presence of faults, realistic rheology, spatially varying heat flow, topographical loading and boundary conditions imposed by plate velocities. The model is therefore very comprehensive. Liu and Bird (2002) find that their model is able to predict the major patterns of deformation that occur throughout the country. Liu and Bird (2002) were able to compare their strain field with that based upon GPS data of Beavan and Haines (2001). Importantly, Liu and Bird (2002) also find that the generally E-W contraction through the Buller-NW Nelson is again found in their analysis but that the magnitude of this contraction is greater than that found from the GPS analysis. Liu and Bird (2002) predict long-term slip rates of approximately 2-4 mm/yr in addition to a small, but significant, contractional strain rate. Again, this suggests that reactivated faults in the Buller – NW Nelson region are actively accommodating a portion of the inter-plate deformation and have the potential for generating further large thrust or reverse earthquakes.

The two studies just mentioned, in addition to the findings of Ghisetti and Sibson (2006), suggest that the historical record of seismicity in the Buller – NW Nelson region may not be as anomalously high as has been previously asserted. The deformation analyses also indicate that the strain conditions that have existed during this instrumental period continue to be present and that consequently the seismicity may be a better indicator of future earthquake occurrence than is suggested by Yeats and Berryman (1987), among others.

A.2.8. Interactions Between Large Events in the Buller – NW Nelson Region

Another interesting issue to address is the relationship and interactions between the occurrences of the large recorded events in the Buller region, in particular the Buller and Inangahua events. Given their close proximity to each other and the similarity of their focal mechanisms a prudent question that should be

posed is whether or not the occurrence of the Buller event acted to trigger the Inangahua event (as well as the Westport, and Hawks Crag events). If this was the case, then the apparent clustering of the events in the region may be linked to the occurrence of a major event such as the Buller earthquake, or possibly even to the 1868 event. A prime example of the effect that the occurrence of a large event can have on the subsequent seismicity of a region is given by the San Andreas Fault, the fault that has received by far the most attention from the research community. The great San Francisco earthquake of 1906 has been found to have cast a stress shadow over the greater San Francisco Bay area and offset the occurrence of large events over the last century (Harris and Simpson 1998; Working Group for California Earthquake Probabilities 2003). The practice of using Coulomb stress fields (King et al. 1994) coupled with rate-and-state friction models (Dieterich 1994) to infer interactions between earthquake events has emerged over the last decade or so. Interactions between large earthquakes have been shown to be related to the modifications in the Coulomb stress field in the region with increases in the Coulomb stress field increasing the likelihood that a future event will occur and decreases doing the opposite. Such an analysis has recently been performed for the Buller region (Hincapie et al. 2005) and an interesting conclusion was found. Rather than finding that the Buller Earthquake increased the likelihood of subsequent events, the Buller event was found to delay the occurrence of the Inangahua event. Therefore, if the fault responsible for the Inangahua event was already in a state close to failure when the Buller event occurred then an enormous amount of stored strain energy must have been distributed throughout the lithosphere in the Buller region over a considerable amount of time. The occurrence of these large events in the region must therefore be the result of sustained contractional deformation throughout this region. This is opposed to some model in which a cascade of events is somehow initiated through the occurrence of a single major event such as the Buller Earthquake.

A.2.9. Constraint from Tree – Ring Analyses

Another form of constraint that is available for the region comes from a recent study that investigates the correlation between the occurrence of strong ground shaking and alterations to the behaviour of tree-ring growth (Wells and Yetton 2004). The occurrence of strong ground shaking, and associated secondary effects, can affect the growth of trees in both positive and negative ways. While most of the affects act to perturb the growth of trees following the earthquake, some trees may subsequently experience periods of heightened growth due to an increased share of the available light, and resources, in general. These impacts manifest themselves in the width of tree-rings and can therefore be used to accurately date the occurrence of past events. The time period for which this method is useful depends strongly upon the typical age of trees in the study area. For the region in the present study, tree-ring data can be used to provide information on the occurrence of major events over a period of approximately 800 years. Wells and Yetton (2004) found strong evidence for the occurrence of both the Buller and Inangahua events as well as possible evidence of the last two ruptures of the Alpine Fault (events in c. 1717 AD and c. 1620-30 AD). These authors do not report evidence of any additional events in the region. However, it should be noted that while this method is capable of revealing information regarding earthquake occurrence over a

reasonable time period, the observed effects of the ground shaking will be spatially dependent. Therefore, there may have been other events, such as the 1868 Cape Farewell event, that need to be considered when determining a long-term moment release rate, but whose effects are not perceived because of the relative distance between the source of the event and the site of the tree-ring study. The findings of this study are in agreement with the findings of Berryman (1980) in that the recurrence intervals for large events on the White Creek, and Inangahua (or Rotokohu) Faults are much longer than those that would be obtained from using the historical record of earthquake occurrence and tree life cycles also.

A.2.10. Seismic Moment Release Rates for the Buller – NW Nelson Region

Given the findings of previous researchers, constraints on the likely rate of seismic moment release in the Buller – NW Nelson region may be inferred. As previously mentioned, the moment release rate from the 'nonuniform' model of Holt and Haines (1995) may be regarded as a lower bound due to the fact that no account is taken of folding in the region and that the assumed slip rates for faults in the model do not reflect the present rate of shortening in the region (i.e. Saul 1994; Beavan and Haines 2001; Ghisetti and Sibson 2006). The upper bound is probably close to the moment rate inferred from the observed seismicity. The rate that should be assigned to the region for the purpose of predicting future events via the PSHA procedures is most likely to be towards the lower end of this range. This level would reflect the partial accommodation of the long-term plate motion by the Buller – NW Nelson region that is predicted by both the Beavan and Haines (2001) and Liu and Bird (2002) deformation studies. One is therefore justified in using seismicity data to infer activity rates as long as the consequent moment release rate that is obtained as a result of the overall fault model is consistent with this range. In order to meet this requirement, careful consideration of the maximum magnitudes assigned to the various fault sources in the fault model must be made as the rate of occurrence of these largest events contribute most significantly to the overall moment release rate for a region. The process by which characteristic activity parameters are assigned to the sources included in the fault model is the subject of the next chapter.

Thus far, our consideration of the geological setting has been primarily with respect to regional deformation. While it is of critical importance to ensure that the final fault model is consistent with this regional constraint, it is also desirable, if possible, to consider the processes of deformation internal to the overall region. Describing the deformation at higher spatial resolution is the objective of the following section.

A.2.11. Regional Seismic Domains

In addition to considering the overall deformation of the Buller – NW Nelson region as it relates to the governing tectonic motions, it is also worth considering various smaller tectonic domains within the Buller

– NW Nelson region itself. As can be appreciated from Figure A.2.4, there appears to be groups of faults whose activity at depth is governed by a series of master faults. While the individual splays from these faults may act independently, they are most likely to do so in an attempt to equilibrate stresses in the crust induced by driving motions on these master faults. This type of activity is likely to be responsible for the generation of small to moderate sized events. Activity on the master faults on the other hand is more likely to reflect the large-scale tectonic loading that is applied to the region. The depths at which these governing structures act as individual faults correspond to regions of the crust that are able to maintain high lithospheric pressures and can consequently be expected to release correspondingly high amounts of stress in the form of large scale seismic events. In the case of both the Buller and Inangahua events, the most likely focal depths that have been calculated support this statement.

The division of the overall region into subdomains also recognises the relative proximity of the faults in the study region to the sites of interest for the PSHA. All other things being equal, seismic sources that are closest to the sites of interest will dictate the level of hazard for these sites. As a consequence of the above two considerations, the Buller – NW Nelson region has been subdivided into three primary domains, A, B, and C, one of which (A) is further subdivided into three subdomains. The definition of the various domains, and subdomains, is depicted in Figure A.2.10.

Based primarily upon topographical and structural geology considerations, the overall Buller – NW Nelson region can be partitioned into smaller domains and these in turn, into smaller subdomains. These domains reflect differing amounts of uplift as seen from topographical maps, as well as groups of faults that have similar mechanisms and are known to have acted similarly in the past. The deformation associated with each domain can be regarded as being the manifestation of different driving processes associated with the external constraints from regional tectonics. The characteristic properties of the faults in each domain reflect, in part, their role in accommodating this regional deformation.

The domain of primary interest (Domain A) includes all the faults that are known to have experienced moderate to large events throughout the course of European settlement. Within this domain, further groups of faults may be identified. The two most important ones, in terms of their observed, and inferred, levels of activity as well as their proximity to sites of interest in the region are labelled A1 and A2 in Figure A.2.10.

Subdomain A1 includes the Kongahu Fault, a section of the Cape Foulwind Fault, the Inangahua and Maimai Faults, as well as the Mount William Fault (e.g. Figure A.2.2). The combined effect of this group of faults is to uplift the Paparoa Range. This uplift of the range is accommodated primarily by the east dipping faults on its western margin (Cape Foulwind and Kongahu), with an associated contribution from the west dipping faults on the eastern margin (Inangahua and Maimai). The Mount William Fault probably does little to accommodate deformation in the region, and is likely to join, or be curtailed by, the Inangahua Fault at mid to low crustal depths. Coseismic displacement on the Mount William Fault is therefore considered to represent an upper crustal partitioning of slip as a function of structural complexity.

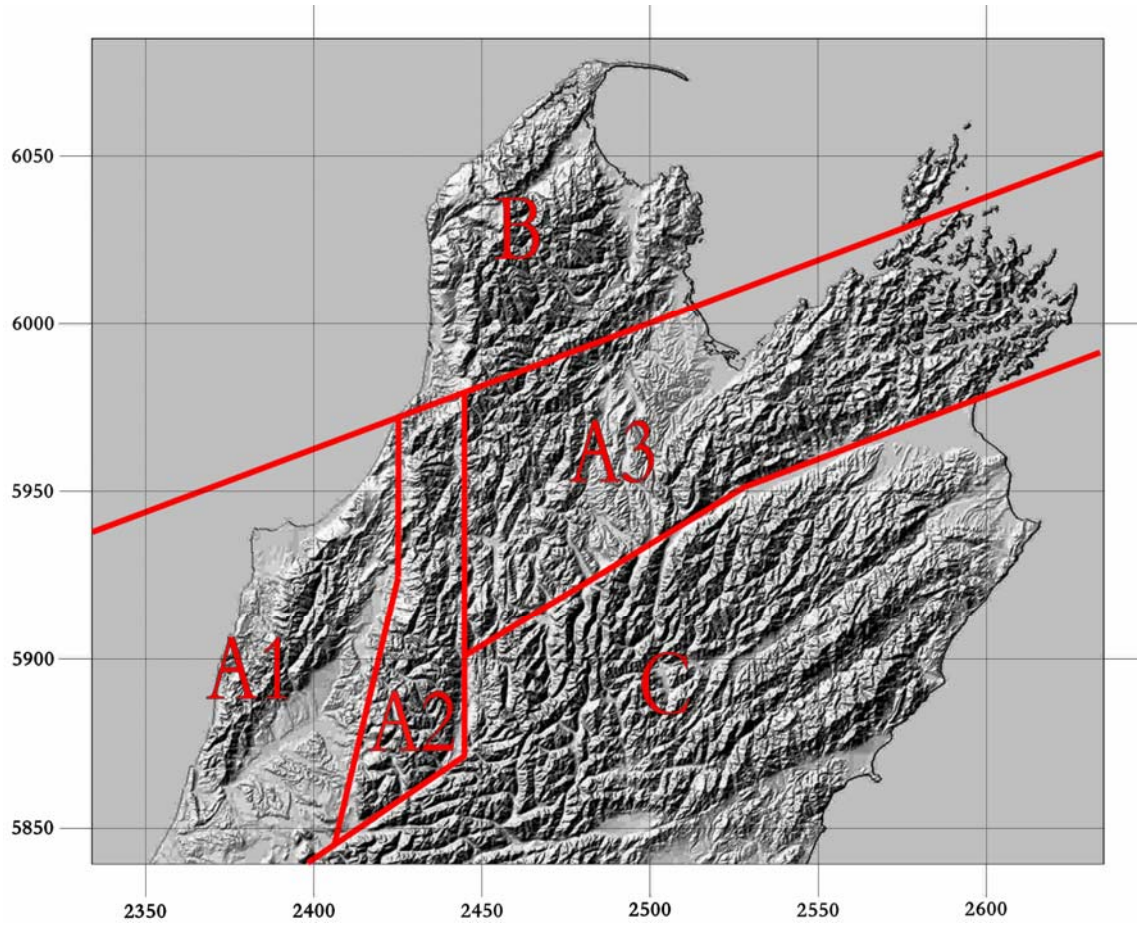

Figure A.2.10: Division of the study area into various domains (A,B,C), and subdomains (A1,A2,A3). Co-ordinates are given in terms of the NZMG system and have units of kilometres.

The uplift associated with this subdomain is clearly visible from topographic maps (e.g. NZMS 260 topographic map series), and the derived digital elevation models (DEM), such as that presented in Figure A.2.10. It is postulated that the faults in this subdomain respond primarily to the overall regional contraction and are not strongly coupled with activity associated with the Alpine Fault.

The next subdomain, A2, however, is likely to be strongly related to overall activity on the Alpine Fault, particularly with respect to differential activity on the central and northern sections of the Alpine Fault. At its southernmost end, subdomain A2 is bounded by the northern end of the central section of the Alpine Fault. The south eastern boundary of this subdomain is bounded by the bend in the Alpine Fault. Throughout this southern part of the subdomain there appears to be significant amounts of uplift, with the eastern side upthrown. The western margin of subdomain A2, at this southern end, is bounded by the White Creek Fault.

To the north, in subdomain A2, significant uplift again takes place, but with opposite orientation. Here, the western margin is upthrown and is bounded by the Glasgow Fault. The northern limit to this subdomain is the Karamea Bight where the Glasgow Fault turns inland at an approximately northeasterly strike. Within this subdomain the Lyell and White Creek faults trend from southwest to northeast.

The combined effect of significant uplift in the north western and south eastern parts of subdomain A2, coupled with the long linear faults (Lyell and White Creek) trending obliquely across the subdomain gives the impression that this subdomain is a zone of torsion. This torsional action is driven by the constraint of the bend in the Alpine Fault at its southern end, and by regional contraction in the north. The long, linear, relatively steeply dipping faults obliquely traversing the interior of the subdomain are a manifestation of the region equilibrating itself to this induced torsion.

If this torsional mechanism is correct, then seismic activity in this subdomain would be relatively high with respect to its consequent contribution to regional horizontal shortening. This agrees with what has been observed throughout the past 150 years or so.

The remaining subdomain, A3, in this central domain, A, is probably the least significant in terms of its contribution to hazard for sites of interest in the present study. While it contains the Karamea Fault, which is a reasonably long and well defined structure, and the Waimea Fault, with a recently determined paleoseismic history (Fraser 2005); these faults are relatively distant from sites of primary interest in the region. There have also been relatively low amounts of seismic activity observed through this subdomain, with respect to subdomains A1 and A2, over the period of European occupation.

Domain B, to the north of the overall region, contains faults that can be associated with significant amounts of uplift, and possibly historic seismicity[†]. The complicated partitioning of the overall regional deformation between strike-slip action on the Alpine Fault, and reverse faulting in the Buller region, that characterises domain A is not so prevalent in domain B as the distance from the influential Alpine Fault is sufficiently large. Here the faults consequently respond primarily to regional contraction on a relatively large scale. To the west, the region is bound by the offshore Cape Foulwind fault as well as the Wakamarama and Kohaihai Faults which define the Tasman Range. These faults are most likely to accommodate the majority of deformation in this domain. To the east, the region is bounded by the Pikikiruna and Pisagh Faults. These faults, in turn, bound the Moutere Depression, a region notorious for its very low levels of crustal seismic activity (Pettinga 2004). At its southern end, the Pikikiruna Fault defines the interface between domains A and B and runs sub-parallel to the northern section of the Alpine Fault. While the lengths of these faults, and their clear association with uplift in the region imply noteworthy levels of seismic activity, their large distances from sites of importance precludes their contributing significantly to estimates of hazard for sites of interest in the Buller region.

The remaining domain, Domain C, to the southeast of Domain A contains primarily the strike-slip faults of the Marlborough Fault Zone. These faults are known to be highly active in relieving the northern section of the Alpine Fault of much of the slip that is observed over its southern and central sections (Berryman et al. 1992) and in linking this major region of lateral deformation with the Hikurangi

[†] See the previous comment regarding the possible association of the 1868 earthquake with the Wakamarama Fault

subduction zone to the east of the lower North Island. As far as their contribution to the seismic hazard in the Buller region however, these faults are deemed to be sufficiently far enough away from most sites of interest so as to model them as simply being part of the general background seismic source. This is true for most of the critical sites in the Buller region (critical here being in terms of representing population centres, or locations of critical importance to the regions economic stability) that are located in the west of the study region. For specific sites that are located in the east of the Buller region, the fault system comprising Domain C would have to be considered more specifically.

This partitioning of the overall Buller – NW Nelson region into the various domains has been done on a relatively subjective and intuitive basis. It will be instructive to compare the final disaggregated hazard estimates with these domains later in the thesis. However, for now, it is worth postulating these subdomains because if they are found to act as identifiable regions in terms of their contributions to the accommodation of deformation, then future estimates of hazard may be estimated conditional upon recent activity in these subdomains. In this way, regional seismicity and total moment release might be partitioned in a more meaningful way within the region rather than simply averaging the deformation over the entire region.

A.2.12. The Final Fault Model

Given the reasonably comprehensive review of existing research related to the geological setting of the Buller – NW Nelson region summarised in this chapter, we are now well placed to specify the final suite of faulting sources that will form the final fault model for the subsequent PSHA analysis. The faults will be treated as individual seismic sources and activity parameters characterising each of these sources will be estimated in the next chapter. However, not all activity will be associated with the suite of faults assumed to make up the fault model. Consequently, an additional background source is also included in the source model to account for all the seismic activity that cannot be attributed to deformation associated with the assumed fault sources.

At the beginning of this chapter it was mentioned that in order to adequately understand the geology of the study region, data from many, and varied, sources must be considered. While this is certainly true, this information cannot really aid in the selection of an appropriate suite of sources for the fault model to be used in the PSHA. The validity of the assumed model can only be appreciated once the time dependent effect associated with the rates of occurrences of earthquake events are considered. For now however, the consideration of the existing literature indicates that a suite of faults that are relatively well distributed throughout the region is necessary to characterise the approximately continuous amounts of contraction that are occurring in the region. Of course, the selection of these faults is also strongly influenced by the presence of strong lineations observed from DEMs and topographic maps. Only the best politician could deny the presence of a mountain range!

In all, fourteen fault sources as well as a background source are included in the final fault model; these fault sources are presented in Table A.2.1 below along with representative geometric properties. Their seismicity characteristics are derived in the next chapter.

Table A.2.1: Fault sources adopted in the final Fault Model and their relevant geometrical parameters. Segments that are specified relate to geometrical segments and do not necessarily correspond to seismogenic, or rupture scenario, segment boundaries for the fault structures. The adopted co-ordinate system is the New Zealand Map Grid (NZMG) system.

Fault Num.	Fault Name	Seg. Num.	Segment Start		Segment End		Segment Length	Fault Dip	Fault Depth^	Fault Area
			N_i [m]	E_i [m]	N_{i+1} [m]	E_{i+1} [m]	L_i [km]	δ_i [°]	Z_{seis} [km]	A_i [km^2]
1	Kongahu	1	5893165	2380000	5929698	2397842	40.7	60	18	836.1
		2	5929698	2397842	5949784	2412158	24.5	60	18	509.9
		3	5949784	2412158	5978705	2428129	33.0	60	18	711.7
		4	5978705	2428129	6011079	2433309	31.3	60	18	710.1
		5	6011079	2433309	6040526	2432631	27.1	60	18	622.0
						ΣL_i	**156.5**		ΣA_i	**3390.0**
2	Glasgow	1	5944850	2431200	5958561	2427841	14.1	60	18	245.0
		2	5958561	2427841	5971741	2436906	13.4	60	18	267.7
		3	5971741	2436906	5977410	2444100	7.5	60	18	201.3
		4	5977410	2444100	5989065	2449136	12.7	60	18	291.2
						ΣL_i	**47.7**		ΣA_i	**1005.2**
3	Inangahua	1	5905036	2409871	5917122	2417043	14.1	125	18	304.7
		2	5917122	2417043	5944381	2431124	30.7	125	18	670.1
						ΣL_i	**44.7**		ΣA_i	**974.9**
4	Lyell	1	5909353	2421053	5956403	2442949	51.9	75	18	967.1
						ΣL_i	**51.9**		ΣA_i	**967.1**
5	White Creek	1	5888633	2422820	5899712	2432691	14.8	75	18	288.5
		2	5899712	2432691	5962446	2445827	62.5	75	18	1214.0
		3	5962446	2445827	5975539	2444100	12.2	75	18	253.8
						ΣL_i	**89.5**		ΣA_i	**1756.3**
6	Mt. William	1	5923309	2404532	5952632	2423816	35.1	73	10	367.0
						ΣL_i	**35.1**		ΣA_i	**367.0**
7	Cape Foulwind	1	5866053	2360000	5925132	2379079	62.1	65	18	1243.2
		2	5925132	2379079	5947632	2380658	22.1	65	18	434.5
		3	5947632	2380658	5991842	2412368	52.1	65	18	1066.5
		4	5991842	2412368	6040526	2432631	52.7	65	18	1056.8
						ΣL_i	**189.0**		ΣA_i	**3801.0**
8	Maimai	1	5887338	2390647	5905036	2408571	25.2	125	18	553.5
						ΣL_i	**25.2**		ΣA_i	**553.5**
9	Kohaihai	1	5982302	2443668	6005468	2446115	23.3	60	18	487.6
		2	6005468	2446115	6029698	2447122	24.2	60	18	507.5
						ΣL_i	**47.5**		ΣA_i	**995.1**
10	Wakamarama	1	6005468	2446115	6016259	2446978	10.8	75	18	201.7
		2	6016259	2446978	6067626	2483050	61.5	120†	18	1304.6
						ΣL_i	**72.3**		ΣA_i	**1506.3**

Table A.2.1: continued… Fault sources adopted in the final Fault Model and their relevant geometrical parameters. Segments that are specified relate to geometrical segments and do not necessarily correspond to seismogenic, or rupture scenario, segment boundaries for the fault structures. The adopted co-ordinate system is the New Zealand Map Grid (NZMG) system.

Fault Num.	Fault Name	Seg. Num.	Segment Start		Segment End		Segment Length	Fault Dip	Fault Depth^	Fault Area
			N_i [m]	E_i [m]	N_{i+1} [m]	E_{i+1} [m]	L_i [km]	δ_i [°]	Z_{seis} [km]	A_i [km^2]
11	Karamea	1	5948489	2454029	5986043	2465468	39.3	60	18	781.3
		2	5986043	2465468	6012518	2500000	39.6	60	18	851.8
		3	6012518	2500000	6015125	2507750	6.8	60	18	152.0
						ΣL_i	**85.6**		ΣA_i	**1785.1**
12	Pikikiruna	1	6000576	2481727	6014245	2495396	19.3	75	18	377.0
		2	6014245	2495396	6035971	2496978	19.2	75	18	408.2
		3	6035971	2496978	6056000	2513625	25.4	75	18	470.9
						ΣL_i	**63.9**		ΣA_i	**1256.1**
13	Pisagh	1	6017554	2496403	6025612	2497842	8.2	75	18	144.3
		2	6025612	2497842	6033000	2502250	8.3	75	18	152.1
						ΣL_i	**16.5**		ΣA_i	**296.4**
14	Alpine★	1	5840000	2391472	5854914	2416670	29.3	45	18	743.6
		2	5854914	2416670	5859522	2424734	9.3	45	18	249.5
		3	5859522	2424734	5882852	2455515	38.5	45	18	1069.1
		4	5882852	2455515	5906927	2463503	21.3	45	18	654.9
		5	5906927	2463503	5929064	2488631	33.5	45	18	765.2
		6	5929064	2488631	5939104	2506928	20.4	45	18	494.1
		7	5939104	2506928	5957505	2550667	45.7	45	18	1196.0
						ΣL_i	**197.9**		ΣA_i	**5172.4**

^ Assumed depth to the base of the seismogenic layer

† This structure has a change of dip along strike; however, the entire structure is referred to as the Wakamarama Fault

★ The entire Alpine Fault is not specified; only sections that could result in nearest distances to sites in the Buller Region are given

The selection of this suite of faults, as well as the assumption that the earthquake activity in the Buller region can be related to seismic activity on specific faults, represents the first major element of epistemic uncertainty introduced into the overall Probabilistic Seismic Hazard Analysis (PSHA). Epistemic uncertainty reflects a lack of knowledge in the governing physical processes related to earthquake activity. The shear quantity of data that must be considered during the process of conducting a probabilistic seismic hazard analysis means that many assumptions must be made in order for a model to be developed that reflects reality, to sufficient accuracy, but that is also manageable in terms of the number of calculations that are required as part of the analysis. As well as subjectively adopting the various faulting sources listed above, one must make some significant assumptions regarding the orientation and position of these faults in the crust. Of all the data considered thus far, very little of it provides much in the way of a constraint on the geometry of the fault system. Therefore, when proceeding with the seismicity analyses, and the subsequent hazard analyses, some representative geometry must be assumed. The geometry that is assumed for these sources is determined using a combination of techniques. The fault sources themselves are identified using a combination of field investigations techniques, viewing of aerial photographs, inspection

of existing geological maps, and primarily through the inspection of digital elevation models constructed for the region. Details of the assumed geometry in terms of the geometric segmentation of the fault sources on the surface of the earth as well as the assumed fault dips and the depths to the base of the seismogenic layer are provided in Table A.2.1. The simplified geometrical segmentation given in Table A.2.1 is an approximation to the true fault geometry that is governed by the topography as well as the governing tectonic mechanisms of the region. The mapped fault sources for the region, from which the approximate geometry given in Table A.2.1 is obtained, is shown diagrammatically in Figure A.2.11.

It is possible to consider multiple suites of fault geometries in the PSHA framework but these suites must essentially form equivalent sets in terms of their overall moment release rates and consequent regional deformation. Without having any sound external constraint upon the expected moment release rates for the Buller – NW Nelson region the selection of multiple suites of fault geometries is vexed by the fact that while we may well modify activity rates, geometries, maximum magnitudes, and other descriptive

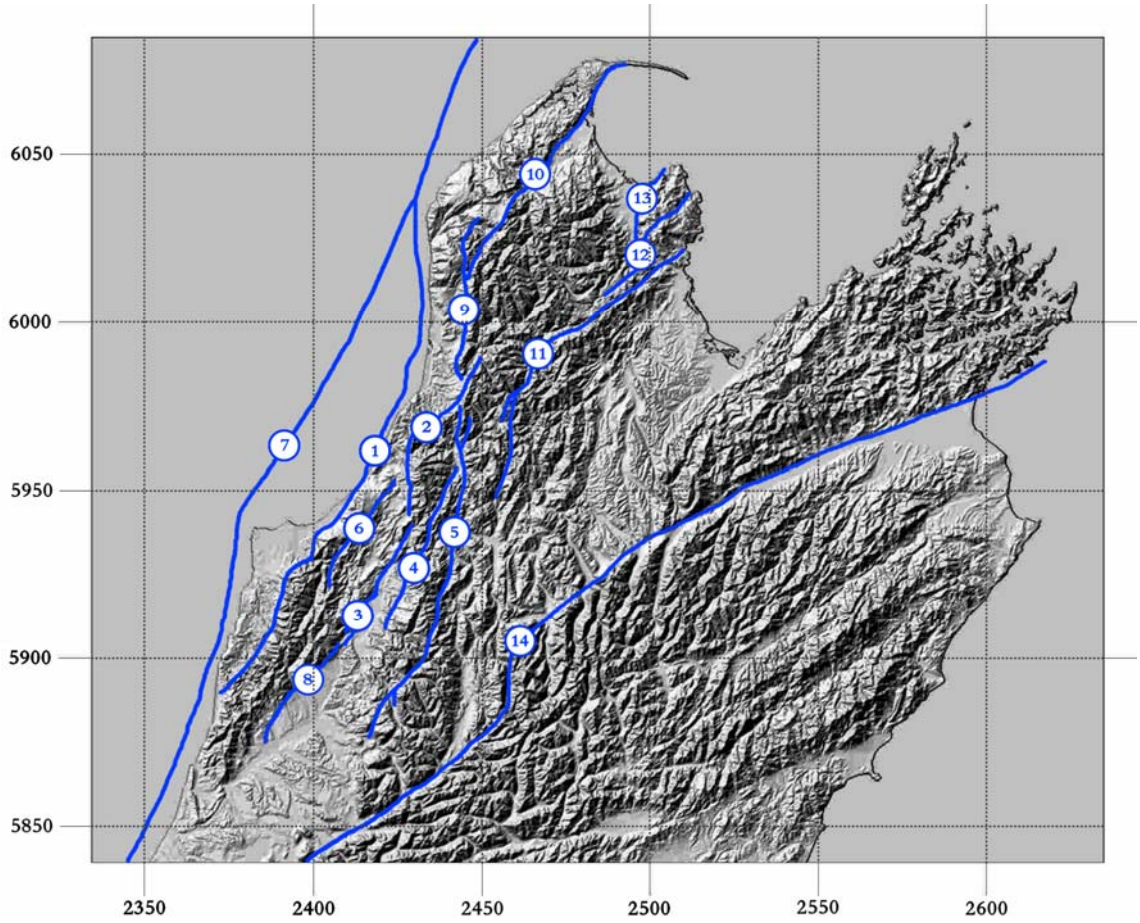

Figure A.2.11: Mapped fault sources in the Buller region. Each of the fourteen fault sources adopted for the final fault model are depicted. Each fault is referenced according to the fault numbers given in Table A.2.1. These fault sources are; (1) Kongahu, (2) Glasgow, (3) Inangahua, (4) Lyell, (5) White Creek, (6) Mt. William, (7) Cape Foulwind, (8) Maimai, (9) Kohaihai, (10) Wakamarama, (11) Karamea, (12) Pikikiruna, (13) Pisagh, (14) Alpine. Co-ordinates are given in terms of the NZMG system, with units of kilometres.

parameters for particular fault sources in order to obtain relatively equivalent fault sets, we have no way of telling if we are merely being consistent with out own initial intuitions or whether we are being consistent with reality. How realistic the adopted suite of faults is in terms of its ability to model the seismic activity of the Buller – NW Nelson region can only be ascertained as we proceed through the analysis. At all possible points one should check that any new findings or results are in fact consistent with the initial assumptions of the model. In this way it is possible to develop an overall model that is consistent with physical constraints, theoretical constraints, and intuition without having to push the total probability theorem to its extreme and consider every conceivable hazard scenario. The main problem associated with not conducting the PSHA on many possible fault models, and many possible suites of activity parameters, etcetera, is that the estimate of the uncertainty associated with the final hazard estimates becomes more difficult to assess. Issues such as these will frequently come up again in subsequent chapters; such is the nature of PSHA.

For now however, we may be content that we have selected a working fault model based upon a sound literature review and a comprehensive understanding of the most likely modes of long term deformation in the Buller – NW Nelson region based upon the geological data that is available. Once again, it is important to continually check that consistency is retained with respect to the initial assumptions made in this chapter when deriving all subsequent results. The first, and most important, check upon our internal consistency comes from deriving activity parameters for the selected suite of faults and then comparing the corresponding moment release rates obtained from these parameters with estimates made by other researchers. This exercise defines the focus of the next chapter.

A.3. Seismicity Analysis for the Buller Region

A.3.1. Introduction

In Chapter Two, a seismic source model was selected based upon geological considerations. The source model that was selected consisted of fourteen individual fault sources and one background source. The objective of the present chapter is to analyse the seismicity in the Buller – NW Nelson region, and from this analysis assign levels of activity to these various seismic sources. The levels of activity ultimately determine how frequently earthquake events occur in any particular spatial area of the Buller – NW Nelson region. Consequently, the activity parameters that are defined for each of the seismic sources will be strongly correlated to the exceedance of ground motions at sites throughout the Buller – NW Nelson region.

The parameters that are sought in order to define the rates of activity within the various sources are the average annual rate of earthquakes occurring within each source that exceed some particular magnitude level, the form of the magnitude – frequency distribution (essentially the Gutenberg-Richter *b* value), and the maximum assumed magnitude that each source is capable of generating. In order to determine these parameters a combination of geological knowledge and various statistical techniques are employed. The overall regional seismicity is partitioned amongst the various fault and background sources and statistical analyses are performed upon each subgroup of seismicity data. The overall rate of activity that is determined for the total fault model must be consistent with the limiting moment release rates mentioned in the previous chapter.

The chapter begins by detailing the seismicity dataset used and by describing the various adjustments and modifications that had to be made in order to prepare this dataset for use in obtaining the activity parameters for each seismic source. Particular attention is given to the procedure used to decluster the seismicity dataset in order to obtain a dataset reflecting Poissonian earthquake occurrence. In addition, significant detail is given to the method employed to partition the total seismicity dataset between the various individual sources in the fault model. Finally, methods used to obtain the final parameters characterising the activity of the sources that are

required for subsequent input into the PSHA calculations are described and some general discussion regarding these parameters is made.

A.3.2. The Seismicity Dataset

The seismicity data has been taken from the New Zealand seismicity database. This database is openly available through the GeoNet project (http://www.geonet.org.nz/). The data extracted from this site for the purposes of this study represent all events recorded either through instrumental means, or by anecdotal evidence. The earliest event that was included for consideration in this analysis occurred in 1846, well prior to the advent of modern strong motion recording instruments. All events occurring prior to August 20, 2004 were included in the analysis. This end limit to the temporal range of earthquake events bears no other significance than that imposed by the finite nature of this study.

Seismicity data was obtained for a region subjectively thought to be large enough to capture the general nature of seismic activity in the Buller – NW Nelson region. More precisely, the spatial extent of the region in standard co-ordinates of longitude and latitude are [170.83°, 173.49°] and [-42.64°, -40.85°]. A more practical co-ordinate system specifically developed for use in New Zealand is the New Zealand Map Grid (NZMG) co-ordinate system. In NZMG, positions have a metric equivalence with the standard metric being 1m at the surface of the earth. Relative positions can therefore be related in what effectively becomes, for all intents and purposes, a Cartesian representation of position as opposed to the less intuitive spherical representation. To account for the Earth's slight, but significant, departure from true spherical geometry as well as to take advantage of New Zealand's approximately oblate shape, complex mathematical algorithms are required. These algorithms are easily programmed and the process of converting between the two systems consequently becomes very simple. This process has been well documented (Reilly 1973; Stirling 1973; Bevin 1998). The spatial extent of the considered region in NZMG co-ordinates is therefore [2329710, 2550569] and [5840001, 6039963] in Eastings and Northings respectively. Given that the NZMG system gives values in metres, the region considered is approximately 220km East-West and 200km North-South. Events occurring through all depths were initially considered.

A.3.2.1. Magnitude Corrections

Various measures of earthquake size are utilised in the New Zealand seismicity catalogue. For the purpose of analysing the seismicity, it is desirable to be able to compare events on an equivalent basis. All magnitude values are therefore converted to a common consistent measure. For this study, the Moment Magnitude (M_W or $\mathbf{M}$) (Hanks and Kanamori 1979) scale has been chosen due to its sound physical basis and its suitability for application over all conceivable ranges of magnitude.

The other magnitude scales that are used in the catalogue are Surface Wave Magnitude (M_S), Body Wave Magnitude (m_b), Duration Magnitude (M_D), and Local Magnitude (M_L). By far the most common of these magnitudes is the Local Magnitude scale for New Zealand earthquakes (Haines 1981). Comparisons between the various magnitude scales have also been made and are regarded when making the conversions between the various scales (Haines 1983; Dowrick and Rhoades 1998).

For the purposes of this study, all events assigned magnitude values less than 5.0, regardless of the magnitude scale in which the event is reported, have been assumed to possess the equivalent magnitude on the Moment Magnitude scale. The founding logic governing this assumption is that the conversion formulae between magnitude scales are often approximate and regionally variable. The standard error in the estimate of individual magnitude values is also typically larger than the error resulting from conversion between scales so while making some empirical conversion may, in principle, be more appropriate, the alterations to the actual observed values are small in comparison to the estimate of the central value anyway. These technicalities aside, the predominant reason for the assumption is that the actual values of the magnitudes over this range have little consequence for the purpose of estimating regional energy release. The events having magnitudes in this range have more importance when comparing the relative frequencies of their occurrence, for example, when determining magnitude-frequency relationships. Therefore, so long as these events are defined consistently, the relative rates of occurrence of differing sized events can be ascertained.

All other events, those with magnitude assignments greater than or equal to 5.0, regardless of scale, are considered on an individual basis. Earthquake events of this size typically warrant suitable investigation so that Moment Magnitude values for the events are available in the literature. In the Buller region there are relatively few events of this size, and those that have occurred have received the required attention to enable the assignment of Moment Magnitude values. The moderate to large events in the catalogue are comprised of the 1929 Buller (Murchison) Earthquake (Berryman 1980; Dowrick and Rhoades 1998; Doser et al. 1999), and associated aftershocks, the 1960 Westport Earthquakes (Adams and Le Fort 1963; Dowrick and Rhoades 1998; Doser et al. 1999), the 1968 Inangahua Earthquake (Anderson et al. 1993; Anderson et al. 1994; Dowrick and Rhoades 1998), and associated aftershocks (Adams and Lowry 1971; Adams et al. 1971), and the 1991 Hawk's Crag Earthquakes (Cousins et al. 1991; Anderson et al. 1993; Dowrick and Rhoades 1998). An example of some significant alterations to the catalogue magnitudes is demonstrated in

All of the events in the magnitude-corrected catalogue are thus represented with a consistent magnitude scale. Subsequent analysis of the seismicity catalogue is performed on Moment Magnitude values and reference to magnitude values henceforth should be understood as drawing reference to the Moment Magnitude scale.

Table A.3.1.

All of the events in the magnitude-corrected catalogue are thus represented with a consistent magnitude scale. Subsequent analysis of the seismicity catalogue is performed on Moment Magnitude values and reference to magnitude values henceforth should be understood as drawing reference to the Moment Magnitude scale.

Table A.3.1: Examples of significant magnitude corrections resulting from the conversion of all catalogued magnitudes to the Moment Magnitude (M_W) scale. Reference numbers refer to the following works, 1. Dowrick and Rhoades (1998), 2. Dowrick and Rhoades (2004), 3. Anderson et al. (1993), 4. Anderson et al. (1994), 5. Cousins et al. (1991)

Earthquake Event		Magnitude Data for Original Catalogue		Magnitude Data for Adjusted Catalogue		References
Name	Date	Magnitude Type	Magnitude	Magnitude Type	Magnitude	
Buller (Murchison)	16/06/1929	M_S	7.8	M_W	7.7	2
Inangahua	23/05/1968	M_L	6.7	M_W	7.1	1,3,4
Hawk's Crag 1	28/01/1991	M_L	6.143	M_W	5.79	1,3,5
Hawk's Crag 2	28/01/1991	M_L	6.286	M_W	5.93	1,3,5
Hawk's Crag 3	15/02/1991	M_L	5.971	M_W	5.42	1,3,5

A.3.2.2. Levels of Magnitude Completeness in the Catalogue

Within any earthquake catalogue there exists a certain level of magnitude for which those administering the seismic network can be confident of recording all events that occur of that size, or greater. The level of completeness of a network is a related primarily to the density and quality of the instruments in the area being observed. As the amount of money available for earthquake research has increased with time, the number and quality of instruments that constitute the New Zealand seismic network have also increased and improved. Throughout the period spanning the earthquake dataset there are four primary periods for which the limiting magnitude of completeness has decreased. These levels of completeness reflect the completeness on a national level. In some parts of New Zealand, such as Wellington, the number of instruments per square kilometre is well above the national average. It can reasonably be expected that the actual magnitude of completeness in these regions is lower than the national limits. The Buller region is not currently one of the heavily monitored regions and as such the national levels of completeness have been adopted. The levels of completeness that have been adopted in previous seismicity studies vary (Stirling, Wesnousky et al. 1998; Stirling et al. 2000; McGinty 2001; Stock 2001; Stirling et al. 2002). These magnitude limits are listed in Table A.3.2. The largest degree of variation associated with the assumed levels of magnitude completeness relate to the largest earthquakes occurring prior to the installation of recording instruments (seismographs or accelerographs). Stirling et al. (2002) adopt 1840 as the year beyond which all $M6.5$ events are identified, however, in contradiction of this date, McGinty (2001), while preparing the seismicity catalogue for the same study, adopts 1900 as the year beyond which all $M6.5$ events are identified. Stock (2001) then reports that routine reporting of moderate to large earthquakes was not implemented until 1870, and therefore adopts this year as the start of completeness for $M6.5$ events. There is far better consensus regarding the dates corresponding to changes in completeness of the seismicity catalogue for $M5.0$ and $M4.0$ events, with dates of 1940 and 1964 typically assumed. The only reported year corresponding to a level of completeness for $M3.0$ events is given by Stock (2001); in this study 1991 is adopted as the year beyond which the catalogue is complete for these events. However, both McGinty (2001) and Stock (2001) note that the national network was upgraded in 1987 through the introduction of the University of

Canterbury strong motion instrument network. Stock (2001) also notes that the values he adopts are typically conservative. In addition, the relatively high rates of seismicity observed in the early nineties would tend to bias the results obtained using his method to slightly higher values. The value of 1990 adopted in this study for the level of completeness for $M3.0$ events is therefore justified.

Magnitudes in the catalogue are often specified to a precision higher than the typical one decimal place commonly associated with modern earthquake catalogues. For this reason the effective magnitudes of completeness are slightly lower than those stated to account for rounding up of magnitudes for events with magnitudes specified at a higher precision than one decimal place.

The accuracy with which the events in the catalogue are measured also increases as the number of instruments recording each event increases. The moderate to large events occurring prior to 1940 have magnitudes inferred from felt intensity data and as such can have associated errors in the estimation of their magnitudes of the order of 0.6 magnitude units; present day events have magnitudes estimated to at least two decimal places in most cases.

Table A.3.2: Levels of magnitude completeness for the New Zealand earthquake catalogue adopted for use in this study

Year from which the Catalogue is deemed Complete	Magnitude Level of Completeness
1850	6.5
1940	5.0
1964	4.0
1990	3.0

The brevity of the catalogue results in there being few events in this moderate to large class. One such event occurring prior to the limiting date of 1850, a magnitude 6.5 occurring in 1846, has been included in the analysis. The event has poor position and no depth location, but was regarded by the author as being important to better restrain the estimates of activity over the range where the least amount of data is available, and where many years would have to pass before this situation might change. The inclusion of this event in the subsequent analysis is also consistent with the levels of completeness adopted by Stirling et al. (2002) in deriving the national seismic hazard maps.

A.3.2.2.1. Temporary Installation of instruments following the 1968 Inangahua Earthquake

Shortly after the occurrence of the 1968 Inangahua Earthquake two temporary instruments were installed in the region (Adams and Lowry 1971). The instruments were only placed for a period of 40 days, but throughout this period the local level of completeness was reduced significantly. The level of completeness for the region prior to the installation is thought to be M_L 3.7 based upon consideration of the aftershock sequence (Adams and Lowry

1971). Following the installation of the two temporary stations, 2.5 days after the occurrence of the mainshock, the level of completeness is thought to have been reduced to M_L 3.1 (Adams and Lowry 1971), again based upon consideration of the aftershock sequence. Adams and Lowry (1971) fitted Modified Omori's Law (Utsu 1961) distributions to the data and estimated the level of completeness through the departure of the recorded data to the well established Modified Omori Law.

As mentioned, the two temporary instruments remained in the field for a period of 40 days after their installation. Over this time 800 events were recorded, from which good constraint on the aftershock parameters for the Inangahua sequence can be obtained. The events recorded by the temporary instruments were considered during the analysis of the seismicity of the Buller region made during the course of this study. These events receive considerable additional attention later in this chapter when the parameters for the Modified Omori Law are recalculated for the aftershock sequence using modern techniques.

A.3.2.3. Magnitude Error Assignment

The standard error estimates for each event in the catalogue are originally made using the magnitude scale in which the event is listed. Therefore, when one converts between the magnitude scales one should also convert the error estimates. However, because no specific conversion rule was adopted for the majority of the events in the catalogue the original values of the standard errors listed in the catalogue have been retained and associated with the corresponding Moment Magnitude values for each event. It is recognized that this procedure is not ideal, but it is also recognized that the magnitude of the error thus incorporated is relatively small to the point that it is reasonable to ignore this issue.

A.3.2.4. Position Corrections

A.3.2.4.1. Lateral Position

As was mentioned earlier, a conversion from co-ordinates of longitude and latitude to those of the NZMG presents some advantages. The primary advantage of the NZMG system is that distances between points in three dimensional space are readily measured, and measured in terms of S.I. units. However, due to the mapping required, some approximation must be made when converting the standard error estimates of lateral position from longitude and latitude to NZMG. For this investigation the assigned latitude and longitude values were converted to NZMG as well as the assigned values plus, and minus, the standard error estimates for the event location in each direction. When this conversion is made, the resulting standard errors in the 'plus' and 'minus' directions differ in the NZMG system whereas they were once equivalent in the original longitude – latitude system; therefore a slight adjustment needs to be made. The two NZMG errors corresponding to each direction are found from the difference between the calculated plus and minus NZMG values and the original NZMG value. The two differences are then arithmetically averaged to obtain the standard error estimate in the Eastings and Northing convention of the NZMG system.

A.3.2.4.2. Vertical Position

While the lateral position error adjustment is really an academic formality, the vertical position assignment presents a far more significant problem. For a significant duration of the catalogue, locating algorithms were either not sophisticated enough, or the instrument density was not high enough, to enable accurate assessments of the focal depth of most earthquakes. For this reason seismologists would assume that the event occurred at a certain restricted depth so that they could optimise the constraint on position in the lateral directions. The result of this procedure is that many events in the catalogue prior to 1987 (McGinty 2001) have been assigned 'restricted depths' at certain particular depths (commonly 5, 12, and 33 km).

As a result of the enforced depth restrictions the distribution of earthquake events vertically does not resemble that which occurs in reality. The significance of this effect is observed when one considers cross sectional views of deep seismicity in an area of plate subduction such as the subduction occurring along the east coast North Island Hikurangi Subduction margin and impinging on the northern part of the area considered in this study (McGinty 2001; Reyners and Robertson 2004). When completing a thorough assessment of the seismicity of a region the spatial and temporal relationships between the occurrences of events must be considered. If the catalogue is analysed leaving events that have been assigned restricted depths uncorrected, the catalogue will exhibit an unnatural clustering of events along depth ranges corresponding to the restricted depths. No appropriate inferences can be made regarding the spatio-temporal relationships between events under this circumstance.

McGinty (2001) describes a procedure by which the restricted events could be redistributed so as to mimic the typical spatial distribution of seismicity in a region. In this work McGinty (2001) estimates the characteristics of the long-term depth distribution of earthquakes by considering those events occurring post 1987 for which good constraint upon position is available. The basic assumption in this method is that the depth distribution of recent seismicity is representative of the long-term distribution. This appears to be a reasonable assumption.

In the present study a slight modification to this method is made. McGinty (2001) considered all post 1987 events, however, the New Zealand catalogue did not become complete for events of magnitude three or greater until 1990 (see Table A.3.2). In order to prevent the introduction of any magnitude bias that may be associated with the inclusion of events below the completeness levels, only post 1990 events are considered in this study.

The first step in the modified procedure is to ascertain the relative percentages of events in the catalogue that can be regarded as being either shallow crustal, or deep events. For this purpose, the limiting depth above which events are regarded as being shallow crustal events is 40km. This definition is consistent with that used by the Institute of Geological and Nuclear Sciences (GNS) for displaying shallow seismicity from New Zealand earthquakes (see for instance http://www.gns.cri.nz/what/earthact/earthquakes/shallowseismicity.html). For the post 1990 catalogue the shallow crustal events represent only a very small portion of the total number of events. Once the catalogue is split into its shallow and deep components the distribution of events within each class is considered and some distribution fit to these events.

For the deep events no discernable spatial correlation between the occurrences of events with depth was observed. Consequently, a uniform distribution was used to model the distribution of deep events. For the shallow events however, the post 1990 distribution showed a distinct concentration of events around the 10-12km region with comparatively few events above or below this level. Initially a normal distribution was fitted to these events but it was seen that the best-fit normal distribution concentrated too much activity about the mean value. A distribution that had a distinct central tendency, but that assigned more weight to its tails, was desired. A Laplacian, or double exponential, distribution was therefore chosen to represent the shallow crustal seismicity.

The restricted events could then be redistributed according to these fitted distributions. For each restricted depth event two uniformly distributed random numbers from the interval $(0,1)$ were generated. The first drawn number was used to assign the restricted depth event to either the shallow crustal, or the deep seismicity catalogues. If the value of the first random number drawn is less than or equal to the decimal percentage of post 1990 events occurring in the shallow crust then the event is assigned to the shallow crustal catalogue, and similarly for the deep events. The second random number that is drawn is set equal to a value of the cumulative distribution function of the distributions fitted to the post 1990 seismicity. Given that the fitted distributions are written in terms of depth the inverse of the cumulative distribution function therefore corresponds to a depth. This depth is the new depth assigned to the restricted event in question.

Obviously, this depth reassignment process is random and while the new depths of events are assigned according to a distribution that reflects the regional seismicity on a large scale, information regarding the interaction of small groups of events is lost. In order to try and compensate for this problem, 20 separate redistributions were made and subsequent analysis was performed on all 20 catalogues. In this way, while actual interactions between events cannot be captured, typical, or average interactions can be approximated. Note also that although the analysis cannot be performed on an actual catalogue, this is not a result of this redistribution process as the original catalogue is not a true representation of reality anyway due to the large number of events set to restricted depths.

McGinty (2001) shows that this process can yield realistic, redistributed catalogues of seismicity. The original redistribution procedure of McGinty (2001) was used in the preparation of the seismicity catalogue employed for the development of the latest seismic hazard maps for New Zealand (Stirling et al. 2002).

A.3.3. Declustering the Catalogues

As was mentioned earlier, a thorough seismicity analysis will involve declustering of the seismicity catalogue. The primary reason for performing this declustering procedure is that the results of seismicity analyses will generally be used as an input into a Probabilistic Seismic Hazard Analysis, a primary assumption of which is that the occurrence of events in time and space is Poissonian in nature (Cornell 1968). The fundamental assumptions underlying a Poisson process are defined more fully in Chapter 5.

The declustering procedure is not just carried out in order to facilitate the use of a mathematical model. When evaluating the seismic hazard at a particular site one is most interested in the occurrence of significant seismic events. As far as the end users of seismic hazard analyses are concerned, a significant seismic event may be a single event causing ground motions of engineering relevance, or a group of these events occurring in a short space of time. Either scenario signifies a disruption in the usual seismically quiescent status quo. Likewise, either scenario must be considered in terms of its likely impact on the physical infrastructure, the disruption to business operation, and to the psyche of the society as a whole. As well as these societal based considerations, physical effects such as the influence that the event, or sequence of events, has on the regional stress state of the seismogenic crust must be considered so that this information can be used to update hazard estimates for the future. The goal of the declustering process is therefore to remove all events, or groups of events that are probably dependent upon each other and replace these clusters of events with singular events that represent the overall effect of each cluster. While there is no formal definition of this dependence, the practical implication is that foreshocks and aftershocks are removed from the catalogue. The resulting earthquake catalogue is then assumed to consist of a series of random, and independent, earthquake occurrences in space and time.

When these groups, or clusters, of earthquake events are removed from the earthquake catalogue it is important that information regarding regional stress relief is not removed in the process. In order to ensure that this does not happen, each identified cluster of events is converted to a singular event. This single equivalent event is assumed to have a size and position that is found from a weighted average of the size and position of the constituent earthquakes in the cluster. The measure of size used to weight the contributions of each event is the seismic moment. The logarithmic nature of this size measure coupled with Båth's Law (Båth 1965) ensures that the mainshock of the sequence is the primary determinant of the size and position of the equivalent event. In this way, the total strain energy released by earthquakes in an earthquake catalogue is conserved. Note that other relevant parameters describing the event, such as the errors associated with the magnitude estimate and position estimates are also processed using the same weighting scheme mentioned above.

Previously it was stated that an ideal declustering process should result in the removal of both foreshocks and aftershocks from an earthquake catalogue. This is generally not the case due to the fact that foreshock events are extremely difficult to identify (even retrospectively), although progress appears to be being made on this front (Ogata et al. 1995; Zhuang et al. 2002; Helmstetter et al. 2003; Felzer et al. 2004; Zhuang et al. 2004; Helmstetter et al. 2005). One of the reasons why foreshock identification is so vexed is that not every large earthquake exhibits an increased of seismic activity prior to an event. Indeed, Ogata (1992) gave evidence that periods of relative seismic quiescence may exist in the period prior to a great earthquake. This evidence was supported through the use of the Epidemic Type Aftershock Sequence (ETAS) model that has subsequently received a significant amount of attention in the literature. If this hypothesis is correct then there may be an argument to not remove aftershock events from the earthquake catalogue but rather to try and transform the observed occurrence of earthquake events onto a more appropriate time scale (Bak et al. 2002). Much of the difficulty in proving or disproving a hypothesis of this nature is due to the relatively short period of instrumental recordings of earthquakes in comparison with the time period required to obtain a truly representative sample of long term seismicity that includes effects related to the occurrence of large events and the related perturbation of smaller earthquake occurrence.

There are many researchers actively engaged in the study of earthquake clusters; in many cases their interest is in developing procedures that may be useful in making short term, or real time, inferences into the nature of future seismic activity. The goal of generic PSHA however, is to estimate hazard over longer time periods and the detailed statistical processes that are entered into are often beyond the scope of the common PSHA. For the present work, the identification and removal of foreshocks is not attempted. The declustering procedure that is used is a generic procedure aimed at the removal of aftershocks, that being the method of Reasenberg (1985). However, it should be noted that within the adopted method of Reasenberg (1985), every event is regarded as being a mainshock event. True mainshocks manifest themselves within this framework by virtue of the fact that larger earthquakes are assigned larger spatial correlation distances. More earthquakes are therefore likely to be correlated with larger events than with small events. This is consistent with observations of real earthquake catalogues in which real clusters† have been identified.

Aftershock sequences are generally well characterised by three models, the Modified Omori Law (Utsu 1961) for the temporal rate of aftershock activity following a mainshock, the Gutenberg-Richter relationship (Gutenberg and Richter 1944) for the size distribution of earthquakes in an aftershock sequence, and Båth's Law (Båth 1965) relating the maximum size of an earthquake in an aftershock sequence to the magnitude of the mainshock. Recently, a model of aftershock occurrence that combines all three of these models has been presented (Shcherbakov et al. 2004). This model provides the motivation for the development of the aftershock distribution used in the present work. Other general characteristics of aftershocks, such as alternative models for the temporal distribution (Kisslinger 1996), and the spatial properties of aftershock zones (Henry and Das 2001; Kagan 2002) are well documented and were considered in the developments that follow.

A.3.3.1. Removing the Influence of the Inangahua Event

The catalogue of observed earthquakes in the Buller region is strongly influenced by events associated with the 1968 Inangahua earthquake. This event creates a significant departure from Poisson occurrence as can be observed in Figure A.3.1 (particularly panels (b) and (c) for the rate of occurrence of events of magnitudes greater than $M_W 4.0$ and $M_W 5.0$ respectively). Figure A.3.1 plots the total number of events recorded in the catalogue for two different cases. The blue circles correspond to a base catalogue that has had corrections made for magnitude and position errors, as well as having had depths redistributed‡. The red triangles correspond to the same catalogue after the declustering algorithm, to be described in detail shortly, has been applied. In plotting these figures, the intention is to try and observe significant departures from an average (Poissonian) rate of earthquake occurrence. If the points plotted in a figure of this nature show strong linear trends then the occurrence process may be well modelled by a Poisson model. Also in Figure A.3.1, dashed vertical lines are included that demarcate the timing of events that are likely to have produced large clusters of seismic activity.

† As opposed to clusters that are defined by some measure of statistical correlation.

‡ The procedures adopted for this purpose have been defined earlier in this chapter

These events are the 1929 Murchison, the 1968 Inangahua, and the 1991 Hawk's Crag sequence. As can be seen from the figure, each of these events causes significant steps in the rate of activity to occur in the base catalogue. It can also be seen that the declustering procedure does not completely remove these steps, particularly in the case of the Inangahua event, but does a pretty good job of removing dependent events and creates earthquake catalogues that can reasonably be considered Poissonian in nature.

Because the Inangahua event has such a significant impact on the regional seismicity the aftershock distribution of this event is considered in depth and specific parameters characterising the sequence are derived. In the declustering procedure, events that are probably associated with the Inanagahua aftershock sequence are identified on the basis of these derived parameters. For other events, generic aftershock sequence parameters derived for New Zealand are employed (Eberhart-Phillips 1998). These generic parameters are remarkably consistent with parameters derived for use in California and are based upon the analysis of 17 New Zealand earthquake sequences with mainshock magnitudes of $M_W \geq 5.5$, from 1987 through to 1995. This dataset includes the Hawk's Crag 1 event that occurred in the Buller region on January 28, 1991.

Following the Inangahua mainshock of May 23, 1968, additional temporary seismographs were installed in the region to monitor the resulting seismicity from the event. This aftershock sequence is analysed by Adams and Lowry (1971) and is also documented in a special publication of the New Zealand Seismological Observatory (Adams et al. 1971). Adams and Lowry (1971) fit an Omori Law (Omori 1894) of the form shown in Equation (A.3.1) below.

$$n(t) = At^{-p} \qquad \text{(A.3.1)}$$

Using a least squares regression, they found the value of the parameter p to be 1.05 ± 0.06. In Equation (A.3.1) $n(t)$ is the rate of earthquake occurrence at time t, A is a parameter that reflects the total number of events in the sequence and is related to the size of the mainshock. The parameter p controls the time dependent rate (the slope of the distribution). However, as Weichert (1980) points out, least squares regression techniques should only be applied to independent data; in all other cases Maximum Likelihood Estimation (MLE) techniques are more appropriate. Ogata (1983) provides the framework within which to determine parameters of the Modified Omori Law (Utsu 1961) using MLE techniques. This method is described in detail later as the Modified Omori Law is adopted in the present work. Additionally, Nyffenegger and Frohlich (1998) provide recommendations for determining the value of p as well as its associated error estimate.

The original seismicity catalogue that was downloaded from the GeoNet website contained the events recorded by the temporarily installed instruments, but differed in some cases from the data in the New Zealand Seismological Observatory report for depth assignments. The downloaded datasets were therefore modified to include the information recorded by the temporary network deployed in the region on an earthquake by earthquake basis. The temporary network was active for a period of 40 days and recorded some 800 odd earthquakes. At the time of the Inangahua event the level of magnitude completeness for the New Zealand

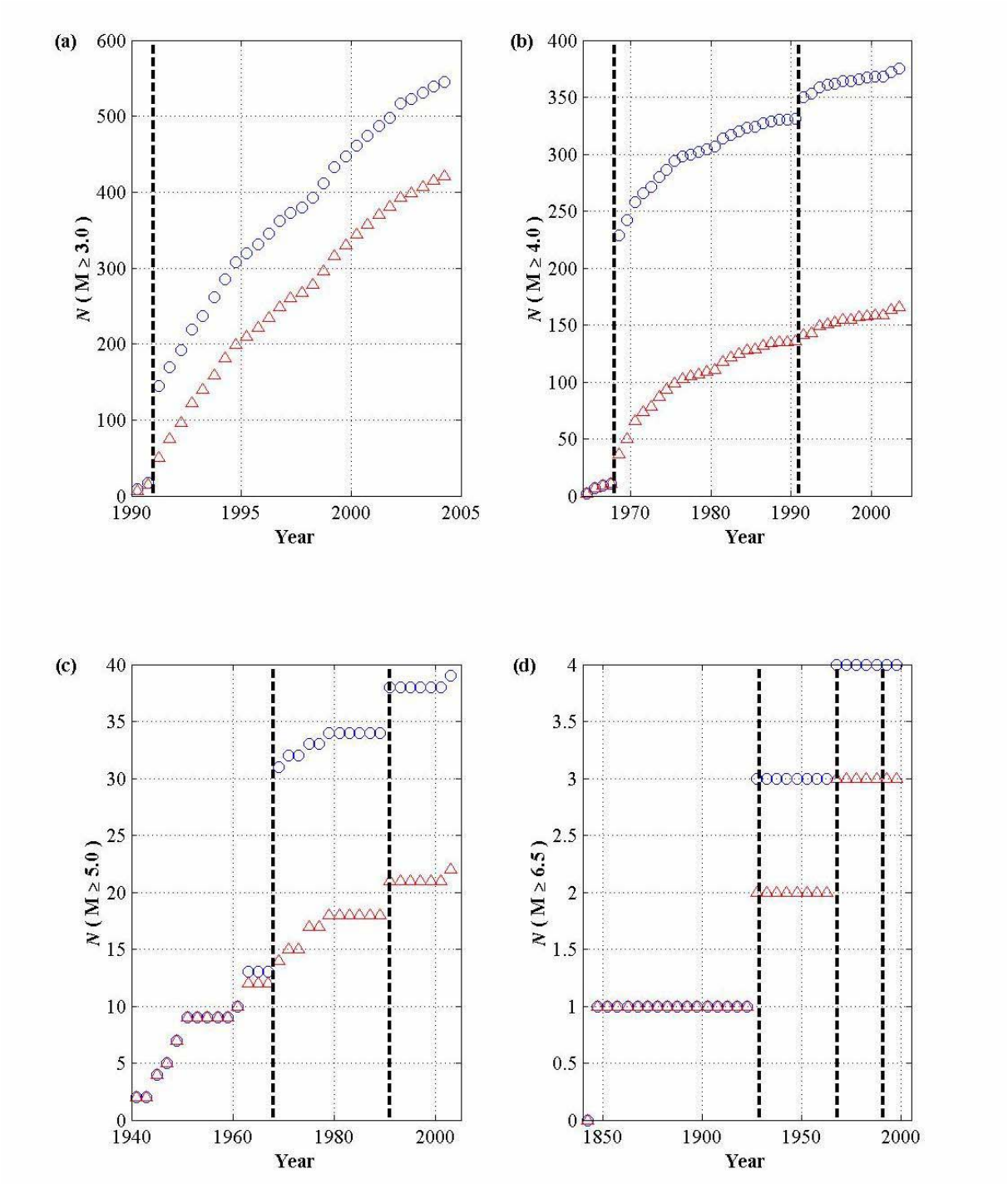

Figure A.3.1: The effect of declustering the earthquake catalogue at the various levels of completeness of the New Zealand seismic network. Panels a-d show the cumulative number of earthquake events having magnitudes greater than 3.0, 4.0, 5.0, and 6.5. In all panels, blue circles represent a raw catalogue whereas red triangles represent a declustered catalogue. The vertical dashed lines represent clusters associated with significant events, 1929 Murchison, 1968 Inangahua, and 1991 Hawk's Crag sequence.

seismic network was 4.0 (see Table A.3.2). The installation of the temporary instruments in the region enabled this level of completeness to be locally lowered in two steps that correspond to the times at which the additional instruments were installed. The first temporary instrument was placed at Cape Foulwind and was able to record aftershocks within 17 hours of the mainshock occurring. The second instrument was placed at Denniston but was not able to satisfactorily record events until 2.5 days after the mainshock (Adams and Lowry 1971). The level of completeness was reduced to 3.7 following the installation of the Cape Foulwind instrument, and then further to a level of 3.1 following the installation of the Denniston instrument. Because the rate of earthquake activity, as defined by the Modified Omori Law, is dependent upon the minimum magnitude of completeness a distinction between the two intervals corresponding to the two levels of completeness must be made when deriving parameters to describe the Inangahua aftershock distribution.

As mentioned above, the declustering of earthquake catalogues in this study is based upon the method of Reasenberg (1985). In this method the rate of aftershock occurrence is modelled by the Omori Law and generic parameters applicable to California are employed. For the present analysis the aftershock rates are modelled using the Modified Omori Law (Utsu 1961), given in Equation (A.3.2) below.

$$n(t) = \frac{K}{(t+c)^p} \tag{A.3.2}$$

In this equation, $n(t)$ is the number of aftershock events occurring at time t, and K, c, and p are parameters specific to a given aftershock sequence. It is these three parameters that are to be determined in order to most appropriately model the Inangahua sequence and consequently remove its effect from the seismicity catalogues.

A.3.3.2. Temporal Dependence

The value of parameter K is actually a function of the completeness level of the aftershock sequence as well as the size of the mainshock itself. In effect, the parameter K describes the total number of events in the aftershock above some minimum magnitude level. The Reasenberg (1985) method incorporates this magnitude dependence by making K a function of both $m_{\min}$ and $m_{\max}$, the minimum and maximum magnitudes in the aftershock sequence. The following relationship is adopted in that original work.

$$\log_{10} K = \frac{2}{3}(m_{\max} - m_{\min} - 1) \tag{A.3.3}$$

However, following the lead of Shcherbakov et al. (2004) (as well as previous similar work, such as that of Reasenberg and Jones (1989; 1990)), the parameter K can be related to the Gutenberg-Richter relationship (Gutenberg and Richter 1944), and Båth's Law (Båth 1965), via the following construction. The total number of

events having magnitude greater than some minimum magnitude, $N(m \geq m_{\min})$, can be found from the familiar expression below†.

$$N(m \geq m_{\min}) = 10^{a-bm} \tag{A.3.4}$$

Here, a represents the number of events with magnitude greater than or equal to zero, and b is the standard Gutenberg-Richter *b*-value. Now, given that the parameters a and b are defined for the specific aftershock sequence in question, the expected value of the largest aftershock can be found by finding the value m for which $N(m \geq m_{\min}) = 1$. This condition is met when $a = bm$. Shcherbakov et al. (2004) then introduced Båth's Law (Båth 1965) in which the difference between the magnitude of the mainshock, m_{MS}, and the largest aftershock, $m_{AS}^{\max}$, is relatively constant (Helmstetter and Sornette 2003), and is termed Δm. This is explicitly expressed in Equation (A.3.5) below.

$$\Delta m = m_{MS} - m_{AS}^{\max} \tag{A.3.5}$$

Therefore, equating $m_{AS}^{\max}$ in Equation (A.3.5) with the previously defined magnitude corresponding to the condition of $N(m \geq m_{\min}) = 1$, the generalised Gutenberg-Richter relationship for aftershock sequences can be described by Equation (A.3.6).

$$N(m \geq m_{\min}) = 10^{b(m_{MS} - \Delta m - m)} \tag{A.3.6}$$

One can therefore determine the number of events in an aftershock sequence that have magnitudes larger than any given value. Recalling the definition of K as being the total number of events above the completeness level of the recorded aftershock sequence, the Modified Omori Law can be restated as in Equation (A.3.7), with $m \equiv m_{\min}$ applying to the case of the complete aftershock sequence.

$$n(t,m) = \frac{10^{b(m_{MS} - \Delta m - m)}}{(t+c)^p} \tag{A.3.7}$$

The numerator in the above expression replaces Equation (A.3.3) in the original Reasenberg (1985) algorithm. In order to implement the above aftershock distribution in the declustering algorithm an estimate of the relevant parameters of Equation (A.3.2) must be obtained.

† While the form of this expression is similar for both incremental and cumulative distributions, the expression given in this sense relates to the cumulative distribution.

The parameters of the original Modified Omori Law were initially determined for the two completeness levels of the aftershock sequence ($m_{\min} = 3.1$ and $m_{\min} = 3.7$). The value of the parameter p should be the same in both cases as it describes the same population. The values of parameter K that are determined are then compared to the numerator of Equation (A.3.7) for each case, and an appropriate b-value is then determined. Ogata (1983) showed how the optimal parameters of the Modified Omori Law might be determined using Maximum Likelihood Estimation techniques. The optimum parameters are defined as the combination of K, c, and p that maximise the following log-likelihood expression.

$$\ln L(\boldsymbol{\theta}) = \sum_{i=1}^{N} \ln n(t_i) - \int_{S}^{T} n(t)\,dt \tag{A.3.8}$$

In this expression, $\boldsymbol{\theta} = \{K, c, p\}$ is the vector of desired parameters, S and T represent the start and finish times of the sequence being considered. These parameters will consequently take on specific values depending upon which of the two sequences is being considered. Time in this expression (as in all previous and subsequent expressions in this section) is given in units of days. With the integral expression evaluated, the above log-likelihood function is equivalent to Equation (A.3.9) below.

$$\ln L(\boldsymbol{\theta}) = N \ln K - p\sum_{i=1}^{N} \ln(t_i + c) - KA(c, p) \tag{A.3.9}$$

Here, the function $A(c, p)$ is defined as below.

$$A(c,p) = \begin{cases} \ln(T+c) - \ln(S+c) & , \text{ for } p = 1 \\ \dfrac{(T+c)^{1-p} - (S+c)^{1-p}}{1-p} & , \text{ for } p \neq 1 \end{cases} \tag{A.3.10}$$

The optimal solution is found using an optimisation process in which the following gradient functions are invoked (Ogata 1983).

$$\frac{\partial \ln L(\boldsymbol{\theta})}{\partial K} = \frac{N}{K} - A(c, p) \tag{A.3.11}$$

$$\frac{\partial \ln L(\boldsymbol{\theta})}{\partial c} = -p\sum_{i=1}^{N} \frac{1}{(t_i + c)} - K\left[(T+c)^{-p} - (S+c)^{-p}\right] \tag{A.3.12}$$

$$\frac{\partial \ln L(\boldsymbol{\theta})}{\partial p} = -\sum_{i=1}^{N} \ln(t_i + c) - \frac{K\left[(T+c)^{1-p} - (S+c)^{1-p}\right]}{(1-p)^2} + \frac{K\left[(T+c)^{1-p}\ln(T+c) - (S+c)^{1-p}\ln(S+c)\right]}{(1-p)} \tag{A.3.13}$$

The errors associated with the parameter estimates are also important. In the method of Ogata (1983) it is assumed that the error of the MLE procedure, $\hat{\boldsymbol{\theta}}-\boldsymbol{\theta}_0$ (where $\hat{\boldsymbol{\theta}}$, and $\boldsymbol{\theta}_0$ represent the MLE and true values of the parameter set), is asymptotically distributed according to a three dimensional normal with zero mean and the variance-covariance matrix $J\left(\boldsymbol{\theta}_0;S,T\right)^{-1}$. Here, $J\left(\boldsymbol{\theta}_0;S,T\right)$ is the Fisher Information Matrix which can be defined by the formulae below.

$$J\left(\boldsymbol{\theta};S,T\right)=\int_S^T \frac{1}{n\left(t;\boldsymbol{\theta}\right)}\frac{\partial n\left(t;\boldsymbol{\theta}\right)}{\partial \boldsymbol{\theta}'}\frac{\partial n\left(t;\boldsymbol{\theta}\right)}{\partial \boldsymbol{\theta}}dt \tag{A.3.14}$$

Upon evaluation of the integrand in Equation (A.3.14), the Fisher Information Matrix is found to be symmetric and equivalent to the integrand of Equation (A.3.15).

$$J\left(\boldsymbol{\theta};S,T\right)=\int_S^T \begin{bmatrix} K^{-1}\left(t+c\right)^{-p} & -p\left(t+c\right)^{-p-1} & -\left(t+c\right)^{-p}\ln\left(t+c\right) \\ * & Kp^2\left(t+c\right)^{-p-2} & Kp\left(t+c\right)^{-p-1}\ln\left(t+c\right) \\ * & * & K\left(t+c\right)^{-p}\left\{\ln\left(t+c\right)\right\}^2 \end{bmatrix} dt \tag{A.3.15}$$

The asterisk entries denote symmetry about the trace. The marginal error for each parameter can then be found from Equation (A.3.15) using the following expression.

$$\sigma_{\boldsymbol{\theta}}=\mathrm{tr}\left[\sqrt{J\left(\hat{\boldsymbol{\theta}};S,T\right)^{-1}}\right] \tag{A.3.16}$$

Of the two sequences analysed, the analysis of the full duration of the aftershock sequence with the larger minimum magnitude of completeness yielded the most robust results. It is these results that are therefore adopted in the subsequent declustering procedure. The observed rates of aftershock occurrence and the corresponding optimal distribution found from the MLE technique are shown diagrammatically in Figure A.3.2. It can be appreciated from inspection that the modelled distribution agrees very well with the observed aftershock sequence.

While the fit to the observed aftershock sequence is very good, it should be appreciated that there is a reasonable range of parameter values over which the fit would appear similarly as good. This fact is highlighted in Figure A.3.3 in which the log-likelihood values for a range of parameter values are shown. Figure A.3.3 is essentially a representation of a four dimensional distribution of log-likelihood values; in each contour plot two of three variables of $\boldsymbol{\theta}$ are plotted against the optimal value of the third, i.e. $\ln L\left(\theta_1,\theta_2,\theta_3=\hat{\theta}_{3,\mathrm{MLE}}\right)$.

Because of the relative insensitivity of the log-likelihood values to variations in the parameter values it is desirable to have some external check on the parameters derived. Fortunately, a check can be provided from the analysis of the magnitude-frequency distribution of the aftershock sequence. As has been previously stated, the magnitude-

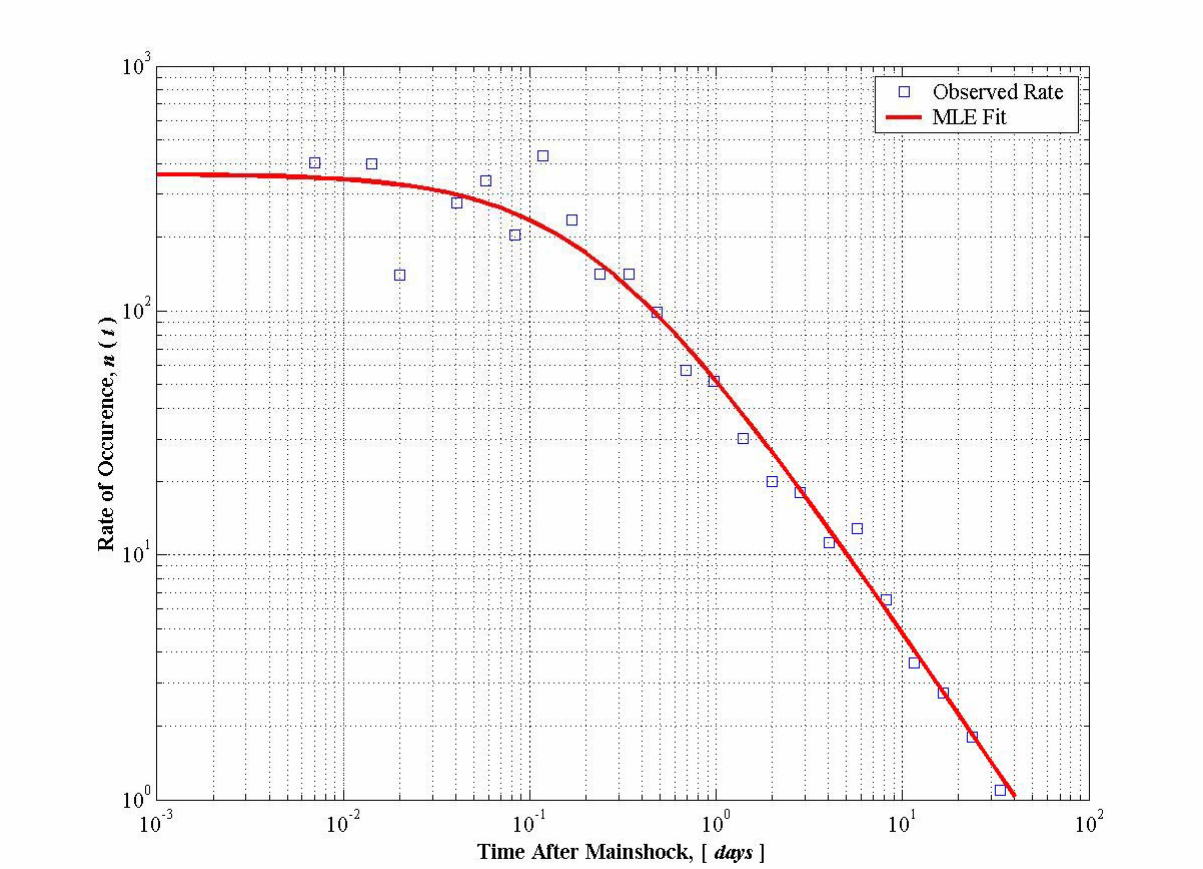

Figure A.3.2: Observed rates of aftershock occurrence for the Inangahua aftershock sequence. Fitted curve is that obtained using the Maximum Likelihood Estimation technique of Ogata (1983).

frequency distribution of the aftershock sequence can be represented by the Gutenberg-Richter relationship. The optimal b-value that describes this distribution can be found for the doubly bounded Gutenberg-Richter relationship (Cornell and Vanmarcke 1969) using the MLE technique of Weichert (1980). In this method, the optimal b-value is found from the solution to the following equation.

$$\frac{1}{2\beta}\left[\frac{\beta\delta}{\tanh(\beta\delta/2)}-\frac{\beta(m_x-m_n)}{\tanh(\beta(m_x-m_n)/2)}\right]=\bar{m}-\frac{m_x-m_n}{2} \qquad \text{(A.3.17)}$$

Here, $\beta=\ln(10)b$, δ is the size of the magnitude bin (0.1 magnitude units), $\bar{m}$ is the mean magnitude of the sequence, and m_x is the maximum possible magnitude of the aftershock sequence, which may be larger than the mainshock magnitude due to the grouping of magnitudes into bins (i.e. m_x is related to the previously defined $m_{\max}$, via $m_x=m_{\max}+\delta/2$). The above formula takes into account the magnitude bin size used in the incremental counts. Note that while previous authors have used MLE procedures to estimate parameters of the Inangahua aftershock sequence (Adams and Lowry 1971; Robinson et al. 1975). These authors used the MLE procedures of either Aki-Utsu (Aki 1965; Utsu 1965) or Page (1968), which are both derived based on the assumption of a continuous magnitude distribution. While in actuality magnitude is a continuous variable,

catalogued magnitudes are recorded at discrete increments. As Bender (1983) points out, Equation (A.3.17) can be recovered from Page's equation,

$$\frac{1}{\beta} = \bar{m} - m_n - \frac{m_x \exp\left[-\beta\left(m_x - m_n\right)\right]}{1 - \exp\left[-\beta\left(m_x - m_n\right)\right]} \tag{A.3.18}$$

provided that Equation (A.3.18) is corrected for the grouping of magnitudes into discrete bins. This modified formula is given in Equation (A.3.19).

$$\frac{1}{\beta} = \bar{m} - m_n - \frac{m_x \exp\left[-\beta\left(m_x - m_n\right)\right]}{1 - \exp\left[-\beta\left(m_x - m_n\right)\right]} - \frac{\delta}{2}\frac{1 + \exp\left[-\beta\delta\right]}{1 - \exp\left[-\beta\delta\right]} \tag{A.3.19}$$

Equation (A.3.19) is easily shown to be equivalent to Equation (A.3.17) once some manipulations have been made.

The optimal b-value found from the above equations must be consistent with the equivalent aftershock parameters found from the Ogata MLE procedure. This condition is satisfied if the b-value found from Equation (A.3.20), from rearrangement of the Modified Omori model, b_{AS}, is the same as that found from the Gutenberg-Richter relationship.

$$b_{AS} = \frac{\log_{10} K}{m_{MS} - \Delta m - m_n} \tag{A.3.20}$$

It is found that this condition is satisfied very well as can be seen from the final parameters given below.

$$\hat{K} = 63.68 \pm 6.10$$
$$\hat{c} = 0.210 \pm 0.050$$
$$\hat{p} = 1.117 \pm 0.030$$
$$b\left(\hat{K}, m_{MS}, \Delta m, m_n\right) = 0.893 \pm 0.021$$
$$\hat{b}_{GR,MLE} = 0.894 \pm 0.052$$

The MLE fit to the doubly-bounded Gutenberg-Richter relationship is shown in Figure A.3.4. Note that the b-value and p-value found in this study are respectively lower and higher than those found in previous studies (Adams and Lowry 1971; Robinson et al. 1975).

The detailed analysis described above is warranted in the case of the Inangahua aftershock sequence because of the large impact that the event had on the regional seismicity. In addition, the events of this sequence were well defined. We do not have the luxury of having such detailed information regarding the aftershock sequences of

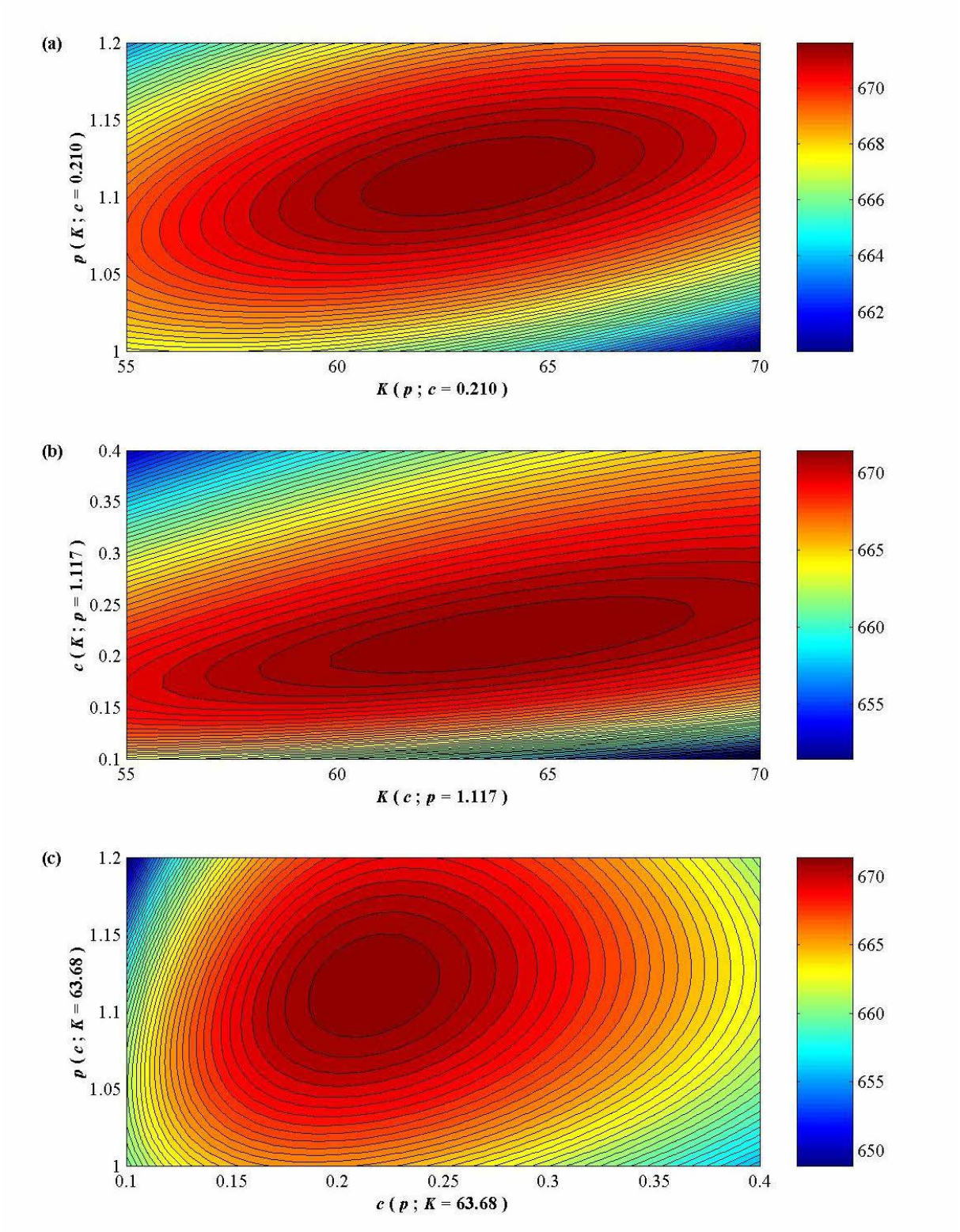

Figure A.3.3: Contour plots of the MLE determined parameters of the aftershock sequence. Plots show the calculated Log-Likelihoods for a range of parameter values. Panel (a) plots *K* against *p*, panel (b) plots *K* against *c*, and panel (c) plots *p* against *c*.

other events occurring in the region over the period of instrumental observation. Therefore, in order to decluster the entire catalogue, the parameters derived above are used for those events defined as being part of the Inangahua sequence only. For all other events the generic parameters derived for use in New Zealand by Eberhart-Phillips (1998) are used. These parameters relate to the model proposed by Reasenberg and Jones (1989) given in Equation (A.3.21) below.

$$n(t,m) = \frac{10^{a+b(m_{MS}-m)}}{(t+c)^{p}} \qquad \text{(A.3.21)}$$

The generic values of the parameters, $\boldsymbol{\theta} = \{a, b, p, c\}$, for this model are given below. The above model with these parameters is that used for the declustering process.

$$a = -1.66$$
$$b = 1.03$$
$$p = 1.02$$
$$c = 0.03$$

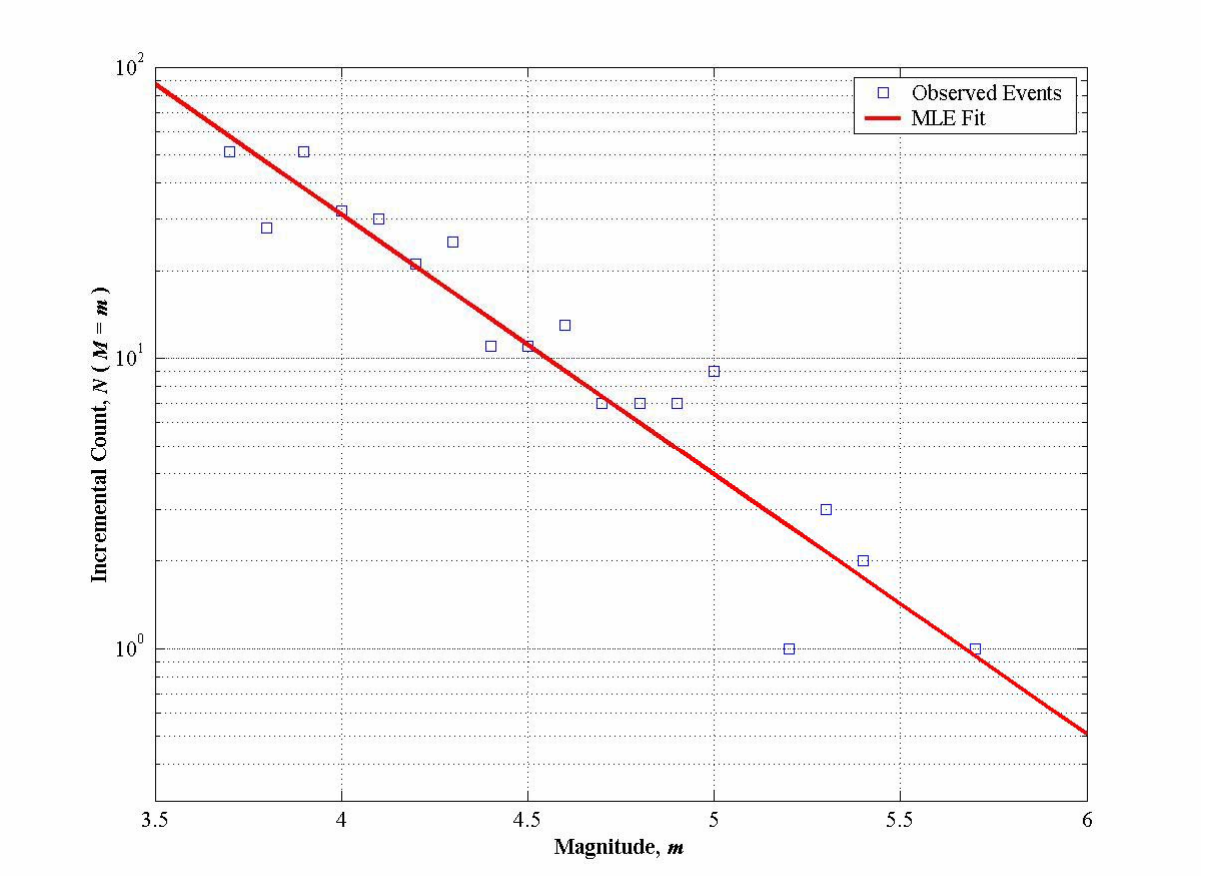

Figure A.3.4: Incremental magnitude-frequency distribution of the Inangahua aftershock sequence. Fitted curve is that obtained from the Maximum Likelihood Estimation technique of Weichert (1980).

A.3.3.3. Spatial Dependence

As well as a temporal dependence, a spatial dependence must be incorporated into the declustering procedure. The Reasenberg (1985) method adopts an interaction radius that has a physical basis, but then scales this using an arbitrary factor, R_{fact}. This interaction radius is meant to define the spatial region in which the occurrence of one earthquake may influence the occurrence of a subsequent event. The interaction radius adopted for this analysis gets its physical basis from the Kanamori and Anderson (1975) relation for Seismic Moment.

$$M_0 = \frac{16}{7}\Delta\sigma a^3 \tag{A.3.22}$$

In Equation (A.3.22), a is the radius of a circular rupture surface. For a particular event we can estimate the stress drop, $\Delta\sigma$, of the event using another expression in the Kanamori and Anderson (1975) paper coupled with some more recent work by Dowrick and Rhoades (2004). For a rectangular fault plane, the equivalent expression to that above is given by Equation (A.3.23).

$$M_0 = \frac{\pi(\lambda + 2\mu)}{4(\lambda + \mu)}\Delta\sigma W^2 L \tag{A.3.23}$$

The Lamé constant, λ, can be related to the shear modulus, μ, and Poisson's ratio, ν, via the following expression in Equation (A.3.24).

$$\lambda = \frac{2\mu\nu}{1-2\nu} \tag{A.3.24}$$

Then, noting that for the widely adopted value of Poisson's ratio for rock, $\nu = 0.25$, $\lambda = \mu$, the expression for Seismic Moment for a rectangular fault plane can be given as in Equation (A.3.25).

$$M_0 = \frac{3\pi}{8}\Delta\sigma W^2 L \tag{A.3.25}$$

Consequently, if one knows, or can estimate, the dimensions of the fault plane, a value of the stress drop may be obtained for earthquakes in the New Zealand context. Dowrick and Rhoades (2004) provide dimensions of the fault rupture area for the Inangahua event allowing a stress drop of approximately $\Delta\sigma = 3.5$ MPa (35 bar) to be obtained. The interaction radius for the Inangahua event that is used in the declustering algorithm can therefore be determined via the following expression.

$$a = \left(\frac{7}{16}\right)^{\frac{1}{3}} \left(\frac{M_0}{\Delta\sigma}\right)^{\frac{1}{3}} \tag{A.3.26}$$

For general implementation of the declustering algorithm for events other than the Inangahua event, a stress drop was assumed and the interaction radius was left as a magnitude dependent parameter.

The selection of an appropriate value for R_{fact} was determined by considering the declustered catalogue determined for various values of R_{fact}. After declustering, the cumulative number of events was plotted with respect to time for the varying levels of completeness in the New Zealand catalogue†. The declustering algorithm is actually quite insensitive to this spatial parameter but reasonable results were able to be found using a relatively large value of $R_{fact} = 30$.

A.3.3.4. Application of the Reasenberg Algorithm

Once the relations describing the spatio-temporal correlations between earthquake events for the region were found the Reasenberg (1985) algorithm could be applied. The method can be summarised briefly as follows.

The probability of observing x earthquakes during an interval $(t, t+\tau)$ is given by a time dependent Poisson process. The time dependent aftershock rate that is used in this relation is that derived in the previous sections, i.e. $n(t)$. The relevant time dependent Poisson model is given below in Equation (A.3.27).

$$P(x, n(t), \tau) = \frac{(n(t)\tau)^x \, e^{-n(t)\tau}}{x!} \tag{A.3.27}$$

The probability of observing one or more events in the same interval is therefore given by Equation (A.3.28).

$$\begin{gathered} P = \sum_{x=1}^{\infty} P(x, n(t), \tau) = 1 - P(x = 0, n(t), \tau) \\ \therefore P = 1 - e^{-n(t)\tau} \end{gathered} \tag{A.3.28}$$

One can therefore solve the above expression for τ to obtain the time window in which you would be P likely to observe an event. In this analysis, P was set at 95%.

$$\tau = \frac{-\ln(1-P)}{n(t)} \tag{A.3.29}$$

† This procedure is demonstrated for one of the initial and declustered seismicity catalogues in Figure A.3.1.

Given this time window, and an interaction radius, one can then say that following a mainshock, if any subsequent events occur within τ days, and within $R_{fact}a$ km of this mainshock, then one is 95% confident that these events are aftershocks. Dependent events are therefore defined in this context and the base seismicity catalogues have these dependent events removed according to this definition.

Following the lengthy procedure detailed thus far in this chapter twenty separate seismicity datasets were prepared for use in the subsequent PSHA analysis (each dataset corresponding to a different depth redistribution). At the beginning of this chapter it was stated that the overall goal is to derive activity parameters for each of the seismic sources selected in the previous chapter. These activity parameters are determined based upon the observed activity associated with each of the individual sources. One must therefore be able to partition the overall seismicity catalogues between the various sources; the method employed to meet this end is described in the next section.

A.3.4. Association of Earthquakes to Seismic Sources via Bayesian Inference

When conducting a PSHA it is preferable to be able to calculate the hazard at a site due to the contributions from the various seismic sources that are capable of generating ground motions of engineering relevance. The more accurately one can model the spatial locations of seismic sources, the more accurately one is able to ascertain the spatial distribution of the contributions to the hazard at a site. In most tectonically active regions the seismic hazard is most appropriately modelled by considering individual fault sources as well as some spatially distributed background level of seismicity. A model set up in this manner allows the occurrence of large events to be constrained to occur on faults that are thought to be capable of generating such events rather than to entertain the possibility that such events could occur absolutely anywhere within a region. Because these large events are most likely to generate significant ground motions, it is important to define the possible locations of these events as well as possible.

Given knowledge of the typical activity of the various faulting sources, it is also possible to account for the modifications to hazard that would result from the known occurrence of a large recent event, or the known quiescence on a fault that is known to be active. These time dependent probability considerations are discussed in more detail in Chapter 5.

In order to develop a fault source based seismicity model one must firstly be able to define specific active faults within a region, as well as be able to determine the typical seismic activity that is associated with each of the identified fault sources. The issue of identifying the relevant fault sources for the region has been addressed in the previous chapter. The other issue of determining the seismic activity for these sources is the topic of the present discussion. The description of the seismic activity is given in terms of the mean rates at which earthquakes of various magnitudes occur, i.e. a magnitude-frequency relationship for each source must be derived.

In order to derive the required magnitude-frequency relationship for a seismic source one must first have a dataset of events that can be attributed to this particular seismic source. In the case of large events, the relationship with particular faults is relatively well defined due to the large amount of investigation that these events receive. The bulk of recorded earthquakes receive far less attention and their association with particular faults is therefore far more ambiguous. The relevance of these small to moderate events is largely dependent upon their frequency of occurrence and their proximity to the site for which the hazard is being determined. A procedure must therefore be employed that is capable of attributing all the events in a seismicity dataset to an assumed set of seismic sources. Fortunately, a method has recently been developed as a means to this end.

As part of the latest Working Group on California Earthquake Probabilities project (WGCEP 2003), Wesson et al. (2003) used Bayesian Inference to associate earthquake events in the San Francisco Bay area with identified faulting structures in the region. Their procedure, governed by Equation (A.3.30), has been adopted in this study to partition the overall seismicity catalogues to the respective faulting sources identified in Chapter 2 given only the instrumental observations of the position of events.

$$P(F_i \mid O) = \sum_k P(F_i \mid H_k) P(H_k \mid O) \qquad \text{(A.3.30)}$$

Here, $P(F_i \mid O)$ denotes the probability of a particular event occurring on the i^{th} fault given the observation of the position of this event. In order to calculate this conditional probability, the study region is divided up into cubic cells of 1 km dimension. There are on the order of one million such cells, each being defined by its index k. The term $P(H_k \mid O)$ therefore represents the conditional probability that an event occurs in the k^{th} cell, given the observation of this event. The remaining term, $P(F_i \mid H_k)$, represents the probability that an event is caused by the i^{th} fault given that it is observed to occur in the k^{th} cell. The final conditional probability of an event occurring on the i^{th} fault given the observation of that event is therefore found from the summation of the product $P(F_i \mid H_k) P(H_k \mid O)$ over all the cells in the region.

The value of $P(F_i \mid O)$ is determined for each fault in the model for every earthquake in the twenty seismicity catalogues. Each event is consequently attributed to one of the various faulting sources, or the background source, based on the highest probability that is calculated for the sources.

Before one can apply the expression in Equation (A.3.30) one must be able to determine the constituent terms of this expression. The required procedure is outlined below.

The probability that an event is caused by the i^{th} fault given that it is located in the k^{th} cell is a function of the geometry of the assumed fault model and is not dependent upon the particular earthquakes in the catalogue. This probability is calculated using Equation (A.3.31).

$$P(F_i \mid H_k) = \frac{P(H_k \mid F_i)P(F_i)}{\sum_i P(H_k \mid F_i)P(F_i)} \tag{A.3.31}$$

In this equation, $P(F_i)$ is the prior probability that an event in the region occurs on the i^{th} fault. This probability must be assigned on the basis of some very general assumptions regarding fault activity in the region. The most general assumption is that every fault in the region is equally likely of generating an event. Naturally, this is a fairly crude assumption as if it were true then there would be no point in conducting the current analysis in the first place as all sources would be equally likely of generating a given earthquake. However, in the case that this assumption is adopted, $P(F_i)$ is calculated via Equation (A.3.32).

$$P(F_i) = \frac{(1 - P(B))}{N} \tag{A.3.32}$$

Here, N is the total number of fault sources that are assumed in the model of the region and $P(B)$ is the prior probability that an event is the result of background activity rather than the result of a fault source. This prior background probability must be assumed before the analysis is conducted, but the suitability of the assumed value can be checked against the final estimate of this value following the application of the procedure. For the present study, an initial value of $P(B) = 0.40$ is assumed. This assumption is made on a subjective basis but is guided by visual inspection of the spatial distribution of seismicity with respect to the assumed geometry of the fault model.

If the assumption of equal prior probabilities for fault sources is thought to be too crude other options are available. These alternatives include assignment of fault priors on the basis of fault slip rates, moment release rates, and fault areas. However, Wesson et al. (2003) show that the final results are not very sensitive to the method of assigning fault priors that is adopted. In this study, fault prior probabilities are assigned according to a scaling of fault areas. This assumption essentially asserts that the faults that are most likely to generate large events are the fault most likely to generate events of all sizes. The fault prior probabilities are therefore calculated according to Equation (A.3.33), in which A_i denotes the area of the i^{th} fault.

$$P(F_i) = \frac{A_i(1 - P(B))}{\sum_{j=1}^{N} A_j} \tag{A.3.33}$$

The term $P(H_k \mid F_i)$ denotes the probability that an earthquake would locate in the k^{th} cell given that it is generated as a result of activity on the i^{th} fault. In order to determine such a probability the distribution of events about a known fault plane must be considered. Once again, the well defined Inangahua aftershock sequence proves valuable for this purpose. Because the Inangahua event received a significant amount of attention, the spatial location of its fault plane is relatively well defined when compared to other faults in the region (Anderson et al. 1994). While this is more a statement regarding the lack of certainty of the positions and orientations of

assumed fault sources in the region, it also implies that this is the best fault that is available to work with for the purpose of estimating the $P(H_k \mid F_i)$ term. The temporary installation of seismographs that have previously been mentioned also helped to locate the positions of these aftershocks and consequently enable one to consider the distribution of these events about an assumed fault plane.

It is recognised that the fact that an event is regarded as being an aftershock of a particular event in no way implies that it was caused by the same fault, or even has the same mechanism or nature. However, when the positions of the located aftershocks are plotted about the fault plane one can see that the distribution of distances about the fault plane is approximately normal; this distribution along with a fitted distribution, fitted according to a least squares solution using a normal distribution as a model, is shown in Figure A.3.5. The suitability of the normal distribution for modelling this data is clear. The standard deviation of the data is 4.905 km.

Not all of the observed events that are considered in the above figure occur on the Inangahua fault plane, many will have been events triggered on other crustal fissures in the vicinity of the Inangahua fault plane. However, the fact that they are all recognised as being events that are dependent upon activity associated with the Inangahua fault means that the standard deviation found above is an upper bound to that defining the distribution of events about a fault plane. Given that the distribution of events about a fault plane can be modelled in this manner, the

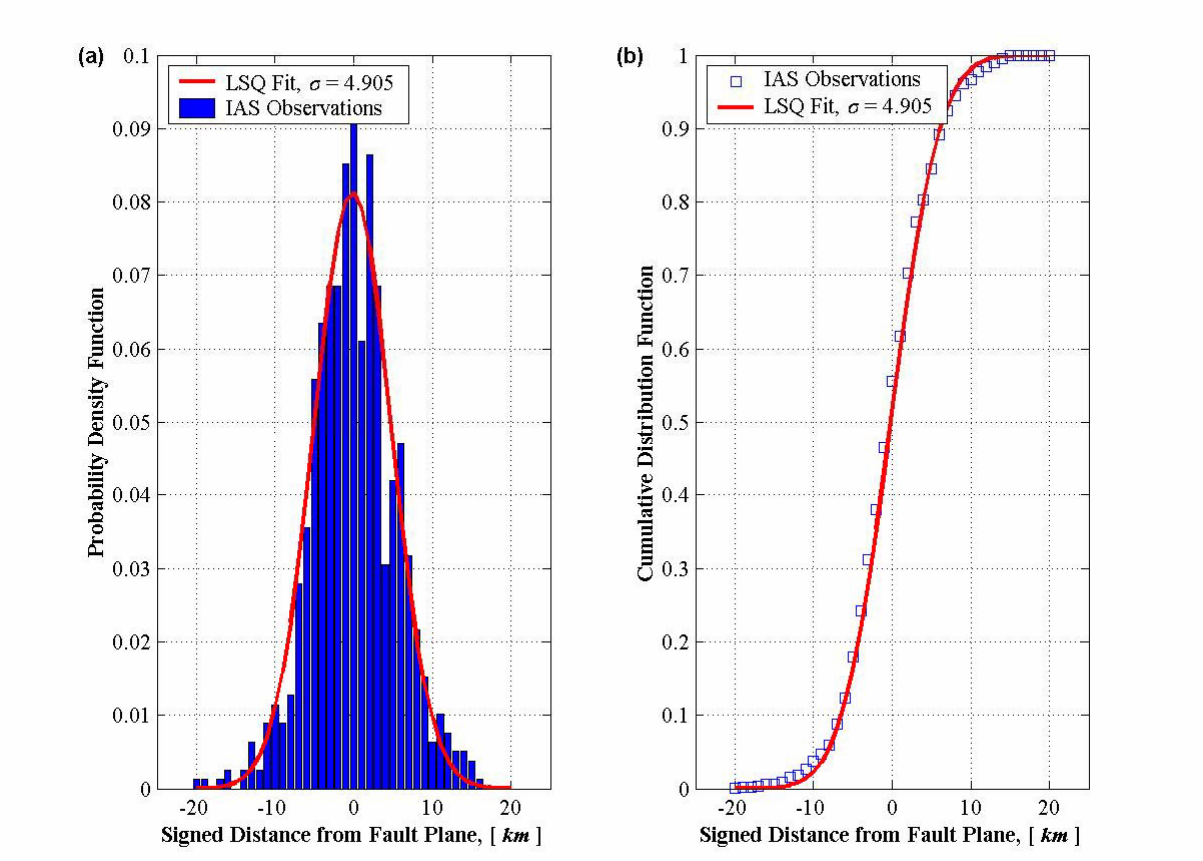

Figure A.3.5: Distribution of events in the Inangahua aftershock sequence about an assumed fault plane. Panel (a) depicts the probability density function while panel (b) shows the associated cumulative distribution function.

probability of an event occurring within a certain distance of a fault plane, $p(r)$, can be modelled using a function having the form of Equation (A.3.34).

$$p(r) = \exp\left[-\frac{r^2}{2\sigma_f^2}\right] \tag{A.3.34}$$

Here, r is the closest distance to the fault plane, and σ_f is the standard deviation of events located about this plane. The term $P(H_k \mid F_i)$ is therefore modelled via Equations (A.3.34) and (A.3.36).

$$P(H_k \mid F_i) = \alpha_i \iiint_{\mathbf{x}\pm\Delta\mathbf{x}} \exp\left[-\frac{x_{ki}^2}{2\sigma_f^2}\right] d\mathbf{x} \tag{A.3.35}$$

In Equation (A.3.35) above, α_i is given by the expression below.

$$\alpha_i = \left(\sum_k \iiint_{\mathbf{x}\pm\Delta\mathbf{x}} \exp\left[-\frac{x_{ki}^2}{2\sigma_f^2}\right] d\mathbf{x}\right)^{-1} \tag{A.3.36}$$

Wesson et al. (2003) tested the sensitivity of their association results to the value of the standard deviation and found their results to not be overly sensitive to this value. This is most likely due to the existence of a trade off between increasing the spatial region of association, and reducing the probability assigned to events in this region. The integral expressions in Equations (A.3.35) and (A.3.36) define a three dimensional probability density with respect to space. If one increases the standard deviation, σ_f, one also increases the extent of the region over which this density function applies, but at the same time, decreases the value of the density at every point in space previously existing in this region. As mentioned before, a value of approximately five kilometres can be regarded as an upper limit to the value of σ_f for instrumental observations in the study region. For the present study a value of $\sigma_f = 3.0$ km was chosen, after trialling other potential values (with an upper limit of 5 km).

The selection of this value is somewhat arbitrary, albeit guided by the result of the consideration depicted in Figure A.3.5. As well as the taking into account the natural scatter of events about a fault plane, we have also lumped a degree of epistemic uncertainty into the parameter as the true scatter occurs about a known fault plane. In this study, the true position of fault planes is uncertain, particularly at the most common depths associated with rupture nucleation. In addition, the location errors of the events in the seismicity catalogue are not constant over time. Rather than trying to formally take these factors into account, the selection of a value of three kilometres is thought to be conservative enough to account for some of the aforementioned uncertainty whilst still favouring a fault source based seismicity model. Using the formulae outlined above, the $P(F_i \mid H_k)$ terms for each fault can be determined. An example of this determination is presented in Figure A.3.6 for the White Creek fault. This

example is given for the row of cells corresponding to a depth of 10 km. Similar spatial distributions would be obtained at other depths with variations coming from the dip of the assumed fault plane and the relative positions of the other fault planes in the vicinity of the White Creek fault.

The focus of the discussion of the Bayesian Inference procedure thus far has been upon probabilistically defining the fault model for the region with a view to attributing observed seismic activity to fault sources. However, a large portion of the regional seismicity cannot be attributed to fault sources and for this purpose a background source is incorporated in the modelling of seismic sources. This source must also have events assigned to it within the framework that is currently being described. The analyst is afforded the means to this end from some of the most fundamental postulates of probability theory.

The term required in order to determine the association of events to the background source is the equivalent to that recently presented above for individual fault sources, namely $P(H_k \mid B)$. Now, the expression describing this conditional probability can be found from the total probability theorem, i.e. the sum of the probabilities of all possible outcomes is equal to one. The relevant equation for the probability of an event locating in the k^{th} cell given that it is generated by the background source is given below.

$$P(H_k \mid B) = \frac{P(H_k) - \sum_i P(H_k \mid F_i) P(F_i)}{P(B)} \tag{A.3.37}$$

Wesson et al. (2003) show that the probability of an event occurring in the k^{th} cell, $P(H_k)$ can be given by the following expression.

$$P(H_k) = \frac{1 - \sum_k \sum_i P(H_k \mid F_i) P(F_i)}{N_{cells}} + \sum_i P(H_k \mid F_i) P(F_i) \tag{A.3.38}$$

Consequently, Equation (A.3.38) may be simplified, and defined in terms of expressions whose definitions have previously been given.

$$P(H_k \mid B) = \frac{1 - \sum_k \sum_i P(H_k \mid F_i) P(F_i)}{N_{cells} P(B)} \tag{A.3.39}$$

At this point the geometrical aspects of the Bayesian Inference procedure have been described. We can therefore move on to discussing how the instrumentally recorded earthquake events in the seismicity catalogues fit into this framework.

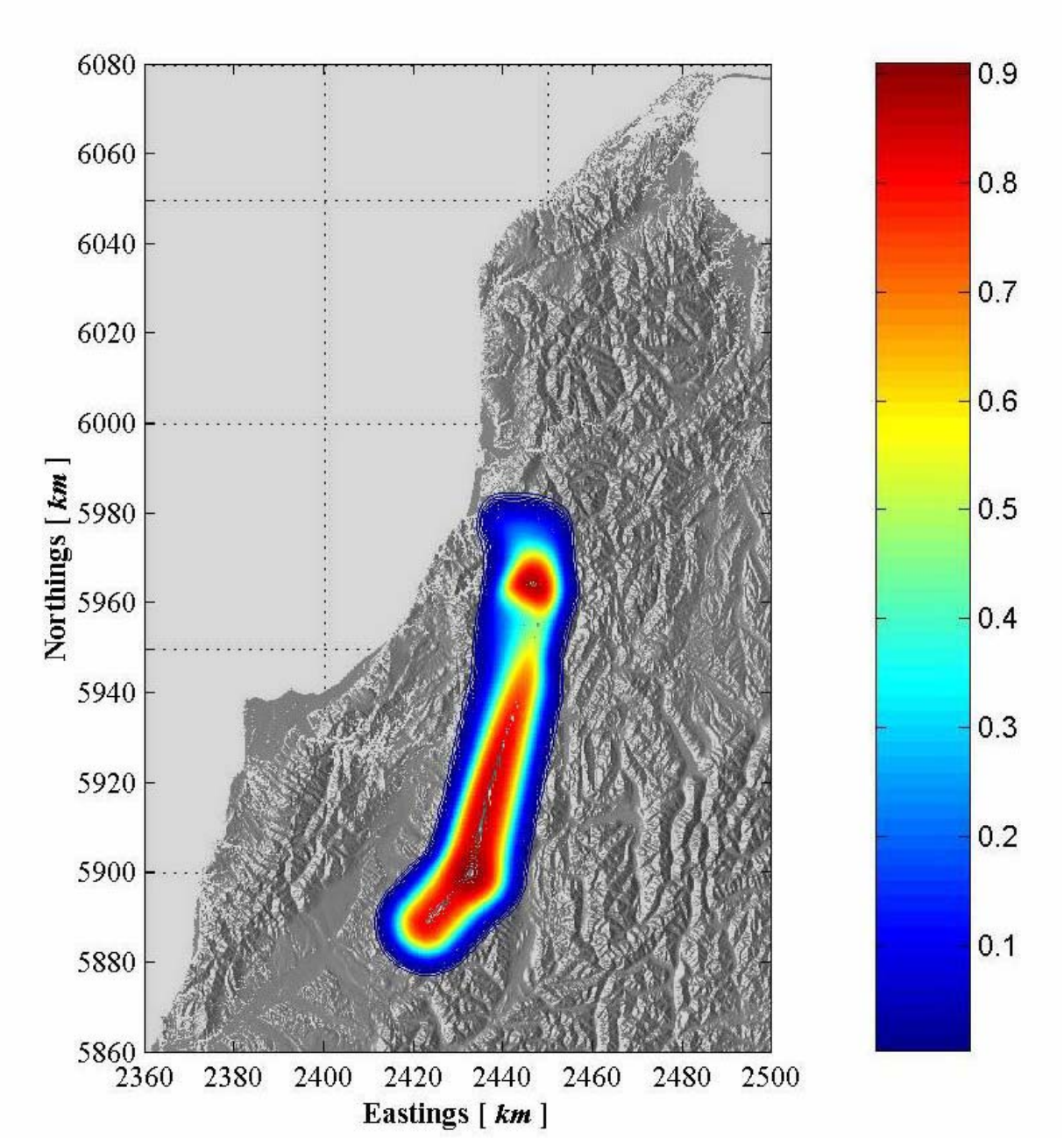

Figure A.3.6: Example of the $P(F_i|H_k)$ term calculated for the White Creek fault. The plotted contours correspond to a depth of 10 km. The Northings and Eastings co-ordinates used in this plot are given in units of kilometres. The effect of the presence of other faults, such as the Glasgow and Lyell Faults, can be seen towards the northern end of the White Creek Fault where the probability contours become perturbed.

Earlier in this chapter the position errors associated with the location of earthquakes in the catalogue were discussed. Making the very reasonable assumption that these errors are normally distributed we note that the three orthogonal error values that are provided for each event define an error ellipsoid. Also, as has already been noted, the error in the vertical direction is commonly larger than those in the Northings or Eastings directions. The probability that the event is located at a particular point in three-space is therefore described by a multivariate normal distribution. This distribution is defined in Equation (A.3.40).

$$p(\mathbf{x}) = \prod_{i=1}^{3} \frac{1}{\sigma_i \sqrt{2\pi}} \exp\left[-\frac{(x_i - \mu_i)^2}{2\sigma_i^2} \right] \tag{A.3.40}$$

If one wished to find the probability that the location of an event was to be found in a particular region of three-space one would simply integrate the above equation over the region in question. This is the procedure that must be undertaken in order to calculate the conditional probability of an event occurring in the k^{th} cell given the observation of that event.

Defining the spatial dimension of a grid cell in a particular direction by $2\Delta x_i$, where $i = 1,2,3$, the probability that an event occurs in the k^{th} cell given the observation of that event is expressed in Equation (A.3.41) below.

$$P(H_k \mid O) = \prod_{i=1}^{3} \frac{1}{2} \left[\operatorname{erf}\left(\frac{x_i^k + \Delta x_i}{\sigma_i \sqrt{2}} \right) - \operatorname{erf}\left(\frac{x_i^k - \Delta x_i}{\sigma_i \sqrt{2}} \right) \right] \tag{A.3.41}$$

In the above equation, x_i^k denotes the position of the centre of the k^{th} grid cell with respect to the i^{th} coordinate direction. The term σ_i represents the error in position of the location of the event, again with respect to the i^{th} direction. The function $\operatorname{erf}(\bullet)$ represents the error function which in turn is formally defined in Equation (A.3.42) below. There is a close association between the error function and the cumulative normal distribution function.

$$\operatorname{erf}(z) = \frac{2}{\sqrt{\pi}} \int_0^z \exp\left[-t^2 \right] dt \tag{A.3.42}$$

As Wesson et al. (2003) noted, the principal axes of the location solution will not coincide with the geographically defined coordinate directions, so in order to be completely thorough a transformation of coordinates would need to be applied so as to accurately asses the above probability. However, in the New Zealand seismicity catalogue, position errors are given with respect to the geographic coordinates, longitude, latitude and depth. Therefore, provided the conversion to New Zealand Map Grid coordinates is performed, in this study Equation (A.3.41) can be applied directly.

The above procedure was performed for each of the twenty depth redistributed seismicity catalogues and therefore twenty realistic reduced datasets were obtained for each of the seismic sources in the fault model. These datasets can then be analysed to derive a magnitude-frequency relationship for each of the seismic sources in the region. The procedure required to obtain these magnitude-frequency distributions is detailed in the next section.

The results of the final application of the Bayesian Inference procedure will be realised when the magnitude-frequency distributions are determined later in this chapter. For now however, the results of the Bayesian Inference procedure will be given in terms of the average number of events that are allocated to the various seismic sources. These results are summarised in

Table A.3.3. The values presented in this table represent the statistics obtained from the processing of the twenty individual datasets created as a consequence of the depth distribution procedure previously outlined. It will be noted that the Alpine Fault is not included in this table. The reason for this is that the Alpine Fault is treated as a Characteristic fault source in the probability calculations. The activity rate of large events associated with this source are already well constrained.

Table A.3.3: Summary of the association of regional seismicity to the modelled seismic sources for the Buller region. $N_{i,\min}, N_{i,\max}, N_{i,50}, N_{i,\mathrm{mean}}$ represent the minimum, the maximum, the median, and the mean number of events associated with the i^{th} seismic source, and σ_{Ni} is the standard deviation of the number of events associated with the i^{th} seismic source. The $\%_{i,\min}, \%_{i,\max}, \%_{i,50}, \%_{i,\mathrm{mean}}, \sigma_{\%i}$ headers are simply the previously defined values expressed as a percentage of the total number of events in a given seismicity catalogue.

Seismic Source	$N_{i,\min}$	$N_{i,\max}$	$N_{i,50}$	$N_{i,\mathrm{mean}}$	σ_{Ni}	$\%_{i,\min}$	$\%_{i,\max}$	$\%_{i,50}$	$\%_{i,\mathrm{mean}}$	$\sigma_{\%i}$
Kongahu Fault	57	66	60.5	60.60	2.87	4.67	5.41	4.96	4.99	0.23
Glasgow Fault	89	103	97.5	96.75	3.34	7.34	8.44	8.04	7.97	0.27
Inangahua Fault	83	114	102	101.30	6.73	6.82	9.43	8.42	8.34	0.55
Lyell Fault	55	65	61	60.45	2.21	4.56	5.32	5.00	4.98	0.17
White Creek Fault	47	58	53	53.20	2.53	3.89	4.77	4.39	4.38	0.21
Mt. William Fault	55	71	67.5	66.00	4.63	4.55	5.89	5.54	5.44	0.39
Cape Foulwind Fault	22	29	26	25.90	2.05	1.80	2.39	2.15	2.13	0.17
Maimai Fault	33	38	35	35.05	1.36	2.70	3.11	2.89	2.89	0.11
Kohaihai Fault	57	70	63	63.30	4.21	4.72	5.80	5.19	5.21	0.35
Wakamarama Fault	10	18	15	14.80	2.12	0.83	1.47	1.24	1.22	0.17
Karamea Fault	35	48	44.5	43.95	3.07	2.87	3.97	3.67	3.62	0.26
Pikikiruna Fault	20	26	23.5	23.35	1.50	1.66	2.16	1.93	1.92	0.13
Pisagh Fault	13	18	16	15.85	1.39	1.06	1.47	1.32	1.31	0.11
Background Source	540	567	552	553.75	7.93	44.67	46.51	45.48	45.60	0.53

As can be seen from Table A.3.3 the initial assumption of a background prior probability, $P(B)$, of 40% is reasonable given that the posterior background probability is typically about 45%. One can also see the value of regarding a suite of declustered catalogues rather than simply applying the redistribution procedure of McGinty (2001) once and then proceeding. This point is supported by the range in the number of events assigned to the various sources over the twenty considered catalogues. As a general rule, it is fair to say that as the dip of the fault plane becomes steeper, the standard deviations become smaller. This finding makes perfect sense when one recalls that the effect of the depth redistribution only effects the vertical positioning of event locations. One would expect no difference in the association of events for multiple redistributed datasets if one was dealing with a purely vertical strike-slip fault†.

Given that the Bayesian Inference procedure has now allowed the total datasets to be partitioned between the various seismic sources in the region the magnitude-frequency relationships that characterise the activity of these sources can be determined. This determination is the topic of the following section of this chapter.

A.3.5. Magnitude-Frequency Relationships for Seismic Sources

"Statistics looks backwards in time while probability looks forward. Both meet in the present, and it is there that a connection must be made" (Elms 1998). This assertion is an important one when selecting the form of the magnitude-frequency relationships to be used in the PSHA. So far in this chapter a method for obtaining seismicity datasets related to individual seismic sources has been presented. The sizes of the datasets thus created are not large, particularly for some sources (see Table A.3.3). Therefore, if the form of the magnitude-frequency relations were selected based purely on this data then there is no guarantee that the trends applicable to the observed data would accurately predict future trends of activity for these same sources. It is therefore desirable to select a model that has demonstrated the ability to predict the magnitude-frequency behaviour of seismic sources and then to obtain the parameters of such a model based upon the datasets obtained.

Two primary candidate models come to mind for this purpose, the Gutenberg-Richter model (Ishimoto and Iida 1939; Gutenberg and Richter 1944) and the Characteristic Earthquake model (Schwartz and Coppersmith 1984). There is a lot of evidence to support both models, and a great deal of controversy regarding which of the two is the most appropriate for application in a given situation (see for example Wesnousky 1994; Kagan 1996; Wesnousky 1996). It should be noted from the outset that both of these models are essentially empirical statistical models; there is no generally accepted physical basis to either of them. Additionally, there are many other models that may be employed, and that may produce a stronger statistical fit to the data. Many of these models are described in Utsu (1999) and almost all of them require the specification of more parameters than the Gutenberg-Richter model and at least as many parameters as the Characteristic model. Given the size of the datasets for each source, the requirement of specifying these additional parameters becomes restrictive.

† Provided of course, that other faults having non-vertical dips were not in the vicinity of the hypothesized vertical fault.

Both the Gutenberg-Richter and Characteristic models share many common attributes. For small to moderate sized events the two distributions are the same and are based upon the general form of the Gutenberg-Richter relation. The original form of this relation is typically expressed by Equation (A.3.43) below,

$$\log_{10} N(m) = a - bm \qquad \text{(A.3.43)}$$

where $N(m)$ is the number of events of magnitude equal to or greater than m occurring throughout the observation period, a is the number of events of $m \geq 0$, and is termed the activity parameter, while b defines the relative frequency of occurrence between events of differing sizes. Ishimoto and Iida (1939) first expressed this relationship in terms of felt intensities before Gutenberg and Richter (1944) expressed the above equation in terms of magnitudes, and used it to characterise observed Californian seismicity. In their initial study, Gutenberg and Richter found values of b close to 1 over a reasonable range of magnitudes. Since this time, Equation (A.3.43) has been applied to many other regions of the world, at many different geometric scales and magnitude ranges, and only small departures from a b value of 1.0 have been observed (see, for example, amongst many others Rundle 1989; Frohlich and Davis 1993; Kagan 1999; Utsu 1999; Wesnousky 1999; Godano and Pingue 2000; Marzocchi and Sandri 2003).

The basic form of the Gutenberg-Richter relationship given in Equation (A.3.43) is usually modified for use in general applications in two fundamental ways. Firstly, the range of magnitudes is restricted so that only events having a magnitude larger than some particular value are considered, and secondly, the form of the relation at large magnitudes is modified. This modification at large magnitudes constitutes the difference between the general Gutenberg-Richter model and the Characteristic model. The nature of these two modifications is discussed in more detail below.

A.3.5.1. Modification of the General Gutenberg-Richter Model at Low Magnitudes

There are four generic issues to address in regard to this lower bound modification. Firstly, is there some lower physical limit to the size that an earthquake, in the most general sense of the expression, may possess? Secondly, does the power law scaling of earthquake sizes break down at some low level of magnitude? Thirdly, and irrespective of the previous two points, what is the smallest size earthquake that the national seismic network can consistently, and accurately, detect? And finally, what is the magnitude of the smallest size earthquake that is capable of generating ground motions large enough to cause damage to engineered structures?

Each of these issues, particularly the first three, has attracted considerable attention from the research community as advances in technology have enabled the acquisition, and analysis, of data over broader and broader ranges. Despite the quantity of research each issue remains one of contention.

For the purposes of the present work, the first issue of a theoretical lower limit on the size of magnitudes is of little practical relevance as seismic events at the scales in question are not capable of generating ground motions of interest. The research does have some relevance however when it is used to support the selection of various models, or the making of certain assumptions. Currently, magnitudes as low as -3 can be detected in places such as deep mines where the background noise levels are very low. Events of this size correspond to source dimensions of 1m or less (von Seggern et al. 2003). There is no reason to suspect that the limit of earthquake size will not relate to microscopic dislocations at its minimal limit. All such dislocations must release energy, and some of this energy will inevitably manifest in the form of vibrations, i.e. earthquakes.

The second issue however, is of much greater relevance. Various researchers (Abercrombie and Brune 1994; Abercrombie 1995; 1996; von Seggern et al. 2003) have given evidence to support the validity of the power-law scaling to very small magnitudes. However, there also exists evidence to the contrary (Aki 1987; Dieterich 1992; Knopoff 2000). The emergence of the concept of Self-Organized Criticality (SOC) (Bak et al. 1988; Bak and Tang 1989) has provided an elegant theoretical framework with strong coupling to many other physical phenomena exhibiting power law scaling. Within this framework, there is no reason to suspect departure from power law scaling until spatial scales on the order of particle diameters. If however, SOC fails to adequately model real physical processes, as some evidence purportedly demonstrates (Knopoff 2000), then one may find that observed departures from power law scaling in instrumental catalogues are more than artefacts of the inability to detect seismic events and may relate to some real physical mechanism. The model of Self Organised Criticality will receive further attention later in this section. The general consensus however, is that the Gutenberg-Richter relation is applicable to very low magnitude levels.

The issue of the smallest magnitude able to be consistently detected for the New Zealand seismic network is of direct relevance to this work. This lower level of completeness has decreased as more instruments have been installed across the country. Typically, large scale upgrades have occurred at certain times that enable one to partition the total catalogue into various intervals of completeness. These levels of completeness have already been described and were summarised earlier in Table A.3.2. The levels of completeness for the New Zealand catalogue are much larger than the limits imposed by the previous two issues discussed above.

The last of the four issues mentioned above is perhaps the most important issue to consider in the present work, and is an issue that has received surprisingly little attention from the research community. As will be demonstrated later, when conducting a Probabilistic Seismic Hazard Analysis (Cornell 1968), the probabilistic contributions to ground motion exceedances at a particular site are calculated for all magnitudes above a certain minimum size. Therefore, the numerical values assigned to seismic hazard for a site are directly related to the selection of the minimum magnitude.

There are several issues relating to the selection of the minimum magnitude, some of which are discussed by Bender and Campbell (1989). One reason for there not being universally accepted values for this parameter is that the value chosen should be problem specific. Whether or not a certain size event should be considered or not depends upon the structure for which the assessment is being undertaken. The selection of the most appropriate value of the minimum magnitude will receive further attention in Chapter 5. Until then however, it

will suffice to say that almost all potential magnitude-frequency models that are considered in this work are equally applicable for any choice of minimum magnitude.

Given the above considerations, no distinction can be made between the Gutenberg-Richter and Characteristic models based upon considerations of the lower magnitude limit. The limit that is imposed in determining the parameters of the models will coincide with the completeness levels of the New Zealand earthquake catalogue. The actual modification that is made to the relation is a simple truncation of the model at the lowest magnitude considered. Consequently, the probability distributions related to this curtailment need to be normalised to ensure that the total probability theorem is not violated.

A.3.5.2. Modification of the General Gutenberg-Richter Model at Large Magnitudes

The modification that is made over the domain of large magnitudes represents the point of departure of the Characteristic model from the Gutenberg-Richter model. Schwartz and Coppersmith (1984) considered paleoseismic information regarding the timing of large earthquakes in the Wasatch and San Andreas Fault zones. They found evidence for recurrence intervals for large magnitudes that significantly exceeded the rates expected from the extrapolation of the Gutenberg-Richter relation to the equivalent magnitudes of the large events. Since that time, more evidence has been found of similar behaviour leading some authors, such as Wesnousky (1994), to postulate that this behaviour is more representative of the magnitude-frequency nature of earthquakes from fault sources. However, there are also many examples where faults do not exhibit this behaviour (Yeats et al. 1997; Grant 2002).

One of the arguments presented in support of a Characteristic fault model is that the Gutenberg-Richter relation that is commonly observed is the result a huge number of Characteristic earthquake sources, each relating to varying spatial scales, acting together (Wesnousky 1994; Turcotte 1997; Turcotte and Malamud 2002). Within this framework, a fractal distribution of earthquake faults is required in order to reproduce the Gutenberg-Richter relation. Bak (1996) however, highlights that the recurrence intervals estimated for these large events are usually based upon a very small dataset of a few points at most and that inferences made with respect to departures from power-law scaling are more to do with the incompleteness of the earthquake data than any real physical process.

An obvious way to determine whether the Characteristic model is more appropriate for modelling future earthquake occurrence than the Gutenberg-Richter relation is to consider the datasets obtained from the seismicity procedures outlined above. However, the datasets are far too incomplete at large magnitudes to provide any insight into the problem. The other source of information is from paleoseismic investigations, but as has been mentioned in the previous chapter, very little data exists from such studies. The information that is available does not agree with the Characteristic model as the tentative rates of large earthquake occurrence on the White Creek and Inangahua faults, based upon the only paleoseismic information available for the region, are lower than the rates found from the extrapolation of small magnitude occurrence, rather than larger.

Previously, it was implied that the Characteristic model requires more parameters to define the recurrence rates at the upper magnitude ranges. This is true, but these parameters are usually provided by geologic information rather than from statistics. In the case where geologic information does not exist, as in this case, it is still possible to employ the Characteristic distribution by making some assumptions based upon the form of Characteristic models for faults where data are available (Schwartz and Coppersmith 1984; McGuire 2004). The lack of data available in the present study does not therefore preclude the use of the Characteristic model.

Again, regardless of which model is finally adopted, the probability distributions must be normalised in order to satisfy the total probability theorem. The normalisation process for the Characteristic model must be done on a case by case basis as the magnitude, and the distribution of the magnitude, of the annual rate at large magnitudes will vary depending upon the fault source in question. For the Gutenberg-Richter relation however, the appropriate normalisation is defined by Cornell and Vanmarcke (1969). The Gutenberg-Richter relation under this condition is referred to as the doubly bounded Gutenberg-Richter relation (i.e. Kramer 1996).

Returning now to the discussion of model selection; it is appropriate to examine any existing physical theories that might help distinguish between the potential models for the magnitude frequency relationships. Previously it was stated that both models have empirical foundations and limited supporting physical theory. There are some theoretical models of earthquake recurrence processes that are relevant however and these are discussed very briefly below.

A.3.5.3. Elastic Rebound, Self-Organized Criticality, and Intermittent Criticality

Reid (1910) proposed the Elastic Rebound Theory after witnessing the effects of the 1906 San Francisco Earthquake. The essence of his theory was that strain energy is accumulated in the crust in a gradual manner and then released when this stored energy exceeds some threshold in an abrupt fashion. This abrupt release of strain energy is manifest as an earthquake. The mechanisms causing this accumulation of strain energy cannot have been thoroughly understood at the time however as it was only at a similar time that the first public thoughts on continental drift were aired. Even following Wegener's (1924) publication of the seminal work on continental drift the notion of plate tectonics as the fundamental driving force behind earthquakes was not accepted until approximately the 1960's.

Given this new theory of the driving force behind earthquakes coupled with the Elastic Rebound Theory, the concept of an earthquake cycle was strengthened and scientists began to believe that perhaps earthquake occurrence, far from being an act of God, may be predictable. That is, at least, quasi-predictable given knowledge of the occurrence of previous large events at some position. This line of thinking continued to develop and reached its climax in the 1980's with the seismic gap hypothesis. However, this hypothesis has been unable to produce reasonable predictions in even the most apparently favourable conditions (Bakun and Lindh 1985).

Now, over the last 15 years or so the question of how predictable earthquakes really are has resurfaced with renewed vigour. There now exist opinions spanning the entire spectrum from those who firmly believe that earthquakes may be predicted to quite significant resolution, to those who argue that the very nature of earthquakes precludes prediction. A central question of the current debate resides over whether or not earthquakes are an example of a self-organised critical phenomenon, whether they are an intermittently critical phenomenon, or whether they are neither. Supportive, although potentially subjectively selected, evidence appears to be mounting for all camps.

While the purpose of a typical PSHA is not to predict specific events, the nature of earthquake occurrence is fundamental to assumptions that are made regarding the occurrence of events and whether or not historical evidence of earthquake occurrence can be extrapolated, in any formal sense, into the future. For this reason it is important to at least address the current state of the art in this research and describe where the methodology eventually adopted sits with respect to these recent, and constantly developing, theories.

The two primary competing theories are self-organized criticality (Bak et al. 1988; Bak and Tang 1989) (SOC), and essentially a theory going by the names of intermittent criticality, critical point theory, or accelerating moment release[†] (Jaumé and Sykes 1999; Sammis and Smith 1999; Bowman and Sammis 2004). As well as these two main theories there are also others that branch from these, such models include the ETAS model (epidemic-type aftershock) (Ogata 1989) and the more recent EEPAS (every earthquake a precursor according to scale) (Evison and Rhoades 2004; Rhoades and Evison 2004).

In terms of adding weight to either the Gutenberg-Richter or Characteristic models, SOC is very much in line with Gutenberg-Richter, and intermittent criticality is somewhere in between the two depending upon the nature of the 'intermittent' part of the model. The Elastic Rebound Theory discussed earlier is more in line with the Characteristic model, particularly for the occurrence of large events.

A.3.5.4. Final Model Selection

Given all of the considerations presented above the doubly bounded Gutenberg-Richter relationship of Cornell and Vanmarcke (1969) was selected as the model for the general fault and background sources in the region. This is a very well known, and frequently used, relationship for which sound methods exist for the estimation of its defining parameters. Over almost the entire magnitude range the selection of this model is consistent with SOC. However, by introducing the upper bound on the size of magnitudes a given fault source may generate the model departs from SOC, as in pure SOC the upper bound on magnitude that we observe is a statistical artefact of a short observation period (Bak 1996). Given that the datasets for the fault sources are not complete, adopting this assumption of the Gutenberg-Richter relation (that is consistent with SOC) allows the observations of the seismicity at low to moderate magnitudes to be extrapolated to higher magnitudes. The choice of this model also

[†] Each of these theories is slightly different, but they each differ from self-organised criticality in essentially the same ways.

agrees with the very limited paleoseismic information that is available (Berryman 1980). While the complete doubly bounded Gutenberg-Richter relationship has not been derived from any physical basis, the general Gutenberg-Richter relation has been derived from a physical basis, albeit after making some potentially prohibitive assumptions (i.e. Rundle 1989). In further support of its selection, the doubly bounded Gutenberg-Richter relation has also been shown to be the natural result of the maximum entropy principle (Berrill and Davis 1980; Dong et al. 1984).

The discussion on this model selection presented in the above text is considerable. The eventual outcome is to adopt essentially the most common, and most simple, model used in modern PSHA. However, it was felt prudent to demonstrate that the selection of this model was not arrived at lightly. The potential impacts that the use of this model may have on the final hazard estimates, and the assumptions that its use entails, are appreciated.

The probability density function for the doubly bounded Gutenberg-Richter relationship is presented below in Equation (A.3.44).

$$f_M(m) = \frac{\beta \exp\left[-\beta(m - m_n)\right]}{1 - \exp\left[-\beta(m_x - m_n)\right]} \tag{A.3.44}$$

The corresponding cumulative distribution function is given in Equation (A.3.45).

$$F_M(m) = \frac{1 - \exp\left[-\beta(m - m_n)\right]}{1 - \exp\left[-\beta(m_x - m_n)\right]} \tag{A.3.45}$$

The closely associated cumulative complementary distribution function is given below in Equation (A.3.46).

$$G_M(m) = 1 - F_M(m) \tag{A.3.46}$$

From the equation above, the total annual number of events of magnitude greater than some minimum magnitude can be obtained by multiplying the cumulative complementary function given above by the rate of occurrence of events greater than the minimum magnitude. This concept is formalised in Equation (A.3.47) below.

$$N(m) = \nu_{m_n} G_M(m) \tag{A.3.47}$$

The methods used to estimate the parameters for this distribution are presented in the following section.

A.3.6. Maximum Likelihood Estimation of Parameters of the Doubly Bounded Gutenberg Richter Distribution

The estimation of the optimal parameters to describe the magnitude-frequency characteristics of a sample of an earthquake catalogue was briefly discussed earlier when considering the distribution of magnitudes in the Inangahua aftershock sequence. Here, the issues related to the selection of the optimal maximum likelihood estimation procedure are discussed more fully.

The discussion that follows is primarily concerned with the estimation of the b-value as the maximum likelihood estimate of the rate of activity (the a-value, or its equivalent) is simply the total number of events observed throughout the period of observation.

Many approaches to estimating the *b*-value of the Gutenberg-Richter relation have been proposed over the years, many of these are summarised in Marzocchi and Sandri (2003). Least squares fitting procedures have been employed on numerous occasions despite the inappropriateness of such an approach having been highlighted by Weichert (1980). A generalised least squares estimation procedure that performs far better than its ordinary least squares counterpart was presented by Guttorp (1987). This method, while still theoretically inferior to MLE techniques, can be more readily applied to distributions for which the MLE solutions are not available. Methods have also been proposed that account for the various uncertainties inherent in the data. Typically, each event in the catalogue is assumed to be a singular point whereas in reality there is a considerable uncertainty associated with many magnitude estimates. The case of uniform magnitude uncertainty across the dataset was derived by Tinti and Mulargia (1985). This finding gave insight into the effect that these magnitude errors might have on the parameter estimates but was not overly useful in a practical sense as the errors in the magnitude estimates are seldom uniform throughout a seismicity catalogue. A more complete derivation concerning individual magnitude uncertainties was presented by Rhoades (1996). However despite its completeness, this method has not been implemented in many studies since its presentation. This is probably in large part due to the added complexity that is involved in the model when compared to methods such as that of Weichert (1980). As well as accounting for the uncertainties in the data, attention has also been given to the resulting error in the prediction of the *b* value (i.e. Weichert 1980; Shi and Bolt 1982; Bender 1983).

Maximum Likelihood Estimation (MLE) techniques were independently developed for the purpose of selecting parameters for magnitude-frequency distributions by two researchers over forty years ago† (Aki 1965; Utsu 1965). In both of these pieces of work the MLE formulae were derived with respect to the unbounded Gutenberg-Richter relationship, i.e. the distribution defined by Equation (A.3.43). The optimal b-value may be found, via the optimal value of β that satisfies the following equation.

$$\frac{1}{\beta} = \bar{m} - m_n \tag{A.3.48}$$

† Utsu actually arrived at this result via the method of moments (see Utsu, 1965 and 1999)

Here, $\beta = b\ln(10)$, and $\bar{m}$ is the average magnitude of the earthquakes in dataset being considered with magnitude greater than, or equal, m_n, the minimum magnitude that is considered in the dataset. Equation (A.3.48) is derived assuming that magnitude is a continuous variable that may take on any real value equal to or above m_n. Ideally, this is true, but seismologists are only able to routinely determine the value of magnitudes to two decimal places at best. For most catalogues the resolution of magnitudes assignment is 0.1 magnitude units in recent times, and worse than this for large spans of the instrumental records of earthquake activity. Consequently, an adjustment to Equation (A.3.48) needs to be made to account for the bias that is inevitably introduced into the estimation of the average magnitude.

The power law scaling of earthquake magnitudes means that there should be many more events observed having true magnitudes in the lower half of any magnitude increment than in the upper half. Therefore if one groups magnitudes into evenly spaced magnitude bins and uses the number of events in each bin to determine the value of the mean magnitude then the value that is calculated will be higher than what it should be. Consequently, if due account is not taken for the grouping of magnitudes into discrete increments then the optimal estimate of β found using Equation (A.3.48) will be lower than the true value. The bias is removed by applying a relatively simple correction to the determination of the mean magnitude (Utsu 1966; Bender 1983). This equation for the unbiased estimate is given below.

$$\frac{1}{2\beta}\frac{\beta\delta}{\tanh\left[\beta\delta/2\right]} = \bar{m} - m_n \tag{A.3.49}$$

We are interested in the bounded version of the Gutenberg-Richter distribution (Cornell and Vanmarcke 1969). As previously mentioned the equivalent MLE formula for this case was offered by Page (1968), and the correction in order to account for the grouping of magnitudes was provided by both Weichert (1980) and Bender (1983). This formula was presented earlier, but is repeated here in Equation (A.3.50).

$$\frac{1}{2\beta}\left[\frac{\beta\delta}{\tanh\left(\beta\delta/2\right)} - \frac{\beta\left(m_x - m_n\right)}{\tanh\left(\beta\left(m_x - m_n\right)/2\right)}\right] = \bar{m} - \frac{m_x - m_n}{2} \tag{A.3.50}$$

All of the MLE formulae presented thus far deal with the case for which the period of observation is equal for all values of magnitude in the catalogue. In reality this is seldom the case. One would like to be able to use as much information as is possible to determine the parameters that best represent the activity of a seismic source and it is therefore desirable to have a MLE method that takes into account the varying periods of observation in a given catalogue. The periods of observation for the New Zealand catalogue were discussed earlier in this chapter and were summarised in Table A.3.2. The solution to the problem of varying completeness levels was addressed, and solved by Weichert (1980).

Weichert's method takes into account all the factors that are deemed relevant when determining the optimal parameters for the doubly bounded Gutenberg-Richter relationship. The relevant factors are the time dependent completeness levels, the maximum magnitude of the distribution, and the grouping of magnitudes into discrete bins. Weichert showed that the likelihood function for this scenario can be given by Equation (A.3.51) below.

$$L\left(\beta \mid n_i, m_i, t_i\right) = \frac{N!}{\prod_i n_i!} \prod_i p_i^{n_i} \tag{A.3.51}$$

In this formula, n_i is the number of events observed in the magnitude bin defined by m_i over the period of time, t_i. The term N is the total number of events observed for all completeness levels, and the term p_i is given by the equation below.

$$p_i = \frac{t_i \exp\left[-\beta m_i\right]}{\prod_j t_j \exp\left[-\beta m_j\right]} \tag{A.3.52}$$

The m_i values are separated by the bin size $\delta = 0.1$ magnitude units. In the previous formulae, and in those that follow, the minimum magnitude is related to the central value of the first magnitude increment by $m_1 = m_n + \delta/2$. The expression for optimal b-value is obtained from finding the maximum of the natural logarithm of the likelihood expression in Equation (A.3.51). The optimal b-value is consequently found from the solution to the expression given in Equation (A.3.53) below.

$$\frac{\sum_i t_i m_i \exp\left[-\beta m_i\right]}{\sum_j t_j \exp\left[-\beta m_j\right]} = \frac{\sum_i n_i m_i}{N} = \bar{m} \tag{A.3.53}$$

Weichert also provides a means with which to estimate the standard deviation in the estimate of the parameter β. This expression makes use of the second partial derivative of the log-likelihood function and is given below.

$$\sigma_\beta = \sqrt{-\left(\frac{\partial^2 \ln L\left(\beta \mid n_i, m_i, t_i\right)}{\partial \beta^2}\right)^{-1}} \tag{A.3.54}$$

Using this approach, optimal parameters were fitted to each of the twenty datasets found from the Bayesian Inference procedure for each of the seismic sources. The optimal parameters found for these models are given in Table A.3.4 as well as diagrammatically portrayed in Figure A.3.7 through to Figure A.3.10.

The fit of the parameters depends not only upon the dataset being analysed, but also the value assigned to the maximum magnitude. It is therefore very important to define this magnitude as well as possible and to take into account the relevant uncertainty in the estimation of this parameter. In the figures above each dataset has been fit

with five different distributions (the solid black lines). Each one of these fits corresponds to a selection of a potentially appropriate maximum magnitude for the source in consideration. The dashed lack lines represent the error estimates related to these various maximum magnitudes. The heavy blue line denotes the distribution that is used in the PSHA to follow. This curve has been obtained using a logic tree procedure in which each of the curves corresponding to a given maximum magnitude is assigned a weighting that reflects the author's belief in the appropriateness of this maximum magnitude. This belief while somewhat subjective, is not entirely so.

Table A.3.4: Summary of the optimal parameters of the doubly bounded Gutenberg-Richter relationship for the various fault sources in the PSHA model. Here, b is the GR 'b – value' for each source, σ_b is the standard deviation of this parameter, N is the average number of events for which these parameters were obtained, $\nu_{m,min}$ is the annual number of events greater than or equal to m_{min}, $\sigma_{\nu\, m,min}$ is the standard deviation of this value, and M_{max} is the weighed average of the maximum magnitude values used in the determination of these values. The star superscript on the b value for the Pisagh Fault indicates an assumed value due to insufficient data.

Seismic Source	b	σ_b	N	$\nu_{m,min\ =\ 3}$	$\sigma_{\nu\, m,min\ =\ 3}$	M_{max}
Kongahu Fault	1.014	0.122	34.7	1.99	0.34	7.56
Glasgow Fault	1.068	0.089	73.4	4.30	0.50	7.40
Inangahua Fault	0.859	0.078	59.2	3.15	0.41	7.36
Lyell Fault	0.898	0.148	18.2	0.99	0.23	7.31
White Creek Fault	0.777	0.103	27.1	1.37	0.26	7.85
Mt. William Fault	0.819	0.112	27.7	1.44	0.27	6.96
Cape Foulwind Fault	0.906	0.187	11.5	0.63	0.19	7.60
Maimai Fault	0.890	0.121	27.8	1.51	0.29	6.89
Kohaihai Fault	0.965	0.125	30.0	1.69	0.31	7.30
Wakamarama Fault	0.882	0.233	7.1	0.38	0.14	7.46
Karamea Fault	1.061	0.203	13.9	0.81	0.22	7.61
Pikikiruna Fault	1.015	0.261	7.7	0.44	0.16	7.41
Pisagh Fault	1.000*	--	4.3	0.29	0.14	6.86
Background Source	0.874	0.044	207.9	11.20	0.78	6.78
Total Region	0.915	0.027	550.1	30.21	1.29	7.86

The possible range of values for the maximum magnitude considered for each source is governed by scaling relationships appropriate for use in New Zealand (Wells and Coppersmith 1994; Anderson et al. 1996; Stirling, Rhoades et al. 1998; Stock 2001; Dowrick and Rhoades 2004), as well as world wide relations (Wells and Coppersmith 1994). The scaling referred to in the above relationships typically relate observable physical parameters (or at least physical parameters that may be estimated) to magnitudes. These physical parameters include surface fault length, sub-surface fault length, fault widths, fault areas, and fault slip rates. In some cases the values of these parameters may be reasonably accurately obtained from the analysis of large earthquake events that have occurred on known faults throughout time. This is the case for the Alpine, Inangahua and White Creek faults. For the other fault sources, the assignment of a maximum magnitude is far more subjective. The physical size of the regional faults may be estimated from geologic considerations. These considerations include the analysis of aerial photographs, geologic maps, topographic maps, digital elevation models, field investigations,

seismic profiles, and cross sections. From such considerations, estimates of the fault lengths, dips, widths and areas can be made. These parameters are the required inputs into most scaling relations.

Additional parameters that can be incorporated to aid in the estimation of the maximum magnitude is the fault slip rate (Anderson et al. 1996). Anderson et al. (1996) show that faults with low slip rates tend to generate larger magnitude events than those with high slip rates, given the same rupture size for both. The Quaternary slip rates estimated for faults in the Buller – NW Nelson area by Berryman (1980) place the sources in the fault model into the class of low slip rate faults. The rupture dimensions estimated for the Inangahua earthquake are also smaller than that which would be estimated from the basis of the recorded magnitude and the various scaling relationships that are considered.

An additional consideration that should be made when estimating the fault areas for the various sources is the cross sectional profile of Ghisetti and Sibson (2006) reproduced in the previous chapter. This cross section speculated that the dips of the primary faults become shallower near the base of the seismogenic layer. Therefore, the fault areas that are estimated based upon the near surface dips are likely to underestimate the total fault area.

A typically comprehensive summary of the statistical analysis of maximum magnitudes is presented by Cornell (1994). Other statistical approaches to the estimation of maximum magnitudes can also be found (see for example Kijko and Graham 1998; Kijko 2004 and references therein). However, these methods generally require more data than is available for the individual fault sources in the Buller region. The statistical methods would also give poor approximations to realistic maximum magnitudes for the case where the maximum event observed is much lower than that which is estimated based upon geological considerations. The approach of using scaling relations is therefore employed in preference to these statistical methods.

The actual maximum magnitudes that have been used in the final PSHA have already been presented in Table A.3.4. The range of maximum magnitude values used in order to determine these final maximum magnitudes and the weights of the logic tree branches assigned in order to calculate these final values are documented in Table A.3.5 below. It can be noted from Table A.3.5 that the weights assigned to the various possible maximum magnitude values are not symmetrical about a given value. The weights reflect the author's belief in the appropriateness of a given value and the strength of this belief is governed by various factors that interact in a nonlinear manner. These factors include the power law scaling of rupture size with magnitude as well as the power law scaling of earthquake occurrence. The combined effect of these two dominant factors influences the subjective assignment of weights to the various values of maximum magnitude given in Table A.3.5.

As can be seen from the fit of the doubly bounded Gutenberg-Richter relationship to the seismicity data displayed in Figure A.3.7 through to Figure A.3.10, the fit to the small magnitude range is generally very good, but the fit to the larger magnitude events is often quite poor. It should how ever be noted that the fitted line generally appears to under-predict the rate of occurrence of events over this upper magnitude range. This is in part due to the smaller number of events in this range that are able to influence the fit, but it is also in large part due to the fact that the period of observation for these events is shorter than the average return period for these events. For example, even if a magnitude 7 event has a very well constrained return period from paleoseismic evidence of

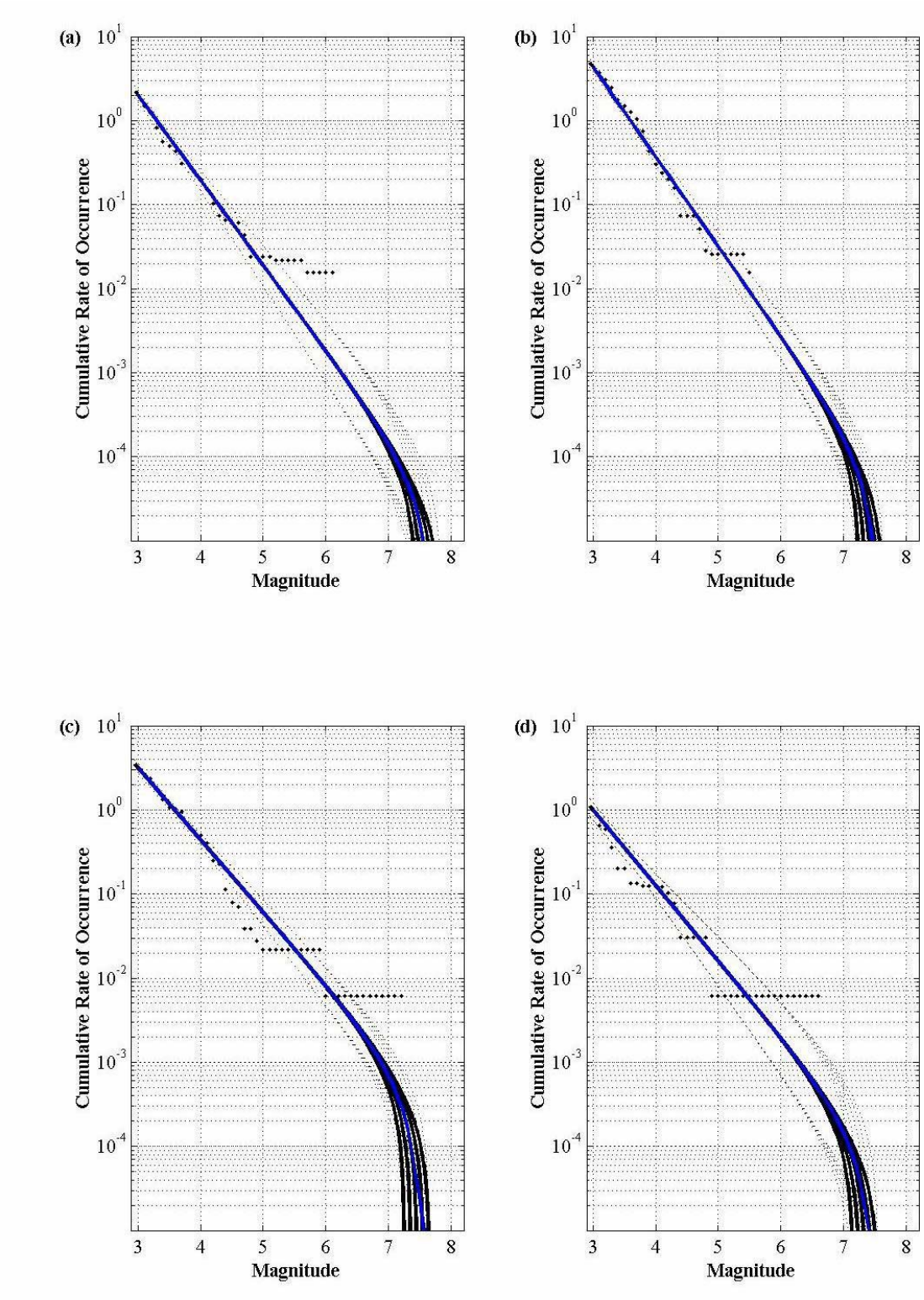

Figure A.3.7: Magnitude-frequency distributions for various fault sources derived from the Bayesian Inference catalogues for each source using Weichert's MLE procedure. Panels (a)-(d) correspond to the Kongahu, Glasgow, Inangahua, and Lyell Faults respectively. Black dots represent observations, solid black lines are MLE fits for various values of M_{max}, dashed black lines are the corresponding errors, and the solid blue line is the final distribution.

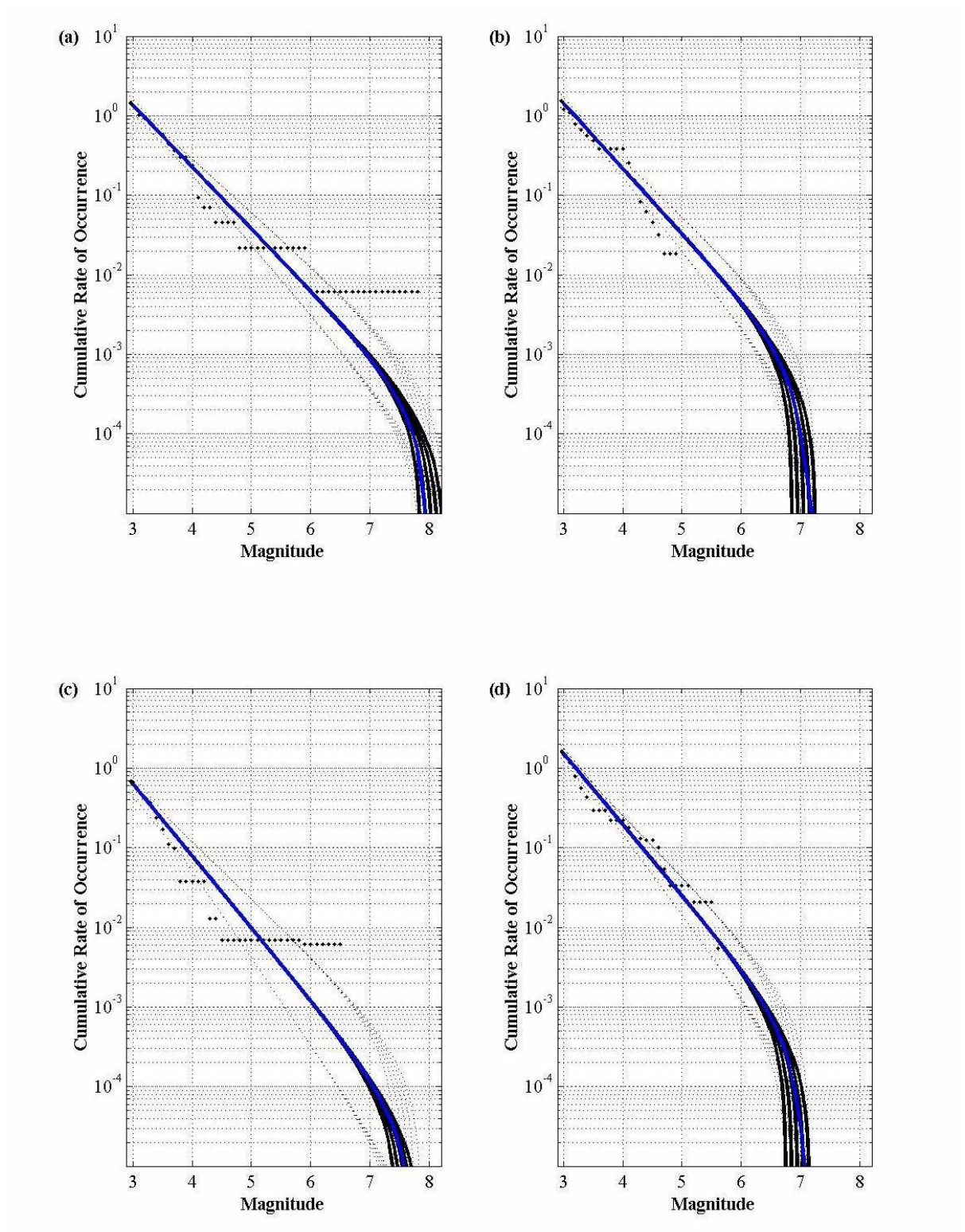

Figure A.3.8: Magnitude-frequency distributions for various fault sources derived from the Bayesian Inference catalogues for each source using Weichert's MLE procedure. Panels (a)-(d) correspond to the White Creek, Mount William, Cape Foulwind, and Maimai Faults respectively. Black dots represent observations, solid black lines are MLE fits for various values of Mmax, dashed black lines are the corresponding errors, and the solid blue line is the final distribution.

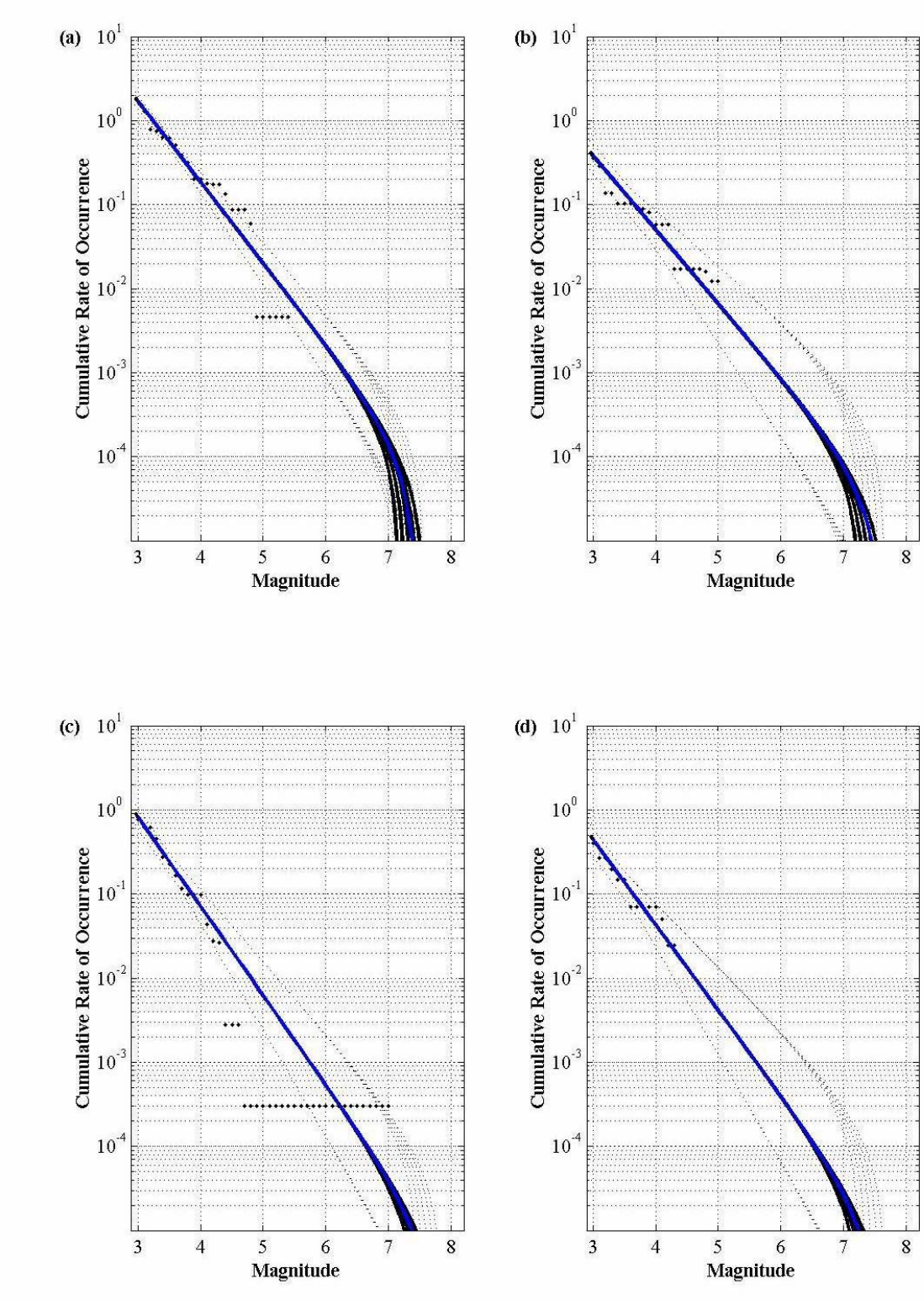

Figure A.3.9: Magnitude-frequency distributions for various fault sources derived from the Bayesian Inference catalogues for each source using Weichert's MLE procedure. Panels (a)-(d) correspond to the Kohaihai, Wakamarama, Karamea, and Pikikiruna Faults respectively. Black dots represent observations, solid black lines are MLE fits for various values of M_{max}, dashed black lines are the corresponding errors, and the solid blue line is the final distribution.

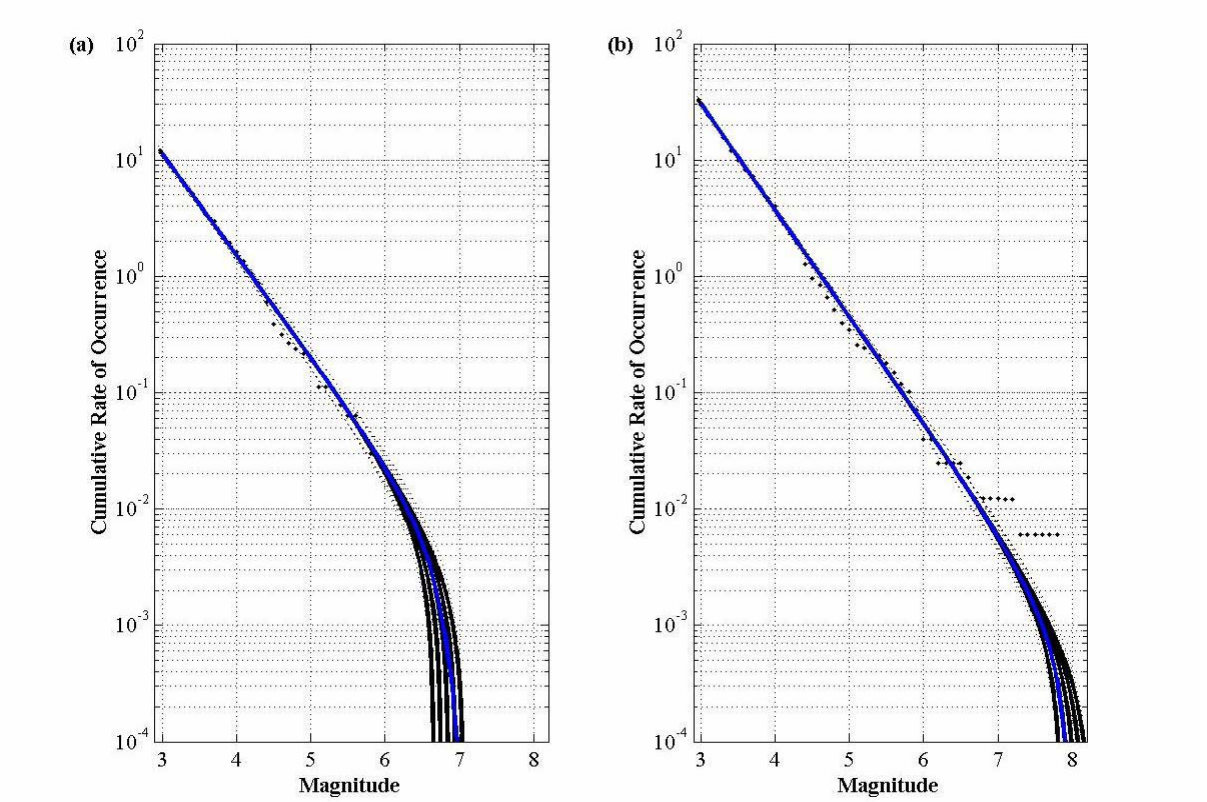

Figure A.3.10: Magnitude-frequency distributions for various fault sources derived from the Bayesian Inference catalogues for each source using Weichert's MLE procedure. Panels (a) and (b) correspond to the Background Source and the entire Buller region respectively. Black dots represent observations, solid black lines are MLE fits for various values of M_{max}, dashed black lines are the corresponding errors, and the solid blue line is the final distribution.

1000 years, but the period of instrumental observation is only 100 years then the estimated return period based upon the observation of a single magnitude 7 event during the period of observation would result in an order of magnitude over estimate of the recurrence interval. While this example is hypothetical, real situations of a similar nature frequently characterise the misfit in the figures above. The visual misfit of the modelled magnitude-frequency distributions can therefore be misleading. This effect is quite clearly evident when the plot to the full seismicity catalogues is presented in panel (b) of Figure A.3.10. In this figure, the Inangahua and Murchison earthquakes plot quite clearly above the fitted curves even though the rest of the events are modelled very well. The doubly bounded Gutenberg-Richter relation should also fit this regional data very well, this is seen to be the case for both panels of Figure A.3.10 where plots for the background source and the entire region are shown. The use of maximum likelihood techniques under these conditions should enable relatively unbiased estimates of the activity parameters to be made. If a least squares fitting procedure was applied in its place the resulting magnitude frequency distributions obtained would significantly overestimate the activity of the region.

The other significant point that the figures above demonstrate is that in many cases the modelled distributions must be extrapolated over a significant magnitude range in order to move from the maximum observed magnitude in the seismicity catalogues to the maximum magnitude assigned to the fault source. These extrapolations rely heavily on the assumptions inherent in the choice of the Gutenberg-Richter form of the

magnitude frequency relation. Under the assumption that the majority of magnitude sizes are governed by SOC behaviour, these extrapolations are not of significant concern. It does however highlight the importance of using a robust method for the estimation of the maximum magnitudes for each source.

A.3.7. External Constraint to the Selection of Magnitude-Frequency Distributions from Plate Motion Modelling

There are very few checks that are available to ascertain the suitability of the selected magnitude-frequency relationships for the region. The relatively frequent occurrence of small earthquakes enables a check on the fit at low magnitudes, but the models are already predominantly based upon events of this magnitude. The real test of the seismicity model is how well it models the rates of occurrence of large earthquakes. These events occur far too infrequently to be able to constrain their mean rates of occurrence based upon seismicity analyses alone.

One option for constraining these rates is to gather more paleoseismic information regarding the individual faults. However, as has been mentioned in the previous chapter, the options for attaining such data appear very limited. Even if good trenching sites were able to be found we may only have an additional point or two with which to constrain our model. The statistical impact of these additional constraints would therefore be very limited.

A second option that is becoming more readily available is the use of Global Positioning Systems (GPS) to gather geodetic data on the deformation of crustal masses in near continuous time. One can analyse a region and observe the average rate of deformation of the region with time. If one can then relate this observed deformation with an appropriate allocation between seismic and aseismic strain energy release then the geodetic rates and the seismicity rates can be compared.

The problem with using geodetic information though is that the combined effect of many small events and gradual build up of strain energy does not really reflect the way that land masses deform. The trend is for significant large events to inflict relatively large scale changes through catastrophic events such as large earthquakes. Consequently, unless the geodetic observations are able to include one or more of these large scale events then there will be an incompatibility between the geodetic results and the seismicity models over the magnitude range where rates of occurrence are low. The result of using geodetic data to constrain seismicity rates is really simply to relate the typical rates of crustal deformation to the occurrence of small events. Therefore, geodetic data will really just provide additional constraint on the selection of models over the small magnitude range.

Over the past few years another check on the accuracy of PSHA predictions has been developed based on observing precariously balanced rocks (Brune et al. 1996; Anderson and Brune 1999; Brune 2001b; 2002; 2003; Anooshehpoor et al. 2004). Researchers go out into the field and find precariously balanced rock masses and estimate how long they have been perched in this precarious state. They then calculate the strength of ground

Table A.3.5: Table showing the subjective weights assigned to the various potential values of the Maximum Magnitude for use in the MLE determination of the optimal parameters for the doubly bounded Gutenberg-Richter relationship.

Seismic Source		$M_{max,i}$; W_i					Weigthed Mmax
Kongahu Fault	M_{max}	7.40	7.50	7.60	7.70	7.80	7.56
	W	0.20	0.30	0.30	0.10	0.10	
Glasgow Fault	M_{max}	7.20	7.30	7.40	7.50	7.60	7.40
	W	0.10	0.20	0.40	0.20	0.10	
Inangahua Fault	M_{max}	7.20	7.30	7.40	7.50	7.60	7.36
	W	0.20	0.30	0.30	0.10	0.10	
Lyell Fault	M_{max}	7.10	7.20	7.30	7.40	7.50	7.31
	W	0.10	0.20	0.30	0.30	0.10	
White Creek Fault	M_{max}	7.80	7.90	8.00	8.10	8.20	7.85
	W	0.60	0.30	0.10	0.00	0.00	
Mt. William Fault	M_{max}	6.80	6.90	7.00	7.10	7.20	6.96
	W	0.20	0.30	0.30	0.10	0.10	
Cape Foulwind Fault	M_{max}	7.40	7.50	7.60	7.70	7.80	7.60
	W	0.10	0.20	0.40	0.20	0.10	
Maimai Fault	M_{max}	6.70	6.80	6.90	7.00	7.10	6.89
	W	0.10	0.30	0.30	0.20	0.10	
Kohaihai Fault	M_{max}	7.10	7.20	7.30	7.40	7.50	7.30
	W	0.10	0.20	0.40	0.20	0.10	
Wakamarama Fault	M_{max}	7.20	7.30	7.40	7.50	7.60	7.46
	W	0.10	0.10	0.20	0.30	0.30	
Karamea Fault	M_{max}	7.40	7.50	7.60	7.70	7.80	7.61
	W	0.10	0.20	0.30	0.30	0.10	
Pikikiruna Fault	M_{max}	7.20	7.30	7.40	7.50	7.60	7.41
	W	0.10	0.20	0.30	0.30	0.10	
Pisagh Fault	M_{max}	6.60	6.70	6.80	6.90	7.00	6.86
	W	0.10	0.10	0.20	0.30	0.30	
Background Source	M_{max}	6.60	6.70	6.80	6.90	7.00	6.78
	W	0.20	0.20	0.30	0.20	0.10	
Total Region	M_{max}	7.80	7.90	8.00	8.10	8.20	7.86
	W	0.50	0.40	0.10	0.00	0.00	

motions that would be required to topple such a rock mass. Given that the rock mass has not been toppled during the period for which it has remained precariously placed a constraint is provided either on the rate of occurrence of large earthquakes, or upon the strength of ground motions that may result from large earthquakes. This information can be very useful in ascertaining the suitability of a particular PSHA model in estimating the occurrence of large ground motions, and on the occurrence of the events that cause such motions. The method therefore looks promising in terms of it being able to help constrain the magnitude-frequency relations for the Buller region. There is one obvious catch though. One must have precariously balanced rocks in the area in order to be able to apply this method. In the field investigations that were conducted as part of this study, no suitable rock masses were observed, and consequently the method cannot be used in this instance.

The only external constraint that we can use on long term seismicity rate comes from plate motion modelling, or large scale deformation of some other form. Holt and Haines (1995) modelled plate motions and associated strain rates across the northern South Island and were able to relate these motions and rates with long term seismic moment release rates (see the previous chapter for more detail). These plate motion models take into account

very long periods of movement and consequently are able to provide constraints upon the long term deformation of a region. From their study, Holt and Haines were able to estimate that the most likely long term moment release rate for the Buller – NW Nelson area was 3.5×10^{17} Nm/yr†.

Now, given the parameters of the doubly bounded Gutenberg-Richter magnitude-frequency distribution McGuire (2004) shows how the associated seismic moment release rates can be determined. Given the probability density function of the doubly bounded Gutenberg-Richter relationship stated above in Equation (A.3.44), one can obtain the equivalent formula in terms of seismic moment.

$$f_{M_0}\left(M_0\right)=\frac{\beta\exp\left[\beta\left(m_n+d/c\right)\right]M_0^{-\left(1+\left(\beta/\gamma\right)\right)}}{\gamma\left[1-\exp\left[-\beta\left(m_x-m_n\right)\right]\right]} \tag{A.3.55}$$

In Equation (A.3.55) the parameters c and d are the coefficients of the Hanks and Kanamori (1979) relationship for seismic moment in terms of moment magnitude. This relationship is presented below.

$$\log_{10} M_0 = cM_W + d \tag{A.3.56}$$

Where, for seismic moments given in units of Newton-metres $c=1.5$ and $d=9.05$. The parameter γ is simply related to the value c via $\gamma=c\ln\left(10\right)$. The seismic moment release rate can then be obtained from the solution to the expression in Equation (A.3.57).

$$\dot{M}_0=\int_{M_{0,\min}}^{M_{0,\max}} M_0\nu_{m_n} f_{M_0}\left(M_0\right)dM_0 \tag{A.3.57}$$

Once evaluated, Equation (A.3.57) is equivalent to the following expression.

$$\dot{M}_0=\frac{\nu_{m_n}\beta\exp\left[\beta\left(m_n+d/c\right)\right]}{\left(\gamma-\beta\right)\left[1-\exp\left[-\beta\left(m_x-m_n\right)\right]\right]}\left(M_{0,\max}^{1-\left(\beta/\gamma\right)}-M_{0,\max}^{1-\left(\beta/\gamma\right)}\right) \tag{A.3.58}$$

The moment rates for each source, as well as for the entire region, were calculated using the formulae above. These results are provided in Table A.3.6. As can be seen from Table A.3.6, the model used in the PSHA entailing the various individual fault sources generates a value of the total seismic moment release rate that is very

† This value of 3.5×10^{17} Nm/yr corresponds to the Holt and Haines (1995) non-uniform model. This was the model that they believed captured the long term regional deformation most appropriately. They also determine moment rates for other models, the most relevant being the uniform and uniform-NUVEL for which the calculated moment rates are 5.8×10^{17} and 4.1×10^{17} Nm/yr respectively. No error estimates are given for these values.

close to, but slightly higher than, that of Holt and Haines (1995). While the estimate from the sum of the individual sources exceeds the optimal estimate given by Holt and Haines (1995), it is below their estimate based upon their uniform model. Given the likely errors associated with estimates of this nature, the agreement between seismic moment release rates based on plate motion modelling estimates and seismicity analyses is good.

This seismic moment rate determined here from the seismicity model is also in extremely good agreement with the desired value proposed in the previous chapter. There it was stated that the Holt and Haines (1995) estimate should provide a lower bound to the seismic moment rate, while the total seismicity for the region should provide a likely upper bound. Following the consideration of current literature relevant to this issue, it was hypothesised that the optimal value would be towards the lower end of this range. The seismicity analysis that has been performed and summarised in this chapter therefore obtains results that are very much in agreement with the constraints applied by the regional geology regarded in the previous chapter. This fault model can therefore be used with confidence for the remainder of the PSHA. The next stage in this overall PSHA process is to relate the recently found rates of earthquake occurrence to corresponding rates of exceedance of ground motion levels. This aspect of the project is the focus of the next chapter.

Table A.3.6: Summary of the contribution to the total regional seismic moment release rate from the individual seismic sources. Also tabulated is the sum of these individual contributions as well as the estimate of the moment release rate for the total region based upon the MLE fit of the doubly bounded Gutenberg-Richter relation to the entire seismicity catalogue. Here, $\nu_{m,\min=3}$ and $\nu_{m,\min=5}$ represent the annual rate of earthquake occurrence of events greater than or equal to 3 and 5 respectively; β is related to the GR *b* value via $\beta = b\ln(10)$; and $M_{0,rate}$ represents the seismic moment release rate for each source.

Seismic Source	$\nu_{m,min\ =\ 3}$	β	$\nu_{m,min\ =\ 5}$	$M_{0,\text{rate}}$ [*Nm/yr*]
Kongahu Fault	1.99	2.335	0.019	2.29E+16
Glasgow Fault	4.30	2.459	0.031	2.74E+16
Inangahua Fault	3.15	1.977	0.060	9.17E+16
Lyell Fault	0.99	2.068	0.016	1.99E+16
White Creek Fault	1.37	1.790	0.038	1.66E+17
Mt. William Fault	1.44	1.886	0.033	2.99E+16
Cape Foulwind Fault	0.63	2.085	0.010	1.80E+16
Maimai Fault	1.51	2.050	0.025	1.75E+16
Kohaihai Fault	1.69	2.222	0.020	2.04E+16
Wakamarama Fault	0.38	2.031	0.007	1.07E+16
Karamea Fault	0.81	2.443	0.006	6.86E+15
Pikikiruna Fault	0.44	2.338	0.004	4.20E+15
Pisagh Fault	0.29	2.303	0.003	1.56E+15
Background Source	11.20	2.012	0.200	1.23E+17
			$\Sigma M_{0,\text{rate}}$	5.60E+17
Total Region	30.21	2.107	0.447	1.15E+18

A.4. Attenuation Relationships (Predictive Equations)

A.4.1. Introduction

The overall goal of a PSHA is to determine how frequently some measure of ground motion is exceeded. Thus far the thesis has been concerned with ascertaining how frequently, and where, earthquakes in the Buller – NW Nelson region occur. In order to achieve the goal of the PSHA one therefore needs to relate this spatial and temporal earthquake occurrence to the consequent occurrence of ground motions. Ground motion attenuation relations, or predictive equations, provide the means to this end.

In the development of early attenuation relations the aim was primarily to reveal the underlying functional dependence of ground motions upon various parameters such as magnitude and distance. It is still desirable to understand how various parameters effect the scaling of ground motions, but since the inception and proliferation of PSHA as the primary method with which to conduct hazard analyses the primary focus has been upon quantifying the magnitude and nature of the errors associated with the predictions of the equations. These error estimates are fundamental to the calculation of hazard required in the PSHA procedure.

The selection of the attenuation equation(s) used in the PSHA can have a marked effect on the results that are consequently obtained. The contribution that a particular earthquake scenario makes to the total hazard determined for a given site depends upon the relative difference between the logarithm of the median ground motion predicted given this scenario and the logarithm of the design ground motion level in question. Ground motions are justifiably assumed to be lognormally distributed (Restrepo-Velez and Bommer 2003), consequently, this deviation of the logarithmic median motion and the logarithmic design motion is equivalent to the z statistic of the standard normal distribution. The probability that the ground motion related to the particular scenario exceeds the design ground motion level can therefore be readily determined from the well known cumulative distribution function for the normal distribution.

The procedure briefly outlined above takes account of the natural variability that is associated with ground motions from earthquakes. This variability is commonly referred to as aleatory variability in current PSHA terminology. However, there is also uncertainty related to the functional form of the model for the attenuation relationship. There are many published attenuation relations in the worldwide literature (see references in the summary papers of Idriss 1978; Douglas 2001). While all of these relations have some common characteristics, there are many different functional forms employed. There is no universally accepted functional form for any given ground motion index, therefore the uncertainty regarding which model is the most appropriate should be taken into account when conducting a PSHA. This modelling uncertainty is known as epistemic uncertainty and is typically accounted for through the use of logic trees.

The use of logic trees to account for the epistemic uncertainty related to the selection of a particular attenuation relation has been employed in PSHA since about the mid 1980's (i.e. Kulkarni et al. 1984; Coppersmith and Youngs 1986). There are some nuances related to the practical implementation of this method (Bommer et al. 2005; Scherbaum et al. 2005), but the theory behind the method is very simple. Rather than consider a single attenuation relation, one considers a suite of relations that are thought to be appropriate for the application to some degree. The degree to which each relation is considered as being appropriate is specified by the analyst. Each relation is therefore assigned a weight (the sum of which is equal to one) that reflects this suspected degree of appropriateness. Hazard curves are generated using standard PSHA methodology (i.e. Cornell 1968) for each relation and then the mean hazard curve is found from the sum over all relations of the product of the hazard determined for each relation and the weight assigned to that relation.

This logic tree approach is adopted as part of the state-of-the-art PSHA methodology employed in this study. The main focus of this chapter is consequently on the selection of the various attenuation models that are included in the suite of models for the various ground motion measures considered in the PSHA. The chapter begins with a summary of the relations that have previously been employed in PSHA for New Zealand before selecting a suite of relations.

A.4.2. Precedent for Predictive Equations in New Zealand PSHA

Naturally, the first port of call when considering the selection of the most appropriate predictive equations to use in PSHA for New Zealand is to review the existing literature and find the models that have been implemented for this purpose in the past. Unfortunately, after carrying out this procedure one is not far from where one started. There are surprisingly few published studies of modern implementations of PSHA in New Zealand, and none, to the author's knowledge that make use of logic tree methodology in which multiple hypotheses regarding the nature of ground motion attenuation is accounted for.

The most recent PSHA carried out for New Zealand (Stirling et al. 2002) made use of just one equation, the McVerry et al. (2000) model. This is the only existing model for predicting response spectral ordinates that is based upon a large enough dataset to give credence to its form in New Zealand. However, the coefficients for this model have not been published in the public domain. The only other model of this nature available to be considered is the Matuschka and Davis (1991) model that is based upon a relatively small dataset and employs some questionable regression techniques in order to determine its parameters. A brief discussion of this model is given in the general introduction to Section B of this thesis.

Prior to the above study Stirling et al. (1998) used an unpublished attenuation relation that was in a developmental stage and was referenced to Norman Abrahamson. This relation is likely to be an early prototype of the McVerry et al. (2000) model. These two hazard analyses represent the most current applications of PSHA on a national scale in New Zealand. Both of these studies use a single attenuation relation, and both of the attenuation relations that are used cannot be implemented from the published literature.

The other applications of PSHA for New Zealand date back to the early to mid 1980's (Matuschka 1980; Peek 1980; Smith and Berryman 1983; Matuschka et al. 1985; Smith and Berryman 1986). These studies provide no aid in the selection of relevant attenuation relations as the models that are employed in these studies are now regarded as being obsolete by modern standards. Therefore, one can conclude that there is almost no relevant precedent for the use of ground motion attenuation relations within a modern framework for New Zealand. This must be regarded as being a surprising conclusion given the active tectonic setting that New Zealand is characterised by.

A.4.3. Selection of Attenuation Relations

In the general introduction of Section B of this thesis a discussion of the strong motion predictive equations developed primarily for application in New Zealand is presented. The general result of this literature review, with respect to the current problem of selecting a suite of ground motion equations, is that there are an insufficient number of relations developed for New Zealand, for any measure of ground motion, to enable a suite to be selected. The relations that are selected for implementation in this study are consequently a combination of available New Zealand relations and relations developed primarily for other regions of the world.

It should be emphasised that the reason for including multiple attenuation relations is to account for the variety of functional forms that are currently adopted in modern ground motion predictive equations. There are a suite of attenuation relations that are pretty well suited for this purpose. These relations appeared in a special volume of Seismological Research Letters and are the Abrahamson and Silva

(1997), Boore et al. (1997; 2005), Campbell (1997), and Sadigh et al. (1997) models. These relations were developed at essentially the same time using similar quality datasets of strong motion records from shallow crustal earthquakes; the differences between them are therefore primarily related to the functional forms chosen for the models and the analytical procedures adopted for the determination of the defining coefficients. They all use a consistent magnitude scale (moment magnitude) which means that no conversions need to be made between various scales to make the relations truly comparable. They encompass the current measures of distance employed in strong motion predictive relations and each has a different functional form. For the actual implementation in the PSHA an updated version of the Campbell (1997) model is used (Campbell and Bozorgnia 2003b; 2003a; 2004). This updated version uses a larger dataset and makes some functional changes to the form of the model.

Each of the Abrahamson and Silva (1997), and Campbell and Bozorgnia (2003b; 2003a; 2004) are developed from datasets that consist of primarily Californian strong motion records, but that also include various foreign events. The Sadigh et al. (1997) is based upon a dataset of almost entirely Californian data with the exception being one record from the 1976 Gazli, USSR earthquake, and three records from the 1978 Tabas, Iran earthquake. The Boore et al. (1997; 2005) model is based purely on Western North American data.

All of these models are able to predict 5% damped acceleration response spectral ordinates as well as peak ground accelerations. The site classification scheme used in each model is slightly different and one therefore needs to take care when using the models in the PSHA that the ground motions that are predicted are predicted on a consistent basis.

It is notable that all of these foreign relations are predominantly based upon records from the United States. In the past models based upon Japanese strong motions such as the Katayama (1982) model have found favour for use in New Zealand. However, many of the Japanese models make use of the JMA magnitude scale and their implantation for PSHA would therefore require a conversion to be made. Two similar studies were conducted in 1993 that compared peak ground accelerations recorded in some New Zealand earthquakes to predictive models from various regions (Dowrick and Sritharan 1993; 1993a). Dowrick and Sritharan (1993) considered a group of events that included both the Hawk's Crag 1 and 2 events from the Buller region. It was found that the Japanese model of Fukushima and Tanaka (1990) did a reasonable job of modelling these recorded motions, particularly for the first Hawk's Crag event, but that the Joyner and Boore (1981) significantly underestimated the ground motions. The Campbell (1981) and Ambraseys and Bommer (1991) models were also shown to underestimate the ground motions for these general events. Similar findings using the Joyner and Boore (1981) and Campbell (1981) models were found when Dowrick and Sritharan (1993a) attempted to model the peak accelerations, although in this case the Campbell model performed significantly better than the Joyner Boore model. These findings suggest that perhaps models developed using predominantly U.S. based data are not appropriate for use in New Zealand. However, one should take into account the significantly larger datasets that the current U.S. based models are derived from with respect to these earlier attempts.

More recently, during the selection of the functional form for the response spectral model of McVerry et al. (2000) a fit was made to each of the Idriss (1991), Abrahamson and Silva (1997), Boore et al. (1997; 2005), and Sadigh et al. (1997) models. McVerry et al. (2000) found that each of the models gave an adequate fit to the New Zealand strong motion data. In addition, recent research by Douglas (2004) has shown that the hypothesis that strong motion records from both California and New Zealand are the same cannot be rejected from a statistical point of view. Therefore, the findings of Dowrick and Sritharan (1993; 1993a) may not be as valid for modern regression models based upon strong motion data from the U.S. as they were for their earlier counterparts.

In light of the considerations above, coupled with the underlying goal of accounting for the epistemic uncertainty associated with the selection of attenuation models, the suite of relations used for the current analysis incorporate New Zealand relations, where applicable, and the predominantly U.S. based relations. The suites employed for the determination of response spectral ordinates differ slightly from those used for the peak ground acceleration as in the latter case two New Zealand models were used. The suites of relations are given below.

For 5% damped acceleration response spectral ordinates:

- Abrahamson and Silva (1997)
- Boore, Joyner and Fumal (1997; 2005)
- Sadigh, Chang, Egan, Makdisi, and Youngs (1997)
- Campbell and Bozorgnia (2003b; 2003a; 2004)
- McVerry, Zhao, Abrahamson, and Somerville (2000)

For peak ground acceleration:

- Abrahamson and Silva (1997)
- Boore, Joyner and Fumal (1997; 2005)
- Sadigh, Chang, Egan, Makdisi, and Youngs (1997)
- Cousins, Zhao, and Perrin (1999)
- Campbell and Bozorgnia (2003b; 2003a; 2004)
- McVerry, Zhao, Abrahamson, and Somerville (2000)

For Arias Intensity:

- Travasarou, Bray, Abrahamson (2003)
- Stafford (2006, see Section B - Chapter 6 of this thesis)

The performance of the various predictive relations over a range of magnitudes and distances are presented in a series of figures to follow.

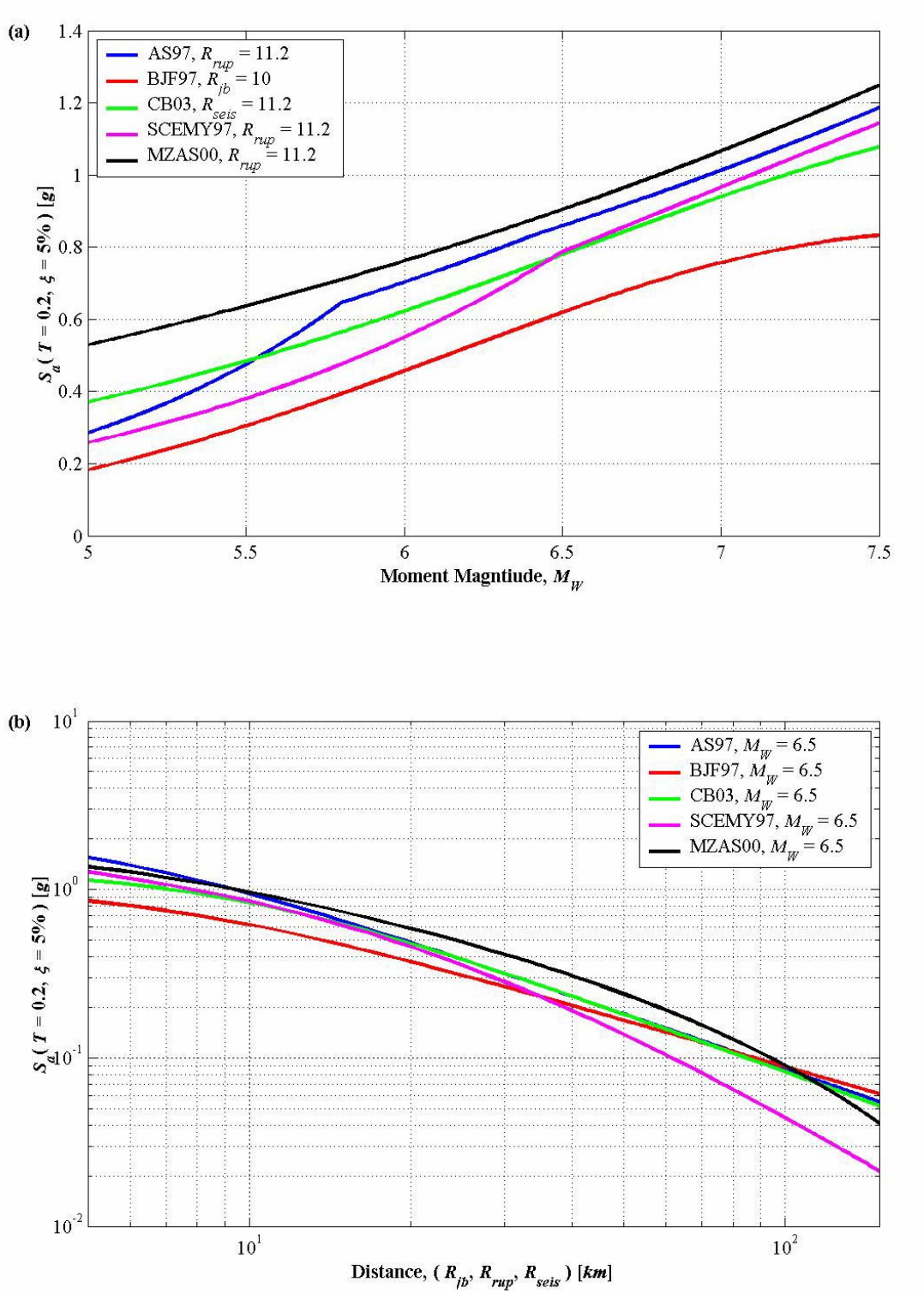

Figure A.4.1: Comparison of 5% Damped Spectral Amplitudes at a Period of 0.2 seconds determined for the various predictive models included in the PSHA. Panel (a) shows the scaling against magnitude, while panel (b) shows the scaling with distance. The three different distance measures are calculated perpendicular to the strike of a fault dipping 60 degrees away from the site. Abreviations are as follows: AS97 – Abrahamson & Silva (1997), BJF97 – Boore, Joyner and Fumal (1997), CB03 – Campbell and Bozorgnia (2003), SCEMY97 – Sadigh, Chang, Egan, Makdisi and Youngs (1997), MZAS00 – McVerry, Zhao, Abrahamson and Somerville (2000).

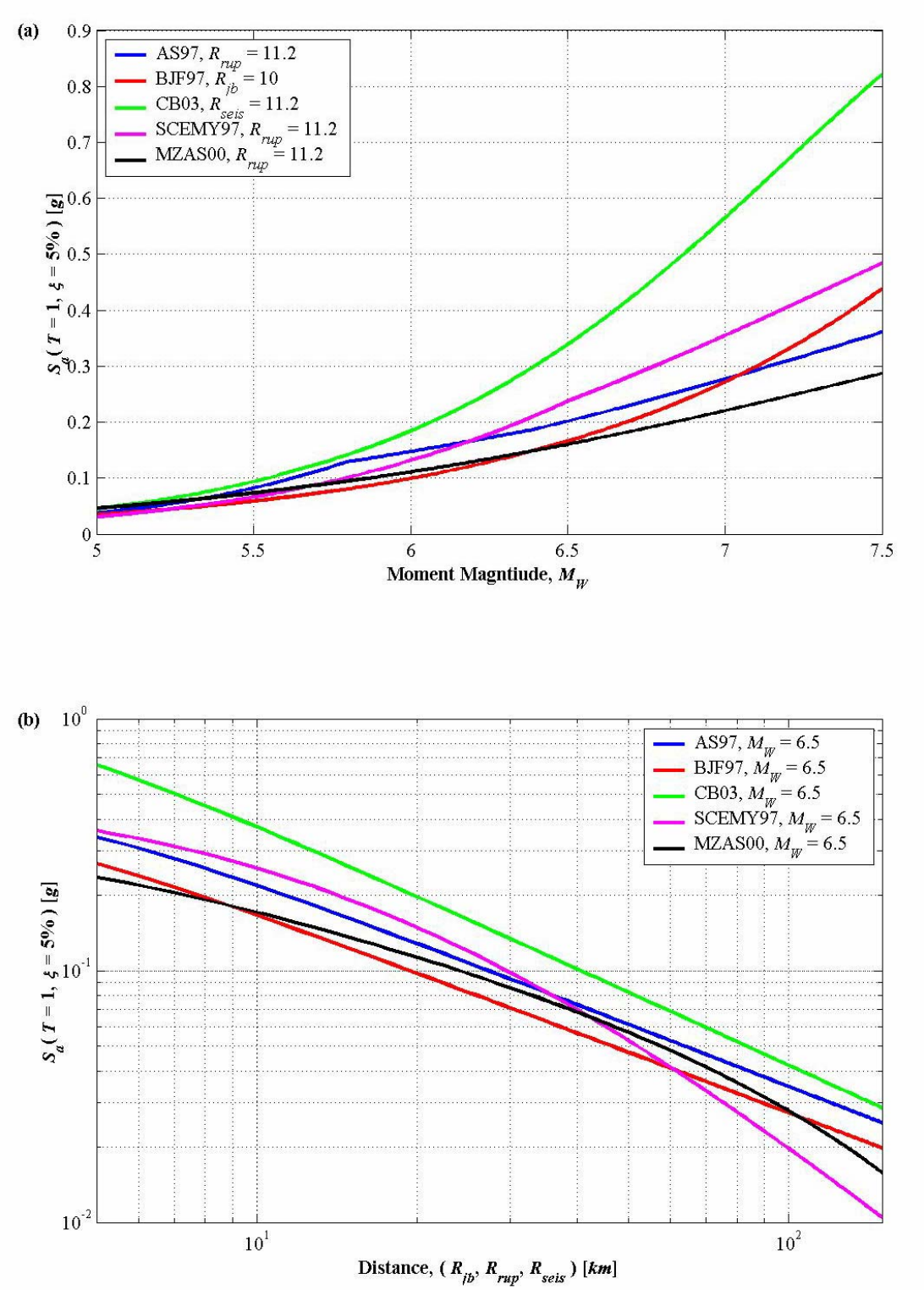

Figure A.4.2: Comparison of 5% Damped Spectral Amplitudes at a Period of 1.0 seconds determined for the various predictive models included in the PSHA. Panel (a) shows the scaling against magnitude, while panel (b) shows the scaling with distance. The three different distance measures are calculated perpendicular to the strike of a fault dipping 60 degrees away from the site. Abreviations are as follows: AS97 – Abrahamson & Silva (1997), BJF97 – Boore, Joyner and Fumal (1997), CB03 – Campbell and Bozorgnia (2003), SCEMY97 – Sadigh, Chang, Egan, Makdisi and Youngs (1997), MZAS00 – McVerry, Zhao, Abrahamson and Somerville (2000).

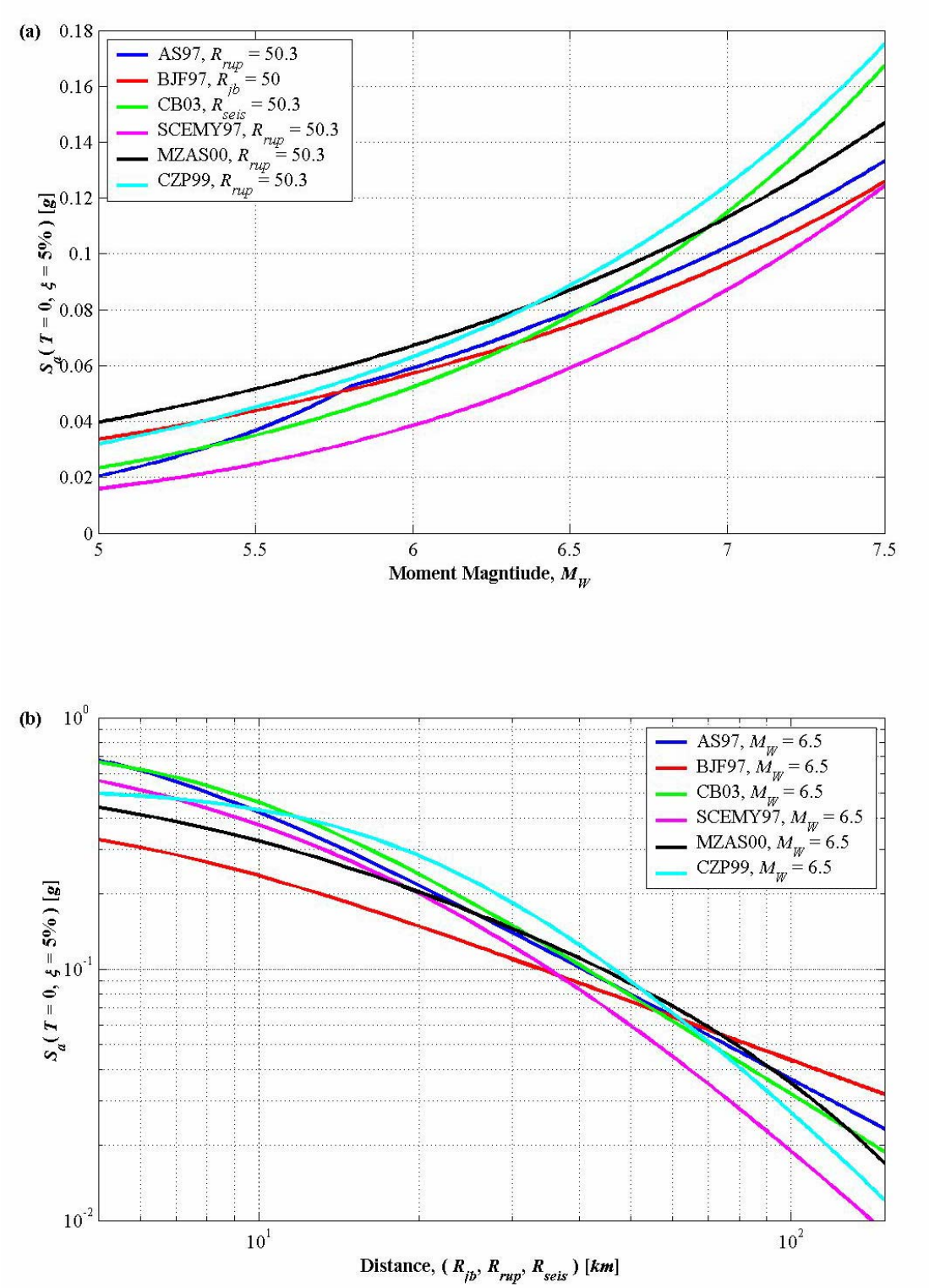

Figure A.4.3: Comparison of Peak Ground Accelerations determined for the various predictive models included in the PSHA. Panel (a) shows the scaling against magnitude, while panel (b) shows the scaling with distance. The three different distance measures are calculated perpendicular to the strike of a fault dipping 60 degrees away from the site. Abreviations are as follows: AS97 – Abrahamson & Silva (1997), BJF97 – Boore, Joyner and Fumal (1997), CB03 – Campbell and Bozorgnia (2003), SCEMY97 – Sadigh, Chang, Egan, Makdisi and Youngs (1997), MZAS00 – McVerry, Zhao, Abrahamson and Somerville (2000), CZP99 – Cousins, Zhao and Perrin (1999).

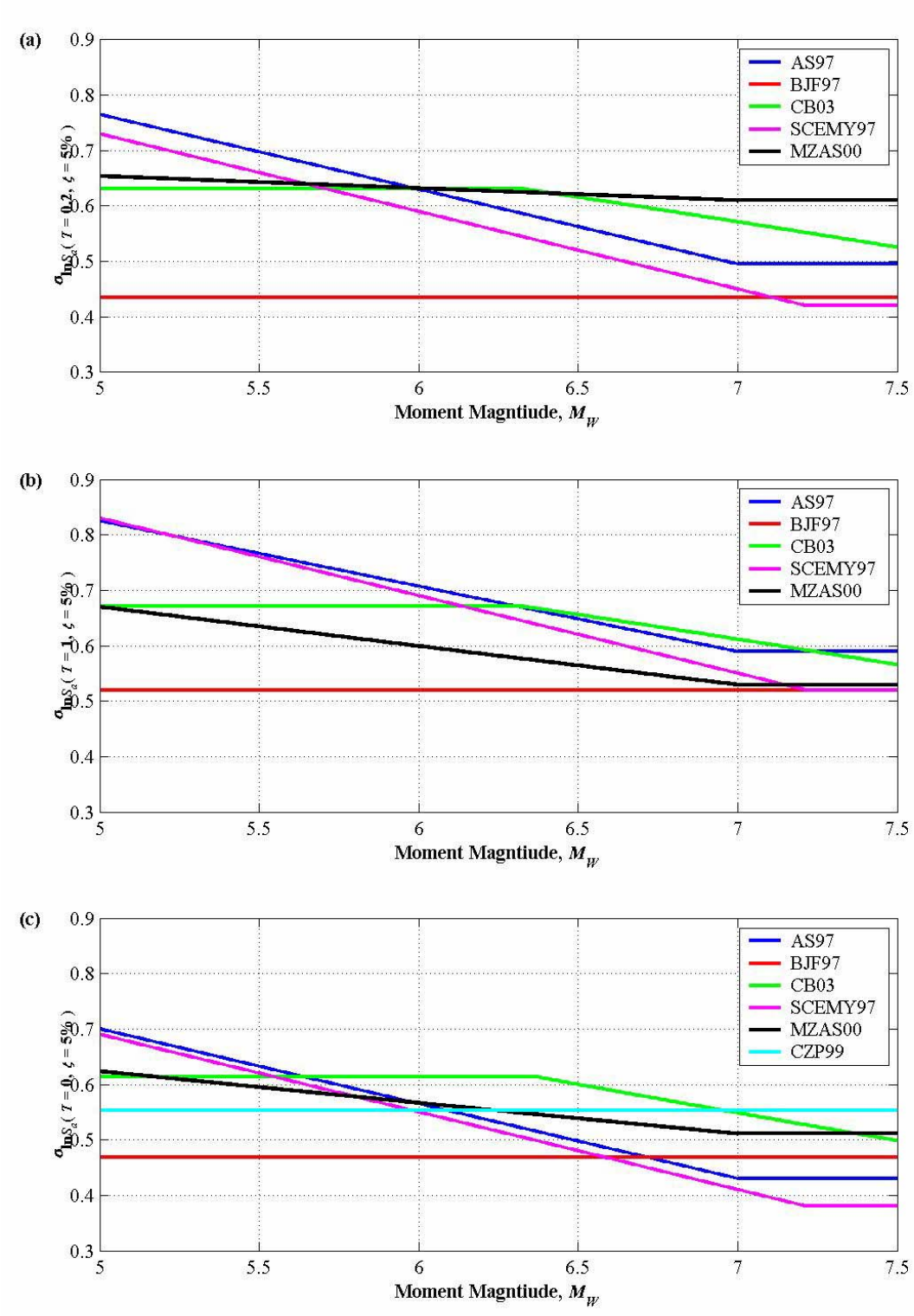

Figure A.4.4: Magnitude Dependence of the Standard Deviations of the various predictive relations employed in the PSHA. In the case where the models provide error estimates for the average or random component, the error for the average component is shown. Abbreviations are the same as for previous figures.

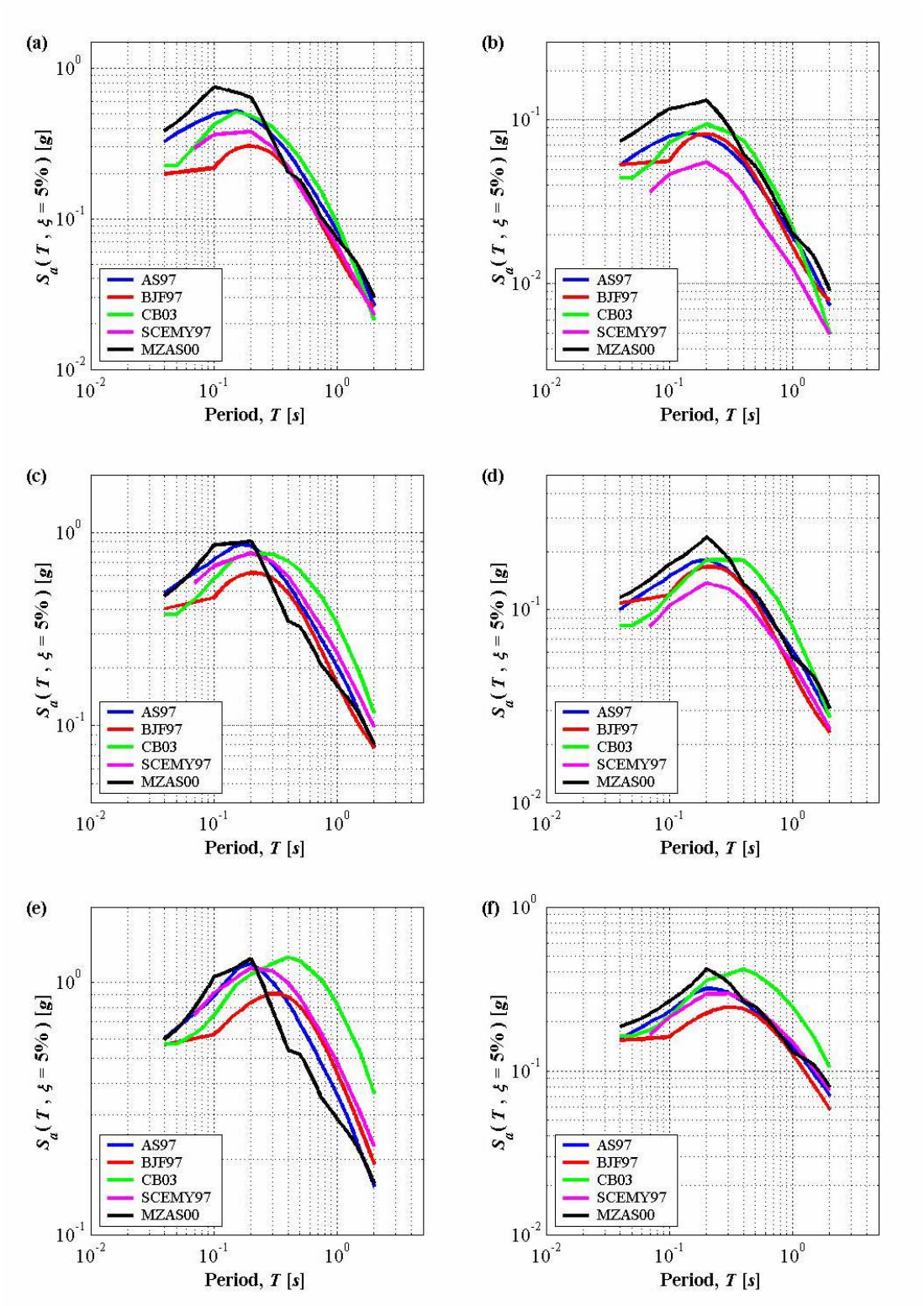

Figure A.4.5: Comparison of 5% Damped Acceleration Response Spectra. Panel (a) is for M_W5.5, R_{jb} = 10km, R_{rup} = R_{seis} = 11.2km; panel (b) for M_W5.5, R_{jb} = 50km, R_{rup} = R_{seis} = 50.3km; panel (c) for M_W6.5, R_{jb} = 10km, R_{rup} = R_{seis} = 11.2km; panel (d) for M_W6.5, R_{jb} = 50km, R_{rup} = R_{seis} = 50.3km; panel (e) for M_W7.5, R_{jb} = 10km, R_{rup} = R_{seis} = 11.2km; while panel (f) is for M_W7.5, R_{jb} = 50km, R_{rup} = R_{seis} = 50.3km.

Diagrammatic representations of the predictive models for Arias Intensity (Arias 1970) are not shown here as they are given in Chapter Six of Section B of this thesis where a model relevant for use in New Zealand is derived.

A.4.4. Logic Tree Weights

Once the suite of attenuation models for the PSHA have been chosen, weights must be allocated to each of the various models in order for them to be included in the overall logic tree. As previously mentioned, these weights reflect the belief in the model's ability to predict future ground motions in the region of interest.

When one regards any of Figure A.4.1, Figure A.4.2, or Figure A.4.3 in isolation it appears as though some models would do a much better job of predicting New Zealand ground motions than others might. However, when one regards the forms of the individual curves for various other magnitude, distance, and frequency (period) scenarios it is found that none of the curves systematically depart from the others on a consistent basis. Each of the curves does a better job than the others for some range of ground motion scenarios. This is due to both the values of the coefficients used in the models, but more importantly, it is due to the range of functional forms that are encompassed by the suite of relations. This is the reason for undertaking this procedure in the first place. It is also noteworthy that in Figure A.4.4, where the standard error estimates for each model are plotted as a function of magnitude for three periods, there is a considerable variation in the magnitude and nature of these error estimates. The nature of this error term has a very significant impact upon the form of the final hazard curves that are calculated for the PSHA. Encapsulating the range of uncertainties in these parameters in the methodology of the PSHA is therefore very important when endeavouring to properly account for the epistemic uncertainty inherent in the process.

Although the performance of the McVerry et al. (2000) predictive model should, in principle, be better than that of the Abrahamson and Silva (1997) model, when applied in New Zealand, the fact that the model has not been fully released into the public domain despite having been developed years ago makes one tentative to give this model special preference over the other models. In addition, it should be noted that the magnitude scaling of this model is entirely inherited from the Abrahamson and Silva (1997) model; the main distinction between the two models being the rate of attenuation with distance as well as the use of different site class categories. As well as this McVerry (2002) acknowledges that there is insufficient magnitude dependence in the McVerry et al. (2000) model over the small magnitude range, and particularly for short period response (up to about 0.4 seconds). This recognised deficiency is a significant one in terms of its impact upon hazard computations in PSHA as events of this nature are by far the most numerous and can contribute significantly to hazard estimates, particularly for areal sources close to the site (Cornell and Vanmarcke 1969). This characteristic of the model was deemed important enough to force the selection of the minimum magnitude value of $M_W 5.25$ being used in the latest PSHA analysis for

New Zealand (Stirling et al. 2002). The significance of this parameter is discussed in more detail in the following chapter. For now though it will suffice to say that the selection of this value is another source of epistemic uncertainty that can have a significant impact of the hazard curves calculated for high frequency ground motion measures and for short return periods. In the present study values of the minimum magnitude less than $M_W 5.25$ will be considered and it is therefore undesirable to give preference to the McVerry et al. (2000) when it is known that unreliable results would be obtained under these circumstances.

The Campbell and Bozorgnia (2003b; 2003a; 2004) model appears to predict larger response than the other models for large earthquakes over the high period range. However, this model is developed from the largest dataset and includes more worldwide events than the other models. The functional form of this model is also the most elaborate of all the models considered. One is therefore reluctant to downgrade to importance of this model. Consequently, for the PSHA calculations for the 5% damped acceleration response spectral ordinates an equal 20% weighting is therefore assigned to each of the five models that are considered.

For the weights associated with the peak ground acceleration models, a higher weighting is applied to the Cousins et al. (1999) model than to the other relations. This is largely due to the fact that this relation is the most comprehensive relation of its type for the prediction of peak ground acceleration in New Zealand. It has also been shown to model the variation of peak ground motions from earthquakes in the Buller region (see both of Zhao et al. 1997; Cousins et al. 1999). The Cousins et al. (1999) model is consequently assigned a weight of 40% while the remaining five models receive 12% each. The Zhao et al. (1997) model for peak ground accelerations is not included in the analysis because it is so similar to the Cousins et al. (1999) model. As the purpose of including multiple models in the PSHA methodology is to encapsulate the range of functional forms, there is little point in including models that are very similar. Therefore, rather than include both, the more modern, and more robust model of Cousins et al. (1999) effectively represents both models as is consequently assigned a relatively larger weight than the other models that are included.

A.4.5. Hanging Wall Effects

There is strong evidence supporting the notion that sites on the hanging walls of dip-slip faults experience larger ground motions than those on the footwall (i.e. Abrahamson and Somerville 1996; Brune 2001a; Shabestari and Yamazaki 2003). The Buller – NW Nelson region contains predominantly reverse faults and consequently, hanging wall effects must be taken into account for some sites. Not all of the models used in this study allow for this effect to be considered. The spectral models of Abrahamson and Silva (1997) and McVerry et al. (2000) necessarily include the same factors for the hanging wall effect. The most recent model of Campbell and Bozorgnia (2003b; 2003a; 2004) also includes quite a comprehensive functional expression for this purpose. The Boore et al. (1997; 2005) does not explicitly include terms to

account for the hanging wall effect, but their use of the R_{jb} distance measure (Joyner and Boore 1981) acts to take this factor into account anyway. Therefore, only the Sadigh et al. (1997) model does not account in some way for hanging wall effects. The dataset used for that study included very few records from the near field of reverse faults and consequently could not have been used to determine a stable representation of this effect anyway. The peak ground acceleration model of Cousins et al. (1999) also does not include any hanging wall factors in their model. At least some qualitative account should be made in the case where these factors are deemed necessary to truly represent the near field ground motions.

A.4.6. Rupture Directivity

As well as the increased motions due to effects associated with the hanging wall, there is also strong evidence in support of the modification of ground motions from directivity effects. None of the models mentioned thus far explicitly take into account this azimuthal variation of ground motion strength, although there are correction factors that can be applied for this purpose (Somerville et al. 1997). There has also been recent progress in characterising the frequency dependence of these directivity factors (Somerville 2000; Somerville 2003; Somerville 2005). It seems certain that inclusion of factors such as these will become common place in future ground motion attenuation relations.

However, currently, these modifications are still relatively in their infancy. It is not entirely apparent to what extent the regression models already account for these effects. Before applying additional scaling factors to attenuation models it must be clear that these effects are currently not taken into account, otherwise the ground motions may be over estimated. Therefore, rather than implementing these factors as part of the standard PSHA methodology, hazard disaggregation is used to identify the critical earthquake scenarios relevant to the sites considered in the analysis. If it appears that the critical scenarios may correspond to cases for which directivity effects are appropriate then these cases are considered individually. This method is adopted because most of the faults in the Buller – NW Nelson region are relatively steeply dipping and also have fault traces located in sparsely populated areas. Rupture directivity effects will therefore be spatially very localised, as well as commonly irrelevant when specifying design scenarios.

A.4.7. Range of Applicable Values

The Attenuation Relations considered in this study have been empirically derived from finite datasets. The relations are therefore only statistically constrained over certain ranges of the input variables. Each Attenuation relation has a different dataset and consequently a different range of variables over which it is applicable. Distance ranges are generally of the order of 70km or greater, while Magnitude ranges are generally valid over a range from about M5 to M7.5 or so. Care must be taken when utilising relations

that boast confidence at high magnitude ranges. Naturally, the often sparse datasets will be most sparse at these magnitude ranges and there will generally be some degree of extrapolation in order to provide coefficients that reflect the predictive properties over this magnitude range.

The maximum magnitudes that have been hypothesised for the various fault sources frequently exceed the upper limit magnitudes of the strong motion datasets used to develop the regression equations. Therefore, when calculating the hazard associated with the largest events in the region, commonly those governing the hazard at long return periods, the ground motions that are predicted must be extrapolated beyond the applicable range of the regression models. This practice must be undertaken with caution, and it should be expected that the models with the most sound theoretical basis will perform most admirably during this extrapolation.

A.5. Probabilistic Seismic Hazard Analysis (PSHA) Methodology

A.5.1. Introduction

Although a considerable amount of time has now passed since the original Probabilistic Seismic Hazard Analysis (PSHA) methodology was proposed (1968), the essence of the method remains unaltered. The analyst determines the mean rate at which a given measure of ground motion is exceeded at a site by integrating a ground motion probability density function for all possible combinations of magnitude and distance pairs. Throughout the interim period between the inception of the methodology and the present, numerous researchers have contributed to our current understanding of the optimal way in which to perform this exercise in integration.

A succinct and formal definition of the PSHA procedure is offered by Bazzurro and Cornell (1999); this definition is repeated here. For this definition, the measure of ground shaking intensity that is adopted is Spectral Acceleration, $S_a(f,\xi)$, corresponding to a particular oscillator frequency f and damping ξ. Any other measure of ground shaking intensity, such as Spectral Velocity or Arias Intensity, is interchangeable with Spectral Acceleration in the framework that is presented. Note also that peak ground acceleration is simply a special case of spectral acceleration corresponding to a frequency of zero hertz, and that damping becomes irrelevant in this limiting case. The PSHA methodology allows computation of the mean annual frequency of exceedance, $\lambda_{S_a>S_a^*}$, at a site of a specified level S_a^* of S_a at an oscillatory frequency f and damping ξ based on the aggregated hazard from N sources located at different distances, r, and capable of generating different magnitudes, m. Mathematically, the above definition is represented by equation (A.5.1) below.

$$\lambda_{S_a>S_a^*} = \sum_{i=1}^{N}\left(\lambda_{S_a>S_a^*}\right)_i = \sum_{i=1}^{N}\nu_i\left\{\iiint I\left[S_a > S_a^*\middle| m,r,\varepsilon\right] f_{M,R,\varepsilon}(m,r,\varepsilon)\,dm\,dr\,d\varepsilon\right\}_i \qquad \text{(A.5.1)}$$

Here, ν_i is the mean annual rate of occurrence of earthquakes generated by source i with magnitude greater than some specified lower bound (e.g. $m_{\min} = 5.0$). The expression $I\left[S_a > S_a^* \middle| m, r, \varepsilon\right]$ is an indicator function for the S_a of a ground motion (generated by source i) of magnitude m, distance r, and ε standard deviations away from the median with respect to level S_a^*. This indicator function is equal to 1 if $\ln S_a(m, r, \varepsilon) > \ln S_a^*$ and 0 otherwise. The remaining term, $f_{M,R,\varepsilon}(m, r, \varepsilon)$ is the joint probability density function of magnitude, M, distance, R, and ε for source i. It should be observed that because ε is stochastically independent of M and R (although $\sigma_{\ln S_a}$ is not functionally so), then the joint probability density function may be expressed as,

$$f_{M,R,\varepsilon}(m, r, \varepsilon) = f_{M,R}(m, r)\, f_{\varepsilon}(\varepsilon), \tag{A.5.2}$$

in which $f_{\varepsilon}(\varepsilon)$ represents the standardized Gaussian distribution of the form below.

$$f_{\varepsilon}(\varepsilon) = \frac{1}{\sqrt{2\pi}} \exp\left[-\frac{\varepsilon^2}{2}\right] \tag{A.5.3}$$

The nature of the now reduced joint probability density function of magnitude and distance, $f_{M,R}(m, r)$, will be discussed later in this chapter.

The framework outlined above essentially provides a means with which to take into account the natural variability that is inherent in earthquake generated ground motions. As was discussed in Chapter 4, while the aim of any ground motion predictive equation is to define the Aleatoric variability of ground motions generated by a set of characterising parameters, present knowledge of seismic wave generation, and propagation, mechanisms is not sufficiently advanced as to suggest a single functional form describing the mean ground motion. The generic ground motion predictive equation for spectral acceleration is of the form given in Equation (A.5.4).

$$\ln S_a = g(M, R, \boldsymbol{\theta}) + \varepsilon \sigma_{\ln S_a}, \tag{A.5.4}$$

Here, $\sigma_{\ln S_a}$ is the standard deviation of $\ln S_a$, and $g(M, R, \boldsymbol{\theta})$ is the functional form of the predictive model. The term, $\boldsymbol{\theta}$, represents a vector of possible additional parameters that may be included in the model to improve the characterisation of the earthquake rupture, and wave propagation scenario. Typically these additional parameters include factors relating to the generative fault mechanism, the site classification at the point of prediction, hanging wall effects, and others. Each predictive model adopted in this study, while sharing some functional features, differ from each other in a variety of ways. This uncertainty in the functional form of the models, termed epistemic uncertainty, may also be taken into account in modern PSHA methodology using logic trees. Exactly how one uses a logic tree, in particular,

how one deals with the resulting outputs from a logic tree has recently been questioned (Abrahamson and Bommer 2005; McGuire et al. 2005; Musson 2005). This issue is one of fundamental importance as logic tree methodology has been used extensively in many modern hazard analyses, it is therefore critical that the methodology is fully understood; consequently this issue will receive some further attention later in this chapter.

Equation (A.5.1) shows that a triple integral must be evaluated for each of the seismic sources considered in the analysis. As with any other definite integral, the procedure must be performed over some finite range of the variables in question. The following section considers some issues related to specifying the limits of these integrals.

A.5.2. The Limits of Integration

In the situation defined by equation (A.5.1), the integration must be performed with respect to magnitude, m, distance, r, and epsilon, ε. In order to proceed practically, one must define the range of each of these variables for which the integration must be performed. Some of these limits have received considerable attention in the literature, in particular the upper limit on magnitude, while the remaining limits have received relatively little attention. Frequently, the limits assumed by the hazard analyst are not explicitly mentioned. Modifying the limits of the integration necessarily engenders a modification to the final estimate of the hazard that is calculated. If the limits of the integrals are not specified then it becomes impossible to compare hazard estimates between projects on an even playing field. Given the degree of effort that goes into performing a comprehensive PSHA it should be deemed prudent by the analyst to fully describe the context within which the analysis has been conducted. For that reason, each limit of the integration required by Equation (A.5.1) is described below as well as issues relating to the selection of the most appropriate value for each limit.

A.5.2.1. Limiting Bounds on Magnitude

As previously mentioned, considerable attention has gone into developing procedures for estimating the upper bound on the range of magnitudes that a given source can generate. Conversely, very little attention has been given to the specification of the minimum magnitude, even though this parameter can have a significant influence upon hazard estimates, particularly for short period ordinates of spectral acceleration (Bender and Campbell 1989).

A.5.2.1.1. Minimum Magnitude

Bender and Campbell (1989) discussed some of the pertinent issues related to the selection of the minimum magnitude used in PSHA. As they correctly mention, "The degree to which minimum magnitude affects the calculated seismic hazard depends on many factors, including the level of seismicity, the type of zonation, the maximum magnitude, the variability in ground motion, the period (in the case of response spectra), and the attenuation relationship". Grünthal and Wahlström (2001) also state that "decreasing the minimum magnitude thought to be of engineering relevance causes a drastic increase of the hazard at small mean return periods".

The PSHA procedure must represent the contribution to hazard of all potentially damaging earthquake scenarios. The problem of specifying a minimum magnitude is therefore a problem in defining what a potentially damaging earthquake scenario is. As has been previously mentioned, an earthquake scenario consists of, at least, a magnitude-distance pair. This coupling between the magnitude of the event and the distance between the source and the site is critical here because what we are really looking to define are ground motion levels at the site of interest. These ground motion levels are partially controlled by the magnitude of the causative earthquake, but as we have demonstrated in the previous chapter distance also has a significant influence.

The damage that is inflicted by ground motions at a site is not simply a reflection of the amplitude of these ground motions, other factors such as the duration of the shaking and the overall frequency content of the motions are also strongly correlated to damage of many structures. Until recently, the framework of PSHA has only admitted the possibility of describing the hazard at a site in terms of a single scalar representation of the ground motions. While the procedure may be repeated for multiple scalar quantities, in many cases, the real measure of damage potential is found from the manner in which these various scalars interact with each other. Bazzurro and Cornell (2002) have proposed a new framework in which these effects may be taken into account. The framework considers a vector of ground motion indices, such as spectral accelerations at different periods, simultaneously in what is termed Vector-Valued Probabilistic Seismic Hazard Analysis (VPSHA). This methodology is currently in its developmental stage, as correlations between various ground motion indices must be determined, but the method promises to lead the way into the future of seismic hazard analyses. Consequently, for the present, we are limited to dealing with scalar quantities.

It can be shown that the source spectrum of seismic waves is dependent upon the size of the earthquake producing this spectrum (Aki 1967; Brune 1970; 1971, also see Section B of this thesis). Large magnitude events generate stronger spectral amplitudes at low frequencies than do small earthquakes; this effect is modelled well by the ω^2 spectrum (Aki 1967). The amplitudes of the source spectrum are modified as the waves propagate through the earth's crust and this modification is frequency dependent. High frequency components are attenuated more strongly than low frequency components for two main reasons (Aki and Richards 1980). Firstly, anelastic material losses occur on a per cycle basis, consequently, the high frequency components, experiencing a greater number of cycles for any given distance travelled, are

attenuated at a greater rate than the low frequency counterparts. The effect of anelastic material losses becomes more pronounced as the travel distance increases. The second effect is due to attenuation via scattering of the propagating waves. The earth's crust is a heterogeneous material with a fractal distribution of irregularities (Turcotte 1997; Turcotte and Malamud 2002). There is a positive correlation between the wavelength of the propagating wave and the minimum size of heterogeneity that causes this wave to scatter, i.e. long period waves are not perturbed by small heterogeneities while short period waves are. Therefore, the extent to which a particular frequency component is scattered is governed by the fractal nature of the heterogeneities in the crust.

Given the two conditions mentioned above, it can be appreciated that reducing the minimum magnitude of engineering relevance will have a more marked effect on increasing the calculated hazard for short period spectral accelerations (peak ground acceleration included) than long period motions. This effect is shown diagrammatically in panels (a) and (b) of Figure A.5.1 where the hazards calculated for three different minimum magnitudes are shown for the case of peak ground acceleration and 1.0 second, 5% damped spectral acceleration. In this figure, and particularly in panels (c) and (d), it is clear that the effect of modifying the minimum magnitude, even over these relatively small increments, is more pronounced for the peak ground acceleration than it is for the longer period ground motion measure. The example curves shown relate to the hazard estimated for the proposed Island Block mine site (approximately NZMG [2424330, 5893600]). It should also be appreciated that the degree to which this effect is observed depends upon the relative rates of activity of the seismic sources in the vicinity of the site being considered. If sources proximal to the site have high rates of activity then the high frequency components of the ground motions generated by these sources will not suffer significant attenuation. The converse case of distal sites is obviously also true. The influence of the distance is minimised, however, by the fact that the high frequency ground motions are severely attenuated in the near surface where lithospheric pressures are low and allow cracks and fissures to exist in the propagating medium (Abercrombie 1998). This issue will receive further attention in Section B of this thesis.

The likelihood of damage occurring to a structure, or of liquefaction occurring in a potentially liquefiable soil deposit, is strongly correlated with not only the amplitude of ground motion, but to the duration of this motion as well. A measure of ground motion that captures both of these aspects of ground motions is the Arias Intensity (Arias 1970). Recent work has shown Arias Intensity to be a superior predictor of damage that traditional measures such as peak ground acceleration or the square of peak ground velocity (Travasarou et al. 2003). This superiority is particularly valid for applications in which the damage response of a high frequency system† is considered. Travasarou et al. (2003) found that for periods up to 1.0 seconds Arias Intensity is a very strong predictor of damage. For periods longer than this they suggest the use of a period dependent predictor.

† By high frequency system, the use of 'system' is intended to infer applicability to both structural and geotechnical applications.

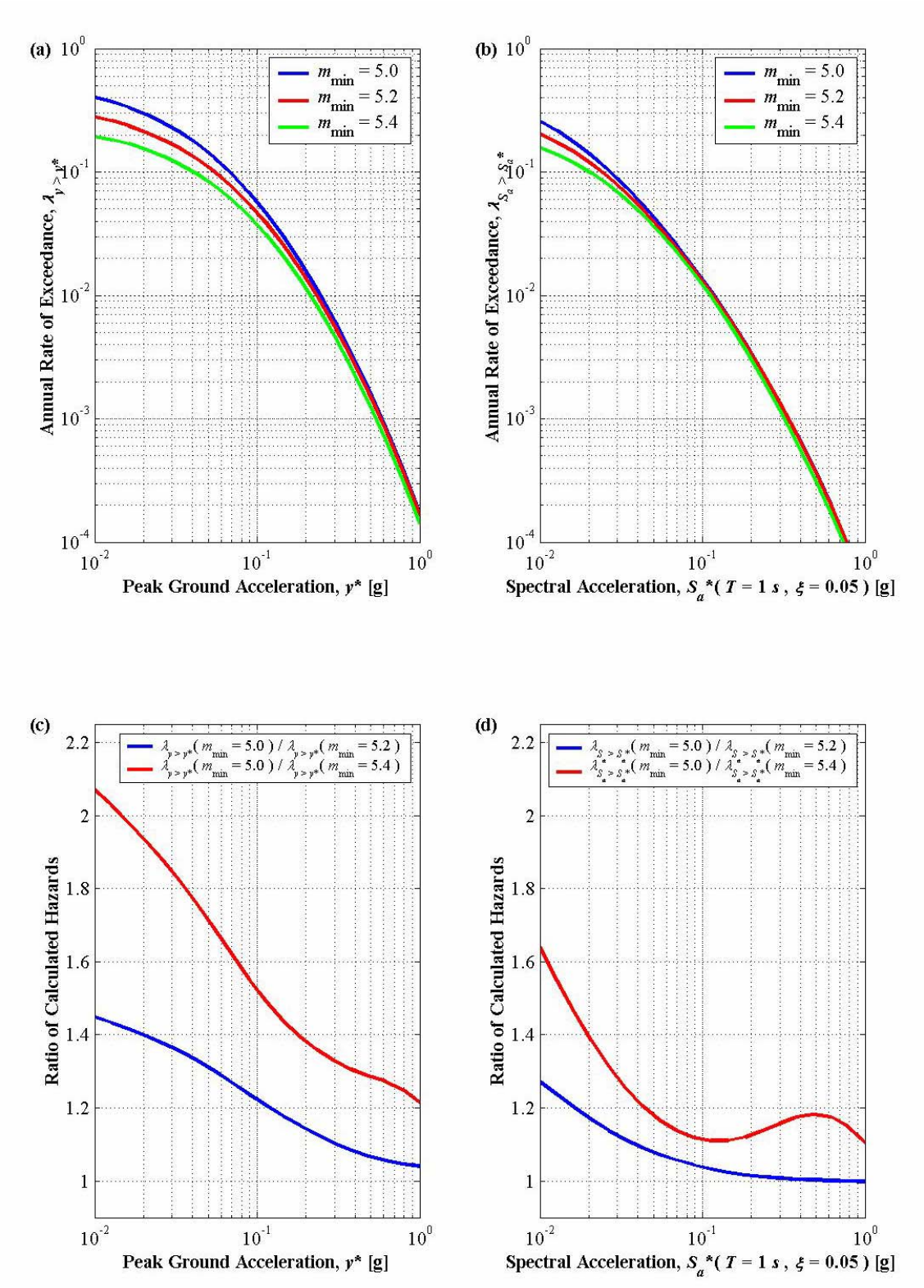

Figure A.5.1: Example of the effect of minimum magnitude selection on the calculated hazard at the Island Block site. Panel (a) shows the effect as it relates to Peak Ground Acceleration, whereas panel (b) demonstrates the effect for 1s Spectral Acceleration. Ratios of the hazard curves calculated for the Island Block site are also shown; panel (c) for Peak Ground Acceleration shows a considerably larger effect on the selection of minimum magnitude than the 1s Spectral Acceleration hazard curves shown in panel (d)

While the role of Arias Intensity is likely to become more prevalent in the future, currently the use of response spectral amplitudes is common place. It is therefore desirable to consider how the duration of a ground motion and the magnitude of the causative earthquake are related. In a very thorough review of currently available measures of strong motion duration Bommer and Martinez-Pereira (1999) propose a model relating magnitude and duration‡ that has the form given in Equation (A.5.5).

$$\ln D = aM_W + b \tag{A.5.5}$$

In Equation (A.5.5) the duration is represented by D, the moment magnitude of the causative event is M_W, and a and b are regression coefficients. Given this functional form one can readily appreciate that a small change to the magnitude results in a large change to the duration of the predicted ground motion. Therefore, when considering the most appropriate level for the minimum magnitude of engineering relevance, one must also consider how the implied durations of the ground motions corresponding to the calculated hazard relate to the concept of 'engineering relevance'. If one decreases the minimum magnitude the calculated hazard will increase, implying that these small events are capable of generating ground motions above the target level. However, because the duration simultaneously decreases (drastically), this increase in hazard may merely account for the occurrence of short, sharp, spikes in the ground motion records. Often these spikes will be of such short duration that the response of the system will be minimal.

As previously mentioned Cornell and Vanmarcke (1969) presented evidence of the influence that proximal, small magnitude events have on the calculation of hazard. In light of this finding, and in continuing the theme of the present discussion, it is very important to ascertain the destructive potential of these small, close, events. Bommer et al. (2001) investigated some historical events of only small-moderate magnitude that caused significant destruction. It should be noted that many of these scenarios relate to locations where the building stock is very dense and is probably not likely to be as seismically resilient as building stock in New Zealand. Many of the cases studied also corresponded to scenarios in which there was considerable site amplification and/or directivity effects. In the Buller region this combination of conditions are unlikely to eventuate. The building stock in the region is relatively sparse and the predominantly reverse faulting regime that exists means that the influence of directivity effects should be concentrated in small spatial areas around the surface expression of ground breaking faults, or in the vicinity of the up dip projection of blind faults. The highest density of building stock is concentrated in the low lying coastal areas around Westport. In these areas soil deposits are relatively deep in comparison to the terrain on the plateau above but these areas are also located on the foot wall of the nearest faulting source. Historically, this area has been susceptible to liquefaction with recorded instances following both the 1929 Murchison Earthquake and the 1968 Inangahua Earthquake (Carr 2004). It is therefore likely

‡ In their paper, Bommer and Martinez-Pereira use 'effective duration' as their measure of ground motion duration. Other similar measures (particularly those based upon significant duration) may have the same functional form.

that the critical ground motion intensity of engineering relevance in this region will relate to the onset of liquefaction in the region, rather than strong ground shaking. It also should be recalled from Chapter Two, that the moderate sized 1962 Westport earthquakes caused damage to building stock in Westport. Given that these events occurred with epicentral distances of approximately 15-20 km from Westport the ground motions from these events can be used to constrain the estimate of the minimum magnitude used for the PSHA.

A key finding of the Bommer et al. (2001) research was the strong correlation between the destructive potential of these small-moderate events and the focal depth of these events. Shallow events were found to be far more likely to cause destruction than deeper ones; note that relatively shallow depths also characterised the Westport sequence of events. This is a natural consequence of the rate at which near field effects attenuate coupled with the initial strength of these waves (Aki and Richards 1980). Another finding of the above research was that there appears to be evidence of directivity effects being observed in small-moderate sized events. Traditionally, the small rupture areas associated with small to moderate events implied that these events could be regarded as point sources. Consideration of directivity effects was therefore constrained to cases of magnitudes of 6.5 and above (Somerville et al. 1997). Ground motions recorded during the 1986 San Salvador Earthquake may provide reason to lower this magnitude limit. As Bommer et al. (2001) point out, the more recent interpretation of forward directivity as a magnitude dependent near-field pulse (Somerville 2000; Somerville 2003; Somerville 2005) increases the likelihood that small to moderate events will generate ground motions of engineering relevance. This finding comes about because the period range at which the directivity pulse acts increases with magnitude. Whereas the directivity pulse for large magnitude events occurs at long periods, the amplification of ground motions due to directivity effects from to small to moderate events occurs at periods that are likely to match the natural periods of common building stock. Given the propensity for liquefaction in the region it is important to take into consideration the possibility of relatively small events occurring at shallow focal depths causing ground motions of engineering relevance.

It is also worth noting that while the probability of a small events causing significant damage to engineered structures remains low, even taking into account shallow focal depths, site amplification, and forward directivity effects, many of these small events occur. The effect of these numerous events may act in conjunction with each other, i.e. while a single event may not be significant enough to incite large scale damage, it may be significant enough to weaken the existing building stock to the point where a successive event of a similar nature may cause ensuing damage. The cumulative effect of numerous small events should therefore be considered in the selection of the minimum magnitude used in the PSHA.

A.5.2.1.2. Maximum Magnitude

The assignment of maximum magnitudes to fault sources was discussed previously in Chapter Three. In this chapter the magnitude-frequency relationship was also specified as being the doubly bounded Gutenberg-Richter relationship. The upper bound of this relationship automatically precludes the

consideration of any magnitude event greater than this value. The upper limit on the magnitude range is therefore automatically imposed from the fault source model and does not need to be discussed in any more detail here.

A.5.2.2. Limiting Bounds on Distance

A.5.2.2.1. Minimum Distance

The selection of a lower bound to the distance range may seem trivial, i.e. the minimum distance must be zero. However, this may not necessarily be the case. Cornell and Vanmarcke (1969) comment on the influence of this selection with respect to area sources. In addition, Campbell (1997) uses a measure of distance, r_{seis}, that precludes the occurrence of earthquake events in the 'non-seismogenic' near surface. While Campbell (1997) gives a clear and explicit reason for requiring all events to occur at some distance from the site in question, most other attenuation relationships inadvertently include a parameter that essentially increases the theoretical distance between the source and site. This parameter that modifies the distance is usually simply described as a regression parameter that enables a better fit to the empirical data. Regardless of its physical meaning, the result is that while the trivial case of a lower bound of zero for the distance variable is commonly adopted, in reality the effective lower bound on the distance is slightly above zero.

A.5.2.2.2. Maximum Distance

The upper bound on distance is rarely mentioned in PSHA. This parameter may have influence upon the results of the hazard analysis if care is not taken in being consistent when defining the seismicity rates for various sources. Again, Cornell and Vanmarcke (1969) address this issue in arriving at the conclusion that small events, close to the site, contribute strongly to the total hazard at a site. There is a coupling between the frequency of events of magnitude greater than some threshold level, $\nu_{m_{\min}}$, and the volume of the region considered in the derivation of this value. Obviously, the larger the region considered, the higher the frequency of events exceeding a given magnitude (all other things being equal). One must therefore ensure that the activity rates assigned to seismic sources are consistent with the region used in the derivation of these activity rates.

For the present work this issue is of particular importance when dealing with the background seismicity. It is assumed that the spatial region of the crust between fault sources is seismically homogeneous. As the nature of the seismicity within the background source is relatively unknown and consists of small to moderate size events, the probability density function of distance is based upon hypocentral distances, i.e. earthquakes are assumed to be point sources. Der Kiureghian and Ang (1977) outlined a method for

taking finite rupture effects into consideration when analysing various types of faulting sources. However, their analysis of areal sources with unknown orientation of faulting essentially required inverting attenuation relationships. In addition to this inversion, their original analysis hypothesised horizontally propagating ruptures; in reality these events are free to rupture in any direction making the mathematics untowardly cumbersome, consequently their method is not adopted in the present work for the background source. It is recognised that assuming that background events are focussed at their hypocentres is not conservative†, however, the effect should have a minimal influence upon the final results.

As well as the above assumptions, the background source is assumed to be a truncated hemisphere of radius $r_{\max}$. This truncation occurs at a depth equal to the base of the seismogenic layer, z_{seis}. In the actual PSHA program written for this study, this volume is actually modified slightly to remove the volume occupied by fault sources within this region. For demonstrative purposes here though, the above idealised model is sufficient. In this case, the probability density function of distance can be given by the ratio of the surface area of a sphere bounded by this volume, and the volume of the space internal to this surface and the bounding volume. The probability density function can therefore be given by Equation (A.5.6) below.

$$f_R(r) = \begin{cases} \dfrac{2r^3}{z_{seis}\left(3r_{\max}^2 - z_{seis}^2\right)} & , 0 \le r \le z_{seis} \\ \dfrac{3r^2 - z_{seis}^2}{3r_{\max}^2 - z_{seis}^2} & , z_{seis} < r \le r_{\max} \end{cases} \tag{A.5.6}$$

Now, consider the form of this probability density function as shown diagrammatically in Figure A.5.2 where the pdf is plotted for various values of $r_{\max}$. Clearly, the probability density assigned to a given hypocentral distance is markedly different for each value of $r_{\max}$. This is a natural, and obvious, consequence of requiring each curve to include the same unit area. This realisation however, does nothing to help resolve the problem of selecting the most appropriate value for $r_{\max}$.

The solution is found after considering the earlier comment regarding the positive correlation between the frequency of occurrence of events above some specified magnitude and the size of the region the frequency applied to. In order to be consistent with the activity rates found from the seismicity analysis, the total volume regarded as being the background source must equal the total volume attributed to the background source when performing the Bayesian Inference analysis and accompanying seismicity analyses. The volume considered in the seismicity analysis was a simple right prism whereas the volume considered in the hazard analysis, as previously mentioned, is a truncated hemisphere.

† The degree to which this assumption is not conservative is related to the magnitude of the event. For small to moderate sized events, having relatively small rupture *planes*, the net difference in total hazard estimates is small.

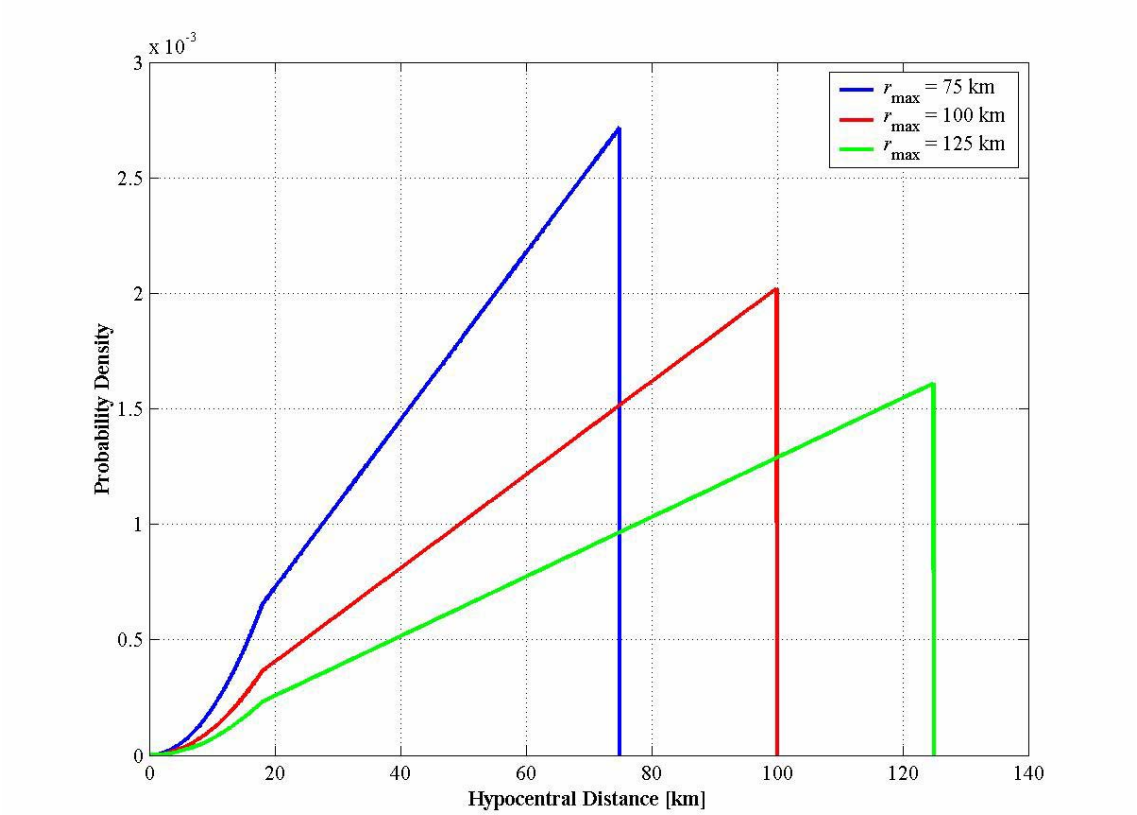

Figure A.5.2: Comparitive plot of probability density functions for the Background source given varying values of the upper bound on hypocentral distance

Now, the total volume of this truncated hemisphere can be given by Equation (A.5.7).

$$V_{background} = \frac{\pi}{3} z_{seis} \left(3r_{\max}^2 - z_{seis}^2 \right) \tag{A.5.7}$$

Therefore, in order to be consistent, one must ensure that the volume, $V_{background}$, is the same as the volume of the region used to determine the seismicity parameters for the seismic sources. Once this condition is met, the upper bound on the distance to be used in the integration can be found after rearranging Equation (A.5.7); this expression for the upper limit to the distance considered is given in Equation (A.5.8) below.

$$r_{\max} = \sqrt{\frac{V_{background}}{\pi z_{seis}} + \frac{z_{seis}^2}{3}} \tag{A.5.8}$$

It is possible to consider other values of $r_{\max}$ in the analysis but one must be sure to scale the activity rates assigned to the source on a pro rata, by source volume, basis.

A.5.3. Limiting Bounds on Epsilon

The essence of PSHA is to determine the rate at which some ground motion level is exceeded. By definition of the Standard Gaussian distribution, the probability that a normalised random variable, X, takes on a value above some specified value, x^*, is given by Equations (A.5.9) and (A.5.10) below.

$$P\left[X > x^*\right] = 1 - \Phi\left(x^*\right) \tag{A.5.9}$$

$$\Phi\left(x^*\right) = \left(1/\sqrt{2\pi}\right)\int_{-\infty}^{x^*} \exp\left(-x^2/2\right)dx \tag{A.5.10}$$

One can appreciate that the standard normal distribution is symmetric about zero, and from the above equations one can also see that as the value of x^* decreases the probability that the condition $X > x^*$ is met increases. In terms of ground motions, this implies that negative values of epsilon characterise events in which the recorded ground motions resulting from an earthquake scenario (magnitude-distance pair) are lower than that which would ordinarily be expected. Therefore, if it is fair to assume that ground motions are lognormally distributed, which many authors (for example Campbell 1985; Douglas and Smit 2001; Restrepo-Velez and Bommer 2003) suggest it is, one can use the limits of the above equations for the normal distribution to infer the lower limit on the value of epsilon to be used in PSHA. The lower bound on epsilon is consequently trivial, and corresponds to the condition where it is certain that a magnitude-distance pair will exceed the target ground motion measure; that being epsilon equal to negative infinity.

The upper bound on epsilon on the other hand is far from trivial. Positive values of epsilon represent ground motions that are in excess of the median predicted ground motion given a magnitude-distance pair (as well as other relevant parameters). The question that must be addressed when selecting an upper bound on epsilon is; what degree of exceedance of this median will we allow in the PSHA? This is not a simple question to answer. For a start, we assume that the ground motions associated with a particular magnitude-distance pair are lognormally distributed. This appears to be a very good assumption (see, for example Restrepo-Velez and Bommer 2003) over a wide range of epsilon values ($\pm 2\varepsilon$ at least). However, with any empirical dataset, the number of recorded data points lying in the tails of the distribution is very low, and it is in these regions that only the weakest statistical inferences can be made. That said, Restrepo-Velez and Bommer (2003) found that the hypothesis that residuals of ground motion predictive equations are normally distributed[†] could not be rejected when tested using the Anderson-Darling goodness of fit test. This measure of the goodness of fit is a modification of the Kolmorgorov-

[†] The residuals of the ground motion predictive equations are typically given by $\delta = \ln S_{a,recorded} - \ln S_{a,predicted}$. Here however, a transformation is made to $\delta = \ln\left(S_{a,recorded}/S_{a,predicted}\right)$ in order to remove any amplitude dependence in the residuals. In either case, if the residuals, δ, are normally distributed, the ground motions must be lognormally distributed.

Smirnov test (Benjamin and Cornell 1970); modified to better indicate the goodness of fit in the tails of a distribution. Therefore, if the conditions of the Anderson-Darling test are satisfied, one can be confident that the upper bound on epsilon would indeed extend beyond the previously mentioned level of positive two if more data were collected.

The satisfaction of statistical tests is one aspect of the matter, the most important condition that we should seek to meet though relates to the physical limits on the magnitude of ground motions. There must be a physical limit, while conservation of energy is maintained, to the level of ground motion that a particular size event can generate. Exactly what this limit is though, is currently an area of active investigation (Bommer et al. 2004). In the future, it may be desirable to modify the assumption of lognormality at large values of epsilon. Restrepo-Velez and Bommer (2003) propose the upper limit lognormal (ULLN) distribution for this purpose. The ULLN distribution requires the specification of the upper limit on epsilon. As we have already alluded to, current datasets of ground motion records are not complete enough to infer what this upper limit is, however, the framework is in place for this purpose.

For the present work, the common assumption of lognormality is adopted and hazard estimates are computed for upper bounds on epsilon of $\varepsilon_{\max} = 2$ and $\varepsilon_{\max} = 3$. Note that these two conditions correspond to neglecting 2.275% and 0.135% of potential outcomes from a particular earthquake scenario. The influence that the selection of this limit has upon the final hazard estimate depends upon how the hazard is made up. Figure A.5.3 shows an example of the hazard curves for the Island Block site (NZMG position [2424330, 5893600]) computed for various upper limiting values of epsilon.

These hazard curves are determined with respect to two different measures of ground motion. Firstly, the effect on Peak Ground Acceleration is demonstrated in panel (a) of Figure A.5.3; in this case the scenario depicted is for an individual fault source, the Glasgow Fault. Additionally, panel (b) shows the same effect as it relates to Arias Intensity[†], this time computed for all seismic sources except for the Alpine Fault. The same effect is evident in both cases; that being the progressive departure from unbounded case as one moves to lower and lower rates of exceedance. This effect results from the fact that the seismic source(s) in question can only generate ground motions above the target level if the ground motions are much larger than the median motions expected for the various earthquake scenarios in the PSHA. In the unbounded case, it is still theoretically possible for these earthquake scenarios to produce such high ground motions but the probability that they will do so is very low. However, if enough of these finite contributions are included the hazard at low rates of exceedance continues to build. In the bounded cases of $\varepsilon_{\max} = 2$ and $\varepsilon_{\max} = 3$ we see that these small, but finite, contributions are not considered and as a result the contribution to the hazard at these low rates of exceedance falls away asymptotically to zero as one moves to lower and lower annual rates of exceedance. In the example cases that are given, the difference

[†] Only the predictive model of Travasarou et al. (2003) is used for this purpose.

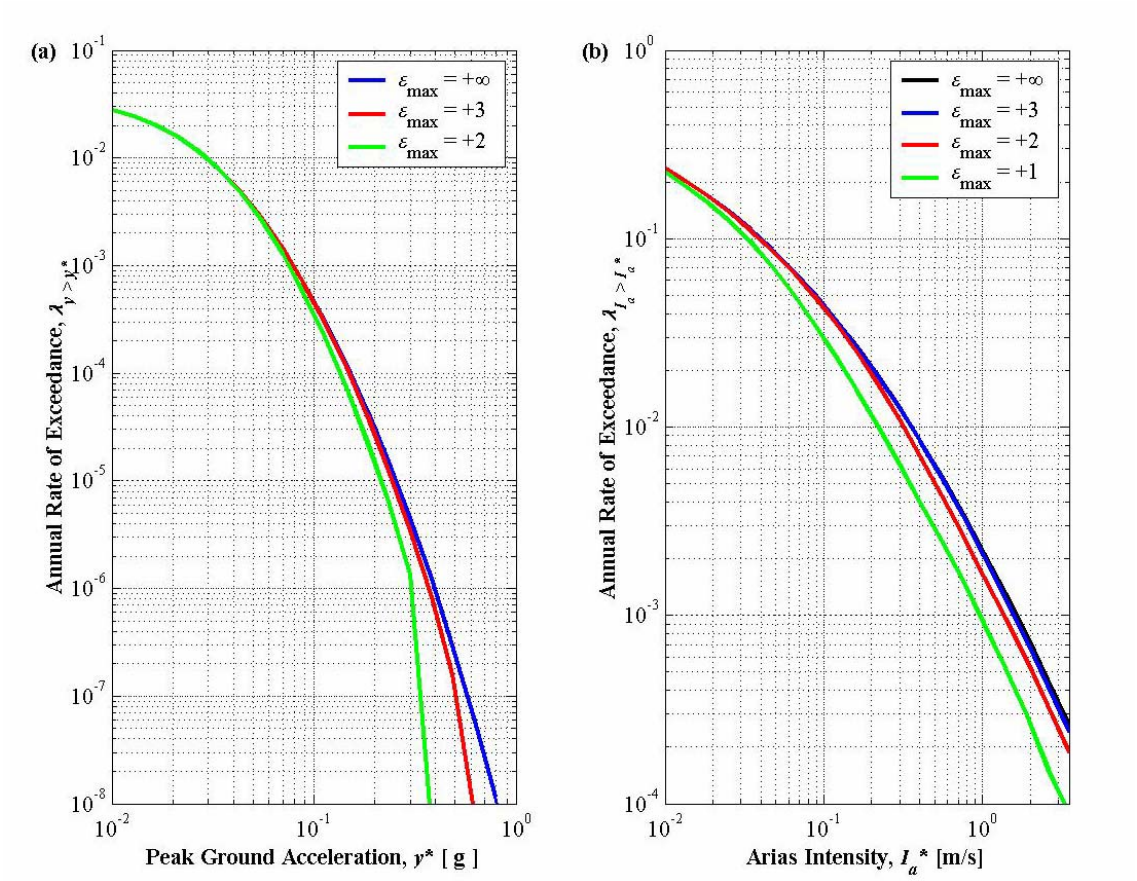

Figure A.5.3: Comparison of hazard curves computed for differing upper limits on epsilon, (a) shows the contribution to the total hazard from the Glasgow fault; here the hazard is determined with respect to Peak Ground Acceleration, (b) shows the total hazard (excluding the time dependent effect of the Alpine Fault) determined with respect to Arias Intensity

between hazard curves appears to be small. One must appreciate however, the logarithmic nature of the plots and that small deviations may represent significant differences in design ground motions. This effect is particularly pronounced as the design return period increases. The degree of influence is also strongly related to the general slopes of the hazard curves in the vicinity of the target rate. The example that is given for the case of the spectral acceleration is given for demonstrative purposes only. In reality, the departures from the unbounded epsilon case for this set of hazard curves are negligible at rates of interest to common design.

The consideration given above to the selection of the most appropriate values of the limits of integration adopted in the PSHA is a procedure that every hazard analyst should perform. The decisions made regarding the specific values implemented in the final calculations should also be explicitly mentioned so that the results of the analysis can be compared with the results of other comparative analyses either presently existing, or undertaken in the future. Once the integrals are fully defined a numerical procedure is implemented in order to calculate the rate of exceedance of the strong motion measure in question.

This rate must then be converted to a probability; how this probability is determined is the subject of the next section.

A.5.4. Probability Calculations

In the original presentation of PSHA methodology (Cornell 1968) three fundamental assumptions were made. These were, firstly, that within any given seismic source, there is equal probability of an event occurring at any point within that source, secondly, that the average rate of occurrence of events is independent of time (i.e. earthquake generation is a stationary process), and finally, that these events can be described by a Poisson model of occurrence. At the time of presentation, qualifying remarks were given with respect to these assumptions. The general PSHA framework easily allows for violation of the first assumption. The analyst simply subdivides the source into smaller elements and assigns differing rates of occurrence to these elements. The second assumption is also relatively simple to relax. The difficulty in modifying this assumption does not result from alterations to the PSHA framework but rather to obtaining data to support the departure from a time independent rate of occurrence for a seismic source. For almost all earthquake sources that are considered in current PSHA models, the duration of observation of activity on these sources is small in comparison to the typically rate of occurrence of large events in these sources. Consequently, any postulated departure from an average rate is difficult to justify in a statistical sense. The third assumption is one that has attracted the most attention of the three mentioned since the original presentation of the methodology. Cornell (1968) acknowledged that the assumption of Poisson occurrence contradicted Elastic Rebound Theory (Reid 1910). Other researchers have developed time dependent earthquake forecasting models that take into account the time since the last event of significant magnitude. Of particular note are the lognormal distribution (Nishenko and Buland 1987) and the more recent Brownian Passage Time distribution (Matthews et al. 2002). Both of these distributions take into account the current position of a seismic source with respect to its earthquake cycle. The result is to reduce the probability of an event occurring in the period immediately following a large earthquake (obviously excluding aftershock sequences), and for the probability of occurrence to gradually build as the time since the last significant event approaches the average time interval between significant events for that source. Whether or not these time dependent models are able to be applied to a given seismic source is strongly related to whether paleoseismic data (McCalpin 1996) are available for that fault source. Almost exclusively, the duration of instrumental observation of activity on an individual fault is too short to confidently infer an average recurrence interval for that fault source. The concept of self-organised criticality (SOC), mentioned in Chapter Three of this section, also warrants mention here. If it is found that the crust is genuinely in a self organised critical state then it becomes theoretically impossible to predict the occurrence of future earthquake events. In this case, the issue of time dependence obviously becomes irrelevant. However, until this issue is resolved either way, the evidence in support of time dependent earthquake behaviour warrants the consideration of time dependent probability calculations here.

This lack of paleoseismic data is generally not a significant problem for active tectonic regions because the Poisson assumption has been shown to be very good in almost all instances (Cornell and Winterstein 1988). The only exception to this statement occurs for the case where the hazard is dominated by a single feature for which the elapsed time since the previous significant event exceeds the average time between such events. In the Buller region it is most probably conservative to assume that Poisson conditions apply. The occurrence of two large earthquakes, the 1929 Murchison and the 1968 Inangahua events, on faults that are otherwise thought to be relatively inactive should mean that the probability of having another similar large event on these sources is reduced.

The exception that Cornell and Winterstein (1988) suggest may well relate to the Alpine Fault when calculating hazard for the Buller region. This is particularly likely when considering the exceedance of ground motion measures at low rates of occurrence. Consequently, in the present study, all seismic sources except for the Alpine Fault are assumed to act in a Poissonian manner. The time dependence of the activity associated with the Alpine Fault is discussed in the next section where a closer look at the potential models is taken.

A.5.4.1. Probability Distributions

A.5.4.1.1. Poisson Distribution (Exponential Distribution)

If the occurrence of earthquakes in time is to be considered a Poisson process, three conditions must be met (Benjamin and Cornell 1970).

1. *Stationarity.* The probability of an earthquake event in a *short* interval of time t to $t+\tau$ is approximately $\lambda\tau$, for any t.
2. *Nonmultiplicity.* The probability of two or more earthquakes in a short interval of time is negligible compared to $\lambda\tau$ (i.e., it is of smaller order than $\lambda\tau$).
3. *Independence.* The number of earthquakes in any interval of time is independent of the number in any other (non-overlapping) interval of time.

Although the Poisson process has been widely used since it was used in the initial introduction of PSHA, it can be appreciated why there have been numerous other alternative models proposed. The validity of both the second and third axioms can be questioned. The condition of nonmultiplicity is not met by foreshock or aftershock sequences of earthquakes. Also, the condition of independence does not agree with the long standing earthquake regeneration model of Elastic Rebound Theory (Reid 1910). However, the Poisson model, whose probability density function is given in Equation (A.5.11) below, is remarkably simple and easy to implement, requiring only knowledge of the average rate of earthquake occurrence, λ.

$$p_X(x) = \frac{(\lambda t)^x e^{-\lambda t}}{x!} \tag{A.5.11}$$

In Equation (A.5.11), $x = 0, 1, 2, \ldots$ represents the number of earthquake events, and t again represents time.

The partial violation of the two conditions above does not generally pose significant problems for PSHA for the following reasons. The violation of the second condition may be remedied by removing spatially and temporally dependent events from the earthquake catalogues used to estimates the rates of activity for the various seismic sources in the PSHA model, i.e. declustering the seismicity catalogues. This issue of declustering earthquake catalogues was addressed in more detail in the discussion of seismicity analyses earlier in this work. The violation of the third condition may present more of a problem, particularly in the case where evidence of characteristic behaviour is observed (Schwartz and Coppersmith 1984), or where the hazard calculation at a site is strongly dependent upon the contribution from a single source (Cornell and Winterstein 1988). However, Cornell and Winterstein (1988) point out that the sum of non-Poissonian processes may be approximately Poissonian, before more formally asserting (Cornell and Winterstein 1989), following the prompt of Lomnitz (1989), that the Poisson model is the limit of a sum of point processes (and under appropriate conditions, marked point processes as well). Therefore, regardless of the temporal dependence of the individual seismic sources within a region, the combination of these sources will yield a regional model of seismic activity that will approach a Poisson model as the number of sources (or the size of the region) increases. The preponderant use of the Poisson model in PSHA is therefore reasonably justified when the model is applied to a site for which the total calculated hazard reflects contributions from a number of individual sources.

Adopting the Poisson process as a model for earthquake occurrence, one is readily able to calculate the probability of an event occurring in a given period of time (a calculation that is pivotal to PSHA). Defining T as a random variable representing the time to the first occurrence of an earthquake, the probability that T exceeds some value t ($P[T > t] = 1 - F_T(t)$), is equal to the probability that no events occur during this interval of time. The probability of no events occurring is found from Equation (A.5.12) for $x = 0$, i.e.,

$$p_X(x = 0) = \frac{(\lambda t)^0 e^{-\lambda t}}{0!} = e^{-\lambda t} \tag{A.5.12}$$

Therefore, the probability that at least one event occurs during this interval must be the compliment of this expression, and is equal to the cumulative distribution function for the occurrence of an earthquake, this function is defined in Equation (A.5.13) below along with the associated probability density function in Equation (A.5.14).

$$F_T(t) = 1 - e^{-\lambda t} \tag{A.5.13}$$

$$f_T(t) = \frac{dF_T(t)}{dt} = \lambda e^{-\lambda t} \tag{A.5.14}$$

Both the above equations are valid for $t \geq 0$ only. The above pair of equations define the Exponential distribution and we can therefore assert that, given the acceptance of the hypothesis that earthquakes follow a Poisson process, the interarrival time of earthquakes are independent and exponentially distributed (Benjamin and Cornell 1970).

A.5.4.1.2. Lognormal Distribution

In an effort to address the violation of axiom three of the Poisson process stated above, Nishenko and Buland (1987) considered the distribution of interarrival times of repeated earthquakes of similar magnitude on individual fault sources. In this work they found that these interarrival times could be modelled well by the lognormal distribution. The lognormal distribution has the probability density function and cumulative distribution function given by Equations (A.5.15) and (A.5.16) respectively.

$$f_T(t) = \frac{1}{\sigma t \sqrt{2\pi}} \exp\left[-\frac{\left(\ln(t) - \mu\right)^2}{2\sigma^2} \right] \tag{A.5.15}$$

$$F_T(t) = \Phi\left[\frac{\ln(t) - \mu}{\sigma} \right] \tag{A.5.16}$$

In Equation (A.5.16) $\Phi[\bullet]$ is the standard normal integral defined earlier in Equation (A.5.10). The lognormal model was fit to an empirical dataset that consisted of faults that had at least three documented earthquake events in their history. This dataset consequently consisted of 53 recurrence intervals and the fundamental ergodic assumption was made; that being that because the events included in the dataset are the result of a similar mechanism events distributed in space can be regarded as events distributed in time. In this manner, the 53 recurrence intervals, while compiled from different regions throughout the world, can be regarded as originating from the same population. Following this assumption, it was found that the best fit to the data corresponded to a standard deviation for the recurrence interval of $\sigma_D = 0.205$. This is a surprisingly small standard deviation given the large uncertainties involved with the estimation of the timing of paleoseismic events. Yetton et al. (1998) added paleoseismic findings from their study of the Alpine Fault as well as new information from other fault sources to increase the Nishenko and Buland dataset by 16 intervals. They recalculated the standard deviation using this extended dataset and found it to be $\sigma_D = 0.34$.

However, Matthews et al. (2002) claim that "Nishenko and Buland's entire approach,…, is seriously flawed and their goal impossible to achieve". The primary flaw apparently comes about due to data-dependent normalization to a common scale (i.e. in fitting the lognormal distribution to a fictitious dataset of T/T_{ave} values), and is discussed in the appendix to their paper. This consequently draws into question the validity of the estimates of time dependent probabilities made for the Alpine Fault by Yetton et al. (1998).

A.5.4.1.3. Brownian Passage Time Distribution

While the lognormal distribution does an admirable job of modelling the form of the time dependence of earthquake occurrence on individual faults, it has the undesirable feature that its hazard rate function tends to zero at long times. The hazard rate function for any distribution can be given by the ratio of the probability density function to the complimentary cumulative distribution function. This definition is given below in Equation (A.5.17).

$$h(t) = \frac{f_T(t)}{1 - F_T(t)} \tag{A.5.17}$$

The hazard rate function describes the instantaneous failure propensity of the fault in question (Matthews et al. 2002). Given our current understanding of the earthquake cycle, the most desirable behaviour of the hazard rate function would be that it starts at zero (following the occurrence of a major event), and then gradually increases with time suggesting that the instantaneous likelihood of failure in turn increases with time (as tectonic stresses build in the vicinity of the fault). Following a period of increase of the hazard rate function it would then be desirable for the function to approach some asymptotic limit that represents the case in which the stress state around the fault is conducive to failure and that the occurrence of next event can now be modelled as a random process. A model that achieves all of these desired behaviours is the Brownian Passage Time (BPT) model (Matthews et al. 2002). This model was derived from a physical basis by adding Brownian perturbations to a steady loading cycle of tectonic stress. The model has a sound physical basis and is in strong accord with the current understanding of stress cycles and earthquake cycles; for these reasons the model was adopted in place of the lognormal distribution in the Working Group on California Earthquake Probabilities (WGCEP 2003) study. Another point of merit of the BPT model is that its functional form is very similar to the lognormal distribution and consequently the strong correlation between modelled and observational data that Nishenko and Buland (1987) found is maintained when the BPT model is fitted to this same data.

Mathematically, the probability density function for the Brownian Passage Time model is defined as in Equation (A.5.18).

$$f_T(t) = \sqrt{\frac{\mu}{2\pi\alpha^2 t^3}} \exp\left[-\frac{(t-\mu)^2}{2\mu t\alpha^2}\right] \tag{A.5.18}$$

Here, as in the case of the lognormal distribution, two parameters are required to define the distribution. For the BPT model these parameters are the mean recurrence interval, μ, and the aperiodicity parameter, α †. The associated cumulative distribution function is defined in terms of the cumulative Gaussian probability function (Rhoades and Van Dissen 2003); again see Equation (A.5.10), and is given in Equation (A.5.19).

$$F_T(t) = \Phi\left[\frac{t-\mu}{\alpha\sqrt{\mu t}}\right] + \exp\left[\frac{2}{\alpha^2}\right]\Phi\left[\frac{t+\mu}{\alpha\sqrt{\mu t}}\right] \tag{A.5.19}$$

Because the derivation of the BPT model is physically based upon the regional stress fields induced by tectonic loading, the model is also able to be modified to incorporate stress steps, or perturbations, that may be caused by the interactions between various faulting sources (Matthews et al. 2002). This modified version of the BPT model, the BPT-step model, was employed to account for the stress shadow cast by the Great San Francisco earthquake of 1906 in the WGCEP (2003) study. Recently, some investigation has been made into the fault interactions that may exist between fault sources in the northern South Island (Robinson 2004; Hincapie et al. 2005). Hincapie et al. (2005) paid particular attention to the Buller region with a view to trying to find correlations between the modifications to the regional stress field caused by the major historical events that the region has experienced and subsequent events. While some events (typically aftershocks) can be shown to lie strongly in regions where secular Coulomb stress accumulation (ΔCFS) changes are strongly positive, they eventually conclude that there does not appear to be a clear relationship between areas of increased secular Coulomb stress accumulation and the location of subsequent mainshocks of moment magnitude greater than $M_W = 7.0$. As a result of this finding, the BPT-step model will not be incorporated in the present work. Another finding of the Hincapie et al. (2005) research that is noteworthy is that the occurrence of the 1968 Inangahua event is likely to have been *delayed* as a result of the 1929 Buller event. The relevance of this finding may be important when one considers the amount of literature suggesting that the historical record of seismicity in the region is anomalously high. This issue was mentioned previously in Chapter Two.

Having now settled upon the use of the standard BPT model (as well as the lognormal model) for modelling time dependent probabilities for the Buller region, all that remains is to define applicable parameter values for these distributions. Ellsworth et al. (1999) suggest the use of $\alpha = 1/2$ as a generic value of the aperiodocity based upon 37 recurrent earthquake sequences with a magnitude range of $-0.7 \le M_W \le 9.2$. Note that when one regards the aperiodicity as being equivalent to the coefficient

† In the BPT model, the aperiodicity parameter, α, is for all intents and purposes equivalent to the coefficient of variation, i.e., it is defined by the relationship $\alpha = \sigma/\mu$.

variance as well as appreciating the normalisation of reccurence intervals used by Nishenko and Buland, it is clear that this value for the aperiodicity is significantly larger than the estimate of 0.205 of Nishenko and Buland (Nishenko and Buland 1987). While this value is suggested as a generic value, there is still considerable uncertainty regarding the applicability of this value for a given fault source as well as equally large uncertainty regarding the selection of the appropriate value of μ for a given fault. Unfortunately, specific datasets for a given fault, such as the Alpine Fault, are not likely to improve drastically in the foreseeable future. Fortunately, however, a methodological framework has been developed in which time dependent probabilities may be estimated in a relatively robust manner. This methodology is outlined in the next section.

A.5.4.2. Application of Time Dependent Probabilities to the Alpine Fault

Rhoades and Van Dissen (2003) considered the time dependence of probabilities of characteristic earthquakes occurring on the central and southern sections of the Alpine Fault. In this work both the lognormal and BPT models were used (as well as the exponential and Weibull distributions). The research presents a methodology that can be used to effectively ascertain descriptive parameters of the distributions by taking into account the various large uncertainties that are related to working with small numbers of data points. Their methodology does not generate specific parameters for the distributions that they considered; rather it generates an estimate of the instantaneous hazard rate which in turn can be used to obtain time dependent probabilities. A brief summary of this methodology is presented here for the case of the BPT model‡. The methodology summarised below applies to all of the distributions that can be considered for modelling time dependent earthquake probabilities.

Let $f_T(t \mid \mathbf{x})$ be the recurrence time probability density function, in which $\mathbf{x}$ is the vector of data points of past rupture times. For a given time dependent model (such as the BPT model in this case), this probability density function can be expressed by the following expression.

$$f_T(t \mid \mathbf{x}) = \int_{\boldsymbol{\theta}} f_T(t \mid \boldsymbol{\theta}, \mathbf{x}) g(\boldsymbol{\theta} \mid \mathbf{x}) d\boldsymbol{\theta} \tag{A.5.20}$$

Here, $f_T(t \mid \boldsymbol{\theta}, \mathbf{x})$ is the BPT recurrence time model for particular values of the model parameters, given in the vector $\boldsymbol{\theta} = \{\mu, \alpha\}$, and data values, $\mathbf{x}$. In addition, $g(\boldsymbol{\theta} \mid \mathbf{x})$ represents the conditional probability density of the parameters $\boldsymbol{\theta}$, given $\mathbf{x}$, commonly known as the likelihood function. For the BPT model, the term $f_T(t \mid \boldsymbol{\theta}, \mathbf{x})$ has the form given in Equation (A.5.18), while the likelihood function is proportional to the following expression.

‡ Note that in their original paper, Rhoades and Van Dissen refer to the BPT model as the Inverse Gaussian model.

$$g\left(\boldsymbol{\theta} \mid x_1,\ldots,x_k\right) \propto \left(\frac{\mu_s}{2\pi\alpha_s^2}\right)^k \prod_{i=1}^{k}\left(\frac{1}{x_i^3}\right)\exp\left[-\frac{\left(x_i-\mu_s\right)^2}{2\alpha_s^2\mu_s x_i}\right] \tag{A.5.21}$$

In Equation (A.5.21), μ_s is the mean recurrence interval for a particular sample, drawn from a prior distribution of probable mean recurrence intervals. This prior distribution of recurrence intervals is found from consideration of the likely distributions of rupture displacement and fault slip rate. Both the probable rupture displacement and the fault slip rate are modelled as lognormally distributed parameters based upon observations of previous events on the Alpine fault as well as variations in these parameters for other faults with longer paleoseismic records. The prior distribution of recurrence intervals is calculated from the ratio of the rupture displacement distribution and the fault slip rate distribution. Likewise, the term, α_s is also drawn from a prior distribution; this time, randomly from a uniform distribution over the interval $(0,1)$.

Now the hazard rate function, conditioned upon the particular set of data values can be determined using the standard form for the hazard rate function, given below in Equation (A.5.22).

$$h_T\left(t \mid \mathbf{x}\right) = \frac{f_T\left(t \mid \mathbf{x}\right)}{1-F_T\left(t \mid \mathbf{x}\right)} \tag{A.5.22}$$

The final estimate of the hazard rate function can then be found after consideration of the possible range of data values. This is essentially as estimate found by calculating the weighted average of the conditional hazard rate values and is defined in Equation (A.5.23).

$$h_T\left(t\right) = \int_{\mathbf{x}} h_T\left(t \mid \mathbf{x}\right) f_X\left(\mathbf{x}\right) dx \tag{A.5.23}$$

Finally, the probability of an earthquake occurring in the future interval (t_1,t_2) is given by Equation (A.5.24) below.

$$P\left[E_{(t_1,t_2)}\right] = 1-\exp\left[-\int_{t_1}^{t_2} h_T\left(t\right)dt\right] \tag{A.5.24}$$

After following this rigorous procedure Rhoades and Van Dissen (2003) found that the hazard levels for the BPT model should be set equal to 0.0073 events per year, while the lognormal distribution should have a corresponding hazard of 0.010 events per year. Both of these estimates of the instantaneous hazard rate correspond to the 2002 value for the central section of the Alpine Fault. Employing these values in Equation (A.5.24) yields significantly lower time dependent probability estimates than those obtained by Yetton et al. (1998).

This finding has significant implications for the determination of seismic hazard for regions proximal to the Alpine Fault, such as the Buller region. However, although the instantaneous hazard rate values given above are very rigorously, and robustly, determined, they correspond to the central section of the Alpine Fault and the sections of the Alpine Fault that are closest to the region of interest in this study are northern and Wairau sections (Yetton 2002). A method must therefore be devised to ascertain the equivalent instantaneous hazard rates for these sections also. Obviously, the method outlined above provides a means with which to do this. However, for the cases of the central and southern sections of the Alpine Fault, more paleoseismic information exists, as well as more constraint from other sources such as landslide and terrace records, forest age data, and tree ring chronologies (Rhoades and Van Dissen 2003). For these sections it is therefore possible to identify approximate sequences of historical events. For the northern and Wairau sections of the Alpine Fault, while more paleoseismic information has been obtained for these sections (Yetton 2002), the potential for identifying sequences of events is very limited. Therefore, because even the robust methodology of Rhoades and Van Dissen (2003) would still only provide relatively approximate hazard rates for the northern and Wairau sections of the Alpine Fault a more simple approximation is made to determine the instantaneous hazard rates for these northern sections.

As previously mentioned, one of the primary advantages of the Brownian Passage Time model over the lognormal model is that the BPT model has the desirable characteristic that its hazard rate function tends asymptotically to a constant value at times greater than the mean inter event time. This rate can be thought of as being reflective of the long term rate of occurrence for the given fault. As Rhoades and Van Dissen (2003) point out, a relatively long period of time has passed since the last rupture of the central and southern sections of the Alpine Fault. Consequently, the instantaneous hazard rates that they calculate for the BPT model are very stable with time and these values can therefore be associated with the average occurrence of earthquakes on these sections. Another measure of the typical recurrence interval of a fault is the combination of the slip rate on the fault and the average single event displacement of events on these faults. This information was made use of in the method of Rhoades and Van Dissen (2003) detailed above. However, the observed displacements are often highly variable along the strike of a fault (Thatcher et al. 1997; Yetton 2002). The paleoseismic evidence on the northern section of the Alpine Fault (Yetton 2002) suggests that smaller single event displacements are observed along this section of the Alpine Fault; the significant degree of uncertainty related to this observation must be recognised. In order to estimate the instantaneous hazard rates for the northern and Wairau sections the probably conservative assumption was made that the displacements along these sections are similar to those observed on the central section and that the relative slip rates can therefore be used to approximate the hazard rates for these sections. The typical slip rate along the central section of the Alpine Fault is approximately 27 ± 5 mm/yr (Norris and Cooper 2000), whereas the slip rate along the northern section is approximately 7.7 ± 1.0 mm/yr (Berryman et al. 1992; Yetton 2000; Yetton 2002), and the slip rate on the Wairau section is relatively well defined at approximately 4.5 ± 1 mm/yr (Lensen 1968; 1976; Grapes and Wellman 1986; Knuepfer 1988; 1992; Zachariasen et al. 2001). Yetton (2002) also notes that both the northern and Wairau sections of the Alpine Fault have not experienced significant events for quite some time. Yetton (2002) estimates the time of last rupture of the northern section to be approximately 1620 ± 10 AD and that consequently enough strain energy would have built up on this section to suggest that the next rupture of this section is

most likely to correspond to a coincident rupture of the central section. This scenario of a joint rupture of both the central and northern sections is thought to be the most likely scenario involving the northern section of the Alpine Fault (Yetton 2002). Another scenario is also postulated by Yetton (2002) for this section however, that of a smaller event rupturing a relatively smaller section of 100km contained just to the northern section of the fault. The suggestion that the most likely event on the northern section coincides with that on the central section is very useful for constraining the instantaneous hazard rate for this section as it can simply be taken to equal the value of Rhodes and Van Dissen (2003) for the central section. The relative likelihood of the other scenario, involving only the rupture of the northern section in isolation, is estimated by multiplying the value Rhoades and Van Dissen (2003) by the ratio of the slip rates of the northern and central sections. The Wairau section of the Alpine Fault is suspected of acting independently of the northern section due in large part to the bend in the Alpine Fault acting as a barrier to rupture propagation (Zachariasen et al. 2001; Yetton 2002). The single scenario of a full rupture of this section of the Alpine Fault is therefore considered in the present hazard analysis. The instantaneous hazard rate for this section is again approximated by taking the ratio of the slip rates of the Wairau and central sections of the Alpine Fault and multiplying this by the instantaneous hazard rate of the central section defined by Rhoades and Van Dissen (2003). In this way the time dependent probability of a large event occurring on the Alpine Fault diminishes as one moves progressively north; this is in keeping with the general consensus of the geological community (Yetton 2002).

Therefore, in order to calculate the time dependent contribution to hazard from the Alpine Fault, three scenarios are considered; these are:

- Combined rupture of both the central and northern sections of the Alpine Fault, with corresponding magnitude of approximately $M_W 8.05 \pm 0.2$, and an instantaneous hazard rate of 0.0073 events per year for the BPT model and 0.010 events per year for the lognormal model. The source site distances for the various attenuation models used for this scenario correspond to the combined rupture surface (i.e. the distance will be governed by northern section),
- An independent rupture of the northern section only with an associated magnitude of approximately $M_W 7.4 \pm 0.2$, and an instantaneous hazard rate of approximately 0.0021 events per year for the BPT model and 0.0029 events per year for the lognormal model. In this scenario, if the northern section is assumed to act independently of the central section the hazard from the central section must also be accounted for. The assumed magnitude for the rupture of the central section is $M_W 7.95 \pm 0.2$, and instantaneous hazard rates of 0.0073 and 0.010 events per year for the BPT and lognormal models respectively. The relevant distance to each source is determined for each attenuation model,
- An independent rupture of the Wairau section with an associated magnitude of approximately $M_W 7.5 \pm 0.2$, and an instantaneous hazard rate of approximately 0.0012 events per year for the BPT model and 0.0017 events per year for the lognormal model.

In order to calculate the hazard associated with these three scenarios a logic tree methodology was implemented. The general form of this logic tree as well as the weights assigned to the branches is shown in Figure A.5.4.

Only two pairs of weights need to be defined. Working from left to right through the tree, the first number of unity assigned to both of the main branches of the tree is more for completeness than anything else and simply represents the hypothesis that the scenarios of ruptures on the northern and Wairau sections of the Alpine fault are independent due to the segmentation imposed by the bend in the Alpine Fault. The next pair of numbers, for the upper branches is essentially a 2:1 ratio between the scenarios of a combined rupture on both the central and northern section together, and the northern section, and the central section acting independently. This ratio has been selected somewhat subjectively but is based primarily upon the conclusions of Yetton (2002) that the extent of elapsed time on both the central and northern sections makes their mutual occurrence the most probably scenario. Performing the required calculations for a range of other values for these relative contributions shows that the influence of this subjective allocation of weights upon the total hazard is limited as the difference in overall contribution to hazard between these two scenarios is relatively small. For the scenario of the northern and central sections acting independently the branches are again given a full value of one each; simply representing that both of these events define this scenario. The final branch weights define the relative confidence in the time dependent probability models for modelling these scenarios. The models may have their parameters selected so that the form of the distributions is reasonably similar; this would suggest the assignment of a more even weighting. However, the definition of the instantaneous hazard rates used in this tree are strongly reliant upon the assumption that the instantaneous hazard rate tends to a constant level and only the BPT model has this property; the lognormal hazard rate asymptotically tends to zero at large elapsed times. In addition, the estimates of the instantaneous hazard rate for the BPT model was found to be the most stable in the analysis of Rhoades and Van Dissen (2003). This stability was both with respect to increases in elapsed time (i.e. the estimate of the hazard rate is very similar for the next 100 years, provided the Alpine Fault does not rupture during this time), as well as with respect to alterations to the initial information upon which the model was based (i.e. if more paleoseismic information was added to the dataset). These considerations, as well as the stronger physical basis of the BPT model as outlined by Matthews et al. (2002) are the reasons for assigning a 4:1 ratio to the BPT model over the lognormal model for the calculation of time dependent probabilities related to ruptures on the Alpine Fault.

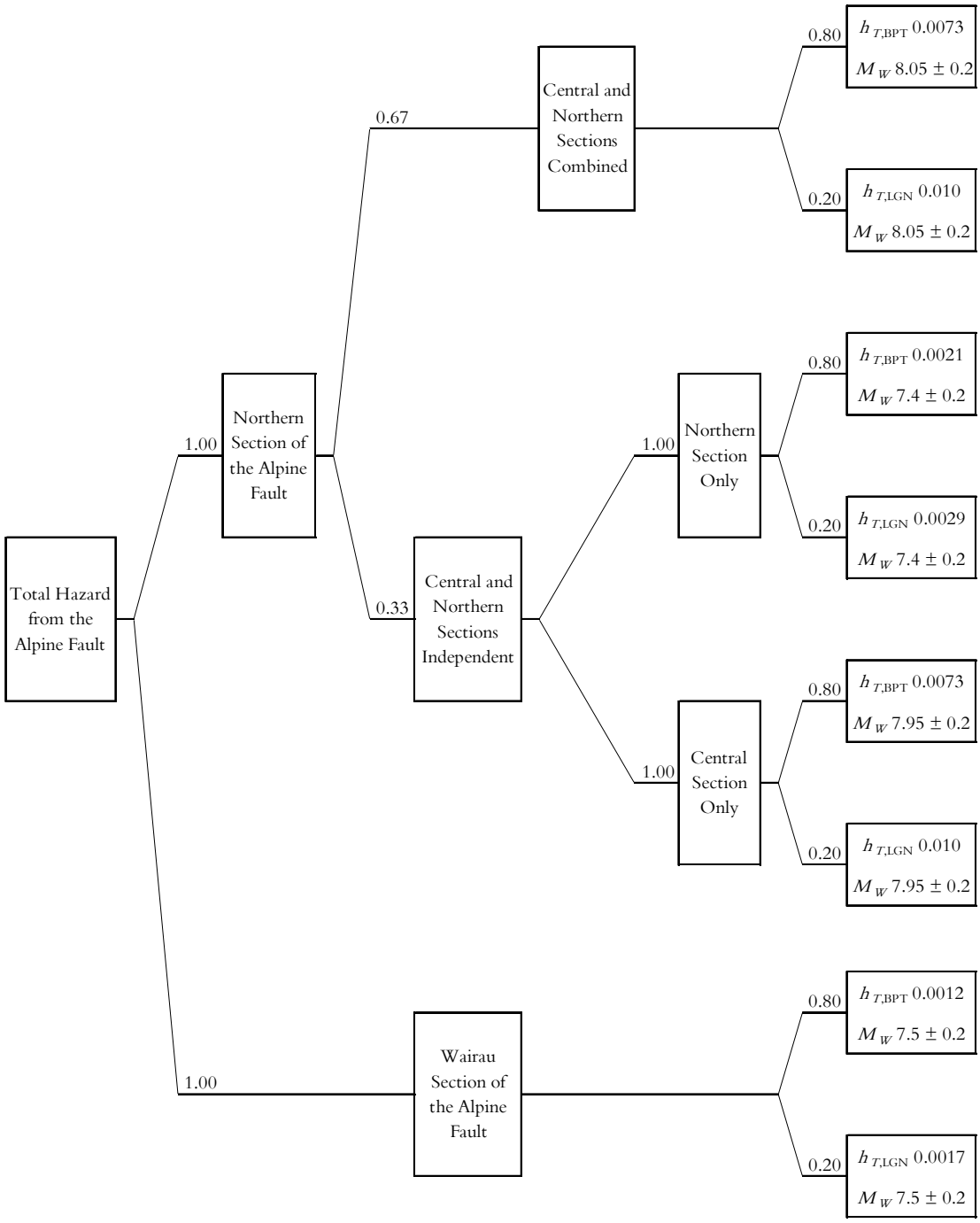

Figure A.5.4: Logic Tree implemented to determine the total hazard contribution from the northern and Wairau sections of the Alpine Fault. Numbers near branch nodes represent weights associated with that branch. Magnitude distributions are assumed to be truncated normal distributions with standard deviation of $\sigma_M = 0.1$ magnitude units and with applicability over the range specified in this figure i.e. distribution truncated and renormalized according to $\pm 2\sigma_M$.

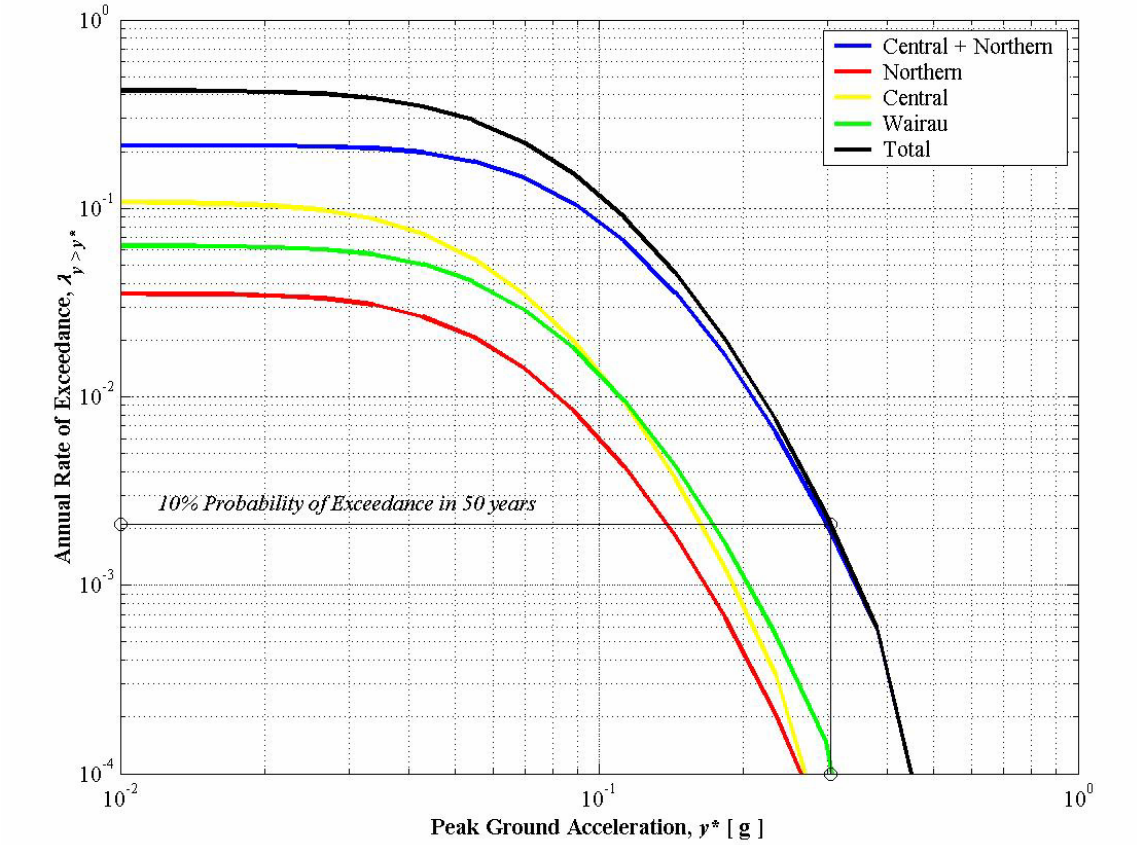

Figure A.5.5: Total contribution to hazard at Westport from the Alpine Fault. The various rupture scenarios are shown as well as their combined effect. Curves correspond to a maximum epsilon value of +3.

A.5.5. Disaggregation of Seismic Hazard

Commonly the results of a Probabilistic Seismic Hazard Analysis (PSHA) are disaggregated in order to show how the resulting hazard at a particular site relates to its constituent components. While analytical solutions may exist for the integral expression given in Equation (A.5.1) for the most simple cases (Ordaz 2004), there are invariably no analytical solutions to the integral expressions that result from modern seismic hazard assessments. The integration of the joint probability density function in magnitude, distance, and epsilon is consequently approximated in reality by performing a series of simple summations for discrete increments of each variable between the limits of integration. The true value of the integral is recovered in the limit where the increment size of each variable tends to zero. This process of approximation is summarised in Kramer (1996) In its most basic form this disaggregation can be performed with respect to one parameter such as magnitude or distance. In this case the hazard is said to be marginally disaggregated. Typically though, the total hazard is disaggregated with respect to at least two variables; usually magnitude and distance. Because of the numerical procedure adopted to evaluate the

integrals this is a relatively simple exercise. One simply stores the contributions to hazard determined for every combination of increments between each of the variables before the numerical integration is performed. The contributions to the total hazard for every scenario considered can then be extracted from these stored values.

The representation of the hazard at a site afforded by the disaggregation procedure is very instructive as it takes a step back from the probabilistically framed final outcomes and displays the hazard in terms of readily understandable parameters. Most lay people can easily consider the scenario of an earthquake of some magnitude occurring at some distance from them. When the hazard is disaggregated in this manner the result is a suite of magnitude-distance pairs that occur with various probabilities. The identification of the most critical earthquake scenarios is therefore made relatively transparent to the end user of the PSHA. There are however some subtleties associated with the disaggregation procedure, such as whether or not the probability mass function, or the probability density function is used to portray the hazard (Bazzurro 1998; Bazzurro and Cornell 1999), and how the hazard contributions are assigned to increments of epsilon (McGuire 1995; Bazzurro 1998; McGuire 2004).

As well as disaggregating the total hazard with respect to magnitude and distance one should also consider the contributions to the hazard that are made by various values of epsilon. When the hazard disaggregation is performed in terms of the three primary variables, M, R, ε, one is able to get a complete picture of where the overall hazard comes from. An additional method that provides even greater clarity is the 4D disaggregation methodology proposed by Bazzurro (1998) and Bazzurro and Cornell (1999) in which the positional contributions are also included by disaggregating the distance, R, further into latitude and longitude, or in our case New Zealand Map Grid Northings and Eastings. In this way the spatial distribution of the contributions to hazard can be plotted and one is able to see critical positions and events with great clarity. Note however, that this 4D representation requires much more complex code than the typical 3D version. It also requires the ability to store very large amounts of data (large four dimensional matrices) in physical memory while the calculations are performed. The amount of physical memory required rapidly increases as the bin size used for each of the four variables of Northings, Eastings, magnitude, and epsilon decreases.

Earlier in this chapter, the independence between the values of epsilon as well as magnitude and distance enabled the decomposition of the joint probability density function of $f_{M,R,\varepsilon}(m,r,\varepsilon)$ into the product of the joint probability density function in magnitude and distance and the probability density function of epsilon. This decomposition was defined in Equation (A.5.2). A further decomposition is almost always made; that being to decompose the joint probability density function in magnitude and distance into the product of the probability density functions corresponding to each variable separately. This methodology is that presented in Kramer (1996) and is expressed here in Equation (A.5.25).

$$f_{M,R,\varepsilon}(m,r,\varepsilon) = f_{M,R}(m,r)\, f_{\varepsilon}(\varepsilon) = f_{M}(m)\, f_{R}(r)\, f_{\varepsilon}(\varepsilon) \qquad \text{(A.5.25)}$$

In Equation (A.5.25) the probability density function with respect to distance, $f_R(r)$, is usually generated by assuming that events are equally likely to occur anywhere with a given source and the probability density function is consequently only related to the geometry of the source (Kramer 1996). However, in reality the decoupling presented in Equation (A.5.25) is not possible as modern predictive equations make use of distance measures that do not correspond to point sources. The above decomposition is valid when point source measures of distance are made as in that case one is able to make the assumption that events are equally likely to occur anywhere within the source and that the corresponding source site distances are simply the geometric distance from the site to each point that is considered within the source. It has long been recognised however, that point source distance measures are generally not appropriate for modelling strong ground motions (i.e. Bolt and Abrahamson 2003; Campbell 2003b). The distance measures used in the attenuation models incorporated into this study are all related to the size of the rupture surface, which in turn is related to the size of the earthquake creating this surface. Consequently, the distance from a site to the rupture surface depends upon the hypocentral position as well as the magnitude of the event. The joint probability density function should therefore be written as a conditional distribution dependent upon the magnitude of the causative event. The more appropriate form of the joint probability distribution function is therefore given in Equation (A.5.26).

$$f_{M,R,\varepsilon}(m,r,\varepsilon) = f_R\left(r \mid m, r_{hyp}, \boldsymbol{\theta}\right) f_{R_{hyp}}\left(r_{hyp}\right) f_M(m)\, f_\varepsilon(\varepsilon) \qquad \text{(A.5.26)}$$

In Equation (A.5.26), r_{hyp} denotes the hypocentral distance, and the vector $\boldsymbol{\theta}$ represents a set of parameters that describe the orientation of the rupture surface, such as the strike and dip of the fault, the depth to the bottom of the fault (and in the case of the r_{seis} distance measure of Campbell (1981) the depth to the top of the seismogenic part of the rupture), the segment of the fault the hypocentre is located in, and so on, i.e. $\boldsymbol{\theta} = \{\theta, \delta, z_{seis}, \text{segment}, ...\}$. Now, in this case, the probability density function with respect to hypocentral distance, $f_{R_{hyp}}\left(r_{hyp}\right)$, makes use of the assumption that events are likely to occur anywhere in the source, but the conditional probability density of the actual distance measure used to calculate hazard contributions from the attenuation equations must account for other parameters, including magnitude. The revised framework for hazard calculation presented here mirrors to a large degree that of Der Kiureghian and Ang (1977) in which the effects of rupture propagation are explicitly taken into account in the hazard analysis. Equation (A.5.26) explicitly shows how the hazard computations are dependent upon the nature of the scaling relationships adopted in the analysis. Such a component is a source of epistemic uncertainty and should be addressed accordingly in the analysis.

Note also that when one desires the full 4D representation of the hazard, one must effectively reduce Equation (A.5.26) further to account for the actual hypocentral position (rather than just the hypocentral distance) with respect to the site. For a given source i, the full joint conditional probability density function should therefore be represented by the following equation.

$$f_{M,R,\varepsilon}\left(m,r,\varepsilon\right)_i = f_R\left(r \mid m, \mathbf{x}_{hyp}, \boldsymbol{\theta}_i\right) f_{\mathbf{X}_{hyp}}\left(\mathbf{x}_{hyp}\right) f_M\left(m\right) f_\varepsilon\left(\varepsilon\right) \quad \text{(A.5.27)}$$

Now, $\mathbf{x}_{hyp} = \{x_1, x_2, x_3\} = \{N, E, Z\}$ (e.g., the hypocentral position in three dimensional NZMG co-ordinates) and $\boldsymbol{\theta}_i = \{\theta_i, \delta_i, Z_{seis}, \text{segment}, ...\}$ represent source specific parameters that dictate the position, nature, and orientation of the rupture surface. Note that within this framework, the hazard is actually disaggregated in five dimensions as the contributions from each increment in depth must also be taken into account. This is particularly for hazard analyses that take into account dipping faults such as the present study. While the disaggregation used in this study is therefore a 5D disaggregation procedure the spatial contributions are shown in map form and the contributions with depth are aggregated and shown in terms of their surface projections.

As well as being mathematically precise, the above formulation also makes it simple to see what information must initially be gathered in order to perform the PSHA calculations and ultimately disaggregate the PSHA into four dimensions so that the results are most easily comprehended by the end users of the PSHA.

A.5.6. Hazard Consistent Earthquake Scenarios

The disaggregation procedure outlined above is performed following the derivation of a hazard curve for a given site. Once this hazard curve has been calculated the design level of ground motion, such as the ground motion having a 10% probability of exceedance in 50 years can be picked off the curve. The disaggregation is then performed for this specific level of ground motion and the resulting spatial distribution of hazard contributions (if the 4D disaggregation method is used) relates specifically to this design ground motion level. Once the disaggregation procedure has been performed the most critical earthquake scenarios can be identified. In the most rigorous case this critical scenario corresponds to the triplet M^*, R^*, ε^* which represents the three dimensional mode of the joint probability distribution in these variables (note that in the four dimensional case this becomes the quartic mode $N^*, E^*, M^*, \varepsilon^*$). Commonly in the literature only magnitude - distance pairs are reported without the corresponding value of epsilon; in this case the combination of magnitude and distance when used in an attenuation model may not generate the ground motion level that has been disaggregated as the hazard could be reflecting positive epsilon values.

It is obviously desirable for the design scenario events that are identified from the disaggregation procedure to generate the target ground motion level when the values of magnitude, distance and epsilon are put into an attenuation model. However, this will generally not be the case if the hazard contributions are assigned to bins in epsilon in a manner that reflects that bins incremental contribution to hazard. This issue was addressed by primarily by McGuire (Stepp et al. 1993; McGuire 1995) where a method was employed to

ensure that the design ground motion level is recovered when the design triplet M^*, R^*, ε^* is used in an attenuation model. In this method, for every magnitude – distance bin the minimum value of epsilon is found that generates the ground motion level, then the total hazard contribution of all values of epsilon greater than this value are assigned to this bin. When this procedure is performed, some information is lost in the process but the modal triplet that is recovered will match the target ground motion level. Bazzurro (1998) however points out that while the triplets obtained from applying the more theoretically pure method will specify scenario events that will exceed the target ground motion level, the extent of exceedance is usually less than 20%. Both of these methods have benefits; the McGuire (1995) method matches the target ground motion level, while the Bazzurro (1998; Bazzurro and Cornell 1999) method is theoretically more sound and although it produces scenario earthquakes that exceed the target ground motion level, the exceedance is small. In this study the disaggregation is performed using the method of Bazzurro (1998; Bazzurro and Cornell 1999).

Additional methods for ensuring that the earthquake scenarios used in subsequent design applications are consistent with the results of a hazard analysis include the work of Bommer et al. (2000) in regard to the selection of appropriate time histories, the use of environmental contours of seismic hazard using reliability methods (Bazzurro 1998), and issues relating to the adopted measure of standard deviation used in hazard analyses and design, or response, analyses (Baker and Cornell 2006). While the methods addressed by these authors are not implemented in the present work, they should be consulted when using the outputs of this study for design applications.

A.5.7. Chapter Summary

This chapter has outlined the PSHA methodology adopted in the present study; the method used is primarily the original framework of Cornell (1968). This procedure is essentially an exercise in integration and consequently some time was spent discussing the applicable range over which this integration should be perform with respect to the three controlling variables in the hazard analysis, magnitude, distance and epsilon. The assumption of Poisson earthquake occurrence is made for all of the fault sources and the background source with the only exception being the Alpine Fault for which pure characteristic events are assumed and various different rupture scenarios are assessed before time dependent hazard calculations are made. The time dependent probabilities of occurrence are determined using predominantly the Brownian Passage Time distribution, as well as the lognormal distribution. The robust methodology for ascertaining the relevant parameters for these distributions of Rhoades and Van Dissen (2003) is used for this purpose.

The total site specific hazard estimates that are finally obtained are disaggregated in order to most appropriately display the results of the hazard analysis. The framework with which to do this is fundamentally that of Bazzurro and Cornell (1999) but is framed differently in this study in order to account for the finite effects associated with rupture propagation and in this way reflects the method of Der Kiureghian and Ang (1977).

The methodology outlined in this chapter is implemented in order to obtain the results presented and discussed in Chapter Six of this section.

A.6. Probabilistic Seismic Hazard Analysis: Results and Discussion

A.6.1. Introduction

The overall objective of Section A of this thesis is to quantify the seismic hazard in the Buller region. This quantification of the seismic hazard is performed within the probabilistic framework originally outlined by Cornell (1968). Chapters Two and Three of this section were primarily concerned with the quantification of the frequency in both time and space of earthquake occurrence within the various seismic sources of the Buller – NW Nelson region. Chapter Four then presented the tools that are required to correlate the occurrence of an earthquake to its associated strong ground motions; the predictive equations for typical ground motion measures of engineering interest. In Chapter Five the Probabilistic Seismic Hazard Analysis (PSHA) methodology required to convert the findings of the previous chapters into some estimate of the probable future seismic hazard of the Buller region for the was presented. In addition, methods to portray this derived hazard so that it may be most readily used in structural and geotechnical engineering analyses were outlined.

Thus far an enormous amount of information has been considered and analysed in order to get to the present point where quantitative estimates of the future seismic hazard in the Buller region may be made. As well as there being a wealth of information required to arrive at this point, once the actual hazard analyses are carried out a wealth of new information exists. The purpose of the current chapter is to apply the PSHA methodology discussed in Chapter Five and to portray the consequent results in as transparent a manner as is possible.

True seismic hazard is site specific. Every point in real space will be exposed to a different level of seismic hazard that is dictated by the relative position of seismic sources about this point, the history of seismic activity in the space about this point, and many, many other factors. While sites in close proximity to each other will generally be exposed to very similar levels of seismic hazard, this is not always the case. The spatially observed distribution of ground shaking intensities can be highly variable,

particularly in areas where a variety of soil conditions are present. As well as site effects due to soil response the nature of the local topography can also result in non-uniform distributions of ground shaking. Additionally, two closely located sites may also experience significant differences in the level of ground shaking if they are positioned on opposite sides of a dipping fault plane as hanging wall and directivity effects may occur.

The characteristic output of a PSHA is a hazard curve calculated for a particular site. This hazard curve plots the annual rate of occurrence of a particular ground motion intensity against that ground motion intensity. Given a hazard curve one can pick off a ground motion level that corresponds to a particular probability of occurrence and subsequently use this value in a design application. A common practice is to generate seismic hazard maps. In order to generate a seismic hazard map one simply performs site specific hazard analyses for a large grid of points and uses these points to plot contours of ground motion levels corresponding to a particular probability of occurrence. National seismic hazard maps are available for New Zealand, following the analyses of Stirling et al. (1998) and Stirling et al. (2002). Both of these studies generate hazard maps for particular design levels for the entire country. One can therefore select a position within the country and obtain an estimate of the seismic hazard at that point. However, it must be emphasised that this value will indeed be an estimate. The points made in the previous paragraph relating to the highly localised variation in ground shaking intensities means that the values specified by hazard maps must generally be regarded as ball park estimates. The accuracy of a hazard map will obviously be related to the density of points for which hazard estimates are made in order to construct the hazard contours. To generate hazard maps for the entire country a reasonably course grid must be used in order to make the required calculations manageable.

For the present study it was decided not to generate hazard maps, but rather to compute examples of hazard curves for a selection of sites, and to provide an example of a thorough analysis for a particular site. The main reason for not generating hazard maps for the Buller region was that the calculations required to do so are extremely computationally intensive. In Chapter Five where the disaggregation procedure was outlined, the difference between a hazard analysis that uses point source distance measures to derive the probability density functions with respect to distance, and an analysis that takes into account the magnitude dependent finite fault effects was discussed. The emphasis of that discussion was upon the theoretical differences between the two approaches, it must also be recognised however that there is a significant increase in the computations required to perform the PSHA if the finite fault effects are taken into account. The number of calculations grows to the point where the generation of site specific hazard estimates for a large grid become extremely prohibitive. In addition, if one were to generate accurate hazard maps for the Buller region one would have to be very conscious of the differences in ground motions between sites on the hanging and foot walls of the various reverse faults in the region. In order to accurately portray this effect the grid of points that were used to generate the hazard maps would have to be relatively dense around the surface expressions of the reverse faulting structures in the region. Given the location and spatial distribution of the reverse faults throughout the region this would require a very dense grid to be employed that would in turn require an extremely large number of calculations to be performed for each ground motion index that was considered.

The various parameters that influence the determination of seismic hazard enter the calculations in an extremely nonlinear manner. Therefore, one can not simply determine some generic hazard level for a region, say for one soil class, and then apply site specific correction factors to obtain hazards levels for other soil classes. The various site specific parameters must generally be included in the determination of the hazard for the site from the outset. That said however, the method employed in this study is to generate site specific estimates of hazard that correspond to ground motion probabilities determined for rock sites. A comprehensive disaggregation procedure is then implemented to determine the most descriptive earthquake scenarios that correspond to that site. These earthquake scenarios may then be used to determine actual ground motion time histories required for design by using some method for simulating ground motion time histories, such as the program SMSIM (Boore 2000) that implements the stochastic method (Boore 2003), coupled with some method for computing site response such as one-dimensional site response programs such as SHAKE (Schnabel et al. 1972), or the NRATTLE program included in the SMSIM package, or more comprehensive site response programs such as SUMDES (Li et al. 1992).

The primary example used in this chapter is for a site located in the centre of Westport, the population centre of the Buller region. Hazard curves for various measures of strong ground motion are presented for this location as well as a full disaggregation of the hazard associated with peak ground acceleration.

It is often said that a picture tells a thousand words. With this in mind, many figures are presented in this chapter to help disseminate the huge amount of information that is produced through conducting a full four dimensional probabilistic seismic hazard analysis. Some of these figures, such as the hazard curves will be very familiar and will need little explanation; however, other figures that portray characteristics of the computed hazard that have not been reported from previous, more simplistic, methodologies, either as a result of less sophisticated PSHA code, or due to a lack of appreciation of the importance of the parameters, will require some supporting explanation. These relatively unfamiliar figures convey a wealth of information regarding the origins of the computed hazard and are therefore very instructive for adequately framing the results of the PSHA in both the current, and future, contexts. As well as providing some example results of the probabilistic seismic hazard in the Buller region this chapter will also look to demonstrate how powerful a tool modern PSHA methodology can be. In doing so, some of the inadequacies in previously applied methods will become apparent. In addition, potential issues related to the common practice of simply generating a hazard curve and picking off an ordinate for a design application will be highlighted.

A.6.2. Site Specific Hazard Analysis for Westport

The site used to demonstrate the probabilistic seismic hazard analysis methodology is located at 2393550 Eastings, 5937500 Northings, and corresponds to the central main road in Westport. A plot of the

various hazard curves computed for this site for peak ground acceleration, and 5% damped spectral acceleration at periods of 0.2 seconds and 1.0 seconds are shown in Figure A.6.1 through to Figure A.6.3. In Figure A.6.1, Figure A.6.2, and Figure A.6.3 similar information is portrayed for the three most typically reported ground motion indices computed through PSHA. In each plot, a suite of thin blue lines represent hazard curves computed by employing various modelling assumptions. More specifically, these assumptions correspond to differing values of the minimum magnitude used in the analysis, hazard curves corresponding to minimum magnitudes of $M_W 5.0$, $M_W 5.2$, and $M_W 5.4$ are shown; differing values of the upper bound on epsilon, curves corresponding to $\varepsilon_{\max} + 2$, $\varepsilon_{\max} + 3$, and $\varepsilon_{\max} + \infty$ are shown; and curves corresponding to each of the attenuation relations used in the analysis. While each individual curve is not annotated (purely due to the large number of curves portrayed) the heavy red lines indicate resultant curves computed through the use of a logic tree procedure for subsets of the blue curves. Each solid red line therefore corresponds to one of the minimum magnitudes assumed. The difference between these various curves is most apparent at short return periods where the impact of the relatively more frequent earthquake events is manifest. The height of the red lines therefore decrease as the assumed value of the minimum magnitude increases.

Corresponding to each of the three heavy red lines in the figures are a set of thin blue curves that correspond to the various different ground motion predictive models used in the analysis; six different models for peak ground acceleration, and five different models for spectral ordinates (see Chapter Four of this section for details). In addition, three such curves are shown for each model, minimum magnitude, combination. These three curves correspond to various values of the maximum value of epsilon allowed in the analysis. One of these three curves is computed for the unbounded case of $\varepsilon_{\max} = \infty$, while the other two curves are computed for truncations at $\varepsilon_{\max} = 3.0$, and $\varepsilon_{\max} = 2.0$. Although the difference between the summarising red curves is typically not great for the ground motion measures shown here, the use of a logarithmic scale should be noted, as well as the fact that it is the horizontal distance between curves that defines differences in design ground motion levels. This notion is demonstrated for each of the curves by plotting a horizontal line at the level corresponding to the common design ground motion level of 10% probability of exceedance in 50 years. Note that this value is computed using the rearranged Poisson formula given in Equation (A.6.1) below, where the design rate, λ_y^*, is a function of both the design life, or period, T, and the probability of exceedance, P.

$$\lambda_y^* = \frac{-\ln(1-P)}{T} \tag{A.6.1}$$

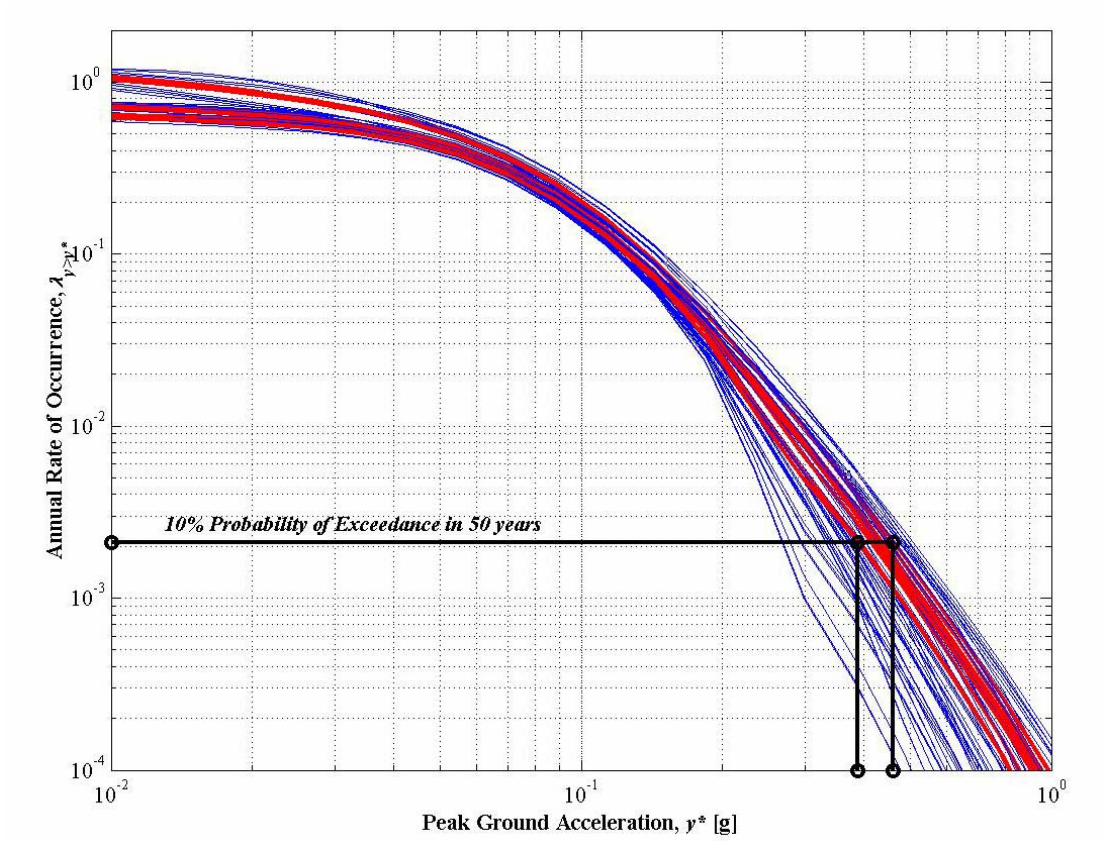

Figure A.6.1: Hazard curves for Peak Ground Acceleration computed for the Westport. A range of probable ground motion levels corresponding to a 10% probability of exceedance in 50 years are also shown. The thin blue lines correspond to hazard curves determined using various modeling assumptions, while the thicker red lines indicate averages of these groups. See main text for further explanation.

As was mentioned in Chapter Five of this section, the differences between curves computed for different assumed values of the minimum magnitude should vary with respect to the ground motion index being determined and the return period in question. The largest effect of lowering the minimum magnitude will be seen in high frequency ground motion measures, such as peak ground acceleration and 5% damped response spectral acceleration at 0.2s at short return periods (high annual rates of occurrence), while longer period ground motion measures such as the 1.0 second 5% damped response spectral acceleration, or ground motion velocities, or displacements, will have larger influence at longer return periods. This is simply a result of longer return periods favouring the occurrence of larger magnitude events, at potentially larger source site distances. There are consequently two main effects that cause the increased differences between curves; firstly, larger earthquakes generate stronger low frequency components of motion than smaller earthquakes, and secondly, high frequency components attenuate more rapidly during their propagation, than their low frequency counterparts,

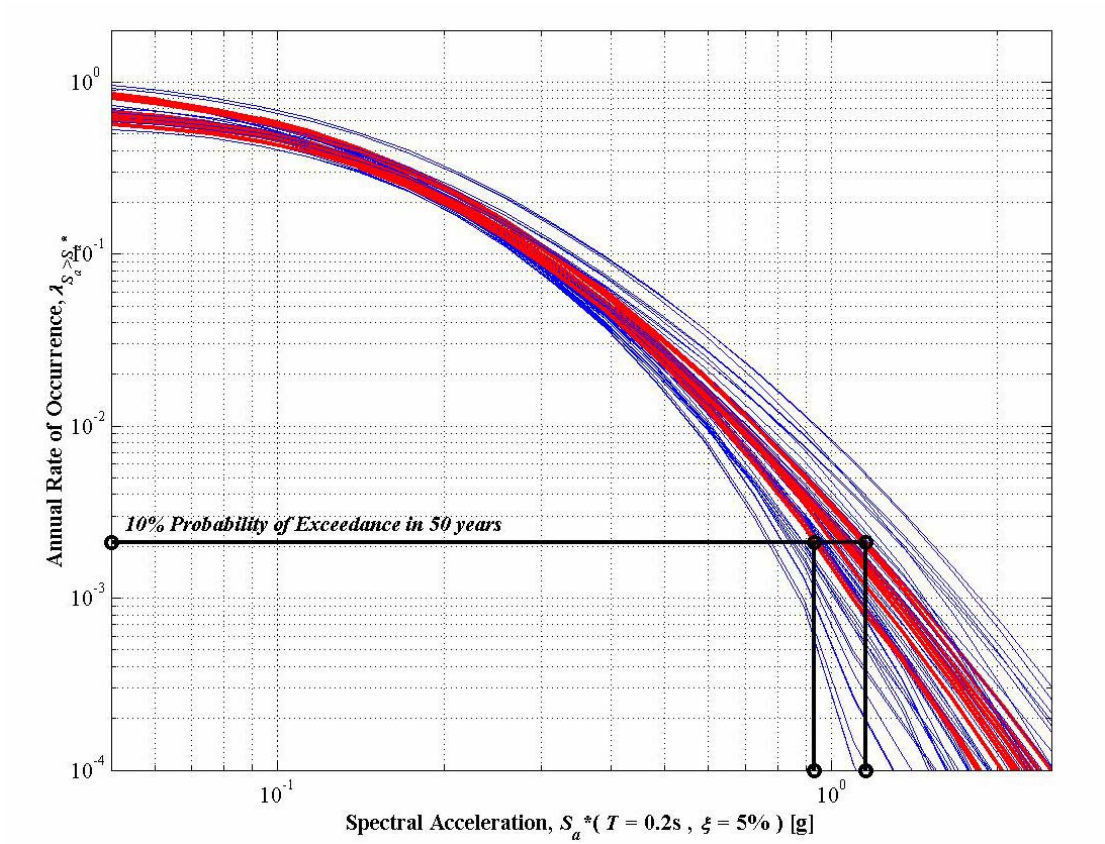

Figure A.6.2: Hazard curves for 5% damped Response Spectral Acceleration computed at period of 0.2 seconds for the Westport site. A range of probable ground motion levels corresponding to a 10% probability of exceedance in 50 years are also shown. Again, the thin blue lines correspond to hazard curves determined using various modeling assumptions, while the thicker red lines indicate averages of these groups.

between the source and the site†. One should therefore expect to see this effect demonstrated through characteristic differences between, say Figure A.6.1 and Figure A.6.3. However, when these curves are inspected for this purpose one notices that some peculiarities exist for the plot of the 1.0 second response spectral ordinates. Although the observed differences between curves at short return periods are in agreement with the previous comments to some extent, it is far more noticeable that the scatter in the blue lines is almost non existent in this case. There are two (main) possible explanations for such behaviour; firstly, the scatter associated with low frequency ground motion is much less than that at high frequency; and secondly, that the hazard curves calculated largely represent the contribution to hazard from a single seismic source, or a small number of sources, and that consequently the condition relating to the hazard curve is very well defined. The first possible explanation is quite simply wrong; the opposite is actually true. High frequency motions are scattered to a much higher degree than low frequency motions with the effect that differences in the initial strength of waves emitted from a source.

† These characteristics are most appropriately modeled by a relationship for the Fourier Amplitude Spectrum. A model of this nature is developed for use in New Zealand in Section B of this thesis.

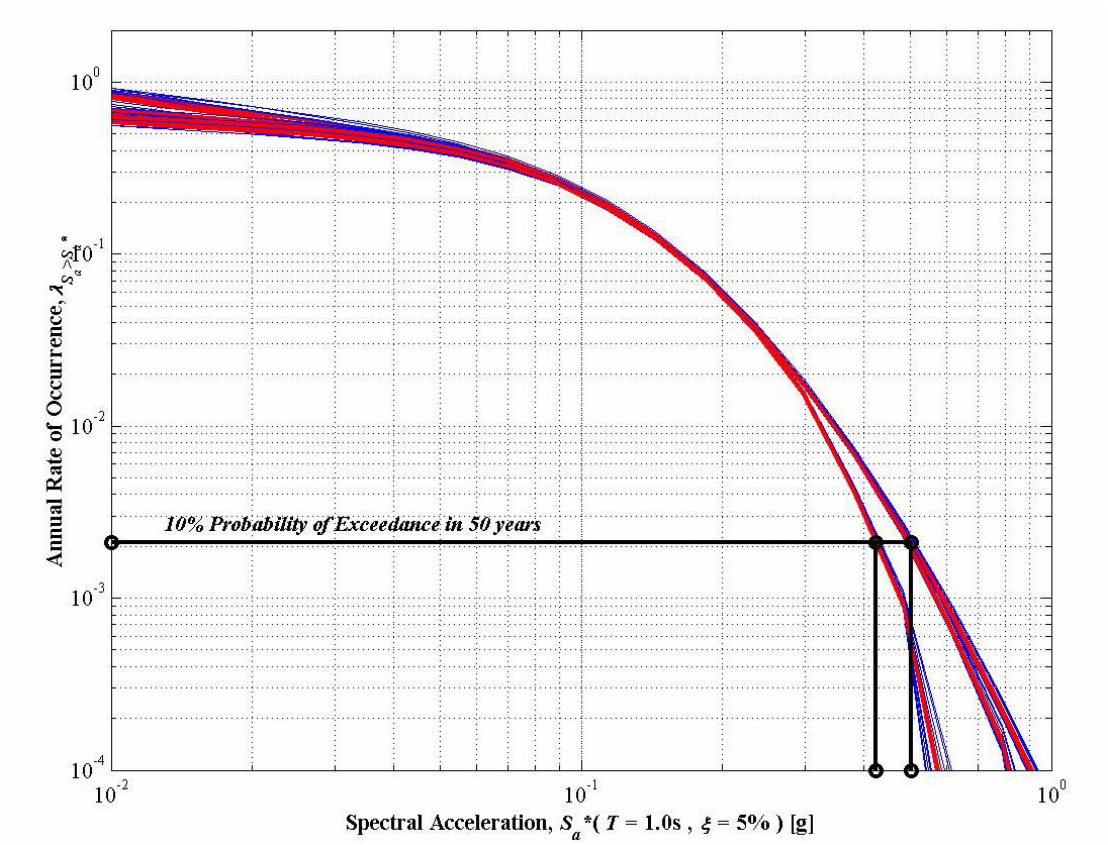

Figure A.6.3: Hazard curves for 5% damped Response Spectral Acceleration computed at period of 1.0 seconds for the Westport site. A range of probable ground motion levels corresponding to a 10% probability of exceedance in 50 years are also shown. Again, the thin blue lines correspond to hazard curves determined using various modelling assumptions, while the thicker red lines indicate averages of these groups.

are averaged out and the strong motion signal effectively resembles random motion (Hanks 1978; 1978a). The low frequency motions on the other hand are able to retain their initial strengths as dictated by the radiation pattern of the rupture as well as finite fault effects or directivity. The strong motion records used to determine predictive models for strong ground motion measures are based upon records from a wide range of source-site azimuths and consequently the range of spectral amplitudes assigned to a given magnitude event are greater in the low frequency case.

It is therefore most likely that a single seismic source is having a very strong impact upon the total hazard computed for the site. The relative contributions from the various sources can be plotted as individual hazard curves, showing the contribution of each seismic source to the total hazard for each level of ground motion considered. An example of such a plot if given in Figure A.6.4 for peak ground acceleration; similar curves for the spectral ordinates are not shown here. When such a curve is generated for the 1.0 second response spectral ordinate it is found that the contribution from the Alpine

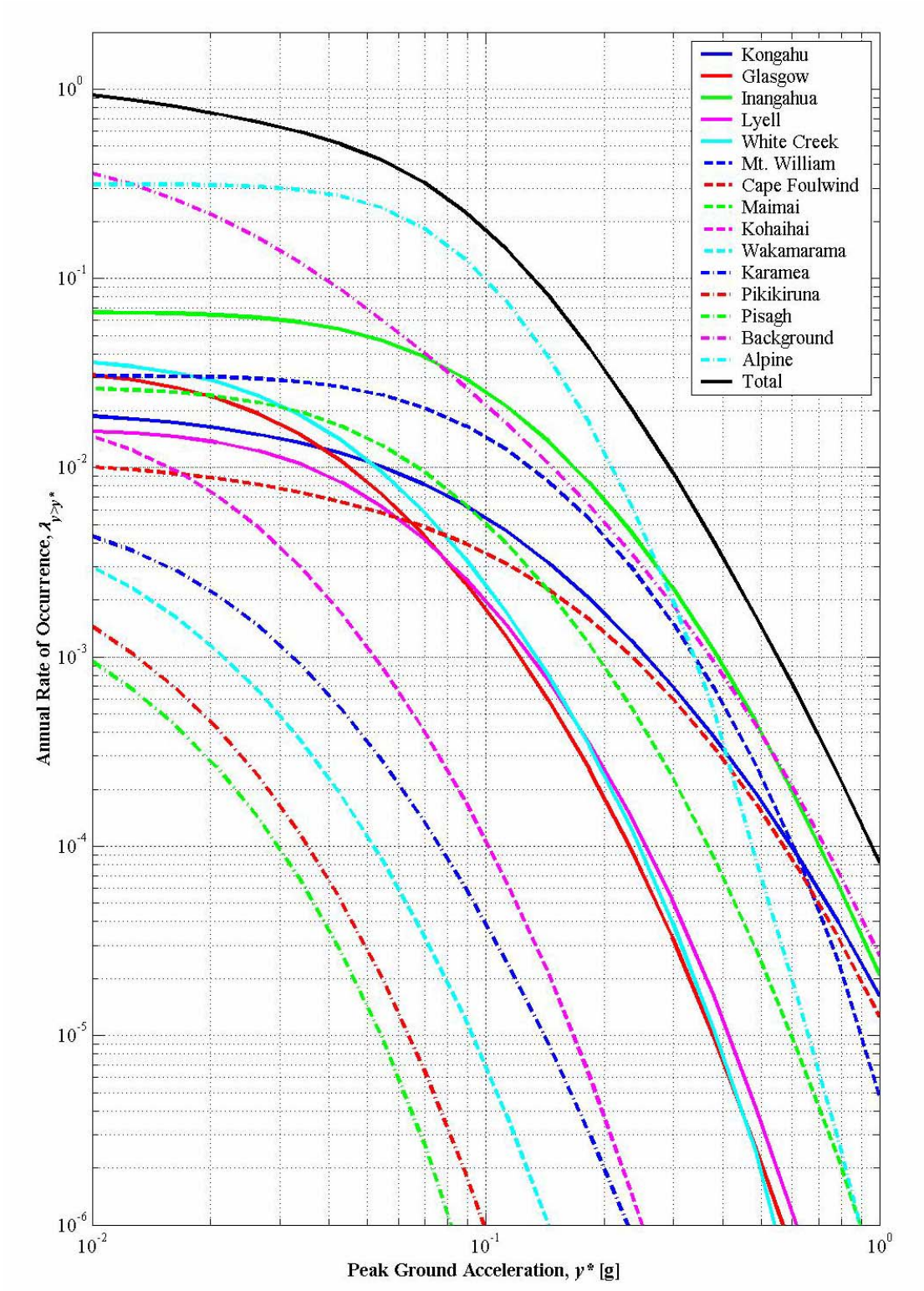

Figure A.6.4: Contributions to the total hazard curve for Peak Ground Acceleration computed for the Westport site from each of the seismic sources in the Buller – NW Nelson region. The curves shown here correspond to a minimum magnitude of $M_W 5.0$ and a maximum epsilon of $\varepsilon_{\max} 3.0$.

Fault far exceeds that of all other sources. This is also tends to be the case for all other ground motion measures as well, although the observed effect is both distance and frequency dependent for reasons previously mentioned.

It is quite important to portray the calculated hazard as in Figure A.6.4, particularly for regions where single large earthquake scenarios can significantly affect the estimate of regional seismic hazard. As was detailed in Chapter Five of this section, the contribution to hazard calculated for the Alpine Fault is determined using time dependent probability models. Because the elapsed time since the last major rupture on all sections of the Alpine Fault is approaching, or is past, the typical return period for such events the current estimate of the instantaneous hazard is quite high. If a single curve was specified such as the mean, median, or some other level, as is essentially the case in Figure A.6.1, Figure A.6.2, and Figure A.6.3, the effect upon the calculated hazard of subsequent major events cannot readily be determined. However, for the case of Figure A.6.4, all other curves apart from that for the Alpine Fault are determined using a model of average, or Poisson, earthquake occurrence and would therefore remain relatively stable regardless of specific rupture scenarios taking place. Consequently, if the Alpine Fault were to rupture tomorrow; rather than having to perform the entire PSHA again from scratch, one could simply assume that a subsequent rupture on the Alpine Fault in the near future was negligible in terms of its contribution to total hazard and then obtain a new estimate for the seismic hazard by summing the contributions from the other fault sources.

Note that the ability to do this is often lost when seismic hazard maps for an entire region are generated. While the required calculations are exactly the same in both cases (varying only in the number of repeat runs that are required) the focus when presenting the results for whole regions commonly precludes specifying the extent of information shown in Figure A.6.4. Therefore, the end user of a regional, or national, hazard map is presented with essentially a point estimate (in time) of the current level of hazard. It is very difficult for end users to then consider various scenarios that could happen, i.e. what is the quantitative effect on the calculated hazard for this site if a large earthquake on a particular fault occurs. It is therefore strongly recommended that the total hazard computed for a particular site is described both in its most general sense, in terms of the aggregate effect of all seismic sources; but also in terms of relative contributions from individual sources. By specifying the calculated results in this way the hazard analyst provides the end used with far more freedom to consider various permutations of future earthquake scenarios and how these scenarios relate to various engineering applications. In this way it is therefore simpler to make connections between hazard estimates and calculated risks associated with these hazards.

A.6.3. A Note on Uncertainties

The suite of blue curves acts to demonstrate some extent of the epistemic uncertainty associated with the PSHA. It is common to assign degrees of belief to the various permutations of assumptions through

the use of a logic tree (for example Working Group for California Earthquake Probabilities 2003). When this is done a single mean, or median hazard curve is reported, although specifically which of these measures is used varies (Abrahamson and Bommer 2005; McGuire et al. 2005; Musson 2005). However, the degree of belief in the appropriateness of various model parameters depends upon the specific scenario that is being considered in a design, or assessment, application (Bender and Campbell 1989). Therefore, rather than collapsing the suites of curves presented in Figure A.6.1, Figure A.6.2, and Figure A.6.3, the distribution of potentially applicable values is left in its current transparent form. In this way, the end user gets both a qualitative appreciation of the likely uncertainty associated with the hazard estimate as well as the freedom to adopt an estimate of the hazard level that is most appropriate for a given application.

The practice of routinely collapsing the results of a probabilistic hazard analysis onto a single curve and then making some estimate of the uncertainty associated with that curve has some shortcomings, both practically and theoretically. For a start, likely estimates of the associated errors are usually computed by considering a subjectively chosen range of input parameters, and modelling assumptions; performing the PSHA for each scenario, using a Monte Carlo simulation technique or simply considering a finite selection of models, and then reporting an estimate of the associated error based upon the distribution of results that are obtained. Consequently, the error that is obtained is conditional upon the particular analysis method employed, the assumptions that are made, and the application for which the PSHA was conducted. One cannot therefore routinely compare error estimates made between different hazard analyses in a consistent manner. Some judgment must be made by the end user as to the quality, and accuracy, of the results that are obtained. For the present case, where the hazard is computed for a particular site, but with no specific application in mind, i.e. the assessment of a given existing structure, or the design of some new facility etc, it would not make sense to perform a probabilistically based determination of the hazard at the Westport site and then report specific values for the hazard and error estimate of this hazard without having knowledge of the particular application for which the values would be used. One of the great strengths of PSHA is its ability to be flexible to changes in the scenario being considered, but associated with this recognition of strength must be a recognition of the coupling between the methodology employed and the intended use of the hazard analysis results.

Further to this brief discussion on error estimation it should be noted that even if the application for which the PSHA results were to be determined was exactly defined, there are still issues related to placing a specific numerical estimate upon the error associated with the results of the analysis. As well as the estimate being somewhat conditional upon the original beliefs and intuitions of the analyst, the estimate is also conditional upon the current knowledge base of engineering seismologists. Much attention has been given in the engineering seismology literature to quantifying both aleatory variability and epistemic uncertainty. However, in risk analysis circles another aspect of uncertainty is frequently discussed, that being ontological uncertainty (Elms 1998). Ontological uncertainty is uncertainty associated with influences that cannot be included into a model because they represent unknown phenomena. To some extent engineering seismologists lump this uncertainty into epistemic uncertainty and generally refer to this as the uncertainty associated with an inadequate knowledge of how to most

appropriately model physical processes relating to earthquakes. However, even if this is the case and the analyst is implicitly aware of incorporating the ontological uncertainty with the epistemic uncertainty, the estimate of the error associated with such a component of a hazard analysis can only ever account for that part of this combined uncertainty that is truly epistemic. Even though there is currently call for the practice of incorporating excessively large numbers of modelling variations into PSHA to cease (Musson 2004; 2004a; 2005); in the hypothetical situation in which every available model was included into a hazard analysis, the error thus obtained must still necessarily underestimate the actual uncertainty of the hazard estimate; because it must neglect ontological uncertainty by definition. Note the distinction here between the theoretically actual uncertainty and the uncertainty that is conditional upon the particular model that is used.

A.6.4. Specific Hazard Results Obtained

Thus far the discussion of the results obtained has been very generic; although specific summarising hazard curves have been presented. Before discussing the nature of the determined results in more depth it is worthwhile making a general comparison between the hazard values calculated in this study with those determined from the latest national seismic hazard maps. While this comparison must be made between hazard determined for a specific site and hazard determined over a very large region, it is instructive to make a comparison nonetheless. The most recent national seismic hazard maps for New Zealand are computed for class B intermediate sites (Stirling et al. 2000; Stirling et al. 2002) and results are given for the same ground motion indices that have been shown here in Figure A.6.1, Figure A.6.2, and Figure A.6.3. Hazard maps for both 10% probability of exceedance in 50 years (475 year return period), and 10% probability of exceedance in 105 years (1000 year return period) are presented. A comparison between the ranges of values given by Stirling et al. (2000; 2002) (maps of New Zealand are coloured in terms of 0.1 increments in the particular ground motion measure shown), and the range found in the present study are given in Table A.6.1. The range values in this table that relate to the present study are defined by the difference between the highest and lowest values given by the heavy red curves in Figure A.6.1 through Figure A.6.3. These upper and lower curves correspond to minimum magnitude values that range from $M_w 5.0-5.4$. The national seismic hazard maps are determined using a minimum magnitude value of $M_w 5.25$. It should again be noted that the national seismic hazard map values presented in Table A.6.1 are determined for site class B as defined in the New Zealand Loadings Code (Standards New Zealand 1992), and also re-presented in Chapter Two of Section B in the present work. All other things being equal, the hazard values obtained for site class B will be larger than those obtained for site class A. In order to make a more appropriate comparison between hazard estimates for ground motions from the two different site classes the values obtained from this study have been scaled up to try and represent the equivalent site class B hazard levels. Note that there is a considerable amount of approximation involved in performing this scaling procedure as if

Table A.6.1: Comparison between regional hazard estimates from the national seismic hazard maps and the site specific analysis performed in the present study. Note that the results presented for here for the present study are those calculated for Westport.

Ground Motion Measure	Probability of Occurrence	Annual Rate of Occrrence	Approx. Return Period	National Seismic Hazard Maps[1]	Present Study[2]	Present Study Scaled[3]
Peak Ground Acceleration	10% in 50 yrs	0.0021	475	0.5 - 0.6	0.40 - 0.46	0.56 - 0.64
	10% in 105 yrs	0.0010	1000	0.7 - 0.8	0.48 - 0.56	0.67 - 0.78
5% Damped Response Spectral Acceleration at 0.2 s	10% in 50 yrs	0.0021	475	1.4 - 1.8	0.91 - 1.14	1.27 - 1.60
	10% in 105 yrs	0.0010	1000	1.8 - 2.2	1.09 - 1.40	1.53 - 1.96
5% Damped Response Spectral Acceleration at 1.0 s	10% in 50 yrs	0.0021	475	0.2 - 0.3	0.40 - 0.47	0.56 - 0.66
	10% in 105 yrs	0.0010	1000	0.3 - 0.4	0.45 - 0.56	0.63 - 0.78

1. Note that these values are calculated for Class B Intermediate Sites
2. Note that these values are calculated for Class A Rock Sites
3. These values are scaled up using approximate factors from the McVerry et al. (2000) attenuation model

hazard estimates were determined using site class B throughout the entire PSHA the subsequent results would not simply be the appropriately scaled up versions of the site class A results. The difference in site class coefficients in the attenuation models affects the mean ground motion, but hazard contributions are also strongly dependent upon the magnitude of the error terms of the attenuation model. The situation in reality is therefore highly nonlinear, but for these comparative purposes, a simple scaling of the rock ground motions is sufficiently accurate, and instructive. The scaling factor was estimated from the coefficients of the McVerry et al. (2000) attenuation model. The difference in ground motions between site class A and site class B is approximately[†] 40% (0.35 natural logarithmic units). Table A.6.1 therefore contains a column of scaled values related to this study, i.e. the calculated design levels for the rock sites multiplied by 1.4. Given the significant differences between the methodologies used in the calculation of PSHA in the present study and in that of Stirling et al. (2000; 2002) the agreement between the peak ground acceleration values and the 5% damped response spectral ordinate at 0.2 seconds can be considered very close. There is however a significant difference between the estimates of the response spectral design level at a period of 1.0 seconds; levels found from scaling the estimates calculated in this study are roughly double those of the national seismic hazard maps.

It should be noted again however, that the hazard calculated for this ordinate is, for all intents and purposes, the hazard associated with the imminent rupture of the Alpine Fault. This single large – great earthquake is expected to generate very strong long period shaking intensities. A much better agreement between the values obtained in this study and that of Stirling et al. (2000; 2002) would be found if the specific influence of the Alpine Fault was reduced. The probabilities of rupture assumed for the Alpine Fault in this study are based upon those derived by Rhoades and Van Dissen (2003) after the

[†] The site class factors in the McVerry et al. (2000) model actually vary with spectral period, but the assumed value of 0.35 is fairly indicative of the difference in ground motions between the two site classes and is sufficiently accurate for the present purposes.

national hazard maps were created. This does little to help explain the difference in estimated hazard levels however as one of the key findings of the Rhoades and Van Dissen (2003) study was that previous time dependent probability forecasts (Yetton et al. 1998; Yetton 2000) overestimated the probability of rupture of this fault.

Another point to make with regard to the contributions made to hazard by the Alpine Fault is that in all cases the ground motions that are predicted for this event during the PSHA procedure require the attenuation models to be extrapolated beyond the range of the datasets used to derive the models. The functional form of a predictive model generally determines how well the model is likely to respond to such an extrapolation. The most likely level of ground motion observed from a magnitude 8+ earthquake is currently ill-defined and this additional degree of uncertainty should be associated with the estimates of hazard for all of the ground motion measures, but particularly those representative of long period components of ground motion as the hazard associated with these measures is strongly governed by the Alpine Fault.

In general then, the estimates of hazard estimated in this study for Westport appear to be fairly consistent with that from the national seismic hazard maps. Later in this chapter some consideration is given to the spatial variability of hazard estimates in the Buller region and it will be prudent to consider this comparison once again at that point.

A.6.5. Four Dimensional Disaggregation

In Chapter Five the optimal methodology for disaggregating the results of a probabilistic seismic hazard analysis was outlined. Currently, the most theoretically robust and informative method available is that of Bazzurro and Cornell (1999); this method forms the basis for the disaggregation performed in the present study for the Westport example. The amount of information to analyse and to convey using the four dimensional disaggregation procedure is immense so only the case of peak ground acceleration for the Westport site will be presented here.

Recall that the main reason for disaggregating hazard estimates is so that the calculated hazard may be related to specific earthquake scenarios that can then be used for design and analysis applications (response analysis). It is also a very worthwhile process to undertake as it enables the probabilistically framed outputs of PSHA to be described in terms that are readily understandable to end users of the hazard estimates that do not have a thorough understanding of PSHA methodology. Most lay people for instance would not be familiar with expressions such as 'the ground motion level with an X% probability of exceedance in Y years', however, they may well appreciate the implications of a magnitude X event occurring at a distance of Y from them. As well as being a useful tool with which to express hazard estimates to lay people, the disaggregation procedure is also a fundamental step in a probabilistic hazard analysis as it enables a complete understanding of the nature of the hazard estimate

to be obtained. It also allows for critical earthquake scenarios to be accurately, and robustly, defined. Proponents of Deterministic Seismic Hazard Analysis (DSHA) often claim that PSHA is inadequate for portraying realistic earthquake scenarios (for example Krinitzsky 1993; 1995a; 2002b; 2003) and in some cases certain disaggregation methods will result in nonsensical earthquake scenarios. However, in many cases PSHA does a very good job of defining critical earthquake scenarios as well as doing a better job than DSHA at determining earthquake scenarios for short return periods, or for less-than-critical events in general.

As a starting point in the presentation of the disaggregation example, the most common disaggregation method for representing contributions to hazard is shown; that being a disaggregation of the total hazard into magnitude - distance bins. This elementary disaggregation method was used for presenting the results from the national seismic hazard maps for the main population centres in New Zealand. Figure A.6.5 shows the conditional joint probability density distribution of hazard with respect to magnitude and distance. The joint probability density is conditional upon the exceedance of a design ground motion level of 0.45g. This design value was obtained from the PSHA as corresponding to the peak ground acceleration with a 10% probability of exceedance in 50 years determined using a minimum magnitude of $M_{W,\min} = 5.0$ and a maximum epsilon value of $\varepsilon_{\max} = 3.0$.

Note that in Figure A.6.5, as well as in all other figures in this section, the contribution to hazard from the Alpine Fault is not presented. The nature of the contribution from this event is trivial as it was explicitly specified in order to include the fault source in the PSHA methodology in the first place. The only ambiguity related to this event is to what extent the various rupture scenarios considered for the Alpine Fault contribute to the hazard in reality. In the derivation of the rupture model, discussed in Chapter Five of this section, subjective weights were assigned to each rupture scenario that effectively imposes the partitioning of hazard from this fault source *a priori*. In the figures that follow then, the Alpine Fault would simply plot as a large spike positioned at the magnitude distance bin of relevance. The inclusion of this spike obscures the definition of the contributions from the other seismic sources and for this reason also it is excluded from the following figures. Often, the disaggregation procedure is curtailed at this point. From both the three dimensional surface and the related contours beneath the surface, points of high hazard contribution can be picked out that correspond to a given magnitude distance pair. In the case shown in Figure A.6.5 this would correspond to a two dimensional magnitude – distance conditional mode of $\left(M^*, R^*\right) = \left(6.7, 21\right)$. One could potentially then use this earthquake scenario for design purposes. However, this simple representation does not paint the whole picture. This earthquake scenario could correspond to any point with an epicentral distance of 21 km from the site at Westport. Also, this scenario does not take into account how likely this magnitude – distance combination is of exceeding the target ground motion level of 0.45g. In order to account for this additional consideration, the modal triplet $\left(M^*, R^*, \varepsilon^*\right)$ must be found. The next step then is to consider the conditional joint probability density distribution of hazard with respect to magnitude and epsilon. A presentation of this distribution analogous to that for magnitude and distance shown in Figure A.6.5 is given in Figure A.6.6.

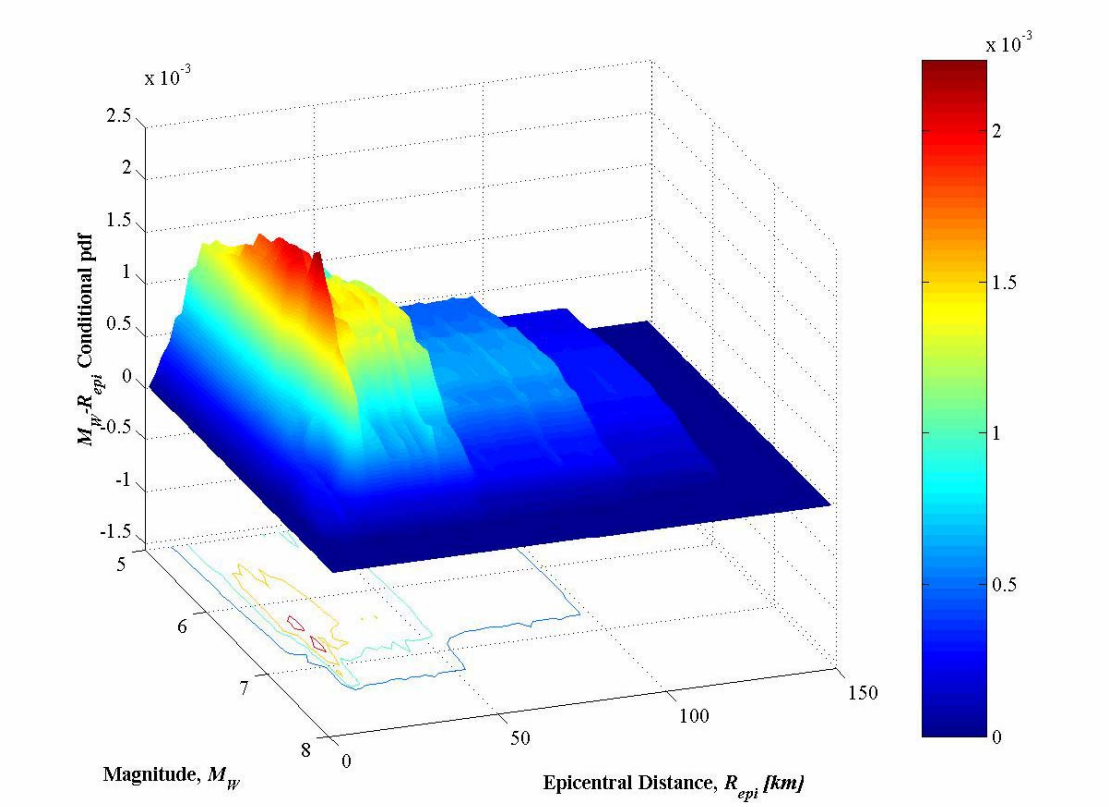

Figure A.6.5: Disaggregation of the hazard estimate for peak ground acceleration for the Westport example with respect to magnitude and distance. Here the peak of the distribution occurs at $\left(M^* = 6.7, R^* = 21\text{km}\right)$.

Now, from Figure A.6.6 the two dimensional conditional mode is defined by $\left(M^*, \varepsilon^*\right) = \left(7.3, 0.2\right)$, the presence of the contribution to hazard at a magnitude of $M_W 6.7$ can still be observed but we note that it occurs at a higher value of epsilon and is therefore less likely to occur on average. At this point we have still only performed the disaggregation with respect to two of the controlling parameters at a time. It is worthwhile considering what further information can be gleaned from this restricted disaggregation process. Given that we have obtained two magnitude values that contribute strongly to the hazard at the Westport site it is instructive to consider which seismic sources are responsible for this contribution. In order to do this separate conditional joint probability density distributions are generated for each of the seismic sources considered in the PSHA. These distributions are shown in Figure A.6.7 through to Figure A.6.10. Inspection of these distributions immediately identifies the possible sources responsible for the large contributions to hazard at both $M_W 6.7$ and $M_W 7.3$ observed from the total conditional joint probability density distributions with respect to magnitude and distance, and magnitude and epsilon respectively. In all of these figures the anticipated general trend of epsilon decreasing with increasing magnitude is observed.

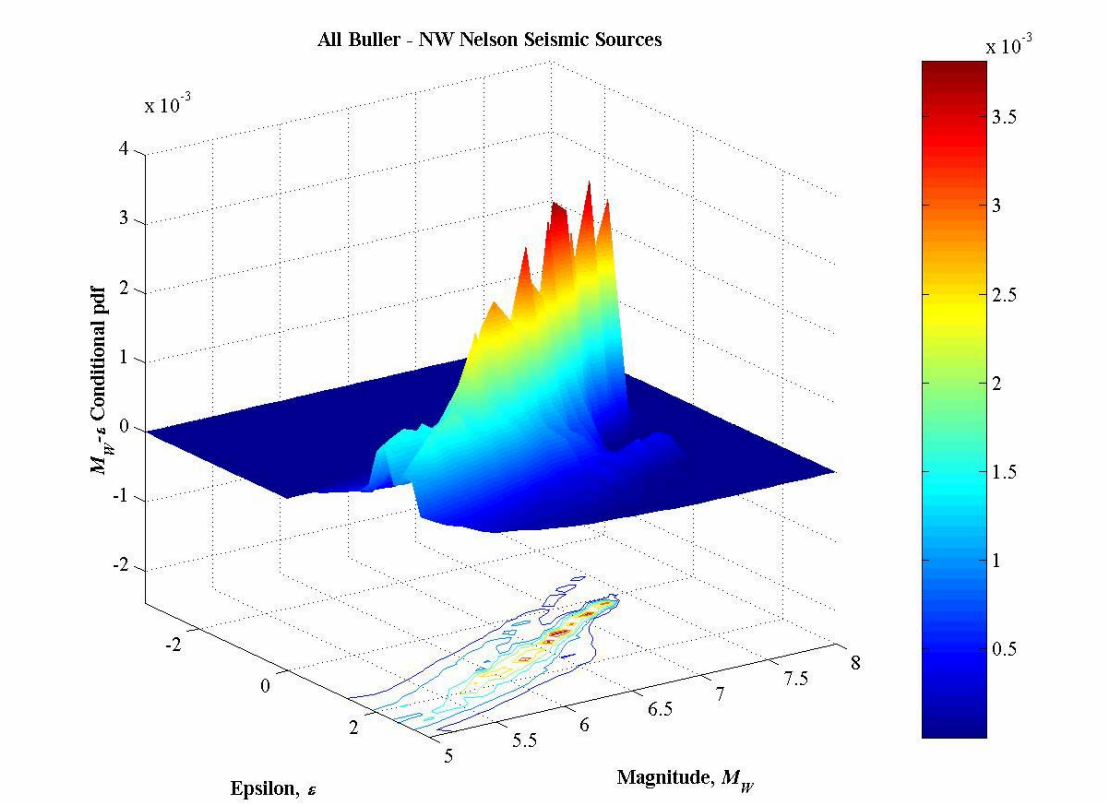

Figure A.6.6: Disaggregation of the hazard estimate for peak ground acceleration for the Westport example with respect to magnitude and epsilon.

Displaying the hazard results in the form of the above figures is somewhat analogous to displaying the individual hazard curves associated with each fault source as in Figure A.6.4. Again, as was readily observed from Figure A.6.4, the fault sources to the north of the Buller – NW Nelson region (Kohaihai, Wakamarama, Karamea, Pikikiruna, and Pisagh Faults) are seen to contribute negligibly to the hazard calculated for Westport. In each of these cases, the condition of exceeding the target peak ground acceleration is only achieved for the case where the faults generate maximum, or very close to maximum, magnitudes and where the ground motions resulting from these large magnitude events significantly exceed the mean ground motion intensity for that magnitude and the relevant distance to the fault source. If in the future, one wanted to refine the PSHA results found from this study one could use the information given in Figure A.6.7 through to Figure A.6.10 to identify the most critical earthquake sources with respect to sites in Westport and consequently focus ones attention upon most appropriately quantifying the earthquake activity related to these sources. Although the essence of this statement could have been intuited from the outset of the PSHA, it is not until an analysis such as that currently being presented is conducted that one can ascertain the relative importance of the various fault sources with respect to a given design level of ground motion. The conditional nature of these results (conditional upon the exceedance of 0.45g) is also very important. If for example, the Alpine Fault had recently ruptured, then the target ground motion level corresponding to a 10% probability of

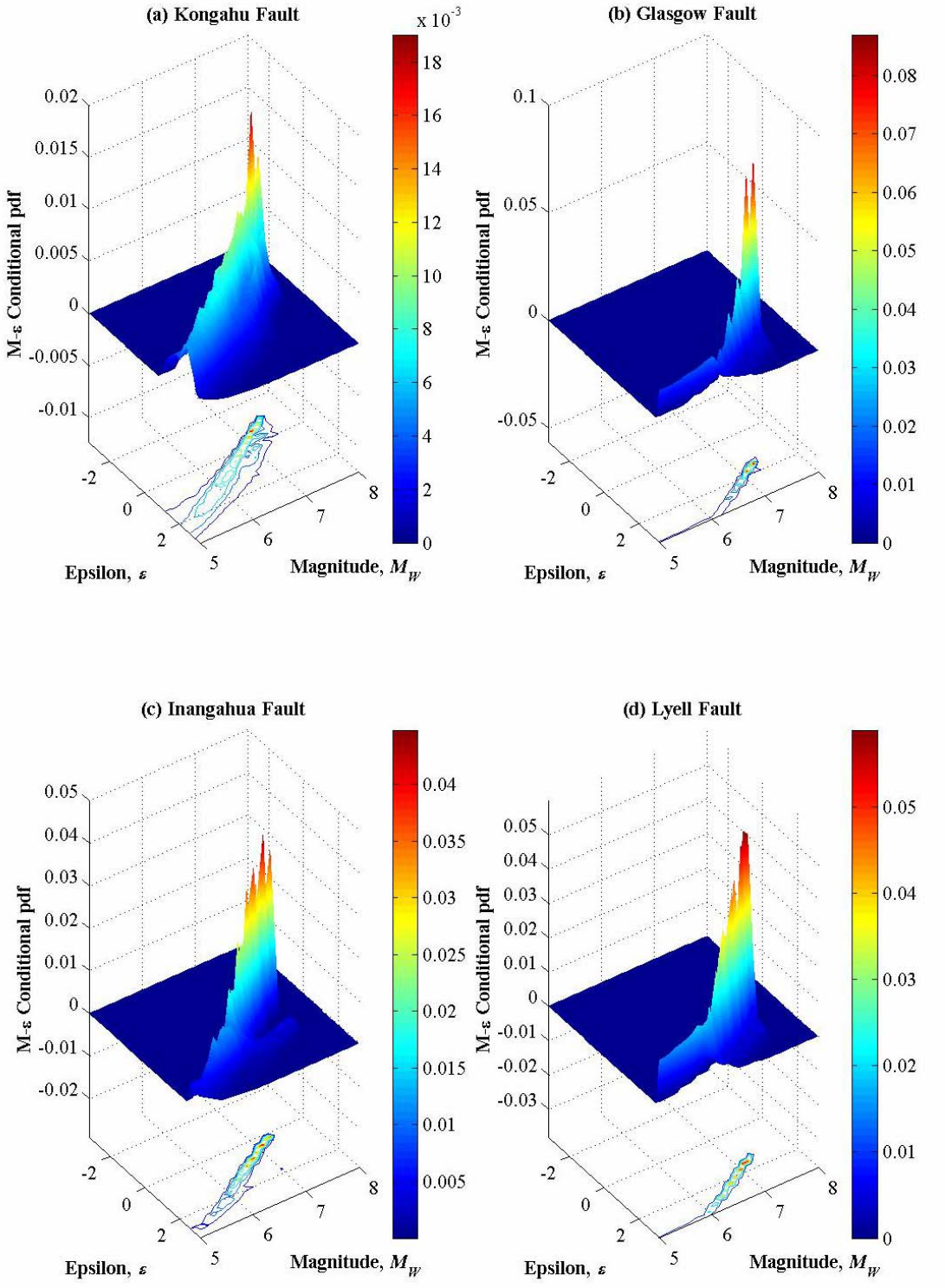

Figure A.6.7: Conditional joint probability density distributions for four fault sources. Panel (a) shows the distribution for the Kongahu Fault, panel (b) for the Glasgow Fault, panel (c) the Inangahua Fault, and panel (d) the Lyell Fault.

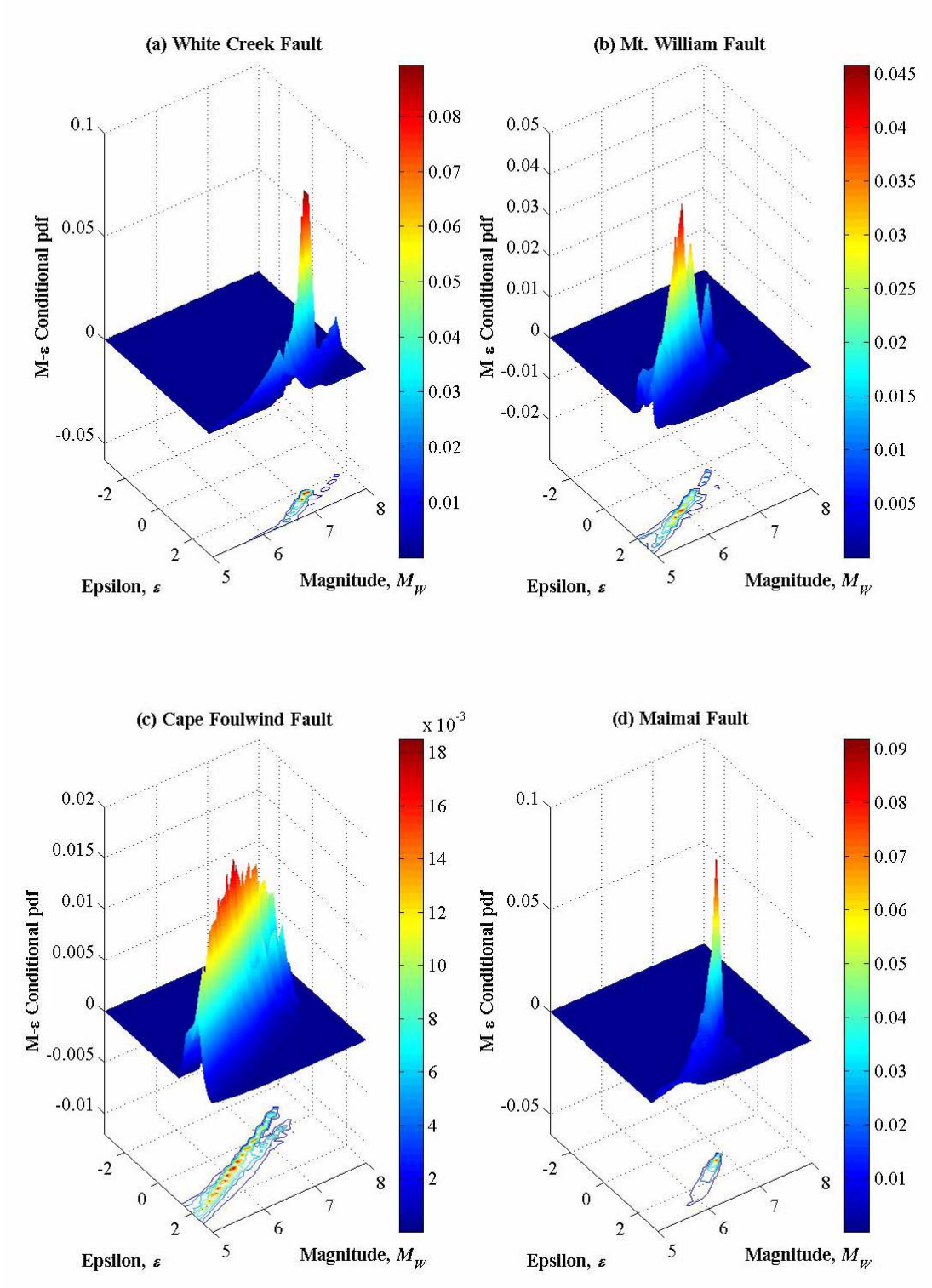

Figure A.6.8: Conditional joint probability density distributions for four fault sources. Panel (a) shows the distribution for the White Creek Fault, panel (b) for the Mount William Fault, panel (c) the Cape Foulwind Fault, and panel (d) the Maimai Fault.

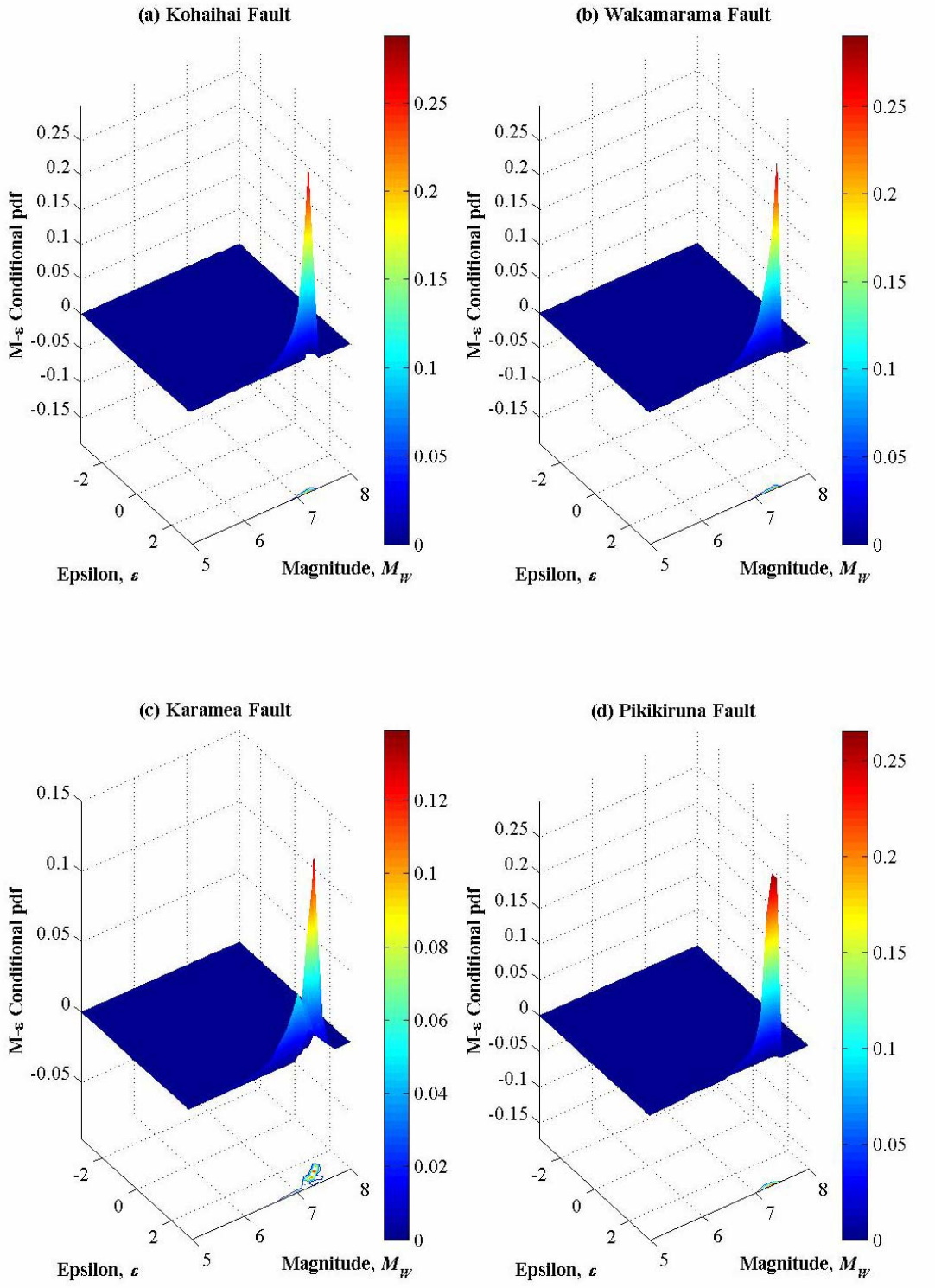

Figure A.6.9: Conditional joint probability density distributions for four fault sources. Panel (a) shows the distribution for the Kohaihai Fault, panel (b) for the Wakamarama Fault, panel (c) the Karamea Fault, and panel (d) the Pikikiruna Fault.

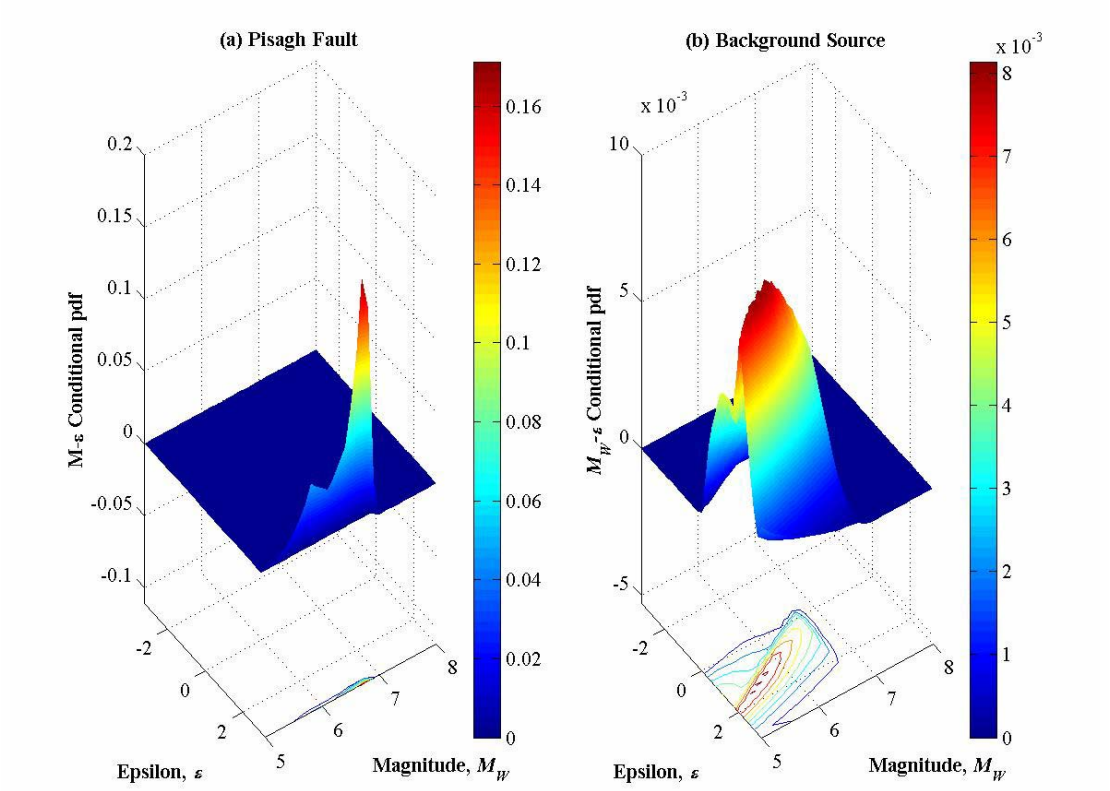

Figure A.6.10: Conditional joint probability density distributions for the Pisagh Fault source, in panel (a), and the Background source in panel (b).

occurrence in 50 years would be significantly less than 0.45g and in this case the northern faults may in fact contribute more strongly, at least in a relative sense, to the total hazard for this revised design criteria.

So far, the disaggregation results that have been shown are simply lower dimensional subsets of a greater disaggregation in four dimensions. It is difficult to portray the full extent of information recovered from a four dimensional disaggregation procedure on a two dimensional page in a three, for all practical purposes, world. However, if the conditional relations between epsilon and magnitude shown for each fault source in Figure A.6.7 through to Figure A.6.10 are firmly kept in mind, the representation of the total information can be largely achieved by plotting the relative contributions to hazard from increments in epsilon over two dimensional space. In other words, one can get a feel for how hard seismic sources distributed throughout the region have to work in order to achieve the target ground motion level by plotting spatial maps showing the contributions to the total hazard from bins of epsilon values. Because such a strong trend between epsilon and magnitude has already been observed, and is seen to be relatively well constrained, the plots of the spatial distribution to hazard associated with the bins in epsilon can serve as a proxy also for the distribution with respect to magnitude. An example of such a plot, or series of plots, is presented in Figure A.6.11 for various increments in epsilon.

In Figure A.6.11 it is evident, as should be expected, that region associated with increasing values of epsilon grows about the site in question. To visualise this effect most appropriately, the contour plots beneath the surfaces are overlaid with a map of the coastline around the Buller – NW Nelson region. Westport is readily located with respect to both this coastline and to the circular contours centred at the site; this 'bull's-eye' type pattern brings new meaning to the term 'target acceleration'!

The spikes that are observed in the surface plots project down onto specific spatial positions on the contour maps. These points will correspond to the surface projection of the nearest point from the site to the rupture plane. The concentrations of hazard contributions will therefore not coincide with mapped surface traces of faults in many cases when dealing with a region containing dipping fault sources. During the process of gathering the information required to present the illustrative results thus far shown in this chapter a simple book-keeping exercise is employed to determine the four dimensional modal combination of spatial position, magnitude, and epsilon that correspond to the most likely combination of parameters that would result in an exceedance of the target ground motions level of 0.45g. The set of parameters that were obtained from this exercise, bearing in mind that the true governing event is still the rupture scenario associated with a combined central and northern section rupture of the Alpine Fault, are $\left(N^* = 5928500, E^* = 2411500, M^* = 7.3, \varepsilon^* = 0.2\right)$. Here, N^* and E^* represent are the conditional modal northings and eastings co-ordinates associated with M^*, ε^*, and 0.45g. Thus, a very specific design scenario earthquake is defined via the four dimensional disaggregation procedure.

This combination of parameters defines the most probably combination of parameters that lead to an exceedance of 0.45g at a site in Westport; after the Alpine Fault rupture. When this spatial location is plotted on a map along with the fault traces of the sources considered in this study one finds that the point lies just east of the trace of the east dipping Mount William Fault. Ones initial impression therefore, is that it is this fault source that contributes most strongly, after the Alpine Fault, to the peak ground acceleration hazard in Westport. However, this is a premature conclusion, as when one considers the conditional probability density distribution of hazard with respect to epsilon and magnitude for this source, Figure A.6.8, one finds that the design event cannot be associated with this source. Rather, the optimal design scenario earthquake is associated with the Inangahua Fault. This is conclusively demonstrated by considering the spatial location defined by the four dimensional modal set $\left(N^*, E^*, M^*, \varepsilon^*\right)$ coupled with the conditional distribution of hazard with respect to magnitude and epsilon in Figure A.6.7.

It should be noted however, when using logic tree methods to calculate seismic hazard, the four dimensional conditional modal parameter set will not necessarily correspond to the target ground motion level when these parameters are used in all of the attenuation models. For the current analysis,

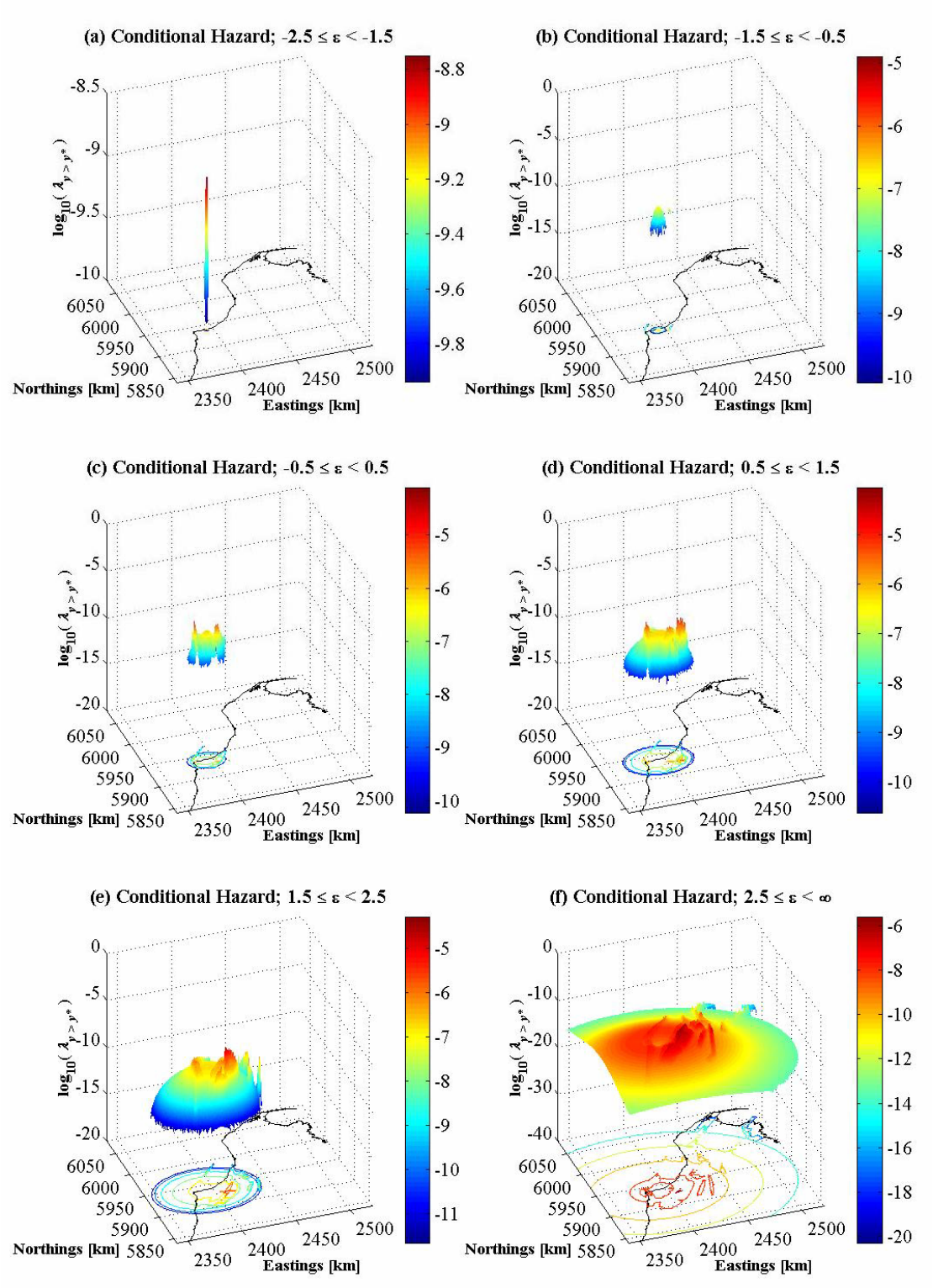

Figure A.6.11: Spatial distribution of hazard contributions associated with various increments of epsilon. Panel (a) depicts epsilon values between -2.5 and -1.5, panel (b) depicts the increment -1.5 to -0.5, panel (c), -0.5 to 0.5, panel (d) 0.5 to 1.5, panel (e) 1.5 to 2.5, and panel (f), all epsilon greater than 2.5.

and for the current example of peak ground acceleration, the Cousins et al. (1999) model will calculate a peak ground acceleration very close to the target level, as this model received a 40% weighting in the logic tree. However, some of the other models predict lower peak ground accelerations than the favoured Cousins et al. (1999) model for the magnitude distance pair defined by the four dimensional conditional mode. In addition, the magnitude of the standard deviation of peak ground acceleration for each of the attenuation models is different, so the modal value of epsilon will correspond to different deviations from the mean ground motion for each model that is included in the PSHA. Issues such as these must be recognised when using the set of modal parameters in subsequent response analyses.

Through the example case considered above, the four dimensional disaggregation procedure has been shown to completely define the characteristics of the hazard estimated for some level of ground motion measure at a particular site. The hazard results, when portrayed within this framework convey far more information than a single point picked off of a hazard curve. It should be noted once again however, that the added complexity related to performing such a comprehensive disaggregation procedure precludes the possibility of generating regional hazard maps for which this sort of information is readily available. If the level of detail described, and generated, through this example is deemed warranted for a given hazard investigation then it is probable that the purpose for conducting such an analysis will be very well defined. In this case, only a site specific hazard analysis would be conducted, and the various modelling assumptions included in the PSHA could be most appropriately matched to the application in question.

It has been pointed out previously that the hazard estimate is calculated assuming rock sites. Now that a very specific earthquake scenario has been defined through the four dimensional disaggregation procedure, a detailed site response analysis could be conducted using acceleration time histories corresponding to the magnitude, distance, and epsilon parameters obtained. In addition, recent developments in hazard and response analysis have lead to vector valued predictive equations for intensity measures such as spectral acceleration and epsilon (Baker and Cornell 2005). Models such as these, which will undoubtedly become more and more common with time, tie in extremely well to disaggregation procedures in PSHA.

A.6.6. PSHA for Arias Intensity

In Chapter Four of this section, as well as discussing models for spectral and peak ground acceleration, two models of Arias Intensity were mentioned. These two models, the Travasarou et al. (2003) model and the model developed in Chapter Six of Section B of the current thesis have been employed to conduct the first probabilistic seismic hazard analysis with respect to Arias Intensity in New Zealand. A thorough discussion of the development of the new model for use in New Zealand is given later in this thesis, so rather than repeat this here, the interested reader is referred to Chapter Six of Section B.

On point that must be made with respect to the use of the newly derived model in PSHA is that currently the standard deviation of the model is probably too large. Therefore, while the model performs very well at predicting mean Arias Intensities from earthquakes in New Zealand the larger than ideal standard deviation of the model will result in hazard estimates that are higher than they should be. The New Zealand model performs much better than the Travasarou et al. (2003) model when used to predict typical values of Arias Intensity. The two models have slightly different functional forms but the main differences between the two models are the extent of near source constraint, and the rate of geometric spreading in each two model. While it would be too conservative to implement the new model for Arias Intensity for New Zealand for PSHA by itself, simply using the Travasarou et al. (2003) model would also lead to misleading hazard estimates for Arias Intensity in New Zealand.

Therefore, a hazard curve for Arias Intensity is computed for the example site in Westport using a variety of different assumptions regarding the most appropriate weight to assign each of the models. Considering the strengths and weaknesses of both models, and without wanting to overestimate the hazard for Arias Intensity too much, weights of 70% and 30% for the Travasarou et al. (2003) and new New Zealand models respectively were used to calculate the hazard curve presented in Figure A.6.12. In this figure, the design level Arias Intensity corresponding to a 10% probability of exceedance in 50 years is indicated. Table A.6.2 shows how this design value varies with the assignment of different weights to each of the two predictive models for Arias Intensity.

The hazard curves shown in Figure A.6.12 display some 'kinks'; these kinks are the related to the rupture scenarios for the Alpine Fault for the independent northern and Wairau section ruptures. In each of these cases, the restriction on the epsilon value becomes inhibitive and causes the contribution from these scenarios to be curtailed at different points depending on the value of $\varepsilon_{\max}$ and the particular rupture segment. Once again, the Alpine Fault has a considerable influence upon the total hazard calculated at the Westport site. The relative contributions from the various fault sources are shown in Figure A.6.13.

This hazard curve for Arias Intensity represents the first of its type in New Zealand. Arias Intensity is an important ground motion parameter that has both structural and geotechnical applications. A thorough

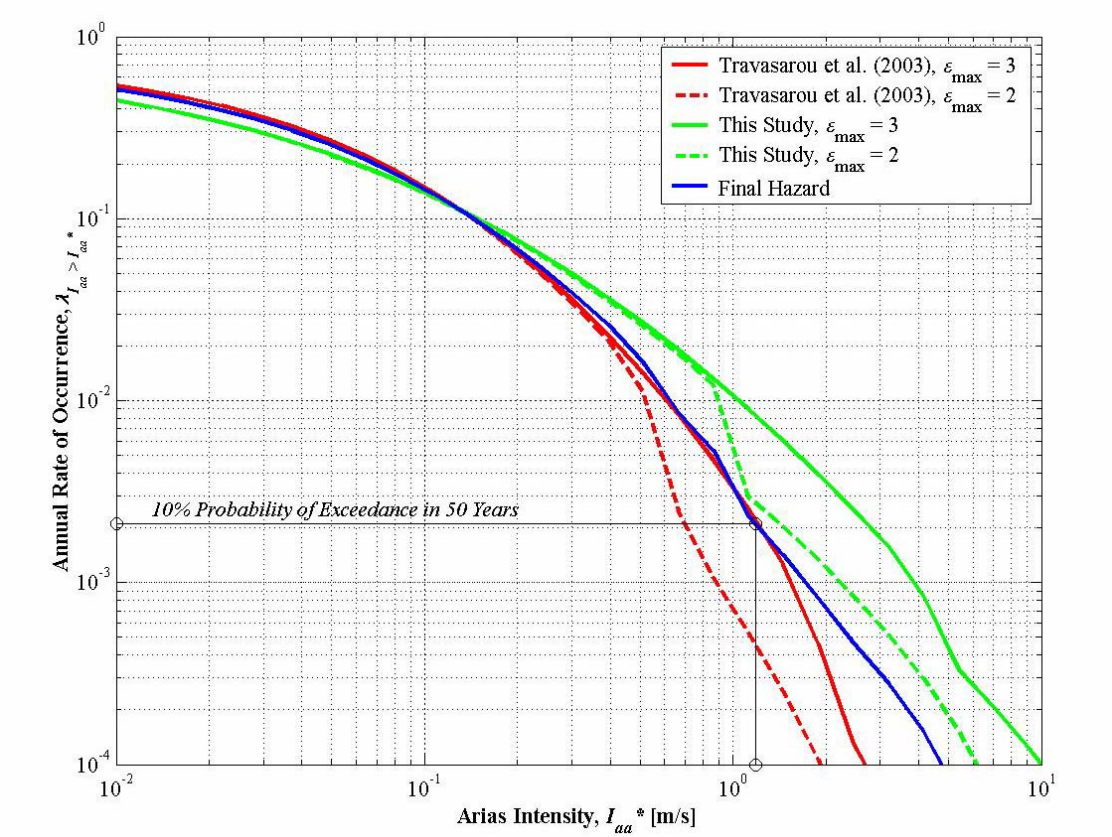

Figure A.6.12: Hazard curve for Arias Intensity calculated for the Westport site. The design level Arias Intensity corresponding to a 10% probability of exceedance in 50 years is indicated. Also shown are two different curves, each for different values of ε_{max} , for each model.

discussion of its nature and possible applications is given in Section B of this thesis. Although the newly derived model for Arias Intensity has been employed to estimate design Arias Intensities for the example Westport site, these values should be regarded with caution until a more thorough understanding of the nature of the standard deviation of the New Zealand model is obtained. The standard deviation of the Travasarou et al. (2003) is very well modelled and is based upon a large dataset of strong motion records from throughout the world. However, the model does not perform very well for predicting mean Arias Intensities for New Zealand. One possible option that was considered, but not implemented, was to retain

intra-event component of uncertainty from the New Zealand model, as this compares relatively well with that of the Travasarou et al. (2003) model, but to adopt their inter-event uncertainty values to essentially obtain a composite ground motion model for Arias Intensity for use in PSHA in New Zealand. While this method was considered, it was not implemented; until a better understanding of the nature of the scatter of Arias Intensity in New Zealand is obtained, hazard estimates for this ground motion measure are best made by implementing the methodology used to generate the curves in Figure A.6.12 and Figure A.6.13, and to acknowledge that these design levels will be conservative. The extent of this conservatism is currently unknown however.

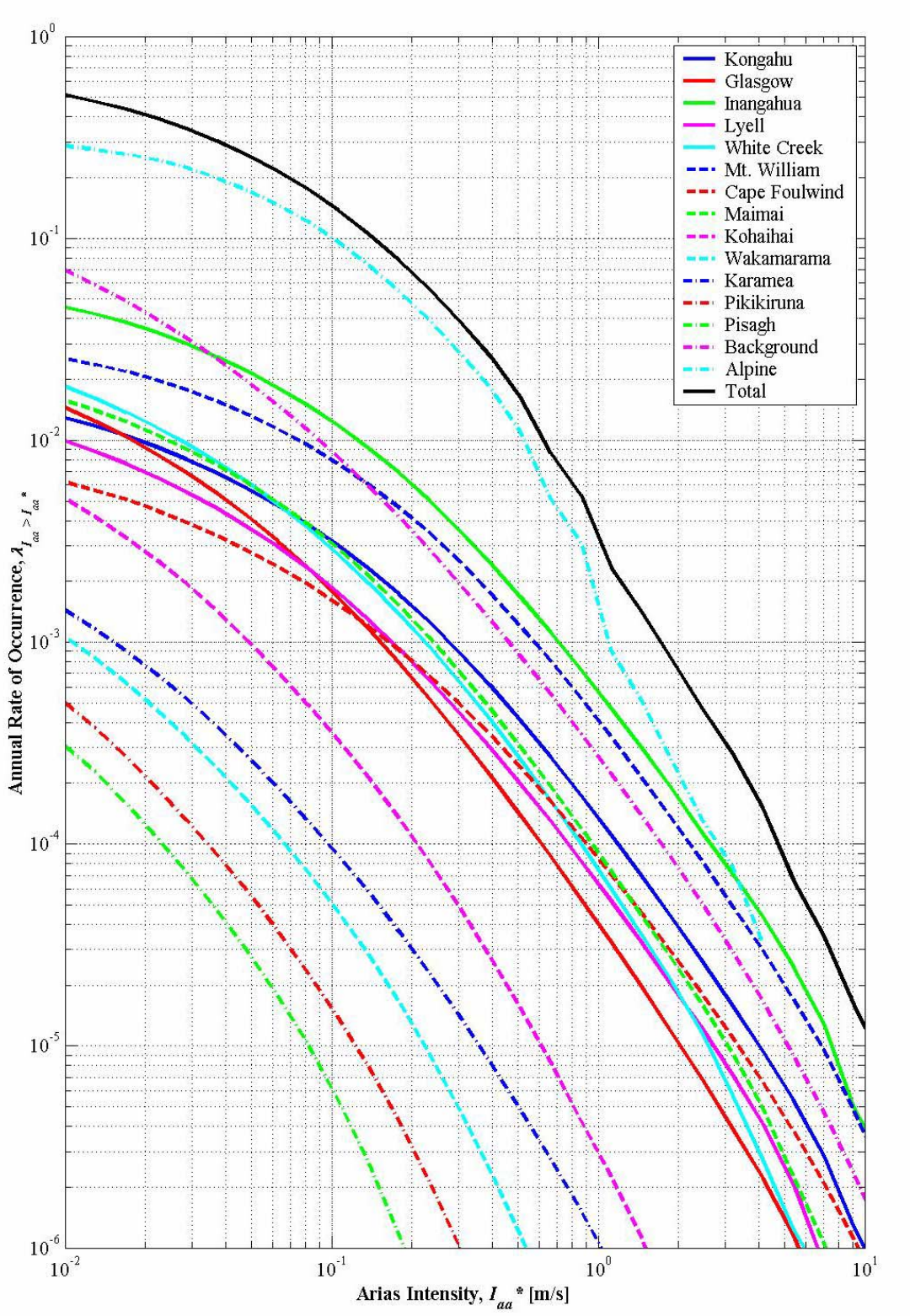

Figure A.6.13: Contributions to the total hazard for Arias Intensity calculated for the Westport site from each of the seismic sources in the PSHA fault model.

Table A.6.2: Dependence of the 10% probability of exceedance in 50 years design Arias Intensity with respect to the weighting factors between the predictive models used.

Model	Model Weight	I_{aa}^{*},10% in 50yrs [m/s]
Travasarou et al. (2003)	1.0	0.8895
This Study	0.0	
Travasarou et al. (2003)	0.9	1.0102
This Study	0.1	
Travasarou et al. (2003)	0.8	1.0922
This Study	0.2	
Travasarou et al. (2003)	0.7	1.1809
This Study	0.3	
Travasarou et al. (2003)	0.6	1.2877
This Study	0.4	

A.6.7. Spatial Variations of Hazard in the Buller Region

All of the PSHA results presented thus far have related to an example site chosen for the population centre of the study region. Reasons for not generating hazard maps have already been mentioned, but it is worthwhile to calculate hazard curves for other spatial positions so that the spatial stability of the hazard estimates may be obtained. In the national seismic hazard maps broad increments of ground motion levels are assigned to large regions. However, one can readily appreciate that for regions where individual fault sources are able to have a strong impact upon the total calculated hazard, such as the present study region, the spatial distribution of hazard for any given ground motion measure may vary significantly in space.

In order to demonstrate the nature of this spatial variation, hazard curves for peak ground acceleration were calculated for two different sites. The two different sites that were selected were selected based upon both their significance to the economic stability of the Buller region, as well as due to their spatial location relative to Westport. In Chapter Two of this section the nature of the faults in the region were observed to trend in a similar direction. Therefore difference between hazard estimates is likely to vary more as one moves perpendicular to the primary orientation of faults than if one moves parallel to these faults. The two site that were selected were the Ngakawau site, at $(E = 2416460, N = 5954600)$, and the Island Block site, at $(E = 2424330, N = 5893600)$ in NZMG co-ordinates. The Ngakawau site is located to the north of Westport, along the coast and is positioned essentially on top of the surface

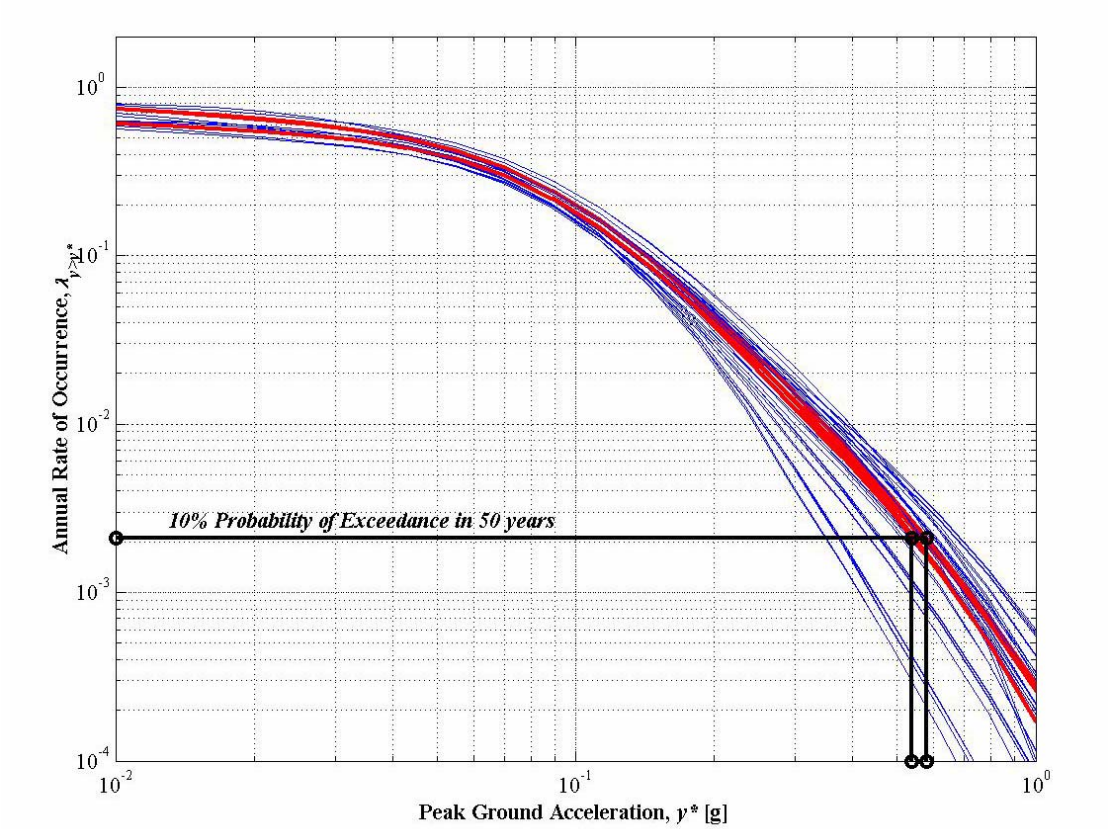

Figure A.6.14: Peak ground acceleration hazard curves computed for the Ngakawau site to the north of Westport. The ground motion level having a 10% probability of exceedance in 50 years is again shown. The blue and red curves retain their definitions from earlier figures.

expression of the Kongahu Fault. This site must therefore consider some interesting near field hazard scenarios related to fault displacements, directivity effects, and hanging wall effects. These effects are not considered further in this study; however, while the rupture of the Kongahu fault would be responsible for these creating these interesting near field effects, the occurrence of this event was not found to be the critical event in terms of contribution to probabilistic hazard at this location. This is an example of where engineering judgement must come into play. Although the average hazard computed for the PSHA suggests alternate critical earthquake scenarios to the rupture of the Kongahu fault, this calculation is based upon average rates of occurrence and measures of strong ground shaking. The PSHA does not consider the consequences of this shaking and in the case of the Ngakawau site special consideration should be made for the near field effects associated with a possible rupture of the Kongahu Fault. This fault should also be considered more specifically in order to determine constraints upon the activity with respect to factors other than observed seismicity. The fault is considered capable of generating large magnitude earthquakes but the relatively small contribution to hazard at the Ngakawau site may be based upon a lack of observed seismicity associated with this source. That said however, the Hawk's Crag Earthquake sequence of 1991 is associated with this fault, so it is known to be currently active and, if anything, the 1991 sequence of events is more likely to overestimate the future hazard associated with this fault source.

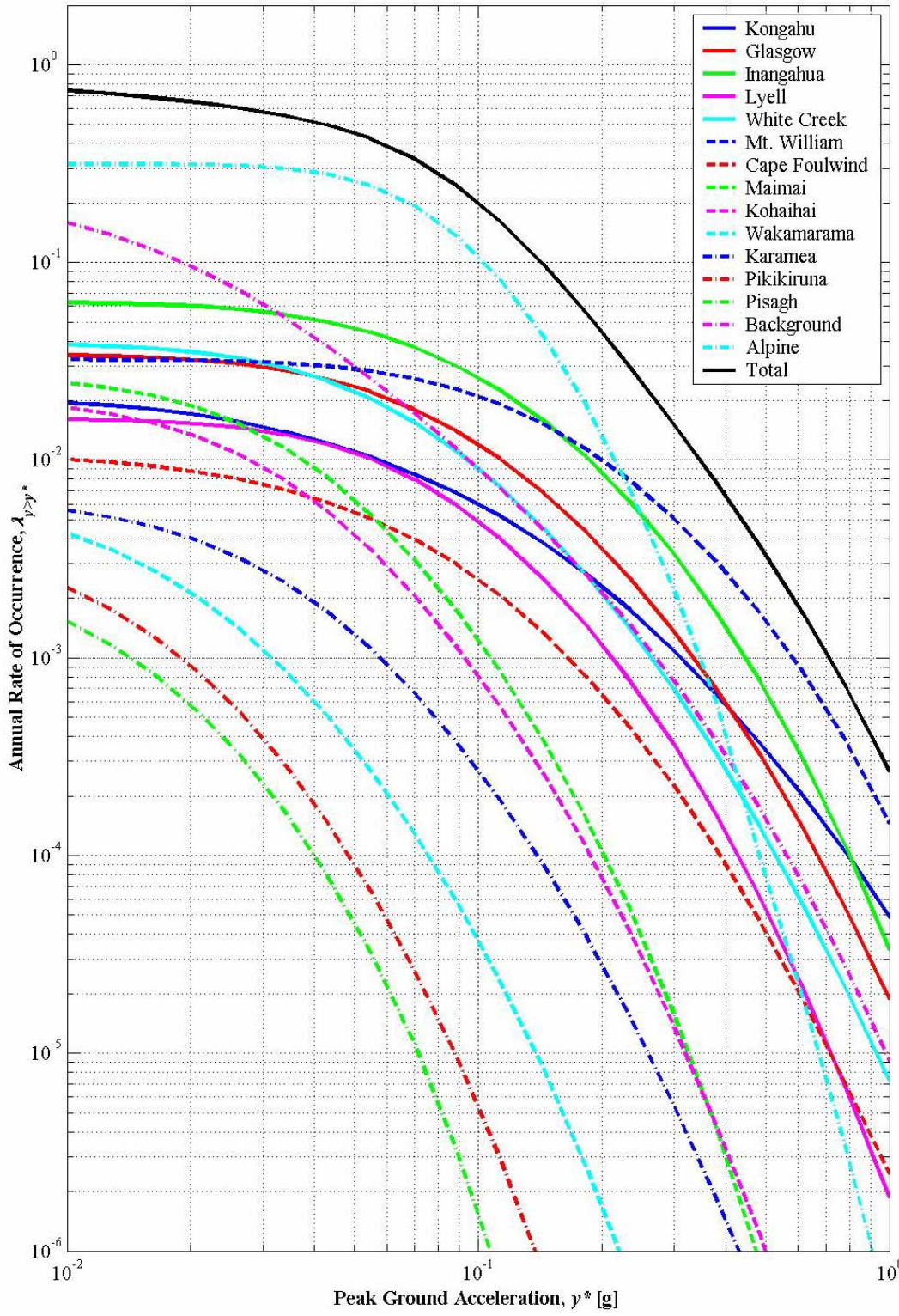

Figure A.6.15: Hazard curves from individual seismic sources for the Ngakawau site. Note that the Kongahu Fault is only a governing fault source at long return periods due to its relatively low levels of observed seismic activity and its close proximity to the site.

Comparing the actual design values calculated for this site to those determined for Westport, ones obtains estimates of 0.54 – 0.58g, and 0.66 – 0.72g, for the 10% probability of exceedance for 50 and 105 years respectively. Note that these values are significantly larger than those computed for the site in Westport despite the two sites being less than 30km from each other. The ground motions computed for rock at Ngakawau are very close to those scaled up from the rock site class for Westport. The ground motions therefore change by increase by approximately 40% over a distance of only 30km.

The Island Block site, in contrast to the Ngakawau site, is located approximately 50km to the southeast of Westport. The directions between Westport and Ngakawau, and Westport and Island Block are approximately orthogonal to each other. As one moves from Westport towards the Island Block site, one moves on a direct line closer to the Alpine Fault. The hazard curves for this site are therefore heavily governed by the hazard contribution from the Alpine Fault. This extent of this domination is such that it is pointless showing a plot of hazard curves such as those in Figure A.6.1 for the Ngakawau site as the plot would simply be a plot of the Alpine Fault hazard curve over the range of peak ground accelerations of interest. This is clearly portrayed in Figure A.6.14 where the contributions from the individual seismic sources to the hazard from peak ground acceleration at the Island Block site are presented. One cannot observe the design ground motion levels in this case as the values are out of the scale of the plot in excess of 1g.

Regardless of the specific hazard values for the Island Block site, it is clear that the difference in hazard for different points within the Buller – NW Nelson region is highly variable and that the accurate determination of the hazard associated with the Alpine Fault is of great significance for the region. Given that a rupture of the Alpine Fault is regarded as being imminent (Yetton et al. 1998; Yetton 2000; 2002) hazard analyses that are conducted in the time period between now and the next rupture of the Alpine Fault should include enough information for hazard estimates after the Alpine Fault rupture to be made. This may simply be through the use of figures such as Figure A.6.14 so that the hazard estimate for the site including and excluding a particular fault source may be estimated.

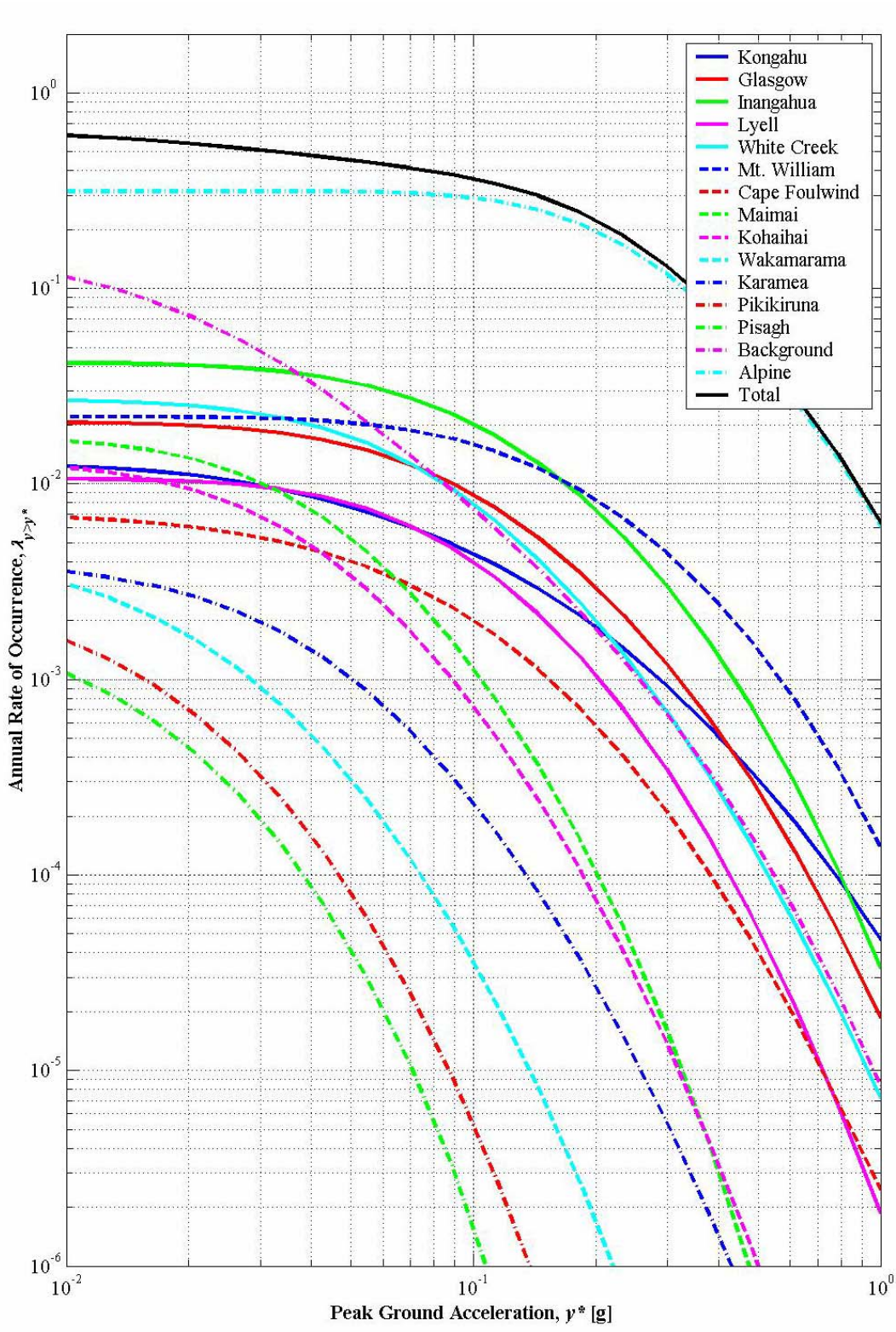

Figure A.6.16: Individual peak ground acceleration hazard curves for the Island Block site for the various fault sources in the Buller region. Note the complete governing of the total hazard curve by the Alpine Fault.

A.6.8. Chapter Summary

Results from probabilistic seismic hazard analyses are presented for example sites within the Buller region. The methodology implemented was previously summarised in Chapter Five of this section of the thesis. Hazard estimates were given for four different ground motion measures for an example site located in Westport, the population centre of the Buller region. These ground motion measures are peak ground acceleration, 5% damped ordinates of acceleration response spectra at 0.2 and 1.0 seconds, and Arias Intensity. A complete four dimensional disaggregation of the peak ground acceleration corresponding to a 10% probability of exceedance in 50 years was presented. The controlling earthquake scenario for this site was found to be an $M_W 7.3$ event occurring on the Inangahua Fault with an associated peak ground acceleration of 0.2 natural logarithmic units above the mean value for this combination of earthquake size and position. This accurately defined earthquake scenario may be used to generate, or select appropriate ground motion time histories that can in turn be used to convert the hazard estimates made for rock sites into those for specific geotechnical site conditions. This is an extremely useful piece of information to have available for a response analyst working with the results of the PSHA.

The predicted ground motions estimated for the Westport site were shown to agree well with those estimated using the latest national seismic hazard maps for New Zealand. However, examples of sites located only 30, and 50km from Westport has hazard estimates determined that were significantly higher than those estimated in the national hazard maps. This significant spatial variation in ground motion hazard in the Buller region means that if general hazard maps were to be computed for the region, the spacing of the grid points used to draw contours of spatially varying hazard would have to be extremely close together. The computation time associated with such an exercise using the sophisticated PSHA code developed as part of this study would be extremely large and the amount of physical storage space, if subsequent disaggregation was desired, would be highly restrictive.

The hazard curves provided for Arias Intensity are the first of their kind determined in New Zealand. There are issues related to the error structure of the model of Arias Intensity for New Zealand, described later in this thesis, that mean that the hazard estimates given here for Westport should be regarded as being conservative. The extent of conservatism is not able to be estimated with any reliability at this point.

A.7. Conclusions and Recommendations

Section A of this thesis was devoted to the description, and application, of modern Probabilistic Seismic Hazard Analysis (PSHA) methodology to the Buller region in the northwest of the South Island of New Zealand. As a consequence of applying this methodology to a specific region, there are specific results and conclusions that are arrived upon. These results formed the basis Chapter A.6. However, in this chapter, as well as briefly recapitulating these results and their implications, conclusions that can be drawn from each of the previous chapters will also be presented

In the remainder of the chapter, the conclusions pertaining to each of the five main chapters of this section are presented in relevant subsections.

A.7.1. Chapter A.2: Geological Setting of the Buller Region

Being the first chapter of this section, the focus was to describe the environment in which the PSHA was to be carried out. The Buller region is known to have a very active recent seismic history, but there are varying degrees of belief in the literature regarding how representative this observed seismicity is of the long term activity in this region. This existing paradox represents a significant challenge when attempting to use observed seismicity to model future earthquake occurrence. However, after having reviewed the literature it was found that the most recent research from geodetic modelling, finite element modelling, and structural geology, all suggest that the observed rates of seismic activity in the Buller region are not as anomalously high as previously suspected. This finding is important in giving support to the predominantly seismicity based methodology employed in this thesis.

A brief review of the most significant historic earthquakes to have been observed in the region was given. Similarities were seen to exist between all of these events, particularly with respect to their focal mechanisms. However, each event also had specific characteristics that were later able to be used to provide constraint on some of the assumptions made in other chapters. The 1868 Cape Foulwind

Earthquake showed that active faulting continues to the north of the Buller region, and that large events have been occurring relatively regularly over the past 150 years or so. The 1929 Buller Earthquake was significant in helping define typical maximum magnitude levels for the region as well as demonstrating the typical types of damage related to such an event. As the Buller Earthquake occurred prior to the development of modern building standards in New Zealand this information regarding the typical forms of damage relate mostly to geotechnical damage such as the onset of liquefaction and the triggering of landslides. Good felt intensity maps were also obtained for this event though which can be correlated to likely damage in modern structures to some extent. The 1961 Westport Earthquakes highlighted the existence of a significant fault source offshore of the Buller region that would not have been identified from the inspection of topographic maps or field inspections. These events were also very useful in placing upper bounds upon the minimum magnitude of engineering significance to be used in the PSHA as significant damage was reported as a consequence of these moderate sized events. The 1968 Inangahua Earthquake contributed to the peak ground acceleration database for New Zealand and still provides the largest recorded peak ground accelerations from a New Zealand earthquake. This earthquake also provided well constrained isoseismal maps over a large region as well as multiple examples of liquefaction. The final events that were considered were those comprising the Hawk's Crag sequence in 1991, these events showed that the Kongahu Fault was definitely active which is significant in that it is the closest source to the main population centre in the Buller region. These events also supported the findings from the consideration of the Buller and Inangahua Earthquakes that the slip vectors of events in the Buller region are rotated from those that would be expected from plate motion modelling. This finding has some significance when considering the modes of deformation across the entire northern South Island, and in particular, when considering the respective roles of the faults in the Buller region and those in the Marlborough Fault Zone in accommodating this overall regional deformation.

The final result of Chapter A.2 was the selection of a suite of seismic sources that were used in the subsequent PSHA. In total, fifteen seismic sources were selected. Of these, fourteen were fault sources while the remaining source represented background seismicity in the region. In general these fault sources were shown to be steeply dipping reactivated reverse faults, with the exception of the Alpine Fault which is predominantly strike-slip. The faults in the region were also shown to be located in hypothesised domains and subdomains that are likely to contribute differently to hazard estimates for sites in the Buller region both due to their locality with respect to these sites, but also due to differences in the nature of the faults comprising each domain and subdomain. This hypothesis is not readily verified in the present, but will be tested in time. If the hypothesis proves to be an accurate representation of the tectonics of the Buller region then the model may be used to partition seismic moment release rates over the region with a greatly spatial resolution. This in turn would lead to better definitions of future seismic hazard in the region.

A.7.1.1. Recommendations for Further Work

At present, many assumptions must be made with respect to the geometry of the faults within the Buller region when performing a PSHA. While the surface expression of the fault structures in the region is quite pronounced, the corresponding geometry throughout the depth of the crust is highly uncertain. The existence of information relating to the total geometry of the fault structures in the region would add greatly to ones ability to characterise the hazard for sites in the Buller region. Such information might be gleaned from taking seismic profiles throughout the region. In this way, hypotheses such as the cross section of Ghisetti and Sibson (2006) could be tested. If the geometries of the faults were known it would also greatly facilitate the determination of the relative contributions made by the various faults in the region to the release of the compressional strain induced in via the governing tectonics.

The availability of paleoseismic information is extremely useful for constraining the activity rates of the individual fault sources at long return periods. Currently, very little paleoseismic information is available for the region. Any more information of this nature that could be obtained would be particularly useful. However, the field investigations that were performed as part of this study suggest that finding appropriate sites will be very difficult.

Deformation models have been developed for New Zealand as a whole, and for the northern South Island, but none have been developed for the Buller – NW Nelson region in particular. Any study of this nature, using geodetic data, Quaternary slip rates, plate motion vectors, or any other method that resulted in estimates of the moment release rate specifically for the Buller – NW Nelson region would be very useful for constraining the rates of seismic activity assigned to the fault sources.

A.7.2. Chapter A.3: Seismicity Analysis of the Buller Region

The seismicity analysis conducted as part of this study employed state of the art techniques. A significant amount of effort was made to ensure that the dataset employed for this study was as accurate as possible in terms of the locations and magnitudes of the earthquakes comprising the dataset. The main focus of the attention in this regard was with respect to ensuring that a consistent magnitude scale was adopted for all records and that the positions assigned to events in the catalogue actually represented physically possible distributions in space. The practice of assigning earthquake events restricted depths compromises the quality of the seismicity catalogue, particularly if one wishes to implement a thorough declustering procedure, and/or employ Bayesian Inference to associate events to fault sources, as was done in this study. To this end, twenty pseudo-datasets were created that retained all information regarding the lateral positions of events, but that redistributed the vertical positions of restricted depth events so that the resulting datasets had events distributed according to the distributions observed since the practice of assigning restricted depths ceased.

The pseudo-seismicity datasets were declustered using a modified version of the Reasenberg (1985) algorithm that incorporated the three key scaling relationships with respect to aftershock sequences, the Modified Omori Law, the Gutenberg-Richter Law, and Båth's Law. The Inangahua Earthquake was identified as having an associated aftershock sequence that had a significant impact upon the rate of earthquake occurrence in the years that followed. For this reason, the Inangahua aftershock sequence was re-analysed using techniques that were not available when the sequence had been previously analysed and new aftershock sequence parameters were obtained. These parameters were then used to remove the majority of events that can be assumed to be associated with the Inangahua aftershock sequence, based upon the fundamental assumptions made in the Reasenberg (1985) algorithm.

Following the declustering of the seismicity catalogues, magnitude – frequency distributions were derived for each of the seismic sources to be included in the PSHA. These magnitude – frequency relations were derived by assuming that the individual seismic sources could be modelled using the doubly bounded Gutenberg - Richter relationship. Each source was assigned a maximum magnitude value that was determined using a combination of observed earthquake occurrence and various fault scaling relationships. The characteristic activity parameters for each source were determined using a range of values for the maximum magnitudes for each of the twenty seismicity catalogues considered in the analysis. The final results that were obtained and carried through the PSHA were found through the use of a logic tree in order to account, in some way, for the epistemic uncertainty associated with the assumptions made throughout the seismicity analysis.

The findings of Chapter A.2 regarding the likely values of seismic moment release rate were compared to those determined from the seismicity analysis and were found to agree very well. This indicates that, contrary to the opinion of some researchers, the observed seismicity can do a good job of representing the extent of long-term deformation typical of the Buller – NW Nelson region. This finding is very important for justifying the use of a seismicity based source model for the region where geological information is not able to provide adequate constraint on long term activity rates.

A.7.2.1. Recommendations for Further Work

Obviously, the more seismicity information that is available for the region, the more accurately the Gutenberg – Richter b -values for the various seismic sources may be obtained. We cannot accelerate the occurrence of earthquakes (nor would we, if we were able), but we can lower the level of completeness of the seismicity dataset in the region by installing more strong motion instruments in the region. This work is currently in the process of happening as part of this project. An additional six accelerographs are to be installed throughout the Buller region and will greatly increase the density of recording stations in this region. While the presence of these instruments will not act to help constrain the rate of occurrence of the critical large earthquakes, it will enable much tighter constraints to be placed on the b -values based upon small earthquakes and provide a stronger platform from which extrapolations may be made to larger magnitudes. The ability to detect smaller events will also allow aftershock sequences to be modelled more

accurately as well as other more general time dependent fluctuations in the observed levels of seismicity. Both of these sources of information may add to the quality of subsequent hazard analyses conducted in the region.

The most important further research that could be conducted in terms of seismicity analyses is to constrain the rate of occurrence of large earthquakes in the region. The method of using precarious rock evidence was mentioned in Chapter A.2, and is currently being investigated practically in other parts of the South Island (Stirling 2005). However, during the field investigations conducted as part of this research, opportunities to conduct studies of this nature appear very limited. Tree – ring analyses may offer some constraint, although the single study that has been conducted in the region thus far (Wells and Yetton 2004) did not present any new information regarding past earthquake occurrence. It is probable that the time frame over which tree-ring analyses may offer information is too short to be of much use for constraining magnitude – frequency relations.

Associated with more seismicity information comes a greater ability to identify regions of heightened activity within the Buller – NW Nelson region. The regional domains and subdomains that were hypothesised in Chapter A.2 may be identified with more accuracy given a larger seismicity catalogue and in this case the background source that is assumed in the present model might be able to be subdivided to reflect spatially varying background seismicity rates.

A.7.3. Chapter A.4: Attenuation Relationships

Chapter A.4 considered the important problem of selecting appropriate strong motion predictive relationship for use in PSHA. An overwhelming conclusion form this section of work was that there are currently too few predictive equations developed specifically for strong ground motion measures in New Zealand. While the primary excuse for this in the past has been the lack of available strong ground motion information, this excuse cannot be maintained *ad infinitum*. For the present work, predictive equations for 5% damped acceleration response spectral ordinates, and peak ground accelerations, based primarily upon data from the United States were adopted in order to encapsulate the variety of functional forms existing in the current literature. These relations supplemented the available New Zealand relations that were regarded as being suitably robust for use in PSHA. A suite of ground motion predictive equations were therefore used in order to take into account some degree of the epistemic uncertainty associated with the selection of a particular strong ground motion model.

Two models for Arias Intensity were also adopted, one based upon a very large worldwide dataset, and one developed in Section B of this thesis based primarily upon New Zealand data, but with supplementary foreign near field records. These relations both have strengths and weaknesses with respect to application in PSHA, but the strong ground motion measure that they predict is considered useful enough to warrant making even a tentative estimate of its associated future hazard.

The all important nature of the standard deviations of these models was considered. Again, the use of multiple ground motion equations enables the wide variety of assumed error structures to be considered. This parameter has a large impact upon hazard estimates and it is therefore important to represent the nature of the variability of this parameter in the available predictive models. Unfortunately, the form of the standard error is strongly related to the size of the dataset used to obtain the relationship. It has been shown that standard errors are magnitude dependent, but the nature of this magnitude dependence cannot be ascertained unless a reasonably large dataset is available for the regression analysis. This actually presents an issue that is commonly not addressed in the selection of predictive models for PSHA. Often the general fit of the model to the observed ground motions in the study region is used to assign logic tree weights to the various models. However, it is just as important, if not more so, to consider the error structure of the relationships and to see how this compares with the observed data for the study region. Weights assigned to branches of a logic tree must therefore take into account both the general fit of the model as well as the nature of the standard deviation of the model.

A.7.3.1. Recommendations for Further Work

The recommendations here are obvious. More predictive models must be developed for use in PSHA for New Zealand. The most important models are those for the attenuation of peak ground acceleration and ordinates of the 5% damped acceleration response spectrum. In addition, models for Arias Intensity, such as the one proposed in Chapter B.6 of this thesis need to be further developed.

The magnitude scaling of the error terms in ground motion predictive models should also be investigated. Currently, models for peak ground acceleration have a constant error with magnitude; while that for the response spectra assumes that the form of a foreign equation holds and then modifies the magnitudes. The foreign model used assumes a trilinear error function; the two magnitudes corresponding to the change of scaling are therefore imposed upon the New Zealand data. However, other relations that include magnitude dependent errors have adopted different magnitude limits and the values assumed in the New Zealand model are therefore by no means fixed.

All New Zealand predictive equations for strong ground motion assume that geometric spreading holds in all regions of New Zealand. This is in contrast to many foreign models for measures of Fourier Amplitude Spectra in which the scaling with distance is modelled as bilinear or trilinear. Given the great variation in crustal structure in New Zealand over relatively short distances, any such scaling may be either difficult to identify, or be not appropriate at all. Regardless, this issue is not raised in the present literature associated with New Zealand strong motion predictive models. There may be comment in the seismological literature of which the author is unaware. If this is the case, then whatever results have been found in these cases must be incorporated into the predictive models for strong ground motion measures. Although the distances in question correspond to ground motions that are not typically regarded as being strong, better knowledge of the scaling of strong motion with distance will enable larger regression datasets to be

obtained and consequently, better constraints upon the magnitude scaling of the ground motion measures. It should be noted however, that if there was a significant bilinear or trilinear geometric scaling of strong ground motion amplitudes then neglecting these would lead to lower estimates of the geometric spreading over short distances. The models for peak ground acceleration for New Zealand, as well as those for the Fourier Amplitude Spectrum of acceleration, and Arias Intensity developed later in this work indicate that the geometric spreading found from regression upon New Zealand data is higher than expected. Given this finding, it is likely that no alternate scaling with distance may be found. This should, however, be verified independently.

It will also be very beneficial to extend the applicable range of periods that are currently able to be predicted to much longer periods. Although the revised building standards that are soon to be implemented in New Zealand are founded upon capacity design, it will no doubt be long before displacement based design becomes the norm in New Zealand as it is doing in Europe and the United States. For this reason, predictive relations for displacement spectral amplitudes will become very useful. Currently, the only available model for acceleration response spectra is the McVerry et al. (2000) model that has coefficients defined up to a maximum period of 3.0 seconds. This limit must be extended much further, up towards the 10 second range in order for many common, and future, displacement based methods to be employed. This goal is achieved if the high pass filter level is reduced for the strong motion recording instruments in New Zealand. This may not be possible in the near future, and work towards the goal of extending the period range of predictive models may have to adopt a methodology similar to that of Cousins et al. (1999) of marrying ground motion records from accelerographs with those from broadband seismographs. The extended bandwidth of the seismographs would enable constraints to be placed upon the high period spectral ordinates, but only for weak ground motions. Extrapolation would need to be made for strong ground motion models.

A.7.4. Chapter A.5: Probabilistic Seismic Hazard Analysis Methodology

In this chapter, standard modern PSHA methodology was outlined. The main focus was placed upon defining the applicable variable range over which the numerical integration procedure was performed. A considerable amount of effort was put into defining, or at least investigating the most applicable range of these variables. In the common practice in PSHA were the final output is a single hazard curve it is important to understand how such fundamental assumptions, such as those regarding the applicable range of the integration, may affect both the magnitudes and form of the final hazard curve. This is all too commonly neglected when performing PSHA.

In the end, specific values were not adopted in preference to others, except for the distance limits that are defined from the seismicity analysis. The values selected for the minimum and maximum magnitudes both have a significant influence upon the hazard curves that are obtained, as does the upper bound on epsilon, although this latter parameter becomes more and more important as hazard is computed at larger and larger

return periods. The reason for not specifying a particular parameter set is that the analysis that has been conducted has not been done with any particular final project in mind, such as for the design of a particular structure, or an assessment of an existing structure etc. The PSHA will be specific for the situation in question. This concept is essentially at the heart of Performance Based Earthquake Engineering (PBEE) that is becoming popular in the United States and elsewhere. Much as in Quantum physics, where Schrödinger's wave equation entertains all possibilities until an observation is made, upon which the wave equation collapses to single state, the hazard curves presented in this study represent a wide range of possibilities with respect to the final application in question. Once this application is defined, the hazard curves may collapse onto the most applicable value for that given situation.

As well as addressing the limits of integration, Chapter A.5 discussed four-dimensional disaggregation of hazard and how this procedure is carried out. An important point of this section was that the commonly adopted formulation for PSHA must be modified when accounting for the finite effects of fault ruptures in the hazard analysis. The most important consequence of reframing the governing disaggregation formulae is that careful attention must be made to ensuring that consistently defined distance measures and source scaling relations are used in the calculation of the conditional probability density function for distance. This is of particular importance when using multiple predictive models in the hazard computations.

An issue that relates to the disaggregation with respect to multiple predictive equations is that the target ground motion level for which the disaggregation is performed will not necessarily be achieved by back substituting the four-dimensional mode of two spatial co-ordinates, magnitude, and epsilon, into the various predictive models (except under very special conditions, i.e. for strike-slip faults, and for only models using r_{rup} and r_{jb}). Even when the relevant logic tree weights are applied to the values of the predictive models obtained using the four-dimensional mode, the target acceleration may not be matched. This is due to the different distance definitions used by the various predictive models. If one wanted to prove that the four-dimensional mode does indeed correspond to the target ground motion desired, one must take explicit account of the fault geometry that is related to the modal value. This assumes from the outset that the modal value will indeed correspond to a particular fault. Without knowledge of the fault geometry, the relevant distance measures cannot be made to reflect the same scenario, and so long as the distance measures determined from the disaggregation procedure are not consist with those used to calculate the hazard in the first place, the target ground motion level will not be achieved. This is an important point for those wishing to use the results of a disaggregation procedure for future design. One must be very careful in using consistent definitions of distance in both the hazard calculations, and the subsequent design application.

A.7.4.1. Recommendations for Further Work

The actual methodology employed in PSHA is now very well established. There has recently been some debate regarding how to obtain the most appropriate results from logic tree formulations. However, these nuances have little practical impact on most general hazard analyses; it is not until very rare ground motion

levels are considered that the difference between whether or not one takes the mean, or median, hazard becomes important.

It would be beneficial to have more information regarding the most appropriate value of minimum magnitude to be assumed for a given application. At the moment there is a considerable degree of freedom left to the analyst in this regard. The implications of this are significant if one is required to meet particular hazard levels by government regulations, or the like. The analyst can readily calculate a lower hazard by modifying the values of the limits of integration, i.e. increasing r_{max}, increasing m_{min}, and decreasing ε_{max}. Indeed, there are so many degrees of freedom within PSHA that the results can almost be produced on demand. Take for example the present case where seismicity rates were extrapolated to large magnitudes, but where they were curtailed at an essentially subjectively chosen point. Simply by decreasing the values of the maximum magnitudes assumed in the analysis, the hazard might significantly be reduced. The influence of all of these parameters is very well appreciated by the hazard analyst, but is almost certainly not appreciated by the end users of the hazard results.

Constraints upon the values of minimum magnitude may come relatively simply as more studies of loss estimation are performed. A fundamental requirement of loss estimation is to relate ground shaking intensities to observed, or expected, levels of damage. Therefore, if the owner of some structure was willing to tolerate a particular degree of damage to their asset then the ground shaking intensity corresponding to this level of damage may be estimated. Given this estimation one could either obtain a representative level of magnitude that would cause shaking intensities such as these. Or, more accurately, one could invert the strong ground motion predictive equations used in the analysis to determine a distance dependent minimum magnitude level that corresponds to the ground shaking intensity relevant to the damage level that is deemed acceptable. Employing a methodology such as that just mentioned would enable standard comparisons between different hazard analyses to be made, as well as allow end users of PSHA to have a greater input in defining the analysis that is to be carried out.

Naturally, this proposed methodology also lends itself well to implementation in design codes. For example, in New Zealand, seismic design criteria are currently specified by a seismic coefficient for typical building types in various regions of the country. These coefficients can be related to ground motion intensities corresponding to particular design levels, such as the serviceability limit state, or the ultimate limit state (essentially the life safety condition). These ground motion intensities can then be used to specify the required minimum magnitude by adopting the method outlined above. In this way, general code specifications could be related more closely to site specific probabilistic hazard analyses in a consistent manner.

A.7.5. Chapter A.6: PSHA Results

This chapter is effectively a summarising chapter in its own right. It outlines the results of hazard computations made with respect to peak ground acceleration, 5% damped acceleration response spectral levels for periods of 0.2 seconds and 1.0 seconds, and also for Arias Intensity. The main design levels that are presented are the 10% probability of exceedance in 50, and 105 years. These design levels correspond to average return periods of approximately 475 and 1000 years respectively.

The effectiveness of portraying the total hazard in terms of the contributions from individual seismic sources is highlighted as is the benefit of using a thorough disaggregation procedure to completely define the outputs of the PSHA. This disaggregation procedure was also shown to be very effective in characterising a hazard consistent earthquake scenario that can subsequently be used for advanced demand and response analyses for geotechnical and structural engineering problems. The specification of a such an earthquake scenario coupled with ground motion relations that are developed in Section B provide extremely powerful tools for performing site specific engineering analyses. Currently in New Zealand, the capacity for performing such analyses is very limited.

Another key finding was the extent to which hazard estimates may vary with respect to time and space within the Buller region. The spatial variation of hazard is primarily related to the relative position of the site in question to the surrounding seismic sources. This is particularly true in the present, where a rupture on the Alpine Fault is anticipated within typical design periods. The hazard calculated for specific sites therefore increases as one moves towards the Alpine Fault. The variation in time is also primarily related to activity on this fault. As soon as the Alpine Fault ruptures, the hazard for sites in the Buller region, as determined using time dependent probabilities for the Alpine Fault, will drop drastically. In this case, the nature of the spatial variation of hazard will also be modified. Because the majority of faults in the region are aligned in a subparallel manner, hazard is most likely to vary as one moves perpendicular to the typical strike angles of these faults, while remaining relatively constant as one move parallel to them.

Some of the more specific findings of Chapter A.6 are presented in bullet point form below.

- Hazard estimates for peak ground acceleration and the 5% damped acceleration response spectral ordinate of 0.2s for a site in central Westport compare well with the estimates of regional hazard for the Buller region based upon the most recent national seismic hazard maps. These comparisons are made for both the 10% probability of exceedance in 50 years and the 10% probability of exceedance in 105 years.
- The estimates of the 5% damped acceleration response spectral ordinate at 1.0s do not agree well at all, with estimated values from this study being significantly higher than those in the national seismic hazard maps.

- Estimates of seismic hazard within the Buller region vary significantly over relatively short spatial distances. Based upon the small set of sites for which hazard estimates were made, the hazard calculated for Westport appears to be towards the lower end of the typical hazard for the region.
- Hazard estimates for peak ground acceleration determined for a site at Ngakawau, less than 30km from the site in Westport, showed an approximately 40% increase in the hazard estimate. Another site, positioned closer to the Alpine Fault, was considered, and in this case the even greater contribution to hazard from the Alpine Fault meant that the total hazard estimated for the site essentially coincided with the curve determined for just the Alpine Fault on its own. The 10% probability of exceedance in 50 years ground motion was in excess of 1g for this site.
- A full four-dimensional disaggregation procedure was implemented, and was shown to be very effective in portraying the contributions to hazard from the constituent seismic sources included in the PSHA. This method also enabled a very specific design scenario earthquake to be identified. For the case of the hazard calculated for peak ground acceleration at the site in Westport, the scenario event was shown to be an $M_W 7.3$ event occurring on the Inangahua Fault with a ground motion of 0.2 natural logarithmic standard deviations above the mean level predicted from an attenuation model. This scenario corresponds to the peak ground acceleration having a 10% probability of exceedance in 50 years; that being approximately 0.45g.
- An incompatibility was identified between the target ground motion measure for which the disaggregation is performed, and the ground motion values that are obtained after inserting the earthquake scenario parameters back into the specific attenuation models included in the analysis. Of all the peak ground acceleration relationships included in this study, the Cousins et al. (1999) model was favoured in terms of the weight that was assigned to it in the logic tree procedure. Consequently, inserting the modal earthquake scenario parameters found from the disaggregation procedure back into this attenuation model gives the closest match to the target peak ground acceleration.

A.7.5.1. Recommendations for Further Work

As far as further work related to performing PSHA for sites in the Buller region is concerned, there is not a huge amount that can be done. It would be desirable to account more rigorously for the uncertainties involved in the PSHA procedure, perhaps by implementing a Monte Carlo simulation framework similar to that of the latest WGCEP project (Working Group for California Earthquake Probabilities 2003), Currently however, much of the data required to implement such an analysis is not available. The focus of future work should therefore be placed upon obtaining this required information, the bulk of which relates to geological constraints.

The hazard results that have been determined in this study relate to ground motions on typical rock sites. Maps accounting for site class could be developed by simply repeating the procedure outlined in Chapter A.5 many times for rock sites and then applying some approximate scaling factor for other classes, as was done in Chapter A.6. Or preferentially, by creating a map of geotechnical site conditions for the region

and then incorporating the spatial distribution of site classes directly into the hazard analysis. Both of these methods would apply for generating regional hazard estimates. In the case where site specific hazard is required however, the method suggested in this section of using rock site estimates to specify an earthquake scenario, and then performing a specific site response analysis is recommended.

SECTION B

DEVELOPMENT OF NEW PREDICTIVE EQUATIONS FOR STRONG GROUND MOTION MEASURES IN NEW ZEALAND

B.1. General Introduction to Section B

In Section A, care was taken to frame the problem of calculating seismic hazard in a probabilistic manner. In this section, the use of probability is generally associated with the acceptance of some degree of uncertainty within the problem being considered. However, when dealing with earthquakes, one thing is certain; they will happen in the future. While there is considerable uncertainty regarding where, and when, these events might take place our societies must be prepared to experience these events and to protect ourselves against foreseeable consequences that may result. This concept was articulated famously by Sun Tzu in the fifth century B.C.[†].

> *"If you know the enemy and know yourself, you need not fear the result of a hundred battles.*
> *If you know yourself and not the enemy, for every victory gained you will also suffer a defeat.*
> *If you know neither the enemy nor yourself, you will succumb in every battle."*

While it may prove to be untowardly arrogant to suppose that we might triumph against the affects of earthquakes any time soon, we can certainly go a long way towards minimising the losses they inflict upon us as a society. In order to adequately prepare ourselves to experience the potentially severe ground motions associated with damaging earthquakes we must develop methods to characterise the nature of this ground shaking, and we must design our structures with these expected ground motion characteristics in mind. In New Zealand, there has been a disproportionate amount of research focussed upon the seismic design of buildings with respect to the amount of research into the likely nature of strong ground motions from New Zealand earthquakes. In keeping with Sun Tzu's principles it could be said that we know ourselves reasonably well, but that our enemy is still somewhat shrouded in mystery. This is in large part due to the lack of available strong ground motion recordings against which potential predictive equations of strong ground motion measures might be tested. The current practice of making strong ground motion records freely available to the research community, through the GeoNet project (http://www.geonet.org.nz/), should go some way towards alleviating this problem, as should the

[†] From James Clavell's "The Art of War by Sun Tzu", 1981, Hodder & Stoughton Publishers

proposed increases in the number of strong motion recording instruments sited throughout the country (for example Avery et al. 2004). Developing predictive equations to aid in the characterisation of New Zealand strong ground motions is the primary objective of Section B of this thesis.

Predictive equations for strong ground motion measures based upon empirical data from various regions of the world have been available since the mid 1950's (Gutenberg and Richter 1956). Since this time the number of relationships available for estimating ground motion measures has increased rapidly in conjunction with the rapid increase in the amount of empirical strong motion data available. Most of the available relationships have been developed for the purpose of estimating peak horizontal ground accelerations, and response spectral ordinates of acceleration at 5% damping. Early studies also placed a reasonable amount of focus upon relationships for peak ground velocity. The proliferation of these types of predictive equations is driven primarily through the strong correlation these measures have with damage in engineered structures, as well as due to the growing acceptance of Probabilistic Seismic Hazard Analysis (PSHA) as the optimal method for estimating seismic hazard. Comprehensive summaries of the available worldwide ground motion predictive equations can be found for early relations in Idriss (1978) and, for more recent relations, in Douglas (2001; 2002; 2003).

While the summary publications mentioned above detail a very large number of predictive equations, very few relate to equations that have been developed based upon empirical datasets from New Zealand earthquakes. Consequently, until relatively recently, hazard estimates for New Zealand locations have had to make use of either worldwide relations, or of relations based upon data from other tectonic regions. Of these adopted relationships, the models of Katayama (1982) and Joyner and Boore (1981) have been implemented most frequently. The use of these equations required the acceptance of the hypothesis that these relations adequately predicted the likely ground motion levels that one might expect from New Zealand earthquakes. As Zhao et al. (1997) point out, whether or not this was the case was a moot point because the only way to test this hypothesis would be to compare the adopted relationships to New Zealand strong motion data. In order for any significant results to be obtained one would have to have a reasonably large empirical dataset with which to test against. If this were the case then relationships specific to New Zealand could be derived anyway. An obvious exception to this argument applies to the case where only a limited magnitude or distance range is required. In this case, how well a model performs beyond the limits of the range is somewhat superfluous.

An observation such as that of Zhao et al. (1997) is easily made in retrospect. However, while researchers were aware of the limited completeness of the New Zealand strong motion catalogue, pioneering attempts to reveal the nature of strong ground motion associated with New Zealand earthquakes were made. The first of these relations was that of Matuschka (1980) for the attenuation of peak ground acceleration. This relationship was based upon 61 records from earthquakes with local magnitudes greater than or equal to $M_L 4.5$ and with hypocentral distances of less than 120 km. The functional form of the model was adopted from that of Esteva and Rosenblueth (1964) and Esteva (1970) and the coefficients were determined using a simple least squares regression analysis. No subsequent relations were developed between this relation and the early 1990's. Rather, throughout this period attention was given to

modifying the Katayama (1982) model for use in New Zealand. The modifications that were made included corrections for instrument response, distance scaling, and modifications to the magnitude of the error terms (see Matuschka and Davis 1991 and references therein). The analysis of residuals, or error terms related to strong motion predictive equations is extremely important when using the equations to determine design ground motion levels. Consequently, due attention was paid to the uncertainties associated with the predictive equations in use in New Zealand during this period (Berrill 1985; McVerry 1986).

In the early 1990's the New Zealand strong motion database was thought to have grown sufficiently to allow the derivation of a predictive relation for acceleration response spectral amplitudes to be made based upon a dataset of entirely New Zealand records (Matuschka and Davis 1991). A total of 160 horizontal components of ground motion acceleration from 30 earthquakes constituted the dataset for this analysis (both horizontal components of motion were used in the regression analysis). The functional form of this model was based upon the models of Campbell (1981), Fukushima and Tanaka (1990), and Abrahamson and Litehiser (1989) and included a modification to the distance term that accounted for the magnitude saturation of spectral amplitudes at small source to site distances. Empirical coefficients were determined for 16 periods ranging from 0.04 seconds to 4.0 seconds and for three different site classes. It should be noted that these limiting periods, which correspond to frequencies of 25 and 0.25 Hz respectively, are at the very extreme ends of the frequencies available in the current strong motion records. The sampling rate of the standard accelerographs in New Zealand of 50 Hz dictates a Nyquist frequency of 25 Hz; consequently, most strong motion records have a low pass filter that starts at 24.5 Hz. In addition, the high pass filter is usually applied above the 0.25 Hz level for which spectral amplitudes are given in the Matuschka and Davis (1991) model. The coefficients derived for these ordinates should therefore be regarded very carefully before their application. Rather than using dummy regression variables to distinguish between various site classes (i.e. Searle 1971), separate models for each class were derived. This method significantly reduced the number of records that could be considered in each dataset and as a result meaningful regression coefficients could not be obtained for two of the three classes that were modelled. In order to address this problem, the model derived for the largest dataset (equivalent to current site class C (Standards New Zealand 1992)) was modified to obtain coefficients for the other two site classes. Given that the soft soil sites typically show the greatest amount of variation in terms of ground motion response, this approach is far from optimal from a statistical point of view. Matuschka and Davis (1991) also found coefficients relating to the vertical component of ground motion from the records in their dataset, given that there were 160 horizontal records, there were consequently only 80 records upon which to base this regression. While there are some obvious shortcomings to this model, these were recognised by the authors and due caution was advised to those wishing to implement this model for hazard analyses.

Following the emergence of the Matuschka and Davis (1991) model, the attenuation characteristics of peak ground motions from two restricted groups of earthquakes were made by Dowrick and Sritharan (1993; 1993a). In the first of these papers (Dowrick and Sritharan 1993), the peak accelerations from a group of eight earthquakes occurring between 1987 and 1991 were fitted with an equation having the same form as the Joyner and Boore (1981) and Ambraseys and Bommer (1991) relationships for the western United

States and Europe respectively. The ground motions, and the equations obtained from them, were compared to ground motion equations derived for other regions in the world. It was found that the ground motions observed during these New Zealand earthquakes were significantly larger than those predicted by the relationships for the western U.S.A. and Europe. However, a reasonable fit was obtained through the use of the Fukushima and Tanaka (1990) relationship derived from a Japanese dataset. In the second paper (Dowrick and Sritharan 1993a), only peak ground accelerations from the 1968 Inangahua earthquake were considered. The same general procedure was applied and similar general conclusions were drawn, i.e. that the attenuation relations developed for the western U.S.A. under predicted the ground motions from this event.

At a similar time, the first steps were being taken to derive a robust new regression relation for peak ground acceleration for New Zealand earthquakes (McVerry et al. 1993; McVerry et al. 1995). These preliminary studies ultimately lead to the Zhao et al. (1997) predictive equation. This relation was derived from a much larger dataset that included 461 records from 51 New Zealand earthquakes as well as 66 records from 17 foreign earthquakes. These foreign records were included so as to make the dataset more complete for large earthquakes at small source to site distances. Five different models were considered in this study that corresponded to differing amounts of prior information available to the user, i.e. does the user know the fault mechanism of the event being modelled. No allowance for the saturation of ground motion with magnitude was included in this model; the inclusion of such a term was tested but was found to be statistically insignificant as well as being relatively unstable. Initially a parameter accounting for the anelastic attenuation throughout the travel path of the seismic waves was included in the regression model but this parameter was found to be statistically insignificant and was not included in the final relationships. The Zhao et al. (1997) model took into account different source depths of earthquakes as well as heightened rates of attenuation through a central volcanic zone in the North Island of New Zealand. The standard deviation of the relationship was assumed to be independent of magnitude, and ground motion level, despite the findings of Abrahamson (1988) and Youngs et al. (1995) that indicate that the standard error of ground motion relations for peak ground acceleration decrease with increasing magnitude. The coefficients for the model were obtained using simple least squares regression analysis. Overall, however, the Zhao et al. (1997) model is statistically robust and accounts for most of the effects currently included in modern strong ground motion relations.

Given that the aim of most ground motion predictive equations is to estimate strong levels of ground shaking the source to site distances of events constituting the empirical dataset are limited to be within some restricted range. Often this restriction precludes the possibility of accurately defining the contribution of anelastic attenuation associated with the passage of seismic waves through the earth. This was found to be the case in the predictive equation of Zhao et al. (1997) discussed above. An estimate of the likely magnitude of this effect was presented however, in a study of the attenuation of weak ground motions recorded by instruments in the New Zealand National Seismograph Network (NNSN) (Pancha and Taber 1997). This study used data extracted from the NNSN as well as from a temporary deployment of instruments about the East Cape of the North Island, the Marlborough region of the South Island, and the central volcanic zone of the North Island. These seismographs are sited upon rock and are far more

sensitive than their strong motion counterparts. Consequently, the recorded motions that have been included in the dataset are typically associated with source to site distances of greater than 100 km. This predictive equation was the first in New Zealand to make use of multiple stage regression analyses by employing the two stage regression procedure of Joyner and Boore (1981). Two functional forms for the regression model were considered, the basic model of Joyner and Boore (1981) as well as the more complicated form of Molas and Yamazaki (1995) which accounts for varying depths of events. The Pancha and Taber (1997) model is a very sound relation in its own right but should only be used with extreme caution for hazard analyses. The model is very useful for constraining the attenuation of ground motions at large distances, particularly with respect to anelastic attenuation. However, the use of the point source approximation as well as only a simple linear magnitude scaling means that the model should be inaccurate for predicting near field ground motions related to the most severe earthquake loading scenarios.

The most recent relationship developed purely for peak ground acceleration that has been published in New Zealand is the Cousins et al. (1999) relationship. This relationship makes the most of the advantages of both of the previous models by utilising the dataset of Zhao et al. (1997), including the foreign earthquake records, as well as supplementing the dataset with recordings from the NNSN. The inclusion of this seismograph data greatly increases the number of records that can be classified as being 'rock' sites. In addition, problems associated with biased ground motion equations at large distances due to non-uniform triggering of recording stations are removed as the seismograph data correspond to much larger distance ranges than the accelerograph data. Through the inclusion of the seismograph data, a coefficient for the anelastic attenuation was able to be determined; otherwise the functional form of the model is essentially the same as that of Zhao et al. (1997). The only other main differences are the partitioning of the general rock site class into two subclasses and the consequent inclusion of two parameters that modify the linear scaling of the peak ground acceleration with magnitude for the strong rock site class. Again, the residuals were assumed to be independent of magnitude. The method employed to determine the coefficients for the model was not specified. This model should be regarded as being the current best predictive equation for estimating peak ground accelerations associated with earthquakes in New Zealand.

The only remaining relationship to have been derived for use in New Zealand is that of McVerry et al. (2000). This relationship is derived for 5% damped acceleration response spectral ordinates and was used in the derivation of the latest seismic hazard maps for New Zealand (Stirling et al. 2002). However, while this relationship is actively used in New Zealand, the actual coefficients of this relationship have not been released in the public domain. This relationship is interesting in that it utilises foreign ground motion data as well as actual regression coefficients derived for a completely different dataset. Acceleration response spectra from two different classes of earthquakes were considered in the model; crustal and subduction earthquakes. Different functional forms for the regression models were adopted for each of the two classes. The models that were selected were too complicated for regression coefficients to be determined from the composite New Zealand dataset used in Zhao et al. (1997) and Cousins et al. (1999). The functional forms of the regression models were that of Abrahamson and Silva (1997) for crustal events, and Youngs et al. (1997) for subduction events. These models were selected from a suite of other candidate relations on the

basis of their fit to the New Zealand dataset. The approach of McVerry et al. (2000) was then to take the models of Abrahamson and Silva (1997) and Youngs et al. (1997) and retain some of their original coefficients while leaving others free to take on new values that corresponded to the composite New Zealand dataset. In both cases the scaling with magnitude, both in the general sense and in terms of the near source constraint, was held fixed at the values of the foreign relations. This immediately imposes a constraint on the source strength of New Zealand earthquakes and assumes them to be the same as events occurring throughout the world. The main degrees of freedom in the models came through the distance and site scaling terms. In keeping with the foreign models, the standard errors of the McVerry et al. (2000) relationship were made to be decreasing functions of magnitude. The regression method employed in the analysis is not specified, but given that the error terms are specified as a function of two components (inter and intra event terms) in addition to the involvement of Norman Abrahamson in the research, it is probable that a random effects approach (almost certainly Abrahamson and Youngs 1992) was employed. While the coefficients of this model are not generally available at present, this model is the only predictive equation for response spectral ordinates that has been based upon a large enough dataset to warrant its inclusion in modern hazard analyses in New Zealand.

As Sabetta and Pugliese (1996) point out, the estimation of strong ground motions can be made primarily from two different perspectives. One method is to employ seismological techniques that incorporate many parameters related to the source and travel paths of seismic waves; parameters that engineers are typically unfamiliar with, and that are rarely available for general application. The other is to use empirical or stochastic methods to estimate ground motions, this method being more familiar to engineers, but usually less accurate and often with tenuous scaling with physical characteristics of the earthquake process. Of the models that have been developed, and mentioned above, for general use in New Zealand, all of them adopt the empirical approach. There is significant scope within the New Zealand research community to couple these two approaches together more strongly. In doing so, some of the issues related to the limitations of the New Zealand strong motion dataset could be overcome through the implementation of models with a stronger theoretical, or seismological, basis. Some steps have been taken to this end, for example, in the study of Eberhart-Phillips and McVerry (2003) the anelastic attenuation parameters from the McVerry et al. (2000) were used to constrain those found for the slab case in consideration. Previously, it was mentioned that the magnitude scaling parameters of the latest relation for response spectral ordinates for New Zealand were held equal to those of foreign relations. Knowledge of the scaling of earthquake ground motions with respect to kinematic, or dynamic, properties of the source as determined from inversion studies could be employed to add constraint specific to New Zealand earthquakes. Many aspects of this potential collaboration are already in place, for example the studies of Haines et al. (1994), Benites et al. (2003), and François-Holden (2004) already make use of important seismological parameters that relate to properties of the seismic source and travel path. There are also foreign examples of relations that have employed attributes of both the engineering and seismological approach such as the hybrid method of Campbell (2003a). Currently in New Zealand however, parameters such as those mentioned above are only acknowledged in a very general sense when developing empirical relations to characterise strong ground motions. In the future, perhaps in association with the

imminent ruptures upon both the Alpine and Wellington faults in New Zealand, descriptive parameters such as slip velocities, and consequently high frequency spectral amplitudes (Beresnev 2001; 2002), or anelastic attenuation, scattering, and geometric spreading parameters consistent with empirical Green's functions, for example, may be incorporated more explicitly in the empirical models of ground motions in New Zealand.

It is the opinion of the author that the direction towards more collaboration between seismologists and earthquake engineers is one that is likely to be pursued in the future. To this end, the present section on the study of strong ground motions has been approached from a predominantly engineering seismology basis. While the end result of this section is the presentation of empirical predictive equations for various ground motion measures, the derivation, where possible, of the functional forms has been done from a seismological point of view. Effort has been made to make the parameters included in the empirical models as transparent as possible in terms of their underlying relationships to seismological properties. The overall structure and emphasis of this section is detailed in the remainder of this general introduction.

B.1.1. Outline of Section B

Section B contains five main chapters (as well as this introduction, some conclusions, and relevant appendices) each of which addresses a different aspect of the characterisation of strong ground motion in New Zealand. A brief description of each of these chapters is given below.

Chapter B2 describes the strong ground motion data set used in the development of the empirical models of ground motion in the chapters to follow. Details of the inclusion of foreign strong motion records to supplement the deficient scenarios in the New Zealand dataset are described. These details include a discussion on the correlation between the New Zealand site classes assigned to each of the foreign records. The processing of the strong ground motion records relevant to each of the subsequent analyses is described. The overall composition of the strong motion dataset is detailed in terms of the contributions from various source mechanisms and site conditions.

In Chapter B3, the general theoretical background to the derivation of the relations for ground motion measures to be modelled later in this section is presented. Much of the backgrounds of each of the three models that are developed are common to each other. By presenting the overall derivation of the relation for the Fourier Amplitude Spectra of ground motion in this section the regression models used in the subsequent chapters are more readily described. As previously mentioned, effort is made in this chapter to present the theoretical background from a strong motion seismology perspective so that the resulting empirical relations may be associated to their seismological origin where possible.

Chapter B4 describes the derivation of the first empirical relationship developed in this section; that of a model for the moment magnitude – corner frequency relationship for source spectra in New Zealand.

This relationship is developed through the implementation of a simple ray tracing procedure coupled with a reasonably comprehensive Monte Carlo simulation procedure. Each of these aspects of the model development is described in full before the actual regression is performed. The main focus of this chapter is to obtain a high quality dataset upon which a relatively simple regression can be performed. An elaborate method is proposed with which to estimate zero frequency displacement spectral amplitudes, and consequently corner frequencies for strong motion records from New Zealand earthquakes. The result of this section of work is employed subsequently in the development of the empirical relation for the Fourier Amplitude Spectrum of acceleration.

In Chapter B5, the first empirical model for the Fourier Amplitude Spectrum of acceleration for New Zealand earthquakes is presented. A relationship of this nature underlies most other measures of ground motion. Consequently, the functional forms of the models considered in the analysis are described in addition to a detailed account of the regression techniques applied to determine the parameters of the final model. The description of the regression procedure has application in both the preceding and following chapters so due attention is given here. The majority of the theoretical background required for this section of work is previously covered in Chapter B3 so the focus of this chapter is the description of the methods used to determine the parameters in the relationship and the consequent analysis of the resulting residuals and the performance of the model.

Starting with the theoretical model for the Fourier Amplitude Spectrum (FAS) of acceleration, Chapter B6 details the derivation of an expression for Arias Intensity primarily by employing Parseval's theorem. Once an analytical model of the Arias Intensity is developed, the functional form of a regression model for Arias Intensity is derived. Upon the presentation of the functional form of the regression model, an associated regression analysis is performed in order to obtain a model for the Arias Intensity for general use in New Zealand. This model, like the model for the FAS of acceleration and the corner frequency presented in the previous chapters, signifies the first relation of its type for New Zealand.

The final chapter in this section summarises the findings of the previous chapters, discusses the implications and applications of the derived relationships and draws conclusions related to the characterisation of strong ground motion relations in New Zealand. Following these conclusions, some suggestions for further areas of research are suggested.

B.2. Strong Ground Motion Dataset and its Preparation

B.2.1. Introduction

In the general introduction to this section of work presented in the previous chapter it was stated that the primary objective of this section is to develop predictive equations for various characteristics of strong ground motion for use in a New Zealand context. While every effort will be made to ensure that the models that are developed agree with generally accepted seismological theory, this theory counts for naught if it in turn does not agree with observations in reality. Thus, for the purpose of developing predictive models for ground motion indices, theory will be applied to derive functional forms of the models before the parameters defining these models are obtained through a fit to an empirical dataset. As this dataset of strong motion recordings ultimately dictates the nature of the derived predictive equations it is important to detail how this dataset is formed as well as how the records in this dataset are prepared so that they lend themselves most optimally to application in the regression analyses.

This chapter begins by detailing the composition of the strong motion dataset in terms of the specific events that make up the total dataset. Relevant magnitudes and fault mechanisms for each event, as well as source to site distances and site classes for each corresponding record are presented. Particular attention is given to the assignment of site classes for records from foreign earthquakes that are introduced into the New Zealand dataset. Following this, the method employed to calculate the closest distance to the rupture surface is outlined as well as details pertaining to the allocation of fault mechanism classifications to events for which this is not previously known. Finally, the manipulation and processing of the strong motion records from signals in the time domain to spectra in the frequency domain is described. This procedure involves the rotation of the strong ground motion records from arbitrary component directions into radial and transverse components. The filtering method used to smooth the strong motion records is also described. The relevant information relating to the individual records included in the strong motion dataset are provided in detail in the appendices.

B.2.2. Composition of the Strong Motion Dataset

In New Zealand, the strong ground motion database is freely available through the GeoNet project (http://www.geonet.org.nz/). Through this source, Volume I uncorrected three component acceleration time histories, Volume II corrected three component acceleration, velocity, and displacement time histories, and Volume III Fourier and response spectra data files based on the Caltech Bluebook system (for example Hudson et al. 1969) are available. Accompanying these data files are reference files detailing the geotechnical characteristics of all the sites of strong motion instruments in New Zealand. This site information is also available in hard copy form in Cousins et al. (1996). Each data file also contains relevant event information such as the epicentral position, the event magnitude, hypocentral depth, time and date of occurrence as well as information specific to the recording and processing of the strong motion record, for example the high and low pass filter limits applicable to the particular record. The instruments that make up the New Zealand strong motion network typically sample at 100 Hz and the time series presented in the uncorrected data files are discrete at 0.01 second intervals, while the corrected data files are discrete at 0.02 second time increments. Associated with this corrected time increment is a Nyquist frequency of 25 Hz (see, for example, Kramer 1996). The spatial distribution of the strong motion recording sites is depicted in Figure B.2.1.

As the predictive equations that are to be derived are done so for use in a New Zealand environment it is important that as many records come from New Zealand earthquakes as is possible. Unfortunately however (from a ground motion analysts point of view), the New Zealand strong motion database is deficient in areas corresponding to critical earthquake scenarios. The primary region for which very few records presently exist corresponds to the most severe loadings scenario; that being large magnitude events with small source to site distance. Given the importance of these earthquake scenarios in terms of their contribution to hazard estimates it is important that empirical data is employed to constraint the theoretical models over this region of magnitude-distance space. To this end it was decided to supplement the New Zealand strong motion database with a selection of records from foreign earthquakes. The inclusion of these records greatly improves the reliability of the predictive equations in the near field of large magnitude events. However, it remains to be seen whether or not New Zealand earthquakes generate ground motions in the near field that are comparable to those in foreign earthquakes. The most likely differentiator between ground motions occurring in different regions of the world comes from differences in regional geology that effect the attenuation of seismic waves with distance. Therefore, it is probably fair to assume that near field records, which do not experience considerable propagation, should be similar from region to region. Consequently, the strong motion dataset used in the development of the predictive relations for the Fourier Amplitude Spectrum and Arias Intensity comprised records from both New Zealand and foreign earthquakes. The development of the moment magnitude – corner frequency relation was based purely on a subset of strong motion records from New Zealand earthquakes.

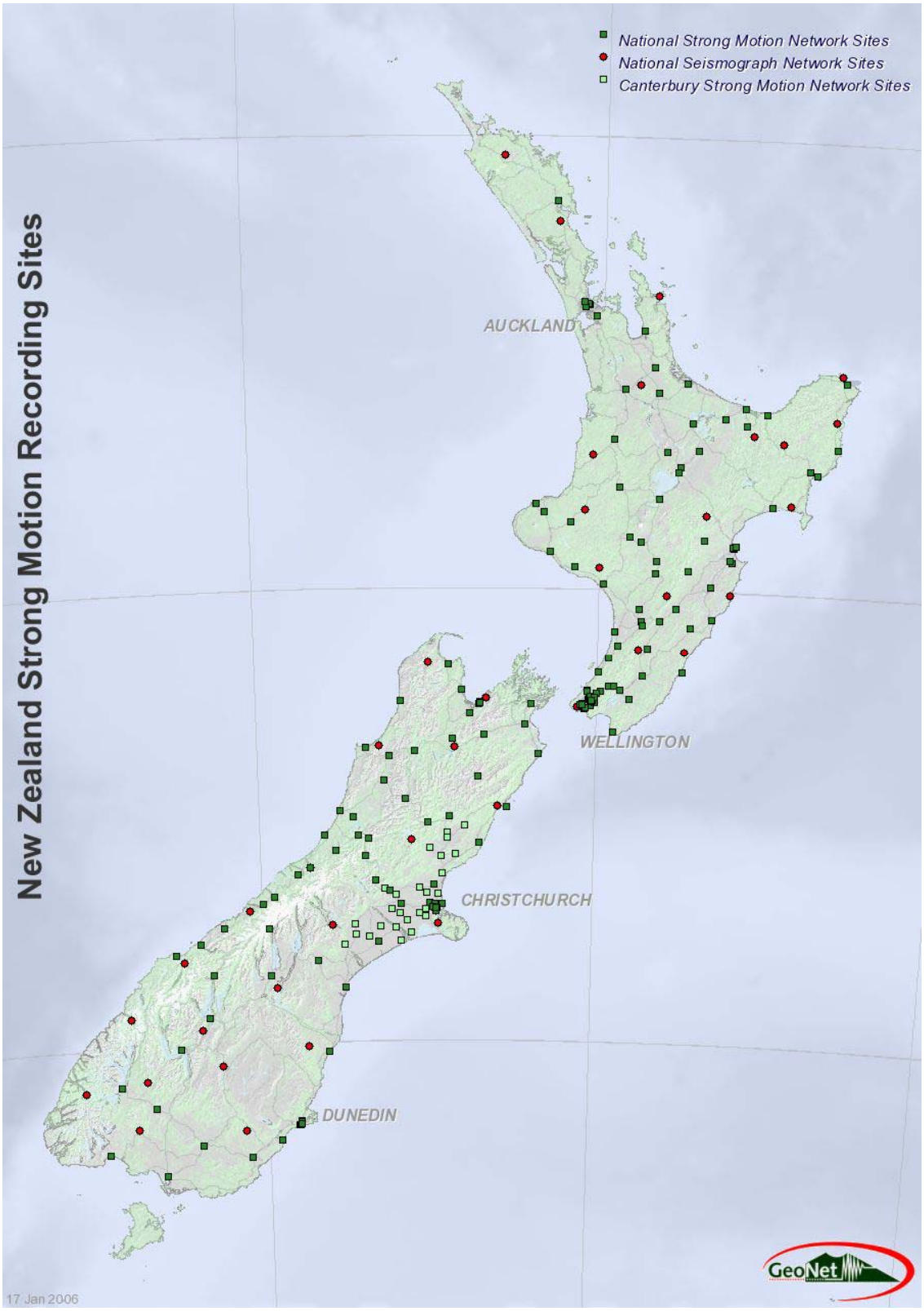

Figure B.2.1: Spatial distribution of the current strong motion recording instruments in New Zealand (reproduced from http://www.geonet.org.nz/strongmotion.html)

Models were derived for two general datasets, one that included, and one that excluded records from the 1999 Chi-Chi earthquake. Comments regarding the need for such a distinction are made later in this chapter. In total, 529 strong motion records from 97 events were included in the dataset that included the Chi-Chi event. The dataset with the Chi-Chi event removed contained a total of 496 records from 96 events. Of the records in the complete dataset, 422 records from 79 earthquakes were from New Zealand while 107 records from 18 earthquakes were foreign. All of these records correspond to earthquake magnitudes greater than or equal to $M_W 5.0$ and with rupture distances less than or equal to 300 km. This restricted magnitude–distance space should encompass all earthquake scenarios capable of generating strong ground motions. The New Zealand events that were used, and their corresponding number of records, are listed in Table B.2.1. The similar table for the foreign events is also presented in Table B.2.2. Tables containing additional information for each record used in the regression analysis, such as rupture distance and site class are presented for both the New Zealand and foreign events in Appendix B1.

As recently mentioned, the reason for including foreign records into the dataset was to supplement the New Zealand catalogue in areas where it is currently deficient. This supplementation should be regarded as a temporary measure as these foreign records will be probably be phased out as relevant New Zealand records become available to replace them. Until that time however, the foreign records provide valuable insight as to the nature of the ground motions that we might expect from large magnitude events occurring close to sites of interest. Time, of course, may prove strong ground motions in the near field of New Zealand earthquakes to be indistinguishable from those recorded in other parts of the world. In this case no revision of the dataset need necessarily take place.

The foreign records were retrieved from the Pacific Earthquake Engineering Research (PEER) centre earthquake catalogue (http://peer.berkeley.edu/smcat/). The table presented in Appendix B1 with details of the foreign records used also contains a PEER reference number that corresponds to the indexing used at the aforementioned website. The bulk of the events that have been used in this analysis have previously been adopted for use in developing predictive equations for peak ground acceleration for New Zealand (Zhao et al. 1997; Cousins et al. 1999); the exceptions being the most recent Turkish events, the 1999 Duzce and Izmit-Kocaeli earthquakes, and the already mentioned 1999 Chi-Chi, Taiwan, earthquake. These events provide valuable additional strong motion records in the near field of large earthquakes and extend the magnitude range up to $M_W 7.6$ for the case where the Chi-Chi records are included in the dataset. As well as maintaining consistency with other recent predictive relations developed for New Zealand, justification for the inclusion of foreign events into the present dataset is provided by Douglas (2004). In this study, ground motions from various regions of the world were compared and it was found that the hypothesis that ground motions from the Californian and New Zealand earthquakes, and European and New Zealand earthquakes, are similar could not be rejected. However, it should be noted that the method that was employed in order to make such comparisons required the strong motion records to be segregated into magnitude-distance bins that resulted in significant reduction of the sample size, and consequently, the statistical significance of the findings. For the present though, it seems reasonable to supplement the New Zealand dataset with records from events occurring in similarly active tectonic environments.

Table B.2.1: New Zealand Earthquakes included in the Strong Motion dataset for the regression analyses

Ev. #	Event Name	Year	Month	Day	UT	M_W	Focal Mech.	# Recs.
1	Palliser Bay	1968	11	1	0132	5.40	R	3
2	Reefton	1971	8	13	1442	5.80	R	3
3	Unnamed	1973	2	21	1442	5.40	N	1
4	Opunaki	1974	11	5	1038	5.44	N	1
5	Milford Sound	1974	9	20	1948	5.50	R	6
6	Dannevirke	1975	6	10	1011	5.62	S	4
7	Cape Campbell	1977	1	18	0541	6.02	N	31
8	Unnamed	1982	2	5	1751	5.36	S	5
9	Oaonui 2	1983	4	16	2129	5.30	N	1
10	Godley River	1984	6	24	1329	6.14	S	2
11	Unnamed	1984	3	5	0207	5.27	N	1
12	Tiniroto	1985	7	19	1433	5.92	N	3
13	Edgecumbe	1987	3	2	0135	6.53	N	8
14	Edgecumbe Aftershock	1987	3	2	0150	5.60	N	4
15	Edgecumbe Aftershock	1987	3	2	0207	5.00	N	1
16	Doubtful Sound	1989	5	31	0554	6.33	S	2
17	Weber 1	1990	2	19	0534	6.23	N	21
18	Weber 2	1990	5	13	0423	6.37	R	22
19	Lake Tennyson	1990	2	10	0327	5.93	S	3
20	Hawk's Crag 1	1991	1	28	1258	5.79	R	7
21	Hawk's Crag 2	1991	1	28	1800	5.93	R	10
22	Hawk's Crag 3	1991	2	15	1048	5.42	R	5
23	Unnamed	1991	2	24	0950	5.10	R	1
24	Cape Palliser 1	1990	10	4	2348	5.57	R	12
25	Bay of Plenty	1992	6	21	1743	6.25	N	6
26	Ormond	1993	8	10	0946	6.19	S	15
27	Tikokino	1993	4	11	0659	5.63	R	10
28	Secretary Island	1993	8	10	0051	6.81	R	5
29	60km North of White Island	1994	12	15	1120	6.31	S	7
30	Offshore East Cape	1995	2	5	2251	7.09	N	12
31	East Cape Aftershock	1995	2	10	0144	6.20	?	6
32	10km north of Gisborne	1995	2	13	1218	5.00	I	5
33	Cass	1995	11	24	0618	6.24	R	11
34	Arthur's Pass 1995	1995	5	29	1006	6.00	R	1
35	Near Hanmer Springs	1996	8	29	0447	5.70	S	1
36	5km north of Hanmer	1996	9	19	1216	5.80	S	1
37	39km west of Oamaru	1998	2	8	1826	5.30	R	2
38	Weber 3	1990	8	15	1554	5.17	N	3
39	Cape Palliser 2	1990	10	6	0241	5.46	R	9
40	Weber 4	1992	3	2	0905	5.54	N	11
41	Near Tokomaru	1992	5	16	1757	5.76	R	2
42	Unnamed	1992	5	17	0106	5.20	R	2
43	Wilberforce River	1992	3	30	0702	5.50	R	3
44	Unnamed	1992	4	1	2257	5.20	R	2
45	Ormond Aftershock	1993	8	10	0946	6.19	S	2
46	Arthur's Pass	1994	6	18	0325	6.81	R	16
47	Inangahua Aftershock	1968	5	24	2057	5.70	R	1
48	Inangahua Aftershock	1968	5	25	2349	5.30	S	1
49	Inangahua Aftershock	1968	6	5	1243	5.20	I	1
50	Te Horo	1994	12	15	1513	5.20	N	2
51	15km west of Porangahau	1996	10	5	2121	5.00	I	1
52	20km east of Hawera	1996	9	27	1354	5.00	N	1
53	Unnamed	1997	6	20	1536	5.20	S	4
54	Unnamed	1979	3	24	2106	5.08	R	1
55	Unnamed	1997	6	19	0855	5.10	S	4
56	Unnamed	1997	6	20	1536	5.40	S	5

Table B.2.1: continued…

Ev. #	Event Name	Year	Month	Day	UT	M_W	Focal Mech.	# Recs.
57	Turangi Swarm	1984	2	21	0823	5.30	N	1
58	5km north of Gisborne City	1989	11	30	0858	5.00	I	1
59	Seddon	1966	4	23	0649	5.75	R	1
60	Napier	1980	10	5	1532	5.66	N	1
61	Gisborne	1982	3	3	2234	5.10	N	4
62	Hawke's Bay	1982	9	2	1558	5.46	N	2
63	Unnamed	1982	6	4	0157	5.10	I	1
64	10km NW Greytown	2000	3	29	1430	5.20	R	11
65	90km north-west of Te Anau	2000	11	1	1035	6.20	S	2
66	Unnamed	2000	11	1	1037	5.00	S	1
67	60km north-west of Te Anau	2000	11	12	1149	5.50	S	1
68	Unnamed	2000	12	31	2156	5.40	I	1
69	Unnamed	2001	5	18	1056	5.50	R	2
70	20km west of Seddon	2001	5	22	0158	5.00	S	4
71	20km south of Porangahau	2001	9	24	0449	5.60	R	6
72	100km north-east of Te Araroa	2001	10	21	0029	6.30	?	3
73	50km west of Haast	2001	12	7	1927	6.20	S	7
74	20km SE of Karamea	2002	5	4	1259	5.60	R	11
75	Unnamed	2002	12	24	0742	5.00	S	5
76	70km north-west of Te Anau	2003	8	21	1212	7.10	S	24
77	70km north-west of Te Anau	2003	8	21	1412	6.20	S	13
78	20km east of Woodville	2003	1	25	2130	5.50	S	9
79	Unnamed	2004	1	2	0349	5.10	S	1

Table B.2.2: Foreign Earthquakes included in the Strong Motion dataset for the regression analysis

Ev. #	Event Name	Year	Month	Day	UT	M_W	Focal Mech.	# Recs.
1	Imperial Valley	1940	5	19	0436	7.0	S	1
2	Parkfield	1966	6	28	0436	6.1	S	3
3	San Fernando	1971	2	28	1400	6.6	R	1
4	Hollister	1974	11	28	2301	5.2	S	3
5	Oroville	1975	8	1	2020	6.0	N	1
6	Gazli	1976	5	17	0258	6.8	R	1
7	Santa Barbara	1978	8	13	1322	6.0	R	1
8	Tabas	1978	9	16	1535	7.4	R	1
9	Coyote Lake	1979	8	6	1705	5.7	S	6
10	Imperial Valley	1979	10	15	2316	6.5	S	20
11	Loma Prieta	1989	10	18	0004	6.9	S	9
12	Erzincan	1992	3	13	1718	6.9	S	1
13	Landers	1992	6	28	1157	7.3	S	3
14	Northridge	1994	1	17	1230	6.7	R	8
15	Kobe	1995	1	16	2046	6.9	S	6
16	Duzce	1999	11	12	1657	7.1	S	6
17	Izmit-Kocaeli	1999	8	17	0001	7.4	S	3
18	Chi-Chi	1999	9	20	1747	7.6	R	33

B.2.2.1. Characterising the foreign site classes

A problem that arises due to the inclusion of the foreign events is that of how to map differing site classifications into the current New Zealand site classification scheme. There is a usually considerable amount of allowable variation, in terms of dynamic response within any individual site class. Additionally, the limiting boundaries between particular classes are often chosen on a relatively subjective basis. It should therefore be expected that there will be some degree of overlap between the earthquake responses of adjacent site classes. These considerations must be made when dealing with a contiguous dataset from a single country let alone when considering composite datasets from different regions of the world. In the common case where countries employ differing numbers of site categories and/or differing ranges for classes that have similar descriptions (such as generic rock, or soil etc) a considerable amount of judgement must be made when attempting to combine data from various regions into a single consistent dataset.

Site classes in New Zealand are assigned according to three reasonably broad classes in the NZS 4203:1992 loadings code; classes A, B, and C (Standards New Zealand 1992). Of these three, only classes A and C are explicitly defined; site class B simply accommodates those sites that cannot be classed as belonging to either site class A or C. The site classification scheme is taken from the Guidelines for the Field Description of Soils and Rocks in Engineering Use (New Zealand Geomechanics Society 1988). The classification scheme used in NZS 4203:1992 ("The Loadings Code") is repeated below.

Site subsoil category A: Rock or very stiff soil sites

Sites where the low amplitude natural period is less than 0.25 s, or sites with bedrock, including weathered rock, with unconfined compressive strength greater than or equal to 500 kPa, or with bedrock overlain by:

(i) Less than 20 m of very stiff cohesive material with undrained shear strength exceeding 100 kPa; or

(ii) Less than 20 m of very dense sand, with N1 >30, where N1 is the SPT (N) value corrected to an effective overburden pressure of 100 kPa; or

(iii) Less than 25 m of dense sandy gravel with N1 >30.

Site subsoil category B: Intermediate soil sites

Sites not described as category A or C may be taken as intermediate soil sites.

Site subsoil category C: Flexible or deep soil sites

Sites where the low amplitude natural period exceeds 0.6 s, or sites with depths of soils exceeding the values in Table B.2.3:

Table B.2.3: Typical deposit information to aid the categorisation of Site Class C

Cohesive Soil	Representative Undrained Shear Strengths (kPa)	Depth of Soil (m)
Soft	12.5 - 25	20
Firm	25 - 50	25
Stiff	50 - 100	40
Very Stiff	100 - 200	60

Cohesionless Soil	Representative SPT (N) Values	Depth of Soil (m)
Loose	4 - 10	40
Medium Dense	10 - 30	45
Dense	30 - 50	55
Very Dense	> 50	60
Gravels	> 30	100

As Cousins et al. (1996) point out, although the site classes are described with adjectives such as rock or stiff soil, for site class A, these descriptors do not preclude the inclusion of soft soil sites that happen to have a natural period of less than 0.25 seconds (which may happen). Similarly, soil deposits with greatly varying shear wave velocities will meet the conditions of having a period of greater than 0.6 seconds depending upon how thick the soil deposit is. Given that knowledge of the soil or rock at the site itself, without information regarding depths of deposits or layering of these deposits, does not directly infer the site class means that the confidence in the classification depends strongly upon the quality of the geotechnical information that is available for the site in question. Some of the sites where strong motion instruments are located have been thoroughly investigated and their likely site response is known very well while others have been classified on the basis of inference from geological maps alone. It is well known that site response can be highly variable (see for example Boore 2004) and would ordinarily be taken as being a major source of aleatory variability. However, given the disparate degree of knowledge regarding the site classifications in the New Zealand dataset, a considerable amount of the overall uncertainty must be assigned to the epistemic uncertainty associated with the inability to accurately classify the ground conditions at sites of recording instruments. These issues associated with site classification are well known and as a result additional qualifiers are appended to the standard A, B, and C designations where they are applicable[†]. These additional qualifiers include descriptors such as 'soft', 'deep', or 'thin soil layer', or 'possible topographic effects' etc and allow the broad classification to be refined to some degree. Regression groups based upon such sub-classifications were used in the Zhao et al. (1997), Cousins et al. (1999), and McVerry et al. (2000) attenuation relationships. Unfortunately though, while this additional information helps, there still remains a great variation between the quality and quantity of geotechnical information available for each site. This means that these additional qualifiers cannot be applied to all sites on a consistent basis and that consequently, the catalogue cannot necessarily be grouped according to these

[†] This additional qualifier is appended to the information provided through the GeoNet project only (see also Cousins et al. 1996) and is not part of the current NZS 4203:1992 loadings code.

additional qualifiers without introducing an unknown degree of bias into the regression analysis. Very little can be done to remedy this situation in the near future; consequently this inherent uncertainty must be accepted and kept in mind throughout the analysis. However, one direction that might be pursued in the future would be to include regressions upon specific site characteristics such as SPT blow counts, or shear wave velocities as has been adopted in the Boore, Joyner, and Fumal (1997) predictive equation for peak and spectral accelerations. A good summary of the assignment of site categories to strong motion recording sites in New Zealand, as well as a discussion of the various limitations and strengths of the method, can be found in Cousins et al. (1996). This report should be consulted if additional information regarding New Zealand site classes is sought.

The loose constraint on the site class that is provided from the existing classification scheme means that when strong motion records are grouped according to these sites one should expect quite a wide variety of response within each of the site classes. While the previous statement is generally a negative one, a positive associated with the loose definition of site classes in New Zealand means that any potential misclassification of foreign sites when converting between classification schemes should not untowardly affect the consequent regression results. This is not necessarily a good thing; however, it does mean that time intensive investigations into the specifics of the foreign recording sites need not be undertaken. In keeping with the principle of consistent crudeness (Elms 1985) it is sufficient to make general correlations between foreign and New Zealand site classification schemes without significantly compromising the quality of the combined dataset.

The foreign records in the PEER dataset are classified according to various schemes depending upon the origin of the record. For the majority of records included in this study, sites are classified according to both the Geomatrix and USGS (United States Geological Survey) classification schemes. The main exception to this rule applies to the Chi-Chi records where the CWB (Central Weather Bureau) scheme is used.

The Geomatrix classification scheme was used, and detailed, in the development of the Abrahamson and Silva (1997) predictive equation; the classification scheme is repeated below in which $V_{S_{30}}$ is the shear wave velocity average over the upper 30m of the site.

- A – Rock ($V_{S_{30}} > 600$ m/s) or very thin soil (< 5 m) over rock
- B – Shallow Soil, soil 5 – 20 m thick over rock
- C – Deep Soil in Narrow Canyon, Soil > 20 m thick, Canyon < 2 km wide
- D – Deep Soil in Broad Canyon, Soil > 20 m thick, Canyon > 2 km wide
- E – Soft Soil ($V_{S_{30}} < 150$ m/s)

Considering the Geomatrix scheme given above, it would seem that the equivalent New Zealand classification would group Geomatrix class A and much of class B together as New Zealand class A. New Zealand class B would account for some of Geomatrix class B and some of class C while New Zealand

class C would probably accommodate the remainder of Geomatrix class C as well as classes D and E. As can be seen from the descriptions of each class given above, this proposed calibration is reasonably subjective and other interpretations are very possible.

The USGS scheme is based upon the average shear wave velocity over the upper 30m of deposit, $V_{S_{30}}$, and is partitioned into four typical categories as given below.

- A - $V_{S_{30}} > 750$ m/s
- B - 360 m/s $< V_{S_{30}} \leq 750$ m/s
- C - 180 m/s $< V_{S_{30}} \leq 360$ m/s
- D - $V_{S_{30}} \leq 180$ m/s

These USGS site classes are very similar to both the NEHRP (Building Seismic Safety Council (BSSC) 1994) and Borcherdt (1994) schemes, with the primary exception being that these two latter schemes subdivide the USGS class A into two categories that essentially represent rock and very hard rock (to account for the Eastern United States where rock sites are very hard).

Cousins et al. (1996) comment on the inadequacy of simply using a single descriptor such as site period or shear wave velocity when classifying a site. The layering of the soil deposit coupled with the actual materials constituting the layers governs the overall response of a site to seismic motions; such factors cannot be described by a scalar identifier. This complicates the correlations between the New Zealand descriptions and the USGS descriptions. Although the USGS descriptions of shear wave velocities correspond to a set depth of 30 metres, the New Zealand descriptions only give rough guidelines as to the depths of deposits corresponding to various site periods. Consequently no clear correlation between the two systems can be inferred.

For the present study the Geomatrix and USGS schemes are used to assign New Zealand site classes to the foreign events. Because there is some overlap between the Geomatrix and USGS schemes they can be used to help differentiate between broad classes. For example, USGS class B covers a wide range of shear wave velocities that may cover both rock and soil categories. If the USGS classification is B but the Geomatrix scheme is A (or B in some cases) then it can be assumed that the site is to the rock end of the spectrum of site classes covered by USGS category B. In this case the record would be assigned an equivalent New Zealand category A site classification. This method of inference is applied to all the foreign records in order to obtain relevant site classes.

It has been mentioned previously that an exception to this rule exists for records taken from the 1999 Chi-Chi earthquake. For these records the site classification is assigned according to the CWB scheme in which category 1 corresponds to 'Hard Sites', category 2 corresponds to 'Medium Sites', and category 3 corresponds to 'Soft Soil Sites'. A correlation between these loosely defined categories and the USGS

scheme is available (Lee et al. 2001) and has been applied to aid in the classification of these records according to the New Zealand classification scheme. The final allocation of New Zealand site classifications to the foreign records can be found in Appendix B1 on a record by record basis.

The complete data set is shown visually in Figure B.2.2. In this figure, the distribution of records with respect to magnitude and distance are plotted with each point also being discriminated in terms of its site class or fault mechanism. The information in Figure B.2.2 is also presented in tabular form in Table B.2.4 and Table B.2.5 below.

Table B.2.4: Subdivision of Dataset by Site Class and Focal Mechanism for the Total Dataset, the New Zealand Dataset, and the Foreign Dataset

Site Class	Total Number of Records	Number of New Zealand Records	Number of Foreign Records
A	152	124	28
B	93	81	12
C	284	217	67
Σ_i	529	422	107

Fault Mechanism	Total Number of Records	Number of New Zealand Records	Number of Foreign Records
Normal	232	231	1
Strike-Slip	117	56	61
Reverse/Thrust	180	135	45
Σ_i	529	422	107

Table B.2.5: Number of records in each site class / fault mechanism bin for (a) the total dataset, (b) the New Zealand dataset, and (c) the foreign dataset

(a)

Total Dataset		Fault Mechanism			
		Normal	Strike-Slip	Reverse/Thrust	All
Site Class	A	81	32	39	152
	B	44	11	38	93
	C	107	74	103	284
	All	232	117	180	529

(b)

NZ Dataset		Fault Mechanism			
		Normal	Strike-Slip	Reverse/Thrust	All
Site Class	A	80	15	29	124
	B	44	5	32	81
	C	107	36	74	217
	All	231	56	135	422

(c)

Foreign Dataset		Fault Mechanism			
		Normal	Strike-Slip	Reverse/Thrust	All
Site Class	A	1	17	10	28
	B	0	6	6	12
	C	0	38	29	67
	All	1	61	45	107

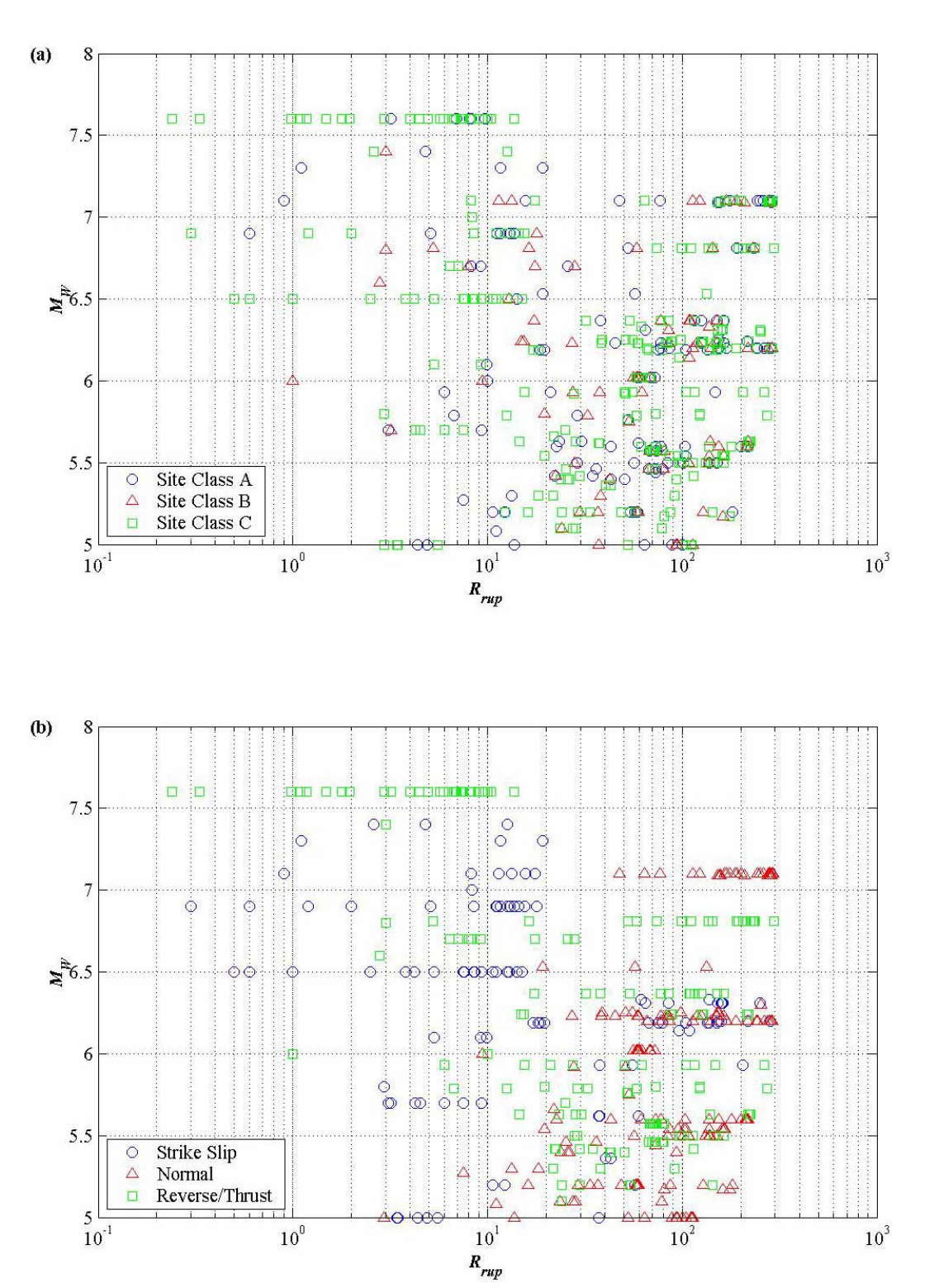

Figure B.2.2: Magnitude-Distance distribution of the Strong Motion Dataset used in the regression analyses. Panel (a) shows the distribution of records with respect to site class. Panel (b) shows the distribution of records with respect to Fault Mechanism

Considering the number of records that can be contributed by a single event from Table B.2.1 and Table B.2.2 above, one can appreciate that single events may constitute a significant portion of the records in any particular fault mechanism category. This may also be the case for the site classes for the foreign events as all records are taken from the near field and it is likely that there is some correlation between geologic conditions in this restricted spatial region. For the general case of the New Zealand records however, it is unlikely that an individual event would have significantly correlated site classes as records in general are measured over much larger spatial regions. Possible exceptions could come from regions in which many strong motion instruments are located, and when these instruments records moderate sized events, such earthquakes of approximately $M_W \sim 5$ around Wellington. The other possible exception could relate to the triggering of strong motion instruments at large distances. It is commonly accepted that strong motion datasets are biased towards larger than average ground motions at large distances due to the limited triggering level of strong motion instruments. However, this issue is commonly addressed when selecting strong motion datasets for regression analysis. For instance, in this study, only records having rupture distances less than a particular limit are considered for inclusion in the dataset. What is not typically taken into consideration is the variation in response of observations made upon differing site conditions. It is generally accepted that soft sites should amplify ground motions more than firm sites, all other things being equal. Therefore, instruments located on soft sites are more likely to be triggered than those on firm sites. The bias associated with such an issue is not considered significant enough to warrant any further attention. However, it should be continually kept in mind how such effects are likely to influence the final results.

The dominance of particular events in making contributions, in terms of the number of records, to a given fault mechanism group is an effect that should be taken into account, where possible, in the regression analysis. Given that we wish to determine predictive equations for use in future events, it is important that the regression is based upon data that reflects the trends observed from the global (in the New Zealand sense) strong motion dataset. It is for this reason that the regression analyses that are conducted make use mixed effects models (see for example Lindstrom and Bates 1988; 1990). These models are able to take into account effects that are associated with particular events that contribute multiple records to the dataset. In a sense they may be regarded as being somewhat similar to weighted regression analyses. These models and their application will receive detailed discussion in the chapters to follow.

Here though it is appropriate to include a comment regarding the inclusion of records from the Chi-Chi earthquake. The $M_W 7.6$ 1999 Chi-Chi, Taiwan, earthquake was recorded by a very large number of strong motion instruments very close to the rupture surface of the event. Consequently, this event may potentially increase the number of near source ground motion records by a significant fraction. However, it is thought that the ground motions from this event are lower than those that might be expected from future earthquakes of similar magnitude. Because this event contributes such a large number of near field records, the inclusion of these records would have a significant impact upon the nature of the near source scaling of ground motion measures. However, if the impact of including this event in a regression analysis is to cause the resulting equations to underestimate ground motions in this important near field region then the inclusion may be ill-advised. For this reason Campbell and Bozorgnia (2003b; 2003a; 2004) refrained from including records from the Chi-Chi event until the reasons for the apparently low ground motions

were better understood. Speculated reasons for the lower than expected ground motions from the Chi-Chi event include large amounts of surface rupturing , large amounts of slip on the fault plane and long rise times over the fault (see Campbell and Bozorgnia 2003b and references therein). Currently, these effects are not taken into account in empirical regression equations. If the reasons mentioned above do indeed explain why the ground motions are lower than expected, then this strongly suggests that factors to account for such influences should be included in empirical ground motion regression models in the future. This adds weight to the comments made in the previous chapter regarding the possibility of including more seismologically based dependencies into future predictive relations.

While there has been precedent to exclude the Chi-Chi records from strong ground motion datasets, there has also been precedent to include them. The Travasarou et al. (2003) predictive equation for Arias Intensity includes the records from the Chi-Chi event. It is probably noteworthy that the coefficients of this predictive equation are obtained using a mixed effects model. As briefly mentioned earlier, mixed effects models are able to take into account systematic differences between events. These models are employed in the present work and as such there may be ample justification for including the Chi-Chi events as the effect of the systematically lower ground motions will be accounted for yet the functional form of the scaling of ground motions with distance can still be used to constrain the form of the predictive models in the near field. In either case, regressions are performed upon datasets that both include and exclude the Chi-Chi records. Later the effect that these records have can be considered further.

B.2.3. Determination of the Distance to the Rupture Surface

Each strong motion record in the New Zealand dataset contains details of the location of the recording site and the epicentre of the recorded event, both in terms of longitude and latitude. An epicentral distance is also provided in the data file based upon these positions. The data files also contain the hypocentral depth and therefore the hypocentral distance can readily be determined. In modern regression analyses however it has become customary to use measures of distance that account in some way for the finite effects of fault rupture. Point source measures of distance can be suitable for small earthquakes where the spatial extent of the rupture is small in relation to the source to site distance. However, the spatial extent of the rupture increases in a exponential manner with magnitude (i.e. Wells and Coppersmith 1994) and the measure of hypocentral distance looses its appropriateness as the magnitude becomes large (see Bolt and Abrahamson 2003; Campbell 2003b for a brief summary of these, and other available, measures).

The distance measure that is adopted for the regression analyses in this study is R_{rup}, the closest distance from the site to the rupture surface first proposed by Schnabel and Seed (1973). In order to apply this distance measure, details of the fault mechanism plus some scaling equation relating the size of the rupture associated with a given magnitude must be available. Recently a new scaling relation based upon New Zealand data that can be employed for this purpose was presented by Dowrick and Rhoades (2004). This

publication provides predictive equations for the rupture length, width, and area associated with an earthquake of a given magnitude. The details regarding the fault mechanism are somewhat harder to come by. For large magnitude events focal mechanism solutions are routinely reported in the Harvard Centroid Moment Tensor catalogue (http://www.seismology.harvard.edu/CMTsearch.html) and in the National Earthquake Information Center [sic] (NEIC) through the USGS (http://neic.usgs.gov/neis/sopar/). In addition to these systematically processed mechanisms, independent researchers will reassess the focal mechanisms of significant events and these solutions are generally published in common seismology literature. However, while focal mechanisms for the largest events (that contribute the bulk of the records in the dataset) are available, there are many events for which no known solution is available. Fortunately, the events that do not have specific solutions generally correspond to the smaller events in the catalogue for which the effect of finite fault rupture does create large differences between the rupture and hypocentral distance. However, fault mechanisms for these events must still be obtained if the associated records are to be included in the strong motion dataset used for the regression analyses.

In order to determine the rupture distances for every event in the catalogue some assumptions have to be made. For the events that did not have focal mechanism solutions (from which the approximate position of the rupture surface could be inferred) a rupture surface was estimated through consideration of the fault most likely to be associated with the event. The New Zealand fault dataset used in the development of the PSHA maps for New Zealand (Stirling et al. 2002) was used to estimate likely strike and dip angles of the faults generating each event. There is a considerable degree of approximation associated with this procedure as it is well known that not all active faults are represented in the New Zealand active fault dataset used in the Stirling et al. (2002) analysis. In addition, the locations, and the assumed orientations, of the faults in this catalogue should be considered as being approximate. However, for the purpose of calculating the rupture distance for each record these approximations should be reasonable as there is a strong trend to the orientation of faults in New Zealand. The orientation of the plate boundary that passes through New Zealand largely governs the orientation of the suite of faults that are distributed throughout the country. In addition, the orientation of New Zealand itself is approximately parallel with this plate boundary and, as the country is relatively thin in the direction transverse to this boundary, most strong motion instruments will be located approximately along strike from active faults. Obviously there are some significant generalisations made in the previous sentence, but as was mentioned before, this method is typically applied to smaller events where finite fault effects are relatively less significant and the approximations can therefore be justified. This procedure for selecting the causative active fault for each event is also used to assign the fault mechanism where this is unknown. Even though it may not always be possible to identify a particular fault based upon the epicentral co-ordinates of the event, the fault mechanism can generally be estimated with some confidence. New Zealand can basically be partitioned into regions in which certain modes of faulting are dominant over others (see for example Stirling et al. 2002). Therefore, one can often guess the correct fault mechanism based purely upon the co-ordinates of the epicentre before even looking at the actual outlay of the active faults in the vicinity. Examples of regions in which such estimations rarely prove inaccurate are reverse faulting in northwest Nelson, and strike slip faulting in the Marlborough region.

Subsequently, each record has a fault mechanism and distance to the rupture surface hypothesised and attributed to it by employing the following method. The epicentre of the event is extracted from the relevant data files. This point is then located on a map of New Zealand that has all the active faults in the New Zealand active fault database plotted on it. If the event locates very close to one of the faults (taking into account the dips of the plotted traces) then a rupture surface is hypothesised based upon the strike and dip of that fault. If the epicentre falls in a region where the association to a particular fault is ambiguous then the orientation of the fault is estimated based upon the orientations of the surrounding faults and knowledge of the regional tectonics. Once the orientation of the rupture surface is estimated, the finite extent of this surface is estimated by assuming a bilateral rupture and applying the Dowrick and Rhoades (2004) scaling relation. Then, given the assumed position and orientation of this hypothesised rectangular fault rupture, the closest distance to the rupture surface can be determined using standard vector relationships. In order to ease the determination of the distance, the location co-ordinates are converted from the spherical longitude and latitude system to the essentially Cartesian New Zealand Map Grid co-ordinate system (Stirling 1973; Bevin 1998).

In the case of the foreign events; all source mechanisms are well known, and almost all records have the distances to the rupture surface specified. Where these distances are not specified, either a hypocentral distance, or a Joyner-Boore distance (Joyner and Boore 1981), or both, are provided. An estimate of the rupture distance is made based upon this information. The records for which such approximations had to be made are marked accordingly in Appendix B1.

Following the methods outlined above, every event included in the strong motion dataset is assigned a source mechanism, and every record relating to each event is assigned a site class and a distance to the rupture surface. At this point the compilation of the data set is complete and the focus can shift to the processing of the actual records themselves.

B.2.4. Preparation of the Strong Motion Records

Strong motion records in the New Zealand dataset generally consist of three component corrected ground motion time histories of acceleration, velocity, and displacement, as well as three component Fourier spectra and response spectra at five values of damping (0, 2, 5, 10 and 20%). The general procedure for processing these records can be found in Hodder (1983). There is no standard convention for the orientation of the two horizontal components of ground motion. Each record therefore includes details of the directions of the recorded components. All provided spectra are given in terms of the originally recorded components.

For the present work it is desirable to rotate the horizontal recorded components of ground motion into radial and transverse directions. This simple operation is done using the co-ordinate transformation matrix given in Equation (B.2.1) below.

$$\begin{bmatrix} \ddot{u}_g^r(t) \\ \ddot{u}_g^\theta(t) \\ \ddot{u}_g^z(t) \end{bmatrix} = \begin{bmatrix} \cos\theta & -\sin\theta & 0 \\ \sin\theta & \cos\theta & 0 \\ 0 & 0 & 1 \end{bmatrix} \begin{bmatrix} \ddot{u}_g^x(t) \\ \ddot{u}_g^y(t) \\ \ddot{u}_g^z(t) \end{bmatrix} \tag{B.2.1}$$

In Equation (B.2.1) above, θ is the angle in the horizontal plane through which one must rotate the co-ordinates and $\ddot{u}_g^i(t)$, with $i \in (x, y, z, r, \theta)$, represent the acceleration time histories for the various components. The notation used is fairly obvious, with x, y, z directions taking their normal Cartesian convention and r, θ, z being another orthogonal set with r and θ indicating the radial and transverse directions respectively.

Once this rotation operation has been performed in the time domain the corresponding spectra of the ground motion must be recomputed. This computation is achieved through application of the Fourier Transform which is generically defined by the transform pair given in Equation (B.2.2) below.

$$\begin{aligned} X(f) &= \int_{-\infty}^{\infty} x(t) \exp(-2\pi i f t)\, dt \\ x(t) &= \int_{-\infty}^{\infty} X(f) \exp(2\pi i f t)\, df \end{aligned} \tag{B.2.2}$$

The Fourier Transform pair given above corresponds to continuous signals in both the time and frequency domains. The strong motion records that constitute the dataset in this analysis are sampled at discrete increments. We also wish to calculate the Fourier spectral amplitudes at a selection of certain frequencies. It is therefore simpler, and more appropriate, to determine the acceleration spectra by using the mechanical energy method rather than the continuous transform (or its discrete fast fourier transform equivalent). The mechanical energy method is also that used in the standard processing of strong motion records in New Zealand (Hodder 1983). A description of this method can be found in Jennings (2002) and the relevant formulae that are used to calculate both the amplitude and phase spectra are given below in terms of angular frequency; here, T_d is the relevant duration of the record for which the transform is made.

$$\left|F^i(\omega)\right| = \left[\left\{ \int_0^{T_d} \ddot{u}_g^i(t) \cos\omega t dt \right\}^2 + \left\{ \int_0^{T_d} \ddot{u}_g^i(t) \sin\omega t dt \right\}^2 \right]^{1/2} \tag{B.2.3}$$

$$\Phi^i(\omega) = \tan^{-1} \left[\frac{-\int_0^{T_d} \ddot{u}_g^i(t) \sin\omega t dt}{\int_0^{T_d} \ddot{u}_g^i(t) \cos\omega t dt} \right] \tag{B.2.4}$$

In Equations (B.2.3) and (B.2.4) the index $i \equiv r, \theta, z$ corresponds to the directions of the three components in consideration. The spectra thus obtained in terms of angular frequency are converted to

natural frequency via a simple mapping between the two frequencies, $\omega = 2\pi f$. Once this simple mapping has been applied, the velocity or displacement spectra corresponding to the strong motion record can be obtained through a simple multiplicative operation. The velocity ($\dot{\mathbf{U}}^i(\mathbf{x}, f)$) and displacement ($\mathbf{U}^i(\mathbf{x}, f)$) spectra are therefore given in the Equation set (B.2.5).

$$\begin{aligned} \ddot{\mathbf{U}}^i(\mathbf{x}, f) &\equiv \left| F^i(f) \right| \\ \dot{\mathbf{U}}^i(\mathbf{x}, f) &= \frac{\ddot{\mathbf{U}}^i(\mathbf{x}, f)}{2\pi f} \\ \mathbf{U}^i(\mathbf{x}, f) &= \frac{\ddot{\mathbf{U}}^i(\mathbf{x}, f)}{(2\pi f)^2} \end{aligned} \tag{B.2.5}$$

When computing the spectra using the method outlined above, it is important to give due attention to the duration of the time series for which the spectra are calculated. We are only interested in the spectral strength of the relatively energetic S waves. The duration, T_d , should therefore not correspond to the entire recording of ground motion, but to that part of the record corresponding to S wave arrivals. Only a windowed portion of the time series is therefore transformed into the frequency domain. The portion of the time series that is sampled should correspond primarily to direct S waves, or S waves that have only undergone a limited degree of scattering. The intention when selecting the relevant window is to omit both obvious P and surface waves. The distinction between the quasi-direct and surface shear waves becomes more obscure as the source-site distance increases for each record. In order to determine the extent of this S wave window a visual inspection process was undertaken that aims to take into account a degree of this obscurity.

Every record that was considered in the subsequent analysis was inspected, and visual picks of the shear wave window were made. This visual picking process is quite subjective and is an obvious potential source of error. Consequently when making the picks, a best estimate as well as two other probable limiting bounds of the S wave window lengths are made. A simple logic tree is then used to take into consideration the epistemic uncertainty associated with the visual picking process. The Fourier spectra are calculated for each of the three window lengths selected. The logarithm of the spectra corresponding to the best pick is given a 50% weighting while the logarithm of the spectra corresponding to the two limiting bound S wave windows receive 25% weighting each. These weights have been selected arbitrarily; the final spectra thus obtained did not appear to be particularly sensitive to various trial values of the weights assigned. Figure B.2.3 visually demonstrates the window picking procedure outlined above. The obscurity that is mentioned above manifests itself in the relative values of the window picks. The difference between the lower and upper bounds of the S wave windows tend to increase as the source to site distance increases.

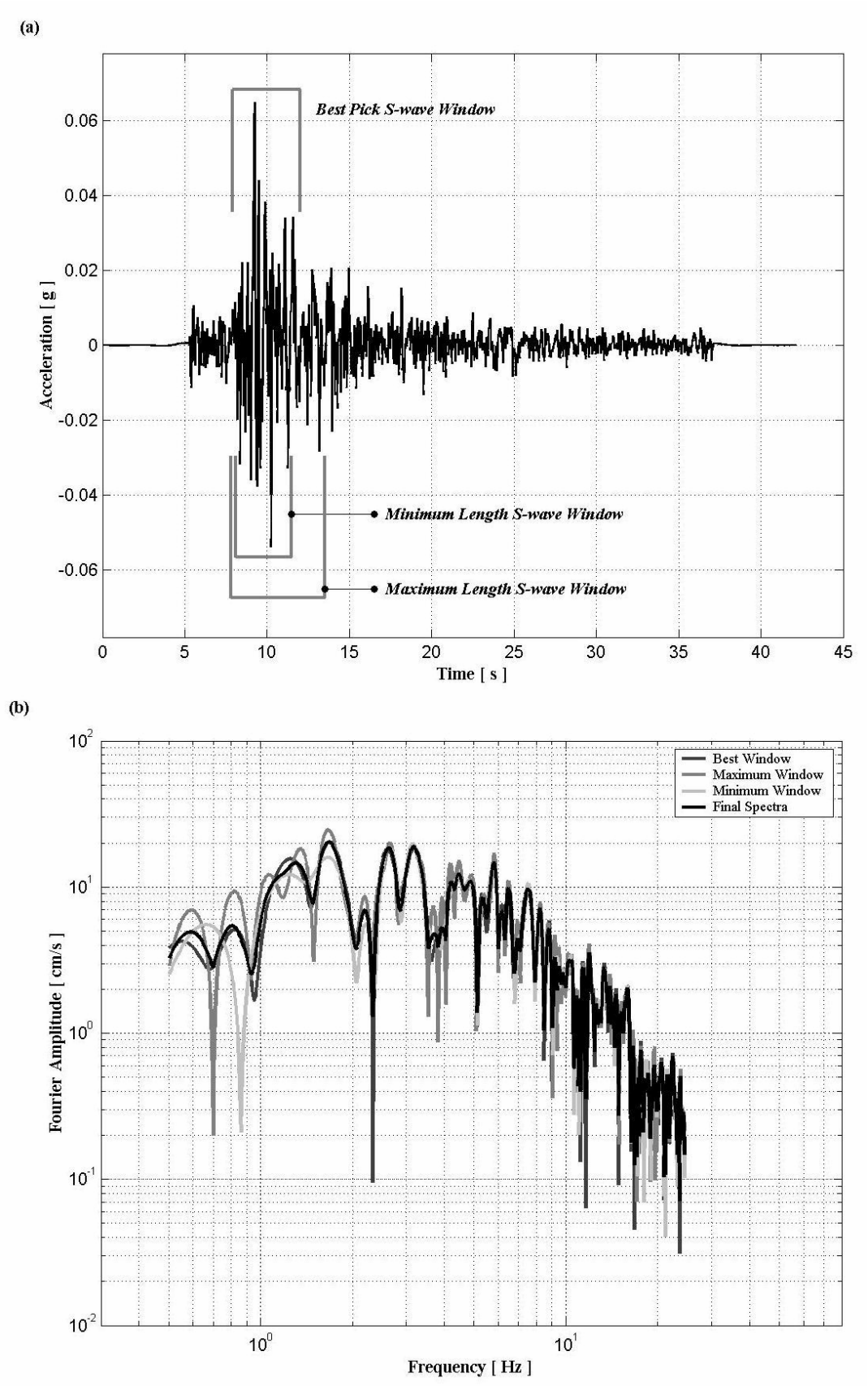

Figure B.2.3: Example of the S-wave window picking process and the resulting Fourier Amplitude Spectra of Acceleration. Time history and resulting spectra are for the Radial Component of 13 August 1971, M_L 5.8, Reefton Earthquake, recorded at Maruia Springs Hotel

Any individual spectrum determined using the above methods (or other methods) will include significant 'spikes' that deviate from an apparent underlying spectral form. The present of such spikes is apparent in panel (b) of Figure B.2.3 where all four of the calculated spectra (the three visual picks and the resultant) for the radial component of the Maruia Springs recording of the 1971 Reefton earthquake are plotted. When developing predictive equations for ground motion spectra we desire a generic relationship that estimates the underlying form of the spectra. To this end it is appropriate to smooth the spectra so that spikes of significant magnitude do not influence the general nature of the fitted spectra in an untoward manner. A very simple method is applied to smooth the spectra. Spectral ordinates are initially computed at 1000 logarithmically spaced frequency values for each spectra, then depending upon the final number of frequency values required frequency bins of the relevant size are obtained. The logarithms of the spectral ordinates corresponding to each frequency bin are averaged, and the value is assigned to the central frequency of the logarithmically spaced bins. It is acknowledged that there are many pre-established filters, as well as infinitely many possible user defined filters, available to achieve the goal of smoothing the spectra. It is also acknowledged however, that considerable effort can go into designing the optimal filter for a given purpose and that the consequent improvement in the final regression model would be almost negligible. The existing literature was examined in an attempt to perceive any standard method of smoothing spectra, During this exercise it was found that rather than there being a standard method, many varying approaches are adopted with each tending to differ slightly from each other and with each varying in complexity from the simple method applied here, to highly elaborate methods. Again, it is worthwhile keeping in mind the principle of consistent crudeness during this process.

When evaluating the integrals in Equations (B.2.3) and (B.2.4), one can select the particular frequency values of interest. For the present work the fit to recorded spectra of the model is assessed in terms of logarithmic residuals and the goodness of fit is typically assessed in terms of plots against the logarithm of frequency. The values of frequency for which the spectra are computed are therefore evaluated at evenly spaced logarithmic increments of frequency.

In following the methodology outlined in this chapter, a strong motion dataset was selected and prepared for use in obtaining predictive equations for both the Fourier Amplitude spectra and Arias Intensity for use in New Zealand. A subset of records from this dataset is also used for the derivation of a moment magnitude – corner frequency relationship for source spectra in New Zealand.

B.3. Theoretical Background to the Predictive Equations for Strong Ground Motion

B.3.1. Introduction

There are many similarities between the theoretical derivations of the functional forms for the regression models of both the Fourier Amplitude Spectrum and Arias Intensity. Therefore, in an attempt to minimise repetition, this chapter addresses the general theoretical basis for the functional forms employed for the predictive equations developed in later chapters. Much of the development presented here draws heavily from the works of Aki and Richards (1980). Their remarkable treatise on the mathematics governing the field of seismology is without peer in terms of scope and content and has provided the working basis for a considerable amount of the current strong motion seismology literature.

The primary objective of this chapter is to justify the use of what is now a relatively common theoretical form for the Fourier Amplitude Spectrum. The model thus derived will be used in the subsequent derivation of the functional form of the Arias Intensity relationship as well as in obtaining the predictive equation for the FAS itself. The derived model is also used as a base from which the source spectra required in the next chapter may be back-calculated.

In keeping with the theme of trying to strengthen the bond between engineers and seismologists in New Zealand, this chapter begins with one of the most fundamental relations in seismology and proceeds to derive an expression that is now familiar to engineering seismologists. Often the seismological literature may initially appear daunting to an engineer not specifically trained in this discipline. Trivial, or common assumptions employed by seismologists may not seem trivial at all to the engineer in this case. For this reason attention is given in this chapter to providing the seismological foundation from which engineering style analyses can be initiated. This background should aid the analyst in discriminating between regression models from the perspective of theory rather than just through the application of statistical measures for goodness of fit or the like.

B.3.2. Theoretical Development

A complete description of the spatio-temporal distribution of ground motion displacements can be found from the following representation theorem (Aki and Richards 1980).

$$u_n(\mathbf{x},t) = \int_{-\infty}^{\infty} d\tau \iint_{\Sigma} \left[u_i(\boldsymbol{\xi},\tau)\right] c_{ijpq} \nu_j \frac{\partial G_{np}(\mathbf{x},t-\tau;\boldsymbol{\xi},0)}{\partial \xi_q} d\Sigma \tag{B.3.1}$$

In this tensor expression, $u_n(\mathbf{x},t)$ gives the n^{th} component of the displacement of the ground at some arbitrary location, $\mathbf{x}$, and at some time, t. The vector, ν_j, is normal to the fault and is used to define the orientation of the slip distribution over the fault plane, Σ. The slip distribution itself is given as a function of the position, $\boldsymbol{\xi}$, on the fault plane at some time after the initiation of rupture, τ. In Equation (B.3.1) the i^{th} component of this slip distribution is represented by Equation (B.3.2), i.e. the relative dislocation over the rupture surface. Note that this slip distribution is allowed to be spatially and temporally variant allowing for almost any conceivable type of rupture.

$$\left[u_i(\boldsymbol{\xi},\tau)\right] = u_i^{+}(\boldsymbol{\xi},\tau) - u_i^{-}(\boldsymbol{\xi},\tau) \tag{B.3.2}$$

The partially differentiated expression in Equation (B.3.1) is the Green's function, $G_{np}(\mathbf{x},t;\boldsymbol{\xi},\tau)$, which gives the motion in the n^{th} direction at location $\mathbf{x}$ and time t caused by a point force acting in the p direction at location $\boldsymbol{\xi}$ and time τ. In this way the representation theorem can be made equivalent to a double couple source. The only remaining expression to be defined is the fourth-order elastic tensor, c_{ijpq}. This tensor is given, using Einstein indicial notation, by Equation (B.3.3).

$$c_{ijpq} = \lambda \delta_{ij} \delta_{pq} + \mu\left(\delta_{ip}\delta_{jq} + \delta_{iq}\delta_{jp}\right) \tag{B.3.3}$$

In Equation (B.3.3), λ and μ are the Lamé constants, and δ_{ij} is the Kronecker delta function ($\delta_{ij} = 0$ for $i \neq j$, and $\delta_{ij} = 1$ otherwise).

Equation (B.3.1) therefore represents the ground motion at the position of interest as a linear combination, through the integral over space, of the contributions from each point on the fault surface. This representation is particularly useful as it enables one to decompose an observed ground motion into constituent components provided by the source mechanism, and the travel path of the seismic waves (including the special case of waves propagating near the surface, i.e. site response). This attribute of the representation theorem will be exploited as we develop our model for the Fourier Amplitude Spectrum of ground motion.

In what follows, progressively simpler approximations to the governing form of Equation (B.3.1) will be adopted. It is not possible to know *a priori* the spatio-temporal characteristics of the slip distribution for a future event. It is therefore useful to generalise the time integrated slip distribution by some generic model for the actions at the source. This generic approximation makes use of the Seismic Moment which, for an infinite, homogeneous, isotropic medium, can be given by Equation (B.3.4) (Aki and Richards 1980).

$$M_0 = \mu A \bar{u} \tag{B.3.4}$$

Here, μ is the shear modulus, A is the fault rupture area, and $\bar{u}$ is the average slip over this surface. This seismic moment is a measure of the source strength of an earthquake event and can be correlated to the strength of strong ground motion recordings. The seismic moment, as can be seen from Equation (B.3.4) above, is also readily obtainable from geologic investigations. Due to the power law scaling of earthquake rupture dimensions (Turcotte and Malamud 2002) the numeric range of values for the seismic moment are immense. Consequently, Hanks and Kanamori (1978; 1979) introduced a new magnitude scale that translates seismic moments into a numeric range similar to existing magnitude scales. For seismic moments measured in terms of Newton-metres, the Moment Magnitude, $\mathbf{M}$ or M_W, is given by Equation (B.3.5) below.

$$\mathbf{M} = \frac{2}{3}\left[\log_{10}\left(M_0\right) - 9.05\right] \tag{B.3.5}$$

This Moment Magnitude is the predominant measure of source strength that will be adopted in the model for the FAS.

Aki and Richards (1980) proceed to represent Equation (B.3.1) in terms of the seismic moment, spherical co-ordinates related to the specific rupture surface, and material properties of the source and propagating medium. The co-ordinate system used in this description can be seen in Figure B.3.1 below. Note that the co-ordinates in this case are selected to coincide with the fault geometry, i.e. x_1 is parallel to fault slip, x_2 is transverse to fault slip but lies in the plane of the fault, and x_3 is orthogonal to the fault plane.

From this development it becomes evident that the various components contributing to an observed ground motion dissipate at varying rates. Consequently, the radiated displacement field can be thought of as being composed of a near, an intermediate, and a far field region. The displacement field can thus be written as in Equation (B.3.6) below.

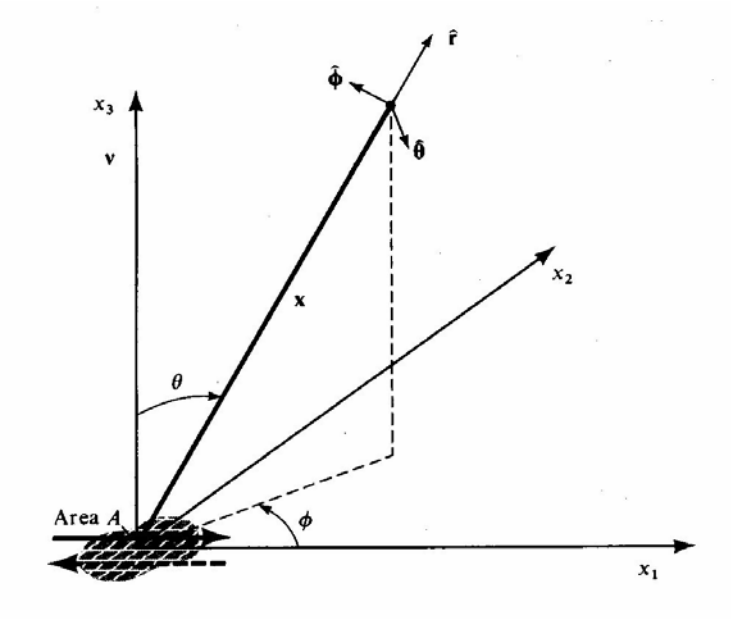

Figure B.3.1: Co-ordinate system initially adopted for the definition of the spatio-temporal displacement field (from Aki and Richards, 1980)

$$\mathbf{u}(\mathbf{x},t) = \underbrace{\frac{1}{4\pi\rho}\mathbf{A}^{N}\frac{1}{r^4}\int_{r/\alpha}^{r/\beta}\tau M_0(t-\tau)\,d\tau}_{\text{near field term}} + \underbrace{\frac{1}{4\pi\rho\alpha^2}\mathbf{A}^{IP}\frac{1}{r^2}M_0\left(t-\frac{r}{\alpha}\right)+\frac{1}{4\pi\rho\beta^2}\mathbf{A}^{IS}\frac{1}{r^2}M_0\left(t-\frac{r}{\beta}\right)}_{\text{intermediate field terms}} + \underbrace{\frac{1}{4\pi\rho\alpha^3}\mathbf{A}^{FP}\frac{1}{r}\dot{M}_0\left(t-\frac{r}{\alpha}\right)+\frac{1}{4\pi\rho\beta^3}\mathbf{A}^{FS}\frac{1}{r}\dot{M}_0\left(t-\frac{r}{\beta}\right)}_{\text{far field terms}} \tag{B.3.6}$$

Here, in Equation (B.3.6) the $\mathbf{A}^i$ terms represent the radiation patterns corresponding to the near field ($i \equiv N$), intermediate field ($i \equiv IP, IS$), and far field ($i \equiv FP, FS$), for P and S waves respectively. The radiation pattern describes the azimuthally varying strength of seismic waves initially emitted from an earthquake source. These radiation pattern terms are given in Equation (B.3.7) below.

$$\begin{aligned}
\mathbf{A}^{N} &= 9\sin 2\theta\cos\phi\hat{\mathbf{r}} - 6\left(\cos 2\theta\cos\phi\hat{\boldsymbol{\theta}} - \cos\theta\sin\phi\hat{\boldsymbol{\varphi}}\right)\\
\mathbf{A}^{IP} &= 4\sin 2\theta\cos\phi\hat{\mathbf{r}} - 2\left(\cos 2\theta\cos\phi\hat{\boldsymbol{\theta}} - \cos\theta\sin\phi\hat{\boldsymbol{\varphi}}\right)\\
\mathbf{A}^{IS} &= -3\sin 2\theta\cos\phi\hat{\mathbf{r}} + 3\left(\cos 2\theta\cos\phi\hat{\boldsymbol{\theta}} - \cos\theta\sin\phi\hat{\boldsymbol{\varphi}}\right)\\
\mathbf{A}^{FP} &= \sin 2\theta\cos\phi\hat{\mathbf{r}}\\
\mathbf{A}^{FS} &= \cos 2\theta\cos\phi\hat{\boldsymbol{\theta}} - \cos\theta\sin\phi\hat{\boldsymbol{\varphi}}
\end{aligned} \tag{B.3.7}$$

There may appear to be a rather abrupt jump from the representation theorem given in Equation (B.3.1) to the expression given in Equation (B.3.6). However, if one recognises that the spatio-temporal dislocation function, and the elastic tensor, have essentially been replaced by the time dependent seismic

moment expression, and that the Green's function has been approximated by a simple scaling with respect to distance, r; the jump is not so abrupt.

In the above equations, the spatial position is defined using spherical co-ordinates related conveniently to the orientation of the shear dislocation at the source, i.e. an optimum co-ordinate system for descriptions in terms of the source. Later it will be convenient to represent the far-field displacement field in terms of an optimal co-ordinate representation from the point of view of the observer. For now though, Equation (B.3.6) is introduced primarily to demonstrate the various rates at which the terms of the displacement field attenuate. In addition the introduction of the radiation pattern acts to demonstrate the fact that the initial source strength of seismic waves varies considerably about the focal sphere (as well as also being frequency dependent, which will be considered later).

Only the far field terms, and in particular the far field term for the shear waves, will be considered when developing the model for the FAS. There are very few near field strong motion records in the New Zealand strong motion database; too few in fact to allow consideration of near and intermediate field terms in the context which we will momentarily develop. Of the far field terms, the S wave term is that which carries the majority of the energy away from the source. It is this component of the emitted seismic radiation that contributes most strongly to damage induced in engineered structures, and therefore this component will receive the bulk of our attention as we proceed. The far field S wave contribution to the displacement field can be given by the following equation.

$$\mathbf{u}^{FS}\left(\mathbf{x},t\right)=\frac{\mathbf{A}^{FS}\left(\theta,\phi\right)}{4\pi\rho\beta^{3}r}\dot{M}_{0}\left(t-\frac{r}{\beta}\right) \tag{B.3.8}$$

In the above equation, one can again appreciate that the expression is comprised of terms relating to both the source, and the travel path.

Equation (B.3.8) contains a radiation pattern term (see Equation (B.3.7)) that corresponds to a given set of co-ordinates defined in terms of directions from the fault source. Later, focal mechanism solutions will be used to calculate theoretical values of this radiation pattern. These focal mechanism solutions are given in terms of geological descriptions of the source orientation, and the nature of the dislocation at this source. These geologic descriptors are the strike, θ, and the dip, δ, of the fault as well as the rake, λ of the slip over this fault; all defined with respect to what are essentially Cartesian geographic co-ordinates (for regional distances), i.e. North, East, Depth. In New Zealand, positions are mostly aptly defined using the New Zealand Map Grid (NZMG) co-ordinate system (Stirling 1973; Bevin 1998). This NZMG co-ordinate system is valid only for New Zealand and maps positions on the earth's surface given in latitude and longitude to a Cartesian metric scale with minimal distortion of angles and areas. This co-ordinate system will be that used throughout the remainder of this work. The geological descriptors mentioned above are diagrammatically defined in Figure B.3.2 below.

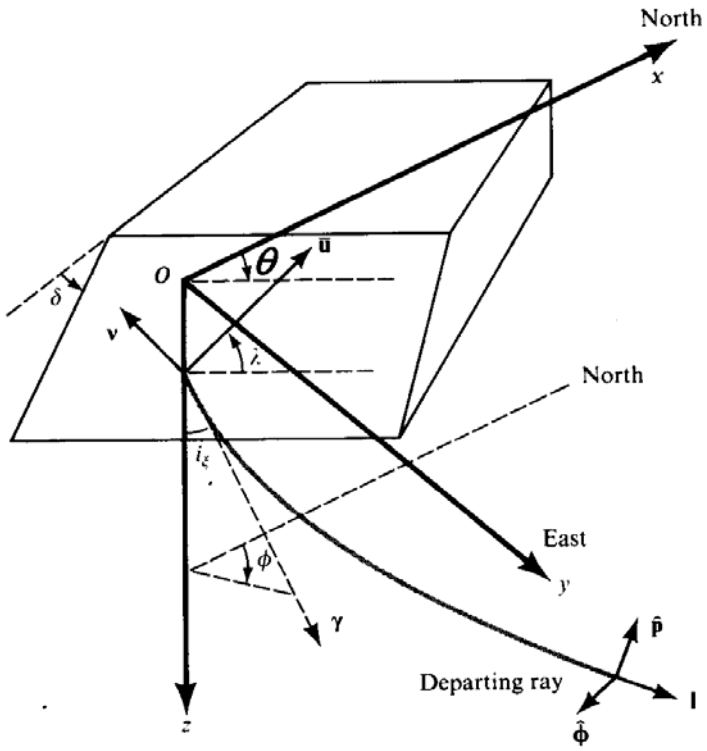

Figure B.3.2: Definition of Cartesian coordinates used to define the far field radiation patterns (slightly modified from Aki and Richards, 1980, page 114)

Also depicted in Figure B.3.2 are unit vectors that define the orientation of a ray departing from the fault surface, $\boldsymbol{\gamma}$, as well as a slip vector, $\bar{\mathbf{u}}$, defining the slip in the plane with respect to Cartesian co-ordinate directions.

If one incorporates the definition of seismic moment, given in Equation (B.3.4), with the far field terms of Equation (B.3.6), one can represent the far field displacement expressions for P and S waves in terms of the vectors in Figure B.3.2; these expression are given by the following equations.

P wave displacement component (α is the P wave velocity)

$$\mathbf{u}^{P}\left(\mathbf{x},t\right)=\frac{2\left(\boldsymbol{\gamma}\cdot\mathbf{v}\right)\left(\boldsymbol{\gamma}\cdot\dot{\bar{\mathbf{u}}}\right)\mu A\boldsymbol{\gamma}}{4\pi\rho\alpha^{3}r} \tag{B.3.9}$$

S wave displacement component (β is the shear wave velocity)

$$\mathbf{u}^{S}\left(\mathbf{x},t\right)=\frac{\left[\left(\boldsymbol{\gamma}\cdot\mathbf{v}\right)\dot{\bar{\mathbf{u}}}+\left(\boldsymbol{\gamma}\cdot\dot{\bar{\mathbf{u}}}\right)\mathbf{v}-2\left(\boldsymbol{\gamma}\cdot\mathbf{v}\right)\left(\boldsymbol{\gamma}\cdot\dot{\bar{\mathbf{u}}}\right)\boldsymbol{\gamma}\right]\mu A}{4\pi\rho\beta^{3}r} \tag{B.3.10}$$

The equivalence between Equations (B.3.10) and (B.3.8) can be appreciated when regarding the moment rate, evaluated at the retarded time $t - r/\beta$, as a function of the average slip velocity on the fault plane evaluated at the same time, $\dot{\bar{\mathbf{u}}}$.

$$\dot{M}_0\left(t - \frac{r}{\beta}\right) \equiv \mu A \dot{\bar{\mathbf{u}}} \tag{B.3.11}$$

The vector terms used in the above equations, and depicted in Figure B.3.2, are defined in terms of the NZMG co-ordinates by the set of equations below. In all the expressions to follow, i_ξ defines the take-off angle, and is measured from the positive $\hat{\mathbf{z}}$ (depth) direction.

Slip vector, $\bar{\mathbf{u}}$

$$\begin{aligned}\bar{\mathbf{u}} = {} & \bar{u}\left(\cos\lambda\cos\theta + \cos\delta\sin\lambda\sin\theta\right)\hat{\mathbf{x}} \\ & + \bar{u}\left(\cos\lambda\sin\theta - \cos\delta\sin\lambda\cos\theta\right)\hat{\mathbf{y}} \\ & - \bar{u}\sin\lambda\sin\delta\hat{\mathbf{z}}\end{aligned} \tag{B.3.12}$$

Fault normal vector, $\mathbf{v}$

$$\mathbf{v} = -\sin\delta\sin\theta\hat{\mathbf{x}} + \sin\delta\cos\theta\hat{\mathbf{y}} - \cos\delta\hat{\mathbf{z}} \tag{B.3.13}$$

P -wave direction, $\mathbf{l}$

$$\mathbf{l} = \boldsymbol{\gamma} = \sin i_\xi\cos\phi\hat{\mathbf{x}} + \sin i_\xi\sin\phi\hat{\mathbf{y}} + \cos i_\xi\hat{\mathbf{z}} \tag{B.3.14}$$

SV -wave direction, $\hat{\mathbf{p}}$

$$\hat{\mathbf{p}} = \cos i_\xi\cos\phi\hat{\mathbf{x}} + \cos i_\xi\sin\phi\hat{\mathbf{y}} - \sin i_\xi\hat{\mathbf{z}} \tag{B.3.15}$$

SH -wave direction, $\hat{\boldsymbol{\varphi}}$

$$\hat{\boldsymbol{\varphi}} = -\sin\phi\hat{\mathbf{x}} + \cos\phi\hat{\mathbf{y}} \tag{B.3.16}$$

Given that we have now defined *SV* and *SH* directions, i.e. shear motion polarised in a vertical and horizontal direction with respect to the radial curvilinear direction, $\mathbf{l}$, we can use the dot product operator on Equation (B.3.10) for the total far field *S* wave displacement field to define contributions to the displacement field from *SV* and *SH* waves respectively. These expressions are consequently defined by Equation (B.3.17), for the *SV* component, and Equation (B.3.18), for the *SH* component respectively.

$$\mathbf{u}^{SV}(\mathbf{x},t) = \left(\mathbf{u}^{S}\cdot\hat{\mathbf{p}}\right)\hat{\mathbf{p}} = \frac{\left[\left(\boldsymbol{\gamma}\cdot\mathbf{v}\right)\left(\dot{\bar{\mathbf{u}}}\cdot\hat{\mathbf{p}}\right)+\left(\boldsymbol{\gamma}\cdot\dot{\bar{\mathbf{u}}}\right)\left(\mathbf{v}\cdot\hat{\mathbf{p}}\right)\right]\mu A\hat{\mathbf{p}}}{4\pi\rho\beta^{3}r} \tag{B.3.17}$$

$$\mathbf{u}^{SH}(\mathbf{x},t) = \left(\mathbf{u}^{S}\cdot\hat{\boldsymbol{\varphi}}\right)\hat{\boldsymbol{\varphi}} = \frac{\left[\left(\boldsymbol{\gamma}\cdot\mathbf{v}\right)\left(\dot{\bar{\mathbf{u}}}\cdot\hat{\boldsymbol{\varphi}}\right)+\left(\boldsymbol{\gamma}\cdot\dot{\bar{\mathbf{u}}}\right)\left(\mathbf{v}\cdot\hat{\boldsymbol{\varphi}}\right)\right]\mu A\hat{\boldsymbol{\varphi}}}{4\pi\rho\beta^{3}r} \tag{B.3.18}$$

Now, comparing Equations (B.3.17) and (B.3.18) with the previously defined Equations (B.3.6) and (B.3.8) one can see that the bracketed expressions in the above equations are simply radiation pattern terms given in terms of the new Cartesian, NZMG, coordinates. The determination of these radiation pattern terms will come under close scrutiny in the procedure of the following chapter so it is worth our while to define them completely here.

Far field P wave radiation pattern, $\mathbb{R}^{P}$

$$\begin{aligned}\mathbb{R}^{P} &= 2\left(\boldsymbol{\gamma}\cdot\mathbf{v}\right)\left(\boldsymbol{\gamma}\cdot\dot{\bar{\mathbf{u}}}\right)/\dot{\bar{u}}\\ &= \cos\lambda\sin\delta\sin^{2}i_{\xi}\sin 2\left(\phi-\theta\right)-\cos\lambda\cos\delta\sin 2i_{\xi}\cos\left(\phi-\theta\right)\\ &\quad+\sin\lambda\sin 2\delta\left(\cos^{2}i_{\xi}-\sin^{2}i_{\xi}\sin^{2}\left(\phi-\theta\right)\right)\\ &\quad+\sin\lambda\cos 2\delta\sin 2i_{\xi}\sin\left(\phi-\theta\right)\end{aligned} \tag{B.3.19}$$

Far field SV wave radiation pattern, $\mathbb{R}^{SV}$

$$\begin{aligned}\mathbb{R}^{SV} &= \left[\left(\boldsymbol{\gamma}\cdot\mathbf{v}\right)\left(\dot{\bar{\mathbf{u}}}\cdot\hat{\mathbf{p}}\right)+\left(\boldsymbol{\gamma}\cdot\dot{\bar{\mathbf{u}}}\right)\left(\mathbf{v}\cdot\hat{\mathbf{p}}\right)\right]/\dot{\bar{u}}\\ &= \sin\lambda\cos 2\delta\cos 2i_{\xi}\sin\left(\phi-\theta\right)-\cos\lambda\cos\delta\cos 2i_{\xi}\cos\left(\phi-\theta\right)\\ &\quad+\tfrac{1}{2}\cos\lambda\sin\delta\sin 2i_{\xi}\sin 2\left(\phi-\theta\right)\\ &\quad-\tfrac{1}{2}\sin\lambda\sin 2\delta\sin 2i_{\xi}\left(1+\sin^{2}\left(\phi-\theta\right)\right)\end{aligned} \tag{B.3.20}$$

Far field SH wave radiation pattern, $\mathbb{R}^{SH}$

$$\begin{aligned}\mathbb{R}^{SH} &= \left[\left(\boldsymbol{\gamma}\cdot\mathbf{v}\right)\left(\dot{\bar{\mathbf{u}}}\cdot\hat{\boldsymbol{\varphi}}\right)+\left(\boldsymbol{\gamma}\cdot\dot{\bar{\mathbf{u}}}\right)\left(\mathbf{v}\cdot\hat{\boldsymbol{\varphi}}\right)\right]/\dot{\bar{u}}\\ &= \cos\lambda\cos\delta\cos i_{\xi}\sin\left(\phi-\theta\right)+\cos\lambda\sin\delta\sin i_{\xi}\cos 2\left(\phi-\theta\right)\\ &\quad+\sin\lambda\cos 2\delta\cos i_{\xi}\cos\left(\phi-\theta\right)\\ &\quad-\tfrac{1}{2}\sin\lambda\sin 2\delta\sin i_{\xi}\sin 2\left(\phi-\theta\right)\end{aligned} \tag{B.3.21}$$

Thus far, the material parameters, ρ, α, β, and the distance, r, have escaped explicit mention. These parameters represent a density, a P wave velocity, an S wave velocity, and a distance measure respectively. The density of the crust typically increases with depth, the wave velocities (being functions of the density, in theory) consequently also increase with depth. Aki and Richards (1980) develop far field

geometrical ray solutions for contributions to the displacement field from P, SV, and SH waves in a spherically symmetric medium (their Equations 4.57, 4.60, and 4.61). These equations give the displacement field amplitude as being related to the material and distance parameters via the proportionality in Equation (B.3.22) below.

$$\mathbf{u}^i(\mathbf{x},t) \propto \left(\frac{1}{\rho(\mathbf{x})v_i(\mathbf{x})}\right)^{1/2} \frac{1}{\Re^i(\mathbf{x},\boldsymbol{\xi})} \tag{B.3.22}$$

Here, $i = P, SV, SH$ and consequently $v_i \Rightarrow \alpha, \beta, \beta$. The function $\Re^i(\mathbf{x},\boldsymbol{\xi})$ represents the geometric spreading of waves propagating from the source. In the expressions that have been presented thus far this function has been equivalent to r and, for far field components, suggests that amplitudes attenuate according to spherical spreading for body waves ($1/r$). In the methodology of the chapter to follow we will also consider how the scattering caused by waves interacting with material interfaces effects this spreading function in a probabilistic sense.

As we will be using some elementary ray tracing in the procedures to follow it is prudent to be consistent with the ray tracing solution and the double couple representation. The final expressions for the far field displacement components should therefore contain the square root dependency on the material parameters at the point of observation as given in Equation (B.3.22).

The final expressions that we will adopt for the far field contributions to the displacement field, in terms of Cartesian co-ordinates oriented consistently with NZMG co-ordinates, are given in Equations (B.3.23), (B.3.24), and (B.3.25).

$$\mathbf{u}^P(\mathbf{x},t) = \frac{\mathbb{R}^P \mu(\boldsymbol{\xi}) A \dot{\bar{u}}\left(t - T^P\right)\mathbf{l}}{4\pi\rho(\boldsymbol{\xi})^{1/2}\,\rho(\mathbf{x})^{1/2}\,\alpha(\boldsymbol{\xi})^{5/2}\,\alpha(\mathbf{x})^{1/2}\,\Re^P(\mathbf{x},\boldsymbol{\xi})} \tag{B.3.23}$$

$$\mathbf{u}^{SV}(\mathbf{x},t) = \frac{\mathbb{R}^{SV} \mu(\boldsymbol{\xi}) A \dot{\bar{u}}\left(t - T^S\right)\hat{\mathbf{p}}}{4\pi\rho(\boldsymbol{\xi})^{1/2}\,\rho(\mathbf{x})^{1/2}\,\beta(\boldsymbol{\xi})^{5/2}\,\beta(\mathbf{x})^{1/2}\,\Re^S(\mathbf{x},\boldsymbol{\xi})} \tag{B.3.24}$$

$$\mathbf{u}^{SH}(\mathbf{x},t) = \frac{\mathbb{R}^{SH} \mu(\boldsymbol{\xi}) A \dot{\bar{u}}\left(t - T^S\right)\hat{\boldsymbol{\phi}}}{4\pi\rho(\boldsymbol{\xi})^{1/2}\,\rho(\mathbf{x})^{1/2}\,\beta(\boldsymbol{\xi})^{5/2}\,\beta(\mathbf{x})^{1/2}\,\Re^S(\mathbf{x},\boldsymbol{\xi})} \tag{B.3.25}$$

In the expressions above, T^P and T^S are the P and S wave travel times respectively for a particular ray (note that these replace the terms r/α and r/β in the previous expressions). It is also very important to note the directions in which these motions act, given by the unit vectors in the numerators of these expressions. A major assumption of the procedure to follow is that the impedance of the crust increases sufficiently with depth to make ray paths emitted from the source curve towards the vertical as they

propagate through the earth and approach the surface. Given that this assumption is reasonable, the vertical motion recorded at a site will be primarily composed of P wave motion (as well as a component of SV wave motion, depending on how far from vertical the arriving rays really are), while the horizontal radial and transverse components of observed motions are strongly correlated to the contributions from the SV and SH motions respectively. The reason that this assumption, and distinction, is important will become evident when we consider the effects of the scattering of waves interacting with material interfaces as they propagate through a layered earth.

B.3.3. From the Time Domain to the Frequency Domain

As the heading of this section suggests, we are ultimately interested in determining the spectrum of ground motions. Thus far the development has considered the space-time dependence of ground motions. In order to represent the preceding equations in terms of the desired space-frequency representation of ground motions one simply makes use of the Fourier transform.

$$X(f) = \int_{-\infty}^{\infty} x(t) e^{-2\pi i f t} dt \tag{B.3.26}$$

One can readily appreciate that the majority of terms in Equations (B.3.23), (B.3.24), and (B.3.25) are independent of time and that consequently, when one applies the above transform the amplitude spectrum retains the proportionality to these parameters. The case for the Fourier Transform of SV waves is shown in Equation (B.3.27) below.

$$\mathbf{U}^{SV}(\mathbf{x}, f) = \frac{\mathbb{R}^{SV} \mu(\xi) A \hat{\mathbf{p}}}{4\pi\rho(\xi)^{1/2} \rho(\mathbf{x})^{1/2} \beta(\xi)^{5/2} \beta(\mathbf{x})^{1/2} \Re^{S}(\mathbf{x}, \xi)} \int_{-\infty}^{\infty} \dot{\bar{u}}\left(t - T^{S}\right) \mathrm{e}^{-2\pi i f t} \, dt \tag{B.3.27}$$

The integral expression, if the temporally independent terms, $\mu(\xi)$ and A, are included, is simply the product of the seismic moment and some function of frequency that represents the seismic source spectrum.

Since its inception (Aki 1967; Brune 1970; 1971) the omega squared, single corner frequency, source model has proven suitable for the majority of applications in strong motion seismology, particularly for small to moderate sized events. In such cases the assumptions made in deriving this spectrum regarding the source dimensions and shape of the rupture (circular) are good. When the source dimensions grow to the extent that this assumption no longer holds (i.e. when the rupture is limited by the thickness of the seismogenic portion of the crust) other source spectra may be more appropriate, such as multiple corner frequency models or partial rupture models (Boatwright and Choy 1992; Atkinson and Boore 1995; Haddon 1996; Atkinson and Silva 2000; Boore 2003). For the present work we desire a generic

description of the spectrum of seismic waves generated by a wide range of magnitude events so the omega-squared model will be adopted in what follows.

Returning now to the integral expression in Equation (B.3.27), it can be shown that the source displacement pulse that results in the omega squared spectrum is of the following form (i.e. Beresnev and Atkinson 1997; Beresnev 2001; 2002).

$$u(t) = u(\infty)\left[1 - \left(1 + \frac{t}{\tau}\right)\exp\left[-\frac{t}{\tau}\right]\right] \tag{B.3.28}$$

In this expression, $u(\infty)$ is the final static displacement over the fault surface and τ is a parameter governing the rate at which this final dislocation is achieved (the rise time). Following Beresnev (2002), the modulus of the Fourier transform of displacement in the radiated field is then,

$$\Omega(\omega) = \left|\int_{-\infty}^{\infty} \dot{u}(t)\exp(-i\omega t)\,dt\right| = \frac{u(\infty)}{1 + (\omega\tau)^2} \tag{B.3.29}$$

where $\omega = 2\pi f$ is the angular frequency. Keeping with the common assumption that the inverse of the rise time is a good approximation to the angular corner frequency of the source spectrum, i.e. $\omega_c \equiv 1/\tau$, one can write the above equation in terms of natural frequency as in Equation (B.3.30).

$$\Omega(f) = \frac{\Omega_0}{1 + (f/f_c)^2} \tag{B.3.30}$$

In Equation (B.3.30), Ω_0 represents the zero-frequency spectral ordinate and is the asymptotic upper limit to the source spectrum of displacement at low frequencies; this parameter is of central importance to the development of the following chapter. In addition, f_c is the corner frequency of the source spectrum.

Now, one can combine Equations (B.3.27) and (B.3.30), and in doing so attain the working base model for the spectrum of ground motion displacements in the far field. This model, for the case of SV waves, is given by Equation (B.3.31) below.

$$\mathbf{U}^{SV}(\mathbf{x}, f) = \frac{\mathbb{R}^{SV} M_0 \hat{\mathbf{p}}}{4\pi\bar{\rho}(\mathbf{x},\boldsymbol{\xi})\bar{\beta}(\mathbf{x},\boldsymbol{\xi})^3 \Re^S(\mathbf{x},\boldsymbol{\xi})\left[1 + (f/f_c)^2\right]} \tag{B.3.31}$$

It must be appreciated that the parameter Ω_0 is related to the seismic moment of the event, i.e. $\Omega_0 = f(M_0) = g(\mathbf{M})$, as well as the radiation pattern and the material parameters of density and wave velocity. Note also that for brevity, the nomenclature for the material parameters of density and wave

velocity has been altered. These new terms should be viewed as composite parameters and are defined in the equation couplet below. The relative contributions of the material properties at the source of the event and at the site of observation are governed by the ray tracing approximation previously mentioned and given in Equation (B.3.32).

$$\begin{aligned} \overline{\rho}(\mathbf{x},\boldsymbol{\xi}) &= \rho(\boldsymbol{\xi})^{1/2}\,\rho(\mathbf{x})^{1/2} \\ \overline{\beta}(\mathbf{x},\boldsymbol{\xi}) &= \left(\beta(\boldsymbol{\xi})^{5/2}\,\beta(\mathbf{x})^{1/2}\right)^{1/3} \end{aligned} \tag{B.3.32}$$

Equation (B.3.31) represents the radiated far field displacement spectrum for a perfectly elastic homogeneous isotropic medium. As mentioned, this model forms the basis for our final model. In addition to the considerations made in arriving at this base model, we also wish to consider the effects of inelastic material attenuation, scattering of waves through the propagation process, and the effects of site response. Given the limited dataset with which we will be working, it will be difficult to place significant constraints on the parameters that reflect these additional considerations. However, it is better to make these distinctions at this point so that we are better placed to partition the uncertainties within the constituent components of the model. For example, there is strong evidence that ground motions undergo significant near surface attenuation, particularly at high frequencies (Abercrombie 1998). If one did not address this phenomenon as part of a site response effect then the estimates of inelastic material, and scattering, attenuation would have to be higher to accommodate the observed reduction in spectral amplitudes. While this distinction may have minimal impact on the final accuracy of the resulting equations in terms of fitting empirical data, it would lead to significantly varying estimates of particular parameters as more developed models arose. This condition is a source of confusion in the literature and should be avoided where possible.

The modifications to the base model that address the anelastic and scattering attenuation are reasonably simple. Firstly, for the scattering attenuation, it is impossible to know the spatial positions of inhomogeneities in the crust that lead to the scattering of waves. For a generic model, this level of detail, even if available, would not be appropriate anyway. Consequently, the only modification to the base model is to allow for an increased rate of attenuation in the geometrical spreading term, $\mathfrak{R}(\mathbf{x},\boldsymbol{\xi})$. This modification will simply be manifest in a multiplicative or exponential parameter applied to the travel distance of seismic waves. Secondly, the anelastic attenuation is accommodated by an exponential multiplier (Boore 2003); the form of which is given in the equation below.

$$\exp\left[\frac{-\pi f R}{Q(f)c_Q}\right] \tag{B.3.33}$$

Here, R is a measure of the distance travelled by the waves, $Q(f)$ is the anelastic material attenuation function, and c_Q is the seismic velocity used in the determination of $Q(f)$ (for this application, this seismic velocity will be assumed equal to the wave velocity).

The modifications to account for site effects are much more vexed with complication. Ideally, one would have knowledge of a near surface transfer function for each site in the New Zealand strong motion network. Unfortunately, reality is somewhat removed from this ideal (Cousins et al. 1996). We have very limited knowledge of how individual sites respond over the range of frequencies required in our model. The reasonably small number of recordings made at each site, in conjunction with the large aleatoric variability inherent in site response (Boore 2004) make it unrealistic to try and ascertain the nature of the required transfer functions at this point. Therefore, for the present work, site response will be handled in a variety of ways. For the determination of a moment magnitude – corner frequency relationship for New Zealand (to be addressed in the next chapter) generic rock and soil transfer functions developed for California, USA, have been adopted (Boore and Joyner 1997) and applied to the New Zealand context. For the determination of the predictive equations for FAS no assumption is made regarding the form of the site response, rather, the site response at particular frequencies is left as a regression parameter. Finally, for the determination of the predictive equation for the Arias Intensity, simple multipliers are adopted to take into account the various site categories.

At this point, it will suffice to incorporate these site amplification terms into our model simply as some function of frequency, $S(f)$. In addition to these generic transfer functions, and in keeping with other authors, it is common practice to include a factor to account for the effects of the free surface on the wave amplitudes. In most models for the Fourier amplitude spectrum, particularly for those derived for use in stochastic applications (see Boore (2003), and references therein), this effect is represented by a parameter, $F = 2$, corresponding to the case of vertically propagating waves.

B.3.4. The Model for the Fourier Amplitude Spectrum

The final functional form of the model can then be written as follows (note again that the case of SV waves is presented).

$$\mathbf{U}^{SV}(\mathbf{x},\xi,f,\mathbf{M},\boldsymbol{\theta}) = \frac{\Omega_0^{SV}(\mathbf{x},\xi,\mathbf{M},\boldsymbol{\theta})}{\left[1+\left(f/f_c(\mathbf{M})\right)^2\right]} \frac{1}{\mathfrak{R}^S(\mathbf{x},\xi)} \exp\left[\frac{-\pi f R}{Q(f)c_Q}\right] S(\mathbf{x},f) \tag{B.3.34}$$

In Equation (B.3.34) above, as well as specifying the functional form of the model, the dependence of terms on fundamental parameters has also been shown. Now, the zero-frequency spectral amplitude, as well as encompassing the seismic moment also includes the previously mentioned effects of the radiation pattern and free surface. This term can therefore be defined by Equation (B.3.35) below.

$$\Omega_0^{SV}(\mathbf{x},\xi,\mathbf{M},\boldsymbol{\theta}) = \frac{\mathbb{R}^{SV}(\mathbf{x},\xi,\boldsymbol{\theta}) F M_0(\mathbf{M})}{4\pi\bar{\rho}(\mathbf{x},\xi)\bar{\beta}(\mathbf{x},\xi)^3} \tag{B.3.35}$$

In both Equation (B.3.34) and Equation (B.3.35) the vector $\boldsymbol{\theta}$ represents the set of parameters defining the orientation of the fault source (strike, dip, and rake). The dependence of the corner frequency upon the moment magnitude, included in Equation (B.3.34), is an important dependence and one that will be the focus of the next chapter.

The theoretical development presented in this chapter begins with the representation theorem in the time domain and proceeds, via various manipulations, into the frequency domain, before ending in the base expression for the Fourier Amplitude Spectrum (FAS) of displacement. This base model for the FAS will be utilised in the three chapters to follow the present one. When obtaining the predictive equations for the Fourier Amplitude Spectrum and Arias Intensity the FAS of acceleration, rather than displacement will be required. For completeness the FAS of acceleration is given here with respect to the FAS of displacement in Equation (B.3.36) below, noting that in the frequency domain time differentiation corresponds to multiplication by frequency.

$$\ddot{\mathbf{U}}^{SV}\left(\mathbf{x},\boldsymbol{\xi},f,\mathbf{M},\boldsymbol{\theta}\right)=\left(2\pi f\right)^{2}\mathbf{U}^{SV}\left(\mathbf{x},\boldsymbol{\xi},f,\mathbf{M},\boldsymbol{\theta}\right) \tag{B.3.36}$$

Here, $\ddot{\mathbf{U}}^{SV}\left(\mathbf{x},\boldsymbol{\xi},f,\mathbf{M},\boldsymbol{\theta}\right)$ represents the FAS of acceleration. It is this term for which a regression model based upon New Zealand strong motion data will be derived in Chapter Five of this section.

B.4. Moment Magnitude – Corner Frequency Relationship for New Zealand

B.4.1. Introduction

At the close of the previous chapter it was stated that the magnitude dependence of the corner frequency term was an important one. In this chapter, the base model for the FAS developed previously will be used in conjunction with existing focal mechanism solutions, simple ray tracing procedures, and Monte Carlo simulation methods to determine the parameters of a predictive equation for the corner frequency as a function of magnitude. The functional form of the model has a well known theoretical basis. The parameters of this relation will be based solely upon New Zealand strong ground motion records and will make use of a linear mixed effects model. The relationship thus derived will be suitable for estimating corner frequencies of Fourier Amplitude Spectra from earthquakes occurring throughout New Zealand. The results of this section of work will also be employed to aid in the determination of the predictive equations for FAS and Arias Intensity in the chapters to follow.

B.4.2. Theoretical Background

The starting point of the development of the moment magnitude – corner frequency relationship is the final form of the FAS of displacement expression arrived at in the previous chapter. This model is repeated below in Equation (B.4.1).

$$\mathbf{U}^{SV}\left(\mathbf{x},\xi,f,\mathbf{M},\boldsymbol{\theta}\right)=\frac{\Omega_0^{SV}\left(\mathbf{x},\xi,\mathbf{M},\boldsymbol{\theta}\right)}{\left[1+\left(f/f_c\left(\mathbf{M}\right)\right)^2\right]}\frac{1}{\Re^S\left(\mathbf{x},\xi\right)}\exp\left[\frac{-\pi fR}{Q(f)c_Q}\right]S\left(\mathbf{x},f\right) \tag{B.4.1}$$

The expression above can be partitioned into components representing three distinct phases in the life of a seismic wave; its emergence from the source, its propagation through the earth, and its arrival at the surface of the earth. The goal of this chapter is to determine a generic relationship to describe the source spectrum of seismic waves. One can appreciate from Equation (B.4.1) that the source spectrum may be recovered from an observed strong motion record once the effects associated with the site response and the wave propagation are removed. This notion is expressed in Equation (B.4.2) below.

$$\begin{aligned}\Omega^{SV}\left(\mathbf{x},\boldsymbol{\xi},f,\mathbf{M},\boldsymbol{\theta}\right) &= \frac{\Omega_0^{SV}\left(\mathbf{x},\boldsymbol{\xi},\mathbf{M},\boldsymbol{\theta}\right)}{\left[1+\left(f/f_c\left(\mathbf{M}\right)\right)^2\right]} \\ &= \frac{\mathbf{U}^{SV}\left(\mathbf{x},\boldsymbol{\xi},f,\mathbf{M},\boldsymbol{\theta}\right)\Re^{S}\left(\mathbf{x},\boldsymbol{\xi}\right)}{S\left(\mathbf{x},f\right)}\exp\left[\frac{\pi fR}{Q(f)c_Q}\right]\end{aligned} \tag{B.4.2}$$

From this point forward, we may relax the formal nature of the two equations above. The source spectrum can therefore be restated simply as in Equation (B.4.3).

$$\Omega^{SV}\left(f\right) = \frac{\Omega_0^{SV}}{1+\left(f/f_c\right)^2} \tag{B.4.3}$$

The source spectrum can therefore be fully described by two parameters, the zero frequency displacement spectral amplitude, Ω_0^{SV}, and the corner frequency, f_c. The theoretical expression for the zero frequency spectral amplitude was presented at the end of the previous chapter; it involves parameters that are typically available, or that can be estimated to reasonable precision. The estimation of the corner frequency is not so simple.

Various methods exist for estimating the corner frequency from a recording of strong ground motion. These methods range from the relatively subjective procedure of visually picking the corner frequency, to more objective and systematic estimation techniques such as spectral integration methods. Any automated picking procedure should be validated by visual inspection to ensure that the resulting corner frequencies appear reliable.

In this study the spectral integration techniques of Andrews (1986) and Snoke (1987) are employed with slight modification. In the original formulation of Andrews (1986), the corner frequency and zero frequency spectral amplitude were described as functions of the power spectra of velocity and displacement. The original method required integration of the square of the velocity and displacement spectra over the entire positive range, $[0,\infty)$, of real frequencies. However, actual recorded spectra are limited in bandwidth due to physical restrictions associated with the recording instrument and its locality, such as the sampling frequency and background noise levels. The integration is therefore only possible over this limited bandwidth. Snoke (1987) recognised this and suggested approximate corrections for both the low and high pass filter limits. In Snoke's formulation, the integration of the velocity power spectrum is modified above and below the band pass limits as given by Equation (B.4.4).

$$J = 2\int_0^{\infty} |V(f)|^2 \, df$$
$$J = \frac{8}{3}\pi^2 \Omega_0 f_1^3 + 2\int_{f_1}^{f_2} |V(f)|^2 \, df + 2|V(f_2)|^2 f_2 \qquad \text{(B.4.4)}$$

In the above expression, $V(f)$ is the Fourier Amplitude Spectrum of velocity, and f_1 and f_2 are the high-pass and low-pass band limits respectively. Note that the correction terms are determined by assuming that the Fourier amplitude spectrum of displacement is constant below the high-pass limit and falls of as f^{-2} above the low-pass limit, consistent with the assumptions in our model. Equation (B.4.4) also includes Ω_0, the zero frequency spectral amplitude of displacement, and this term is at this point an unknown. It is possible to approximate Ω_0 from the band limited spectra, but the appropriateness of this approximation depends upon the magnitude of the corner frequency in relation to the high-pass band limit. If the corner frequency is lower than the high pass limit then the zero frequency spectral amplitude may be significantly underestimated. For large magnitude events, the associated corner frequency will be low and will frequently be lower than the high pass filter limit. Consequently, some other method to estimate the zero frequency spectral amplitude of displacement would be preferable for these large events.

Snoke (1987) provides a method for deterministically estimating this zero frequency spectral amplitude based again upon spectral integration techniques. However, this method requires selecting specific spectral amplitudes corresponding to the band limits and raises the question of how to systematically select such levels, particularly where the spectra fluctuate significantly, or where the corner frequency is below the high-pass limit. To address these issues, an alternate method for estimating the zero frequency spectral amplitude is proposed that incorporates a ray tracing procedure coupled with a Monte Carlo simulation technique. This procedure will be described in detail presently.

Once the value of Ω_0 has been estimated, the corner frequency can be estimated in turn using Equation (B.4.5).

$$f_c = \left[\frac{J}{2\pi^3 \Omega_0^2} \right]^{1/3} \qquad \text{(B.4.5)}$$

Once every record that is considered has been processed, and the above method applied one has a set of magnitude, corner frequency pairs. This data can then be used to obtain the relationship that is the goal of this chapter. In Equation (B.4.2) the corner frequency was written as a function of moment magnitude. To see how one arrives at this dependence it is worth briefly recapitulating the work of Brune (1970; 1971).

As previously defined, the seismic moment is a function of the average slip across some dislocating region of a fault. Assuming that this dislocating region is circular with radius, r, the average slip can be shown to

be a function of the difference in stress across this region before and after the rupture, $\Delta\sigma$ (the stress drop, or stress parameter, see Atkinson and Beresnev (1997)).

$$\bar{u} = \frac{\Delta\sigma}{\mu} r \frac{16}{7\pi} \tag{B.4.6}$$

The radius of this circular rupture is also constrained by the velocity of rupture propagation and the rise time (or equivalently the corner frequency). This constraint is detailed below.

$$r = \frac{2.34\beta}{2\pi f_c} \tag{B.4.7}$$

It should be noted that the specific values given in the original formulae of Brune are subject to several assumptions of varying validity. This issue, and the sensitivity of the final results to these assumptions, are discussed candidly by Beresnev (2001). For now however, we will continue following Brune; substituting Equation (B.4.6) and Equation (B.4.7) into $M_0 = \mu A \bar{u}$ and rearranging terms in order to solve for the corner frequency yields the expression in Equation (B.4.8) below.

$$f_c = \frac{2.34}{2\pi}\left(\frac{16}{7}\right)^3 \beta \left(\frac{\Delta\sigma}{M_0}\right)^{\frac{1}{3}} \tag{B.4.8}$$

In Equation (B.4.8), the stress parameter is specified in units of bars, while the seismic moment has units of dyne-cm. All that remains in order to yield a relationship for the corner frequency in terms of moment magnitude is to substitute the relevant expression for the seismic moment in terms of moment magnitude, i.e. $\log_{10} M_0 = \frac{3}{2}\left(\mathbf{M} + 10.7\right)$. Doing this, as well as some rearranging yields a relationship of the following form,

$$f_c = C_{f_c} \beta \left(\frac{\Delta\sigma}{10^{16.05}}\right)^{\frac{1}{3}} \left(10^{-0.5\mathbf{M}}\right) \tag{B.4.9}$$

where C_{f_c} is simply a coefficient combining the various constants in Equation (B.4.8); for the Brune case, this coefficient takes a value of 4.9×10^6. Finally, taking logarithms enables one to work with a decidedly simpler equation.

$$\log_{10} f_c = \underbrace{\log_{10}\left(C_{f_c}\beta\right) - \frac{1}{3}\left(16.05\right) + \frac{1}{3}\log_{10}\Delta\sigma}_{\text{terms encapsulating various assumptions}} - 0.5\mathbf{M} \tag{B.4.10}$$

For practical purposes, the terms encapsulating the various assumptions of the Brune (1970; 1971) model (as well as those of Hanks and Kanamori (1979)) can be combined into one parameter that we will look to determine from the New Zealand strong motion dataset, a_{f_c}. The functional form of the magnitude-

corner frequency relationship originally introduced in Equation (B.4.10) is therefore given by Equation(B.4.11).

$$\log_{10} f_c = a_{f_c} - 0.5\mathbf{M} \tag{B.4.11}$$

A relationship thus obtained will provide a fundamental component of a total predictive equation for strong ground motions. In what follows, a robust method for estimating the value of the parameter a_{f_c} in equation (B.4.11) will be outlined.

As was mentioned earlier, the key to obtaining the parameter defining the corner frequency relation lies in being able to accurately determine the zero frequency spectral amplitude of displacement. In the previous chapter a theoretical expression for this term was given; it is repeated here in simplified form in Equation (B.4.12). The expression presented applies to SV waves, naturally, a similar expression exists for SH waves as well.

$$\Omega_0^{SV} = \frac{\mathbb{R}^{SV} F M_0}{4\pi\bar{\rho}\bar{\beta}^3} \tag{B.4.12}$$

The ability to estimate the zero frequency spectral amplitude therefore depends upon ones ability to estimate the radiation pattern associated with each strong motion record. The other remaining parameters are all fundamental elements of obtaining focal mechanism solutions for earthquake events. It has previously been mentioned that along with routine determination of such focal mechanism solutions, independent researchers also obtain generally refined estimates of the focal mechanism solutions. These solutions will form the source of the values assigned to all of the parameters required in the above equation, with the exception of the radiation pattern term.

In the previous chapter theoretical formulae for the radiation patterns for P, SV, and SH waves were derived. These terms were seen to be functions of the fault plane geometry, of the direction of dislocation over this fault surface, and of the orientation of the rays that departed the source. Focal mechanism solutions provide estimates of the orientation of the fault plane as well as the direction of the slip vector over this plane. The only unknown parameter in the expressions for the radiation patterns are the take-off angles of the rays that depart the source and arrive at the site. If one can calculate the relevant values of the take-off angles that correspond to rays that reach the recording site then one may determine the radiation pattern, determine the zero frequency spectral amplitude, and consequently estimate the corner frequency. The goal the present analysis is therefore to determine appropriate values of the take-off angles for each strong motion record.

Unfortunately, this problem is not as simple as it initially appears as the solution is non-unique. The anisotropy of the earth's crust means that rays may leave the source and reach the site via a myriad of

pathways. Each pathway involves a varying number of reflections and transmissions across material interfaces.

B.4.3. Simplified Ray Tracing Procedure

Ray tracing is a procedure whereby one traces the path of a seismic ray leaving the source as it propagates through the crust. The path that the ray travels depends upon the nature of the crust. Rays will change their direction where they experience changes in impedance as well as when they interact with heterogeneities in the crust. These heterogeneities can be thought of as being fractal in nature, with many more at a small scale than at a large scale. The degree to which the rays interact with these heterogeneities is related to the wavelength (frequency) of the wave, with high frequencies being scattered far more than low frequencies. This effect cannot be taken into consideration directly for both practical and theoretical reasons. There is some potential for these effects to be incorporated in a stochastic framework but this not directly dealt with in this analysis.

The nature of the crust for this analysis is assumed to be a horizontally layered isotropic homogeneous elastic halfspace. A ray propagating within one layer of such a medium will travel in a straight line in three space with its amplitude attenuating as $1/R$; this attenuation rate being a requirement of the conservation of energy over a spherical surface. However, when this ray reaches a material interface, across which there is some change in impedance, the direction of the ray will be altered, and as a consequence of this, the amplitude of the wave will also be modified. The law that governs the nature of this amplitude and direction change is commonly known as Snell's Law.

We must now consider how the amplitude and direction of waves interacting with a material interface are modified. As a seismic ray travels across a material interface where the density and/or velocity (the seismic impedance) changes the ray is scattered. This scattering must occur in order for the two materials at the boundary to remain in contact as the wave passes. Formally, the horizontal slowness of the propagating wave must be conserved between like waves in the two materials as well as between differing wave types in the two materials. This is a fundamental assumption of Snell's Law and can be represented by the following equation.

$$p = \frac{\sin i_1}{\alpha_1} = \frac{\sin i_2}{\alpha_2} = \frac{\sin j_1}{\beta_1} = \frac{\sin j_2}{\beta_2} \tag{B.4.13}$$

In Equation (B.4.13), p is termed the ray parameter (horizontal slowness), i_1 is the angle of incidence (and reflection) of a P wave in material one, i_2 is the angle of transmission of a P wave passing into material two, j_1 is the angle of incidence (and reflection) of an S wave in material one, while j_2 is the

angle of transmission of an S wave passing into material two. In all the above cases, the angle is measured from the vertical (in the case of horizontal layering).

The nature of the scattering differs for *SV* and *SH* waves. In both cases however, some energy is transmitted into the next layer while some is reflected back into the layer from which the wave came. The relationships defining these interactions are governed by Snell's Law. The difference between the *SV* and *SH* wave types exists due to the nature of the motion of the two waves. For the case of the *SV* waves, motion occurs in the vertical plane, i.e. in the plane coincident with the direction of the change in impedance. Because the angle of transmission and reflection are not equal (as described by Equation (B.4.13)), *P* waves must be generated to ensure continuity at the material interface. For the case of *SH* waves the motion is horizontal (perpendicular to the plane in which the impedance changes) and therefore continuity is maintained across a boundary. Incident *SH* waves consequently only generate transmitted and reflected *SH* waves. This scattering process is shown diagrammatically for downwards and upwards travelling SV waves in Figure B.4.1 below.

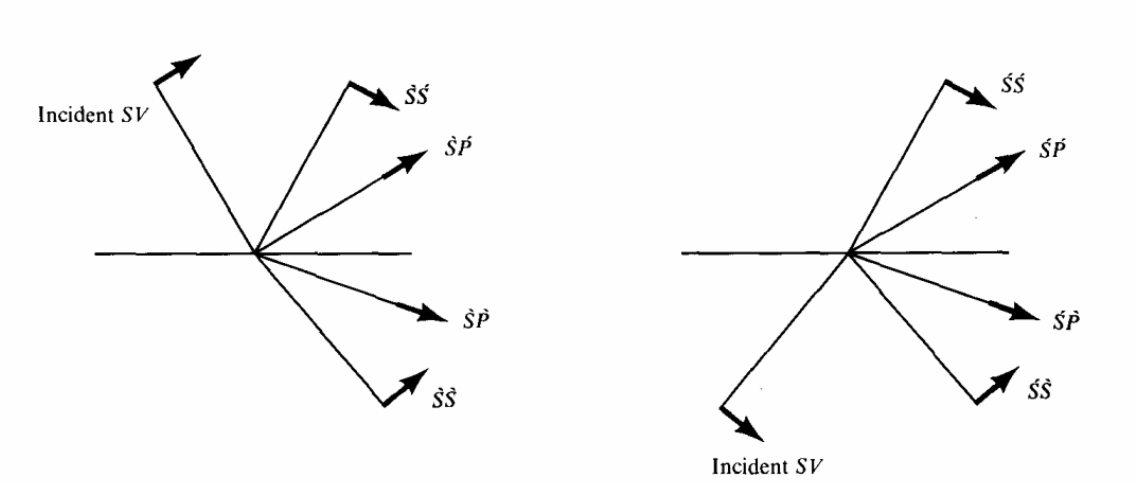

Figure B.4.1: Schematic illustration of the scattering of *SV* waves at a material interface. The figure on the left depicts a downwards travelling *SV* wave propagating into a material with increased impedance. The figure on the right depicts the case where the ray propagates from the high impedance layer upwards into the lower impedance layer (from Aki and Richards, 1980).

The degree to which total initial energy possessed by the incident wave is partitioned to the various resultant wave types is defined by a scattering matrix. The scattering matrices in this analysis describe the displacement amplitudes of the waves. Different scattering matrices exist for differing cases, i.e. incident SV wave upon a material – material interface, or incident SH wave upon a material – air interface (free surface), etc. The elements of the scattering matrix define the displacement amplitude of the created wave components as a ratio of the displacement amplitude of the initial wave. The most general case of the material – material scattering matrix in the vertical plane (the $P-SV$ case) is given in Equation (B.4.14) below. The scattering matrix given in Equation (B.4.14) takes into account the required modification of the base scattering terms to ensure conservation of energy flux across the material interfaces.

The individual elements of the scattering matrix, $\mathbf{S}$, can be interpreted as each of the 16 possible interaction associated with the scattering process. The matrix consists primarily of terms such as $\breve{P}\hat{P}$ which corresponds to a downwards travelling P wave (direction of propagation inferred from the modifier of the character, i.e. $\breve{P}$ is downwards, while $\hat{P}$ is upwards) being converted into an upwards travelling P wave. The additional square root terms containing material parameters and ray angles are the modifying terms to account for the conservation of energy flux. The formulae corresponding to each of the elements of the scattering matrix for the material - material $P-SV$, and SH, cases, as well as for the free surface $P-SV$, and SH, cases are given in Appendix B2.

$$\mathbf{S}=\begin{bmatrix} \breve{P}\hat{P} & \breve{S}\hat{P}\left(\dfrac{\alpha_1\cos i_1}{\beta_1\cos j_1}\right)^{1/2} & \hat{P}\hat{P}\left(\dfrac{\rho_1\alpha_1\cos i_1}{\rho_2\alpha_2\cos i_2}\right)^{1/2} & \hat{S}\hat{P}\left(\dfrac{\rho_1\alpha_1\cos i_1}{\rho_2\beta_2\cos j_2}\right)^{1/2} \\ \breve{P}\hat{S}\left(\dfrac{\beta_1\cos j_1}{\alpha_1\cos i_1}\right)^{1/2} & \breve{S}\hat{S} & \hat{P}\hat{S}\left(\dfrac{\rho_1\beta_1\cos j_1}{\rho_2\alpha_2\cos i_2}\right)^{1/2} & \hat{S}\hat{S}\left(\dfrac{\rho_1\beta_1\cos j_1}{\rho_2\beta_2\cos j_2}\right)^{1/2} \\ \breve{P}\breve{P}\left(\dfrac{\rho_2\alpha_2\cos i_2}{\rho_1\alpha_1\cos i_1}\right)^{1/2} & \breve{S}\breve{P}\left(\dfrac{\rho_2\alpha_2\cos i_2}{\rho_1\beta_1\cos j_1}\right)^{1/2} & \hat{P}\breve{P} & \hat{S}\breve{P}\left(\dfrac{\alpha_2\cos i_2}{\beta_2\cos j_2}\right)^{1/2} \\ \breve{P}\breve{S}\left(\dfrac{\rho_2\beta_2\cos j_2}{\rho_1\alpha_1\cos i_1}\right)^{1/2} & \breve{S}\breve{S}\left(\dfrac{\rho_2\beta_2\cos j_2}{\rho_1\beta_1\cos j_1}\right)^{1/2} & \hat{P}\breve{S}\left(\dfrac{\beta_2\cos j_2}{\alpha_2\cos i_2}\right)^{1/2} & \hat{S}\breve{S} \end{bmatrix} \quad \text{(B.4.14)}$$

Now, given some assumed origin corresponding to the source of an earthquake, and some assumed crustal layering model, one can use the above scattering coefficients in conjunction with Equation (B.4.13) to determine the possible paths that a ray may take to get from the source to the site. In addition to determining the path, the scattering coefficients also dictate what portion of the initial energy is maintained by the various wave components as the wave scatters at each interface. Using this knowledge, one may propagate out a whole suite of possible solutions to what is essentially a geometrical problem and simultaneously calculate the relative amplitudes of each solution. The strongest waves are those that are most likely to govern the magnitude of the zero frequency displacement spectral amplitude and so the solutions corresponding to the waves should be predominantly used to ascertain the most appropriate value of the take-off angle.

The case of the SH waves is the simplest as one needn't consider the influence of P wave motions. The case of the SV waves is for this same reason more complicated. However, when the P waves are created due to the scattering of an SV wave, the amount of energy that the created wave receives is very small in relation to the amount partitioned to the transmitted and reflected SV waves. The P waves that are thus created also then go on to interact with material interfaces and undergo their own scattering, creating new P and SV waves. However, because the amount of energy initially associated with the P wave is always small, the energy transferred to the new waves at each interface is necessarily even smaller. Therefore, it is a reasonable assumption to ignore the influence of the P waves when tracing out the SV

wave paths. By employing this assumption, the tracing procedure for SV waves becomes similar to the SH case. One must still take into account the energy that is transferred to the P waves however when determining the energies associated with the transmitted and reflected SV waves.

One must also consider a special case. As the material impedance increases, downwards travelling waves are bent upwards; this process is shown in the left hand panel of Figure B.4.1. One must therefore consider the case where the incident wave approaches at a shallow angle itself. Figure B.4.1 shows that while the transmitted SV wave is bent upwards, the transmitted P wave is bent event more. There will be some critical angle at which the P wave will be bent beyond the horizontal and will therefore apparently not exist as a transmitted wave. This case corresponds to the creation of inhomogeneous waves. Under this condition, the transmitted wave still exists, but the terms of the scattering matrix begin to take on complex values. One must still account for the energy assigned to these inhomogeneous waves when performing the scattering procedure.

As the incident angle becomes even more shallow, there comes a point at which the SV wave will be bent to the horizontal. In this case the wave will be concentrated in travelling along the material interface as a head wave. This case often corresponds to first arrivals as the head waves travels at the velocity of the higher impedance layer and consequently arrives earlier than waves that either remain in the initial layer, or are forced to travel deeper through the high impedance layer. The different travel times of all the rays that are traced out must also be taken into account when performing the analysis as some solutions will become irrelevant if they take too long to reach the site.

The propagation of all potential rays is a potentially arduous task, but is one that can be performed with reasonably high efficiency using modern computers. An example of some typical travel paths associated with an assumed geometry is given in Figure B.4.2. Not all rays solutions are shown as the figure would become excessively cluttered. However, most of the strongest rays arriving at the site are depicted; note that the ranges of the take-off angles are generally concentrated in groups.

Given that there are so many possible rays that are able to reach the site via so many different paths, the problem of trying to select a representative take-off angle becomes relatively difficult. However, as has already been mentioned, the amplitude of each ray is modified by various factors as it travels through the crust. Firstly, the wave amplitudes attenuate as approximately $1/R$ due to spherical spreading if the real medium is close to elastic. In addition, the wave amplitudes are modified at every interaction with a material interface, with new waves being created etc. Therefore, the further the wave travels, the weaker the arriving wave will be, and the more interactions that the wave experiences, the weaker the arriving wave will be. These two conditions, coupled with the initial strengths of the departing rays which is governed by the strength of the radiation pattern can be used to assign weights to the various possible solutions. After applying these weights, a weighted average take-off angle, and consequently, a weighted average radiation pattern can be determined an assigned to the given scenario. Previously, the travel time was also mentioned. In the chapter addressing the preparation of the strong motion records it was stated that the Fourier Amplitude Spectra that were obtained from the strong motion records were taken from a

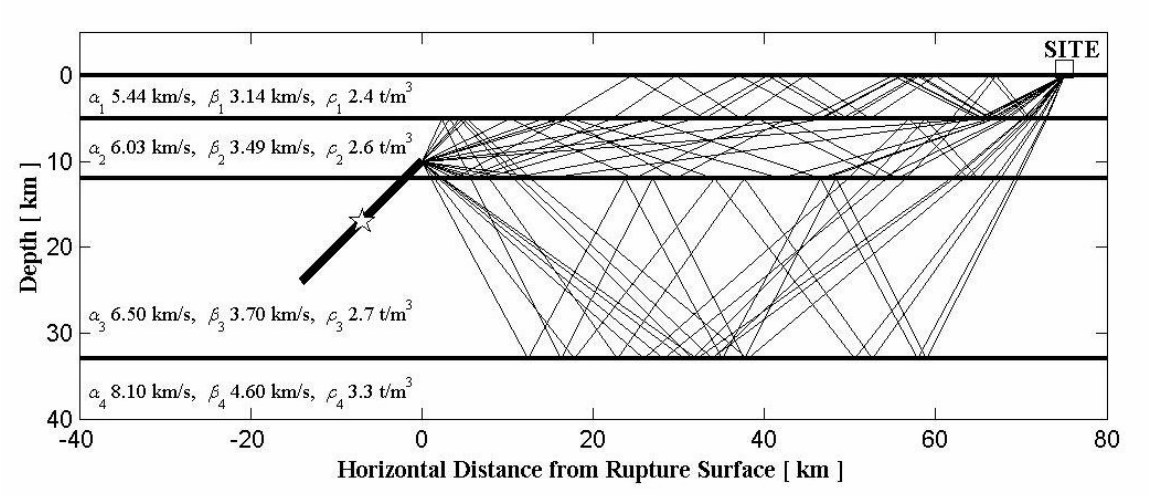

Figure B.4.2: Example of some solutions to the ray tracing problem for an assumed geometry. Note that the source is modelled as a bilateral rupture with the hypocentre marked by the pentagram.

selected window of the acceleration time series. Therefore, one should only consider rays that arrive at the site of observation during this time window if one wishes to replicate the strength of spectral amplitudes during this window.

Taking the above conditions into consideration, expressions for the weighted average of the radiation patterns can be given by Equation (B.4.15) and Equation (B.4.16) below.

$$\overline{\mathbb{R}}^{SV} = \frac{\sum_{i=1}^{n} P_i^{SV} \mathbb{R}_i^{SV} / r_i}{\sum_{i=1}^{n} P_i^{SV} / r_i} \tag{B.4.15}$$

$$\overline{\mathbb{R}}^{SH} = \frac{\sum_{i=1}^{n} P_i^{SH} \mathbb{R}_i^{SH} / r_i}{\sum_{i=1}^{n} P_i^{SH} / r_i} \tag{B.4.16}$$

In the above expression, P_i^{SV} represents the relative magnitude of the displacement amplitude after all the effects of the scattering have been taken into account. The actual value of this parameter must be determined for each specific ray solution as the interactions and magnitudes of the scattering coefficients will be different in every case. The geometric spreading is also taken into account through the r_i parameter. This parameter corresponds to the actual distance travelled by the particular ray in each case. The radiation pattern term for each case is determined from the source geometry as well as from the specific take-off angle calculated for that case.

Because the interactions at material interfaces result in the partitioning of energy, the expressions given above for the representative radiation patterns are primarily governed by the strengths of the most direct rays, as would be expected. Exceptions are possible however when the direct travel paths correspond to very low initial radiation pattern strengths.

Once the representative radiation pattern has been found for the scenario in question the corresponding zero frequency spectral amplitude can be determined from Equation (B.4.12).

B.4.4. Monte Carlo Simulation Procedure

The method for determining the representative zero frequency spectral amplitudes detailed above relies upon various assumptions. These assumptions primarily regard the geometry and material properties of the crust, the orientation of the rupture plane, and the value of the Seismic Moment assigned to each event. All of this information for a given event is available if a focal mechanism solution exists for the event. However, focal mechanism solutions can only ever be determined to a limited degree of precision (Molnar and Chen 1982). The rate of change of the theoretical radiation pattern with respect to the take-off angle at low frequencies and over certain ranges of the take-off angle can be very large. This can be appreciated from consideration of the theoretical expression for the radiation pattern presented in the previous chapter. Consequently, the value that is obtained for the zero frequency spectral amplitude may be strongly dependent upon the assumed geometry and material parameters in the model. It is therefore very desirable to take these errors into account in order to determine how sensitive the values obtained for the zero frequency spectral amplitudes really are. The problem therefore lends itself ideally to a Monte Carlo Simulation procedure in which the parameters defining the problem may be varied and a distribution of results consequently obtained.

In undertaking the ray tracing procedure we implicitly assume that the velocity structure of the crust is known. There are many uncertainties associated with this assumption. The velocity models that have been assumed in this study are typically those that have previously been used to determine focal mechanism parameters for earthquake events in New Zealand. These crustal models have been taken primarily from two sources (Doser et al. 1999; Doser and Webb 2003) and are regionally dependent. The range of take-off angles and consequently the radiation pattern terms will vary depending on the actual position of the assumed interfaces as well as with the actual position of the source within the crustal models. Incorporating this uncertainty via Monte Carlo simulation will enable us to provide error estimates upon the likely range of characteristic radiation patterns.

The Monte Carlo Simulations are run using the @RISK software package. This software package is an add on to the Microsoft Excel program. It is possible to write user defined macros in Visual Basic for Applications to work with the @RISK package. User defined macros were written in order to determine the ray tracing solutions once the geometry of the problem and other parameters were defined by the

@RISK package. The @RISK package has a range of built in distribution that can be assigned to variables and is also able to take into account correlations between variables in the model. In addition, Latin Hypercube Sampling is available to increase the efficiency of the simulations. All of these facilities are utilised in the Monte Carlo model that is set up; more comment regarding the selection of the distributions and the assignment of correlations between variables is given in the following text.

B.4.4.1. Assumed Distributions

The distributions that are assigned to the various parameters of the model must have some assumed shape. Typically a normal distribution is assumed where no other information exists regarding the nature of the parameter. For many of the focal mechanisms considered the errors in the parameter estimates are given with uneven error terms, in this case a triangular distribution has been adopted.

The critical parameters for the determination of the geometrical spreading and scattering of the seismic waves in this model are the values of the *P* and *S* wave velocities, the density of the crustal layers, and the thickness of these layers. The magnitude, and distributions, or the errors associated with each variable are important in defining the reliability of the model and due attention has consequently been paid to these.

In all cases where normal distributions are used truncations have been applied, and the appropriate renormalisation performed. This truncation has been applied at one standard deviation from the mean. This is a consequence of the asymmetrical error estimates given for various focal mechanism parameters. Triangular distributions have been assigned in these cases, not because of any particular theoretical reasoning but rather because one cannot assume any other distribution in this case. The triangular distributions are, by their definition, bounded over a finite range and consequently the variables cannot assume values outside the error bounds given from the focal mechanisms. If untruncated normal distributions were used for the symmetrically distributed errors associated with other parameters in the model then they would entertain the possibility of assigning values to the parameters that lie outside of the error estimates. Allowing some parameters to assumed values that are outside of their specified error values, while restricting others, would introduce a degree of inconsistency into the Monte Carlo simulation. This inconsistency is prevented by applying the truncations to the normal distributions and renormalizing them. A possible problem associated with limiting the values of the parameters is that critical scenarios might be neglected in the analysis. This would certainly be the case if one was looking to determine the extreme values of the radiation pattern terms. In the present case however, the goal is to find the most representative values and consequently, the truncation is more likely to aid in finding the most representative values of the radiation pattern terms.

The distributions adopted for the various parameters in the model are given in Table B.4.1. The values of the errors that have been assumed for the velocities and the densities have been assigned on the basis of the sensitivity analysis as well as prior knowledge of the accuracy of such values. The error value selected for the layer thicknesses is given as a percentage of the expected value of the layer thickness. Again, this

assignment has been made from a subjective basis but couples information gathered from the sensitivity analysis as well as prior knowledge. Layer thicknesses are determined from seismic imaging of the crust, the further you probe the more you entrain inaccuracies due to scattering and other effects. Consequently, it makes intuitive sense to relate the uncertainty to the distance that the imaging waves must travel. The layers tend to become thicker with depth; therefore, representing the error as a percentage of the expected value of the layer thickness acts to represent the increased uncertainty that is associated with making inferences at depth.

B.4.4.2. Initial Sensitivity Analysis

Because some of the error distributions that were assigned to variables were done on a primarily intuitive basis it is important to ascertain how sensitive the model results are to alterations to these error distributions. In order to gain this insight an initial sensitivity analysis was conducted.

Table B.4.1: Distributions assigned to the model parameters in the Monte Carlo Simulation

Parameter	Distribution Type	Error Value	Correlated	Variables Correlated With
M_o	Normal or Triangular†⋆	see Focal Mechanism Table	No	
z_{src}	Normal or Triangular†⋆	see Focal Mechanism Table	No	
θ	Normal or Triangular†⋆	see Focal Mechanism Table	No	
δ	Normal or Triangular†⋆	see Focal Mechanism Table	No	
λ	Normal or Triangular†⋆	see Focal Mechanism Table	No	
α_i	Normal⋆	0.1 km/s	Yes	β_i, ρ_i
β_i	Normal⋆	0.1 km/s	Yes	α_i, ρ_i
ρ_i	Normal⋆	0.05 t/m^3	Yes	α_i, β_i
z_i	Normal⋆	$0.1\times E[z_i]$	No	
a_L	Normal⋆	0.14 or 0.25‡	Yes	a_W, b_L, b_W
a_W	Normal⋆	0.14 or 0.18‡	Yes	a_L, b_L, b_W
b_L	Normal⋆	0 or 0.04‡	Yes	a_W, a_L, b_W
b_W	Normal⋆	0 or 0.03‡	Yes	a_L, a_W, b_L

† The distribution is either normal or triangular depending upon the symmetry of the error estimates
⋆ Normal distributions are truncated at one standard deviation and renormalised
‡ The first value corresponds to magnitudes below M_W 6.0, the second value to all other magnitudes

Initially a model was set up for one arbitrary scenario; one source-site pair from the 1971 Reefton Earthquake. A sensitivity analysis was conducted that considered the relative influences of the assigned errors in both *P* and *S* velocity, in the density and also in the thicknesses of the crustal layers. From this analysis it was found that the parameter with the largest influence on the zero frequency displacement spectral level for the *SV* component of motion was the error in the thickness of the crustal layers. This result agrees with intuition as alterations in the thickness of the layers creates alterations to the overall

geometry of the problem and therefore completely changes the values of the take-off angles that result in rays being recorded at the site. The error in the velocity had the next greatest influence, but it is noteworthy that this initial sensitivity analysis did not include any correlation between the *P* and *S* wave velocities. As can be seen from the terms of the scattering matrices shown in the Appendices, not including some correlation will have an influence on the relative magnitudes of the scattering terms due to a change in the way the energy is partitioned between radial and transverse components of motion. The variation in the estimate of error for the density had a very weak correlation with the variation in the final output spectral level. This fact is useful as accurate estimates of the density at large depths are difficult to constrain. The model's weak dependence upon the value of this parameter consequently circumvents this issue.

B.4.4.3. Correlations Between Variables

B.4.4.3.1. Wave Velocity Correlations

In the final Monte Carlo model the *P* and *S* wave velocities are defined as positively correlated variables. The correlation coefficient for these parameters is assumed to be 0.95, indicating a very strong positive correlation. Justification for the selection of such a correlation is provided from consideration of the velocity profiles that are used in the simulation. The velocity profiles used in this analysis are those used to determine focal mechanism solutions by Doser et al. (1999) and Doser and Webb (2003). These velocity profiles are summarised in Table B.4.2. Compiling the velocity information from these models, and calculating the correlation coefficient (as found from the variance-covariance matrix) yields a correlation coefficient of 0.98. The adopted coefficient value is relaxed in the actual simulations to 0.95 to account for some degree of variability as the values used in the determination of the coefficient are taken as absolute values.

The calculation of the correlation coefficient is made using Equations (B.4.17) and (B.4.18). Equation (B.4.17) defines the variance-covariance matrix, while Equation (B.4.18) gives the resulting matrix of correlation coefficients (Benjamin and Cornell 1970).

$$\sigma_{\alpha,\beta} = \mathrm{Cov}[\boldsymbol{\alpha},\boldsymbol{\beta}] = E\left[\left(\boldsymbol{\alpha} - \mu_{\alpha}\right)\left(\boldsymbol{\beta} - \mu_{\beta}\right)\right] \tag{B.4.17}$$

$$\rho_{\alpha,\beta} = \frac{\sigma_{\alpha,\beta}}{\sigma_{\alpha}\sigma_{\beta}} \tag{B.4.18}$$

Using an iteratively re-weighted least squares fitting algorithm, with weights defined using the bi-square function, gives the line of best fit shown in Figure B.4.3 for the plot of compiled *P* and *S* wave velocities. This line is constrained to pass through the origin, for obvious physical reasons, and gives a straight line fit having the equation $\alpha = (1.7285 \pm 0.0089)\beta$. The slope of this lines is very close to the theoretical value

given by elasticity theory for a crustal rock having Poisson's ratio equal to $\nu = 0.25$. The theoretical relationship between the *P* and *S* wave velocities is given by Equation (B.4.19).

$$\alpha = \sqrt{\frac{2(1-\nu)}{1-2\nu}}\beta \tag{B.4.19}$$

For a Poisson's ratio of $\nu = 0.25$ the expression above gives $\alpha = \sqrt{3}\beta$ (1.7321β c.f. 1.7285β above).

B.4.4.3.2. Correlations Due to the Effects of a Finite Source

A fundamental assumption of this analysis is that the Fourier amplitude spectrum of source can be described by a single corner frequency spectrum (Brune 1970; 1971). This source spectrum is derived based upon the assumption of a circular rupture surface, with the corner frequency being related to the size of the circular dislocation. However, it is generally acknowledged that this assumption does not apply for large magnitude events where the rupture surface is constrained by the thickness of the seismogenic crust. In this case it is often more appropriate to model the source spectrum using a two corner frequency model, where the two corner frequencies are related to the two dimensions of what is essentially a rectangular rupture surface (see for example Haddon 1996; Atkinson and Silva 1997). In this study there is only one large event where it is likely that the single corner frequency model may not be appropriate. It is therefore not possible to derive a two corner frequency source spectrum for New Zealand given this dataset. In order to still take into account the finite effects of the source, a generic scaling relationship for New Zealand is included in the model instead (Dowrick and Rhoades 2004). This scaling relationship gives the dimensions of the source as a function of magnitude as given by Equations (B.4.20) and (B.4.21) below.

$$\log_{10} L_{sub} = \begin{cases} (-2.19 \pm 0.14) + 0.5 M_W & \text{, for} \quad M_W < 6.0 \\ (-2.89 \pm 0.25) + (0.63 \pm 0.04) M_W & \text{, for} \quad M_W \geq 6.0 \end{cases} \tag{B.4.20}$$

$$\log_{10} W = \begin{cases} (-2.19 \pm 0.14) + 0.5 M_W & \text{, for} \quad M_W < 6.0 \\ (-1.02 \pm 0.18) + (0.31 \pm 0.03) M_W & \text{, for} \quad M_W \geq 6.0 \end{cases} \tag{B.4.21}$$

The rays that are traced from the source to the site are therefore taken from the point on this idealized rupture surface that is closest to the site (this is shown in Figure B.4.2). This distance modification is similar to that used in the hazard analysis methodology proposed by Der Kiureghian and Ang (1977). The assumption of a Brune spectrum can be further justified by considering that the energy from a fault plane is not uniformly distributed over this fault plane. The majority of the energy is released from smaller asperities that can be adequately modelled as circular fault sources using a single corner source spectrum (Somerville et al. 1999). The combination of the modified distance and a Brune spectrum can therefore be regarded as a reasonable assumption, this assumption being supported by the use of a similar model in finite fault simulation studies (Beresnev and Atkinson 1997).

Table B.4.2: Crustal Velocity models used in the Monte Carlo Simulation (models presented here have previously been used to obtain the focal mechanism solutions used in this study)

P Wave Velocity α (km/s)	*S* Wave Velocity β (km/s)	Density ρ (t/m^3)	Thickness Δz (km)
Wairarapa Region[1] (events 4, 5, 7, 8)			
3.55	2.1	2.2	4
5.35	3.15	2.4	4
5.94	3.5	2.55	5
6.29	3.7	2.65	6
6.1	3.6	2.6	6
7.49	4	3	10
8.8	4.6	3.3	60
8.9	4.7	3.5	---
Hawke's Bay Region[1] (event 13)			
3.2	1.9	2.2	5
6.2	3.65	2.63	7
5.94	3.5	2.55	21
7.22	3.95	2.9	11
8.4	4.4	3.3	---
Poverty Bay Region[1] (event 14)			
3.2	1.9	2.2	5
6.2	3.65	2.63	7
5.94	3.5	2.55	12.5
7.22	3.95	2.9	11
8.4	4.4	3.3	---
South Island[2] (events 1, 2, 3★, 9, 10, 11, 12, 13, 16)			
5.44	3.14	2.4	5
6.03	3.49	2.6	7
6.5	3.7	2.7	21
8.1	4.6	3.3	---
Fiordland Region[2] (events 6, 7, 15, 17, 18)			
5.06	3	2.3	5
6.3	3.7	2.65	10
6.58	3.87	2.7	10
6.94	4	2.75	10
7.18	4.2	2.8	15
7.48	4.4	3	15
8.06	4.6	3.3	35
8.2	4.8	3.44	---

[1] Profile taken from Doser and Webb (2003)

[2] Profile taken from Doser et al. (1999)

★ Crustal Model Assumed Similar to South Island Model for this Event

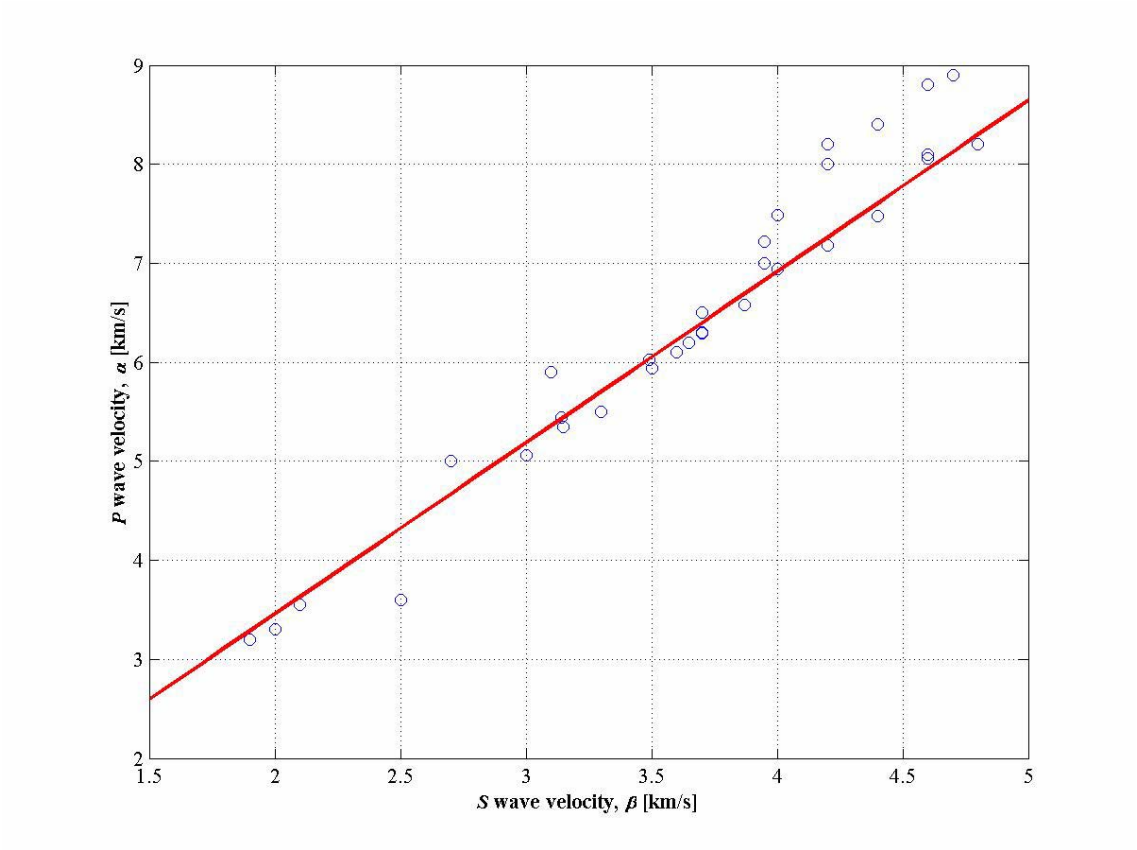

Figure B.4.3: Correlation between the *P* and *S* wave velocities in the Monte Carlo model

When this finite fault effect is implemented into the Monte Carlo model the parameters for the rupture length, L_{sub}, and rupture width, W, are assumed to be correlated. This relationship is governed by the observation that typically the length will exceed the width for a fault plane. Correlations between the parameters, a_L and b_L, and between a_W and b_W are given in Dowrick and Rhoades (2004) and are both given values of -0.996. In the model, as well as correlating the parameters within the estimates of rupture length and width, it is also desirable to define correlations between rupture lengths and widths. Independent correlation coefficients for a relationship defining an L_{sub}/W ratio are given in Dowrick and Rhoades (2004), but these coefficients cannot be incorporated into a correlation matrix as their coefficients are found from a regression on L_{sub}/W ratios rather than for a relationship that assumes *a priori* the scaling relations for L_{sub} and W independently. Consequently, the correlation matrix entries are determined using a trial and error procedure where a target L_{sub}/W ratio is desired. A target ratio of approximately 1.8 (L_{sub}/W) was desired, this corresponds well to studies considering this parameter both in New Zealand and abroad (Somerville et al. 1999; Stock 2001; Dowrick and Rhoades 2004).

The correlation coefficients for the finite source scaling are therefore given in Equation (B.4.22).

$$C_{source} = \begin{bmatrix} C_{a_L,a_L} & C_{a_L,a_W} & C_{a_L,b_L} & C_{a_L,b_W} \\ C_{a_W,a_L} & C_{a_W,a_W} & C_{a_W,b_L} & C_{a_W,b_W} \\ C_{b_L,a_L} & C_{b_L,a_W} & C_{b_L,b_L} & C_{a_W,b_W} \\ C_{b_W,a_L} & C_{b_W,a_W} & C_{b_W,b_L} & C_{b_W,b_W} \end{bmatrix} = \begin{bmatrix} 1 & 0.85 & -0.996 & -0.85 \\ 0.85 & 1 & -0.85 & -0.996 \\ -0.996 & -0.85 & 1 & 0.85 \\ -0.85 & -0.996 & 0.85 & 1 \end{bmatrix} \quad \text{(B.4.22)}$$

B.4.4.4. Sampling

For every recording in the dataset considered, all parameters defining the source mechanism (Seismic Moment, M_0, Focal Depth, z_{src}, Strike, θ, Dip, δ, and Rake, λ) are allowed to vary according to the assumed distributions given in Table B.4.1. The crustal geometry is also allowed to vary with correlated velocities and densities varying according to normal distributions. The layer thicknesses are allowed to vary according to normal distributions. For every simulation, Latin Hypercube Sampling was implemented and the model was put through 10,000 trials per simulation. During each simulation the crustal model is set as well as the focal mechanism. Given the focal mechanism the assumed fault rupture surface defined using the finite fault scaling relation is determined. The ray tracing and scattering analysis is then performed for the given geometry and the radiation patterns, zero frequency spectral levels, and actual distances travelled and travel times are determined. Also determined in the analyses are estimates of distributions for the composite density and shear wave velocity values for the path terms as well as those at the source.

B.4.5. Focal Mechanism Dataset

The proposed methodology detailed above relies heavily upon the availability of focal mechanism solutions. Focal mechanisms are not determined for every moderate to large event that occurs in New Zealand. The solutions that are computed are also not routinely collated so in order to extract the required information an extensive literature search was performed. A total of 18 earthquakes for which focal mechanisms were available could be found; these events along with the relevant parameters defining these solutions are presented in Table B.4.2. Only crustal events were considered for inclusion in the dataset; crustal events were classes as any event having a focal depth of less that 40 km. Table B.4.2 includes the references from which the focal mechanism solutions were obtained.

In addition the number of records having epicentral distances of less than or equal to 100 km are also detailed. Only events that had records that fit this catergory were included in the dataset. The reason for restricting the distance range is that the assumption of spherical spreading only holds up to a certain limit, Aki and Richards (1980) suggest that this limit is approximately twice the crustal thickness. Beyond this, strong motion records attenuate more slowly as reflections from the Moho increase the number of arrivals that are recorded and can cause constructive interference to occur. Then as the distance increases further, the strong motion records become dominated by surface waves that attenuate as $1/\sqrt{R}$. The ray tracing model that was established for this analysis aimed at targeting the spectrum of seismic waves associated with predominantly direct arrivals from the source (or rays that had minimal degrees of scattering associated

Table B.4.3: Focal Mechanism Solutions. Reference Indices are as follows, 1. Webb & Anderson (1998), 2. Anderson, Webb & Jackson (1993), 3. Doser & Robinson (2002), 4. Robinson et al. (2003), 5. Reyners & Webb (2002), 6. Harvard CMT Catalogue Solution, 7. NEIC USGS Catalogue Solution

No.	Event Name	Event Date (YYYYMMDD)	M_W	M_0 ($\times 10^{17}$Nm)		z_{src} (km)		Focal Mechanism						Ref.	No. Records ($R_{epi} \leq 100$km)
								θ (°)		δ (°)		λ (°)			
1	Inangahua Aftershock	19680524	5.78	5.3	+1.8 -1.8	11	+1 -3	179	+10 -15	49	+4 -6	72	+10 -7	1	1
2	Reefton	19710813	5.7	4	+0.5 -0.7	9	+3 -2	242	+15 -10	83	+7 -8	207	+15 -12	2	2
3	Opunake	19741105	5.44	1.6	+0.3 -0.3	17	+3 -3	195	+20 -20	41	+3 -7	213	+15 -15	1	1
4	Dannevirke	19750610	5.62	3	+0.2 -0.2	38	+2 -2	250	+10 -5	56	+5 -5	257	+5 -15	1	4
5	Cape Campbell	19770118	6.02	12	+1 -1	34	+4 -2	213	+15 -10	68	+5 -5	251	+15 -10	1	31
6	Doubtful Sound	19890531	6.33	34.5	+3.5 -2.5	24	+2 -4	26	+10 -20	48	+5 -10	148	+7 -10	2	1
7	Weber 1	19900219	6.23	25	+1 -1	23	+1 -1	220	+5 -7	86	+4 -4	316	+8 -10	1	12
8	Weber 2	19900513	6.37	40	+6 -7	11	+6 -2	182	+27 -15	35	+4 -8	111	+10 -10	1	13
9	Lake Tennyson	19900210	5.93	8.7	+0.6 -0.6	8	+2 -3	55	+10 -10	89	+5 -5	163	+5 -5	2	2
10	Hawk's Crag 1	19910128	5.78	5.3	+0.9 -0.7	10	+3 -2	42	+20 -10	30	+10 -5	99	+10 -10	2	5
11	Hawk's Crag 2	19910128	5.93	8.7	+1.7 -0.5	11	+4 -3	8	+10 -10	48	+5 -5	77	+10 -5	2	6
12	Hawk's Crag 3	19910215	5.42	1.5	+0.5 -0.5	7	+9 -4	33	+10 -10	53	+10 -10	90	+10 -10	6	4
13	Tikokino	19930411	5.62	3	+0.1 -0.3	26	+2 -2	198	+10 -10	15	+10 -10	52	+10 -10	1	4
14	Ormond	19930810	6.19	22	+3 -3	39	+2 -2	354	+10 -10	64	+5 -10	168	+10 -10	1	10
15	Secretary Island	19930810	6.82	190	+20 -20	22	+3 -3	41	+20 -20	41	+5 -5	107	+10 -10	5	2
16	Arthur's Pass	19940618	6.75	150	+25 -25	4	+2 -2	220	+5 -5	47	+5 -5	112	+5 -5	3	3
17	Thompson Sound	20001101	6.17	20	+6 -6	18	+2 -2	171	+10 -5	57	+5 -5	59	+10 -10	4	1
18	Fiordland	20030821	7.15	600	+100 -100	30	+3 -3	215	+15 -15	67	+10 -10	96	+15 -15	6,7	3

with them). It was for this reason that the time window was restricted when obtaining the Fourier Amplitude Spectra, and for limiting the number of interface encounters that the rays were able to experience. While the adopted limit of 100 km is slightly larger than the limit suggested by Aki and Richards (1980) there is no model that accounts for differential rates of attenuation for New Zealand. Consequently, the value chosen was done so on an intuitive basis. The validity of this assumption will be checked in the next chapter where the predictive model for the Fourier Amplitude Spectra is derived.

Given the restrictions upon the records that were included in the dataset, a total of 105 strong motion records were available. Both the radial and transverse horizontal components from each record were considered because the use of theoretical radiation pattern means that a separate zero frequency spectral amplitude can be determined for each component. Consequently, a total of 210 component of strong ground motion were included in the dataset.

In addition to the correction for geometrical spreading that must be made, corrections for anelastic attenuation and site effects must also be made in order to obtain estimates of the source spectrum for each record. These corrections must be made in accord with Equation (B.4.2). At this point however, little is know regarding the nature of anelastic attenuation and site response for New Zealand earthquakes. Consequently, generic relations are applied to back calculate the source spectra.

In Equation (B.4.1) the effect of anelastic attenuation and site response are presented as being two separable terms. However, in reality site response is merely the final part of the overall propagation of seismic waves as they travel from the source to the recording site. Seismic waves undergo extensive attenuation as they approach the near surface, particularly at high frequencies. This is thought to be a result of the decreasing lithospheric pressure allowing fractures to open in the near surface crust. This increases the amount material heterogeneity and therefore the amount of scattering (Abercrombie 1998). As high frequency components of motion are able to be scattered by small heterogeneities it is natural that these high frequency components should experience significant attenuation. The effect that this near surface attenuation has upon the observed spectra is almost indistinguishable from the more typical anelastic attenuation typically associated with the full propagation path through the crust. In most modern studies of ground motion spectra, the near surface attenuation is incorporated into the site response. This has the effect balancing the overall contribution from site response as the general amplification of ground motion due to the softer near surface deposits is countered by the increasing amount of scattering and attenuation due to these same deposits (and the shallow crust). Most models of site response therefore take on a relatively flat broadband response[†]. Boore and Joyner (1997) determine some generic site response profiles by assuming velocity and density profiles and applying the quarter wavelength approximation to determine the site response for a range of frequencies. They include suggested generic site responses for the various categories in the NEHRP (Building Seismic Safety Council (BSSC) 1994) scheme. These generic profiles

[†] Here, by flat, the implication is of amplifications for soil sites, with respect to rock, on the order of two to three. While such magnitudes vary with frequency, these variations are relatively flat in comparison to the exponential type response that the near surface attenuation has on the spectra.

are adopted in the present study to account for the site response term. How suitable it is to use site response profiles that have been derived for a western United States context is not knowable. However, given that the goal is to obtain representations of the source spectra of the strong motion records one must account for the effects of site response in some way. The method currently being employed, of adopting generic Californian site response functions, has been adopted in other situations where site response profiles were not available (for example Margaris and Boore 1998). It is also worth noting that the most significant modifications to the base spectra that occur due to the site response profiles occur at high frequencies. When eventually evaluating the integral of the power spectrum of velocity, in order to determine the corner frequencies for each record, this high frequency range will contribute only a small fraction to the value of the integral.

In order to apply the generic site response profiles of Boore and Joyner (1997) one must relate the site categories of the NEHRP classification scheme to those used in New Zealand. This issue has previously been addressed with respect to the inclusion of foreign strong ground motion records in the datasets for regression analysis. For the purposes of the present component of work, the New Zealand site class A was assumed to correspond to the generic rock category of the Boore and Joyner (1997) paper. New Zealand class B was assumed equivalent to NEHRP category C, while New Zealand class C was assumed equivalent to the generic soil category. By adopting these site response profiles, the appropriate correction to the observed spectra implied by Equation (B.4.2) can be made. Once this operation is performed the only remaining correction that must be made is to correct for the effects of the anelastic attenuation along the path of the seismic waves.

There is considerable evidence in the existing literature that the function $Q(f)$ representing the anelastic attenuation should be frequency dependent (see Abercrombie 1998 and references therein). However, there is also evidence that the effects of anelastic attenuation are adequately modelled using a frequency independent anelastic attenuation parameter (see, for example Olafsson 1999). The use of a frequency independent scaling factor is particularly suitable when one wishes to account for the effects of the near surface attenuation as part of the overall path response. Anderson and Hough (1984) showed that a good approximation that meets this end can be achieved by fitting a straight line to the high frequency part of the spectrum in log-linear space (logarithmic spectral amplitudes plotted against linear frequency). This method is adopted here in order to correct for the anelastic losses incurred along the entire path. The method is adopted primarily due to its simplicity. The anelastic scaling parameter that is sought, κ_Q, is made to be a linearly increasing function of distance. This relation comes about through consideration of the general form of the anelastic loss term and the near surface site diminution that is commonly adopted (Boore 2003). In addition, waves that travel larger distances tend to penetrate deeper into the crust to regions where anelastic losses typically decrease, therefore one should expect that the perceived amount of anelastic loss will increase approximately linearly with distance (Olafsson 1999). These effects are generally accounted for using the functional form given below.

$$\exp\left[-\frac{\pi fR}{Q(f)c_Q}\right]\exp\left[-\pi\kappa_0 f\right] \Rightarrow \exp\left[-\pi f\left(\frac{R}{Q(f)c_Q}+\kappa_0\right)\right] \tag{B.4.23}$$

Because the anelastic function term is assumed to be frequency independent (i.e. $Q(f) \equiv Q_0$), one can see that the scaling factor κ_Q is equivalent to the following expression.

$$\kappa_Q(R) = \kappa_0 + \frac{R}{Q_0 c_Q} \tag{B.4.24}$$

For every record in the dataset that was considered a log-linear fit was made to the high frequency part of the spectra (typically $f > 2-5$ Hz, depending upon the magnitude of the event), thus obtaining a dataset of κ_Q values. A robust fit was then made to the data with respect to distance using the same weighted least squares algorithm that was implemented for the wave velocity correlations mentioned earlier. This fit is shown diagrammatically in Figure B.4.4. There is a large amount of scatter associated with this fit, but the parameters that are consequently obtained are within the bounds of parameters that have been obtained for other regions throughout the world (for example Boore et al. 1992; Margaris and Boore 1998; Chen and Atkinson 2002). The fitted line in Figure B.4.4 is given in Equation (B.4.25) below.

$$\kappa_Q = (0.0504 \pm 0.0043) + (3.706\times10^{-4} \pm 0.628\times10^{-4})R \tag{B.4.25}$$

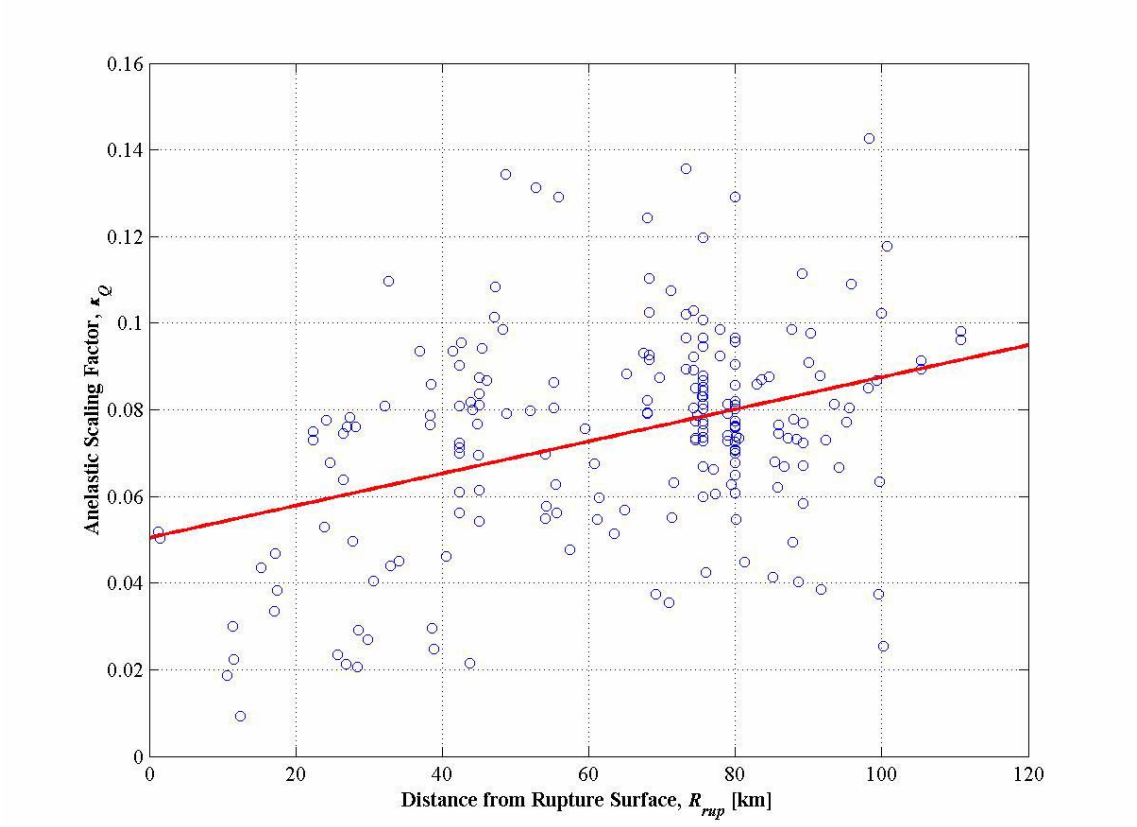

Figure B.4.4: Plot of the anelastic scaling parameter against distance for all of the records in the dataset

By applying the relevant corrections discussed in this section to each of the 210 strong motion components in the dataset one obtains a dataset of displacement source spectra. These displacement source spectra are then converted to velocity source spectra in order to perform the integrations required by Equation (B.4.4) in order to obtain the corner frequencies.

B.4.6. Model Results

Following the procedure detailed in this chapter thus far, 210 source spectra were obtained, and from these 210 estimates of the zero frequency displacement spectral amplitude were made, and correspondingly, 210 estimates of the corner frequency. Each of these points correspond to a particular magnitude earthquake and this compilation of data can therefore be used to determine the parameter a_{f_c} of Equation (B.4.11). From consideration of Table B.4.3 it can be seen that the various events included in the dataset contribute significantly different numbers of components to the dataset. There is therefore a large potential for the components from earthquakes such as the Cape Campbell earthquake to bias the determination of the a_{f_c} parameter if standard regression techniques are employed. To circumvent this problem a linear mixed effects model was employed. These models were mentioned briefly in the previous chapter and they will receive further attention in the next chapter. For the present, the regression model will simply be specified and the corresponding results presented. The nonlinear mixed effects package of the freeware program R was used to perform the regression (Pinheiro et al. 2005), the linear mixed effects model implemented in this package is based upon the theory outlined in Lindstrom and Bates (1988).

The regression model is a very simple one and is described in Equation (B.4.26).

$$\log_{10} f_{c,ij} = a_{f_c} - 0.5M_{W,i} + \eta_i + \varepsilon_{ij} \tag{B.4.26}$$

Here, $f_{c,ij}$ represents the corner frequency determined from the j^{th} component of the i^{th} earthquake in the dataset. The error in the estimation is partitioned between two terms, an inter event term, η_i, and an intra event term, ε_{ij}. Both of these individual error terms are assumed to be normally distributed with standard errors of τ and σ respectively. The total error for the model is subsequently defined as $\sigma_T = \sqrt{\tau^2 + \sigma^2}$. Upon implementing this model, the optimal parameter describing the magnitude scaling of the corner frequency was found to be that given below in Equation (B.4.27).

$$a_{f_c} = 2.645 \pm 0.046 \tag{B.4.27}$$

The fit to the data of this model is shown in Figure B.4.5. From visual inspection it appears that a better fit would be obtained by relaxing the theoretical constraint placed upon the magnitude scaling. However,

this impression is accentuated due to the isolated misfit points at larger magnitudes. It should be kept in mind that the single corner frequency source spectral model is expected to perform poorly when modelling source spectra from large earthquakes. If the theoretical constraint on the magnitude scaling was, in fact, inappropriate then the plot of the inter event residuals given in panel (b) of Figure B.4.6 would show a non horizontal trend. While a straight line fitted to this data would have a positive slope, the observed distribution of inter event residuals about zero appears to be reasonably even. Given the limited number of events considered in the formulation of the model, the model thus far derived appears to do a reasonable job of modelling the moment magnitude – corner frequency relationship for New Zealand earthquakes.

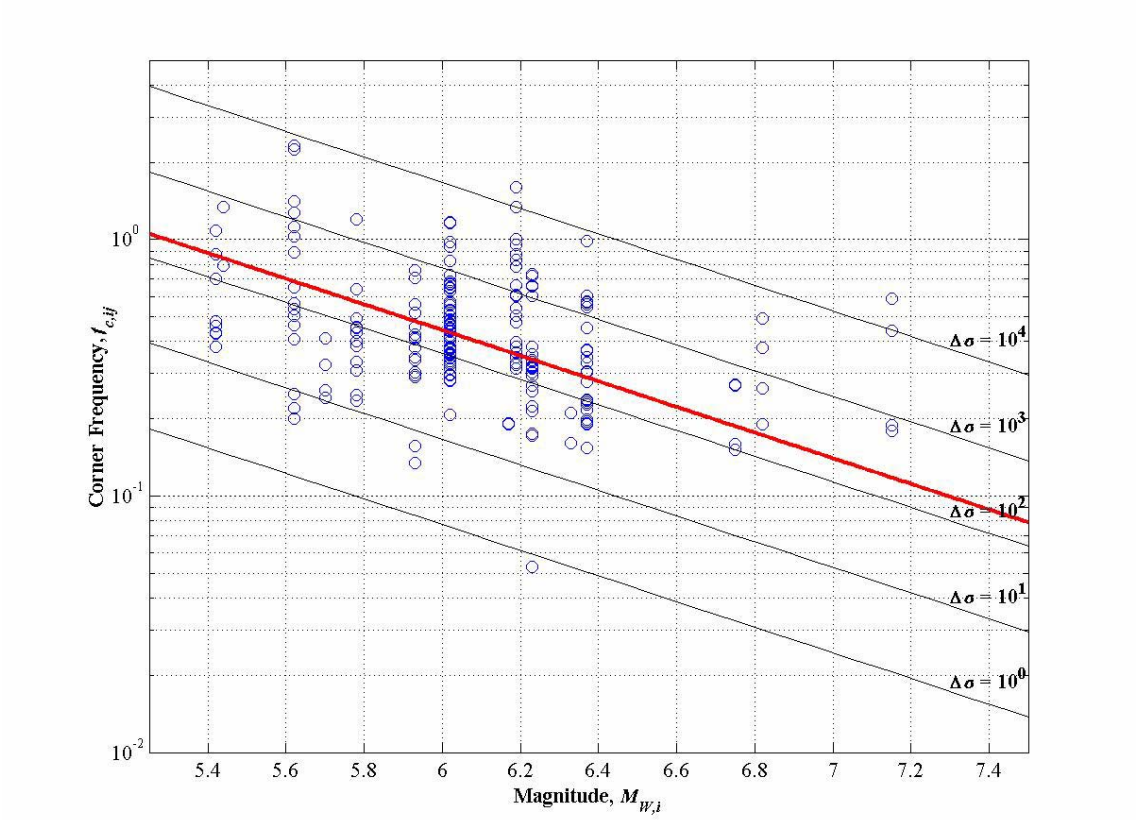

Figure B.4.5: Fit of the Moment Magnitude - Corner Frequency relationship to the processed empirical data. Solid black lines indicate lines of constant stress drop, the values given are in units of bars.

Figure B.4.5, as well as showing the fit to the data of the model, shows lines corresponding to constant values of the stress parameter, $\Delta\sigma$ (commonly called the stress drop). Based upon the coefficient determined from the linear mixed effects regression model the most representative value of the stress parameter for the earthquakes included in the present data set would be approximately 195 bars as determined from Equation (B.4.28). The value of this parameter is very sensitive to changes in the coefficient obtained in Equation (B.4.27). For example, even though the standard error estimate of this parameter of 0.046 may be considered reasonably tight, if the a_{f_c} parameter is changed in Equation (B.4.28) by this amount the resulting range of stress parameter values that one obtains is approximately 140 - 270 bars; quite a considerable range.

$$\Delta\sigma = \frac{f_c^3 M_0}{\left(4.9\times10^6\beta\right)^3} \Rightarrow \frac{10^{3a_{fc}+16.05}}{\left(4.9\times10^6\beta\right)^3} \tag{B.4.28}$$

Kanamori and Anderson (1975) suggested that interplate earthquakes would have values of the stress parameter of approximately 30 bars, while intraplate earthquakes would have values of approximately 100 bars. However, as Lay and Wallace (1995) point out, while most earthquakes have stress drops between 10 and 100 bars, it is not unusual to observe order of magnitude variations up, or down, of this range.

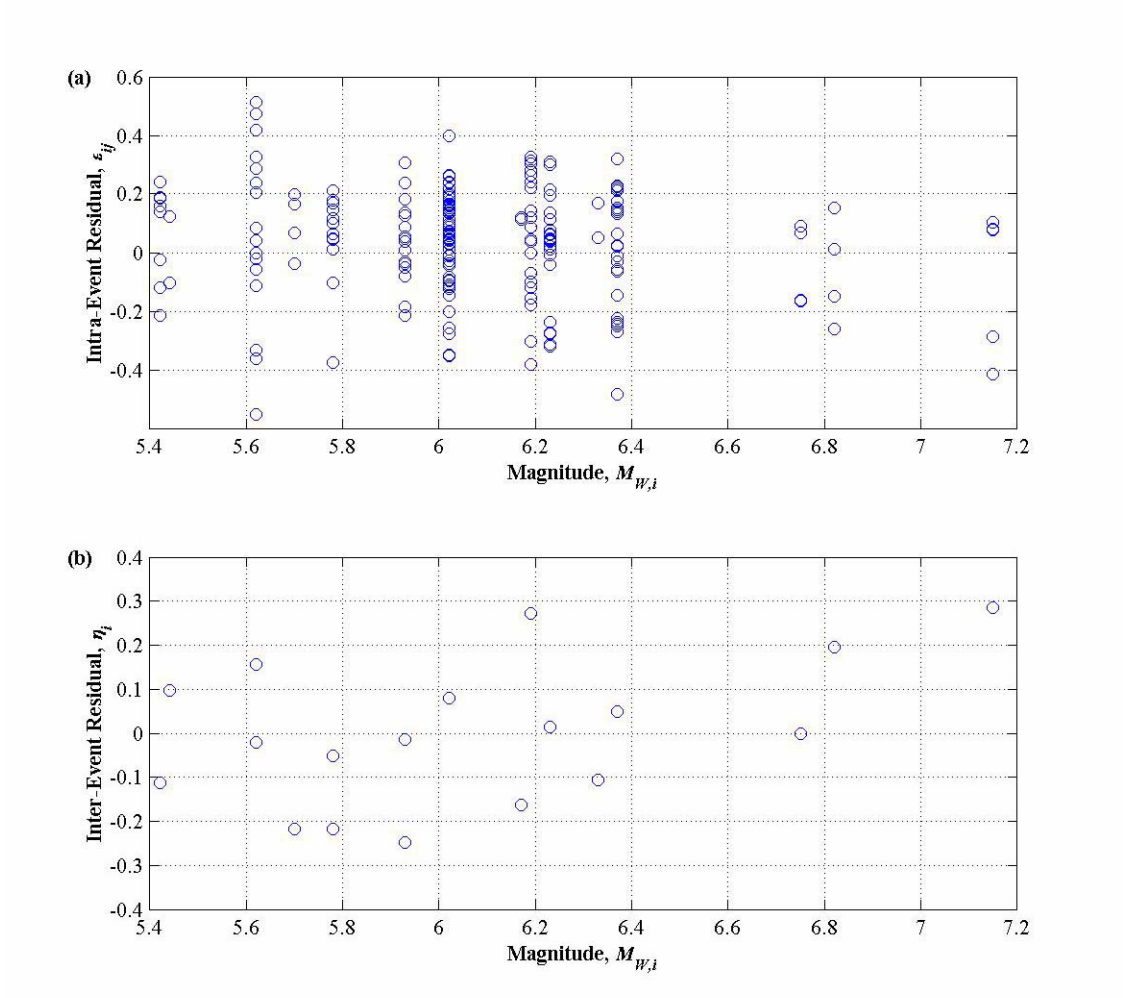

Figure B.4.6: Residuals for the Moment Magnitude - Corner Frequency relationship. Panel (a) shows the intra event residuals (ε_{ij}) while panel (b) shows the inter event residuals (η_i).

B.5. Predictive Equation for the Fourier Amplitude Spectrum of Strong Motion Acceleration in New Zealand

B.5.1. Introduction

The purpose of this chapter is to determine, and present, the underlying form of the Fourier Amplitude Spectrum (FAS) of acceleration for New Zealand earthquakes. There is currently no model of this type in New Zealand. Howfever, understanding the frequency content of ground motions is very important and while response spectral ordinates are currently far more common for application in design scenarios the utility of the FAS is likely to increase as more sophisticated analysis techniques involving ground motion time histories become popular. The possibility of using some model of the Fourier Amplitude Spectrum coupled with a spectrum of random phase angles to model high frequency strong ground motion has been appreciated for over 25 years (Hanks 1979; McGuire and Hanks 1980; Hanks and McGuire 1981; Boore 1983; Beresnev and Atkinson 1998; Boore 2003). This technique for simulating ground motion time histories is a relatively simple way of generating realistic ground motion time histories that scale well with magnitude and distance, as well as other seismological parameters. The method is known as the stochastic method and has been applied widely throughout the world, but not in New Zealand (see Boore 2003 and references therein). In order to apply this method, one requires some model for the source spectrum of seismic shear waves as well as some knowledge of how this source spectrum is modified during its propagation from the source to some site. In the previous chapter a model for the source spectrum of seismic shear waves was developed for New Zealand. In the present chapter, the nature of the effects of propagation on this source spectrum is investigated through the development of an empirical predictive model for the FAS. Consequently, the current and previous chapters together provide the basis from which strong ground motion time histories may be simulated using the stochastic method in New Zealand. The availability of such a technique greatly enhances our ability to utilise state-of-the-art methods in both structural and geotechnical engineering.

Comprehensive regression techniques will be employed to obtain parameters that describe the underlying form of the FAS. Most of the modern advancements that have been made with respect to empirical equations of strong motion measures relate to the quantification of the error associated with the equations. The most advanced models make use of mixed models that are able to partition the overall error observed between a predictive model and an observed ground motion into a random inter-event error associated with the specific earthquake in question, and a fixed intra-event error that represents the inherent variability of strong ground motions. For certain ground motion measures these two terms have been shown to be negatively correlated with magnitude, each to differing extents (Abrahamson 1988; Youngs et al. 1995). It is preferable to obtain a predictive equation for the Fourier Amplitude Spectrum of acceleration that is able to provide similar detail regarding the distribution and nature of the errors associated with the prediction. However, while the general procedure to obtain such characteristics can be applied to Fourier Spectral models, the true quantification of error is vexed by the strong reliance of the magnitude of the observed error upon the processing techniques employed to derive the Fourier Spectra that represent the empirical data set.

There is no universally standard method for the processing of Fourier Spectra. While Caltech Bluebook framework (Hudson et al. 1972) forms the basis of most modern systems for systematically generating Fourier Spectra, there are many alternate methods employed in the literature for processing Fourier Spectra for the purpose of deriving empirical models (for example Boore and Atkinson 1987; Atkinson and Mereu 1992; Sokolov 2000; Sokolov et al. 2000; 2002). In the present study, the simple method described in Chapter Two of this section was used. This method was found to generate spectra that are very similar to those provided through the GeoNet project (http://www.geonet.org.nz/). This is a desirable attribute as it enables the model to be readily updated as more strong motion spectra become available in New Zealand as well as making it relatively easy for other researchers to validate this model, or compare this model to others that are subsequently developed[†].

This chapter begins by giving a brief description of the functional form of the regression model used in the analysis before describing the regression procedure in some detail. The preferred model is then presented and the results and implications discussed.

B.5.2. Model Formulation and Regression Procedure

The theoretical background for the development of the Fourier Amplitude Spectrum has already been presented in Chapter Three of this section. However, when performing the regression analysis it is commonly necessary to modify the ideal theoretical model in order to enable the algorithms involved in the regression to converge. In addition, there are couplings between some parameters that can result in non-unique solutions in the regression model. Most regression techniques are not able to obtain reliable,

[†] Provided the publicly available spectra from the GeoNet project are at least modified enough to extract the shear wave spectra from the total spectra presented.

or stable, solutions in such cases so one must be careful to try and limit the degree of coupling between the parameters in the regression model where possible. A well known coupling between parameters involved in models of the Fourier Spectrum is that between the stress parameter, or stress drop, $\Delta\sigma$ (and consequently the corner frequency), and the high frequency spectral decay parameter, κ (Boore et al. 1992; Margaris and Boore 1998). This known coupling was a primary reason why an independent method was employed to determine a relationship between moment magnitude and corner frequency in the previous chapter. As will be seen shortly, this derived relationship is utilised in the derivation of the predictive model for the FAS and the results that are obtained can therefore be regarded as being somewhat conditional upon the relationship developed in the previous chapter.

The functional form of the model for which parameters estimates must be found is nonlinear. This nonlinearity comes about through two main sources; the theoretical distance scaling function of the FAS presented in Chapter Three must be modified to incorporate a near source factor, and the magnitude dependence of the corner frequency also introduces significant nonlinearity. Nonlinear regression models require starting estimates of the parameters. In almost all cases, the better the starting estimates, the better the results and frequently, the more efficient the performance of the regression algorithm. It is therefore necessary to have a sound understanding of the theoretical basis of a regression model so that the physical meaning of the various terms of the model can be appreciated. Without this understanding it can be very difficult to estimate adequate starting estimates for the nonlinear model. In many cases, the algorithm will not converge at all, or will converge to a local solution rather than the required global solution. This problem becomes more and more critical as the number of parameters in the model increases.

The dataset that the regression analysis is based upon is not large enough for stable estimates to be made for a large number of parameters. Therefore, in order to fit a model that is sophisticated enough to preclude the requirement of being radically modified in the near future, it was necessary to include some theoretical scaling as well as the empirical scaling. For this reason, the relationship between the moment magnitude and the corner frequency developed in the previous chapter was utilised. The initial functional form of the regression model that was used for the Fourier Amplitude Spectrum of acceleration is given below in Equation (B.5.1).

$$y_{k,ij} = c_1 + c_2 M_{W,i} + c_3 \ln\left[\sqrt{r_{rup,ij}^2 + c_4^{\,2}}\right] + c_5 S_{B,ij} + c_6 S_{C,ij} + c_7 F_{N,i} + c_8 F_{R,i} + \eta_i + \varepsilon_{ij} \qquad \text{(B.5.1)}$$

Here, the dependent variable is a combination of the observed spectral amplitudes at the particular frequency in question as well as some theoretical scaling factors representing an omega squared spectrum (Aki 1967) with a single corner frequency (Brune 1970; 1971).

$$y_{k,ij} = \ln\left[A_{k,ij}\right] - \ln\left[\frac{f_k^2}{1+\left(f_k / f_{c,i}\right)^2}\right] \qquad \text{(B.5.2)}$$

In the above equations, $y_{k,ij}$ represents the modified Fourier spectral amplitude at the k^{th} frequency, f_k, for the j^{th} recording from the i^{th} earthquake. The parameters $S_{B,ij}, S_{C,ij}, F_{N,i}, F_{R,i}$ are dummy binary regression variables (Searle 1971) that represent site class B and C for the j^{th} record of the i^{th} earthquake, and the fault mechanism for normal and reverse earthquakes respectively. The corner frequency is specified as a function of magnitude, $M_{W,i}$, using the relationship previously derived from the Monte Carlo ray tracing procedure. The c_i parameters, with $i = 1, 2, \ldots, 8$, are the regression coefficients to be determined, and $r_{rup,ij}$ is the rupture distance for the j^{th} record of the i^{th} earthquake. The only remaining terms are the random inter-event error term, η_i, and the fixed intra-event error term, ε_{ij}. Each of these error terms are assumed to be normally distributed with zero means and variances of τ^2 and σ^2 respectively.

Consequently, the regression is performed on this model on a frequency by frequency basis. Ideally, rather than performing a regression for a functional form that primarily represents the scaling with magnitude and distance, it would be preferable to use a functional form in a third primary dimension of frequency. However, a much larger dataset is required for such an approach to be employed because the additional nonlinearity introduced through the frequency dependence causes the problem to become highly non-unique. Therefore, the frequency by frequency regression is performed before then smoothing the obtained coefficients in order to ensure that the coefficients vary in a smooth manner with respect to frequency. In this way the set of regression coefficients that are obtained are able to predict smooth spectra in the frequency domain as well as smooth scaling of individual spectral ordinates with respect to both magnitude and distance.

A mixed effects model was used in the regression analysis so that the effect of individual earthquake events could be adequately accounted for. The random effects algorithm of Abrahamson and Youngs (1992) was employed in order to determine the regression coefficients. This algorithm requires a normal fixed effects regression to be performed as one of the steps of an iterative procedure. In order to perform the nonlinear fixed effects regression the linearization technique outlined in the one-step method of Joyner and Boore (1993; 1994) is employed. This method uses a Taylor series expansion to linearise the regression problem so that the nonlinear model is transformed to a linear model. The validity and efficiency of this approach is again strongly dependent upon the quality of the initial parameter estimates.

The linearization procedure for the case of ordinary least squares regression analysis is described by Draper and Smith (1981) and is outlined in the following. The Taylor series expansion about the initial trial parameter values, $\boldsymbol{\theta}_0$, can be expressed as in Equation (B.5.3).

$$f(\boldsymbol{\xi}_u, \boldsymbol{\theta}) = f(\boldsymbol{\xi}_u, \boldsymbol{\theta}_0) + \sum_{i=1}^{p} \left[\frac{\partial f(\boldsymbol{\xi}_u, \boldsymbol{\theta})}{\partial \theta_i} \right]_{\boldsymbol{\theta}=\boldsymbol{\theta}_0} (\theta_i - \theta_{i0}) \tag{B.5.3}$$

In Equation (B.5.3), standard nonlinear regression nomenclature is used. Within this framework, $\boldsymbol{\xi}_u$ represents the vector of predictor variables (i.e. magnitude, distance, frequency) for the u^{th} observation (of which there are a total of n). The $\boldsymbol{\theta}$ represent the vector of parameter values; there are a total of p parameters. Given these definitions, $f\left(\boldsymbol{\xi}_u, \boldsymbol{\theta}\right)$ represents the evaluation of the functional form of the regression model for the predictor variables corresponding to the u^{th} observation and with the current parameter values. If we rearrange the various terms of the above equation and reframe the problem as in Equation (B.5.4) it can be seen that following the first order Taylor series expansion the nonlinear regression problem has been transformed into a linear-in-the-parameters problem. To achieve this transformation let,

$$\begin{aligned} f_u^0 &= f\left(\xi_u, \boldsymbol{\theta}_0\right) \\ \beta_i^0 &= \theta_i - \theta_{i0} \\ Z_{iu}^0 &= \left[\frac{\partial f\left(\xi_u, \boldsymbol{\theta}\right)}{\partial \theta_i}\right]_{\boldsymbol{\theta}=\boldsymbol{\theta}_0} \end{aligned} \tag{B.5.4}$$

and then Equation (B.5.3) can be restated as follows.

$$Y_u - f_u^0 = \sum_{i=1}^{p} \beta_i^0 Z_{iu}^0 + \varepsilon_u \tag{B.5.5}$$

It is assumed that the error term, ε_u, in the above equation is normally distributed and that there is no correlation between the various observations in the dataset. This is the ordinary least squares case. It is possible to relax this condition and allow for correlations between observations. This relaxation corresponds to the case of generalised least squares and is the essence of the Joyner and Boore one-stage method (1993; 1994).

The regression problem under these new definitions can be restated in matrix form as in Equation (B.5.6) below.

$$\mathbf{Y} - \mathbf{f}^0 = \mathbf{Z}_0 \boldsymbol{\beta}_0 + \boldsymbol{\varepsilon} \tag{B.5.6}$$

Here the notation is relatively obvious, but is defined for completeness below.

$$\mathbf{Y} - \mathbf{f}^0 = \begin{bmatrix} Y_1 - f_1^0 \\ Y_2 - f_2^0 \\ \vdots \\ Y_u - f_u^0 \\ \vdots \\ Y_n - f_n^0 \end{bmatrix}, \quad \boldsymbol{\beta}_0 = \begin{bmatrix} \beta_1^0 \\ \beta_2^0 \\ \vdots \\ \beta_i^0 \\ \vdots \\ \beta_p^0 \end{bmatrix}, \quad \mathbf{Z}_0 = \begin{bmatrix} Z_{11}^0 & Z_{21}^0 & \cdots & Z_{p1}^0 \\ Z_{12}^0 & Z_{22}^0 & \cdots & Z_{p2}^0 \\ \vdots & & & \\ Z_{1u}^0 & Z_{2u}^0 & \cdots & Z_{pu}^0 \\ \vdots & & & \\ Z_{1n}^0 & Z_{2n}^0 & \cdots & Z_{pn}^0 \end{bmatrix}, \quad \boldsymbol{\varepsilon} = \begin{bmatrix} \varepsilon_1 \\ \varepsilon_2 \\ \vdots \\ \varepsilon_u \\ \vdots \\ \varepsilon_n \end{bmatrix} \tag{B.5.7}$$

Now that the problem has been fully reframed in a linear-in-the-parameters regression problem, the optimal parameter set that minimises the squares of the residuals between the model and the observations can be found using the familiar expression in Equation (B.5.8).

$$\hat{\boldsymbol{\beta}}_0 = \left(\mathbf{Z}_0{}^T \mathbf{Z}_0\right)^{-1} \mathbf{Z}_0{}^T \left(\mathbf{Y} - \mathbf{f}^0\right) \tag{B.5.8}$$

As is evidenced by the '0' subscripts in all the equations in the development above, these equations correspond to the initial parameter estimates. The procedure above should be implemented as an iterative problem until the assumed parameter values stabilise within some tolerable limits. The new parameter estimates for each iteration are found from Equation (B.5.9).

$$\boldsymbol{\theta}_{j+1} = \boldsymbol{\theta}_j + \left(\mathbf{Z}_j{}^T \mathbf{Z}_j\right)^{-1} \mathbf{Z}_j{}^T \left(\mathbf{Y} - \mathbf{f}^j\right) \tag{B.5.9}$$

As has been mentioned earlier, the quality of the initial parameter estimates as well as the nonlinearity of the problem strongly dictates the efficiency of the linearization algorithm. Because the Taylor series is constrained to its first order terms, the accuracy of the approximation given by Equation (B.5.3) depends upon how far the true functional form deviates from a 'plane' in p-space. Naturally, the better the starting estimates the better this approximation.

Previously, it was mentioned that the development presented above applied to the case of ordinary least squares. In this case, all errors are deemed independent of each other and the problem is truly one of least squares parameter estimation. However, in the case where various observations are correlated and one wishes to take this correlation into account, i.e. in the present case where the effects of each earthquake are to be considered, then the standard linear-in-the-parameters regression formulae above need to be modified. The appropriate modification involves the introduction of the variance-covariance matrix as well as the application of maximum likelihood techniques.

If, for some reason, the observations of the ground motions from a particular earthquake event are either higher or lower than the typical level of response associated with the relevant earthquake scenario then all observations of the ground motion for that event will be similarly biased. Within the group of observations associated with this given event there will be some inherent scatter. When aiming to understand the overall nature of the scatter of ground motion data it is important to consider to what extent group action governs the overall scatter of the data. This is particularly important in limited datasets where singular events may contribute a significant portion of the records in the dataset. It is therefore desirable to perform a generalised least squares regression rather than an ordinary least squares regression. In the generalised case, the correlations between various observations can be taken into account. The generalised least squares solution is equivalent to maximum likelihood estimation in the case where the error distribution is assumed to be normal (Searle 1971). Typically, when performing regressions upon ground motion data, models are fitted to the logarithms of observed motions and in this case the errors are

assumed to be normally distributed (Restrepo-Velez and Bommer 2003); therefore generalised least squares and maximum likelihood methods are equivalent.

In keeping with the nomenclature presented for the ordinary least squares case above, the solution to the linearised model is given by Equation (B.5.10).

$$\hat{\boldsymbol{\beta}}_0 = \left(\mathbf{Z}_0{}^T\mathbf{V}^{-1}\mathbf{Z}_0\right)^{-1}\mathbf{Z}_0{}^T\mathbf{V}^{-1}\left(\mathbf{Y}-\mathbf{f}^0\right) \tag{B.5.10}$$

Here, the variance-covariance matrix, $\mathbf{V}$, is a block diagonal matrix (when the data is grouped by event) that can be represented by Equation (B.5.11) below.

$$\mathbf{V} = \sigma^2\mathbf{I}_N + \tau^2\sum_{i=1}^{M}{}^{+}\mathbf{1}_{n_i} \tag{B.5.11}$$

In Equation (B.5.11), $\mathbf{I}_N$ is the identity matrix of dimension N, where N is the total number of observations in the dataset for any given frequency. The term $\mathbf{1}_{n_i}$ is an $n_i \times n_i$ unit matrix, with n_i representing the number of records from the i^{th} earthquake, of which there are a total of M. The summation symbol with the superscript + symbolises a direct sum operation for block diagonal matrices (Searle 1971). If, as mentioned before, the ground motion observations are grouped by event, the variance-covariance matrix can be written as a sparse block diagonal matrix, where each block matrix essentially has total error diagonal terms and inter-event off diagonal terms. The total error is simply obtained from Equation (B.5.12).

$$\sigma_T^2 = \sigma^2 + \tau^2 \tag{B.5.12}$$

The variance-covariance matrix therefore has the following expanded form.

$$\mathbf{V} = \begin{bmatrix} \sigma^2\mathbf{I}_{n_1} + \tau^2\mathbf{1}_{n_1} & 0 & \cdots & 0 \\ 0 & \sigma^2\mathbf{I}_{n_2} + \tau^2\mathbf{1}_{n_2} & \cdots & 0 \\ \vdots & \vdots & \ddots & \vdots \\ 0 & 0 & \cdots & \sigma^2\mathbf{I}_{n_M} + \tau^2\mathbf{1}_{n_M} \end{bmatrix} \tag{B.5.13}$$

The regression solution corresponds to the case where the parameter vector, $\boldsymbol{\beta}$, and error variances σ^2 and τ^2, are selected so that the log-likelihood expression given below is maximised.

$$\ln L = -\frac{N}{2}\ln\left(2\pi\right) - \frac{1}{2}\ln\left|\mathbf{V}\right| - \frac{1}{2}\left(\mathbf{Y}-\mathbf{f}^j-\mathbf{Z}_j\boldsymbol{\beta}_j\right)^T\mathbf{V}^{-1}\left(\mathbf{Y}-\mathbf{f}^j-\mathbf{Z}_j\boldsymbol{\beta}_j\right) \tag{B.5.14}$$

Because the variance-covariance matrix is block diagonal analytical solutions exist for the determinant $|\mathbf{V}|$ and matrix inverse $\mathbf{V}^{-1}$. The log-likelihood expression can therefore be restated into a more convenient working form given in Equation (B.5.15).

$$\begin{aligned}\ln L = &-\frac{1}{2}N\ln(2\pi)-\frac{1}{2}(N-M)\ln(\sigma^2)-\frac{1}{2}\sum_{i=1}^{M}\ln(\sigma^2+n_i\tau^2)\\ &-\frac{1}{2\sigma^2}\sum_{i=1}^{M}\sum_{j=1}^{n_i}(y_{ij}-\bar{Y}_i)^2-\frac{1}{2}\sum_{i=1}^{M}\frac{n_i(\bar{Y}_i-\bar{\mu}_i)^2}{\sigma^2+n_i\tau^2}\end{aligned} \tag{B.5.15}$$

Here, the terms $\bar{Y}_i$ and $\bar{\mu}_i$ are respectively the average observed and modelled response for the i^{th} earthquake, and are defined formally by Equation (B.5.16) below. In this equation $\mu_{ij} = f(M_{W,i}, r_{rup,ij}, \boldsymbol{\theta})$ is simply the functional form, devoid of the error terms, evaluated for the given parameter values.

$$\bar{Y}_i = \frac{1}{n_i}\sum_{j=1}^{n_i} y_{ij}, \quad \bar{\mu}_i = \frac{1}{n_i}\sum_{j=1}^{n_i}\mu_{ij} \tag{B.5.16}$$

Once some parameter and variances have been estimated the specific random effect associated with each event can be obtained from the equation below.

$$\eta_i = \frac{\tau^2\sum_{j=1}^{n_i} y_{ij}-\mu_{ij}}{\sigma^2+n_i\tau^2} \tag{B.5.17}$$

The procedure detailed above follows the method of Abrahamson and Youngs (1992) which in turn is a modification of the method proposed originally by Brillinger and Preisler (1984; 1985) for the analysis of the Joyner and Boore (1981) empirical equation. An essentially equivalent method that is possibly easier to implement has also been proposed, the Joyner and Boore one-stage method (Joyner and Boore 1993; 1994). This method only requires the maximisation of the log-likelihood method over one variable rather than both τ^2 and σ^2. However, an enhanced version of the Abrahamson and Youngs (1992) procedure, based upon that of Rhoades (1997) which allows for the uncertainty associated with individual magnitude values, is employed for the Arias Intensity regression model in Chapter Six of this section and it was therefore more efficient to set up the base Abrahamson and Youngs (1992) model here. Both the Joyner and Boore (1993; 1994) and Abrahamson and Youngs (1992) algorithms should yield very similar results for a given regression requirement.

As previously mentioned, the regression model that is adopted in this analysis is essentially two dimensional, in M_W, r_{rup} space; with additional dummy variables corresponding to site classes and fault mechanisms. The regression model, as it stands, requires coefficients to be determined on a frequency by frequency basis. This requirement means that the coefficients that are obtained for each frequency, when

used, will generate smooth curves when plotted against magnitude or rupture distance. They will not, however, generate smooth curves when actual spectra (response plotted against frequency) are plotted. Ideally, the regression analysis would be performed on a three dimensional model that would obtain regression coefficients for a surface in M_W, R_{rup}, f space. However, in order to do this, functional theoretical, or appropriately estimated, forms of the regression model for the site response and fault mechanism influence would need to be included in the model to tie in the third dimension of frequency into the two dimensional magnitude-distance space. While approximate theoretical models exist for site response, these would typically require additional input variables that are generally not available on a common basis†. The functional form for the fault mechanism terms could probably be derived as a function of focal mechanism properties and source-site azimuth, i.e. through functional dependence upon the radiation pattern. In practice however, the incorporation of the additional terms required to quantify the site and fault effects, even if available, would increase the number of predictive variables to the point where the regression models would become over-parameterized. In addition, the strong motion datasets that are employed would have to be significantly larger and far more complete in terms of their encompassing possible earthquake scenarios in order for this approach to be attempted.

The ability to generate smooth spectra is desirable however, particularly when the base input into the strong motion dataset are actual spectra themselves. It is important to try and generate a model for the Fourier Amplitude Spectra that is actually compatible with real earthquake spectra and not just arbitrarily selected spectral ordinates. To try and meet this end, regression coefficients are typically smoothed after being determined on a frequency by frequency basis, for example Boore, Joyner and Fumal (1997) employed the Joyner and Boore (1993; 1994) two-stage regression model and then smoothed the resulting coefficients with respect to frequency using a cubic polynomial. For the present study the determined coefficients were smoothed by fitting a polynomial of an order that depended upon the particular parameter (but that was either cubic or quartic) against $\log_{10}$-frequency to the determined coefficients. While this smoothing procedure results in final coefficients that will predict residuals that differ to those found from the original regression analysis, the price paid for applying this smoothing is more than made up for by obtaining the desired smooth spectra. The reason for utilising polynomials of varying degrees to fit to the coefficients is to try and minimise consequent alteration to the error that is introduced by employing this smoothing procedure.

B.5.3. Application of the Regression Procedure

The methodology detailed above was applied to two datasets, one that contained records from the Chi-Chi event and one that did not. When performing a regression analysis the stability of the results that are

† Likely additional parameters that would characterize the site response would include information regarding the layering of soil deposits in terms of geometry and the associated physical properties of the layers.

obtained should be checked. This check can be made by determining the errors of the coefficients as well as considering the correlations between the coefficients that are obtained. This is an important step to take because parameters can be found for much more complicated models than that given in Equation (B.5.1) but it is likely that the additional parameters that would be included in these more complex models would be strongly correlated. If the coefficients are strongly correlated then changes to the dataset could result in significant changes to the determined coefficients. This is not desirable, therefore the errors associated with the coefficient estimates as well as the correlations between the coefficients were computed for the model considered in Equation (B.5.1), as well as many other slightly different models. The standard error associated with each coefficient can be found from taking the square root of the relevant diagonal element of the matrix defined by Equation (B.5.18).

$$\mathrm{var}\left(\hat{\boldsymbol{\beta}}\right) = \left(\mathbf{Z}^T\mathbf{V}^{-1}\mathbf{Z}\right)^{-1}\sigma_T{}^2 \tag{B.5.18}$$

The corresponding matrix of correlation coefficients, $\mathbf{C}$, can in turn be found from the equation pair below.

$$\mathbf{Q} = q_{ij} = \left(\mathbf{Z}^T\mathbf{V}^{-1}\mathbf{Z}\right)^{-1} \tag{B.5.19}$$

$$\mathbf{C} = c_{ij} = \frac{q_{ij}}{\left(q_{ii}q_{jj}\right)^{1/2}} \tag{B.5.20}$$

After performing this check it was found that the coefficients c_3 and c_4 were quite strongly coupled as well as being moderately correlated to coefficient c_2 of Equation (B.5.1). This is most undesirable as the parameter c_4 of Equation (B.5.1) is the factor to account for near source constraint and is quite strongly influenced by the ground motion records from the overseas data. The coefficient c_3 that essentially accounts for the geometrical spreading as well as some scattering and anelastic attenuation should model the New Zealand data as well as possible and we consequently do not want this factor to be untowardly influenced by the foreign records. This coupling also affects the magnitude scaling parameter, c_2, which should be reasonably well constrained from theoretical considerations.

In order to address this situation, the factor for near source constraint was set to a fixed value of 19 km. This value was chosen so as to be consistent with the near source factor adopted in the peak ground acceleration predictive models of both Zhao et al. (1997) and Cousins et al. (1999) for New Zealand. This adoption of this value enabled the correlations between parameters to be reduced significantly as well as obtain relatively stable values of the magnitude scaling factor c_2 that agreed quite well with the value expected through theoretical considerations (i.e. the seismic moment, moment magnitude relation of Hanks and Kanamori, 1979, $1.5\ln(10)$).

When analysing the results of the regression analysis for the two different datasets it was found that the dataset that excluded the records from the Chi-Chi earthquake did a slightly better job of modelling the spectra. In light of the controversy associated with the inclusion of the Chi-Chi records in strong motion datasets for regression analyses it was decided that the preferred model was that based upon the dataset that excluded these records.

The final smoothed coefficients that were obtained from the preferred dataset using the methodology described in this chapter are presented here in Table B.5.1. For comparative purposes, the coefficients obtained using the preferred functional form, with the near source term fixed, for the dataset that includes the Chi-Chi records is given in Appendix B3. Also given in this appendix are tables of coefficients for these two datasets for the case where the near source constraint was allowed to be a regression variable. In this case it can be seen that the factor accounting for geometric spreading, as well as that for the magnitude scaling is more variable than the case where the near source factor is constrained.

B.5.4. Note on the Partitioning of Error Components

In Table B.5.1 it can be seen that rather than having the expected three columns for the error components of τ, σ and σ_T, there are five such columns. The inclusion of these additional error terms is very important, as Baker and Cornell (2006) have recently pointed out. When using predictive equations for engineering design, structural engineers typically apply a ground motion in some direction. This ground motion is usually assumed to be a random component of ground motion. However, when deriving the empirical ground motion equations the engineering seismologist usually, as in this case, performs the regression on the geometric mean of the two horizontal ground motion components. By performing the regression analysis upon the geometric mean, the data have less scatter and more stable regression parameters can be obtained. When this approach is adopted though, the magnitude of the error terms that are obtained correspond to the geometric mean of the ground motion parameter and not to a random component of ground motion. There is consequently an incompatibility between the definitions of the ground motions typically used by structural engineers and engineering seismologists. As Baker and Cornell (2006) demonstrate, this is not merely semantics, because hazard analyses are conducted by engineering seismologists where the error relevant to the geometric mean of the ground motions is most appropriate, while the subsequent structural response analysis is performed by structural engineers where the error relevant to a random component of ground motion is relevant. Baker and Cornell (2006) suggest options for addressing this incompatibility. Most of these options rely on the engineering seismologist clearly stating exactly which error estimate is being provided, the geometric mean, or the random component. The additional columns in Table B.5.1 are given for this purpose.

Table B.5.1: Regression coefficients of the predictive model for the Fourier Amplitude Spectrum of Acceleration in New Zealand. Column headings correspond to the coefficients found from the regression analysis; additionally, *f* represents frequency, *M* is the number of events at each frequency, and *N* is the number of records used for each frequency.

f	c_1	c_2	c_3	c_4	c_5	c_6	c_7	c_8	τ	σ_1	σ_c	σ	σ_{lnY}	M	N
0.333	-6.040	2.845	-1.090	19	0.088	0.218	-1.085	-0.290	0.978	0.868	0.152	0.881	1.316	59	265
0.357	-6.387	2.886	-1.088	19	0.068	0.234	-1.031	-0.266	0.963	0.866	0.151	0.879	1.303	64	288
0.370	-6.556	2.907	-1.087	19	0.060	0.248	-1.003	-0.254	0.954	0.865	0.151	0.878	1.296	64	288
0.400	-6.884	2.946	-1.085	19	0.046	0.285	-0.944	-0.228	0.934	0.863	0.150	0.876	1.280	69	343
0.417	-7.042	2.965	-1.083	19	0.041	0.309	-0.914	-0.215	0.923	0.861	0.149	0.874	1.272	69	343
0.455	-7.343	3.001	-1.081	19	0.036	0.364	-0.851	-0.187	0.899	0.859	0.148	0.872	1.252	70	355
0.476	-7.486	3.019	-1.080	19	0.035	0.396	-0.818	-0.173	0.885	0.858	0.148	0.870	1.241	70	355
0.526	-7.753	3.051	-1.078	19	0.039	0.464	-0.749	-0.142	0.855	0.855	0.146	0.867	1.218	74	399
0.556	-7.875	3.067	-1.078	19	0.043	0.500	-0.712	-0.126	0.838	0.853	0.145	0.866	1.205	76	407
0.625	-8.094	3.095	-1.078	19	0.059	0.572	-0.636	-0.092	0.802	0.850	0.144	0.862	1.177	85	445
0.667	-8.188	3.108	-1.080	19	0.070	0.606	-0.596	-0.074	0.782	0.848	0.143	0.860	1.163	85	446
0.769	-8.339	3.130	-1.085	19	0.100	0.663	-0.512	-0.036	0.739	0.844	0.140	0.856	1.130	88	458
0.833	-8.393	3.140	-1.090	19	0.119	0.685	-0.467	-0.015	0.715	0.842	0.139	0.853	1.113	90	473
1.000	-8.448	3.155	-1.108	19	0.166	0.701	-0.372	0.029	0.665	0.837	0.135	0.848	1.078	93	480
1.053	-8.448	3.158	-1.114	19	0.180	0.698	-0.347	0.041	0.652	0.836	0.134	0.846	1.069	93	480
1.176	-8.432	3.163	-1.130	19	0.210	0.680	-0.296	0.066	0.626	0.833	0.131	0.843	1.050	93	480
1.250	-8.415	3.165	-1.140	19	0.226	0.664	-0.269	0.079	0.613	0.831	0.130	0.841	1.041	94	482
1.429	-8.359	3.168	-1.165	19	0.260	0.618	-0.215	0.107	0.587	0.828	0.126	0.838	1.023	94	484
1.481	-8.340	3.168	-1.172	19	0.269	0.602	-0.201	0.115	0.581	0.827	0.125	0.837	1.019	94	484
1.600	-8.298	3.169	-1.189	19	0.287	0.567	-0.173	0.130	0.569	0.825	0.123	0.835	1.010	94	484
1.667	-8.273	3.170	-1.199	19	0.296	0.547	-0.159	0.138	0.563	0.824	0.122	0.833	1.006	94	484
1.818	-8.220	3.170	-1.221	19	0.314	0.501	-0.131	0.154	0.553	0.823	0.119	0.831	0.998	94	484
1.905	-8.190	3.171	-1.233	19	0.322	0.476	-0.117	0.162	0.548	0.822	0.118	0.830	0.995	94	484
2.000	-8.159	3.171	-1.246	19	0.331	0.448	-0.103	0.171	0.543	0.821	0.116	0.829	0.991	94	484
2.174	-8.106	3.172	-1.269	19	0.344	0.401	-0.080	0.185	0.537	0.819	0.113	0.827	0.986	94	484
2.381	-8.051	3.172	-1.296	19	0.357	0.349	-0.059	0.200	0.533	0.818	0.110	0.825	0.982	94	484
2.500	-8.022	3.173	-1.311	19	0.362	0.322	-0.048	0.207	0.532	0.817	0.108	0.824	0.981	94	484
2.632	-7.995	3.173	-1.327	19	0.367	0.294	-0.038	0.215	0.531	0.816	0.106	0.823	0.980	94	484
2.703	-7.981	3.174	-1.335	19	0.369	0.279	-0.033	0.219	0.531	0.816	0.105	0.822	0.979	94	484
2.857	-7.954	3.174	-1.353	19	0.373	0.250	-0.023	0.227	0.532	0.815	0.103	0.821	0.978	94	484
2.941	-7.941	3.175	-1.362	19	0.375	0.235	-0.019	0.232	0.532	0.814	0.102	0.821	0.978	94	484
3.125	-7.917	3.176	-1.381	19	0.377	0.206	-0.010	0.240	0.534	0.814	0.100	0.820	0.978	94	484
3.226	-7.906	3.177	-1.391	19	0.378	0.191	-0.006	0.244	0.536	0.813	0.098	0.819	0.979	94	484
3.448	-7.887	3.178	-1.412	19	0.379	0.161	0.001	0.253	0.539	0.813	0.096	0.818	0.980	94	484
3.571	-7.879	3.179	-1.423	19	0.379	0.146	0.005	0.258	0.541	0.812	0.094	0.818	0.981	94	484
3.846	-7.868	3.181	-1.447	19	0.377	0.118	0.010	0.267	0.547	0.812	0.091	0.817	0.983	94	484
4.000	-7.865	3.182	-1.459	19	0.375	0.104	0.012	0.272	0.551	0.812	0.090	0.816	0.985	94	484
4.348	-7.868	3.184	-1.484	19	0.370	0.079	0.015	0.281	0.559	0.811	0.086	0.816	0.989	94	484
4.545	-7.874	3.185	-1.497	19	0.367	0.067	0.016	0.286	0.564	0.811	0.084	0.815	0.991	94	484
5.000	-7.899	3.188	-1.523	19	0.357	0.046	0.014	0.296	0.576	0.811	0.080	0.815	0.998	94	484
5.263	-7.919	3.189	-1.536	19	0.351	0.037	0.012	0.302	0.583	0.811	0.078	0.814	1.001	94	484
5.882	-7.980	3.192	-1.562	19	0.336	0.023	0.005	0.312	0.598	0.811	0.073	0.814	1.010	94	484
6.250	-8.024	3.194	-1.574	19	0.326	0.018	-0.001	0.318	0.607	0.811	0.070	0.814	1.016	94	484
7.143	-8.148	3.196	-1.595	19	0.303	0.014	-0.019	0.329	0.627	0.812	0.065	0.815	1.028	94	484
7.692	-8.233	3.196	-1.603	19	0.290	0.015	-0.032	0.334	0.638	0.813	0.062	0.815	1.035	94	484
9.091	-8.470	3.194	-1.608	19	0.258	0.024	-0.069	0.345	0.661	0.815	0.055	0.817	1.051	94	484
10.000	-8.633	3.190	-1.601	19	0.240	0.031	-0.094	0.351	0.672	0.817	0.051	0.819	1.059	94	484
11.111	-8.837	3.183	-1.586	19	0.221	0.038	-0.127	0.357	0.682	0.819	0.047	0.821	1.067	94	483
11.765	-8.958	3.178	-1.573	19	0.211	0.042	-0.146	0.359	0.686	0.821	0.045	0.822	1.071	94	483
13.333	-9.249	3.164	-1.533	19	0.193	0.049	-0.193	0.365	0.691	0.824	0.041	0.825	1.077	94	483
14.286	-9.424	3.153	-1.503	19	0.185	0.052	-0.221	0.367	0.692	0.826	0.039	0.827	1.078	94	483
16.667	-9.851	3.121	-1.415	19	0.175	0.053	-0.291	0.372	0.684	0.832	0.036	0.833	1.077	94	483
18.182	-10.114	3.098	-1.351	19	0.174	0.051	-0.335	0.374	0.673	0.835	0.034	0.836	1.073	93	481
20.000	-10.419	3.067	-1.268	19	0.179	0.047	-0.387	0.376	0.656	0.840	0.032	0.840	1.066	93	481

The regression analysis in this study was performed on the geometric mean of the two horizontal components of the Fourier spectra. Consequently, the error estimates of τ, σ and σ_T that are obtained by following the procedure detailed thus far correspond to the error of the geometric average of the FAS. In order to determine what the relevant error is for the case of the random, or arbitrarily oriented, component of FAS the original Fourier spectra must be analysed and an estimate of the error associated with the two horizontal components from each strong motion records made. Boore et al. (1997) describe the procedure that is required to meet this end, however, their actual formulae contain errors and these are corrected in Boore (2005). In terms of the column headers of Table B.5.1, the value of τ retains it original definition, that being the standard deviation of the inter-event terms, η_i. The error term previously referred to as σ for the standard deviation of the intra-event terms, ε_{ij}, refers to the geometric component of ground motion and is therefore the error estimate for the first stage of the overall process, it is renamed σ_1 in Table B.5.1. Consequently, the total error associated with the geometric mean, or the average component of ground motion, $\sigma_{\ln Y,ave}$, is given by Equaiton (B.5.21).

$$\sigma_{\ln Y,ave} = \sqrt{\tau^2 + \sigma_1^{\,2}} \tag{B.5.21}$$

The component variance, $\sigma_c^{\,2}$, can be found from Equation (B.5.22) below.

$$\sigma_c^{\,2} = \frac{1}{N}\sum_{j=1}^{N}\frac{\left[\ln\left(y_{1j}\right) - \ln\left(y_{2j}\right)\right]^2}{4} \tag{B.5.22}$$

In Equation (B.5.22), N is again the total number of records in the dataset, and y_{1j} and y_{2j} are the two components of the j^{th} record in the dataset. Given this component variance, the standard deviation of the intra-event terms for the random, or arbitrary, component now referred to as σ can be found from Equation (B.5.23).

$$\sigma = \sqrt{\sigma_1^{\,2} + \sigma_c^{\,2}} \tag{B.5.23}$$

Now, the total standard deviation related to the arbitrary component of ground motion ($\sigma_{\ln Y}$ in Table B.5.1) can be found from combining the previous definitions and is given in Equation (B.5.24).

$$\sigma_{\ln Y,arb} = \sqrt{\tau^2 + \sigma_1^{\,2} + \sigma_c^{\,2}} \tag{B.5.24}$$

One should be careful when using the model presented here that the appropriate error for the application in question is used. One should refer to Baker and Cornell (2006) for further details of how to ensure compatibility between hazard analyses and response, or demand, analyses.

B.5.5. Discussion of the Final Model

Examples of the predictive model for the FAS are shown in Figure B.5.1 and Figure B.5.2. Figure B.5.1 shows the scaling of the predictive model with respect to both magnitude and distance. Figure B.5.2 shows the influence of the dummy variables for fault mechanism and site class for fixed values of magnitude and distance. In both of these figures, the modelled spectra are shown over a range of 0.4 – 20 Hz (0.05 – 2.5 second period range). The actual regressions were performed over a range of frequencies greater than this but the coefficients that were obtained at low frequencies were determined for progressively smaller datasets as can be appreciated from Table B.5.1. In addition, the data that was available at lower frequencies was heavily dominated by foreign data in the near field and consequently would not have provided very strong constraint on the geometric spreading at distance. It is worth noting however that the coefficient values for the geometric spreading terms are reasonably close to the theoretical value for these frequencies though and also when considering the unconstrained regression coefficients given in Appendix B3 the factor for near source constraint agrees well with the value that was assumed over this low frequency range. This finding provides further justification for the adoption of the 19 km value used in the studies of peak ground acceleration of Zhao et al. (1997) and Cousins et al. (1999). Extrapolating the spectra to lower frequencies than 0.4 Hz is strongly advised against, but extrapolation up to at least 24.5 Hz using the coefficients presented here could be done with some confidence in the resulting spectral amplitudes. The frequency range provided here covers the majority of frequencies of relevance to general engineering applications. A discussion of how to extend models of the Fourier Amplitude spectra beyond the range specified here can be found in Trifunac (1994). An example of where extensions above and below the typical range of reliable frequencies given from strong motion records is also given in Trifunac and Todorovska (2004).

Panel (a) of Figure B.5.1 shows the scaling of the FAS with respect to magnitude. Unfortunately, as was also seen in Chapter Four of this section, the validity of the magnitude – corner frequency model cannot readily be ascertained from these visual inspections as the majority of events in the dataset would have corner frequencies that are close to, or lower than, the range in which the modelled spectral amplitudes become less reliable. The general form of the model appears reasonable with the exception that between about 0.4 – 0.5 Hz the spectra appear to trend slightly upwards. The modelled spectra should therefore be regarded with caution over this range. Panel (b) of this same figure shows the scaling with distance and in this case one would expect that the general form of the spectra be maintained whilst being shifted vertically downward with increasing distance. The spectra plotted here for distances of 10, 50, and 100 km show this trend well.

In Figure B.5.2, panel (a), the influence of the site class is shown. Here, the observed trends agree well with the findings of Sabetta and Pugliese (1996) in which the amplification of spectra for softer sites peak at lower frequencies than those for intermediate sites. We also see that the site class C spectra amplifies the rock motion more than the site class B spectra. These are both expected results when one considers the likely range of response frequencies of the various site classes. Recalling the site classification scheme used in the loadings code for New Zealand (Standards New Zealand 1992), site class C was described as

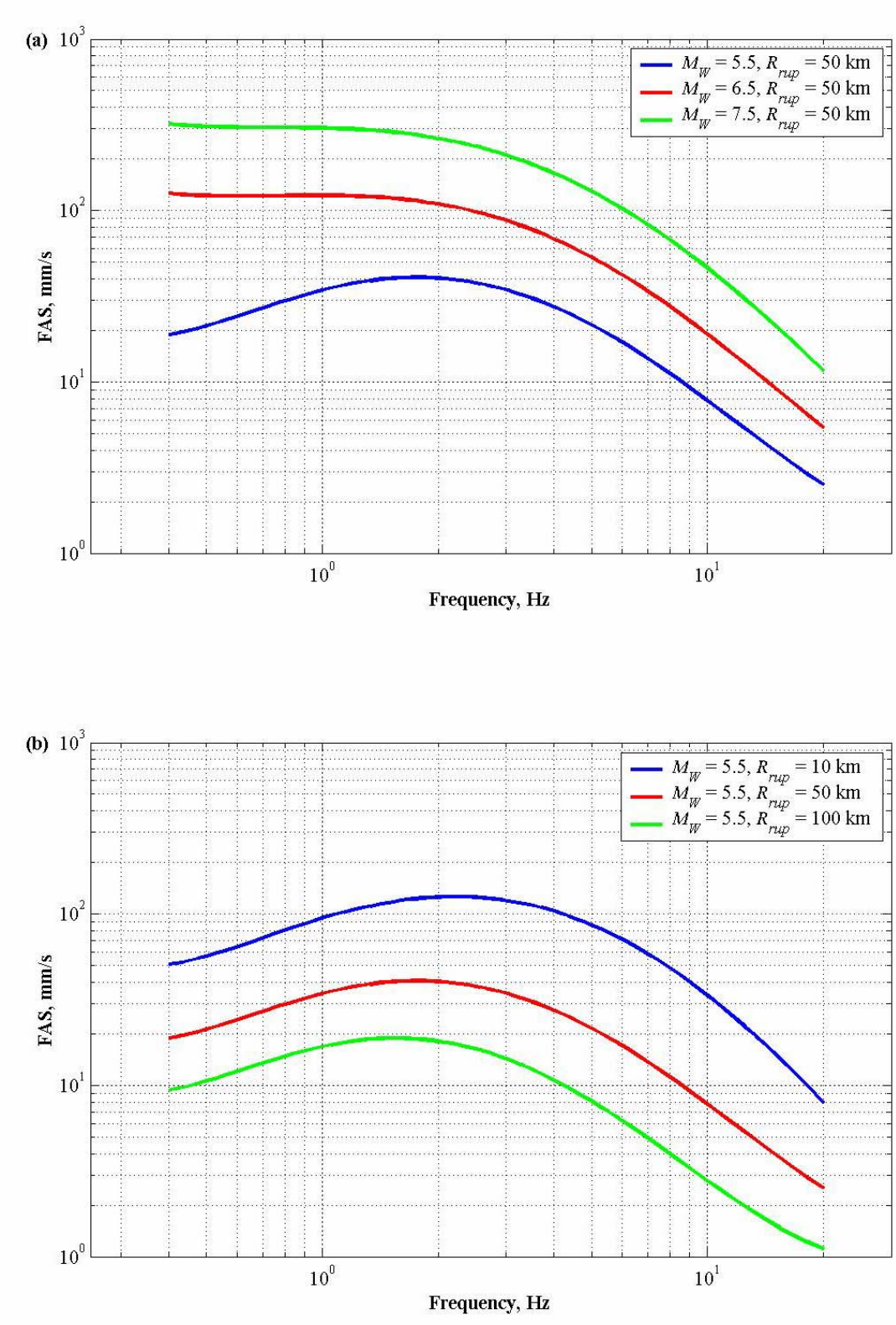

Figure B.5.1: Scaling of the predictive model for the Fourier Amplitude Spectrum of Acceleration with both magnitude, panel (a), and distance, panel (b). Both panels depict the scenario of a strike-slip fault mechanism and site class A.

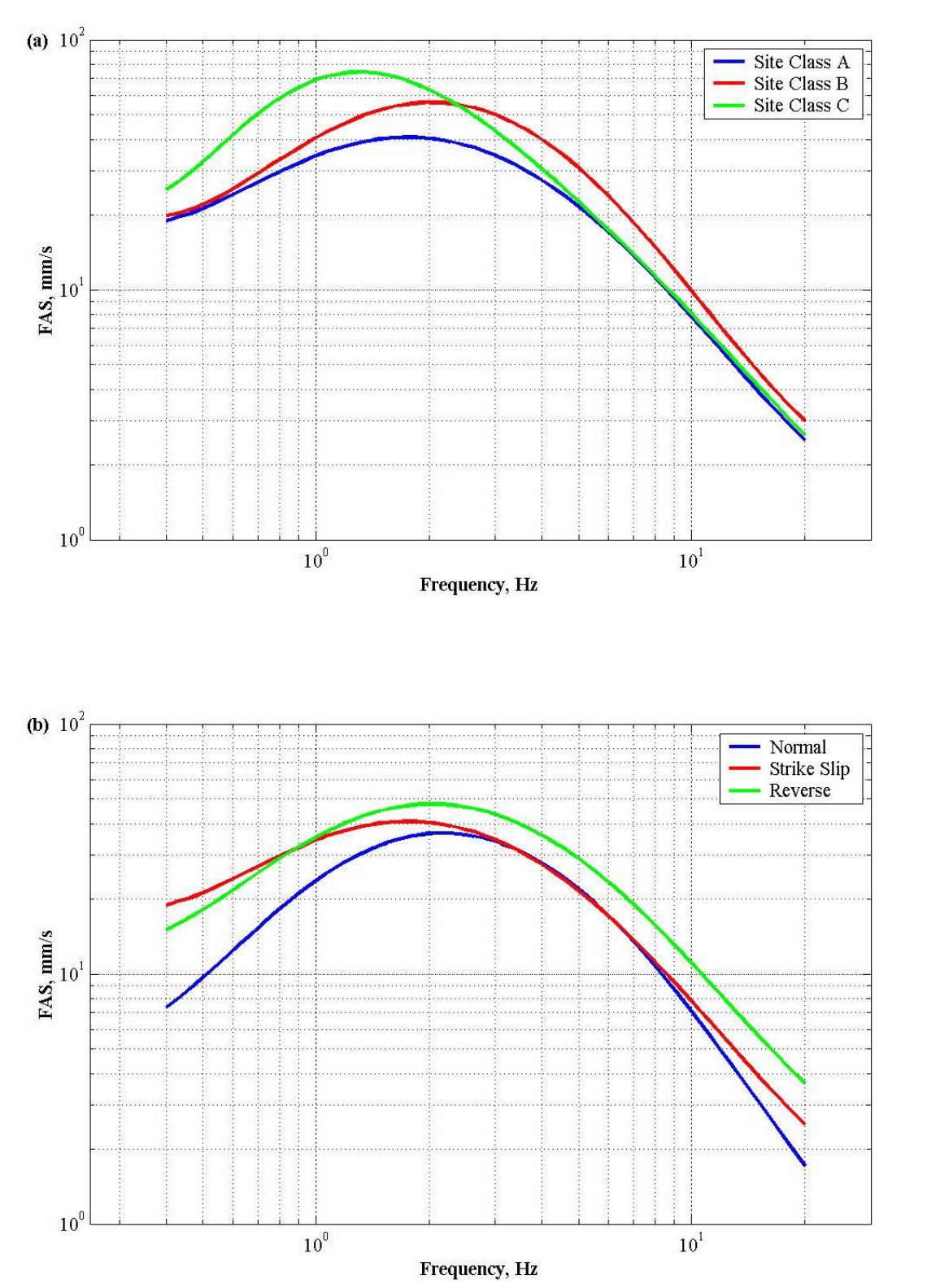

Figure B.5.2: Scaling of the predictive model for the Fourier Amplitude Spectrum of Acceleration with both site class, panel (a), and fault mechanism, panel (b). Both panels depict the scenario of a magnitude 5.5 earthquake at a distance of 50 km.

representing sites where the low amplitude natural period exceeds 0.6 seconds. This period range corresponds to frequencies below approximately 1.7 Hz and it is in this range where the amplification for site class C is seen most prolifically. The suggested upper limit for site class A is 0.25 seconds, corresponding to a frequency of 4 Hz; intermediate sites should therefore peak in between this value and the 1.7 Hz value of site class C. Panel (a) of Figure B.5.2 again shows this expected response well. It therefore appears as though the site response is adequately modelled by the predictive equation.

The influence of fault mechanism is not as well modelled. Panel (b) of Figure B.5.2 shows that although the general trends that should be expected are seen over a reasonable frequency range, but that there is some unexpected behaviour at low frequencies. Although the plot shown is for site class A, the same trends are observed for both site classes B and C as well. The reverse mechanism spectra are systematically higher than the strike-slip spectra over the majority of frequencies apart from the low frequency range. The strike-slip and normal mechanism spectra are relatively similar over a reasonable range of frequencies which is again to be expected as often the strong motion records from these events are grouped together. However, significant departures are observed between the two fault types at both high and low frequencies justifying the distinction made in this study between these two site classes.

In general it can be said that the functional form of the model and the regression coefficients obtained in this analysis generate strong motion spectra that agree reasonably well with the expected form of such a model over wide range of frequencies. This statement is based primarily upon consideration of the form of the model rather than any revelation gleaned from the observed fit to the actual strong motion data. In order to ascertain the quality of the fit to the actual data it is more appropriate to consider the residuals determined for various frequency values that show the fit of the model to the data with respect to magnitude and distance. As coefficients were obtained for a large number of frequencies it is not appropriate to show plots of residuals for all of these frequencies here. Rather, two examples are shown for frequencies of 1 Hz and 5 Hz; these frequencies correspond to the commonly used response spectral ordinates of 1 and 0.2 seconds respectively. As can be seen from Table B.5.1, these frequencies have associated errors that are fairly typical in terms of their overall magnitude; they have therefore only been chosen due to their familiarity when dealing with response spectra. Here though, rather than considering the overall magnitude of the errors we are interested in the distribution of the individual error estimates with respect to both magnitude and distance.

Figure B.5.3 and Figure B.5.4 both show plots of the inter-event residuals with respect to magnitude in panel (a), the intra-event residuals with respect to magnitude in panel (b), and the intra-event residuals with respect to rupture distance in panel (c) for frequencies of 1 and 5 Hz respectively. In both cases it can be appreciated that there are no obvious trends that depart from the ideal case of zero mean and normally distributed errors over large magnitude and distance ranges. This situation is also found to be the case when the residuals are plotted in a similar fashion but for each of the individual site classes and for each of individual fault types. These plots are presented here for a frequency of 2 Hz in Figure B.5.5 through to Figure B.5.8. Figure B.5.5 plots the intra-event residuals against magnitude for each of the three site

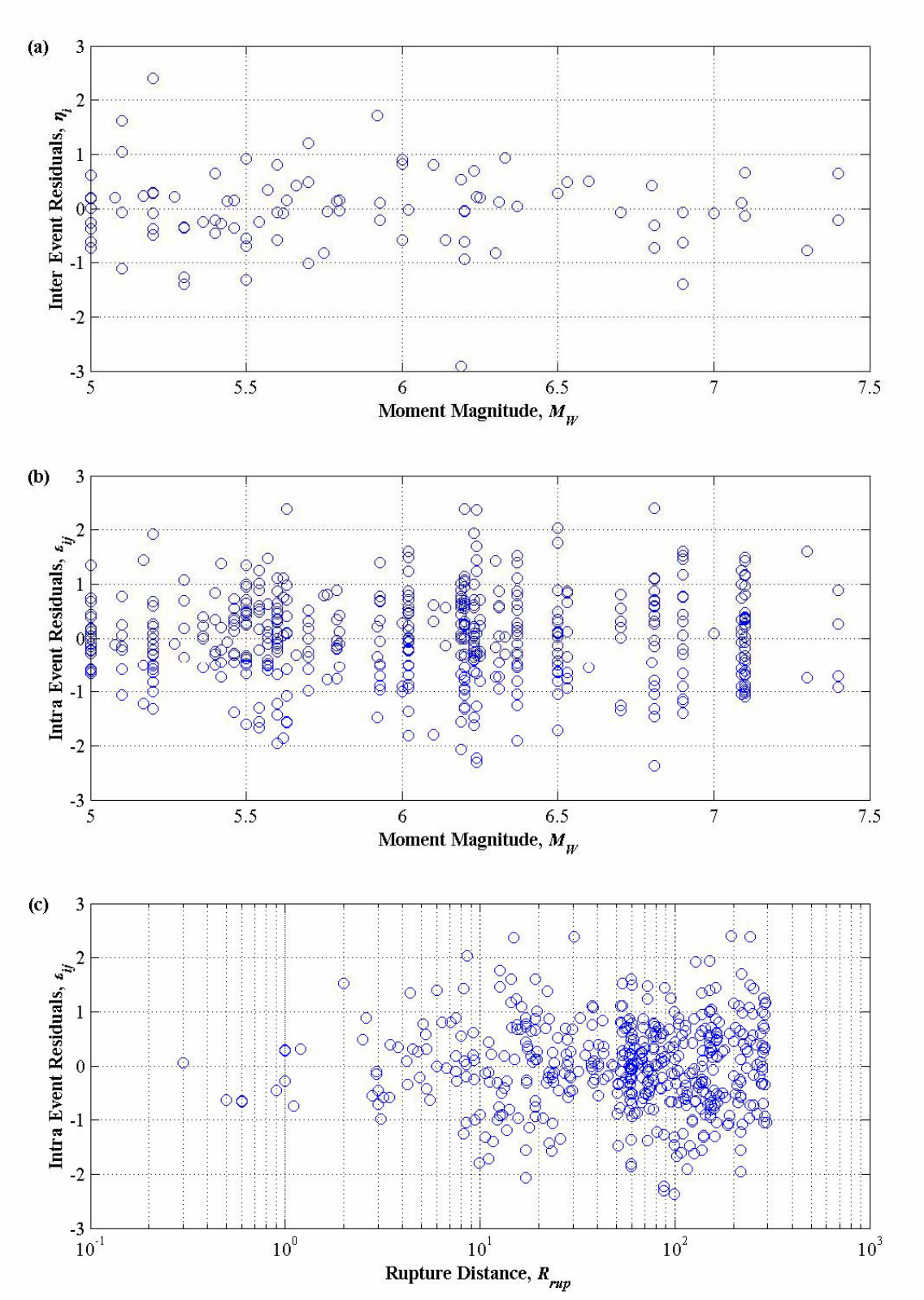

Figure B.5.3: Residuals for the predictive model for the Fourier Amplitude Spectrum of Acceleration for New Zealand. Residuals are shown here for a frequency of 1 Hz (1 second period). Panel (a) shows the inter event residuals plotted against magnitude, panel (b) shows the intra event residuals plotted against magnitude, and panel (c) shows the intra event residuals plotted against the rupture distance.

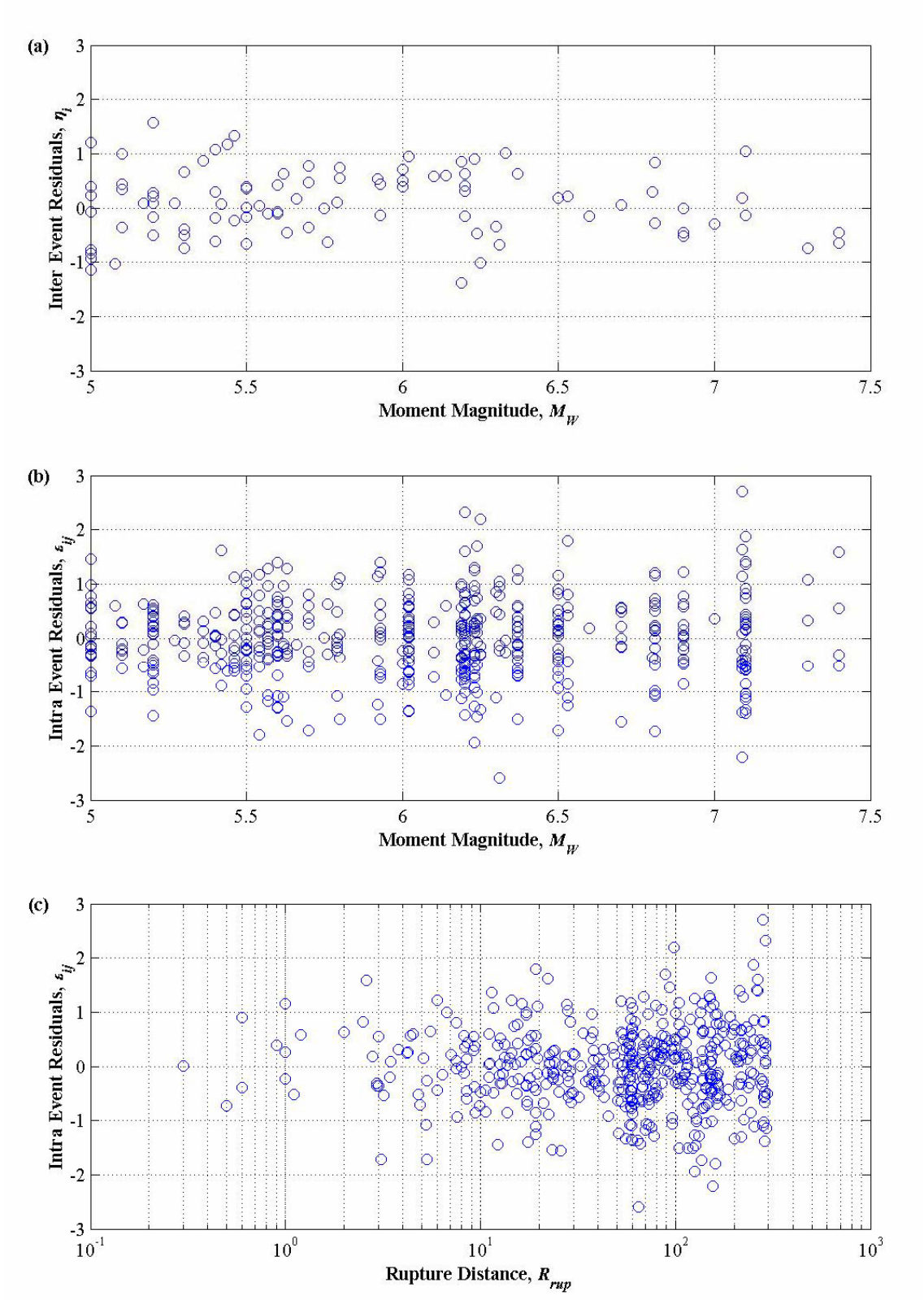

Figure B.5.4: Residuals for the predictive model for the Fourier Amplitude Spectrum of Acceleration for New Zealand. Residuals are shown here for a frequency of 5 Hz (0.2 second period). Panel (a) shows the inter event residuals plotted against magnitude, panel (b) shows the intra event residuals plotted against magnitude, and panel (c) shows the intra event residuals plotted against the rupture distance.

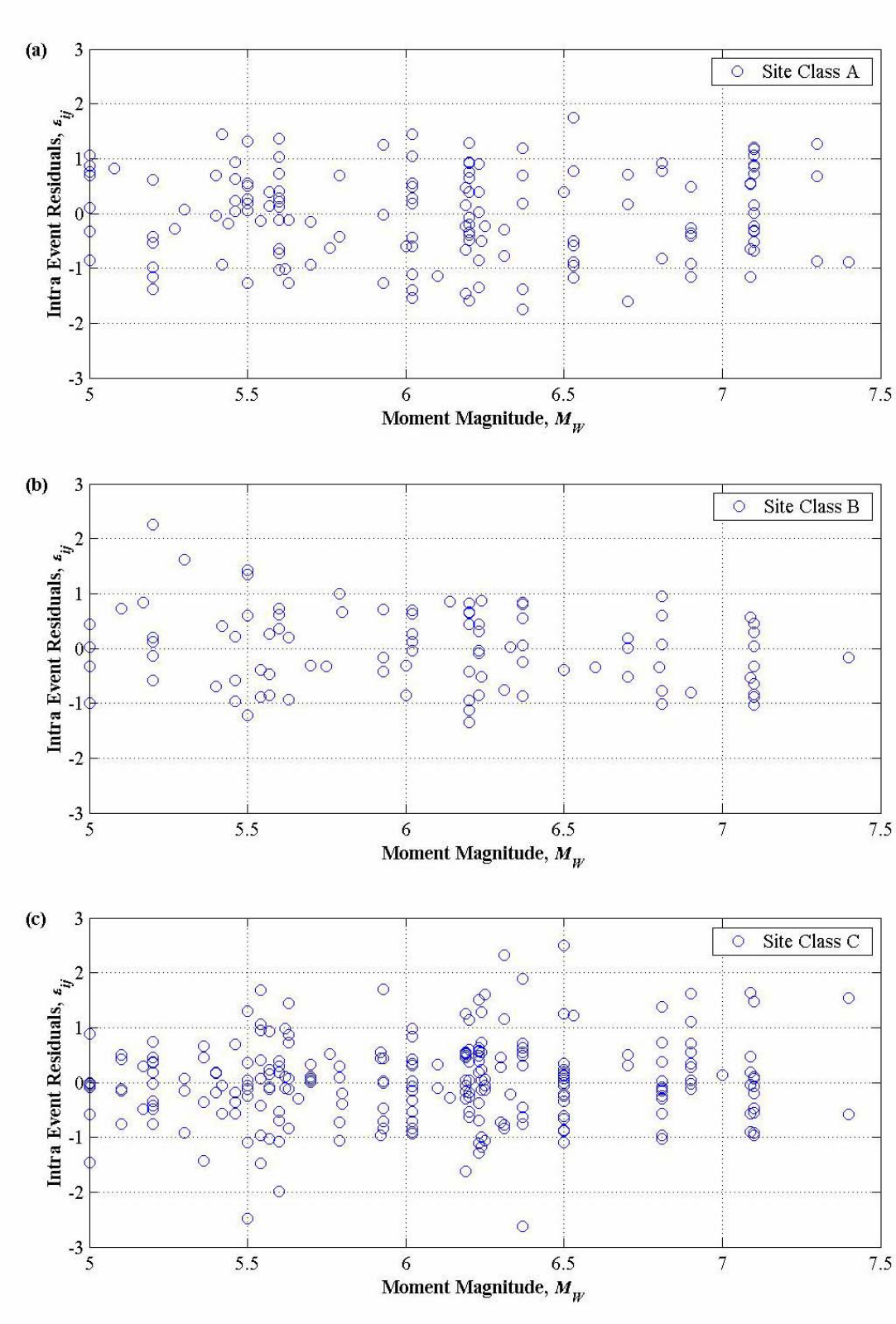

Figure B.5.5: Distribution of the Intra-event residuals with respect to magnitude for a frequency of 2 Hz. Panel (a) shows only site class A residuals, panel (b) shows only site class B residuals, and panel (c) shows only site class C residuals.

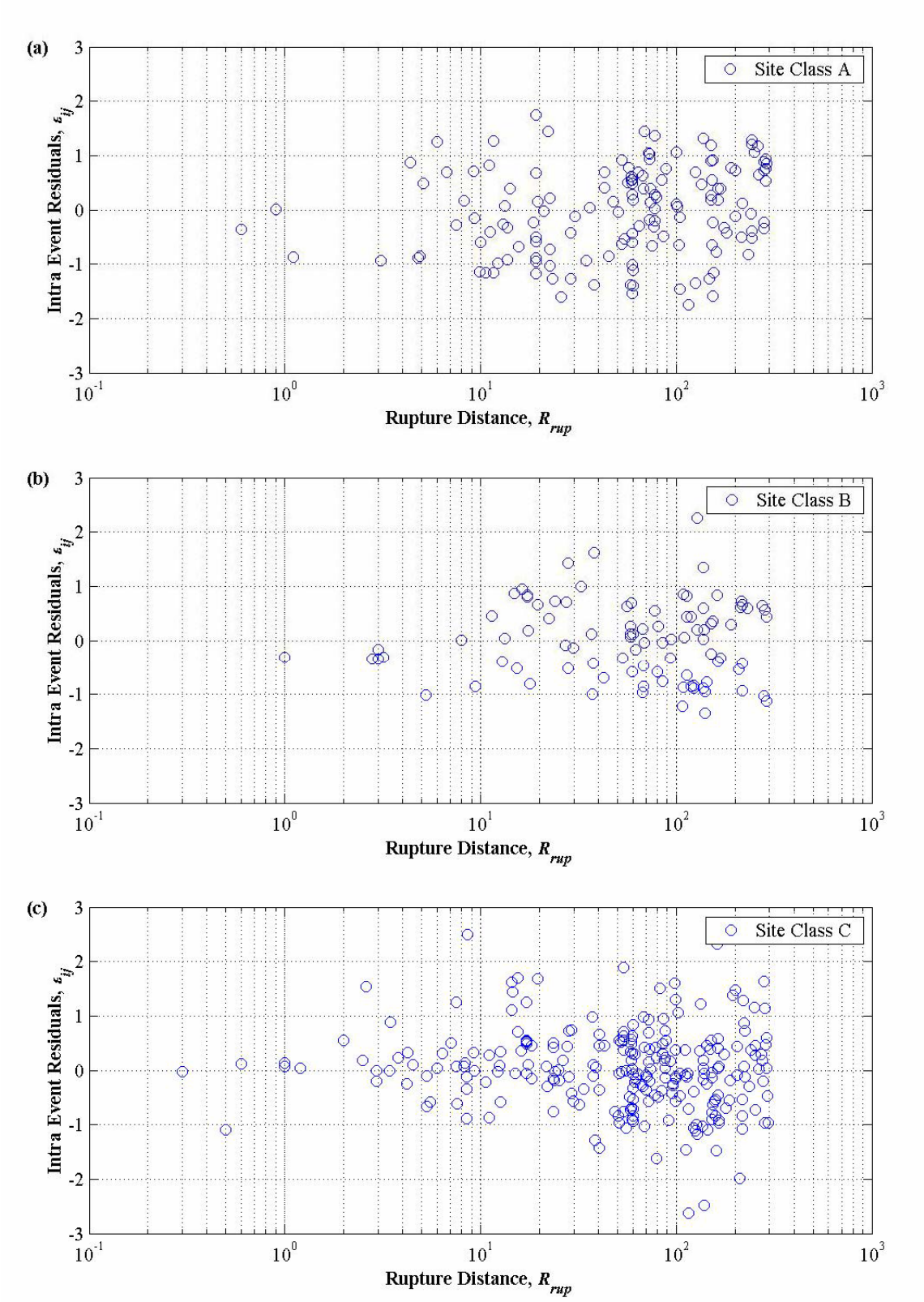

Figure B.5.6: Distribution of the Intra-event residuals with respect to rupture distance for a frequency of 2 Hz. Panel (a) shows only site class A residuals, panel (b) shows only site class B residuals, and panel (c) shows only site class C residuals.

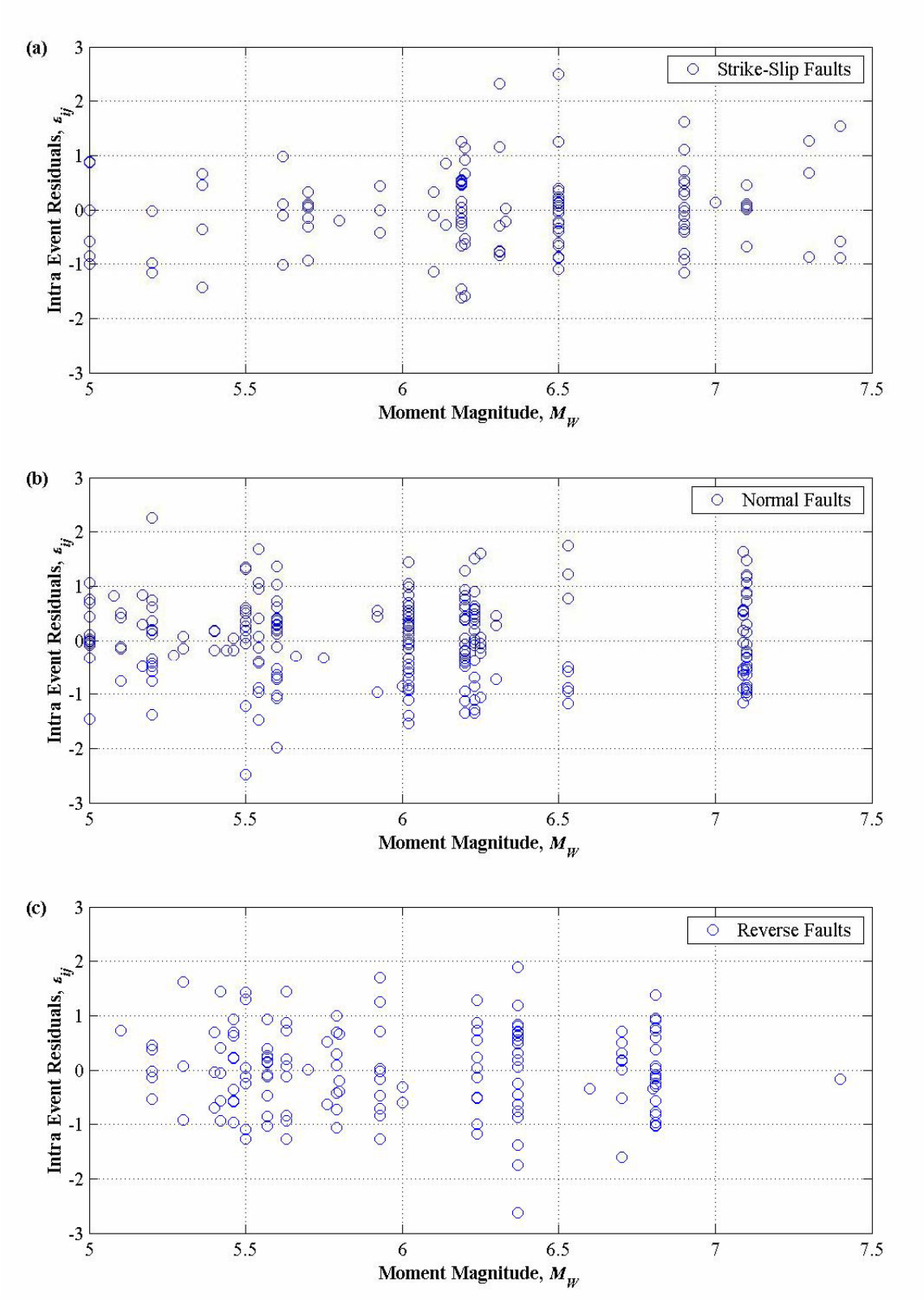

Figure B.5.7: Distribution of the Intra-event residuals with respect to magnitude for a frequency of 2 Hz. Panel (a) shows only Strike-Slip event residuals, panel (b) shows only Normal event residuals, and panel (c) shows only Reverse event residuals.

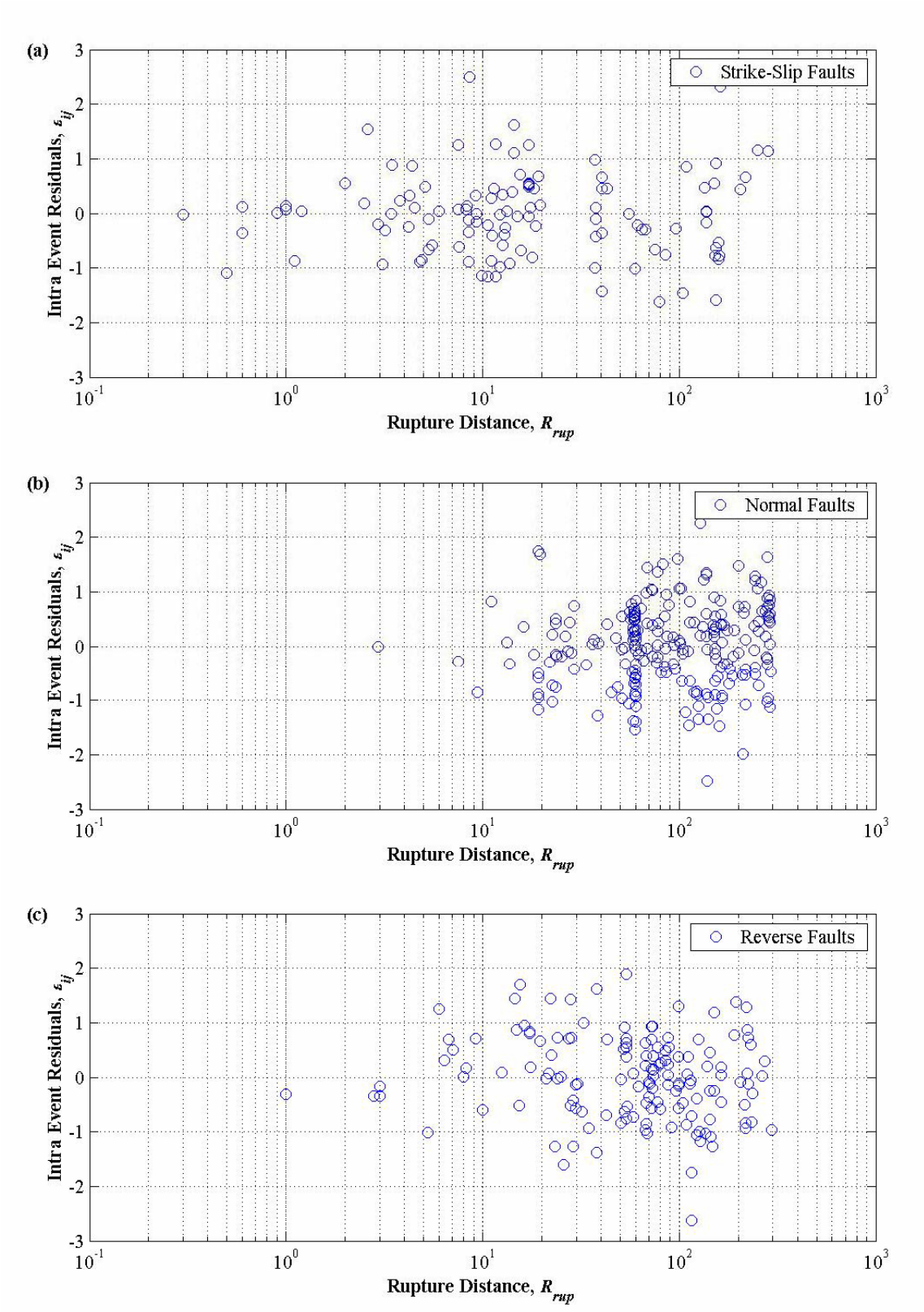

Figure B.5.8: Distribution of the Intra-event residuals with respect to rupture distance for a frequency of 2 Hz. Panel (a) shows only Strike-Slip event residuals, panel (b) shows only Normal event residuals, and panel (c) shows only Reverse event residuals.

classes, Figure B.5.6 plots the same residuals against rupture distance for the three site classes. Figure B.5.7 and Figure B.5.8 show the same plots respectively as the two previous figures with the exception that rather than distinguishing between site classes, these figure plot the intra-event residuals for the three different fault categories. As well as acting to demonstrate the stability of the predictive model with respect to the different subsets of the total dataset these figures also help to demonstrate how the data is distributed with respect to the various categories in the analysis. Note also that the use of dummy variables to partition the dataset enables the total dataset to support the determination of the regression coefficients applicable to the various subsets because they are able to share common scaling factors (Searle 1971).

B.5.6. Chapter Summary

This chapter has demonstrated how a comprehensive regression procedure was implemented to derive a predictive model for the Fourier Amplitude Spectrum of strong ground motion acceleration for general use in New Zealand. This model has been shown to give reasonably stable estimations of the mean spectral amplitudes over a wide range of frequencies of interest to engineers. The form of the regression model made use of the magnitude – corner frequency relation derived in the Chapter Four of this section by modifying the observed response to account for the magnitude dependent frequency scaling applicable to each frequency that was considered. The total predictive model for the Fourier Amplitude Spectrum of strong ground motion in New Zealand can therefore be written as in Equation (B.5.25).

$$\ln A = c_1 + c_2 M_W + 2\ln f - \ln\left[1 + \left(f^2 / f_c^{\,2}\right)\right] + c_3 \ln\left[\sqrt{r_{rup}^2 + c_4^{\,2}}\right] + c_5 S_B + c_6 S_C + c_7 F_N + c_8 F_R \tag{B.5.25}$$

In Equation (B.5.25) the Fourier Amplitude for the given frequency, f, is denoted by A. The coefficients are as given in Table B.5.1 and the corner frequency is given by the following equation.

$$\log_{10} f_c = 2.645 - 0.5 M_W \tag{B.5.26}$$

The errors associated with this model have been thoroughly determined and have been provided for both the random, or arbitrary, component of ground motion as well as for the geometric mean of two horizontal components. The model is therefore suitable for use in both hazard analyses and response, or demand analyses. As well as the nature of the errors being robustly defined, the magnitude of the errors is reasonable when compared with the more complicated empirical model of Trifunac (1994). However, it was noted at the beginning of the chapter that the magnitude of the errors will be somewhat dependent upon the processing method used to obtain the observed spectra that form the strong motion dataset. It should be noted though that the processing method should essentially only have influence on the intra-event variance, σ^2. The inter-event variance should remain relatively stable as it reflects systematic

deviations from the mean of groups of records associated with a particular earthquake; these systematic deviations should still exist regardless of the processing technique.

In order to reduce the overall error associated with the prediction of Fourier spectral amplitudes more strong motion records must be obtained so that more complicated functional forms may be used without compromising the quality of the regression coefficients that are obtained. In addition, a significant reduction in the inter-event variance may be achieved if the individual uncertainties in the magnitude values are taken into account (Rhoades 1997). The potential impact that this additional consideration may have is demonstrated in the next chapter where a predictive model for Arias Intensity is derived. This technique was not able to be readily applied in this section however as the dependence of the model upon magnitude is highly nonlinear due to the dependence of the corner frequency upon magnitude and the mathematics would become too complicated in this case.

It was found that the dataset that excluded the records from the 1999 Chi-Chi earthquake obtained better results albeit over a slightly smaller magnitude range. The current model can be regarded as being suitable for application over a range of frequencies of 0.4 – 20 Hz, a range of magnitudes of 5.0 – 7.4, and for distances up to at least 100 km. The model actually appears to be stable up to a much larger distance range, but the question of whether ground motions from magnitudes of up to 7.4 can truly be considered as being strong ground motion must be raised over these ranges. It can be safely assumed however that the model is capable of predicting accurate spectra for all distances corresponding to earthquake having magnitudes of less than approximately 7.5 that would create strong ground shaking.

The ability of the model to accurately estimate Fourier Spectral amplitudes over a relatively large distance range using essentially a simple spherical geometric spreading function is contrary to findings from world wide models that have found that a bilinear or trilinear (in log space) distance scaling is more appropriate for modelling motions at large distances (Aki and Richards 1980; Atkinson and Mereu 1992; Olafsson 1999; Boore 2003). The findings of this study are however consistent with every predictive model for strong motion that has been derived for use in New Zealand as thus far no relation has incorporated effects associated with changes in the rate of attenuation with distance.

B.6. Predictive Equation for Arias Intensity in New Zealand

B.6.1. Introduction

The Arias Intensity is an important measure of the strength of a ground motion as it reflects multiple characteristics of the motion in question. Whereas typical scalar ground motion indices such as peak ground acceleration and peak ground velocity, or particular ordinates of spectral acceleration, reflect the nature of the ground motion in a very one dimensional sense[†], Arias Intensity is able to capture and represent additional aspects of the nature of the overall ground motion. In particular the ability to reflect the energy of a ground motion signal across the entire frequency spectrum, or equivalently, to reflect the influence of the entire duration of a ground motion is a property of Arias Intensity that lends itself to useful application in many structural and geotechnical applications.

Recently, Travasarou et al. (2003) have demonstrated the effectiveness of using Arias Intensity as a measure of the likelihood of damage to short period structures, showing that the correlation between Arias Intensity and structural damage is stronger than that between peak ground acceleration and structural damage. Arias Intensity is also a very useful ground motion measure that can be used in geotechnical applications such as determining the likelihood of rock falls and landslides (Harp and Wilson 1995; Del Gaudio et al. 2003) or for estimating the propensity of a site to experience liquefaction (Egan and Rosidi 1991; Kayen and Mitchell 1997). In applications such as these it is not necessarily the peaks of a strong motion record that determine the response, rather it is a combination of the frequency content of the motion, the duration of the motion, and the amplitude of the motion. The Arias Intensity is able to capture all of these aspects of a ground motion.

[†] Although the various measures are deemed suitable for use in particular situations, such as peak ground acceleration being associated with high frequency motion, thus effectively adding an additional 'partial' dimension to the ground motion measure.

In light of this utility probabilistic hazard analyses have begun to consider Arias Intensity as one of the ground motions measures assessed as part of the methodology. An example of this is the recent probabilistic hazard analysis with respect to Arias Intensity for southeastern Spain by Peláez et al. (2005). In order to conduct hazard analyses in terms of Arias Intensity stable predictive equations must be available for this purpose. In comparison to other measures of strong motion there are very few equations of this nature available (Wilson and Keefer 1985; Keefer and Wilson 1989; Wilson 1993; Sabetta and Pugliese 1996; Travasarou et al. 2003). In addition to these, generally regional, models earthquake specific investigation into the scaling of Arias Intensity have also been carried out (Hwang et al. 2004). Of these models, the Travasarou et al. (2003) model is based upon the largest dataset by far and uses the most complicated functional form for the regression model. Of the other models, most are either derived for a specific site class, or use dummy variables to distinguish between site classes. None of the models (apart from Travasarou et al., 2003) take into account the differences between ground motions generated by faults of differing mechanism.

In this chapter a comprehensive model for the attenuation of Arias Intensity in New Zealand is derived using a sophisticated regression technique and by employing a functional form that distinguishes between three site classes and three fault mechanism types. The errors associated with the model are robustly defined and the model is therefore able to be used for probabilistic hazard analyses in New Zealand. The dataset used for this analysis is the same as that previously used for the derivation of the predictive equation for the Fourier Amplitude of strong ground motion acceleration presented in Chapter Five of this section. Once again, two separate dataset were considered; one including the events from the Chi-Chi earthquake, and one excluding these events. This chapter begins by deriving a theoretical model for Arias Intensity before performing the regression analysis and then discussing the results.

B.6.2. Theoretical Development of the Functional Form of the Model

Arias Intensity (Arias 1970) relates to the cumulative energy per unit weight absorbed by an infinite set of single degree of freedom (SDOF) oscillators having fundamental frequencies uniformly distributed in $(0,\infty)$. In the most general case, the expression for Arias Intensity may be written as in Equation (B.6.1) below (Kayen and Mitchell 1997).

$$I_{xx}(\xi) = \frac{\arccos(\xi)}{g\sqrt{1-\xi^2}} \int_0^\infty a_x^2(t)\,dt \tag{B.6.1}$$

In the above expression, the term $I_{xx}(\xi)$ represents the Arias Intensity observed by SDOF oscillators with damping, ξ, aligned in the x-direction, responding to ground shaking in the x-direction. Naturally, there will be additional similar expressions representing the response of SDOF oscillators aligned in orthogonal directions responding to ground motions in other orthogonal directions. In this sense, the

expression given by Equation (B.6.1) is but one term of a second order tensor. The trace of this tensor ($I_{xx} + I_{yy} + I_{zz}$) is an invariant and consequently, all pairs of orthogonal axes passing through a predefined origin have the same Arias Intensity (i.e. $I_{xx} + I_{yy} = \text{const}$) (Travasarou et al. 2003).

The most common representation of the Arias Intensity is recovered for the case of zero damping in the SDOF oscillators; given this condition, the expression in Equation (B.6.1) reduces to that below in Equation (B.6.2).

$$I_{xx} = \frac{\pi}{2g}\int_0^\infty a_x^2(t)\,dt \tag{B.6.2}$$

The expression given in Equation (B.6.2) portrays the Arias Intensity in terms of the integral of what is essentially a transient stochastic signal. In order to develop the functional form of the regression equation for the Arias Intensity we make use of the well known Parseval's Theorem. This theorem is restated for completeness in terms of natural frequency below.

$$\int_{-\infty}^{\infty} |a(t)|^2\,dt = \int_{-\infty}^{\infty} |A(f)|^2\,df \tag{B.6.3}$$

Parseval's theorem states that the total power of a signal in both the time and frequency domains is equivalent. Therefore, given that we already have a theoretical model for the Fourier Amplitude Spectrum (FAS) of acceleration we are able to obtain an expression for Arias Intensity in terms of the strength of the FAS. Note that as we are considering real valued acceleration signals in the positive time domain the expression in (B.6.3) can be simplified to consider only positive times and frequencies without any loss of practical generality.

Now recalling the typical expression for the FAS developed in Chapter Three and restating it here in Equation (B.6.4) below for convenience,

$$A(f) = \frac{\mathbb{C}M_0(2\pi f)^2}{\left[1+(f/f_c)^2\right]}\frac{1}{R}\exp\left[-\frac{\pi fR}{Q(f)\beta}\right]S(f), \tag{B.6.4}$$

we see that the frequency dependence of this expression arises from aspects of the source, the path, and the site. The purpose of introducing the above expression into that for the Arias Intensity is not to obtain an exact closed theoretical expression for the Arias Intensity, but rather to guide us in the selection of an appropriate functional form for a regression model. With this in mind, it is prudent to make some simplifying assumptions to the expression in Equation (B.6.4) in order to relax some of the frequency dependence inherent in this model. Two such simplifications shall be made, firstly, the assumption of a frequency dependent anelastic attenuation function, $Q(f)$, may be relaxed to the case of a constant

attenuation rate, Q_0. This relaxation is not regarded as being overly inhibitive to the accuracy of the resulting model as the true frequency dependence of anelastic attenuation is not accurately known over a broad range of frequencies (Abercrombie 1998) and good models have been obtained for the FAS using the assumption of constant anelastic attenuation in the past (Anderson and Hough 1984; Olafsson 1999). The second relaxation is made with regard to the site response term. While it is well known that site response varies with frequency, and approximate models of this variation exist (Boore and Joyner 1997), it is also appreciated that our understanding of site response is limited (Boore 2004). Consequently, for the purpose of incorporating the effect of site response into a predictive equation for Arias Intensity we will ignore any frequency dependence of this function and simply introduce constant site class factors to account for the associated varying responses. This is in keeping with almost all existing predictive equations for strong motion indices.

One further adjustment to Equation (B.6.4) can be made to make the derivation slightly more general. In Equation (B.6.4) the geometric spreading is assumed to be perfectly elastic spherical spreading at a rate of R^{-1}. However, in reality this ideal spreading rate is seldom observed. Frequently the rate of spreading is observed to be greater than -1 but there are also many examples of attenuation at lower rates than this. Therefore, in the following derivation, the geometric spreading rate is assumed to be $R^{-\zeta}$.

The form of the model for the FAS that we will carry into the development of the functional form of the Arias Intensity relationship can therefore be given by the expression below (after some substitution and cancelling).

$$A(f) = \frac{\pi \mathbb{R}_{\phi\theta} VFM_0 f^2}{\rho \beta^3 R_0 \left[1+\left(f/f_c\right)^2\right]} \frac{1}{R^{\zeta}} \exp\left[-\frac{\pi f R}{Q_0 \beta}\right] S_i \tag{B.6.5}$$

In Equation (B.6.5), the term S_i represents the site response with the subscript, i, corresponding to the various site classes incorporated into the final model. Now, inserting Equation (B.6.5) into the expression for Arias Intensity in terms of frequency we obtain the following equation.

$$I_{aa} = \frac{\pi}{2g}\left[\frac{\pi \mathbb{R}_{\phi\theta} VFM_0}{\rho \beta^3 R_0 R^{\zeta}}\right]^2 S_i \int_0^{\infty} \frac{f^4}{\left[1+\left(f/f_c\right)^2\right]^2} \exp\left[-\frac{2\pi f R}{Q_0 \beta}\right] df \tag{B.6.6}$$

In order to evaluate the integral in Equation (B.6.6), it is worthwhile following Ólafsson and Sigbjörnsson (1999) and make a change of variable. Letting $\overline{f} = f/f_c$, $\kappa_Q = 2\pi R/Q_0\beta$, and then further letting $\lambda = \kappa_Q f_c$, the above integral expression can be recast as follows.

$$\Lambda = f_c^5 \int_0^\infty \frac{\overline{f}^4}{\left[1+\overline{f}^2\right]^2} \exp\left[-\lambda \overline{f}\right] d\overline{f} = \frac{f_c^5 \Psi}{\lambda} \tag{B.6.7}$$

Here, the capital psi term is a function of lambda and involves forms of both the sine and cosine integrals†.

$$\Psi = 1 - \frac{\lambda}{2}\left\{\mathrm{Ci}(\lambda)\left[\lambda\cos\left(\lambda + 3\sin(\lambda)\right)\right] + \mathrm{Si}(\lambda)\left[\lambda\sin\left(\lambda - 3\cos(\lambda)\right)\right]\right\} \tag{B.6.8}$$

The sine and cosine integral terms in the above expression are given respectively in Equations (B.6.9) and (B.6.10) below.

$$\mathrm{Si}(\lambda) = -\frac{\pi}{2} + \int_0^\lambda \frac{\sin t}{t} dt \tag{B.6.9}$$

$$\mathrm{Ci}(\lambda) = \gamma + \ln(\lambda) + \int_0^\lambda \frac{\cos t - 1}{t} dt \tag{B.6.10}$$

In Equation (B.6.10), γ is Euler's Constant, all other terms have previously been defined. Unfortunately, upon first inspection, the indefinite form of the above integral expressions precludes the selection of a simple functional form for the regression model based upon theoretical considerations. Fortunately however, as highlighted by Ólafsson and Sigbjörnsson (1999), the solution to the integral expression given in Equation (B.6.7) can be very well approximated over a wide range of practical values by a surprisingly simple expression, i.e. by simply letting the expression for Ψ simply equal one. A demonstration of the effectiveness of this approximation can be seen by making a plot of $\Psi(\lambda)$ against λ. Such a plot is presented in Figure B.6.1.

Note that in Figure B.6.1, the deviation from unity is small over this range of lambda values, with the worst case being less than a 20% deviation. The appropriateness of the previously mentioned approximation can be appreciated when one recognises that the range of parameter values that would result in values of lambda in the range where the deviation becomes significant is very limited. In practice (i.e. for commonly anticipated parameter values) relatively high values of lambda are only achieved in the case of either low magnitude ($M \to 5$) and large distance ($R \to 100$ km). As these two conditions correspond to the earthquake scenario that is of least concern for most engineering applications the approximation of $\Psi \cong 1$ is a good one. As already mentioned, the worst case error given this assumption is still only 20% and this corresponds to earthquake scenarios that are generally outside the scope of concern for most engineering applications.

† Various analytic forms of these integrals exist in the literature. Generally they differ from each other by a simple factor.

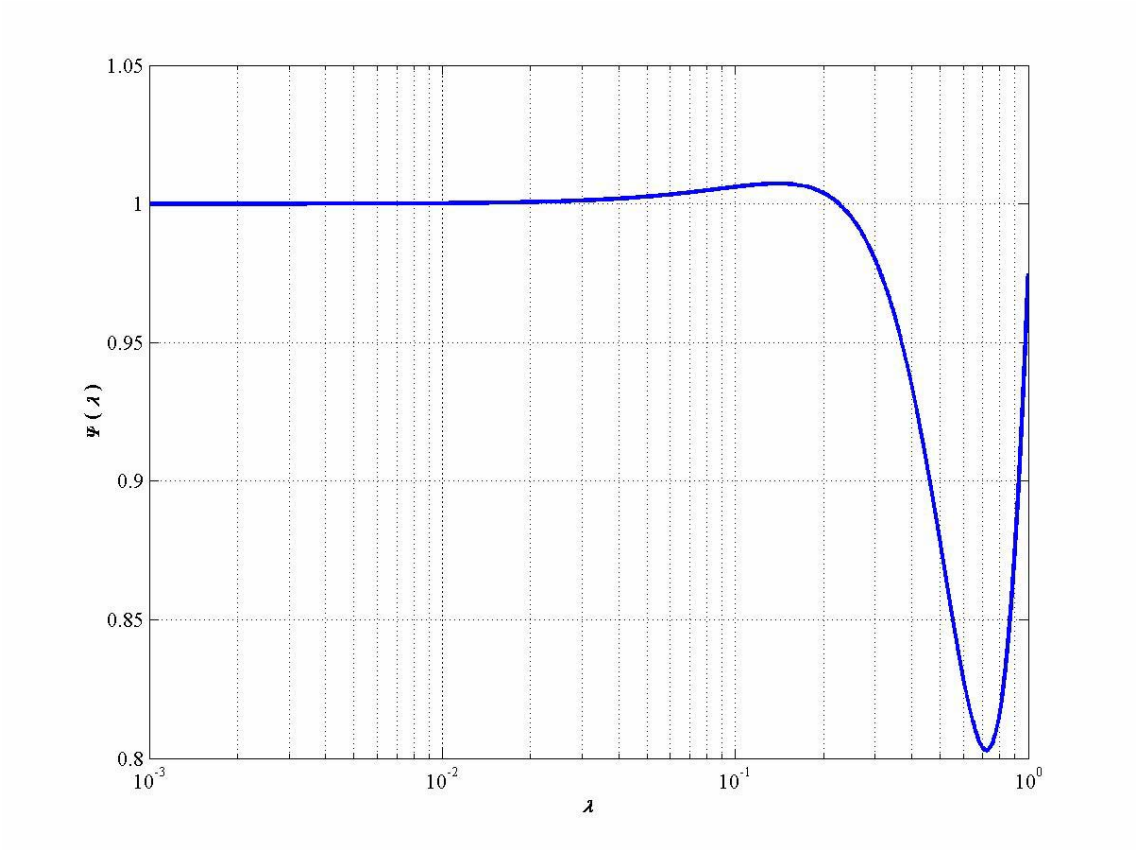

Figure B.6.1: Variation of the analytical integral solution, $\Psi(\lambda)$, against λ

Therefore, proceeding with this approximation in mind, the theoretical expression for the Arias Intensity is now greatly simplified as can be seen in Equation (B.6.11) below.

$$I_{aa} = \frac{\pi}{2g}\left[\frac{\pi \mathbb{R}_{\phi\theta} VFM_0}{\rho\beta^3 R_0 R^{\zeta}}\right]^2 \frac{f_c^{\,5}}{\lambda} S_i \tag{B.6.11}$$

Upon back-substituting the expression for lambda, the equation above becomes that in Equation (B.6.12) below.

$$I_{aa} = \frac{\pi}{2g}\left[\frac{\pi \mathbb{R}_{\phi\theta} VFM_0}{\rho\beta^3 R_0 R^{\zeta}}\right]^2 \frac{f_c^{\,4} Q_0 \beta}{2\pi R} S_i \tag{B.6.12}$$

And upon some simplification the overall theoretical model for the Arias Intensity can be expressed as in Equation (B.6.13).

$$I_{aa} = \frac{\pi^2 \mathbb{R}_{\phi\theta}^2 Q_0 f_c^{\,4} M_0^{\,2} S_i}{2g\rho^2\beta^5 R_0 R^{2\zeta+1}} \tag{B.6.13}$$

However, it can also be noted that while the anelastic attenuation factor, Q_0, has been assumed to be independent of frequency for this derivation, it is typically found to be a linearly increasing function of distance (Anderson and Hough 1984; Olafsson 1999). This is due to the fact that waves travelling greater distances typically penetrate deeper into the crust where they experience relatively less attenuation than their counterparts in the shallower crust (Olafsson 1999). It can therefore be appreciated that rather than being an increasing function of distance, the term κ_Q that was previously defined is constant with respect to distance. Therefore, rearranging the expression for κ_Q and replacing this back into Equation (B.6.13) the theoretical model can be simplified to that in Equation (B.6.14).

$$I_{aa} = \frac{\pi^3 \mathbb{R}_{\phi\theta}^2 f_c^4 {M_0}^2 S_i}{g \rho^2 \beta^6 R_0 R^{2\zeta} \kappa_Q} \tag{B.6.14}$$

In the above equation the terms for both the corner frequency and the seismic moment are essentially functions of moment magnitude. Representing both of these terms as functions of magnitude using the common relations below and taking the natural logarithm of the completed equation yields the functional form of our regression model.

$$\log_{10} f_c = a - 0.5 M_W \tag{B.6.15}$$

$$\log_{10} M_0 = c M_W + d \tag{B.6.16}$$

Making the relevant substitution, and consequent rearrangements results in Equation (B.6.17).

$$\ln\left[I_{aa}\right] = \ln\left[\frac{\pi^3 \mathbb{R}_{\phi\theta}^2}{g \rho^2 \beta^6 R_0}\right] + \ln[10]\left(2cM_W + 2d + 4a - 2M_W\right) - 2\zeta \ln[R] - \ln\left[\kappa_Q\right] + \ln\left[S_i\right] \tag{B.6.17}$$

The primary magnitude scaling can be revealed after inserting the common value of $c = 1.5$ (Hanks and Kanamori 1979).

$$\ln\left[I_{aa}\right] = \left\{\ln\left[\frac{\pi^3 \mathbb{R}_{\phi\theta}^2}{g \rho^2 \beta^6 R_0}\right] + \ln[10]\left(4a + 2d\right)\right\} + \ln[10] M_W - 2\zeta \ln[R] - \ln\left[\kappa_Q\right] + \ln\left[S_i\right] \tag{B.6.18}$$

It should also be recognised that the primary factor that controls the differing strengths of ground motions from different source mechanisms using the above theoretical model is the radiation pattern term, $\mathbb{R}_{\phi\theta}$. This term, as has already been discussed in detail in previous chapters, reflects the azimuthal variation of the strength of seismic waves leaving the source of a shear dislocation. In the final regression equation, factors for various styles of faulting will be included that essentially reflect the variation in the radiation pattern.

As was mentioned in Chapter Five of this section, a regression model would not be able to distinguish between the initial terms in the parentheses and the anelastic scaling term. As far as obtaining the functional form of the regression model is concerned these two terms should be grouped together to represent a single constant. In addition to this grouping together of these terms the standard modification to the distance scaling to account for the near source constraint also needs to be made. The functional form of the regression model is therefore made to be equivalent to the initial model used for the regression analysis conducted for the Fourier Amplitude Spectrum in the previous chapter. The similarities that exist between empirical models for various ground motion measures was also recognised and implemented by Sabetta and Pugliese (1996) where they used the same functional model for 5% damped pseudo-spectral velocity, peak ground acceleration, peak ground velocity, Arias intensity, and ground motion duration.

The theoretically derived model in Equation (B.6.18) therefore provides very strong constraints upon the likely values of the parameters that should be obtained during the regression procedure. This knowledge is very useful as no other models of this type exist for New Zealand and there is consequently no local basis for comparison. The derivation outlined above also acts to help identify potential correlations that may exist between the parameters. If the regression model is over-parameterised then there may be a suite of parameter values that could give similarly accurate results. However, knowledge of the expected values of these parameters will aid in distinguishing between these various parameter sets.

Another effect that is commonly included into predictive equations is the saturation of ground motions from large magnitude events. Commonly this effect is modelled as a higher order term of the magnitude scaling, i.e. a quadratic function of magnitude. This effect was taken into account by using a logarithmic scaling factor in the Travasarou et al. (2003). The inclusion of terms corresponding to a higher order scaling with magnitude also allows the model to accommodate any deviation from the theoretical linear scaling with magnitude that may be present in the empirical data. Higher order scaling terms have typically not been employed in the empirical models of Arias Intensity derived thus far[†]. The inclusion of this additional term also increases the number of parameters in the model and can influence the correlations between the parameters. For these reasons, as well as for reasons relating to the application of a particular regression technique, a higher order scaling with magnitude was initially left out of the functional form for the regression analysis.

The functional form of the regression model for Arias Intensity can therefore be expressed by the Equation (B.6.19) below.

$$\ln\left[I_{aa}\right] = c_1 + c_2 M_W + c_3 \ln\left[\sqrt{r_{rup}{}^2 + c_4{}^2}\right] + c_5 S_B + c_6 S_C + c_7 F_N + c_8 F_R \qquad \text{(B.6.19)}$$

[†] With the exception of the Travasarou et al. (2003) model.

All terms in this equation have been previously defined. The actual regression analysis is performed on the arithmetic average of two horizontal components of Arias Intensity as shown in Equation (B.6.20) below.

$$I_{aa} = \frac{I_{xx} + I_{yy}}{2} \tag{B.6.20}$$

This is the same average measure of ground motion that was adopted in the Travasarou et al. (2003) analysis.

B.6.3. Mixed Effects Regression Models

Mixed effects models are implemented to obtain the relevant coefficients of the empirical predictive model for the Arias Intensity. The theoretical model derived above acts as a firm functional form for the model. However, as in the case of the Fourier Amplitude Spectrum of acceleration the modification of the distance scaling to account for near field acts to introduce stronger coupling between the magnitude and distance scaling.

Once again, the general form of the mixed effects model can be written as in Equation (B.6.21), where $f\left(M_{W,i}, r_{ij}, \boldsymbol{\theta}\right)$ represents the functional form of the regression model, η_i is the random effect associated with the i^{th} earthquake, and ε_{ij} are the fixed effects. Both η_i and ε_{ij} are normally distributed (independent of each other) with zero means and have variances of τ^2 and σ^2 respectively.

$$y_{ij} = f\left(M_{W,i}, r_{ij}, \boldsymbol{\theta}\right) + \eta_i + \varepsilon_{ij} \tag{B.6.21}$$

Given the theoretical derivation presented in the previous section, the initial mixed effects model can be written as in Equation (B.6.22) below (where $y_{ij} = \ln\left[I_{aa,ij}\right]$ now represents the general response).

$$y_{ij} = c_1 + c_2 M_{W,i} + c_3 \ln\left[\sqrt{r_{ij}^{\ 2} + c_4^{\ 2}}\right] + c_5 S_{B,ij} + c_6 S_{C,ij} + c_7 F_{N,i} + c_8 F_{R,i} + \eta_i + \varepsilon_{ij} \tag{B.6.22}$$

Usually, in order to partition the overall model error between the inter and intra event components either the Abrahamson and Youngs (1992) or the Joyner and Boore (1993; 1994) algorithms are implemented. However, there is another more comprehensive algorithm that can also take into account the individual uncertainties inherent in the magnitude values in the strong motion dataset. This algorithm, presented by Rhoades (1997) has only been utilised sparingly since its introduction, yet it is very effective in reducing the variance associated with the inter event terms, particularly for datasets that include magnitude estimates

of varying degrees of accuracy. The methodology of Rhoades (1997) is implemented here for the determination of the regression coefficients of the predictive model for Arias Intensity.

The starting point of the Rhoades (1997) algorithm for uncertain magnitudes is to recognise the linear magnitude dependence of the functional form above and to reframe the general regression model in Equation (B.6.22) as in Equation (B.6.23) below.

$$y_{ij} = c_1 + c_2 M_{W,i} + f\left(r_{ij}, \boldsymbol{\theta}\right) + \eta_i + \varepsilon_{ij} \tag{B.6.23}$$

Now, in order to account for the individual magnitude uncertainties, the magnitudes, $M_{W,i}$, are assumed to be normally distributed (independent of both η_i and ε_{ij}), with known means, $\hat{M}_{W,i}$, and known variances, s_i^2. Then, letting $\delta_i = M_{W,i} - \hat{M}_{W,i}$, and consequently letting $\xi_i = c_2\delta_i + \eta_i$; Equation (B.6.23) can be restated as in Equation (B.6.24) below.

$$y_{ij} = c_1 + c_2 \hat{M}_{W,i} + f\left(r_{ij}, \boldsymbol{\theta}\right) + \xi_i + \varepsilon_{ij} \tag{B.6.24}$$

In Equation (B.6.24) the ξ_i terms are now normally distributed with zero means and variances of $c_2^2 s_i^2 + \tau^2$. The maximum likelihood solutions for the parameters of the regression model in Equation (B.6.22) are found from maximising the log likelihood equation below (Searle 1971).

$$\ln L = -\frac{N}{2}\ln\left(2\pi\right) - \frac{1}{2}\ln\left|\mathbf{V}\right| - \frac{1}{2}\left(\mathbf{y}-\boldsymbol{\mu}\right)^T \mathbf{V}^{-1}\left(\mathbf{y}-\boldsymbol{\mu}\right) \tag{B.6.25}$$

In this case the covariance matrix, $\mathbf{V}$, is defined as a function of the individual magnitude variances and, provided that the Arias Intensity values are grouped by event, is given by the block diagonal form of Equation (B.6.26) (provided that observations from each event are grouped together in the dataset). In Equation (B.6.26) $\mathbf{I}_N$ represents the identity matrix of dimension N, where N is the total number of records in the dataset. The term M represents the total number of earthquakes in the dataset, each of which has n_i records. The $\mathbf{1}_{n_i}$ term is consequently the $n_i \times n_i$ unit matrix. The vectors $\mathbf{y}$ and $\boldsymbol{\mu}$ are the observed and predicted values associated with a given set of parameter estimates respectively.

$$\mathbf{V} = \sigma^2 \mathbf{I}_N + \sum_{i=1}^{M} {}^{+} \left(c_2^2 s_i^2 + \tau^2\right)\mathbf{1}_{n_i} \tag{B.6.26}$$

The block diagonal nature of the covariance matrix allows analytical expressions for both the inverse and the determinant of the covariance matrix to be determined (Rhoades 1997), and consequently direct evaluation of the log likelihood to be made through the use of Equation (B.6.27) below.

$$\ln L = -\frac{N}{2}\ln\left(2\pi\right) - \frac{1}{2}\left(N-M\right)\ln\left(\sigma^2\right) - \frac{1}{2}\sum_{i=1}^{M}\ln\left[\sigma^2 + n_i\left(c_2{}^2 s_i{}^2 + \tau^2\right)\right] - \frac{1}{2\sigma^2}\sum_{i=1}^{M}\sum_{j=1}^{n_i}\left[y_{ij} - f\left(r_{ij},\boldsymbol{\theta}\right) - v_i\right]^2 - \frac{1}{2}\sum_{i=1}^{M}\frac{n_i\left(v_i - c_1 - c_2\hat{M}_{W,i}\right)^2}{\sigma^2 + n_i\left(c_2{}^2 s_i{}^2 + \tau^2\right)} \tag{B.6.27}$$

In Equation (B.6.27) the term v_i is defined in Equation (B.6.28) below.

$$v_i = \frac{1}{n_i}\sum_{i=1}^{n_i}\left[y_{ij} - f\left(r_{ij},\boldsymbol{\theta}\right)\right] \tag{B.6.28}$$

Given the set of model parameters $\left(c_1, c_2, \boldsymbol{\theta}, \tau, \sigma\right)$, the conditional maximum likelihood estimate of ξ_i is given by Equation (B.6.29) below.

$$\tilde{\xi}_i = \frac{\left(c_2{}^2 s_i{}^2 + \tau^2\right)\sum_{j=1}^{n_i}\left(y_{ij} - \mu_{ij}\right)}{n_i\left(c_2{}^2 s_i{}^2 + \tau^2\right) + \sigma^2} \tag{B.6.29}$$

The term μ_{ij} in Equation (B.6.29) represents the fitted values based upon the set of model parameters that Equation (B.6.29) is conditional upon. This term is defined completely, for this case, in Equation (B.6.30) .

$$\mu_{ij} = c_1 + c_2\hat{M}_{W,i} + f\left(r_{ij},\boldsymbol{\theta}\right) \tag{B.6.30}$$

Then, given the estimate of ξ_i, the conditional maximum likelihood estimate of the random effects terms for the regression model are given by Equation (B.6.31).

$$\tilde{\eta}_i = \frac{\tau^2\xi_i}{c_2{}^2 s_i{}^2 + \tau^2} \tag{B.6.31}$$

The above methodology was implemented in order to determine the regression coefficients of the model in Equation (B.6.22). In addition, the analogous methodology of Abrahamson and Youngs (1992) was also applied in order to ascertain the effect of accounting for the individual magnitude uncertainties. In both cases the fixed effects regression operations that are required by the methods were performed using a linearization procedure (i.e. Joyner and Boore 1993; Draper and Smith 1998). The values of the regression coefficients for both the exact and uncertain magnitude cases are given in Table B.6.1.

Obviously, in order to apply this methodology estimates of the errors associated with the magnitudes in the dataset must be available. The regression analysis is performed with respect to moment magnitude but error estimates for moment magnitude are not available for the majority of the earthquakes in the New

Zealand dataset. The standard errors of the magnitude values that have been adopted for this analysis are assumed to be equal to the standard errors provided through GeoNet (http://www.geonet.org.nz/) project. These standard errors relate to various different magnitude scales and while there are known differences between the likely errors associated with different magnitude scales (Dowrick and Rhoades 1998) there are no robust methods for converting the standard error from one magnitude scale to another. Dowrick and Rhoades (1998) do however state that estimates made of moment magnitude from surface wave magnitudes and from local magnitudes would have associated errors of about 0.15 and 0.3 respectively. The errors that are assigned to each event are typically of this order. In addition to the actual error associated with each magnitude value, account must also be made of the rounding of magnitude values that takes place.

Standard error estimates of the magnitudes of the foreign earthquakes included in the dataset were not available. The standard error of magnitude assigned to these events was therefore assumed to be a uniform value of 0.1. This value is likely to overestimate the error associated with some of the more recent events in the dataset, but it is likely to underestimate the error associated with some of the earlier events in the dataset.

Boxplots showing the distributions of the η_i values determined from each model using the parameter estimates in Table B.6.1 are shown in Figure B.6.2; the effect of accounting for individual magnitude uncertainties is clear.

In Table B.6.1 the values of the parameter estimates agree quite well with theory for the magnitude scaling but the distance scaling appears to have coefficients that result in too high a rate of attenuation with distance. Given the theoretical considerations previously outlined, the geometric scaling corresponds to a

Table B.6.1: Maximum Likelihood parameter estimates for the base model of Arias Intensity for both the exact (Abrahamson and Youngs, 1992) and uncertain (Rhoades, 1997) magnitude cases. Coefficients are also given for both datasets considered in this study.

Parameter	Chi-Chi Data Excluded		Chi-Chi Data Included	
	Abrahamson and Youngs (1992)	Rhoades (1997) ($\sigma_{M,foreign}$ = 0.1)	Abrahamson and Youngs (1992)	Rhoades (1997) ($\sigma_{M,foreign}$ = 0.1)
c_1	-4.672	-4.175	-3.844	-3.344
c_2	2.226	2.119	2.113	2.010
c_3	-3.083	-3.052	-3.084	-3.056
c_4	34.186	32.502	34.824	33.330
c_5	0.618	0.622	0.546	0.550
c_6	0.842	0.855	0.708	0.720
c_7	-0.359	-0.345	-0.449	-0.443
c_8	0.463	0.405	0.334	0.267
τ	1.237	1.069	1.243	1.092
σ	1.130	1.131	1.149	1.151
σ_T	1.675	1.557	1.693	1.586

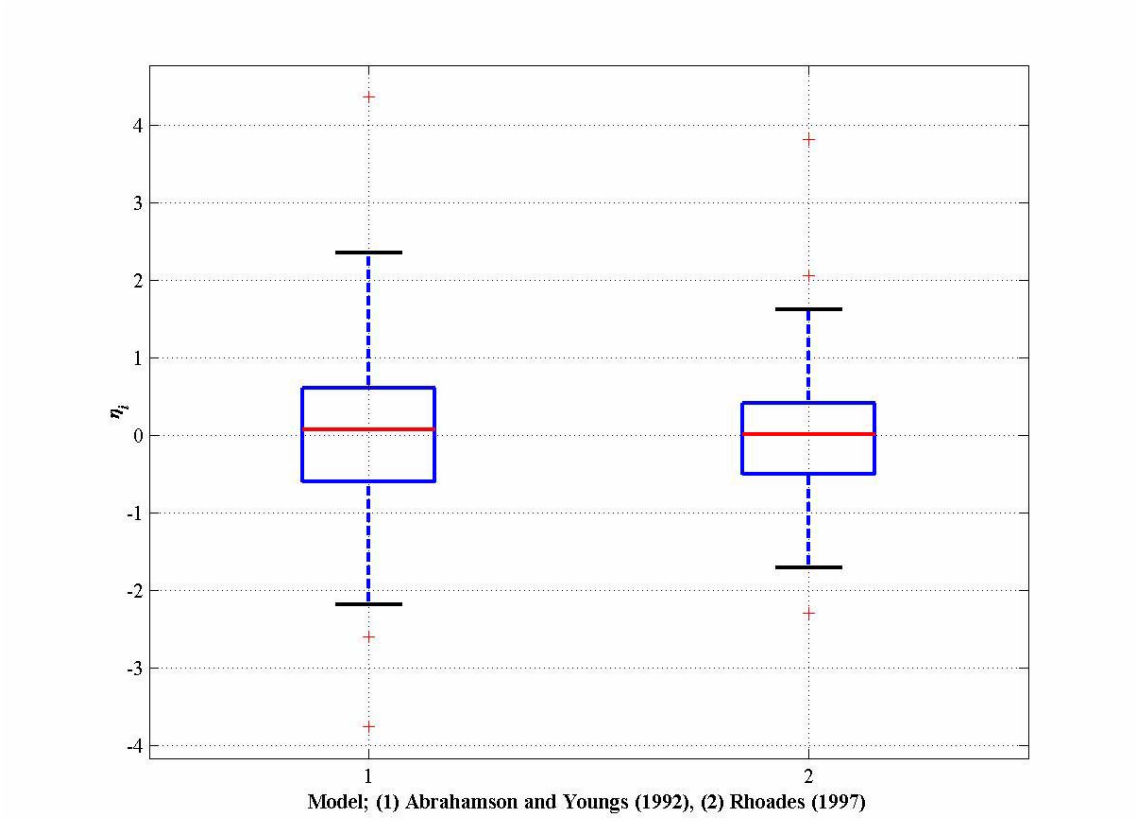

Figure B.6.2: Boxplot showing the distribution of the random effects terms for the base model of Arias Intensity for the certain and uncertain magnitude algorithms. Horizontal blue lines represent the lower and upper quartiles; horizontal red lines represent the median, while outliers are marked by red crosses. The limiting 'whiskers' are placed at 1.5 times the interquartile range. Only results for the case where the Chi-Chi records are excluded are shown.

ζ value of approximately 1.5, whereas the pure elastic case in theory would be 1.0. The near source distance constraint also appears relatively large although values of this parameter tend to vary over quite a significant range and there is not real theoretical basis for preferring any certain value. We must therefore consider whether the factor for geometrical spreading is being driven too high due to the larger near source constraint factor, or whether these values actually reflect reality. A starting point is to compare this geometric spreading factor with other spreading rates determined for regression models of other ground motion measures in New Zealand. In the model for the Fourier Amplitude Spectrum developed in Chapter Five of this section the geometric spreading factor varied with frequency over the approximate range 1.0 – 1.6, with an average value of approximately 1.3. Note however that these values corresponded to a near source constraint of 19 km and that these values are correlated to a degree. If the near source constraint increases then the geometric spreading parameter would also have to increase. Another comparison can be made between the coefficients in Table B.6.1 and those obtained for the peak ground acceleration model of Zhao et al. (1997) and Cousins et al. (1999); in these models the geometric spreading coefficient was -1.56 and -1.603 respectively. The absolute values of these parameters are equivalent to the parameter ζ in this study and it can be seen that these models actually predict even stronger geometric spreading than those estimated in Table B.6.1. It therefore appears that ground

motions attenuate relatively strongly with distance in New Zealand and that the values found in Table B.6.1 are consistent with both theoretical magnitude scaling as well as local distance scaling.

As well as the considerations made above it is also worth conducting a residual analysis to see how well the model predicts the observed ground motions in the empirical dataset. In the boxplots of Figure B.6.2 the median of the η_i values, shown by the horizontal red lines, are very close to zero for both models. From this point of view these results look promising, with parameter values from Table B.6.1 being close to the theoretical magnitude and the approximately expected distance scaling parameter as well as the inter event errors being distributed nicely. However, when the inter event residuals are plotted against magnitude a trend is apparent; this is demonstrated below in Figure B.6.3. The trend that is evident in Figure B.6.3 suggests that a more appropriate model would be obtained if some higher order scaling with magnitude were included into the functional form of the regression model.

In order to incorporate some higher order magnitude scaling into the functional form of the regression model the Rhoades (1997) algorithm must be modified. The details of the modifications that had to be made to the Rhoades (1997) algorithm are detailed below.

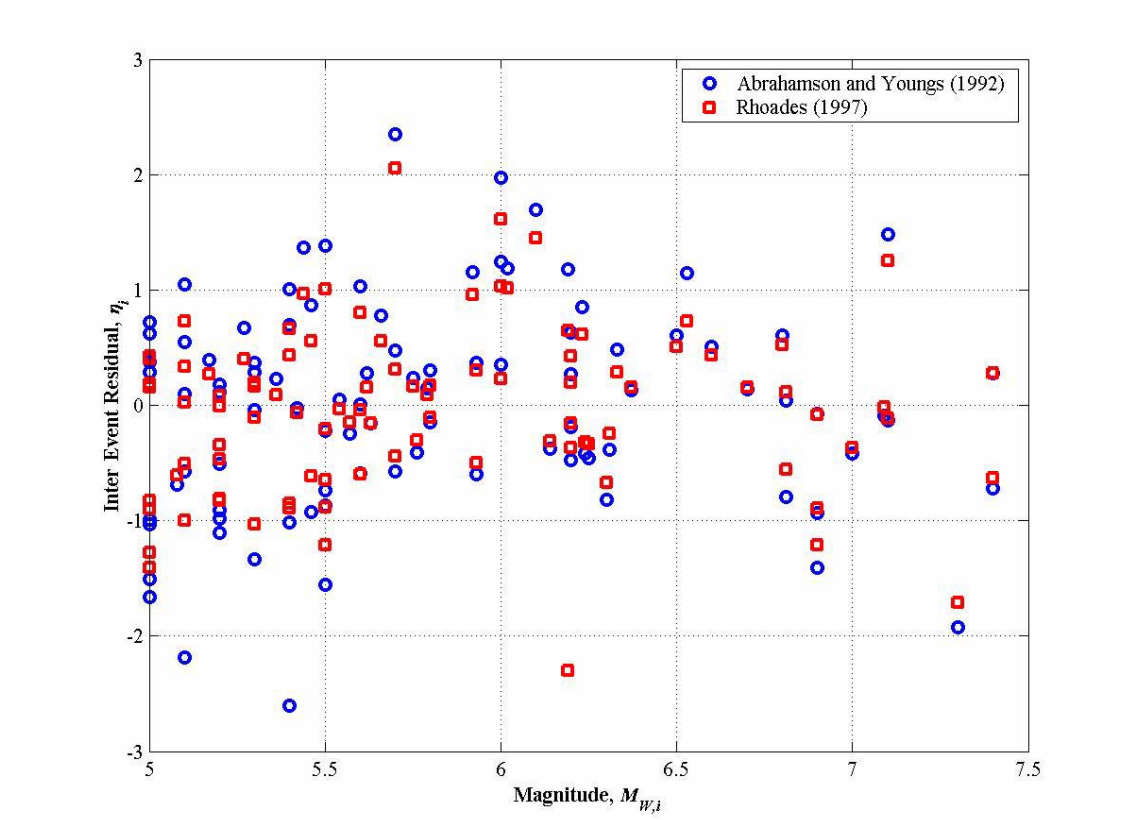

Figure B.6.3: Magnitude dependence of the inter event residuals for the base models for Arias Intensity. Residuals for both the certain and uncertain magnitude cases are shown. Only results for the case where the Chi-Chi records are excluded are shown.

The revised functional form of the regression model is given in Equation (B.6.32).

$$y_{ij} = c_1 + c_2\hat{M}_{W,i} + c_3\left(\hat{M}_{W,i} - 6\right)^2 + f\left(r_{ij}, \boldsymbol{\theta}\right) + \xi_i + \varepsilon_{ij} \tag{B.6.32}$$

In this case the ξ_i terms include the original coefficient of the linear magnitude scaling, but also include some magnitude dependence associated with the second order term. The full form of the ξ_i term is given below in Equation (B.6.33); in addition an approximation to this term is given which makes use of the assumption that the term including δ_i^2 is relatively small in comparison to the other terms.

$$\begin{aligned} \xi_i &= c_2\delta_i + 2c_3\delta_i\hat{M}_{W,i} - 12c_3\delta_i + c_3\delta_i^2 + \eta_i \\ &\cong \left(c_2 + 2c_3\hat{M}_{W,i} - 12c_3\right)\delta_i + \eta_i \end{aligned} \tag{B.6.33}$$

Upon making this approximation, the ξ_i are normally distributed with zero mean and approximate variances $\left(c_2 + 2c_3\hat{M}_{W,i} - 12c_3\right)^2 s_i^2 + \tau^2$. The maximum likelihood solution can again be found from maximising Equation (B.6.25) but with a modified covariance matrix given by Equation (B.6.34) below.

$$\mathbf{V} = \sigma^2\mathbf{I}_N + \sum_{i=1}^{M} + \left[\left(c_2 + 2c_3\hat{M}_{W,i} - 12c_3\right)^2 s_i^2 + \tau^2\right]\mathbf{1}_{n_i} \tag{B.6.34}$$

Associated with this new covariance matrix is a new analytic expression for log likelihood; this new expression is given in full in Equation (B.6.35).

$$\begin{aligned} \ln L = &-\frac{N}{2}\ln\left(2\pi\right) - \frac{1}{2}\left(N - M\right)\ln\left(\sigma^2\right) - \frac{1}{2}\sum_{i=1}^{M}\ln\left(\sigma^2 + n_i\left[\left(c_2 + 2c_3\hat{M}_{W,i} - 12c_3\right)^2 s_i^2 + \tau^2\right]\right) \\ &-\frac{1}{2\sigma^2}\sum_{i=1}^{M}\sum_{j=1}^{n_i}\left[y_{ij} - f\left(r_{ij}, \boldsymbol{\theta}\right) - \nu_i\right]^2 - \frac{1}{2}\sum_{i=1}^{M}\frac{n_i\left[\nu_i - c_1 - c_2\hat{M}_{W,i} - c_3\left(\hat{M}_{W,i} - 6\right)^2\right]^2}{\sigma^2 + n_i\left[\left(c_2 + 2c_3\hat{M}_{W,i} - 12c_3\right)^2 s_i^2 + \tau^2\right]} \end{aligned} \tag{B.6.35}$$

In this equation the term ν_i is again represented by Equation (B.6.28). The associated conditional maximum likelihood estimate of the ξ_i values can be found from Equation (B.6.36).

$$\tilde{\xi}_i = \frac{\left[\left(c_2 + 2c_3\hat{M}_{W,i} - 12c_3\right)^2 s_i^2 + \tau^2\right]\sum_{j=1}^{n_i}\left(y_{ij} - \mu_{ij}\right)}{n_i\left[\left(c_2 + 2c_3\hat{M}_{W,i} - 12c_3\right)^2 s_i^2 + \tau^2\right] + \sigma^2} \tag{B.6.36}$$

Similarly, The associated conditional maximum likelihood estimate of the η_i values can now be found from Equation (B.6.37).

$$\tilde{\eta}_i = \frac{\tau^2 \xi_i}{\left(c_2 + 2c_3 \hat{M}_{W,i} - 12c_3\right)^2 s_i^{\,2} + \tau^2} \tag{B.6.37}$$

The similarities between the new expressions presented above and the original formulation of Rhoades (1997) are readily observed. Although the new formulae appear more formidable, their application is almost identical to the original formulae and consequently regression parameters for the revised predictive model can be obtained with relative ease once the derivation above has been made. Note that in Chapter Five it was mentioned that this method was not employed due to the more complicated magnitude scaling associated with the corner frequency dependence making the derivation of analogous formulae to those above unnecessarily cumbersome. While the functional form of the regression model was the same in the previous chapter, the observed values were modified by terms that included magnitude dependence. This dependence would have to be included in order for the present method to be applied.

The regression coefficients obtained using this revised method are presented in Table B.6.2 and the resulting distribution of the inter event residuals for the dataset excluding the Chi-Chi records are shown in boxplot form in Figure B.6.4. This boxplot also shows the relevant distributions associated with the original regression model for comparison. There is clearly a significant benefit to accounting for individual magnitude uncertainties as can be see from the error terms given in Figure B.6.4. It can also be noted that the difference in the total standard deviations obtained for the two different datasets are almost identical, but that the standard deviations of the fixed and random components are different. It can also be noted that the effect of excluding the Chi-Chi records acts to increase the relative amplification that occurs due to both reverse faults and site class C. These results are to be expected if the Chi-Chi event is influencing the results. Consequently, because the inclusion of the Chi-Chi records does not act to make the regression model more accurate, or stable, the model based upon the dataset that excludes the Chi-Chi events is preferred. An additional consideration that influenced this decision to exclude the Chi-Chi records was that the study of Hwang et al. (2004) derived regression models based upon the Chi-Chi event that were significantly different in nature to those found in the present analysis. While these records would only be used here to constraint the near source scaling of ground motions rather than to model the over all form of the regression model, this incompatibility between the regression models provides another reason to simply use the less contentious records from the New Zealand dataset and the other foreign records.

The residuals associated with the dataset excluding the Chi-Chi records and the coefficients obtained from this dataset using the revised regression model are shown in Figure B.6.5. In this figure both the inter and intra event residuals are plotted with respect to magnitude and the intra event residuals are also plotted against rupture distance. It can clearly be seen that the trend of the inter event residuals with respect to magnitude observed in Figure B.6.3 has effectively been removed by using the revised regression model.

Table B.6.2: Maximum Likelihood parameter estimates for the revised model of Arias Intensity for both the exact and uncertain magnitude cases.

Parameter	Chi-Chi Data Excluded		Chi-Chi Data Included	
	Abrahamson and Youngs (1992)	Rhoades (1997) ($\sigma_{M,foreign}$ = 0.1)	Abrahamson and Youngs (1992)	Rhoades (1997) ($\sigma_{M,foreign}$ = 0.1)
c_1	-5.069	-4.465	-4.872	-4.246
c_2	2.297	2.184	2.270	2.158
c_3	-0.690	-0.657	-0.774	-0.740
c_4	-3.035	-3.015	-3.017	-3.000
c_5	31.911	30.571	31.482	30.278
c_6	0.616	0.623	0.540	0.546
c_7	0.839	0.852	0.710	0.720
c_8	-0.329	-0.273	-0.361	-0.304
c_9	0.400	0.332	0.355	0.277
τ	1.188	0.983	1.165	0.958
σ	1.132	1.134	1.153	1.155
σ_T	1.641	1.500	1.640	1.501

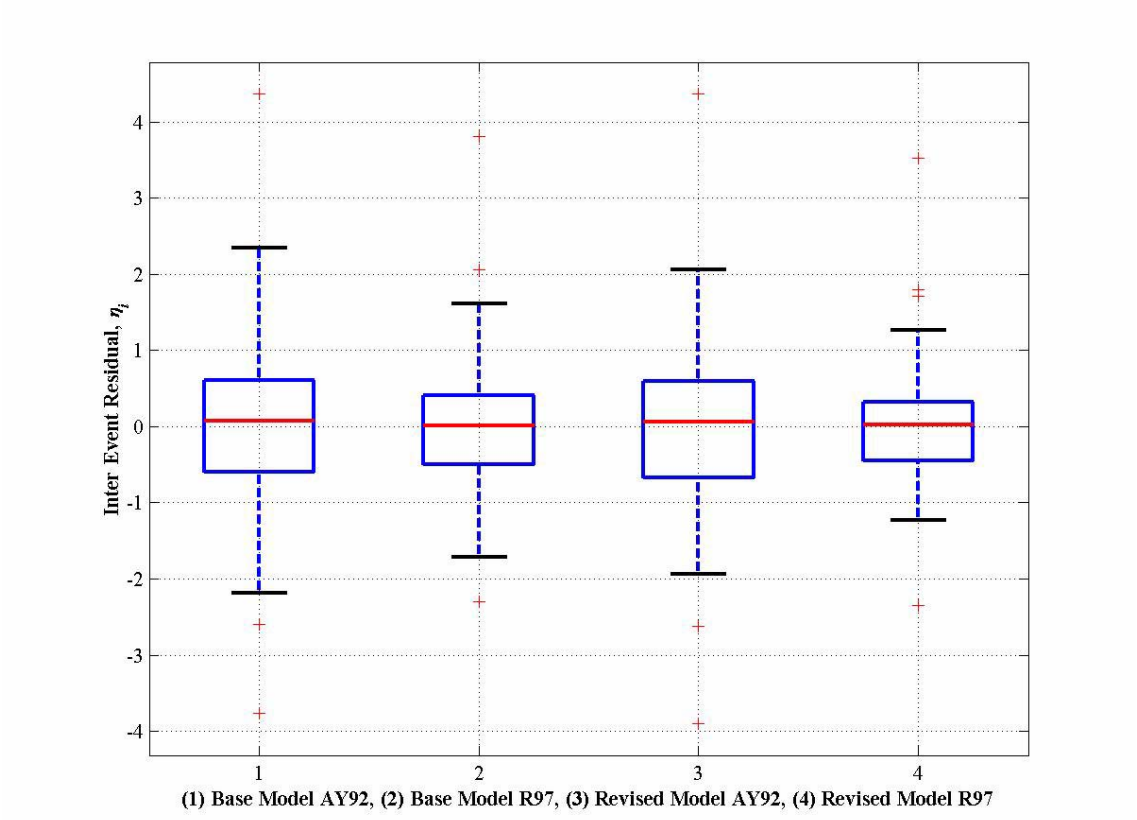

Figure B.6.4: Boxplots for the base and revised models for both certain and uncertain magnitude data. See the caption to Figure B.6.2 for details regarding the box and whisker limits. Only results for the case where the Chi-Chi records are excluded are shown.

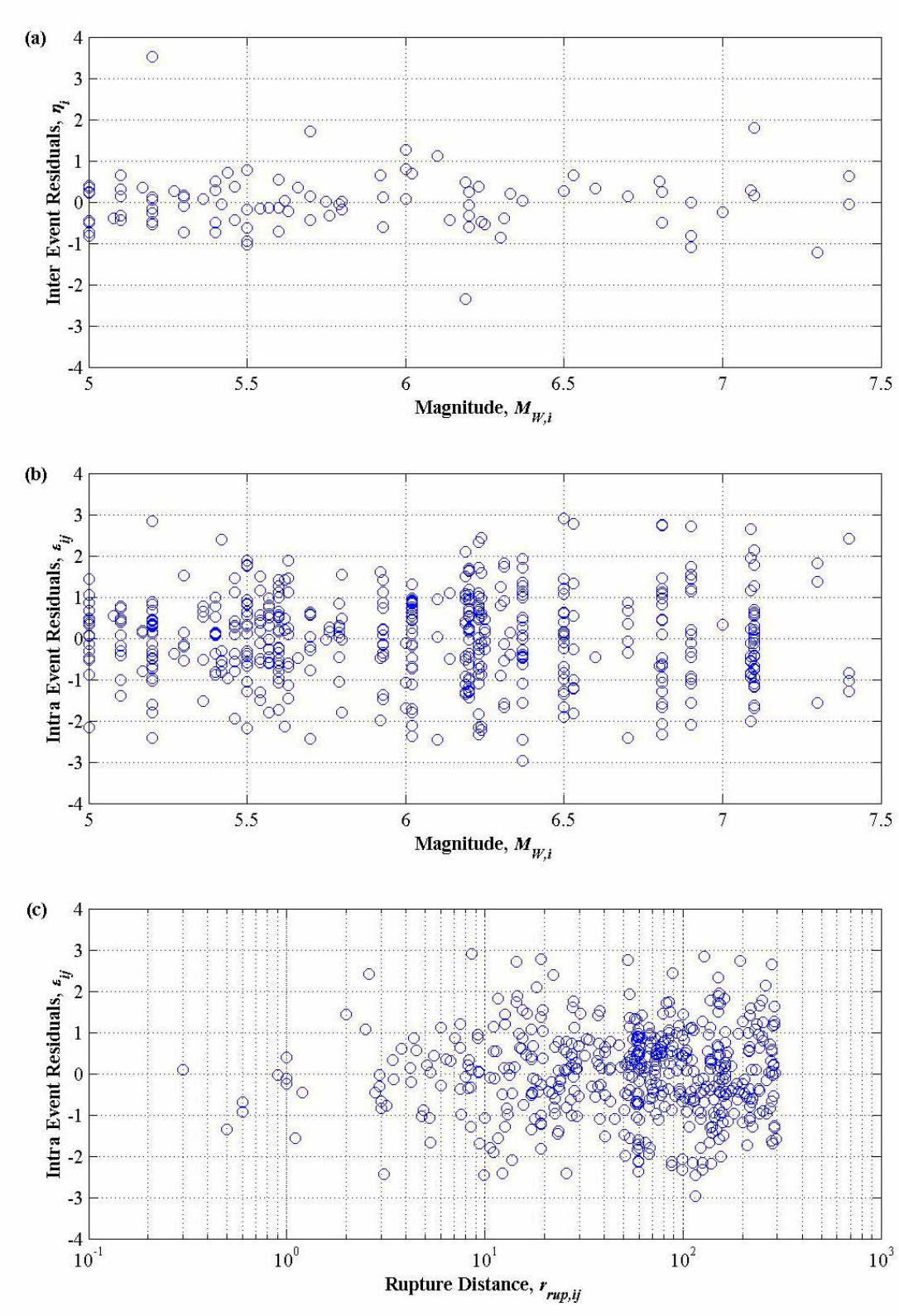

Figure B.6.5: Residuals associated with the preferred model of Arias Intensity for New Zealand. Panel (a) shows the inter-event residuals plotted with respect to magnitude, panel (b) shows the intra-event residuals plotted against magnitude, and panel (c) shows the intra-event residuals plotted against rupture distance.

B.6.4. Arbitrary Component Variability

In Chapter Five a discussion was presented in light of the recent research of Baker and Cornell (2006) highlighting the importance of distinguishing between the average and arbitrary components of ground motion. For the regression model developed in this section it is again important to make this distinction by considering the variability between two orthogonal components of ground motion and including this additional error into the error terms previously determined.

In this case the component variance may be determined from Equation (B.6.38).

$$\sigma_c^{\,2} = \frac{1}{N}\sum_{j=1}^{N}\frac{\left[\ln\left(I_{xx,j}\right)-\ln\left(I_{yy,j}\right)\right]^2}{4} \tag{B.6.38}$$

Given this component variance, the standard deviations applicable to both the average and arbitrary components of ground motion can be calculated. The value of σ previously defined in the derivation of the regression model is the standard deviation of the intra event residuals determined with respect to the average component of ground motion. This standard deviation is henceforth referred to as σ_1. The equations defining the total standard deviation for the average and arbitrary components are presented in Equation (B.6.39) and Equation (B.6.40) respectively.

$$\sigma_{\ln I,ave} = \sqrt{\tau^2 + \sigma_1^{\,2}} \tag{B.6.39}$$

$$\sigma_{\ln I,arb} = \sqrt{\tau^2 + \sigma^2}, \qquad \sigma = \sqrt{\sigma_1^{\,2} + \sigma_c^{\,2}} \tag{B.6.40}$$

These values are computed and presented in Table B.6.3.

B.6.5. Final Predictive Model for Arias Intensity

After performing the above operation on the individual components of the Arias Intensity the same error structure that was presented in Chapter Five for the FAS is presented along with the final values of the coefficients for the preferred regression model in Equation (B.6.41) in Table B.6.3below.

$$\ln I_{aa} = c_1 + c_2 M_W + c_3\left(M_W - 6\right)^2 + c_4 \ln\left[\sqrt{r_{rup}^{\,2} + c_5^{\,2}}\right] + c_6 S_B + c_7 S_C + c_8 F_N + c_9 F_R \tag{B.6.41}$$

Table B.6.3: Final coefficients for the model of Arias Intensity for New Zealand. Standard deviations are provided for both the average and arbitrary components of ground motion.

c_1	c_2	c_3	c_4	c_5	c_6	c_7	c_8	c_9
-4.465	2.184	-0.657	-3.015	30.571	0.623	0.852	-0.273	0.332
	τ	σ_1	σ_c	σ		$\sigma_{\ln I,ave}$	$\sigma_{\ln I,arb}$	
	0.983	1.134	0.203	1.152		1.500	1.514	

B.6.6. Performance of the Predictive Model

Now that the predictive model for the Arias Intensity has been developed it is instructive to examine the performance of the model with respect to modelling the ground motions in the empirical dataset as well as analysing the general form of the model with respect to the required input parameters. Figures demonstrating the form of the model with respect to both magnitude and distance for various values of rupture distance and magnitude respectively are shown in Figure B.6.6. In these figures the simple nature of the scaling of the relation is evident. There is no coupling between the magnitude and distance and consequently the model scales vertically up and down the figures whilst retaining its form. The same comments apply to the case in Figure B.6.7 where the distance scaling is again considered but with the different site classes and fault mechanisms also plotted. Again, as the categories are simply modelled by constant terms the curves simply move vertically up or down with respect to the other categories for any given earthquake scenario. Plots of the intra event residuals plotted against both magnitude and rupture distance are then shown for each of the site classes and fault categories in Figure B.6.8 through to Figure B.6.11. As well as show the distribution of the intra event residuals associated with the various categories these plots also act to show how the strong motion dataset is made up from data in each of the categories. The importance of using dummy regression variables rather than partitioning the dataset is clear as for some the category – magnitude, or category – distance regions of parameter space there are few data points when compared to both the total number of data points, but also to the other categories over similar regions.

The figures showing the residuals are typically the most revealing when considering the goodness of fit of a model to the data. In all cases the distribution of residuals about the mean is relatively consistent over the range of magnitudes and distances for which the data are available. This observation suggests that the model does a very good job of modelling the current dataset of Arias Intensity from New Zealand earthquakes.

It can also be appreciated that whereas a magnitude dependence of the residuals of strong ground motion models is commonly observed (Abrahamson 1988; Youngs et al. 1995) and frequently modelled, the plots of the residuals do not give sufficient evidence to warrant modelling the errors in this

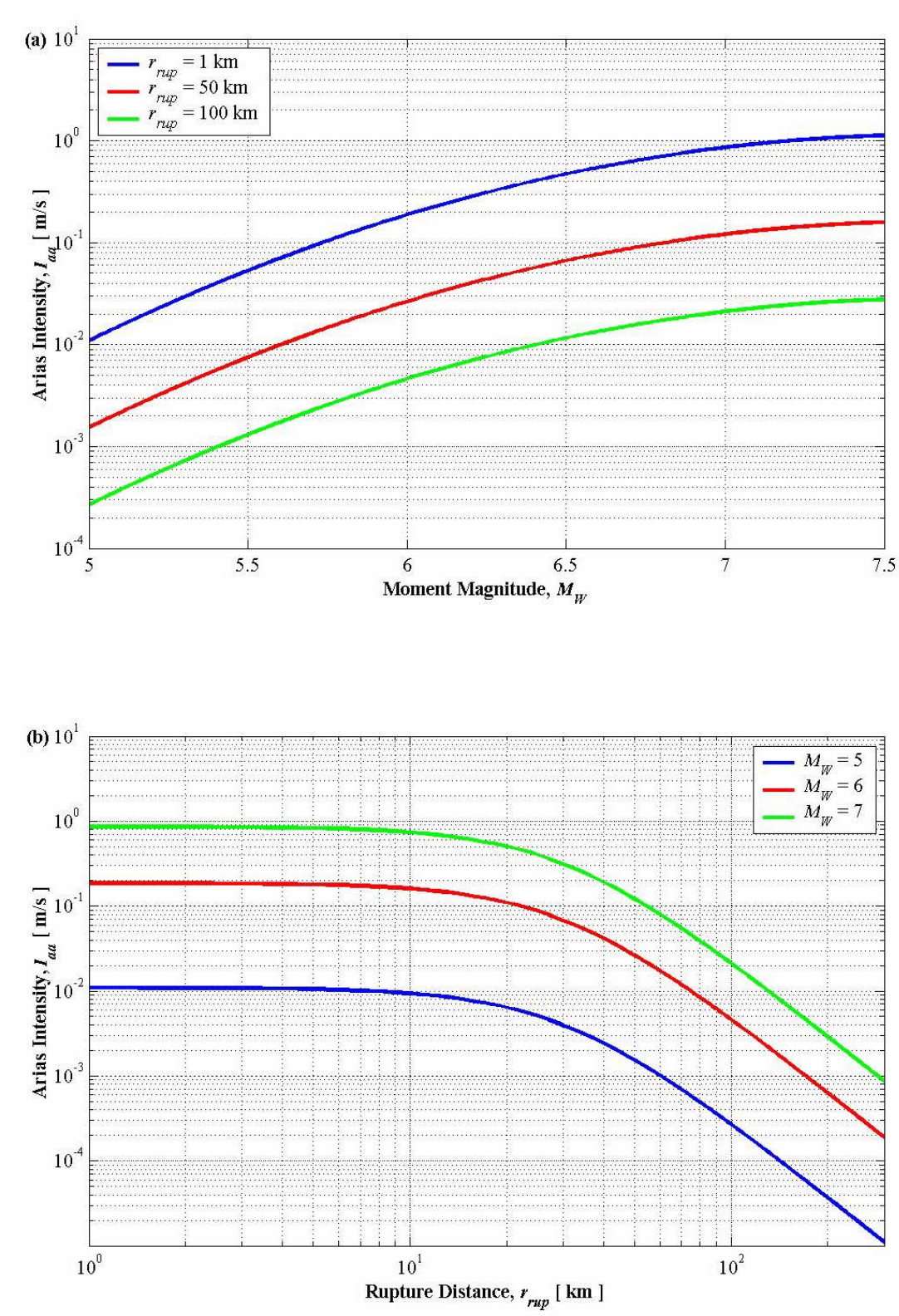

Figure B.6.6: Predictive Equation for Arias Intensity. Panel (a) shows the scaling with moment magnitude while panel (b) shows the scaling with distance

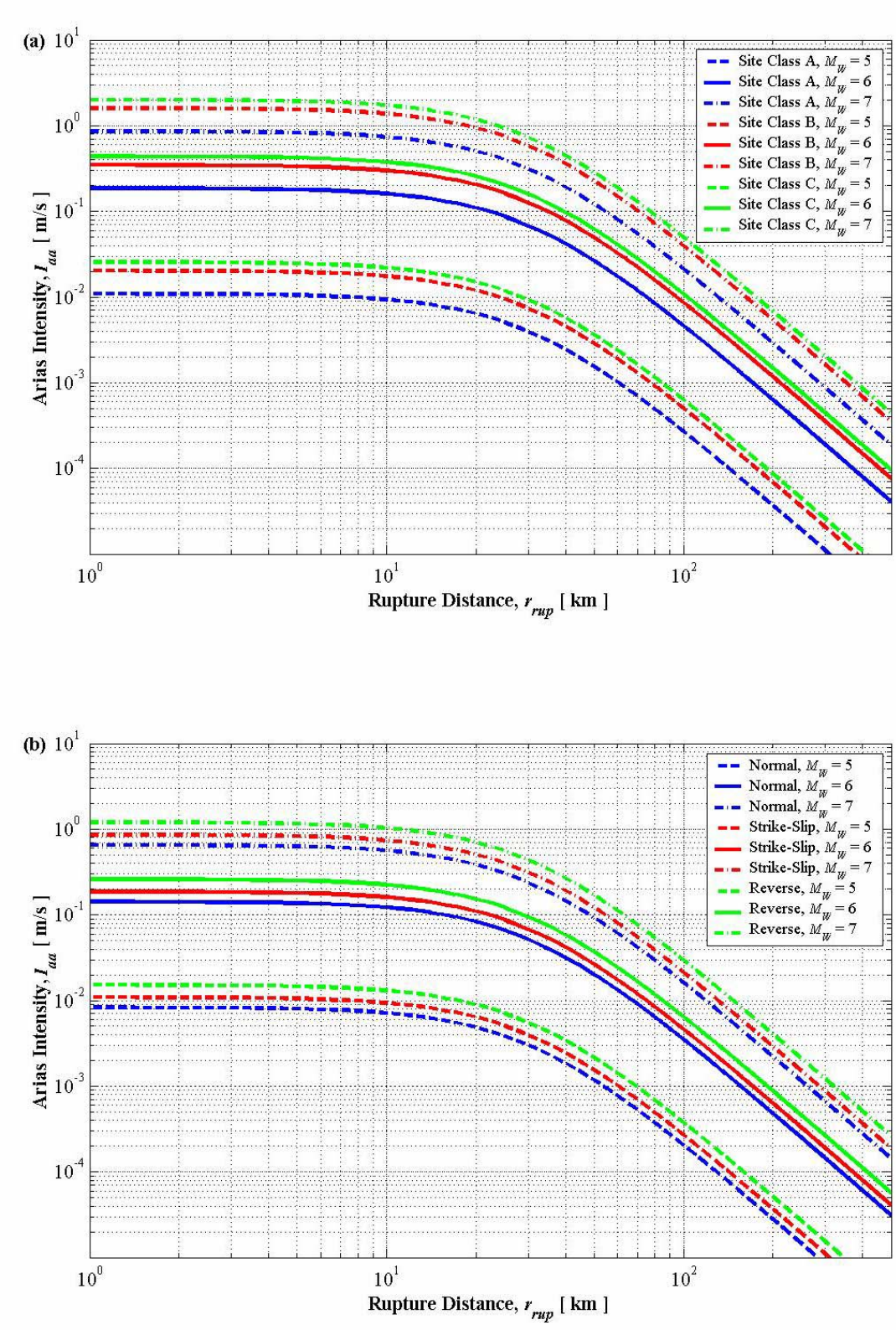

Figure B.6.7: Predictive Equation for Arias Intensity. Panel (a) shows the differences in the scaling with distance for the three site classes in the model while panel (b) shows the differences in scaling with distance for the three fault types included in the model. Note that the modifications are simply vertical shifts with respect to the other classes in all cases.

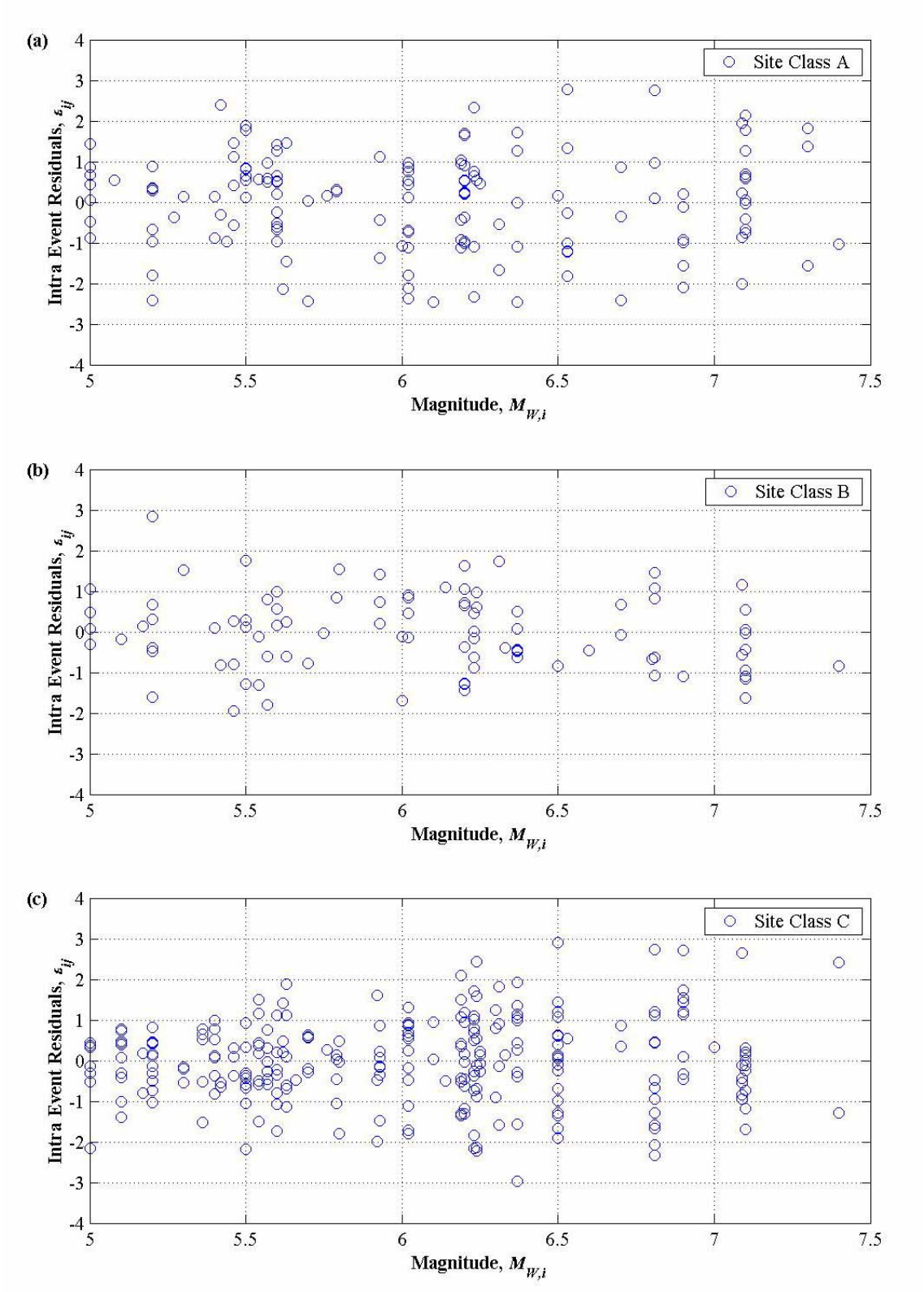

Figure B.6.8: Residuals of the Arias Intensity Predictive Equation. Panel (a) plots the intra event residuals against magnitude for Site Class A, panel (b) plots the intra event residuals against magnitude for Site Class B, and panel (c) plots the intra event residuals against magnitude for Site Class C.

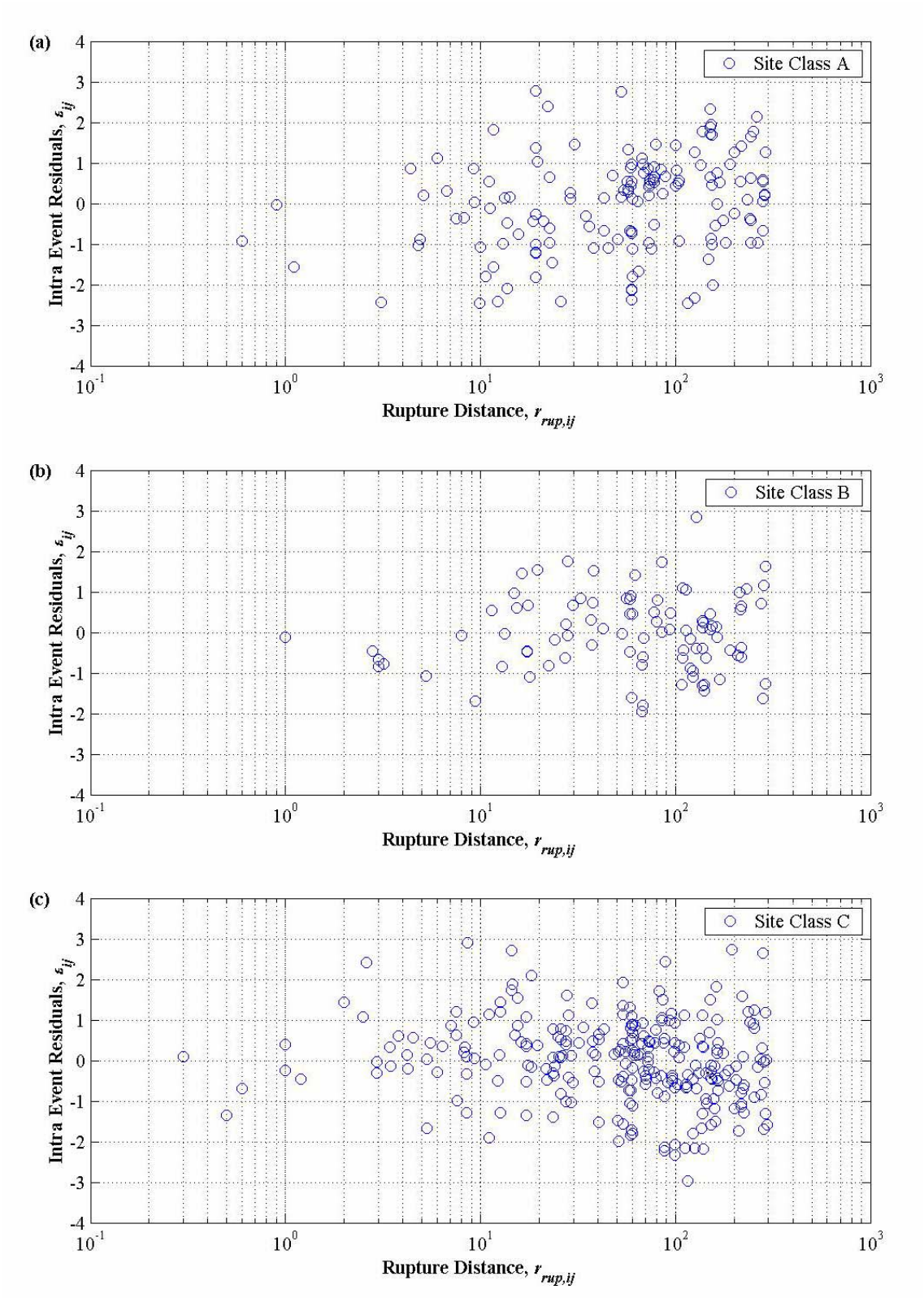

Figure B.6.9: Residuals of the Arias Intensity Predictive Equation. Panel (a) plots the intra event residuals against rupture distance for Site Class A, panel (b) plots the intra event residuals against rupture distance for Site Class B, and panel (c) plots the intra event residuals against rupture distance for Site Class C.

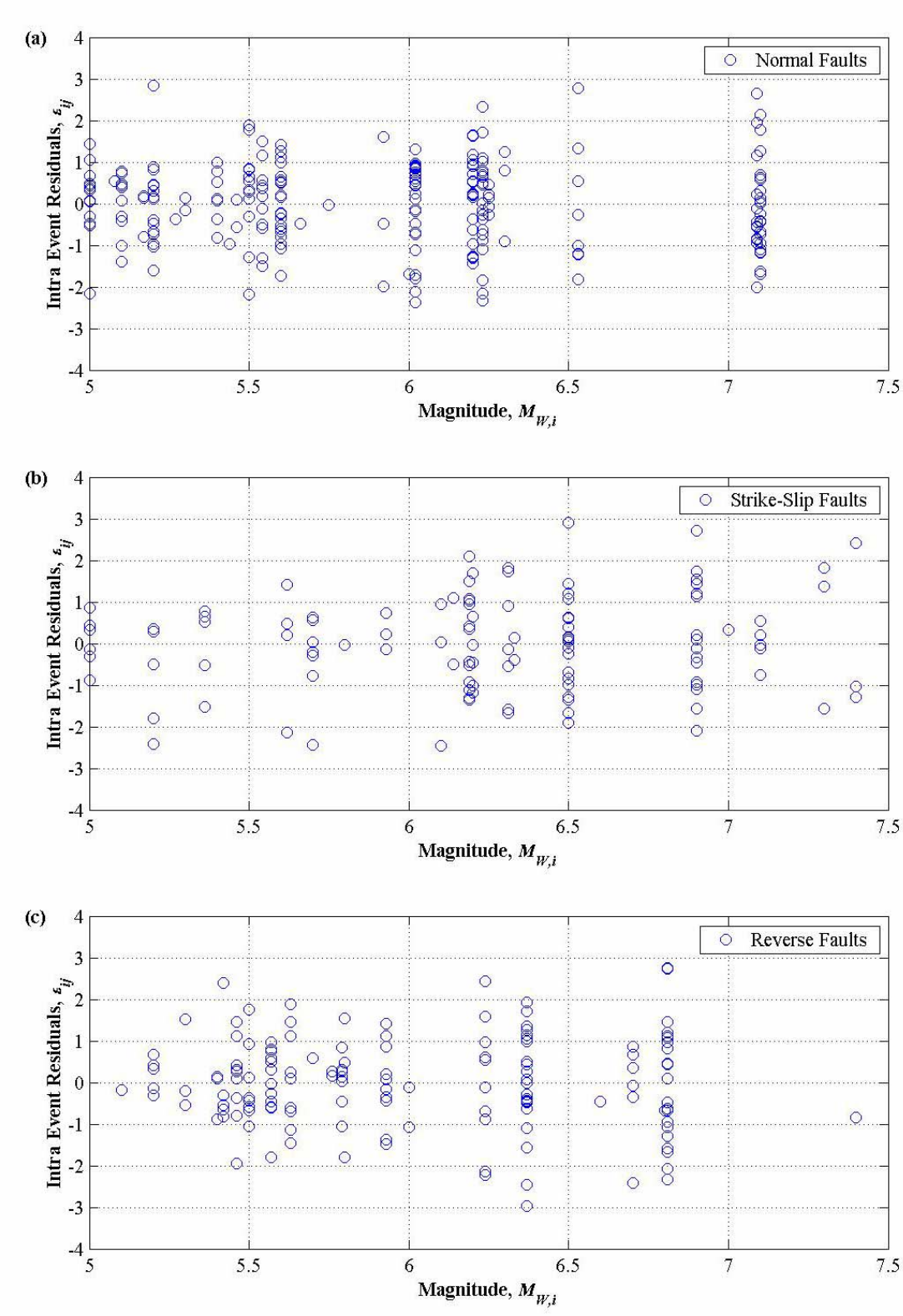

Figure B.6.10: Residuals of the Arias Intensity Predictive Equation. Panel (a) plots the intra event residuals against magnitude for Normal Faults, panel (b) plots the intra event residuals against magnitude for Strike-Slip Faults, and panel (c) plots the intra event residuals against magnitude for Reverse Faults.

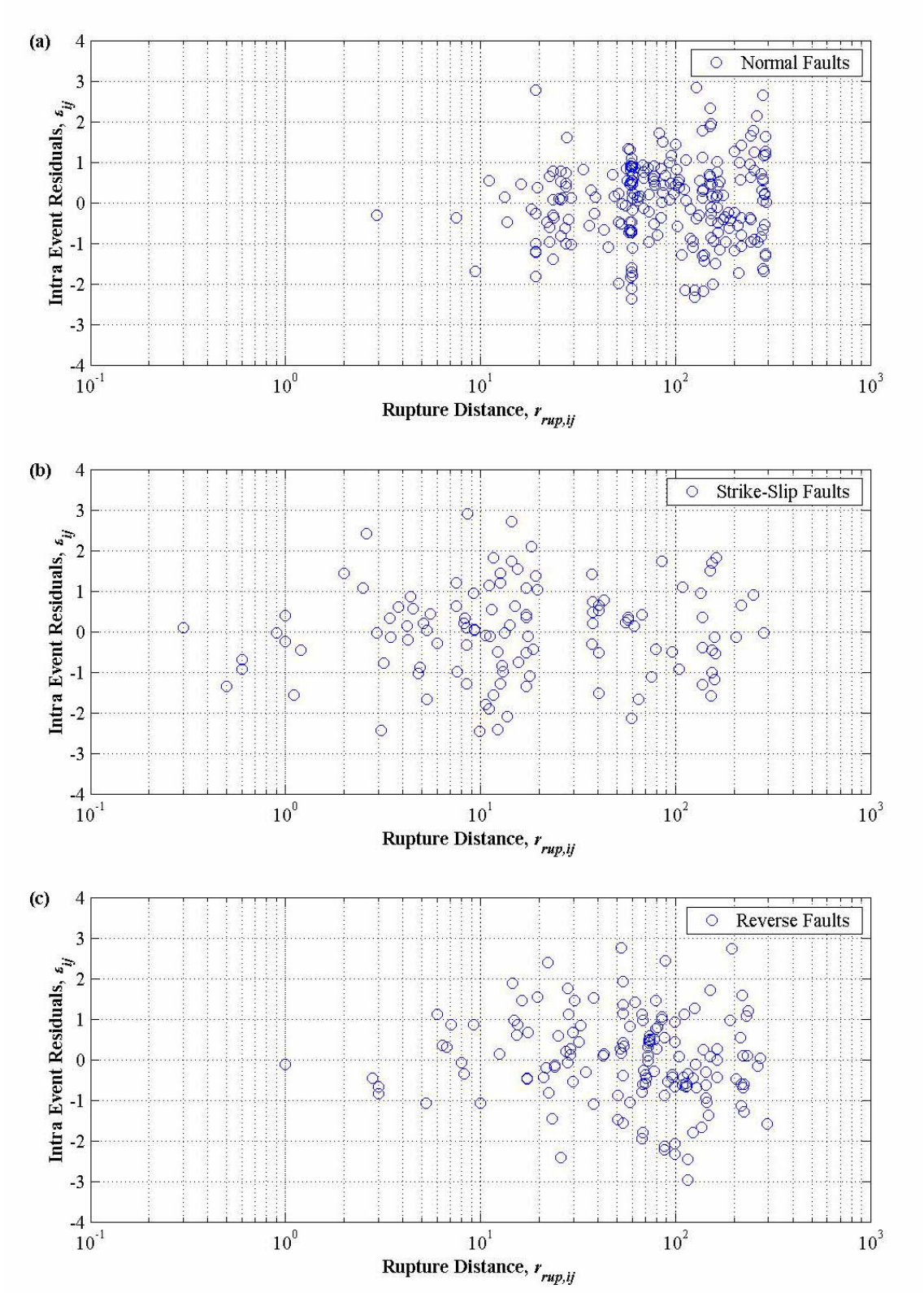

Figure B.6.11: Residuals of the Arias Intensity Predictive Equation. Panel (a) plots the intra event residuals against rupture distance for Normal Faults, panel (b) plots the intra event residuals against rupture distance for Strike-Slip Faults, and panel (c) plots the intra event residuals against rupture distance for Reverse Faults.

manner. In addition, the dataset is too sparse to obtain any statistically robust estimates of the likely magnitude dependence of the residuals at large magnitudes. The recent model of Travasarou et al. (2003) did find a magnitude dependency for the inter event residuals and modelled this accordingly, but modelled the intra event residuals using a function that decreased with increasing Arias Intensity and that had separate parameters for each site category. It should be noted however that their dataset included 1208 strong motion records from 75 earthquakes which amounts to roughly three times the number of records for roughly the same number of earthquakes than were considered in this analysis. Consequently, the simple case of magnitude independent error values was assumed. The magnitudes of the errors should also be compared as these values can have a significant impact upon the results of a seismic hazard analysis if the models are used for that purpose. The structure of the Travasarou et al. (2003) error terms means that quite a wide range of error values may be found, however the total range that their values may take is [0.871, 1.330]. This error represents the error associated with the average component of ground motion and should be compared to the value of $\sigma_{\ln I,ave}$ found in this study of 1.500. They do not give estimates of the magnitude of the arbitrary error term. The model of Kayen and Mitchell (1997) found errors that are equivalent to 1.451 and 1.405 for rock and alluvium sites respectively. Sabetta and Pugliese (1996) obtained an error of approximately 0.914, Keefer and Wilson (1989) a value of approximately 1.151, and Wilson (1993)a value of 0.840. These errors are referred to as being approximate as the actual reported values were reported in terms of $\log_{10} I_{aa}$ rather than $\ln I_{aa}$ as in this study. From consideration of these errors its appears that the errors obtained through this study are at the upper end of those that could be expected for models of this type. It is likely that the error obtained from the present study could be reduced given more accurate site classifications and more accurate estimates of the rupture distance. Currently there is a considerable amount of uncertainty associated with both of these aspects of the model. Note also that while the use of the uncertain magnitudes algorithm of Rhoades (1997) was implemented and was found to reduce the overall error, it is still preferable to simply use more accurately defined magnitude values in the first place so that the effect of magnitude uncertainties becomes irrelevant.

Although this model is currently the only one of its type available for general use in New Zealand it should be implemented with caution in PSHA as the relatively large errors will tend to over-predict the hazard calculated at a site. An ideal predictive equation will have very little uncertainty associated with the initial dataset so that the error terms subsequently determined reflect the inherent errors associated with strong ground motions rather than the quality of data used and the analysis technique implemented to obtain the model. It should be noted that although the present model predicts larger errors than that of the Travasarou et al. (2003) model, the difference between the two model is almost entirely associated with the value of τ that has been determined from the two different studies. The values of the intra event standard deviation, σ, actually compare very well (their σ being the σ_1 in this study). This strongly suggests that the errors will most likely be reduced by concentrating on improving the quality of the dataset. The intra event component should represent the inherent scatter that is associated with a particular earthquake, this aspect of the error is much harder to reduce than the inter event standard deviation. The focus of future modifications to this relationships should therefore focus primarily upon the inter event term, τ.

B.6.7. Chapter Summary

In this chapter a new ground motion attenuation relation for use in New Zealand was developed for modelling Arias Intensity. This ground motion measure is currently becoming more and more popular for use in predicting damage levels associated with structures as well as in geotechnical applications, particularly where the duration of the ground motion is significant such as liquefaction studies and landslide analyses. The functional form of the regression model was obtained after making a theoretical derivation that started with the theoretical model of the Fourier Amplitude Spectra derived in Chapter Three of this section. This derivation enables the regression parameters to easily be related to actual physical parameters and consequently as more seismological information becomes available this can be used to further constrain the expected values of the various parameters in the model.

The actual regression analysis was performed using a sophisticated mixed effects model that allowed for the individual uncertainties associated with the estimation of magnitudes in the strong motion catalogue. The use of this algorithm allowed the inter event variance to be reduced from that which is obtained using the common random effects model of Abrahamson and Youngs (1992).

An analysis of the residuals showed that the model performs equally well for the prediction of Arias Intensity over all fault types and site classes and over a wide range of magnitudes [5, 7.4], and distances up to at least 150 km (regression was performed on data up to 300 km). Although the residuals were found to be well distributed, their magnitudes appear to be higher than they should be and this is most likely to be due to inaccuracies in the original dataset used to determine the relationship.

While there is still significant room for improvement of this model, it is the first of its type developed for New Zealand and while the error estimates may be too large at this stage for the model to be used to accurately define hazard values, the median Arias Intensities that it predicts can be regarded with some confidence.

B.7. Conclusions and Recommendations

The present section of work has recognised the current deficiencies that exist in New Zealand with respect to our ability to estimate measures of strong ground motion for use in engineering applications. This section of the thesis has gone some way to addressing these deficiencies by proposing three new predictive models of strong ground motion measures. While the first two of these, the scaling relation for corner frequency, and the model for the Fourier Amplitude Spectrum (FAS) of acceleration are not currently used in seismic hazard analyses, the development of models of this nature enable a more thorough understanding of other ground motion measures to be made. An example of this was seen during the derivation of the functional form of the predictive equation for Arias Intensity. The knowledge of how the model of the Fourier Amplitude Spectrum scaled with respect to various parameters enabled constraints to be placed upon the likely scaling of the parameters involved in the relationship for Arias Intensity. Ensuring that there is consistency between strong ground motion measures may also become increasingly important as more sophisticated analyses using multiple, correlated, measures of strong ground motion are developed, i.e. Vector-Valued Probabilistic Seismic Hazard Analysis, VPSHA (Bazzurro 1998; Bazzurro and Cornell 2002).

As was highlighted in the conclusions and recommendations of Chapter A.7 with respect to the attenuation models used for the PSHA in this thesis; there is a need to develop more predictive models of strong ground motion measures for use in PSHA in New Zealand. A review of the existing models was presented in Chapter B.1 of this section of work, and there it was seen just how limited ones options are when it comes to selecting a predictive model for use in New Zealand.

In the present chapter, as in the similar chapter for Section A of this thesis, the major conclusions to be drawn from each of the chapters comprising Section B will be summarised along with some brief discussion, before making suggestions related to potential areas in which future research might be directed. For obvious reasons, the general introductory chapter will not be considered in what follows.

B.7.1. Chapter B.2: Strong Ground Motion Dataset

This chapter considered the composition of the strong ground motion dataset available in New Zealand for the purpose of deriving predictive models of strong ground motion measures. It was found that while there are a reasonable number of strong motion records at distances applicable to common hazard analyses, these events are significantly biased towards the upper end of this distance range. There are very few near field records from New Zealand earthquakes, and those that do exist typically correspond to moderate sized earthquakes. The most critical magnitude – distance pairs in terms of their relative contributions to seismic hazard tend to correspond to the range of magnitude – distance pairs for which the New Zealand strong motion dataset is deficient. For this reason, the lead of previous researchers was followed, and supplementary strong ground motion records recorded in the near field of moderate to large earthquakes were included in the strong motion dataset used for the regression models of the Fourier Amplitude Spectrum of acceleration and Arias Intensity. The records that were included in the dataset for this study included the majority of the records that had been incorporated in previous studies, but also included some additional more recent strong motion records. The constraint that these records offer in the near – field region is very important for ensuring that the regression models that are obtained are realistic. In all, 529 strong motion records, each with two horizontal components, were included in the total dataset. Of these, 422 were from New Zealand earthquakes, while 107 were from foreign earthquakes. Site class B, and C, were found to have the lowest, and highest, number of records respectively; while the same can be said of strike – slip, and normal faulting events.

The main issue related to the inclusion of the foreign strong motion records was the conversion between foreign and local site classification schemes. It was realised that while there was some considerable uncertainty associated with trying to match site classes from different international schemes, there was also significant uncertainty in simply specifying local site classes anyway. The errors associated with converting between foreign and local classification schemes were therefore thought to be of similar order to those associated with characterising New Zealand site classes.

In order to obtain a dataset of this size, the records that comprised the New Zealand portion of the data were allowed to have rupture distances up to 300 km, while magnitudes were above $M_W 5.0$. While the magnitude range is standard, the allowable distance range is unusually high for studies of strong ground motion measures; in fact, it may well be considered an oxymoron to regard records recorded over such distances as being representative of strong ground motion. However, these records were retained as there did not appear to be any significant break in the scaling of strong motion amplitudes with distance for either the FAS, or Arias Intensity data.

The distance measure used in the derivation of the predictive models was the closest distance to the rupture surface, r_{rup}. For the majority of records in the New Zealand dataset, this distance was unknown and a method for making an approximation to this distance was outlined. This is far from satisfactory, but there are very few other options.

The method used to convert the acceleration time histories into their respective Fourier spectra was discussed. In that section it was highlighted that the focus of the predictive equations was to model the strengths of shear waves, and therefore a method for extracting that part of the time history that related to shear wave arrivals was explained. This method used multiple shear wave windows with varying weights assigned to each in order to account for the degree of subjectivity associated with this selection process.

The Fourier spectra were then computed using the mechanical energy method before being smoothed using a very simple windowing method. It was noted that the methods used to process the Fourier spectra can have a significant impact upon the values of regression coefficients found for empirical models fitted to these spectra.

B.7.1.1. Suggestions for Further Research

As McGuire (2004) points out; it is far better to have a smaller dataset that is of very high quality than it is to have a large dataset of poor quality. In the case of developing strong motion equations from the New Zealand strong motion dataset one is forced to include events that have lower quality than that which is ideal. It is therefore important to try and determine the parameters relevant to developing strong ground motion models for as many records in the dataset as possible. Currently, most events can have their focal mechanism specified, but besides that, there are considerable errors associated with many magnitude estimates, the distance measures for the individual records is very poorly constrained, and there are inherent uncertainties related to the site classification. If accurate strong motion predictive models are to be developed for New Zealand earthquakes then the quality of the relevant parameters used in the models must be improved.

An obvious way to improve this state of affairs is to obtain more strong ground motion records. There is currently provision for a significant upgrade to the number of strong motion recording stations to be located in the South Island in conjunction with the anticipated rupture of the Alpine Fault. These new instruments should allow the number of strong motion records to increase. Of course, we are still solely reliant upon the occurrence of moderate to large earthquakes that can generate additional strong motion records. In association with the previous paragraph, it is not simply enough to increase the number of strong motion records. There must be a systematic process in place by which an accurate determination of the parameters required for obtaining strong ground motion predictive equations are made.

As was also mentioned in Chapter A.7, it will become important in the near future to have predictive models that are able to generate the amplitudes of response spectral ordinates at longer periods than which are currently available from New Zealand strong ground motion records. The applicable bandwidth of the strong motion records currently ranges between about 0.3 – 0.4 Hz at its lower end, up to 25 Hz at its upper end. It would be beneficial to be able to reduce the high pass limit down to 0.1 Hz, or lower so that regressions can be made on the associated long period ordinates.

B.7.2. Chapter B.3: Theoretical Background

This chapter was essentially a recapitulation of existing work in order to set the scene for the remaining chapters of this section; there are therefore few relevant conclusions. The general theme of this presentation was to relate seismological descriptions of strong ground motion measures to those more familiar to engineers. This is not necessarily a major issue; but it cannot hurt to try and make the connections between pure seismology and pure engineering more transparent. If nothing else, simply allowing proponents from either field to more readily observe the origins of fundamental relationships that are used by their colleagues would facilitate future research in the field of engineering seismology.

B.7.3. Chapter B.4: Moment Magnitude – Corner Frequency Relationship

The ultimate purpose of this chapter was to determine a relationship between the moment magnitude and the corner frequency of earthquakes in New Zealand. While this is a useful relationship in its own right, it primary use was to help constrain the regression model for the Fourier Amplitude Spectrum of acceleration. Because the model obtained from this section was to be incorporated into the model for the FAS of acceleration, it was important to try and obtain the parameters of the model in an independent manner so that the subsequent regression coefficients found for the predictive model of the FAS of acceleration weren't untowardly conditional upon the adopted relationship between the corner frequency and moment magnitude.

In order to try and achieve an independent approximation of the moment magnitude – corner frequency relationship a combination of theoretical and probabilistic techniques was employed. The crux of the approach was to obtain a best estimate of the radiation pattern relevant to each record in the dataset considered. From this radiation pattern term, an estimate of the zero frequency spectral amplitude could be determined, and consequently an estimate of the corner frequency of the spectrum in question.

The radiation pattern can be estimated from theoretical considerations in the case where focal mechanism, and crustal velocity model, information is known exactly. This is never the case however, as all of the parameters comprising these data sources carry significant errors with their best estimates. In order to take these errors into account, a comprehensive Monte Carlo simulation methodology was employed in which the relevant parameters of the model were allowed to vary according to various probability distributions.

The final model for the moment magnitude - corner frequency relation was found to be associated with higher stress drops than those of similar models developed for other regions of the world. The parameters of the model were obtained from a relatively small dataset however and this may not be indicative of the true behaviour of New Zealand earthquakes. It is noted that the values of the stress parameter that one obtains from the moment magnitude – corner frequency relation are very sensitive to deviations of the parameters in the model. There is evidence to suggest that New Zealand earthquakes do produce stronger

ground motions than those in other parts of the world; if this evidence is supported as more strong earthquakes occur in New Zealand then the reason may well be associated with a typically higher stress drop, or equivalently, a typically higher slip velocity.

B.7.3.1. Suggestions for Further Research

The methodology employed for this chapter relied heavily upon the existence of focal mechanism solutions. There are currently relatively few available mechanisms for New Zealand earthquakes, and while the routine processing schemes such as the Harvard CMT catalogue, or the NEIC catalogue of the USGS, generate solutions for New Zealand earthquakes having approximately moment magnitudes of $M_W 5.0$ or greater, the solutions found through these programs can often deviate quite markedly from those found from independent studies of the same events. In addition, issues relating to the distinction between the actual rupture plane and the auxiliary plane exist. Therefore, any research that might work towards routinely obtaining more focal mechanism solutions from New Zealand earthquakes would be very beneficial.

This study also made use of a relatively simple ray tracing procedure that was applied within an idealised horizontally layered crust. Any additional detail regarding crustal velocity models, as well as a more comprehensive ray tracing program for the scattering of waves in the shallow crust would enhance the quality of the results obtained in the present work.

A major reason why the elaborate methodology employed in this section was followed was because it was not possible to obtain reliable estimate of the corner frequency of the recorded ground motions because the high-pass filter limit was too high for most of the strong motion records considered. Once again, if this high-pass filter limit could be reduced then such an elaborate methodology to estimate the corner frequency would not need to be employed. However, if the corner frequencies were able to be checked visually, then the accuracy of the proposed method could be quantified through a comparison of the corner frequencies estimated from the techniques.

B.7.4. Chapter B.5: Predictive Equation for the FAS of Acceleration for NZ

A brief chapter summary has already been presented for this section of work; the comments here will therefore be relatively brief. The first predictive model for the FAS of acceleration for New Zealand was developed. This model was shown to perform well over a large range of frequencies, and with respect to both magnitude and distance. A comprehensive regression procedure was employed in order to partition the error components of the model between those related to individual earthquakes, and those related to the inherent variability of strong ground motions. As was previously noted however, the actual magnitudes of the error components that are obtained are strongly related to the processing method used

to obtain the base Fourier spectra upon which the regression is performed. In spite of this, the magnitude of the errors was found to be comparable to those found from other studies.

The actually magnitude of the error components for the model of FAS is not as important as it is for ground motion models that are used for probability calculations, such as peak ground acceleration, or response spectral models. In the case of the FAS, what is of greater importance is the structure of the errors. The error terms should be well distributed with respect to the variables of the model, and this is indeed found to be the case.

The model that has been derived was able to reproduce the expected effects of differing site classes, but was not able to model all the expected effects of different fault mechanisms.

As was mentioned in reference to the quality of the strong ground motion dataset; the general quality, and accuracy of the data comprising the regression dataset must be improved. The magnitudes of the uncertainties associated with the variables that are assumed to be known elements of the regression model are too large to enable accurately determined error estimates to be obtained. However, despite these recognised deficiencies, the model performs well, and as additional data becomes available, and as the quality of this data improves, so too will the performance of this predictive equation.

It should be noted that the parameter estimates found for this model are conditional upon the scaling relationship between moment-magnitude and corner frequency determined in the Chapter B.4.

B.7.4.1. Suggestions for Further Research

The primary area of future research related to this model is the improvement of the quality of the existing strong motion dataset. If the quality and size of the dataset can be improved then the parameters of the regression model may become better defined and the conditional nature of the parameters may be relaxed to some extent. However, a complete relaxation of this dependency is likely to require significantly more records as the correlations between the magnitude scaling terms and the corner frequency parameters would be very strong.

Once again, the spectra used for the development of this regression model are relevant to shear waves only (at least that is the intention). There is some subjectivity currently associated with obtaining the shear wave spectra from the overall spectra that are provided in the New Zealand strong motion records. Routinely defining shear wave windows would enable shear wave spectra to be obtained in a consistent manner, as well as save a considerable amount of time. The spectral ordinates that carried the largest errors were those at low frequencies, this is the region in which the effects of inaccurate shear wave window picks have the most influence. However, as mentioned in Chapter B.5, the observed amplitudes over this range tend to vary more with direction for these ordinates and it is not clear to what extent inaccuracies in

the shear wave window picking process may contribute to the increased error over this low frequency range.

An additional point related to the strong motion dataset is that currently, the near source effect in New Zealand strong ground motion models has to be constrained. This is not desirable as the assumed conditions of constraint dictate to some degree the consequent values associated with the geometric spreading coefficients. This is obviously undesirable, but there are few other options available given that the strong motion database is already being supplemented by foreign near field records. However, this is an area into which research should be directed, i.e. characterising the near field scaling from New Zealand earthquakes.

B.7.5. Chapter B.6: Predictive Equation for Arias Intensity

Many of the conclusions relevant to the predictive model for the FAS are also relevant to the predictive model for Arias Intensity; particularly with respect to data quality.

The model that was obtained for the Arias Intensity was found to model the average Arias Intensity for New Zealand earthquakes very well. A significant attribute of this model is the relatively high rate of geometric spreading for the model. However, this scaling is shown to be consistent with both existing model of peak ground acceleration in New Zealand as well as for the model of the FAS previously determined in Chapter B.5. The magnitude of the error inter-event error term was found to be relatively high however, which makes one tentative to immediately adopt this model in PSHA considerations. The effect of this increased error magnitude was demonstrated in Section A of this thesis.

The regression parameters were obtained for this model using an even more comprehensive framework than that used for the derivation of the parameters in the model for the FAS of acceleration. This framework, developed by Rhoades (1997), enables the individual errors associated with magnitude estimates to be taken into account during the regression procedure. The original formulation of this algorithm was presented for the case of linear magnitude scaling, but in this study, the algorithms were extended to the case of quadratic magnitude scaling in order to correct for an observed trend in the inter-event residuals in the regression model. This adjustment greatly enhanced the performance of the model, particularly with respect to the distribution of inter-event residuals against magnitude.

The result of accounting for the effects of uncertainties in variables such as magnitude is shown to be significant. The benefits are recognised in the reduction of the magnitude of the inter-event error term. One can therefore appreciate how the errors associated with approximating the actual rupture distance would affect the determination of the regression coefficients for this model as well that for the FAS of acceleration.

B.7.5.1. Suggestions for Further Research

Once again, improvement of the defining parameters in the strong motion dataset would enhance the quality of the regression model for Arias Intensity.

Additional investigations into the reduction of the inter-event error should be conducted as well as an attempt to ascertain any magnitude dependence of both the inter-event, and intra-event error components.

Relatively recently, the Vector-Valued Probabilistic Seismic Hazard Analysis (VPSHA) methodology was presented (Bazzurro 1998; Bazzurro and Cornell 2002). Correlations between observed values of Arias Intensity and other ground motion measures, such as peak ground accelerations, spectral accelerations, or duration, could be determined and applied within this framework. There may be potential to apply VPSHA in a liquefaction analysis framework in which joint hazards of both shaking amplitudes and durations were considered simultaneously. This methodological framework has a strong potential to perform well for situations such as the evaluation of liquefaction susceptibility, or the triggering of landslides, or other geotechnical and structural engineering problems in which both ground motion amplitude and duration are significant determinants of the systems response.

References

Abercrombie, R. E. (1995). "Earthquake source scaling relationships from -1 to 5 M(L) using seismograms recorded at 2.5-km depth." Journal of Geophysical Research-Solid Earth 100(B12): 24015-24036.

Abercrombie, R. E. (1996). "The magnitude-frequency distribution of earthquakes recorded with deep seismometers at Cajon Pass, southern California." Tectonophysics 261: 1-7.

Abercrombie, R. E. (1998). "A Summary of Attenuation Measurements from Borehole Recordings of Earthquakes: The 10 Hz Transition Problem." Pure and Applied Geophysics 153: 475-487.

Abercrombie, R. E. and Brune, J. N. (1994). "Evidence for a constant b-value above magnitude 0 in the southern San Andreas, San Jacinto, and San Miguel fault zones, and at the Long Valley caldera, California." Geophysical Research Letters 21(15): 1647-1650.

Abrahamson, N. A. (1988). "Statistical Properties of Peak Ground Accelerations Recorded by the Smart 1 Array." Bulletin of the Seismological Society of America 78(1): 26-41.

Abrahamson, N. A. and Bommer, J. J. (2005). "Probability and uncertainty in seismic hazard analysis." Earthquake Spectra 21(2): 603-607.

Abrahamson, N. A. and Litehiser, J. J. (1989). "Attenuation of Vertical Peak Acceleration." Bulletin of the Seismological Society of America 79: 549-580.

Abrahamson, N. A. and Silva, W. J. (1997). "Empirical Response Spectral Attenuation Relations for Shallow Crustal Earthquakes." Seismological Research Letters 68(1): 94-127.

Abrahamson, N. A. and Somerville, P. G. (1996). "Effects of the hanging wall and footwall on ground motions recorded during the Northridge earthquake." Bulletin of the Seismological Society of America 86(1): S93-S99.

Abrahamson, N. A. and Youngs, R. R. (1992). "A Stable Algorithm for Regression-Analyses Using the Random Effects Model." Bulletin of the Seismological Society of America 82(1): 505-510.

Adams, R. D., Eiby, G. A., Lowry, M. A., Lensen, G. J., Suggate, R. P. and Stephenson, W. R. (1968). Preliminary reports on the Inangahua earthquake, New Zealand, May 1968. Bulletin of the Department of Scientific and Industrial Research, no. 193. Wellington, Department of Scientific and Industrial Research: 38.

Adams, R. D. and Le Fort, J. H. (1963). "The Westport Earthquakes, May 1962." New Zealand Journal of Geology and Geophysics 6(4): 487-509.

Adams, R. D. and Lowry, M. A. (1971). "The Inangahua Earthquake Sequence, 1968." Bulletin of the Royal Society of New Zealand 9: 129-135.

Adams, R. D., Lowry, M. A. and Ware, D. E. (1971). New Zealand Seismological Report Inangahua Earthquakes 1968. Wellington, New Zealand, New Zealand Department of Scientific and Industrial Research, Geophysics Division.

Aki, K. (1965). "Maximum likelihood estimate of b in the formula $\log N = a - bM$ and its confidence limits." Bulletin of the Earthquake Research Insititute, University of Tokyo 43: 237-239.

Aki, K. (1967). "Scaling Law of Seismic Spectrum." Journal of Geophysical Research 72: 1217-1231.

Aki, K. (1987). "Magnitude-frequency relation for small earthquakes: a clue to the origin of f_{max} of large earthquakes." Journal of Geophysical Research 92: 1349-1355.

Aki, K. and Richards, P. G. (1980). Quantitative Seismology: Theory and Methods. San Francisco, W. H. Freeman and Company.

Ambraseys, N. N. and Bommer, J. J. (1991). "Attenuation of ground accelerations in Europe." Earthquake Engineering & Structural Dynamics 20(12): 1179-1202.

Anderson, H., Beanland, S., Blick, G., Darby, D., Downes, G., Haines, J., Jackson, J., Robinson, R. and Webb, T. (1994). "The 1968 May 23 Inangahua, New-Zealand, Earthquake - an Integrated Geological, Geodetic, and Seismological Source Model." New Zealand Journal of Geology and Geophysics 37(1): 59-86.

Anderson, H. and Webb, T. (1994). "New-Zealand Seismicity - Patterns Revealed by the Upgraded National-Seismograph-Network." New Zealand Journal of Geology and Geophysics 37(4): 477-493.

Anderson, H., Webb, T. and Jackson, J. (1993). "Focal Mechanisms of Large Earthquakes in the South-Island of New-Zealand - Implications for the Accommodation of Pacific-Australia Plate Motion." Geophysical Journal International 115(3): 1032-1054.

Anderson, J. G. and Brune, J. N. (1999). "Methodology for using precarious rocks in Nevada to test seismic hazard models." Bulletin of the Seismological Society of America 89(2): 456-467.

Anderson, J. G. and Hough, S. E. (1984). "A Model for the Shape of the Fourier Amplitude Spectrum of Acceleration at High-Frequencies." Bulletin of the Seismological Society of America 74(5): 1969-1993.

Anderson, J. G., Wesnousky, S. G. and Stirling, M. W. (1996). "Earthquake size as a function of fault slip rate." Bulletin of the Seismological Society of America 86(3): 683-690.

Andrews, D. J. (1986). Objective Determination of Source Parameters and Similarity of Earthquakes of Different Size. Earthquake Source Mechanics. Das, S., Boatwright, J. and Scholz, C. Washington, D.C., American Geophysical Union. 6**:** 259-267.

Anooshehpoor, A., Brune, J. N. and Zeng, Y. H. (2004). "Methodology for obtaining constraints on ground motion from precariously balanced rocks." Bulletin of the Seismological Society of America 94(1): 285-303.

Arias, A. (1970). A Measure of Earthquake Intensity. Seismic Design for Nuclear Power Plants. Hansen, R. J. Cambridge, MA, MIT Press**:** 438-483.

Atkinson, G. M. and Beresnev, I. (1997). "Don't Call it Stress Drop." Seismological Research Letters 68(1): 3-4.

Atkinson, G. M. and Boore, D. M. (1995). "Ground-Motion Relations for Eastern North-America." Bulletin of the Seismological Society of America 85(1): 17-30.

Atkinson, G. M. and Mereu, R. F. (1992). "The Shape of Ground Motion Attenuation Curves in Southeastern Canada." Bulletin of the Seismological Society of America 82(5): 2014-2031.

Atkinson, G. M. and Silva, W. (1997). "An empirical study of earthquake source spectra for California earthquakes." Bulletin of the Seismological Society of America 87(1): 97-113.

Atkinson, G. M. and Silva, W. (2000). "Stochastic modeling of California ground motions." Bulletin of the Seismological Society of America 90(2): 255-274.

Avery, H., Berrill, J. B., Coursey, P. F., Deam, B. L., Dewe, M. B., François, C. C., Pettinga, J. R. and Yetton, M. D. (2004). The Canterbury University Strong-Motion Recording Project. 13th World Conference on Earthquake Engineering, Vancouver, B.C., Canada.

Bak, P. (1996). How nature works, the science of self-organized criticality. New York, Springer-Verlag.

Bak, P., Christensen, K., Danon, L. and Scanlon, T. (2002). "Unified scaling law for earthquakes." Physical Review Letters 88(17): Article No. 178501-1.

Bak, P. and Tang, C. (1989). "Earthquakes as a Self-Organized Critical Phenomenon." Journal of Geophysical Research 94(B11): 15,635-15,637.

Bak, P., Tang, C. and Wiesenfeld, K. (1988). "Self-Organized Criticality." Physical Review A 38(1): 364-374.

Baker, J. W. and Cornell, C. A. (2005). "A vector-valued ground motion intensity measure consisting of spectral acceleration and epsilon." Earthquake Engineering & Structural Dynamics 34(10): 1193-1217.

Baker, J. W. and Cornell, C. A. (2006). "Which Spectral Acceleration Are You Using?" Earthquake Spectra submitted.

Bakun, W. H. and Lindh, A. G. (1985). "The Parkfield, California, earthquake prediction experiment." Science 229: 619-624.

Bastings, L. (1933). "Some seismological aspects of the Buller earthquake, 1929, June 16-17." The New Zealand Journal of Science and Technology: 128-142.

Båth, M. (1965). "Lateral inhomogeneities of the upper mantle." Tectonophysics 2(6): 483-514.

Bazzurro, P. (1998). Probabilistic Seismic Demand Analysis: A dissertation submitted to the department of civil and environmental engineering and the committee on graduate studies of Stanford University in partial fulfillment of the requirements for the degree of Doctor of Philosophy. Department of Civil and Environmental Engineering. Palo Alto, CA, Stanford University: 329.

Bazzurro, P. and Cornell, C. A. (1999). "Disaggregation of seismic hazard." Bulletin of the Seismological Society of America 89(2): 501-520.

Bazzurro, P. and Cornell, C. A. (2002). "Vector-Valued Probabilistic Seismic Hazard Analysis (VPSHA)." Proceedings of the Seventh U.S. National Conference on Earthquake Engineering (7NCEE), Boston, Massachusetts, USA 2: 1313-1322.

Beanland, S., Haines, J., Darby, D., Anderson, H., Blick, G., Downes, G., Jackson, J., Robinson, R. and Webb, T. (1994). "The 1968-May-23 Inangahua, New-Zealand, Earthquake - an Integrated

Geological, Geodetic, and Seismological Source Model - Comment - Reply." New Zealand Journal of Geology and Geophysics 37(4): 500-501.

Beavan, J. and Haines, J. (2001). "Contemporary horizontal velocity and strain rate fields of the Pacific-Australian plate boundary zone through New Zealand." Journal of Geophysical Research-Solid Earth 106(B1): 741-770.

Bender, B. (1983). "Maximum-Likelihood Estimation of B-Values for Magnitude Grouped Data." Bulletin of the Seismological Society of America 73(3): 831-851.

Bender, B. and Campbell, K. W. (1989). "Selection of Minimum Magnitude for Use in Seismic Hazard Analysis." Bulletin of the Seismological Society of America 79(1): 199-204.

Benites, R. A., Robinson, R., Webb, T. and McGinty, P. (2003). Modelling realistic ruptures on the Wellington fault. Institute of Geological and Nuclear Sciences Report. Lower Hutt, New Zealand, Institute of Geological and Nuclear Sciences: 46.

Benjamin, J. R. and Cornell, C. A. (1970). Probability, Statistics, and Decision for Civil Engineers. New York, McGraw-Hill.

Beresnev, I. A. (2001). "What we can and cannot learn about earthquake sources from the spectra of seismic waves." Bulletin of the Seismological Society of America 91(2): 397-400.

Beresnev, I. A. (2002). "Source parameters observable from the corner frequency of earthquake spectra." Bulletin of the Seismological Society of America 92(5): 2047-2048.

Beresnev, I. A. and Atkinson, G. M. (1997). "Modeling finite-fault radiation from the omega(n) spectrum." Bulletin of the Seismological Society of America 87(1): 67-84.

Beresnev, I. A. and Atkinson, G. M. (1998). "Stochastic finite-fault modeling of ground motions from the 1994 Northridge, California, earthquake. I. Validation on rock sites." Bulletin of the Seismological Society of America 88(6): 1392-1401.

Berrill, J. B. (1985). "Distribution of Scatter in New Zealand Accelerograph Data." Bulletin of the New Zealand National Society of Earthquake Engineering 18(2): 151-164.

Berrill, J. B. and Davis, R. O. (1980). "Maximum-Entropy and the Magnitude Distribution." Bulletin of the Seismological Society of America 70(5): 1823-1831.

Berryman, K. and Beanland, S. (1991). "Variation in Fault Behavior in Different Tectonic Provinces of New-Zealand." Journal of Structural Geology 13(2): 177-189.

Berryman, K. R. (1980). "Late Quaternary Movement on White Creek Fault, South Island, New-Zealand." New Zealand Journal of Geology and Geophysics 23(1): 93-101.

Berryman, K. R., Beanland, S., Cooper, A. F., Cutten, H. N., Norris, R. J. and Wood, P. R. (1992). "The Alpine Fault, New Zealand: variation in Quaternary structural style and geomorphic expression." Annales Tectonicæ VI: 126-163.

Bevin, T. (1998). Conversion between Latitude and Longitude and New Zealand Map Grid. Wellington, Office of the Surveyor-General, Land Information New Zealand: 6.

Bishop, D. J. and Buchanan, P. G. (1995). Development of structurally inverted basins: a case study from the West Coast, South Island, New Zealand. Basin Inversion, Geological Society Special Publication No. 88. Buchanan, J. G. and Buchanan, P. G. London, The Geological Society: 549-585.

Boatwright, J. and Choy, G. L. (1992). "Acceleration Source Spectra Anticipated for Large Earthquakes in Northeastern North-America." Bulletin of the Seismological Society of America 82(2): 660-682.

Bolt, B. A. and Abrahamson, N. A. (2003). Estimation of Strong Seismic Ground Motions. International Handbook of Earthquake and Engineering Seismology. Lee, W. H. K., Kanamori, H., Jennings, P. C. and Kisslinger, C. London, Academic Press (for the International Association of Seismology and Physics of the Earth's Interior. 81B**:** 983-1001.

Bommer, J. J., Abrahamson, N. A., Strasser, F. O., Pecker, A., Bard, P. Y., Bungum, H., Cotton, F., Fah, D., Sabetta, F., Scherbaum, F. and Studer, J. (2004). "The challenge of defining upper bounds on earthquake ground motions." Seismological Research Letters 75(1): 82-95.

Bommer, J. J., Georgallides, G. and Tromans, I. J. (2001). "Is there a Near-Field for Small-to-Moderate Magnitude Earthquakes." Journal of Earthquake Engineering 5(3): 395-423.

Bommer, J. J. and Martinez-Pereira, A. (1999). "The Effective Duration of Earthquake Strong Motion." Journal of Earthquake Engineering 3(2): 127-172.

Bommer, J. J., Scherbaum, F., Bungum, H., Cotton, F., Sabetta, F. and Abrahamson, N. A. (2005). "On the use of logic trees for ground-motion prediction equations in seismic-hazard analysis." Bulletin of the Seismological Society of America 95(2): 377-389.

Bommer, J. J., Scott, S. G. and Sarma, S. K. (2000). "Hazard-consistent earthquake scenarios." Soil Dynamics and Earthquake Engineering 19(4): 219-231.

Boore, D. M. (1983). "Stochastic Simulation of High-Frequency Ground Motions Based on Seismological Models of the Radiated Spectra." Bulletin of the Seismological Society of America 73(6): 1865-1894.

Boore, D. M. (2000). SMSIM - Fortran Programs for Simulating Ground Motions from Earthquakes: Version 2.0 - A Revision of OFR 96-80-A. U.S. Geological Survey Open File Report; OFR 00-509. Menlo Park, California, U.S. Geological Survey**:** 57.

Boore, D. M. (2003). "Simulation of ground motion using the stochastic method." Pure and Applied Geophysics 160(3-4): 635-676.

Boore, D. M. (2004). "Can site response be predicted?" Journal of Earthquake Engineering 8: 1-41.

Boore, D. M. (2005). "ERRATUM: Seismological Research Letters, Vol. 68, No.1, pp 128--153, January/February 1997, Equations for Estimating Horizontal Response Spectra and Peak Acceleration from Western North American Earthquakes: A Summary of Recent Work, D. M. Boore, W. B. Joyner, and T. E. Fumal." Seismological Research Letters 76: 368-369.

Boore, D. M. and Atkinson, G. M. (1987). "Stochastic Prediction of Ground Motion and Spectral Response Parameters at Hard-Rock Sites in Eastern North-America." Bulletin of the Seismological Society of America 77(2): 440-467.

Boore, D. M. and Joyner, W. B. (1997). "Site amplifications for generic rock sites." Bulletin of the Seismological Society of America 87(2): 327-341.

Boore, D. M., Joyner, W. B. and Fumal, T. E. (1997). "Equations for Estimating Horizontal Response Spectra and Peak Acceleration from Western North American Earthquakes: A Summary of Recent Work." Seismological Research Letters 68(1): 128-153.

Boore, D. M., Joyner, W. B. and Wennerberg, L. (1992). "Fitting the Stochastic Omega(-2) Source Model to Observed Response Spectra in Western North-America - Trade-Offs between Delta-Sigma and Kappa." Bulletin of the Seismological Society of America 82(4): 1956-1963.

Borcherdt, R. D. (1994). "Estimates of site-dependent response spectra for design (methodology and justification)." Earthquake Spectra 10(4): 617-653.

Bourne, S. J., Arnadottir, T., Beavan, J., Darby, D. J., England, P. C., Parsons, B., Walcott, R. I. and Wood, P. R. (1998). "Crustal deformation of the Marlborough fault zone in the South Island of New Zealand: Geodetic constraints over the interval 1982-1994." Journal of Geophysical Research-Solid Earth 103(B12): 30147-30165.

Bowman, D. D. and Sammis, C. G. (2004). "Intermittent Criticality and the Gutenberg-Richter Distribution." Pure and Applied Geophysics 161: 1945-1956.

Boyes, W. S. (1969). Horizontal and vertical crustal movement in the Inangahua earthquake of 1968. Wellington, Department of Lands and Survey.

Brillinger, D. R. and Preisler, H. K. (1984). "An exploratory analysis of the Joyner-Boore attenuation data." Bulletin of the Seismological Society of America 74(4): 1441-1450.

Brillinger, D. R. and Preisler, H. K. (1985). "Further analysis of the Joyner-Boore attenuation data." Bulletin of the Seismological Society of America 75(2): 611-614.

Brune, J. N. (1970). "Tectonic Stress and Spectra of Seismic Shear Waves from Earthquakes." Journal of Geophysical Research 75(26): 4997-&.

Brune, J. N. (1971). "Correction." Journal of Geophysical Research 76(20): 5002-&.

Brune, J. N. (2001a). "Shattered rock and precarious rock evidence for strong asymmetry in ground motions during thrust faulting." Bulletin of the Seismological Society of America 91(3): 441-447.

Brune, J. N. (2001b). "Shattered rock and precarious rock evidence for strong asymmetry in ground motions during thrust faulting (vol 91, pg 443, 2001)." Bulletin of the Seismological Society of America 91(6): 1937-1940.

Brune, J. N. (2002). "Precarious-rock constraints on ground motion from historic and recent earthquakes in southern California." Bulletin of the Seismological Society of America 92(7): 2602-2611.

Brune, J. N. (2003). "Precarious rock evidence for low near-source accelerations for trans-tensional strike-slip earthquakes." Physics of the Earth and Planetary Interiors 137(1-4): 229-239.

Brune, J. N., Bell, J. W. and Anooshehpoor, A. (1996). "Precariously balanced rocks and seismic risk." Endeavour 20(4): 168-172.

Building Seismic Safety Council (BSSC) (1994). NEHRP recommended provisions for seismic regulations for new buildings, Part 1 - Provisions, FEMA 222A, Federal Emergency Management Agency.

Campbell, K. W. (1981). "Near Source Attneuation of Peak Horizontal Accelerations." Bulletin of the Seismological Society of America 71: 2039-2070.

Campbell, K. W. (1985). "Strong Motion Attenuation Relations: A Ten-Year Perspective." Earthquake Spectra 1(4): 759-804.

Campbell, K. W. (1997). "Empirical Near-source Attenuation Relationships for Horizontal and Vertical Components for Peak Ground Acceleration, Peak Ground Velocity, and Psuedo-absolute Acceleration Response Spectra." Seismological Research Letters 68: 154-179.

Campbell, K. W. (2003a). "Prediction of strong ground motion using the hybrid empirical method and its use in the development of ground-motion (attenuation) relations in eastern north America." Bulletin of the Seismological Society of America 93(3): 1012-1033.

Campbell, K. W. (2003b). Strong-Motion Attenuation Relations. International Handbook of Earthquake and Engineering Seismology. Lee, W. H. K., Kanamori, H., Jennings, P. C. and Kisslinger, C. London, Academic Press (for the International Association of Seismology and Physics of the Earth's Interior. 81B**:** 1003-1012.

Campbell, K. W. and Bozorgnia, Y. (2003a). "Updated near-source ground-motion (attenuation) relations for the horizontal and vertical components of peak ground acceleration and acceleration response spectra." Bulletin of the Seismological Society of America 93(1): 314-331.

Campbell, K. W. and Bozorgnia, Y. (2003b). "Updated near-source ground-motion (attenuation) relations for the horizontal and vertical components of peak ground acceleration and acceleration response spectra (vol 93, pg 314, 2003)." Bulletin of the Seismological Society of America 93(4): 1872-1872.

Campbell, K. W. and Bozorgnia, Y. (2004). "Updated near-source ground-motion (attenuation) relations for the horizontal and vertical components of peak ground acceleration and acceleration response spectra (vol 93, pg 314, 2003)." Bulletin of the Seismological Society of America 94(6): 2417-2417.

Carr, K. M. (2004). Liquefaction case histories from the West Coast of the South Island, New Zealand: a thesis submitted in partial fulfilment of the requirements for the degree of Master of Engineering in the University of Canterbury. Department of Civil Engineering. Christchurch, University of Canterbury**:** 170.

Chen, S. Z. and Atkinson, G. M. (2002). "Global comparisons of earthquake source spectra." Bulletin of the Seismological Society of America 92(3): 885-895.

Coppersmith, K. J. and Youngs, R. R. (1986). Capturing uncertainty in probabilistic seismic hazard assessments with intraplate tectonic environments. 3rd U.S. National Conference on Earthquake Engineering, Charleston, South Carolina.

Cornell, C. A. (1968). "Engineering seismic risk analysis." Bulletin of the Seismological Society of America 58(5): 1583-1606.

Cornell, C. A. (1994). Statistical Analysis of Maximum Magnitudes. The earthquakes of stable continental regions. Johnston, A. C. Palo Alto, Electric Power Research Institute**:** 5.1-5.27.

Cornell, C. A. and Vanmarcke, E. H. (1969). The major influences on seismic risk. Proceedings of the Fourth World Conference on Earthquake Engineering, Santiago, Chile.

Cornell, C. A. and Winterstein, S. R. (1988). "Temporal and Magnitude Dependence in Earthquake Recurrence Models." Bulletin of the Seismological Society of America 78(4): 1522-1537.

Cornell, C. A. and Winterstein, S. R. (1989). "Temporal and Magnitude Dependence in Earthquake Recurrence Models - Reply." Bulletin of the Seismological Society of America 79(5): 1663-1664.

Cousins, W. J. (1993). "Highlights of 30 years of strong-motion recording in New Zealand." Bulletin of the New Zealand National Society of Earthquake Engineering 26(4): 375-389.

Cousins, W. J., Hefford, R. T., McVerry, G. H., O'Kane, S. M. and Baguley, D. E. (1991). Computer analyses of New Zealand earthquake accelerograms, Volume 7, Three earthquakes near Westport

in January and February 1991. Computer analyses of New Zealand earthquake accelerograms. Lower Hutt, New Zealand, DSIR, Physical Sciences.

Cousins, W. J., Perrin, N. D., McVerry, G. H., Hefford, R. T. and Porritt, T. E. (1996). Ground conditions at strong-motion recording sites in New Zealand. Wellington, Institute of Geological & Nuclear Sciences: 244.

Cousins, W. J., Zhao, J. X. and Perrin, N. D. (1999). "A Model for the Attenuation of Peak Ground Acceleration in New Zealand Earthquakes Based on Seismograph and Accelerograph Data." Bulletin of the New Zealand Society of Earthquake Engineering 32(4): 193-217.

Davis, G. H. and Reynolds, S. J. (1996). Structural Geology of Rocks and Regions. New York, John Wiley & Sons, Inc.

Del Gaudio, V., Pierri, P. and Wasowski, J. (2003). "An approach to time-probabilistic evaluation of seismically induced landslide hazard." Bulletin of the Seismological Society of America 93(2): 557-569.

DeMets, C., Gordon, R. G., Argus, D. F. and Stein, S. (1990). "Current plate motions." Geophysical Journal International 101: 425-478.

DeMets, C., Gordon, R. G., Argus, D. F. and Stein, S. (1994). "Effect of recent revisions to the geomagnetic reversal time scale on estimates of current plate motions." Geophysical Research Letters 21(20): 2191-2194.

Der Kiureghian, A. and Ang, A. H.-S. (1977). "A Fault-Rupture Model for Seismic Risk Analysis." Bulletin of the Seismological Society of America 67(4): 1173-1194.

Dieterich, J. (1994). "A Constitutive Law for Rate of Earthquake Production and Its Application to Earthquake Clustering." Journal of Geophysical Research-Solid Earth 99(B2): 2601-2618.

Dieterich, J. H. (1992). "Earthquake nucleation on faults with rate- and state- dependent strength." Tectonophysics 211: 115-134.

Dong, W. M., Bao, A. B. and Shah, H. C. (1984). "Use of Maximum-Entropy Principle in Earthquake Recurrence Relationships." Bulletin of the Seismological Society of America 74(2): 725-737.

Doser, D. I. and Robinson, R. (2002). "Modeling stress changes induced by earthquakes in the southern Marlborough region, South Island, New Zealand." Bulletin of the Seismological Society of America 92(8): 3229-3238.

Doser, D. I. and Webb, T. H. (2003). "Source parameters of large historical (1917-1961) earthquakes, North Island, New Zealand." Geophysical Journal International 152(3): 795-832.

Doser, D. I., Webb, T. H. and Maunder, D. E. (1999). "Source parameters of large historical (1918-1962) earthquakes, South Island, New Zealand." Geophysical Journal International 139(3): 769-794.

Douglas, J. (2001). A comprehensive worldwide summary of strong-motion attenuation relationships for peak ground acceleration and spectral ordinates (1969 to 2000). ESEE Report No. 01-1. Engineering Seismology and Earthquake Engineering. London, Imperial College of Science, Technology and Medicine; Civil Engineering Department: 138.

Douglas, J. (2002). Errata of and additions to ESEE Report No. 01-1: 'A comprehensive worldwide summary of strong-motion relationships for peak ground acceleration and spectral ordinates (1969 to 2000)'. Engineering Seismology and Earthquake Engineering. London, Imperial College of Science, Technology and Medicine; Department of Civil & Environmental Engineering: 40.

Douglas, J. (2003). "Earthquake ground motion estimation using strong-motion records: a review of equations for the estimation of peak ground acceleration and response spectral ordinates." Earth-Science Reviews 61(1-2): 43-104.

Douglas, J. (2004). Use of Analysis of Variance for the Investigation of Regional Dependence of Strong Ground Motions. 13th World Conference on Earthquake Engineering, Vancouver, B.C., Canada.

Douglas, J. and Smit, P. M. (2001). "How accurate can strong ground motion attenuation relations be?" Bulletin of the Seismological Society of America 91(6): 1917-1923.

Downes, G. (1995). Atlas of Isoseismal Maps of New Zealand Earthquakes. Lower Hutt, New Zealand, Institute of Geological & Nuclear Sciences Limited.

Dowrick, D. J. (1994). "Damage and Intensities in the magnitude 7.8 1929 Murchison, New Zealand, earthquake." Bulletin of the New Zealand National Society of Earthquake Engineering 27(3): 190-204.

Dowrick, D. J. and Rhoades, D. A. (1998). "Magnitudes of New Zealand Earthquakes, 1901-1993." Bulletin of the New Zealand Society for Earthquake Engineering 31(4): 260-280.

Dowrick, D. J. and Rhoades, D. A. (1999). "Attenuation of Modified Mercalli intensity in New Zealand earthquakes." Bulletin of the New Zealand Society for Earthquake Engineering 32(2): 55-89.

Dowrick, D. J. and Rhoades, D. A. (2004). "Relations between earthquake magnitude and fault rupture dimensions: How regionally variable are they?" Bulletin of the Seismological Society of America 94(3): 776-788.

Dowrick, D. J., Rhoades, D. A. and Davenport, P. N. (2003). "Effects of microzoning and foundations on damage ratios for domestic property in the magntiude 7.2 1968 Inangahua, New Zealand, earthquake." Bulletin of the New Zealand Society of Earthquake Engineering 36(1): 25-46.

Dowrick, D. J. and Smith, E. G. C. (1990). "Surface wave magnitudes of some New Zealand earthquakes 1901-1988." Bulletin of the New Zealand National Society of Earthquake Engineering 23: 198-210.

Dowrick, D. J. and Sritharan, S. (1993). "Attenuation of peak ground accelerations in some recent New Zealand earthquakes." Bulletin of the New Zealand National Society of Earthquake Engineering 26: 3-13.

Dowrick, D. J. and Sritharan, S. (1993a). "Peak Ground Accelerations recorded in the 1968 Inangahua Earthquake and some attenuation implications." Bulletin of the New Zealand National Society of Earthquake Engineering 26(3): 349-355.

Draper, N. R. and Smith, H. (1981). Applied Regression Analysis. New York, John Wiley & Sons.

Draper, N. R. and Smith, H. (1998). Applied Regression Analysis. New York, John Wiley & Sons, Inc.

Eberhart-Phillips, D. (1998). "Aftershock sequence parameters in New Zealand." Bulletin of the Seismological Society of America 88(4): 1095-1097.

Eberhart-Phillips, D. and McVerry, G. (2003). "Estimating slab earthquake response spectra from a 3D Q model." Bulletin of the Seismological Society of America 93(6): 2649-2663.

Eberhart-Phillips, D. and Reyners, M. (2001). "A complex, young subduction zone imaged by three-dimensional seismic velocity, Fiordland, New Zealand." Geophysical Journal International 146(3): 731-746.

Egan, J. A. and Rosidi, D. (1991). Assessment of earthquake-induced liquefaction using ground-motion energy characteristics. Pacific Conference on Earthquake Engineering, Auckland, New Zealand.

Eiby, G. A. (1966). "The Modified Mercalli Scale of Earthquake Intensity and its use in New Zealand." New Zealand Journal of Geology and Geophysics 9: 122-129.

Ellsworth, W. L., Matthews, M. V., Nadeau, S. P., Nishenko, S. P., Reasenberg, P. A. and Simpson, R. W. (1999). A physically based earthquake recurrence model for estimation of long-term earthquake probabilities. U. S. Geological Survey Open File Report 99-522, USGS: 22.

Elms, D. G. (1985). The Principle of Consistent Crudeness. NSF Workshop on Civil Engineering Applications of Fuzzy Sets, Lafayette, Indiana, U.S.A., School of Engineering, Purdue University.

Elms, D. G., Ed. (1998). Owning the Future: Integrated Risk Management in Practice. Christchurch, Centre for Advanced Engineering.

Esteva, L. (1970). Seismic Risk and Seismic Design. Seismic Design for Nuclear Power Plants. Hansen, R. J. Massachusetts, M.I.T. Press: 142-182.

Esteva, L. and Rosenblueth, E. (1964). "Expectios de tremblores distancias moderadas y grandes." Sociedad Mexicana de Ingenieria Sesmica 2.

Evison, F. and Rhoades, D. (2004). "Long-term seismogensis and self-organized criticality." Earth Planets Space 56: 749-760.

Evison, F. F. (1977). "Precursory seismic sequences in New Zealand." New Zealand Journal of Geology and Geophysics 20: 129-141.

Evison, F. F. (1978). "Long-Term Seismic Precursor to 1968 Inangahua Earthquake, New-Zealand." New Zealand Journal of Geology and Geophysics 21(4): 531-534.

Felzer, K. R., Abercrombie, R. E. and Ekstrom, G. (2004). "A common origin for aftershocks, foreshocks, and multiplets." Bulletin of the Seismological Society of America 94(1): 88-98.

François-Holden, C. C. (2004). Direct measurement of fault rupture using seismic dense arrays: method and application to the Alpine Fault, New Zealand and SMART-1, Taiwan data: a thesis submitted in partial fulfillment of the requirements for the degree of Doctor of Philosophy in Civil Engineering. Department of Civil Engineering. Christchurch, University of Canterbury: 131.

Fraser, J. G. (2005). Paleoseismic Investigation of the Waimea-Flaxmore Fault System, Nelson Region. Department of Geological Sciences. Christhurch, University of Canterbury: 210.

Frohlich, C. and Davis, S. D. (1993). "Teleseismic b values; or much ado about 1.0." Journal of Geophysical Research 98: 631-644.

Fukushima, Y. and Tanaka, T. (1990). "A New Attenuation Relation for Peak Horizontal Acceleration of Strong Earthquake Ground Motion in Japan." Bulletin of the Seismological Society of America 80(4): 757-783.

Ghisetti, F. and Sibson, R. H. (2006). "Accomodation of compressional inversion in north-western South Island (New Zealand): old faults versus new?" Journal of Structural Geology *submitted*.

Godano, C. and Pingue, F. (2000). "Is the seismic moment-frequency relation universal?" Geophysical Journal International 142: 193-198.

Grant, L. B. (2002). Paleoseismology. International Handbook of Earthquake & Engineering Seismology. Lee, W. H. K., Kanamori, H., Jennings, P. C. and Kisslinger, C. London, Academic Press; for the International Association of Seismology and Physics of the Earth's Interior. 1: 475-489.

Grapes, R. H. and Wellman, H. W. (1986). "The north-east end of the Wairau Fault, Marlborough, New Zealand." Journal of the Royal Society of New Zealand 16: 245-250.

Grunthal, G. and Wahlstrom, R. (2001). "Sensitivity of parameters for probabilistic seismic hazard analysis using a logic tree approach." Journal of Earthquake Engineering 5(3): 309-328.

Gutenberg, B. and Richter, C. F. (1944). "Frequency of Earthquakes in California." Bulletin of the Seismological Society of America 34: 185-188.

Gutenberg, B. and Richter, C. F. (1956). "Earthquake Magnitude, Intensity, Energy and Acceleration (second Paper)." Bulletin of the Seismological Society of America 46(2): 143-145.

Guttorp, P. (1987). "On Least-Squares Estimation of *b* Values." Bulletin of the Seismological Society of America 77(6): 2115-2124.

Haddon, R. A. W. (1996). "Earthquake source spectra in eastern North America." Bulletin of the Seismological Society of America 86(5): 1300-1313.

Haines, A. J. (1981). "A Local Magnitude Scale for New-Zealand Earthquakes." Bulletin of the Seismological Society of America 71(1): 275-294.

Haines, A. J. (1983). "Magnitudes of New-Zealand Earthquakes - a Comparison of Magnitudes Calculated by Different Methods." Tectonophysics 93(3-4): 245-248.

Haines, A. J., Benites, R. A. and Jiashun, Y. (1994). 3-dimensional modelling of the effects of near-surface ground structure in central Christchurch, New Zealand, on the passage of seismic waves. Institute of Geological and Nuclear Sciences Report. Lower Hutt, New Zealand, Institute of Geological and Nuclear Sciences; for the Earthquake Commission: 31.

Haines, A. J., Jackson, J. A., Holt, W. E. and Agnew, D. C. (1998). Representing distributed deformation by continuous velocity fields. Institute of Geological and Nuclear Sciences Report 98/5. Wellington: 121.

Hancox, G. T., Perrin, N. D. and Dellow, G. D. (2002). "Recent Studies of Historical Earthquake-Induced Landsliding, Ground Damage, and MM Intensity in New Zealand." Bulletin of the New Zealand Society for Earthquake Engineering 35(2): 59-95.

Hanks, T. C. (1978). "Characterization of High-Frequency Strong Ground Motion." Tectonophysics 49(3-4): 263-263.

Hanks, T. C. (1978a). "High-Frequency Spectral Characteristics of Earthquakes and Representation of High-Frequency Strong Ground Motion." Transactions-American Geophysical Union 59(4): 325-325.

Hanks, T. C. (1979). "*b* Values and w-g Seismic Source Models: Implications for Tectonic Stress Variations along Active Crustal Fault Zones and the Estimation of High-frequency Strong Ground Motion." Journal of Geophysical Research 84: 2235-2242.

Hanks, T. C. and Kanamori, H. (1978). "Moment Magnitude Scale." Transactions-American Geophysical Union 59(12): 1128-1128.

Hanks, T. C. and Kanamori, H. (1979). "Moment Magnitude Scale." Journal of Geophysical Research 84(NB5): 2348-2350.

Hanks, T. C. and McGuire, R. K. (1981). "The Character of High-Frequency Strong Ground Motion." Bulletin of the Seismological Society of America 71(6): 2071-2095.

Harp, E. L. and Wilson, R. C. (1995). "Shaking Intensity Thresholds for Rock Falls and Slides: Evidence from 1987 Whittier Narrows and Superstition Hills Earthquake Strong-Motion Records." Bulletin of the Seismological Society of America 85(6): 1739-1757.

Harris, R. A. and Simpson, R. W. (1998). "Suppression of large earthquakes by stress shadows: a comparison of Coulomb and rate-and-state failure." Journal of Geophysical Research 103: 24,439-24,451.

Helmstetter, A., Kagan, Y. Y. and Jackson, D. D. (2005). "Importance of small earthquakes for stress transfers and earthquake triggering." Journal of Geophysical Research-Solid Earth 110(B5).

Helmstetter, A. and Sornette, D. (2003). "Bath's law derived from the Gutenberg-Richter law and from aftershock properties." Geophysical Research Letters 30(20).

Helmstetter, A., Sornette, D. and Grasso, J. R. (2003). "Mainshocks are aftershocks of conditional foreshocks: How do foreshock statistical properties emerge from aftershock laws." Journal of Geophysical Research-Solid Earth 108(B1).

Henderson, J. (1937). "The west Nelson earthquakes of 1929." New Zealand Journal of Science and Technology 19(2): 66-143.

Henry, C. and Das, S. (2001). "Aftershock zones of large shallow earthquakes: fault dimensions, aftershock area expansion and scaling relations." Geophysical Journal International 147(2): 272-293.

Hincapie, J. O., Doser, D. I. and Robinson, R. (2005). "Stress Changes Induced by Earthquakes and Secular Stress Accumulation in the Buller Region, South Island, New Zealand (1929-2002)." Pure and Applied Geophysics 162: 291-310.

Hodder, S. B. (1983). "Computer Processing of New Zealand Strong-Motion Accelerograms." Bulletin of the New Zealand National Society of Earthquake Engineering 16(3): 243-246.

Holt, W. E. and Haines, A. J. (1995). "The Kinematics of Northern South Island, New-Zealand, Determined from Geologic Strain Rates." Journal of Geophysical Research-Solid Earth 100(B9): 17991-18010.

Hudson, D. E., Brady, A. G. and Trifunac, M. D. (1969). Strong-Motion Earthquake Accelerograms, Digitized and Plotted Data, Vol. I, Earthquake Engineering Research Laboratory, EERL 69-20. Pasadena, U.S.A., California Institute of Technology.

Hudson, D. E., Trifunac, M. D. and Udwadia, F. E. (1972). Analyses of Strong Motion Earthquake Accelerograms: Volume IV - Fourier Amplitude Spectra, Part A - Accelerograms IIA001 Through IIA020, EERL 72-100. Earthquake Engineering Research Laboratory. Hudson, D. E. Pasadena, California, California Institute of Technology: 164.

Hwang, H., Lin, C. K., Yeh, Y. T., Cheng, S. N. and Chen, K. C. (2004). "Attenuation relations of Arias intensity based on the Chi-Chi Taiwan earthquake data." Soil Dynamics and Earthquake Engineering 24: 509-517.

Idriss, I. M. (1978). "Characteristics of Earthquake Ground Motions." Earthquake Engineering and Soil Dynamics; Proceedings of the ASCE Geotechnical Engineering Division Specialty Conference 3: 1151-1265.

Idriss, I. M. (1991). Selection of earthquake ground motions at rock sites, Report Prepared for the Structures Division, Building and Fire Research Laboratory, National Institute of Standards and Technology, Department of Civil Engineering, University of California, Davis.

Ishimoto, M. and Iida, K. (1939). "Observations sur les seisms enregistre par le microseismograph construite dernierment (I)." Bulletin of the Earthquake Research Insititute, University of Tokyo 17: 443-478.

Jaumé, S. C. and Sykes, L. R. (1999). "Evolving Towards a Critical Point: A Review of Accelerating Seismic Moment/Energy Release Prior to Large and Great Earthquakes." Pure and Applied Geophysics 155: 279-306.

Jennings, P. C. (2002). An Introduction to the Earthquake Response of Structures. International Handbook of Earthquake & Engineering Seismology. Lee, W. H. K., Kanamori, H., Jennings, P. C. and Kisslinger, C. London, Academic Press. 81B: 1097-1125.

Joyner, W. B. and Boore, D. M. (1981). "Peak Horizontal Acceleration and Velocity from Strong-Motion Records Including Records from the 1979 Imperial Valley, California, Earthquake." Bulletin of the Seismological Society of America 71(6): 2011-2038.

Joyner, W. B. and Boore, D. M. (1993). "Methods for Regression-Analysis of Strong-Motion Data." Bulletin of the Seismological Society of America 83(2): 469-487.

Joyner, W. B. and Boore, D. M. (1994). "Methods for Regression-Analysis of Strong-Motion Data, (Vol 83, Pg 469, 1993)." Bulletin of the Seismological Society of America 84(3): 955-956.

Kagan, Y. Y. (1996). "The Gutenberg-Richter or characteristic earthquake distribution, which is it? Comment." Bulletin of the Seismological Society of America 86(1): 274-285.

Kagan, Y. Y. (1999). "Universality of the seismic moment-frequency relation." Pure and Applied Geophysics 155(2-4): 537-573.

Kagan, Y. Y. (2002). "Aftershock zone scaling." Bulletin of the Seismological Society of America 92(2): 641-655.

Kanamori, H. and Anderson, D. L. (1975). "Theoretical Basis of Some Empirical Relations in Seismology." Bulletin of the Seismological Society of America 65(5): 1073-1095.

Katayama, T. (1982). "An engineering prediction model of acceleration response spectra and its application to seismic hazard mapping." Earthquake Engineering and Structural Design 10: 149-163.

Kayen, R. E. and Mitchell, J. K. (1997). "Assessment of Liquefaction Potential During Earthquakes by Arias Intensity." Journal of Geotechnical and Geoenvironmental Engineering 123(12): 1162-1174.

Keefer, D. K. and Wilson, R. C. (1989). Predicting earthquake-induced landslides, with emphasis on arid and semi-arid environments. Landslides in a Semi-Arid Environment. Sadler, P. M. and Morton, D. M., Inland Geological Society. 2: 118-149.

Kijko, A. (2004). "Estimation of the maximum earthquake magnitude, m(max)." Pure and Applied Geophysics 161(8): 1655-1681.

Kijko, A. and Graham, G. (1998). "Parametric-historic procedure for probabilistic seismic hazard analysis - Part I: Estimation of maximum regional magnitude m(max)." Pure and Applied Geophysics 152(3): 413-442.

King, G. C. P., Stein, R. S. and Lin, J. (1994). "Static Stress Changes and the Triggering of Earthquakes." Bulletin of the Seismological Society of America 84(3): 935-953.

Kisslinger, C. (1996). Aftershocks and fault-zone properties. Advances in Geophysics, Vol 38. San Diego, ACADEMIC PRESS INC. 38: 1-36.

Knopoff, L. (2000). "The magnitude distribution of declustered earthquakes in Southern California." Proceedings of the National Academy of Sciences of the United States of America 97(22): 11880-11884.

Knuepfer, P. L. K. (1988). "Estimating ages of late Quaternary stream terraces from analysis of weathering rinds and soils." Geological Society of America Bulletin 100: 1224-1236.

Knuepfer, P. L. K. (1992). "Temporal Variations in Latest Quaternary Slip across the Australian-Pacific Plate Boundary, Northeastern South Island, New-Zealand." Tectonics 11(3): 449-464.

Kramer, S. L. (1996). Geotechnical Earthquake Engineering. Upper Saddle River, New Jersey, Prentice-Hall.

Krinitzsky, E. L. (1993). "The Hazard in Using Probabilistic Seismic Hazard Analysis." Civil Engineering 63(11): 60-61.

Krinitzsky, E. L. (1995). "Problems with Logic Trees in Earthquake Hazard Evaluation." Engineering Geology 39(1-2): 1-3.

Krinitzsky, E. L. (1995a). "Deterministic versus probabilistic seismic hazard analysis for critical structures." Engineering Geology 40(1-2): 1-7.

Krinitzsky, E. L. (1998). "The hazard in using probabilistic seismic hazard analysis for engineering." Environmental & Engineering Geoscience 4(4): 425-443.

Krinitzsky, E. L. (2002). "How to obtain earthquake ground motions for engineering design." Engineering Geology 65(1): 1-16.

Krinitzsky, E. L. (2002a). "Epistematic and aleatory uncertainty: a new shtick for probabilistic seismic hazard analysis." Engineering Geology 66(1-2): 157-159.

Krinitzsky, E. L. (2002b). "How to obtain earthquake ground motions for engineering design." Engineering Geology 65(1): 1-16.

Krinitzsky, E. L. (2003). "How to combine deterministic and probabilistic methods for assessing earthquake hazards." Engineering Geology 70(1-2): 157-163.

Kulkarni, R. B., Youngs, R. R. and Coppersmith, K. J. (1984). Assessment of confidence intervals for results of seismic hazard analysis. 8th World Conference on Earthquake Engineering, San Francisco.

Lamarche, G. and Lebrun, J. F. (2000). "Transition from strike-slip faulting to oblique subduction: active tectonics at the Puysegur Margin, South New Zealand." Tectonophysics 316(1-2): 67-89.

Lay, T. and Wallace, T. C. (1995). Modern Global Seismology. San Diego, California, Academic Press.

Lee, C. T., Cheng, C. T., Liao, C. W. and Tsai, Y. B. (2001). "Site Classification of Taiwan Free-Field Strong-Motion Stations." Bulletin of the Seismological Society of America 91(5): 1283-1297.

Leitner, B., Eberhart-Phillips, D., Anderson, H. and Nabelek, J. L. (2001). "A focused look at the Alpine fault, New Zealand: Seismicity, focal mechanisms, and stress observations." Journal of Geophysical Research-Solid Earth 106(B2): 2193-2220.

Lensen, G. J. (1968). "Analysis of progressive fault displacement during downcutting at Branch River terraces, South Island, New Zealand." Geological Society of America Bulletin 79: 545-556.

Lensen, G. J. (1976). Late Quaternary tectonic map of New Zealand, Hillersden & Renwick Sheets. Wellington, Department of Scientific and Industrial Research.

Lensen, G. J. and Otway, P. M. (1971). "Earthshift and Post-earthshift Deformation Associated with the May 1968 Inangahua Earthquake New Zealand." Recent Crustal Movements, Bulletin of the Royal Society of New Zealand 9: 107-116.

Lensen, G. J. and Suggate, R. P. (1968). Inangahua earthquake - prelimary account of the geology. Preliminary reports on the Inangahua earthquake. Adams, R. D., Eiby, G. A., Lowry, M. A., Lensen, G. J., Suggate, R. P. and Stephenson, W. R. Wellington, New Zealand Department of Scientific and Industrial Research Bulletin. 193**:** 17-36.

Lewis, K. B. (1980). Quaternary sedimentation on the Hikurangi oblique-subduction and transform margin, New Zealand. Sedimentation in oblique-slip mobile zones. Ballance, P. F. and Reading, H. G., International Association of Sedimentologists Special Publication**:** 171-189.

Lewis, K. B. and Pettinga, J. R. (1994). The emerging imbricate frontal wedge of the Hikurangi Margin. South Sedimentary Basins (Chapter 13), Sedimentay Basins of the World 2. Ballance, P. F. Amsterdam, Elsevier**:** 225-250.

Li, X. S., Wang, Z. L. and Shen, C. K. (1992). SUMDES - A Nonlinear Procedure for the Response Analysis of Horizontally-layered Sites Subjected to Multi-directional Earthquake Loading. Davis, California, Department of Civil Engineering, University of California, Davis.

Lindstrom, M. J. and Bates, D. M. (1988). "Newton-Raphson and EM Algorithms for Linear Mixed-Effects Models for Repeated-Measures Data." Journal of the American Statistical Association 83(404): 1014-1022.

Lindstrom, M. J. and Bates, D. M. (1990). "Nonlinear Mixed Effects Models for Repeated Measures Data." Biometrics 46: 673-687.

Liu, Z. and Bird, P. (2002). "Finite element modeling of neotectonics in New Zealand." Journal of Geophysical Research-Solid Earth 107(B12).

Lomnitz, C. (1989). "Comment on "Temporal and Magnitude Dependence in Earthquake Recurrence Models" by C. A. Cornell and S. R. Winterstein." Bulletin of the Seismological Society of America 79(5): 1662-1662.

Margaris, B. N. and Boore, D. M. (1998). "Determination of Delta sigma and kappa(0) from response spectra of large earthquakes in Greece." Bulletin of the Seismological Society of America 88(1): 170-182.

Marzocchi, W. and Sandri, L. (2003). "A review and new insights on the estimation of the *b*-value and its uncertainty." Annals of Geophysics 46(6): 1271-1282.

Matthews, M. V., Ellsworth, W. L. and Reasenberg, P. A. (2002). "A Brownian model for recurrent earthquakes." Bulletin of the Seismological Society of America 92(6): 2233-2250.

Matuschka, T. (1980). Assessment of Seismic Hazards in New Zealand; Report No. 222. Auckland, Department of Civil Engineering; School of Engineering; University of Auckland**:** 249.

Matuschka, T., Berryman, K. R., O'Leary, A. J., McVerry, G. H., Mulholland, W. M. and Skinner, R. I. (1985). "New Zealand Seismic Hazard Analysis." Bulletin of the New Zealand National Society of Earthquake Engineering 18: 313-322.

Matuschka, T. and Davis, B. K. (1991). Derivation of an Attenuation Model in Terms of Spectral Acceleration for New Zealand. Pacific Conference on Earthquake Engineering, Auckland, New Zealand.

McCalpin, J. P. (1996). Paleoseismology. San Diego, Academic Press.

McGinty, P. (2001). "Preparation of the New Zealand Earthquake Catalogue for a Probabilistic Seismic Hazard Analysis." Bulletin of the New Zealand Society for Earthquake Engineering 34(1): 60-67.

McGuire, R. K. (1995). "Probabilistic Seismic Hazard Analysis and Design Earthquakes: Closing the Loop." Bulletin of the Seismological Society of America 85(5): 1275-1284.

McGuire, R. K. (2004). Seismic Hazard and Risk Analysis. Oakland, California, Earthquake Engineering Research Institute.

McGuire, R. K., Cornell, C. A. and Toro, G. R. (2005). "The case for using mean seismic hazard." Earthquake Spectra 21(3): 879-886.

McGuire, R. K. and Hanks, T. C. (1980). "RMS Accelerations and Spectral Amplitudes of Strong Ground Motion during the San Fernando, California, Earthquake." Bulletin of the Seismological Society of America 70: 1907-1919.

McVerry, G. H. (1986). "Uncertainties in Attenuation Relations for New Zealand Seismic Hazard Analysis." Bulletin of the New Zealand National Society of Earthquake Engineering 19(1): 28-39.

McVerry, G. H. (2002). Personal Communication. Stafford, P. J. Wellington: Electronic Mail.

McVerry, G. H., Dowrick, D. J., Sritharan, S., Cousins, W. J. and Porritt, T. E. (1993). Attenuation of Peak Ground Acceleration in New Zealand. International Workshop on Strong Motion Data, Menlo Park, U.S.A.

McVerry, G. H., Dowrick, D. J. and Zhao, J. X. (1995). Attenuation of peak ground accelerations in New Zealand. Pacific Conference on Earthquake Engineering, Melbourne, Australia.

McVerry, G. H., Zhao, J. X., Abrahamson, N. A. and Somerville, P. G. (2000). Crustal and Subduction Zone Attenuation Relations for New Zealand Earthquakes. 12th World Conference on Earthquake Engineering, Auckland, New Zealand.

Molas, G. L. and Yamazaki, F. (1995). "Attenuation of Earthquake Ground Motion in Japan Including Deep Focus Events." Bulletin of the Seismological Society of America 85(5): 1343-1358.

Molnar, P. and Chen, W.-P. (1982). Seismicity and Mountain Building. Mountain Building Processes. Hsu, K. London, Academic Press: 41-57.

Musson, R. M. W. (2004). Objective validation of seismic hazard source models. 13th World Conference on Earthquake Engineering, Vancouver, Canada.

Musson, R. M. W. (2004a). "Comment on "Communicating with uncertainty: A critical issue with probabilistic seismic hazard analysis." EOS 85(24): 235-236.

Musson, R. M. W. (2005). "Against fractiles." Earthquake Spectra 21(3): 887-891.

National Research Council (NRC) (1988). Probabilistic Seismic Hazard Analysis; Report of the Panel on Seismic Hazard Analysis, Committee on Seismology, Board on Earth Sciences. Washington, D.C., National Academy Press.

New Zealand Geomechanics Society (1988). Guidelines for the field description of soils and rocks in engineering use. Wellington, New Zealand Geomechanics Society: 42.

Nicol, A. and Nathan, S. (2001). "Folding and the formation of bedding-parallel faults on the western limb of Grey Valley Syncline near Blackball, New Zealand." New Zealand Journal of Geology and Geophysics 44: 127-135.

Nishenko, S. P. and Buland, R. (1987). "A Generic Recurrence Interval Distribution for Earthquake Forecasting." Bulletin of the Seismological Society of America 77(4): 1382-1399.

Norris, R. J. and Cooper, A. F. (2000). "Late Quaternary slip rates and slip partitioning on the Alpine Fault, New Zealand." Journal of Structural Geology 23: 507-520.

Nyffenegger, P. and Frohlich, C. (1998). "Recommendations for determining p values for aftershock sequences and catalogs." Bulletin of the Seismological Society of America 88(5): 1144-1154.

Ogata, Y. (1983). "Estimation of the Parameters in the Modified Omori Formula for Aftershock Frequencies by the Maximum-Likelihood Procedure." Journal of Physics of the Earth 31(2): 115-124.

Ogata, Y. (1989). "Statistical Models for Standard Seismicity and Detection of Anomalies by Residual Analysis." Tectonophysics 169: 157-174.

Ogata, Y. (1992). "Detection of Precursory Relative Quiescence before Great Earthquakes through a Statistical-Model." Journal of Geophysical Research-Solid Earth 97(B13): 19845-19871.

Ogata, Y., Utsu, T. and Katsura, K. (1995). "Statistical Features of Foreshocks in Comparison with Other Earthquake Clusters." Geophysical Journal International 121(1): 233-254.

Olafsson, S. (1999). Estimation of Earthquake-Induced Response. Department of Structural Engineering. Trondheim, Norway, Norwegian University of Science and Technology: 140.

Olafsson, S. and Sigbjornsson, R. (1999). "A Theoretical Attenuation Model for Earthquake-Induced Ground Motion." Journal of Earthquake Engineering 3(3): 287-315.

Omori, F. (1894). "On the Aftershocks of Earthquakes." Journal of the College of Science, Imperial University of Tokyo 7: 111-200.

Ordaz, M. (2004). "Some integrals useful in probabilistic seismic hazard analysis." Bulletin of the Seismological Society of America 94(4): 1510-1516.

Page, R. (1968). "Aftershocks and microaftershocks." Bulletin of the Seismological Society of America 58: 1131-1168.

Pancha, A. and Taber, J. J. (1997). Attenuation of Weak Ground Motions; A Report prepared for the New Zealand Earthquake Commission. Wellington, Victoria University of Wellington; School of Earth Sciences: 50.

Pearson, C. (1993). "Rate of co-seismic strain release in the northern South Island, New Zealand." New Zealand Journal of Geology and Geophysics 36(2): 161-166.

Peek, R. (1980). Estimation of Seismic Risk for New Zealand: A Seismicity Model and Preliminary Design Spectra. Christchurch, Department of Civil Engineering, University of Canterbury: 84.

Peláez, J., Delgado, J. and Casado, C. L. (2005). "A preliminary probabilistic seismic hazard assessment in terms of Arias intensity in southeastern Spain." Engineering Geology 77: 139-151.

Pettinga, J. R. (2004). Personal Communication. Stafford, P. J. Christchurch.

Pinheiro, J., Bates, D., DebRoy, S. and Sarkar, D. (2005). nlme: Linear and nonlinear mixed effects models. R package version 3.1-58.

Reasenberg, P. (1985). "2nd-Order Moment of Central California Seismicity, 1969-1982." Journal of Geophysical Research-Solid Earth and Planets 90(NB7): 5479-5495.

Reasenberg, P. A. and Jones, L. M. (1989). "Earthquake Hazard After a Mainshock in California." Science 243(4895): 1173-1176.

Reasenberg, P. A. and Jones, L. M. (1990). "California Aftershock Hazard Forecasts." Science 247(4940): 345-346.

Reid, H. F. (1910). The Mechanics of the Earthquake, The California Earthquake of April 18, 1906, Report of the State Investigation Commission. Washington, D.C., Carnegie Institution of Washington: 16-28.

Reilly, W. I. (1973). "A Conformal Mapping Projection with Minimum Scale Error." Survey Review XXII(168): 57-71.

Restrepo-Velez, L. and Bommer, J. J. (2003). "An Exploration of the Nature of the Scatter in Ground-Motion Prediction Equations and the Implications for Seismic Hazard Assessment." Journal of Earthquake Engineering 7(Special Issue 1): 171-199.

Reyners, M. and Robertson, E. D. (2004). "Intermediate depth earthquakes beneath Nelson, New Zealand, and the southwestern termination of the subducted Pacific plate." Geophysical Research Letters 31(4).

Reyners, M. and Webb, T. (2002). "Large Earthquakes near Doubtful Sound, New Zealand, 1989-1993." New Zealand Journal of Geology and Geophysics 45: 109-120.

Rhoades, D. A. (1996). "Estimation of the Gutenberg-Richter relation allowing for individual earthquake magnitude uncertainties." Tectonophysics 258(1-4): 71-83.

Rhoades, D. A. (1997). "Estimation of attenuation relations for strong-motion data allowing for individual earthquake magnitude uncertainties." Bulletin of the Seismological Society of America 87(6): 1674-1678.

Rhoades, D. A. and Evison, F. F. (2004). "Long-range earthquake forecasting with every earthquake a precursor according to scale." Pure and Applied Geophysics 161(1): 47-72.

Rhoades, D. A. and Van Dissen, R. J. (2003). "Estimates of the time-varying hazard of rupture of the Alpine Fault, New Zealand, allowing for uncertainties." New Zealand Journal of Geology and Geophysics 46(4): 479-488.

Robinson, R. (2004). "Potential earthquake triggering in a complex fault network: the northern South Island, New Zealand." Geophysical Journal International 159: 734-748.

Robinson, R., Arabasz, W. J. and Evison, F. F. (1975). "Long-Term Behavior of an Aftershock Sequence - Inangahua, New-Zealand, Earthquake of 1968." Geophysical Journal of the Royal Astronomical Society 41(1): 37-49.

Robinson, R., Webb, T., McGinty, P., Cousins, J. and Eberhart-Phillips, D. (2003). "The 2000 Thompson Sound Earthquake, New Zealand." New Zealand Journal of Geology and Geophysics 46: 331-341.

Rundle, J. B. (1989). "Derivation of the Complete Gutenberg-Richter Magnitude-Frequency Relation Using the Principle of Scale-Invariance." Journal of Geophysical Research-Solid Earth and Planets 94(B9): 12337-12342.

Sabetta, F. and Pugliese, A. (1996). "Estimation of Response Spectra and Simulation of Nonstationary Earthquake Ground Motions." Bulletin of the Seismological Society of America 86(2): 337-352.

Sadigh, K., Chang, C.-Y., Egan, J. A., Makdisi, F. and Youngs, R. R. (1997). "Attenuation Relationships for Shallow Crustal Earthquakes Based on California Strong Motion Data." Seismological Research Letters 68(1): 180-189.

Sammis, C. G. and Smith, S. W. (1999). "Seismic Cycles and the Evolution of Stress Correlation in Cellular Automaton Models of Finite Fault Networks." Pure and Applied Geophysics 155: 307-334.

Saul, G. (1994). "The basin development and deformation associated with the Kongahu (Lower Buller) fault zone over the last 12 Ma, Mokihinui River, West Coast, South Island, New Zealand." Journal of the Royal Society of New Zealand 24(3): 277-288.

Scherbaum, F., Bommer, J. J., Bungum, H., Cotton, F. and Abrahamson, N. A. (2005). "Composite ground-motion models and logic trees: Methodology, sensitivities, and uncertainties." Bulletin of the Seismological Society of America 95(5): 1575-1593.

Schnabel, P. B., Lysmer, J. and Seed, H. B. (1972). SHAKE, A Computer Program for Earthquake Response Analysis of Horizontally Layered Sites. Earthquake Engineering Research Center, Report No. EERC 72-12. Berkeley, California, College of Engineering, University of California, Berkeley.

Schnabel, P. B. and Seed, H. B. (1973). "Accelerations in rock for earthquakes in the western United States." Bulletin of the Seismological Society of America 63: 501-516.

Scholz, C. H. (2002). The mechanics of earthquakes and faulting. Cambridge, UK, Cambridge University Press.

Schwartz, D. P. and Coppersmith, K. J. (1984). "Fault Behavior and Characteristic Earthquakes - Examples from the Wasatch and San-Andreas Fault Zones." Journal of Geophysical Research 89(NB7): 5681-5698.

Searle, S. R. (1971). Linear Models. New York, John Wiley and Sons, Inc.

Shabestari, K. T. and Yamazaki, F. (2003). "Near-fault spatial variation in strong ground motion due to rupture directivity and hanging wall effects from the Chi-Chi, Taiwan earthquake." Earthquake Engineering & Structural Dynamics 32(14): 2197-2219.

Shcherbakov, R., Turcotte, D. L. and Rundle, J. B. (2004). "A generalized Omori's law for earthquake aftershock decay." Geophysical Research Letters 31(11).

Shi, Y. and Bolt, B. A. (1982). "The standard error of the magnitude-frequency *b* value." Bulletin of the Seismological Society of America 72(5): 1677-1687.

Shimazaki, K. and Nakata, T. (1980). "Time-predictable recurrence model for large earthquakes." Geophysical Research Letters 7: 279-282.

Sibson, R. H. (1995). Selective fault reactivation during basin inversion: potential for fluid redistribution through fault-valve action. Basin Inversion: Geological Society Special Publication No. 88. Buchanan, J. G. and Buchanan, P. G. London, The Geological Society: 3-19.

Sibson, R. H. and Xie, G. Y. (1998). "Dip range for intracontinental reverse fault ruptures: Truth not stranger than friction?" Bulletin of the Seismological Society of America 88(4): 1014-1022.

Smith, W. D. (1992). "Principal Earthquakes in New Zealand in 1991." Bulletin of the New Zealand National Society of Earthquake Engineering 25(1): 1.

Smith, W. D. (2002). "A Model for MM Intensities Near Large Earthquakes." Bulletin of the New Zealand Society for Earthquake Engineering 35(2): 2002.

Smith, W. D. and Berryman, K. R. (1983). "Revised estimates of earthquake hazard in New Zealand." Bulletin of the New Zealand National Society of Earthquake Engineering 16: 259-276.

Smith, W. D. and Berryman, K. R. (1986). "Earthquake hazard in New Zealand: inferences from seismology and geology." Bulletin of the Royal Society of New Zealand 24: 223-243.

Snoke, J. A. (1987). "Stable Determination of (Brune) Stress Drops." Bulletin of the Seismological Society of America 77(2): 530-538.

Sokolov, V. (2000). "Spectral parameters of ground motion in different regions: comparison of empirical models." Soil Dynamics and Earthquake Engineering 19(3): 173-181.

Sokolov, V., Loh, C. H. and Wen, K. L. (2000). "Empirical model for estimating Fourier amplitude spectra of ground acceleration in Taiwan region." Earthquake Engineering & Structural Dynamics 29(3): 339-357.

Sokolov, V., Loh, C. H. and Wen, K. L. (2002). "Evaluation of models for Fourier amplitude spectra for the Taiwan region." Soil Dynamics and Earthquake Engineering 22(8): 719-731.

Somerville, P., Irikura, K., Graves, R., Sawada, S., Wald, D., Abrahamson, N., Iwasaki, Y., Kagawa, T., Smith, N. and Kowada, A. (1999). "Characterizing Earthquake Slip Models for the Prediction of Strong Ground Motion." Seismological Research Letters 70(1): 59-80.

Somerville, P. G. (2000). New Developments in Seismic Hazard Estimation. Proceedings of the Sixth International Conference on Seismic Zonation, Palm Springs, California.

Somerville, P. G. (2003). "Magnitude scaling of the near fault rupture directivity pulse." Physics of the Earth and Planetary Interiors 137(1-4): 201-212.

Somerville, P. G. (2005). Engineering Characterization of Near Fault Ground Motions. Annual Conference of the New Zealand Society for Earthquake Engineering, Wairakei, New Zealand, NZSEE.

Somerville, P. G., Smith, N. F., Graves, R. W. and Abrahamson, N. A. (1997). "Modification of Empirical Strong Ground Motion Attenuation Relations to Include the Amplitude and Duration Effects of Rupture Directivity." Seismological Research Letters 68(1): 199-222.

Stafford, P. J. (2006). Engineering Seismological Studies, and Seismic Design Criteria for the Buller Region, South Island, New Zealand: A thesis submitted in partial fulfilment of the requirements for the degree of Doctor of Philosophy. Department of Civil Engineering. Christchurch, University of Canterbury.

Standards New Zealand (1992). NZS 4203:1992 loadings standard. General structural design and design loadings for buildings. Wellington, Standards New Zealand.

Stepp, J. C., Silva, W. J., McGuire, R. K. and Sewell, R. T. (1993). Determination of Earthquake Design Loads for High Level Nuclear Waste Repository Facility. 4th DOE Natural Phenomena Hazard Mitigation Conference, Atlanta, Georgia, Department of Energy.

Stirling, I. F. (1973). New Zealand Map Grid. Wellington, Department of Lands and Survey: 8.

Stirling, M., McVerry, G., Berryman, K., McGinty, P., Villamor, P., Van Dissen, R., Dowrick, D., Cousins, J. and Sutherland, R. (2000). Probabilistic Seismic Hazard Assessment of New Zealand: New Active Fault Data, Seismicity Data, Attenuation Relatioships and Methods. Institute of Geological and Nuclear Sciences; Client Report 2000/53. Wellington, Institute of Geological and Nuclear Sciences: 117.

Stirling, M. W. (2005). Personal Communication. Stafford, P. J. Christchurch.

Stirling, M. W., McVerry, G. H. and Berryman, K. R. (2002). "A new seismic hazard model for new Zealand." Bulletin of the Seismological Society of America 92(5): 1878-1903.

Stirling, M. W., Rhoades, D. A. and Berryman, K. (1998). Evaluation of Wells and Coppersmith (1994) Earthquake and Fault Relationships in the New Zealand Context. Lower Hutt, NZ, Institute of Geological and Nuclear Sciences: 17.

Stirling, M. W., Wesnousky, S. G. and Berryman, K. R. (1998). "Probabilistic seismic hazard analysis of New Zealand." New Zealand Journal of Geology and Geophysics 41(4): 355-375.

Stock, C. (2001). A Consistent Geological-Seismological Model for Earthquake Occurrence in New Zealand. Department of Geophysics. Wellington, Victoria University of Wellington: 202.

Study Group of the New Zealand National Society for Earthquake Engineering (1992). "A revision of the Modified Mercalli seismic intensity scale." Bulletin of the New Zealand National Society of Earthquake Engineering 25: 346-356.

Suggate, R. P. (1994). "The 1968-May-23 Inangahua, New-Zealand, Earthquake - an Integrated Geological, Geodetic, and Seismological Source Model - Comment." New Zealand Journal of Geology and Geophysics 37(4): 498-499.

Suggate, R. P. and Wood, P. R. (1979). Inangahua earthquake, 1968: damage to houses. NZGS Report, no. 85. Wellington, Department of Scientific and Industrial Research, New Zealand: 57.

Thatcher, W., Marshall, G. and Lisowski, M. (1997). "Resolution of fault slip along the 470-km-long rupture of the great 1906 San Francisco earthquake and its implications." Journal of Geophysical Research 102(B3): 5353-5367.

Tinti, S. and Mulargia, F. (1985). "Effects of Magnitude Uncertainties on Estimating the Parameters in the Gutenberg-Richter Frequency-Magnitude Law." Bulletin of the Seismological Society of America 75(6): 1681-1697.

Travasarou, T., Bray, J. D. and Abrahamson, N. A. (2003). "Empirical attenuation relationship for Arias Intensity." Earthquake Engineering & Structural Dynamics 32(7): 1133-1155.

Trifunac, M. D. (1994). "Fourier Amplitude Spectra of Strong-Motion Acceleration - Extension to High and Low-Frequencies." Earthquake Engineering & Structural Dynamics 23(4): 389-411.

Trifunac, M. D. and Todorovska, M. I. (2004). "Maximum distance and minimum energy to initiate liquefaction in water saturated sands." Soil Dynamics and Earthquake Engineering 24(2): 89-101.

Turcotte, D. L. (1997). Fractals and Chaos in Geology and Geophysics. Cambridge, UK, Cambridge University Press.

Turcotte, D. L. and Malamud, B. D. (2002). Earthquakes as a Complex System. International Handbook of Earthquake Engineering & Engineering Seismology. Lee, W. H. K., Kanamori, H., Jennings, P. C. and Kisslinger, C. London, Academic Press. 81A: 209-227.

Utsu, T. (1961). "A statistical study on the occurrence of aftershocks." The Geophysical Magazine 30: 521-605.

Utsu, T. (1965). "A method for determining the value of *b* in a formula log*n* = *a* - *bM* showing the magnitude-frequency relation for earthquakes (with English summary)." Geophysical Bulletin of Hokkaido University 13: 99-103.

Utsu, T. (1966). "A statistical significance test of the difference in *b*-value between two earthquake groups." Journal of the Physics of the Earth 14: 37-40.

Utsu, T. (1999). "Representation and analysis of the earthquake size distribution: A historical review and some new approaches." Pure and Applied Geophysics 155(2-4): 509-535.

von Seggern, D. H., Brune, J. N., Smith, K. D. and Aburto, A. (2003). "Linearity of the Earthquake Recurrence Curve to M < -1 from Little Skull Mountain Aftershocks in Southern Nevada." Bulletin of the Seismological Society of America 93(6): 2493-2501.

Walcott, R. I. (1978). "Present tectonics and Late Cenozoic evolution of New Zealand." Geophysical Journal of the Royal Astronomical Society 52: 137-164.

Webb, T. H. and Anderson, H. (1998). "Focal mechanisms of large earthquakes in the North Island of New Zealand: slip partitioning at an oblique active margin." Geophysical Journal International 134(1): 40-86.

Wegener, A. (1924). The origin of continents and oceans (translation of 'Die Entstehung der Kontinente und Ozeane' (1915)). London.

Weichert, D. H. (1980). "Estimation of the Earthquake Recurrence Parameters for Unequal Observation Periods for Different Magnitudes." Bulletin of the Seismological Society of America 70(4): 1337-1346.

Wells, A. and Yetton, M. D. (2004). Earthquake Tree-Ring Impacts in the Middle and Upper Buller River Catchment. Earthquake Commission Research Report No. 03/492. Christchurch, Geotech Consulting Ltd: 39.

Wells, D. L. and Coppersmith, K. J. (1994). "New Empirical Relationships among Magnitude, Rupture Length, Rupture Width, Rupture Area, and Surface Displacement." Bulletin of the Seismological Society of America 84(4): 974-1002.

Wesnousky, S. G. (1994). "The Gutenberg-Richter or Characteristic Earthquake Distribution, Which Is It." Bulletin of the Seismological Society of America 84(6): 1940-1959.

Wesnousky, S. G. (1996). "The Gutenberg-Richter or characteristic earthquake distribution, which is it? Reply." Bulletin of the Seismological Society of America 86(1): 286-291.

Wesnousky, S. G. (1999). "Crustal deformation processes and the stability of the Gutenberg-Richter relationship." Bulletin of the Seismological Society of America 89(4): 1131-1137.

Wesson, R. L., Bakun, W. H. and Perkins, D. M. (2003). "Association of earthquakes and faults in the San Francisco Bay area using Bayesian inference." Bulletin of the Seismological Society of America 93(3): 1306-1332.

WGCEP (2003). Earthquake Probabilities in the San Francisco Bay Region: 2002-2031, U.S. Geological Survey.

Wilson, R. C. (1993). Relation of Arias Intensity to magnitude and distance in California; Open File Report 93-556. Reston, Virginia, U.S. Geological Survey: 42.

Wilson, R. C. and Keefer, D. K. (1985). Predicting the areal limits of earthquake-induced landsliding. Evaluating Earthquake Hazards in the Los Angeles Region - An Earth-Science Perspective. Ziony, J. I. Washington D.C., U.S. Geological Survey Professional Paper 1360: 316-345.

Working Group for California Earthquake Probabilities (2003). Earthquake Probabilities in the San Francisco Bay Region: 2002-2031, U.S. Geological Survey.

Yeats, R. S. (2000). "The 1968 Inangahua, New Zealand, and 1994 Northridge, California, earthquakes: implications for northwest Nelson." New Zealand Journal of Geology and Geophysics 43(4): 587-599.

Yeats, R. S. and Berryman, K. R. (1987). "South Island, New Zealand, and Transverse Ranges, California: A Seismotectonic Comparison." Tectonics 6(3): 363-376.

Yeats, R. S., Sieh, K. and Allen, C. R. (1997). The Geology of Earthquakes. Oxford, Oxford University Press.

Yetton, M. D. (2000). The probability and consequences of the next alpine fault earthquake, South Island, New Zealand: a thesis submitted in partial fulfilment of the requirements for the degree of Doctor of Philosophy in Geology at the University of Canterbury. Department of Geological Sciences. Christchurch, University of Canterbury: 312.

Yetton, M. D. (2002). Paleoseismic Investigation Of The North And West Wairau Sections Of The Alpine Fault, South Island, New Zealand. Earthquake Commission Research Report No. 99/353. Christchurch, Geotech Consulting Ltd.: 96.

Yetton, M. D., Wells, A. and Traylen, N. J. (1998). The Probability and Consequences of the Next Alpine Fault Earthquake. Wellington, EQC Research Report 95/193: 160.

Youngs, R. R., Abrahamson, N., Makdisi, F. I. and Sadigh, K. (1995). "Magnitude-Dependent Variance of Peak Ground Acceleration." Bulletin of the Seismological Society of America 85(4): 1161-1176.

Youngs, R. R., Chiou, S.-J., Silva, W. J. and Humphrey, J. R. (1997). "Strong Ground Motion Attenuation Relationships for Subduction Zone Earthquakes." Seismological Research Letters 68(1): 58-73.

Zachariasen, J., Berryman, K. R., Prentice, C., Langridge, R., Stirling, M., Villamor, P. and Rymer, M. (2001). Size and timing of large prehistoric earthquakes on the Wairau Fault, South Island. Earthquake Commission Report No. 99/389; Institute of Geological and Nuclear Sciences client report 2001/13. Wellington: 41.

Zhao, J. X., Dowrick, D. J. and McVerry, G. H. (1997). "Attenuation of Peak Ground Accelerations in New Zealand Earthquakes." Bulletin of the New Zealand National Society of Earthquake Engineering 30(2): 133-158.

Zhuang, J., Ogata, Y. and Vere-Jones, D. (2002). "Stochastic declustering of space-time earthquake occurrences." Journal of the American Statistical Association 97(458): 369-380.

Zhuang, J. C., Ogata, Y. and Vere-Jones, D. (2004). "Analyzing earthquake clustering features by using stochastic reconstruction." Journal of Geophysical Research-Solid Earth 109(B5).

APPENDICES

Appendix A1: The Modified Mercalli Intensity Scale Adapted for use in New Zealand

The first of the following versions of the Modified Mercalli Intensity scale is that proposed by Eiby (1966) for application in the New Zealand context. In 1992 this New Zealand scale was modified to account primarily for the change in the nature of the New Zealand Building stock since the original proposition of Eiby. The updated version of the MMI scale is presented after that of Eiby as it is used for the isoseismal map of the Buller earthquake. The accompanying information for this update may be found in an article in the Bulletin of the New Zealand National Society for Earthquake Engineering (Study Group of the New Zealand National Society for Earthquake Engineering 1992).

Eiby (1966) MMI Scale

MM 1: Not felt by humans, except in especially favourable circumstances, but birds and animals may be disrupted. Reported mainly from the upper floors of buildings more than 10 storeys high. Dizziness or nausea may be experienced.
Branches of trees, chandeliers, doors, and other suspended systems of long natural period may be seen to move slowly.
Water in ponds, lakes, reservoirs, etc. may be set into seiche oscillation.

MM 2: Felt by a few persons at rest indoors, especially by those on upper floors or otherwise favourably placed.
The long period effects listed under MM 1 may be more noticeable.

MM 3: Felt indoors, but not identified as an earthquake by everyone. Vibration may be likened to the passing of light traffic.

It may be possible to estimate the duration, but not the direction. Hanging objects may swing slightly. Standing motorcars may rock slightly.

MM 4: Generally noticed indoors, but not outside. Very light sleepers may be wakened.

Vibration may be likened to the passing of heavy traffic, or to the jolt of a heavy object falling or striking the building. Walls and frame of buildings are heard to creak. Doors and windows rattle. Glassware and crockery rattle. Liquids in open vessels may be slightly disturbed.

Standing motorcars may rock, and the shock can be felt by their occupants.

MM 5: Generally felt outside, and by almost everyone indoors. Most sleepers awakened. A few people frightened.

Direction of motion can be estimated. Small unstable objects are displaced or upset. Some glassware and crockery may be broken. Some windows cracked. A few earthenware toilet fixtures cracked. Hanging pictures move. Doors and shutters may swing. Pendulum clocks stop, start, or change rate.

MM 6: Felt by all. People and animals alarmed. Many run outside. Difficulty experienced in walking steadily.

Slight damage to Masonry D. Some plaster cracks or falls. Isolated cases of chimney damage. Windows, glassware, and crockery broken. Objects fall from shelves, and pictures from walls. Heavy furniture moved. Unstable furniture overturned. Small church and school bells ring.

Trees and bushes shake, or are heard to rustle. Loose material may be dislodged from existing slips, talus slopes, or shingle slides.

MM 7: General alarm. Difficulty experienced in standing. Noticed by drivers of motorcars.

Trees and bushes strongly shaken. Large bells ring. Masonry D cracked and damaged. A few instances of damage to Masonry C. Loose brickwork and tiles dislodged. Unbraced parapets and architectural ornaments may fall. Stone walls cracked. Weak chimneys broken, usually at the roof-line. Domestic water tanks burst. Concrete irrigation ditches damaged.

Waves seen on ponds and lakes. Water made turbid by stirred-up mud. Small slips, and caving-in of sand and gravel banks.

MM 8: Alarm may approach panic.

Steering of motorcars affected.

Masonry C damaged, with partial collapse. Masonry B damaged in some cases. Masonry A undamaged.

Chimneys, factory stacks, monuments, towers, and elevated tanks twisted or brought down. Panel walls thrown out of frame structures. Some brick veneers damaged. Decayed wooden piles broken. Frame houses not secured to the foundation may move. Cracks appear on steep slopes and in wet ground. Landslips in roadside cuttings and unsupported excavations. Some tree

branches may be broken off. Changes in the flow or temperature of springs and wells may occur. Small earthquake fountains.

MM 9: General panic.

Masonry D destroyed. Masonry C heavily damaged, sometimes collapsing completely. Masonry B seriously damaged.

Frame structures racked and distorted. Damage to foundations general. Frame houses not secured to the foundations shift off. Brick veneers fall and expose frames. Cracking of the ground conspicuous. Minor damage to path and roadways. Sand and mud ejected in alleviated areas, with the formation of earthquake fountains and sand craters. Underground pipes broken. Serious damage to reservoirs.

MM 10: Most masonry structures destroyed, together with their foundations. Some well built wooden buildings and bridges seriously damaged. Dams, dykes, and embankments seriously damaged. Railway lines slightly bent. Cement and asphalt roads and pavements badly cracked or thrown into waves. Large landslides on river banks and steep coasts. Sand and mud on beaches and flat land moved horizontally. Large and spectacular sand and mud fountains. Water from rivers, lakes and canals thrown up on the banks.

MM 11: Wooden frame structures destroyed. Great damage to railway lines and underground pipes.

MM 12: Damage virtually total. Practically all works of construction destroyed or greatly damaged. Large rock masses displaced. Lines of sight and level distorted. Visible wave-motion of the ground surface reported. Objects thrown upwards into the air.

The references to various building types, such as Masonry A etc. refer to the descriptions given the following text.

Masonry A: Structure designed to resist lateral forces of about 0.1g, such as those satisfying the New Zealand Model Building Bylaw, 1955. Typical buildings of this kind are well reinforced by means of steel of ferro-concrete bands, or are wholly of ferro-concrete construction. All mortar is of good quality and the design and workmanship is good. Few buildings erected prior to 1935 can be regarded as in category A.

Masonry B: Reinforced buildings of good workmanship and with sound mortar, but not designed in detail to resist lateral forces.

Masonry C: Buildings of ordinary workmanship, with mortar of average quality. No extreme weakness, such as inadequate bonding of the corners, but neither designed nor reinforced to resist lateral forces.

Masonry D: Buildings with low standard of workmanship, poor mortar, or constructed of weak materials like mud brick and rammed earth. Weak horizontally.

Windows: Window breakage depends greatly upon the nature of the frame and its orientation with respect to the earthquake source. Windows cracked at MM5 are usually either large display windows, or windows tightly fitted to metal frames.

Water Tanks: The "domestic water tanks" listed under MM7 are of the cylindrical corrugated-iron type common in New Zealand rural areas. If these are only partly full, movement of the water may burst soldering and riveted seams.
Hot-water cylinders constrained only by supply and delivery pipes may move sufficiently to break the pipes at about the same intensity.

Study Group of the New Zealand National Society for Earthquake Engineering (1992)

MM 1:

People

Not felt except by a very few people under exceptionally favourable circumstances.

MM 2:

People

Felt by persons at rest, on upper floors or favourably placed.

MM 3:

People

Felt indoors; hanging objects may swing, vibration similar to passing of light trucks, duration may be estimated, may not be recognised as an earthquake.

MM 4:

People

Generally noticed indoors but not outside. Light sleepers may be awakened. Vibration may be likened to the passing of heavy traffic or to the jolt of a heavy object falling or striking the building.

Fittings

Doors and windows rattle. Glassware and crockery rattle. Liquids in open vessels may be slightly disturbed. Standing motorcars may rock.

Structures

Walls and frame of buildings, and partitions and suspended ceilings in commercial buildings, may be heard to creak.

MM 5:

People

Generally felt outside, and by almost everyone indoors. Most sleepers awakened. A few people alarmed. Direction of motion can be estimated.

Fittings

Small unstable objects are displaced of upset. Some glassware and crockery may be broken. Hanging pictures knock against the wall. Open doors may swing. Cupboard doors secured by magnetic catches may open. Pendulum clocks stop, start, or change rate (H★).

Structures

Some Windows Type I★ cracked. A few earthenware toilet fixtures cracked (H).

MM 6:

People

Felt by all. People and animals alarmed. Many run outside. Difficulty experienced in walking steadily.

Fittings

Objects fall from shelves. Pictures fall from walls (H★). Some furniture moved on smooth floors. Some unsecured free-standing fireplaces moved. Glassware and crockery broken. Unstable furniture overturned. Small church and school bells ring (H). Appliances move on bench or table tops. Filing cabinets or "easy glide" drawers may open (or shut).

Structures

Slight damage to Buildings Type I★. Some stucco or cement plaster falls. Suspended ceilings damaged. Windows Type I★ broken. A few cases of chimney damage.

Environment

Trees and bushes shake, or are heard to rustle. Loose material may be dislodged from sloping ground, e.g. existing slides, talus slopes, shingle slides.

MM 7:

People

General alarm. Difficulty experienced in standing. Noticed by motorcar drivers who may stop.

Fittings

Large bells ring. Furniture moves on smooth floors, may move on carpeted floors.

Structures

Unreinforced stone and brick walls cracked. Buildings Type I cracked and damaged. A few instances of damage to Buildings Type II. Unbraced parapets and architectural ornaments fall. Roofing tiles, especially ridge tiles may be dislodged. Many unreinforced domestic chimneys broken. Water tanks Type I★ burst. A few instances of damage to brick veneers and plaster or cement-based linings. Unrestrained water cylinders (Water Tanks Type II★) may move and leak. Some Windows Type II★ cracked.

Environment

Water made turbid by stirred up mud. Small slides such as falls of sand and gravel banks. Instances of differential settlement on poor or wet or unconsolidated ground. Some fine cracks appear in sloping ground. A few instances of liquefaction.

MM 8:

People

Alarm may approach panic. Steering of motorcars greatly affected.

Structures

Buildings Type II damaged, some seriously. Buildgins Type III damaged in some cases. Monuments and elevated tanks twisted or brought down. Some pre-1965 infill masonry panels damaged. A few post-1980 brick veneers damaged. Weak piles damaged. Houses not secured to foundation may move.

Environment

Cracks appear on steep slopes and in wet ground. Slides in roadside cuttings and unsupported excavations. Small earthquake fountains and other manifestations of liquefaction.

MM 9:

Structures

Very poor quality unreinforced masonry destroyed. Buildings Type II heavily damaged, some collapsing. Buildings Type III damaged, some seriously. Damage or permanent distortion to some buildings and bridges Type IV. Houses not secured to foundations shifted off. Brick veneers fall and expose frames.

Environment

Cracking of ground conspicuous. Landsliding general on steep slopes. Liquefaction effects intensified, with large earthquake fountains and craters.

MM 10:

Structures

Most unreinforced masonry structures destroyed. Many Buildings Type II destroyed. Many Buildings Type III (and bridges of equivalent design) seriously damaged. Many Buildings and Bridges Type IV have moderate damage or permanent distortion.

Buildings Type I: Weak materials such as mud brick and rammed earth; poor mortar; low standards of workmanship (Masonry D in other MM scales).

Buildings Type II: Average to good workmanship and materials, some including reinforcement, but not designed to resist earthquakes (Masonry B and C in other MM scales).

Buildings Type III: Buildings designed and built to resist earthquakes to normal use standards, i.e. no special damage limiting measures taken (mid-1930's to c. 1970 for concrete and to c. 1980 for other materials).

Buildings and Bridges Type IV: Since c. 1970 for concrete and c. 1980 for other materials, the loadings and materials codes have combined to ensure fewer collapses and less damage than in earlier structures.

This arises from features such as: (i) "capacity design" procedure, (ii) use of elements (such as improved bracing or structural walls) which reduce racking (i.e. drift), (iii) high ductility, (iv) higher strength.

Windows: Type I – Large display windows, especially shop windows. Type II – Ordinary sash or casement windows.

Water Tanks: Type I – External, stand mounted, corrugated iron water tanks. Type II – Domestic hot-water cylinders unrestrained except by supply and delivery pipes.

H – (Historical): Important for historical events. Current application only to older houses, etc.

General Comment: "Some" or "a few" indicates that the threshold of a particular effect has just been reached at that intensity.

Appendix B1: Strong Motion Dataset

Appendix B1.1: Foreign Strong Motion Records included for the regression analysis

Event	Name	Year	Month	Day	UT	M_W	R_{rup}	Site Class	Focal Mech.	PEER Ref. #
1	Imperial Valley	1940	5	19	0436	7.0	8.3	C	S	P0006
2	Parkfield	1966	6	28	0436	6.1	5.3	C	S	P0031
2	Parkfield	1966	6	28	0436	6.1	9.2	C	S	P0032
2	Parkfield	1966	6	28	0436	6.1	9.9	A	S	P0034
3	San Fernando	1971	2	28	1400	6.6	2.8	B	R	P0082
4	Hollister	1974	11	28	2301	5.2	12.2*	C	S	P0099
4	Hollister	1974	11	28	2301	5.2	12.2*	A	S	P0100
4	Hollister	1974	11	28	2301	5.2	10.6*	A	S	P0101
5	Oroville	1975	8	1	2020	6.0	9.4*	B	N	P0107
6	Gazli	1976	5	17	0258	6.8	3.0^	B	R	P0127
7	Santa Barbara	1978	8	13	1322	6.0	10.0^	A	R	P0136
8	Tabas	1978	9	16	1535	7.4	3.0^	B	R	P0144
9	Coyote Lake	1979	8	6	1705	5.7	9.3	A	S	P0146
9	Coyote Lake	1979	8	6	1705	5.7	3.2	B	S	P0147
9	Coyote Lake	1979	8	6	1705	5.7	7.5	C	S	P0148
9	Coyote Lake	1979	8	6	1705	5.7	6.0	C	S	P0149
9	Coyote Lake	1979	8	6	1705	5.7	4.5	C	S	P0150
9	Coyote Lake	1979	8	6	1705	5.7	3.1	A	S	P0151
10	Imperial Valley	1979	10	15	2316	6.5	8.5	C	S	P0159
10	Imperial Valley	1979	10	15	2316	6.5	12.9	B	S	P0160
10	Imperial Valley	1979	10	15	2316	6.5	7.6	C	S	P0171
10	Imperial Valley	1979	10	15	2316	6.5	0.5	C	S	P0172
10	Imperial Valley	1979	10	15	2316	6.5	4.2	C	S	P0176
10	Imperial Valley	1979	10	15	2316	6.5	1.0	C	S	P0177
10	Imperial Valley	1979	10	15	2316	6.5	1.0	C	S	P0178
10	Imperial Valley	1979	10	15	2316	6.5	5.3	C	S	P0185
10	Imperial Valley	1979	10	15	2316	6.5	11.1	C	S	P0190
10	Imperial Valley	1979	10	15	2316	6.5	2.5	C	S	P0161
10	Imperial Valley	1979	10	15	2316	6.5	8.5	C	S	P0162
10	Imperial Valley	1979	10	15	2316	6.5	10.6	C	S	P0163
10	Imperial Valley	1979	10	15	2316	6.5	9.3	C	S	P0175
10	Imperial Valley	1979	10	15	2316	6.5	0.6	C	S	P0179
10	Imperial Valley	1979	10	15	2316	6.5	3.8	C	S	P0180
10	Imperial Valley	1979	10	15	2316	6.5	8.6	C	S	P0181
10	Imperial Valley	1979	10	15	2316	6.5	12.6	C	S	P0182
10	Imperial Valley	1979	10	15	2316	6.5	7.5	C	S	P0186
10	Imperial Valley	1979	10	15	2316	6.5	14.2	A	S	P0188
10	Imperial Valley	1979	10	15	2316	6.5	15.1	C	S	P0193
11	Loma Prieta	1989	10	18	0004	6.9	11.2	A	S	P0733
11	Loma Prieta	1989	10	18	0004	6.9	12.7	C	S	P0735
11	Loma Prieta	1989	10	18	0004	6.9	14.4	C	S	P0736
11	Loma Prieta	1989	10	18	0004	6.9	14.5	C	S	P0744
11	Loma Prieta	1989	10	18	0004	6.9	5.1	A	S	P0745
11	Loma Prieta	1989	10	18	0004	6.9	17.9	B	S	P0749
11	Loma Prieta	1989	10	18	0004	6.9	11.6	A	S	P0764
11	Loma Prieta	1989	10	18	0004	6.9	13.0	A	S	P0779
11	Loma Prieta	1989	10	18	0004	6.9	13.7	A	S	P0780
12	Erzincan	1992	3	13	1718	6.9	2.0	C	S	P0802
13	Landers	1992	6	28	1157	7.3	11.6	A	S	P0816

Appendix B1.1: continued…

Event	Name	Year	Month	Day	UT	M_W	R_{rup}	Site Class	Focal Mech.	PEER Ref. #
13	Landers	1992	6	28	1157	7.3	19.3	A	S	P0817
13	Landers	1992	6	28	1157	7.3	1.1	A	S	P0873
14	Northridge	1994	1	17	1230	6.7	25.7	A	R	P0905
14	Northridge	1994	1	17	1230	6.7	9.2	A	R	P0887
14	Northridge	1994	1	17	1230	6.7	28.0	B	R	P0925
14	Northridge	1994	1	17	1230	6.7	7.1	C	R	P0927
14	Northridge	1994	1	17	1230	6.7	8.2	A	R	P0928
14	Northridge	1994	1	17	1230	6.7	6.4	C	R	P0934
14	Northridge	1994	1	17	1230	6.7	17.5	B	R	P0935
14	Northridge	1994	1	17	1230	6.7	8.0	B	R	P0995
15	Kobe	1995	1	16	2046	6.9	0.6	A	S	P1043
15	Kobe	1995	1	16	2046	6.9	11.1	C	S	P1046
15	Kobe	1995	1	16	2046	6.9	8.5	C	S	P1048
15	Kobe	1995	1	16	2046	6.9	15.5	C	S	P1054
15	Kobe	1995	1	16	2046	6.9	1.2	C	S	P1056
15	Kobe	1995	1	16	2046	6.9	0.3	C	S	P1057
16	Duzce	1999	11	12	1657	7.1	11.4	B	S	P1552
16	Duzce	1999	11	12	1657	7.1	0.9	A	S	P1553
16	Duzce	1999	11	12	1657	7.1	15.6	A	S	P1556
16	Duzce	1999	11	12	1657	7.1	13.3	B	S	P1557
16	Duzce	1999	11	12	1657	7.1	8.2	C	S	P1540
16	Duzce	1999	11	12	1657	7.1	17.6	C	S	P1547
17	Izmit-Kocaeli	1999	8	17	0001	7.4	12.7	C	S	P1096
17	Izmit-Kocaeli	1999	8	17	0001	7.4	4.8	A	S	P1103
17	Izmit-Kocaeli	1999	8	17	0001	7.4	2.6	C	S	P1114
18	Chi-Chi	1999	9	20	1747	7.6	9.1	C	R	P1131
18	Chi-Chi	1999	9	20	1747	7.6	7.3	C	R	P1135
18	Chi-Chi	1999	9	20	1747	7.6	7.0	A	R	P1169
18	Chi-Chi	1999	9	20	1747	7.6	9.7	A	R	P1341
18	Chi-Chi	1999	9	20	1747	7.6	5.7	C	R	P1400
18	Chi-Chi	1999	9	20	1747	7.6	4.5	C	R	P1427
18	Chi-Chi	1999	9	20	1747	7.6	8.3	C	R	P1429
18	Chi-Chi	1999	9	20	1747	7.6	0.2	C	R	P1430
18	Chi-Chi	1999	9	20	1747	7.6	6.7	C	R	P1431
18	Chi-Chi	1999	9	20	1747	7.6	5.9	C	R	P1432
18	Chi-Chi	1999	9	20	1747	7.6	6.9	C	R	P1433
18	Chi-Chi	1999	9	20	1747	7.6	9.5	C	R	P1437
18	Chi-Chi	1999	9	20	1747	7.6	1.0	C	R	P1441
18	Chi-Chi	1999	9	20	1747	7.6	0.3	C	R	P1442
18	Chi-Chi	1999	9	20	1747	7.6	1.1	C	R	P1443
18	Chi-Chi	1999	9	20	1747	7.6	4.9	C	R	P1445
18	Chi-Chi	1999	9	20	1747	7.6	7.4	C	R	P1446
18	Chi-Chi	1999	9	20	1747	7.6	7.5	C	R	P1450
18	Chi-Chi	1999	9	20	1747	7.6	10.0	C	R	P1451
18	Chi-Chi	1999	9	20	1747	7.6	10.4	C	R	P1455
18	Chi-Chi	1999	9	20	1747	7.6	3.2	A	R	P1457
18	Chi-Chi	1999	9	20	1747	7.6	8.2	A	R	P1458
18	Chi-Chi	1999	9	20	1747	7.6	4.0	C	R	P1467

Appendix B1.1: continued…

Event	Name	Year	Month	Day	UT	M_W	R_{rup}	Site Class	Focal Mech.	PEER Ref. #
18	Chi-Chi	1999	9	20	1747	7.6	8.1	A	R	P1481
18	Chi-Chi	1999	9	20	1747	7.6	9.7	A	R	P1484
18	Chi-Chi	1999	9	20	1747	7.6	1.2	C	R	P1532
18	Chi-Chi	1999	9	20	1747	7.6	13.7	C	R	P1447
18	Chi-Chi	1999	9	20	1747	7.6	1.5	C	R	P1448
18	Chi-Chi	1999	9	20	1747	7.6	2.0	C	R	P1449
18	Chi-Chi	1999	9	20	1747	7.6	5.7	C	R	P1453
18	Chi-Chi	1999	9	20	1747	7.6	2.9	C	R	P1465
18	Chi-Chi	1999	9	20	1747	7.6	1.8	C	R	P1466
18	Chi-Chi	1999	9	20	1747	7.6	1.2	C	R	P1485

⋆ - Actual R_{rup} not given; R_{rup} estimated from R_{jb}

^ - Actual R_{rup} not given; R_{rup} estimated from R_{hyp}

Appendix B1.2: New Zealand Strong Motion Records used in the regression analysis

Ev. #	Event Name	Year	Month	Day	UT	Depth	M_W	R_{rup}	Focal Mech.	Site Class
1	Palliser Bay	1968	11	1	0132	33	5.4	42.8	R	A
1	Palliser Bay	1968	11	1	0132	33	5.4	42.7	R	B
1	Palliser Bay	1968	11	1	0132	33	5.4	50.7	R	A
2	Reefton	1971	8	13	1442	12	5.8	72.7	R	C
2	Reefton	1971	8	13	1442	12	5.8	19.6	R	B
2	Reefton	1971	8	13	1442	12	5.8	122.4	R	C
4	Unnamed	1973	2	21	1442	12	5.4	23.8	N	C
6	Opunaki	1974	11	5	1038	17	5.44	73.3	N	A
7	Milford Sound	1974	9	20	1948	12	5.5	99.0	R	C
7	Milford Sound	1974	9	20	1948	12	5.5	29.0	R	A
7	Milford Sound	1974	9	20	1948	12	5.5	113.1	R	C
7	Milford Sound	1974	9	20	1948	12	5.5	96.0	R	C
7	Milford Sound	1974	9	20	1948	12	5.5	113.1	R	C
7	Milford Sound	1974	9	20	1948	12	5.5	96.0	R	C
8	Dannevirke	1975	6	10	1011	38	5.62	59.7	S	A
8	Dannevirke	1975	6	10	1011	38	5.62	37.3	S	C
8	Dannevirke	1975	6	10	1011	38	5.62	37.7	S	C
8	Dannevirke	1975	6	10	1011	38	5.62	37.7	S	C
10	Cape Campbell	1977	1	18	0541	34	6.02	62.1	N	C
10	Cape Campbell	1977	1	18	0541	34	6.02	68.2	N	C
10	Cape Campbell	1977	1	18	0541	34	6.02	68.9	N	C
10	Cape Campbell	1977	1	18	0541	34	6.02	72.3	N	A
10	Cape Campbell	1977	1	18	0541	34	6.02	60.3	N	C
10	Cape Campbell	1977	1	18	0541	34	6.02	59.6	N	C
10	Cape Campbell	1977	1	18	0541	34	6.02	59.6	N	C
10	Cape Campbell	1977	1	18	0541	34	6.02	59.6	N	C
10	Cape Campbell	1977	1	18	0541	34	6.02	59.8	N	A
10	Cape Campbell	1977	1	18	0541	34	6.02	59.8	N	A
10	Cape Campbell	1977	1	18	0541	34	6.02	59.8	N	A
10	Cape Campbell	1977	1	18	0541	34	6.02	59.8	N	A
10	Cape Campbell	1977	1	18	0541	34	6.02	60.2	N	C
10	Cape Campbell	1977	1	18	0541	34	6.02	60.2	N	A
10	Cape Campbell	1977	1	18	0541	34	6.02	60.2	N	A
10	Cape Campbell	1977	1	18	0541	34	6.02	60.2	N	A
10	Cape Campbell	1977	1	18	0541	34	6.02	60.3	N	C
10	Cape Campbell	1977	1	18	0541	34	6.02	60.3	N	C
10	Cape Campbell	1977	1	18	0541	34	6.02	60.3	N	C
10	Cape Campbell	1977	1	18	0541	34	6.02	60.3	N	C
10	Cape Campbell	1977	1	18	0541	34	6.02	60.3	N	B
10	Cape Campbell	1977	1	18	0541	34	6.02	59.2	N	B
10	Cape Campbell	1977	1	18	0541	34	6.02	55.9	N	B
10	Cape Campbell	1977	1	18	0541	34	6.02	59.2	N	A
10	Cape Campbell	1977	1	18	0541	34	6.02	58.5	N	B
10	Cape Campbell	1977	1	18	0541	34	6.02	58.6	N	C
10	Cape Campbell	1977	1	18	0541	34	6.02	68.9	N	A
10	Cape Campbell	1977	1	18	0541	34	6.02	68.7	N	B
10	Cape Campbell	1977	1	18	0541	34	6.02	59.8	N	A
10	Cape Campbell	1977	1	18	0541	34	6.02	59.8	N	A
10	Cape Campbell	1977	1	18	0541	34	6.02	60.2	N	C
13	Unnamed	1982	2	5	1751	34	5.36	40.3	S	C
13	Unnamed	1982	2	5	1751	34	5.36	40.3	S	C
13	Unnamed	1982	2	5	1751	34	5.36	40.3	S	C
13	Unnamed	1982	2	5	1751	34	5.36	40.3	S	C
13	Unnamed	1982	2	5	1751	34	5.36	43.1	S	C
15	Oaonui 2	1983	4	16	2129	12	5.3	18.3	N	C
16	Godley River	1984	6	24	1329	13	6.14	96.5	S	C

Appendix B1.2: continued

Ev. #	Event Name	Year	Month	Day	UT	Depth	M_W	R_{rup}	Focal Mech.	Site Class
16	Godley River	1984	6	24	1329	13	6.14	108.3	S	B
17	Unnamed	1984	3	5	0207	9	5.27	7.5	N	A
20	Tiniroto	1985	7	19	1433	31	5.92	51.2	N	C
20	Tiniroto	1985	7	19	1433	31	5.92	51.2	N	C
20	Tiniroto	1985	7	19	1433	31	5.92	27.8	N	C
23	Edgecumbe	1987	3	2	0135	6	6.53	19.3	N	A
23	Edgecumbe	1987	3	2	0135	6	6.53	19.3	N	A
23	Edgecumbe	1987	3	2	0135	6	6.53	19.3	N	A
23	Edgecumbe	1987	3	2	0135	6	6.53	19.3	N	A
23	Edgecumbe	1987	3	2	0135	6	6.53	19.3	N	A
23	Edgecumbe	1987	3	2	0135	6	6.53	19.3	N	A
23	Edgecumbe	1987	3	2	0135	6	6.53	133.3	N	C
23	Edgecumbe	1987	3	2	0135	6	6.53	57.3	N	A
24	Edgecumbe Aftershock	1987	3	2	0150	11	5.6	22.7	N	A
24	Edgecumbe Aftershock	1987	3	2	0150	11	5.6	22.7	N	A
24	Edgecumbe Aftershock	1987	3	2	0150	11	5.6	22.7	N	A
24	Edgecumbe Aftershock	1987	3	2	0150	11	5.6	73.0	N	A
30	Edgecumbe Aftershock	1987	3	2	0207	5	5	13.7	N	A
43	Doubtful Sound	1989	5	31	0554	24	6.33	138.2	S	B
43	Doubtful Sound	1989	5	31	0554	24	6.33	61.7	S	C
44	Weber 1	1990	2	19	0534	27	6.23	45.2	N	A
44	Weber 1	1990	2	19	0534	27	6.23	27.2	N	B
44	Weber 1	1990	2	19	0534	27	6.23	125.0	N	A
44	Weber 1	1990	2	19	0534	27	6.23	125.5	N	C
44	Weber 1	1990	2	19	0534	27	6.23	119.1	N	B
44	Weber 1	1990	2	19	0534	27	6.23	77.9	N	A
44	Weber 1	1990	2	19	0534	27	6.23	84.7	N	B
44	Weber 1	1990	2	19	0534	27	6.23	38.5	N	C
44	Weber 1	1990	2	19	0534	27	6.23	59.5	N	C
44	Weber 1	1990	2	19	0534	27	6.23	59.1	N	C
44	Weber 1	1990	2	19	0534	27	6.23	59.1	N	C
44	Weber 1	1990	2	19	0534	27	6.23	59.1	N	C
44	Weber 1	1990	2	19	0534	27	6.23	59.1	N	C
44	Weber 1	1990	2	19	0534	27	6.23	84.1	N	C
44	Weber 1	1990	2	19	0534	27	6.23	82.9	N	C
44	Weber 1	1990	2	19	0534	27	6.23	118.7	N	B
44	Weber 1	1990	2	19	0534	27	6.23	150.2	N	A
44	Weber 1	1990	2	19	0534	27	6.23	150.4	N	B
44	Weber 1	1990	2	19	0534	27	6.23	163.5	N	C
44	Weber 1	1990	2	19	0534	27	6.23	163.7	N	A
44	Weber 1	1990	2	19	0534	27	6.23	149.7	N	C
45	Weber 2	1990	5	13	0423	13	6.37	38.2	R	A
45	Weber 2	1990	5	13	0423	13	6.37	17.3	R	B
45	Weber 2	1990	5	13	0423	13	6.37	85.6	R	C
45	Weber 2	1990	5	13	0423	13	6.37	115.4	R	A
45	Weber 2	1990	5	13	0423	13	6.37	115.9	R	C
45	Weber 2	1990	5	13	0423	13	6.37	108.9	R	B
45	Weber 2	1990	5	13	0423	13	6.37	77.7	R	B
45	Weber 2	1990	5	13	0423	13	6.37	31.9	R	C
45	Weber 2	1990	5	13	0423	13	6.37	53.5	R	C
45	Weber 2	1990	5	13	0423	13	6.37	53.7	R	C
45	Weber 2	1990	5	13	0423	13	6.37	53.7	R	C
45	Weber 2	1990	5	13	0423	13	6.37	53.7	R	C
45	Weber 2	1990	5	13	0423	13	6.37	53.7	R	C
45	Weber 2	1990	5	13	0423	13	6.37	77.7	R	C
45	Weber 2	1990	5	13	0423	13	6.37	85.6	R	C

Appendix B1.2: continued

Ev. #	Event Name	Year	Month	Day	UT	Depth	M_W	R_{rup}	Focal Mech.	Site Class
45	Weber 2	1990	5	13	0423	13	6.37	110.0	R	B
45	Weber 2	1990	5	13	0423	13	6.37	150.9	R	A
45	Weber 2	1990	5	13	0423	13	6.37	151.1	R	B
45	Weber 2	1990	5	13	0423	13	6.37	164.3	R	A
45	Weber 2	1990	5	13	0423	13	6.37	164.1	R	C
45	Weber 2	1990	5	13	0423	13	6.37	17.3	R	B
45	Weber 2	1990	5	13	0423	13	6.37	125.8	R	A
46	Lake Tennyson	1990	2	10	0327	8	5.93	37.8	S	B
46	Lake Tennyson	1990	2	10	0327	8	5.93	55.4	S	C
46	Lake Tennyson	1990	2	10	0327	8	5.93	204.0	S	C
48	Hawk's Crag 1	1991	1	28	1258	10	5.79	12.6	R	C
48	Hawk's Crag 1	1991	1	28	1258	10	5.79	32.8	R	B
48	Hawk's Crag 1	1991	1	28	1258	10	5.79	6.7	R	A
48	Hawk's Crag 1	1991	1	28	1258	10	5.79	28.7	R	A
48	Hawk's Crag 1	1991	1	28	1258	10	5.79	58.5	R	C
48	Hawk's Crag 1	1991	1	28	1258	10	5.79	122.8	R	C
48	Hawk's Crag 1	1991	1	28	1258	10	5.79	272.0	R	C
49	Hawk's Crag 2	1991	1	28	1800	11	5.93	15.4	R	C
49	Hawk's Crag 2	1991	1	28	1800	11	5.93	27.5	R	B
49	Hawk's Crag 2	1991	1	28	1800	11	5.93	104.7	R	C
49	Hawk's Crag 2	1991	1	28	1800	11	5.93	6.0	R	A
49	Hawk's Crag 2	1991	1	28	1800	11	5.93	21.1	R	A
49	Hawk's Crag 2	1991	1	28	1800	11	5.93	62.2	R	B
49	Hawk's Crag 2	1991	1	28	1800	11	5.93	147.9	R	A
49	Hawk's Crag 2	1991	1	28	1800	11	5.93	50.8	R	C
49	Hawk's Crag 2	1991	1	28	1800	11	5.93	115.8	R	C
49	Hawk's Crag 2	1991	1	28	1800	11	5.93	264.5	R	C
50	Hawk's Crag 3	1991	2	15	1048	9	5.42	29.9	R	C
50	Hawk's Crag 3	1991	2	15	1048	9	5.42	22.4	R	B
50	Hawk's Crag 3	1991	2	15	1048	9	5.42	22.1	R	A
50	Hawk's Crag 3	1991	2	15	1048	9	5.42	34.8	R	A
50	Hawk's Crag 3	1991	2	15	1048	9	5.42	114.0	R	C
51	Unnamed	1991	2	24	0950	12	5.1	24.0	R	B
54	Cape Palliser 1	1990	10	4	2348	15	5.57	68.7	R	C
54	Cape Palliser 1	1990	10	4	2348	15	5.57	70.5	R	C
54	Cape Palliser 1	1990	10	4	2348	15	5.57	79.3	R	C
54	Cape Palliser 1	1990	10	4	2348	15	5.57	67.8	R	A
54	Cape Palliser 1	1990	10	4	2348	15	5.57	67.9	R	B
54	Cape Palliser 1	1990	10	4	2348	15	5.57	67.9	R	B
54	Cape Palliser 1	1990	10	4	2348	15	5.57	80.6	R	B
54	Cape Palliser 1	1990	10	4	2348	15	5.57	72.4	R	C
54	Cape Palliser 1	1990	10	4	2348	15	5.57	73.7	R	A
54	Cape Palliser 1	1990	10	4	2348	15	5.57	70.5	R	C
54	Cape Palliser 1	1990	10	4	2348	15	5.57	72.4	R	C
54	Cape Palliser 1	1990	10	4	2348	15	5.57	73.6	R	A
56	Bay of Plenty	1992	6	21	1743	4	6.25	38.8	N	C
56	Bay of Plenty	1992	6	21	1743	4	6.25	50.9	N	C
56	Bay of Plenty	1992	6	21	1743	4	6.25	154.0	N	A
56	Bay of Plenty	1992	6	21	1743	4	6.25	152.6	N	C
56	Bay of Plenty	1992	6	21	1743	4	6.25	98.5	N	C
56	Bay of Plenty	1992	6	21	1743	4	6.25	55.5	N	C
57	Ormond	1993	8	10	0946	39	6.19	17.2	S	C
57	Ormond	1993	8	10	0946	39	6.19	17.2	S	C
57	Ormond	1993	8	10	0946	39	6.19	79.4	S	C
57	Ormond	1993	8	10	0946	39	6.19	104.7	S	A
57	Ormond	1993	8	10	0946	39	6.19	67.2	S	C

Appendix B1.2: continued

Ev. #	Event Name	Year	Month	Day	UT	Depth	M_W	R_{rup}	Focal Mech.	Site Class
57	Ormond	1993	8	10	0946	39	6.19	75.5	S	A
57	Ormond	1993	8	10	0946	39	6.19	137.1	S	C
57	Ormond	1993	8	10	0946	39	6.19	134.9	S	A
57	Ormond	1993	8	10	0946	39	6.19	18.7	S	A
57	Ormond	1993	8	10	0946	39	6.19	17.2	S	C
57	Ormond	1993	8	10	0946	39	6.19	137.3	S	C
57	Ormond	1993	8	10	0946	39	6.19	151.5	S	C
57	Ormond	1993	8	10	0946	39	6.19	17.2	S	C
57	Ormond	1993	8	10	0946	39	6.19	17.2	S	C
57	Ormond	1993	8	10	0946	39	6.19	17.2	S	C
58	Tikokino	1993	4	11	0659	24	5.63	23.3	R	A
58	Tikokino	1993	4	11	0659	24	5.63	28.4	R	C
58	Tikokino	1993	4	11	0659	24	5.63	30.4	R	A
58	Tikokino	1993	4	11	0659	24	5.63	14.6	R	C
58	Tikokino	1993	4	11	0659	24	5.63	139.4	R	B
58	Tikokino	1993	4	11	0659	24	5.63	223.7	R	C
58	Tikokino	1993	4	11	0659	24	5.63	217.3	R	C
58	Tikokino	1993	4	11	0659	24	5.63	222.8	R	C
58	Tikokino	1993	4	11	0659	24	5.63	222.3	R	C
58	Tikokino	1993	4	11	0659	24	5.63	218.4	R	B
59	Secretary Island	1993	8	10	0051	22	6.81	73.8	R	C
59	Secretary Island	1993	8	10	0051	22	6.81	52.6	R	A
59	Secretary Island	1993	8	10	0051	22	6.81	142.9	R	B
59	Secretary Island	1993	8	10	0051	22	6.81	297.0	R	C
59	Secretary Island	1993	8	10	0051	22	6.81	224.2	R	C
60	60km North of White Island	1994	12	15	1120	12	6.31	249.9	S	C
60	60km North of White Island	1994	12	15	1120	12	6.31	160.8	S	A
60	60km North of White Island	1994	12	15	1120	12	6.31	159.4	S	C
60	60km North of White Island	1994	12	15	1120	12	6.31	161.3	S	C
60	60km North of White Island	1994	12	15	1120	12	6.31	152.7	S	C
60	60km North of White Island	1994	12	15	1120	12	6.31	85.2	S	B
60	60km North of White Island	1994	12	15	1120	12	6.31	64.6	S	A
61	Offshore East Cape	1995	2	5	2251	10	7.09	288.0	N	C
61	Offshore East Cape	1995	2	5	2251	10	7.09	285.8	N	A
61	Offshore East Cape	1995	2	5	2251	10	7.09	152.7	N	A
61	Offshore East Cape	1995	2	5	2251	10	7.09	152.4	N	C
61	Offshore East Cape	1995	2	5	2251	10	7.09	274.9	N	C
61	Offshore East Cape	1995	2	5	2251	10	7.09	156.6	N	C
61	Offshore East Cape	1995	2	5	2251	10	7.09	152.8	N	A
61	Offshore East Cape	1995	2	5	2251	10	7.09	208.0	N	B
61	Offshore East Cape	1995	2	5	2251	10	7.09	284.4	N	B
61	Offshore East Cape	1995	2	5	2251	10	7.09	280.2	N	C
61	Offshore East Cape	1995	2	5	2251	10	7.09	152.1	N	C
61	Offshore East Cape	1995	2	5	2251	10	7.09	154.7	N	A
63	East Cape Aftershock	1995	2	10	0144	12	6.2	153.6	?	A
63	East Cape Aftershock	1995	2	10	0144	12	6.2	153.5	?	C
63	East Cape Aftershock	1995	2	10	0144	12	6.2	282.8	?	C
63	East Cape Aftershock	1995	2	10	0144	12	6.2	158.7	?	C
63	East Cape Aftershock	1995	2	10	0144	12	6.2	153.8	?	A
63	East Cape Aftershock	1995	2	10	0144	12	6.2	218.6	?	B
64	10km north of Gisborne	1995	2	13	1218	33	5	4.9	I	A
64	10km north of Gisborne	1995	2	13	1218	33	5	3.5	I	C
64	10km north of Gisborne	1995	2	13	1218	33	5	5.5	I	C
64	10km north of Gisborne	1995	2	13	1218	33	5	4.4	I	A
64	10km north of Gisborne	1995	2	13	1218	33	5	3.4	I	C
66	Cass	1995	11	24	0618	5	6.24	88.8	R	C

Appendix B1.2: continued

Ev. #	Event Name	Year	Month	Day	UT	Depth	M_W	R_{rup}	Focal Mech.	Site Class
66	Cass	1995	11	24	0618	5	6.24	15.4	R	B
66	Cass	1995	11	24	0618	5	6.24	219.5	R	C
66	Cass	1995	11	24	0618	5	6.24	127.3	R	C
66	Cass	1995	11	24	0618	5	6.24	216.2	R	A
66	Cass	1995	11	24	0618	5	6.24	128.2	R	C
66	Cass	1995	11	24	0618	5	6.24	14.8	R	B
66	Cass	1995	11	24	0618	5	6.24	88.0	R	C
66	Cass	1995	11	24	0618	5	6.24	88.0	R	C
66	Cass	1995	11	24	0618	5	6.24	88.0	R	C
66	Cass	1995	11	24	0618	5	6.24	88.0	R	C
67	Arthur's Pass 1995	1995	5	29	1006	4	6	1.0	R	B
68	Near Hanmer Springs	1996	8	29	0447	10	5.7	4.3	S	C
70	5km north of Hanmer	1996	9	19	1216	11	5.8	2.9	S	C
75	39km west of Oamaru	1998	2	8	1826	12	5.3	91.9	R	C
75	39km west of Oamaru	1998	2	8	1826	12	5.3	37.9	R	B
81	Weber 3	1990	8	15	1554	28	5.17	81.1	N	C
81	Weber 3	1990	8	15	1554	28	5.17	162.7	N	B
81	Weber 3	1990	8	15	1554	28	5.17	175.8	N	C
82	Cape Palliser 2	1990	10	6	0241	15	5.46	67.5	R	A
82	Cape Palliser 2	1990	10	6	0241	15	5.46	67.5	R	B
82	Cape Palliser 2	1990	10	6	0241	15	5.46	67.5	R	B
82	Cape Palliser 2	1990	10	6	0241	15	5.46	80.3	R	B
82	Cape Palliser 2	1990	10	6	0241	15	5.46	79.2	R	A
82	Cape Palliser 2	1990	10	6	0241	15	5.46	72.0	R	C
82	Cape Palliser 2	1990	10	6	0241	15	5.46	73.3	R	A
82	Cape Palliser 2	1990	10	6	0241	15	5.46	70.1	R	C
82	Cape Palliser 2	1990	10	6	0241	15	5.46	72.0	R	C
86	Weber 4	1992	3	2	0905	26	5.54	102.8	N	C
86	Weber 4	1992	3	2	0905	26	5.54	104.4	N	A
86	Weber 4	1992	3	2	0905	26	5.54	86.4	N	C
86	Weber 4	1992	3	2	0905	26	5.54	95.0	N	C
86	Weber 4	1992	3	2	0905	26	5.54	137.9	N	B
86	Weber 4	1992	3	2	0905	26	5.54	165.8	N	C
86	Weber 4	1992	3	2	0905	26	5.54	159.7	N	C
86	Weber 4	1992	3	2	0905	26	5.54	164.3	N	B
86	Weber 4	1992	3	2	0905	26	5.54	165.8	N	C
86	Weber 4	1992	3	2	0905	26	5.54	163.8	N	C
86	Weber 4	1992	3	2	0905	26	5.54	19.6	N	C
89	Near Tokomaru	1992	5	16	1757	22	5.76	52.9	R	A
89	Near Tokomaru	1992	5	16	1757	22	5.76	52.2	R	C
90	Unnamed	1992	5	17	0106	18	5.2	54.6	R	A
90	Unnamed	1992	5	17	0106	18	5.2	54.0	R	C
91	Wilberforce River	1992	3	30	0702	5	5.5	145.3	R	C
91	Wilberforce River	1992	3	30	0702	5	5.5	163.7	R	C
91	Wilberforce River	1992	3	30	0702	5	5.5	28.0	R	B
92	Unnamed	1992	4	1	2257	5	5.2	143.0	R	C
92	Unnamed	1992	4	1	2257	5	5.2	29.8	R	B
93	Ormond Aftershock	1993	8	10	0946	39	6.19	19.6	S	A
93	Ormond Aftershock	1993	8	10	0946	39	6.19	18.2	S	C
95	Arthur's Pass	1994	6	18	0325	4	6.81	111.5	R	C
95	Arthur's Pass	1994	6	18	0325	4	6.81	235.8	R	C
95	Arthur's Pass	1994	6	18	0325	4	6.81	135.5	R	C
95	Arthur's Pass	1994	6	18	0325	4	6.81	205.6	R	C
95	Arthur's Pass	1994	6	18	0325	4	6.81	233.9	R	A
95	Arthur's Pass	1994	6	18	0325	4	6.81	143.2	R	C
95	Arthur's Pass	1994	6	18	0325	4	6.81	195.4	R	C

Appendix B1.2: continued

Ev. #	Event Name	Year	Month	Day	UT	Depth	M_W	R_{rup}	Focal Mech.	Site Class
95	Arthur's Pass	1994	6	18	0325	4	6.81	5.3	R	B
95	Arthur's Pass	1994	6	18	0325	4	6.81	230.4	R	B
95	Arthur's Pass	1994	6	18	0325	4	6.81	58.2	R	B
95	Arthur's Pass	1994	6	18	0325	4	6.81	191.3	R	A
95	Arthur's Pass	1994	6	18	0325	4	6.81	16.3	R	B
95	Arthur's Pass	1994	6	18	0325	4	6.81	98.8	R	C
95	Arthur's Pass	1994	6	18	0325	4	6.81	98.8	R	C
95	Arthur's Pass	1994	6	18	0325	4	6.81	98.8	R	C
95	Arthur's Pass	1994	6	18	0325	4	6.81	98.8	R	C
96	Inangahua Aftershock	1968	5	24	2057	12	5.7	25.0	R	C
97	Inangahua Aftershock	1968	5	25	2349	12	5.3	21.7	R	C
98	Inangahua Aftershock	1968	6	5	1243	12	5.2	23.9	R	C
99	Te Horo	1994	12	15	1513	28	5.2	57.5	S	A
99	Te Horo	1994	12	15	1513	28	5.2	57.5	S	A
102	15km west of Porangahau	1996	10	5	2121	33	5	37.2	I	B
103	20km east of Hawera	1996	9	27	1354	33	5	52.9	N	C
105	Unnamed	1997	6	20	1536	33	5.2	33.6	S	C
105	Unnamed	1997	6	20	1536	33	5.2	37.0	S	B
105	Unnamed	1997	6	20	1536	33	5.2	29.2	S	C
105	Unnamed	1997	6	20	1536	33	5.2	29.2	S	C
107	Unnamed	1979	3	24	2106	10	5.08	11.1	R	A
108	Unnamed	1997	6	19	0855	38	5.1	27.5	S	C
108	Unnamed	1997	6	19	0855	38	5.1	27.5	S	C
108	Unnamed	1997	6	19	0855	38	5.1	27.5	S	C
108	Unnamed	1997	6	19	0855	38	5.1	27.5	S	C
109	Unnamed	1997	6	20	1536	34	5.4	25.9	S	C
109	Unnamed	1997	6	20	1536	34	5.4	25.9	S	C
109	Unnamed	1997	6	20	1536	34	5.4	25.9	S	C
109	Unnamed	1997	6	20	1536	34	5.4	25.9	S	C
109	Unnamed	1997	6	20	1536	34	5.4	26.4	S	C
112	Turangi Swarm	1984	2	21	0823	8	5.3	13.3	N	A
117	5km north of Gisborne City	1989	11	30	0858	30	5	3.0	I	C
118	Seddon	1966	4	23	0649	19	5.75	53.4	R	B
120	Napier	1980	10	5	1532	36	5.66	22.0	N	C
121	Gisborne	1982	3	3	2234	33	5.1	23.5	N	C
121	Gisborne	1982	3	3	2234	33	5.1	23.5	N	C
121	Gisborne	1982	3	3	2234	33	5.1	23.5	N	C
121	Gisborne	1982	3	3	2234	33	5.1	23.5	N	C
122	Hawke's Bay	1982	9	2	1558	31	5.46	25.3	N	C
122	Hawke's Bay	1982	9	2	1558	31	5.46	36.0	N	A
123	Unnamed	1982	6	4	0157	30	5.1	28.3	I	C
126	10km NW Greytown	2000	3	29	1430	31	5.2	16.1	R	C
126	10km NW Greytown	2000	3	29	1430	31	5.2	57.7	R	C
126	10km NW Greytown	2000	3	29	1430	31	5.2	181.5	R	A
126	10km NW Greytown	2000	3	29	1430	31	5.2	48.7	R	C
126	10km NW Greytown	2000	3	29	1430	31	5.2	58.8	R	A
126	10km NW Greytown	2000	3	29	1430	31	5.2	59.5	R	B
126	10km NW Greytown	2000	3	29	1430	31	5.2	58.3	R	B
126	10km NW Greytown	2000	3	29	1430	31	5.2	86.5	R	C
126	10km NW Greytown	2000	3	29	1430	31	5.2	58.6	R	A
126	10km NW Greytown	2000	3	29	1430	31	5.2	127.9	R	B
126	10km NW Greytown	2000	3	29	1430	31	5.2	127.9	R	B
143	90km north-west of Te Anau	2000	11	1	1035	9	6.2	285.4	S	A
143	90km north-west of Te Anau	2000	11	1	1035	9	6.2	86.2	S	A
144	Unnamed	2000	11	1	1037	9	5	88.9	S	A
146	60km north-west of Te Anau	2000	11	12	1149	26	5.5	84.7	S	A

Appendix B1.2: continued

Ev. #	Event Name	Year	Month	Day	UT	Depth	M_W	R_{rup}	Focal Mech.	Site Class
154	Unnamed	2000	12	31	2156	30	5.4	93.4	I	C
159	Unnamed	2001	5	18	1056	5	5.5	101.6	R	A
159	Unnamed	2001	5	18	1056	5	5.5	56.4	R	A
161	20km west of Seddon	2001	5	22	0158	13	5	63.9	S	A
161	20km west of Seddon	2001	5	22	0158	13	5	104.6	S	C
161	20km west of Seddon	2001	5	22	0158	13	5	93.4	S	B
161	20km west of Seddon	2001	5	22	0158	13	5	94.7	S	B
169	20km south of Porangahau	2001	9	24	0449	37	5.6	137.0	R	C
169	20km south of Porangahau	2001	9	24	0449	37	5.6	103.5	R	A
169	20km south of Porangahau	2001	9	24	0449	37	5.6	178.6	R	C
169	20km south of Porangahau	2001	9	24	0449	37	5.6	200.4	R	A
169	20km south of Porangahau	2001	9	24	0449	37	5.6	153.2	R	B
169	20km south of Porangahau	2001	9	24	0449	37	5.6	73.3	R	C
173	100km north-east of Te Araroa	2001	10	21	0029	12	6.3	254.8	?	C
173	100km north-east of Te Araroa	2001	10	21	0029	12	6.3	254.8	?	C
173	100km north-east of Te Araroa	2001	10	21	0029	12	6.3	254.8	?	C
182	50km west of Haast	2001	12	7	1927	5	6.2	282.2	S	A
182	50km west of Haast	2001	12	7	1927	5	6.2	264.6	S	A
182	50km west of Haast	2001	12	7	1927	5	6.2	244.4	S	A
182	50km west of Haast	2001	12	7	1927	5	6.2	275.3	S	B
182	50km west of Haast	2001	12	7	1927	5	6.2	240.5	S	C
182	50km west of Haast	2001	12	7	1927	5	6.2	239.9	S	A
182	50km west of Haast	2001	12	7	1927	5	6.2	77.4	S	A
188	20km SE of Karamea	2002	5	4	1259	5	5.6	61.3	R	C
188	20km SE of Karamea	2002	5	4	1259	5	5.6	78.0	R	A
188	20km SE of Karamea	2002	5	4	1259	5	5.6	211.6	R	C
188	20km SE of Karamea	2002	5	4	1259	5	5.6	77.5	R	A
188	20km SE of Karamea	2002	5	4	1259	5	5.6	43.1	R	A
188	20km SE of Karamea	2002	5	4	1259	5	5.6	217.8	R	C
188	20km SE of Karamea	2002	5	4	1259	5	5.6	216.6	R	A
188	20km SE of Karamea	2002	5	4	1259	5	5.6	214.4	R	B
188	20km SE of Karamea	2002	5	4	1259	5	5.6	214.3	R	B
188	20km SE of Karamea	2002	5	4	1259	5	5.6	216.7	R	C
188	20km SE of Karamea	2002	5	4	1259	5	5.6	201.4	R	A
192	Unnamed	2002	12	24	0742	18	5	112.3	S	C
192	Unnamed	2002	12	24	0742	18	5	111.4	S	C
192	Unnamed	2002	12	24	0742	18	5	113.0	S	B
192	Unnamed	2002	12	24	0742	18	5	100.5	S	A
192	Unnamed	2002	12	24	0742	18	5	100.0	S	A
200	70km north-west of Te Anau	2003	8	21	1212	12	7.1	260.7	S	A
200	70km north-west of Te Anau	2003	8	21	1212	12	7.1	244.3	S	A
200	70km north-west of Te Anau	2003	8	21	1212	12	7.1	250.1	S	A
200	70km north-west of Te Anau	2003	8	21	1212	12	7.1	281.6	S	A
200	70km north-west of Te Anau	2003	8	21	1212	12	7.1	282.0	S	A
200	70km north-west of Te Anau	2003	8	21	1212	12	7.1	281.9	S	B
200	70km north-west of Te Anau	2003	8	21	1212	12	7.1	280.3	S	A
200	70km north-west of Te Anau	2003	8	21	1212	12	7.1	291.4	S	C
200	70km north-west of Te Anau	2003	8	21	1212	12	7.1	200.9	S	C
200	70km north-west of Te Anau	2003	8	21	1212	12	7.1	175.5	S	A
200	70km north-west of Te Anau	2003	8	21	1212	12	7.1	168.7	S	B
200	70km north-west of Te Anau	2003	8	21	1212	12	7.1	47.5	S	A
200	70km north-west of Te Anau	2003	8	21	1212	12	7.1	279.1	S	C
200	70km north-west of Te Anau	2003	8	21	1212	12	7.1	191.4	S	B
200	70km north-west of Te Anau	2003	8	21	1212	12	7.1	113.2	S	B
200	70km north-west of Te Anau	2003	8	21	1212	12	7.1	76.9	S	A
200	70km north-west of Te Anau	2003	8	21	1212	12	7.1	123.0	S	B

Appendix B1.2: continued

Ev. #	Event Name	Year	Month	Day	UT	Depth	M_W	R_{rup}	Focal Mech.	Site Class
200	70km north-west of Te Anau	2003	8	21	1212	12	7.1	283.0	S	C
200	70km north-west of Te Anau	2003	8	21	1212	12	7.1	64.3	S	C
200	70km north-west of Te Anau	2003	8	21	1212	12	7.1	290.2	S	A
200	70km north-west of Te Anau	2003	8	21	1212	12	7.1	165.7	S	C
200	70km north-west of Te Anau	2003	8	21	1212	12	7.1	244.7	S	A
200	70km north-west of Te Anau	2003	8	21	1212	12	7.1	186.0	S	C
200	70km north-west of Te Anau	2003	8	21	1212	12	7.1	123.0	S	B
201	70km north-west of Te Anau	2003	8	21	1412	21	6.2	244.6	S	A
201	70km north-west of Te Anau	2003	8	21	1412	21	6.2	287.1	S	A
201	70km north-west of Te Anau	2003	8	21	1412	21	6.2	168.8	S	A
201	70km north-west of Te Anau	2003	8	21	1412	21	6.2	217.5	S	B
201	70km north-west of Te Anau	2003	8	21	1412	21	6.2	113.4	S	B
201	70km north-west of Te Anau	2003	8	21	1412	21	6.2	140.8	S	B
201	70km north-west of Te Anau	2003	8	21	1412	21	6.2	66.0	S	C
201	70km north-west of Te Anau	2003	8	21	1412	21	6.2	187.7	S	C
201	70km north-west of Te Anau	2003	8	21	1412	21	6.2	288.7	S	B
201	70km north-west of Te Anau	2003	8	21	1412	21	6.2	289.9	S	C
201	70km north-west of Te Anau	2003	8	21	1412	21	6.2	288.7	S	B
201	70km north-west of Te Anau	2003	8	21	1412	21	6.2	289.9	S	C
201	70km north-west of Te Anau	2003	8	21	1412	21	6.2	140.8	S	B
203	20km east of Woodville	2003	1	25	2130	35	5.5	107.4	S	B
203	20km east of Woodville	2003	1	25	2130	35	5.5	138.6	S	C
203	20km east of Woodville	2003	1	25	2130	35	5.5	138.6	S	C
203	20km east of Woodville	2003	1	25	2130	35	5.5	132.7	S	C
203	20km east of Woodville	2003	1	25	2130	35	5.5	137.2	S	A
203	20km east of Woodville	2003	1	25	2130	35	5.5	137.7	S	B
203	20km east of Woodville	2003	1	25	2130	35	5.5	137.4	S	B
203	20km east of Woodville	2003	1	25	2130	35	5.5	150.6	S	A
203	20km east of Woodville	2003	1	25	2130	35	5.5	151.1	S	A
206	Unnamed	2004	1	2	0349	22	5.1	78.8	S	C

Appendix B2: Individual Terms of the Scattering Matrices

For the case of waves being scattered in a vertical plane (*P-SV*) the 16 terms of the scattering matrix are those below. Each expression of the scattering matrix in turn makes use of some common expressions. These are given below.

Common terms:

$$a = \rho_2\left(1-2\beta_2^2 p^2\right)-\rho_1\left(1-2\beta_1^2 p^2\right) \tag{B2.1}$$

$$b = \rho_2\left(1-2\beta_2^2 p^2\right)+2\rho_1\beta_1^2 p^2 \tag{B2.2}$$

$$c = \rho_1\left(1-2\beta_1^2 p^2\right)+2\rho_2\beta_2^2 p^2 \tag{B2.3}$$

$$d = 2\left(\rho_2\beta_2^2-\rho_1\beta_1^2\right) \tag{B2.4}$$

$$E = b\frac{\cos i_1}{\alpha_1}+c\frac{\cos i_2}{\alpha_2} \tag{B2.5}$$

$$F = b\frac{\cos j_1}{\beta_1}+c\frac{\cos j_2}{\beta_2} \tag{B2.6}$$

$$G = a-d\frac{\cos i_1}{\alpha_1}\frac{\cos j_2}{\beta_2} \tag{B2.7}$$

$$H = a-d\frac{\cos i_2}{\alpha_2}\frac{\cos j_1}{\beta_1} \tag{B2.8}$$

$$D = EF + GHp^2 \tag{B2.9}$$

Scattering Matrix terms:

$$\breve{P}\hat{P} = \left[\left(b\frac{\cos i_1}{\alpha_1} - c\frac{\cos i_2}{\alpha_2}\right)F - \left(a + d\frac{\cos i_1}{\alpha_1}\frac{\cos j_2}{\beta_2}\right)Hp^2\right] \Big/ D \tag{B2.10}$$

$$\breve{P}\hat{S} = -2\frac{\cos i_1}{\alpha_1}\left(ab + cd\frac{\cos i_2}{\alpha_2}\frac{\cos j_2}{\beta_2}\right)p\alpha_1 \Big/ (\beta_1 D) \tag{B2.11}$$

$$\breve{P}\breve{P} = 2\rho_1\frac{\cos i_1}{\alpha_1}F\alpha_1 \Big/ (\alpha_2 D) \tag{B2.12}$$

$$\breve{P}\breve{S} = 2\rho_1\frac{\cos i_1}{\alpha_1}Hp\alpha_1 \Big/ (\beta_2 D) \tag{B2.13}$$

$$\breve{S}\hat{P} = -2\frac{\cos j_1}{\beta_1}\left(ab + cd\frac{\cos i_2}{\alpha_2}\frac{\cos j_2}{\beta_2}\right)p\beta_1 \Big/ (\alpha_1 D) \tag{B2.14}$$

$$\breve{S}\hat{S} = -\left[\left(b\frac{\cos j_1}{\beta_1} - c\frac{\cos j_2}{\beta_2}\right)E - \left(a + d\frac{\cos i_2}{\alpha_2}\frac{\cos j_1}{\beta_1}\right)Gp^2\right] \Big/ D \tag{B2.15}$$

$$\breve{S}\breve{P} = -2\rho_1\frac{\cos j_1}{\beta_1}Gp\beta_1 \Big/ (\alpha_2 D) \tag{B2.16}$$

$$\breve{S}\breve{S} = 2\rho_1\frac{\cos j_1}{\beta_1}E\beta_1 \Big/ (\beta_2 D) \tag{B2.17}$$

$$\hat{P}\hat{P} = 2\rho_2\frac{\cos i_2}{\alpha_2}F\alpha_2 \Big/ (\alpha_1 D) \tag{B2.18}$$

$$\hat{P}\hat{S} = -2\rho_2\frac{\cos i_2}{\alpha_2}Gp\alpha_2 \Big/ (\beta_1 D) \tag{B2.19}$$

$$\hat{P}\breve{P} = -\left[\left(b\frac{\cos i_1}{\alpha_1} - c\frac{\cos i_2}{\alpha_2}\right)F + \left(a + d\frac{\cos i_2}{\alpha_2}\frac{\cos j_1}{\beta_1}\right)Gp^2\right] \Big/ D \tag{B2.20}$$

$$\breve{PS} = 2\frac{\cos i_2}{\alpha_2}\left(ac + bd\frac{\cos i_1}{\alpha_1}\frac{\cos j_1}{\beta_1}\right)p\alpha_2 \Big/ \left(\beta_2 D\right) \tag{B2.21}$$

$$\breve{SP} = 2\rho_2\frac{\cos j_2}{\beta_2}Hp\beta_2 \Big/ \left(\alpha_1 D\right) \tag{B2.22}$$

$$\breve{SS} = 2\rho_2\frac{\cos j_2}{\beta_2}E\beta_2 \Big/ \left(\beta_1 D\right) \tag{B2.23}$$

$$\breve{SP} = 2\frac{\cos j_2}{\beta_2}\left(ac + bd\frac{\cos i_1}{\alpha_1}\frac{\cos j_1}{\beta_1}\right)p\beta_2 \Big/ \left(\alpha_2 D\right) \tag{B2.24}$$

$$\breve{SS} = \left[\left(b\frac{\cos j_1}{\beta_1} - c\frac{\cos j_2}{\beta_2}\right)E + \left(a + d\frac{\cos i_1}{\alpha_1}\frac{\cos j_2}{\beta_2}\right)Hp^2\right] \Big/ D \tag{B2.25}$$

When a wave front interacts with the free surface no energy is transmitted across the interface and the scattering matrix reduces to just four terms in the *P-SV* case. These four terms are again given below.

$$\breve{PP} = \frac{-\left(\frac{1}{\beta^2} - 2p^2\right)^2 + 4p^2\frac{\cos i}{\alpha}\frac{\cos j}{\beta}}{\left(\frac{1}{\beta^2} - 2p^2\right)^2 + 4p^2\frac{\cos i}{\alpha}\frac{\cos j}{\beta}} \tag{B2.26}$$

$$\breve{PS} = \frac{4\frac{\alpha}{\beta}p\frac{\cos i}{\alpha}\left(\frac{1}{\beta^2} - 2p^2\right)}{\left(\frac{1}{\beta^2} - 2p^2\right)^2 + 4p^2\frac{\cos i}{\alpha}\frac{\cos j}{\beta}} \tag{B2.27}$$

$$\breve{SP} = \frac{4\frac{\beta}{\alpha}p\frac{\cos j}{\beta}\left(\frac{1}{\beta^2} - 2p^2\right)}{\left(\frac{1}{\beta^2} - 2p^2\right)^2 + 4p^2\frac{\cos i}{\alpha}\frac{\cos j}{\beta}} \tag{B2.28}$$

$$\breve{SS} = \frac{\left(\frac{1}{\beta^2} - 2p^2\right)^2 - 4p^2\frac{\cos i}{\alpha}\frac{\cos j}{\beta}}{\left(\frac{1}{\beta^2} - 2p^2\right)^2 + 4p^2\frac{\cos i}{\alpha}\frac{\cos j}{\beta}} \tag{B2.29}$$

The case of *SH* waves is considerably more simple as the motion is transverse to the interface only *SH* waves are transmitted or reflected. The solid-solid scatter matrix is therefore only comprised of four terms

and the solid–air matrix is singular, i.e. all energy is reflected back into the original layer. The terms for the solid–solid case are given below.

$$\breve{S}\hat{S} = \frac{\rho_1\beta_1 \cos j_1 - \rho_2\beta_2 \cos j_2}{\rho_1\beta_1 \cos j_1 + \rho_2\beta_2 \cos j_2} \tag{B2.30}$$

$$\hat{S}\hat{S} = \frac{2\rho_2\beta_2 \cos j_2}{\rho_1\beta_1 \cos j_1 + \rho_2\beta_2 \cos j_2} \tag{B2.31}$$

$$\breve{S}\breve{S} = \frac{2\rho_1\beta_1 \cos j_1}{\rho_1\beta_1 \cos j_1 + \rho_2\beta_2 \cos j_2} \tag{B2.32}$$

$$\hat{S}\breve{S} = -\breve{S}\hat{S} \tag{B2.33}$$

Appendix B3: Regression Coefficients for FAS

Appendix B3.1: Regression coefficients for the Fourier Amplitude Spectrum of Acceleration in New Zealand (coefficients in this table are derived for the dataset including the Chi-Chi records).

f	c_1	c_2	c_3	c_4	c_5	c_6	c_7	c_8	τ	σ_1	σ_c	σ	σ_{lnY}	M	N
0.333	-5.531	2.769	-1.071	19	0.014	0.085	-1.165	-0.377	0.966	0.879	0.152	0.892	1.315	60	297
0.357	-5.882	2.811	-1.069	19	-0.004	0.104	-1.109	-0.352	0.950	0.878	0.151	0.891	1.303	65	320
0.370	-6.053	2.832	-1.068	19	-0.012	0.119	-1.080	-0.339	0.942	0.878	0.151	0.890	1.296	65	320
0.400	-6.386	2.872	-1.067	19	-0.024	0.160	-1.021	-0.313	0.922	0.876	0.150	0.889	1.281	70	375
0.417	-6.547	2.891	-1.066	19	-0.028	0.185	-0.990	-0.299	0.912	0.876	0.149	0.888	1.273	70	375
0.455	-6.856	2.928	-1.064	19	-0.032	0.243	-0.925	-0.270	0.887	0.874	0.148	0.887	1.254	71	387
0.476	-7.003	2.946	-1.063	19	-0.031	0.276	-0.891	-0.255	0.874	0.873	0.148	0.885	1.244	71	387
0.526	-7.280	2.980	-1.061	19	-0.026	0.347	-0.820	-0.223	0.845	0.871	0.146	0.883	1.222	75	431
0.556	-7.408	2.996	-1.061	19	-0.020	0.384	-0.783	-0.206	0.829	0.869	0.145	0.881	1.210	77	439
0.625	-7.639	3.026	-1.061	19	-0.003	0.458	-0.705	-0.171	0.793	0.866	0.144	0.878	1.183	86	477
0.667	-7.740	3.040	-1.063	19	0.009	0.494	-0.664	-0.152	0.774	0.864	0.143	0.876	1.168	86	478
0.769	-7.907	3.064	-1.069	19	0.041	0.554	-0.578	-0.112	0.732	0.859	0.140	0.870	1.137	89	490
0.833	-7.969	3.075	-1.074	19	0.062	0.577	-0.532	-0.091	0.709	0.856	0.139	0.867	1.120	91	505
1.000	-8.043	3.092	-1.091	19	0.112	0.597	-0.434	-0.045	0.661	0.850	0.135	0.860	1.085	94	513
1.053	-8.049	3.096	-1.097	19	0.126	0.595	-0.408	-0.033	0.649	0.848	0.134	0.858	1.076	94	513
1.176	-8.043	3.102	-1.113	19	0.158	0.579	-0.355	-0.007	0.624	0.844	0.131	0.854	1.057	94	513
1.250	-8.031	3.104	-1.123	19	0.175	0.565	-0.328	0.007	0.611	0.841	0.130	0.851	1.048	95	515
1.429	-7.986	3.108	-1.148	19	0.211	0.522	-0.272	0.036	0.587	0.836	0.126	0.846	1.029	95	517
1.481	-7.970	3.109	-1.156	19	0.221	0.508	-0.257	0.043	0.581	0.835	0.125	0.844	1.025	95	517
1.600	-7.933	3.111	-1.173	19	0.240	0.475	-0.228	0.059	0.570	0.832	0.123	0.841	1.016	95	517
1.667	-7.911	3.111	-1.182	19	0.250	0.456	-0.214	0.067	0.565	0.831	0.122	0.839	1.012	95	517
1.818	-7.862	3.112	-1.204	19	0.270	0.414	-0.185	0.083	0.555	0.828	0.119	0.836	1.004	95	517
1.905	-7.835	3.113	-1.216	19	0.280	0.390	-0.170	0.092	0.551	0.826	0.118	0.834	1.000	95	517
2.000	-7.807	3.113	-1.229	19	0.290	0.365	-0.155	0.101	0.547	0.824	0.116	0.832	0.996	95	517
2.174	-7.757	3.114	-1.253	19	0.305	0.321	-0.132	0.115	0.542	0.822	0.113	0.829	0.991	95	517
2.381	-7.705	3.115	-1.280	19	0.319	0.273	-0.109	0.130	0.538	0.819	0.110	0.826	0.986	95	517
2.500	-7.679	3.115	-1.295	19	0.326	0.248	-0.098	0.138	0.538	0.817	0.108	0.824	0.984	95	517
2.632	-7.652	3.116	-1.311	19	0.332	0.222	-0.088	0.146	0.537	0.816	0.106	0.823	0.983	95	517
2.703	-7.639	3.116	-1.319	19	0.335	0.209	-0.082	0.150	0.537	0.815	0.105	0.822	0.982	95	517
2.857	-7.613	3.117	-1.337	19	0.341	0.183	-0.072	0.159	0.538	0.814	0.103	0.820	0.981	95	517
2.941	-7.601	3.117	-1.346	19	0.343	0.170	-0.067	0.163	0.539	0.813	0.102	0.819	0.981	95	517
3.125	-7.578	3.118	-1.365	19	0.347	0.143	-0.058	0.172	0.542	0.812	0.100	0.818	0.981	95	517
3.226	-7.567	3.119	-1.375	19	0.349	0.130	-0.054	0.176	0.543	0.811	0.098	0.817	0.981	95	517
3.448	-7.548	3.120	-1.397	19	0.351	0.104	-0.046	0.185	0.547	0.810	0.096	0.815	0.982	95	517
3.571	-7.540	3.121	-1.408	19	0.352	0.091	-0.042	0.189	0.550	0.809	0.094	0.815	0.983	95	517
3.846	-7.529	3.122	-1.432	19	0.353	0.067	-0.036	0.199	0.556	0.808	0.091	0.813	0.985	95	517
4.000	-7.526	3.123	-1.444	19	0.352	0.055	-0.033	0.204	0.560	0.807	0.090	0.812	0.987	95	517
4.348	-7.528	3.125	-1.469	19	0.349	0.034	-0.030	0.213	0.568	0.807	0.086	0.811	0.991	95	517
4.545	-7.533	3.126	-1.482	19	0.347	0.025	-0.029	0.218	0.574	0.806	0.084	0.811	0.993	95	517
5.000	-7.557	3.128	-1.509	19	0.340	0.009	-0.030	0.228	0.586	0.806	0.080	0.810	0.999	95	517
5.263	-7.576	3.130	-1.522	19	0.336	0.003	-0.031	0.234	0.593	0.806	0.078	0.810	1.003	95	517
5.882	-7.635	3.132	-1.548	19	0.324	-0.006	-0.038	0.244	0.608	0.806	0.073	0.810	1.013	95	517
6.250	-7.677	3.133	-1.561	19	0.316	-0.007	-0.044	0.250	0.617	0.807	0.070	0.810	1.018	95	517
7.143	-7.798	3.134	-1.583	19	0.297	-0.005	-0.061	0.261	0.636	0.809	0.065	0.811	1.031	95	517
7.692	-7.882	3.134	-1.591	19	0.285	-0.001	-0.074	0.266	0.647	0.810	0.062	0.813	1.039	95	517
9.091	-8.117	3.131	-1.596	19	0.257	0.013	-0.110	0.277	0.669	0.815	0.055	0.817	1.056	95	517
10.000	-8.280	3.128	-1.590	19	0.240	0.022	-0.135	0.283	0.679	0.819	0.051	0.820	1.065	95	517
11.111	-8.484	3.121	-1.575	19	0.223	0.032	-0.167	0.288	0.688	0.823	0.047	0.825	1.074	95	515
11.765	-8.606	3.116	-1.562	19	0.214	0.037	-0.186	0.291	0.691	0.826	0.045	0.828	1.078	95	515
13.333	-8.901	3.102	-1.522	19	0.197	0.044	-0.233	0.296	0.695	0.834	0.041	0.835	1.086	95	515
14.286	-9.079	3.092	-1.492	19	0.190	0.047	-0.261	0.299	0.694	0.838	0.039	0.839	1.089	95	515
16.667	-9.517	3.062	-1.405	19	0.179	0.046	-0.332	0.303	0.683	0.850	0.036	0.851	1.091	95	515
18.182	-9.788	3.040	-1.340	19	0.178	0.043	-0.376	0.305	0.671	0.858	0.034	0.859	1.090	94	512
20.000	-10.105	3.012	-1.257	19	0.181	0.037	-0.428	0.307	0.651	0.867	0.032	0.868	1.085	94	511

Appendix B3.2: Regression coefficients for the Fourier Amplitude Spectrum of Acceleration in New Zealand (coefficients in this table are derived for the dataset excluding the Chi-Chi records, with no constraint placed upon the near field scaling terms).

f	c_1	c_2	c_3	c_4	c_5	c_6	c_7	c_8	τ	σ_1	σ_c	σ	σ_{lnY}	M	N
0.333	-6.393	2.796	-0.982	11.405	0.088	0.224	-0.988	-0.212	0.970	0.867	0.152	0.880	1.310	59	265
0.357	-6.821	2.839	-0.965	12.244	0.068	0.239	-0.942	-0.194	0.955	0.865	0.151	0.878	1.298	64	288
0.370	-7.023	2.860	-0.958	12.683	0.060	0.252	-0.918	-0.185	0.947	0.864	0.151	0.877	1.291	64	288
0.400	-7.399	2.901	-0.948	13.606	0.047	0.289	-0.869	-0.166	0.928	0.862	0.150	0.875	1.275	69	343
0.417	-7.571	2.921	-0.945	14.091	0.042	0.312	-0.843	-0.156	0.917	0.861	0.149	0.874	1.267	69	343
0.455	-7.881	2.961	-0.943	15.116	0.036	0.367	-0.789	-0.136	0.894	0.859	0.148	0.871	1.248	70	355
0.476	-8.016	2.981	-0.946	15.658	0.035	0.398	-0.762	-0.126	0.881	0.857	0.148	0.870	1.238	70	355
0.526	-8.242	3.018	-0.956	16.808	0.039	0.466	-0.703	-0.104	0.852	0.854	0.146	0.867	1.216	74	399
0.556	-8.330	3.037	-0.965	17.421	0.044	0.502	-0.673	-0.093	0.836	0.853	0.145	0.865	1.203	76	407
0.625	-8.447	3.072	-0.991	18.734	0.059	0.573	-0.609	-0.069	0.802	0.849	0.144	0.861	1.177	85	445
0.667	-8.473	3.089	-1.009	19.438	0.071	0.607	-0.575	-0.057	0.783	0.847	0.143	0.859	1.162	85	446
0.769	-8.450	3.121	-1.056	20.963	0.101	0.664	-0.504	-0.030	0.741	0.843	0.140	0.854	1.131	88	458
0.833	-8.396	3.137	-1.087	21.792	0.120	0.685	-0.467	-0.016	0.719	0.840	0.139	0.852	1.115	90	473
1.000	-8.187	3.165	-1.167	23.608	0.167	0.701	-0.387	0.013	0.671	0.835	0.135	0.845	1.080	93	480
1.053	-8.112	3.172	-1.191	24.101	0.181	0.698	-0.367	0.021	0.659	0.833	0.134	0.844	1.071	93	480
1.176	-7.933	3.184	-1.245	25.139	0.211	0.679	-0.324	0.038	0.634	0.830	0.131	0.840	1.052	93	480
1.250	-7.828	3.190	-1.276	25.686	0.227	0.663	-0.302	0.047	0.621	0.828	0.130	0.838	1.043	94	482
1.429	-7.586	3.202	-1.344	26.847	0.261	0.616	-0.257	0.065	0.597	0.824	0.126	0.834	1.025	94	484
1.481	-7.520	3.205	-1.363	27.152	0.269	0.600	-0.246	0.070	0.591	0.823	0.125	0.833	1.021	94	484
1.600	-7.379	3.210	-1.404	27.779	0.287	0.564	-0.223	0.080	0.579	0.821	0.123	0.830	1.012	94	484
1.667	-7.305	3.213	-1.425	28.103	0.296	0.544	-0.211	0.085	0.574	0.820	0.122	0.829	1.008	94	484
1.818	-7.152	3.218	-1.470	28.770	0.314	0.497	-0.188	0.096	0.563	0.818	0.119	0.826	1.000	94	484
1.905	-7.074	3.221	-1.494	29.114	0.323	0.471	-0.177	0.101	0.559	0.817	0.118	0.825	0.996	94	484
2.000	-6.994	3.224	-1.519	29.465	0.332	0.444	-0.165	0.107	0.555	0.815	0.116	0.824	0.993	94	484
2.174	-6.866	3.228	-1.560	30.041	0.345	0.395	-0.147	0.116	0.549	0.813	0.113	0.821	0.988	94	484
2.381	-6.741	3.233	-1.604	30.635	0.357	0.343	-0.130	0.126	0.545	0.812	0.110	0.819	0.984	94	484
2.500	-6.680	3.235	-1.627	30.937	0.363	0.315	-0.122	0.131	0.543	0.811	0.108	0.818	0.982	94	484
2.632	-6.622	3.237	-1.650	31.244	0.368	0.286	-0.114	0.137	0.543	0.810	0.106	0.817	0.980	94	484
2.703	-6.594	3.239	-1.662	31.398	0.370	0.271	-0.110	0.139	0.543	0.809	0.105	0.816	0.980	94	484
2.857	-6.542	3.241	-1.686	31.709	0.374	0.241	-0.102	0.145	0.543	0.808	0.103	0.815	0.979	94	484
2.941	-6.517	3.242	-1.698	31.865	0.375	0.226	-0.099	0.148	0.544	0.808	0.102	0.814	0.979	94	484
3.125	-6.473	3.245	-1.723	32.178	0.378	0.196	-0.092	0.154	0.545	0.807	0.100	0.813	0.979	94	484
3.226	-6.454	3.246	-1.735	32.334	0.379	0.181	-0.089	0.157	0.546	0.806	0.098	0.812	0.979	94	484
3.448	-6.423	3.249	-1.760	32.647	0.379	0.151	-0.084	0.163	0.550	0.805	0.096	0.811	0.980	94	484
3.571	-6.412	3.250	-1.773	32.802	0.379	0.136	-0.081	0.167	0.552	0.805	0.094	0.810	0.981	94	484
3.846	-6.400	3.253	-1.797	33.108	0.377	0.107	-0.078	0.174	0.557	0.804	0.091	0.809	0.983	94	484
4.000	-6.399	3.254	-1.809	33.258	0.375	0.093	-0.076	0.177	0.561	0.804	0.090	0.809	0.984	94	484
4.348	-6.414	3.257	-1.832	33.550	0.370	0.067	-0.075	0.185	0.569	0.803	0.086	0.808	0.988	94	484
4.545	-6.431	3.258	-1.844	33.690	0.367	0.055	-0.076	0.189	0.574	0.803	0.084	0.807	0.990	94	484
5.000	-6.485	3.261	-1.864	33.952	0.357	0.034	-0.078	0.197	0.585	0.803	0.080	0.807	0.996	94	484
5.263	-6.526	3.262	-1.873	34.071	0.351	0.025	-0.081	0.201	0.591	0.802	0.078	0.806	1.000	94	484
5.882	-6.639	3.264	-1.888	34.277	0.336	0.011	-0.089	0.211	0.606	0.803	0.073	0.806	1.008	94	484
6.250	-6.716	3.264	-1.893	34.358	0.326	0.007	-0.095	0.216	0.614	0.803	0.070	0.806	1.013	94	484
7.143	-6.918	3.264	-1.897	34.457	0.303	0.004	-0.112	0.228	0.633	0.804	0.065	0.807	1.025	94	484
7.692	-7.049	3.263	-1.895	34.463	0.290	0.006	-0.124	0.234	0.643	0.805	0.062	0.807	1.032	94	484
9.091	-7.386	3.256	-1.876	34.346	0.258	0.017	-0.158	0.248	0.665	0.808	0.055	0.809	1.048	94	484
10.000	-7.601	3.250	-1.857	34.195	0.240	0.026	-0.182	0.256	0.676	0.810	0.051	0.811	1.056	94	484
11.111	-7.853	3.240	-1.829	33.956	0.221	0.035	-0.211	0.265	0.686	0.812	0.047	0.814	1.064	94	483
11.765	-7.993	3.234	-1.811	33.793	0.212	0.040	-0.228	0.271	0.690	0.814	0.045	0.815	1.068	94	483
13.333	-8.307	3.216	-1.762	33.356	0.194	0.048	-0.270	0.282	0.695	0.818	0.041	0.819	1.074	94	483
14.286	-8.481	3.203	-1.731	33.066	0.186	0.051	-0.295	0.288	0.695	0.821	0.039	0.822	1.077	94	483
16.667	-8.859	3.168	-1.648	32.288	0.175	0.052	-0.358	0.303	0.688	0.828	0.036	0.828	1.077	94	483
18.182	-9.060	3.143	-1.594	31.769	0.175	0.048	-0.397	0.312	0.679	0.832	0.034	0.833	1.074	93	481
20.000	-9.264	3.111	-1.528	31.132	0.180	0.042	-0.442	0.321	0.663	0.837	0.032	0.838	1.068	93	481

Appendix B3.3: Regression coefficients for the Fourier Amplitude Spectrum of Acceleration in New Zealand (coefficients in this table are derived for the dataset including the Chi-Chi records, with no constraint placed upon the near field scaling terms).

f	c_1	c_2	c_3	c_4	c_5	c_6	c_7	c_8	τ	σ_1	σ_c	σ	σ_{lnY}	M	N
0.333	-5.543	2.768	-1.066	18.666	0.015	0.085	-1.164	-0.375	0.966	0.879	0.152	0.892	1.315	60	297
0.357	-5.978	2.808	-1.046	19.109	-0.003	0.103	-1.110	-0.351	0.951	0.878	0.151	0.891	1.303	65	320
0.370	-6.185	2.827	-1.038	19.346	-0.011	0.118	-1.082	-0.339	0.943	0.878	0.151	0.890	1.297	65	320
0.400	-6.573	2.867	-1.025	19.851	-0.022	0.159	-1.024	-0.314	0.924	0.876	0.150	0.889	1.283	70	375
0.417	-6.754	2.886	-1.020	20.122	-0.026	0.184	-0.994	-0.300	0.914	0.876	0.149	0.888	1.275	70	375
0.455	-7.084	2.924	-1.014	20.706	-0.030	0.242	-0.931	-0.273	0.891	0.874	0.148	0.886	1.257	71	387
0.476	-7.231	2.942	-1.013	21.020	-0.030	0.275	-0.899	-0.259	0.878	0.873	0.148	0.885	1.247	71	387
0.526	-7.486	2.978	-1.018	21.702	-0.024	0.346	-0.831	-0.230	0.849	0.870	0.146	0.882	1.224	75	431
0.556	-7.591	2.995	-1.023	22.073	-0.019	0.383	-0.796	-0.215	0.833	0.869	0.145	0.881	1.212	77	439
0.625	-7.748	3.029	-1.042	22.883	-0.001	0.457	-0.722	-0.184	0.798	0.865	0.144	0.877	1.186	86	477
0.667	-7.798	3.045	-1.056	23.329	0.011	0.493	-0.683	-0.167	0.779	0.863	0.143	0.874	1.171	86	478
0.769	-7.826	3.076	-1.094	24.315	0.043	0.553	-0.602	-0.132	0.738	0.858	0.140	0.869	1.140	89	490
0.833	-7.801	3.090	-1.120	24.864	0.064	0.576	-0.559	-0.114	0.716	0.854	0.139	0.866	1.123	91	505
1.000	-7.658	3.117	-1.188	26.099	0.114	0.596	-0.468	-0.075	0.668	0.847	0.135	0.858	1.087	94	513
1.053	-7.601	3.124	-1.209	26.442	0.128	0.594	-0.445	-0.065	0.656	0.845	0.134	0.856	1.078	94	513
1.176	-7.459	3.136	-1.257	27.175	0.160	0.578	-0.396	-0.044	0.631	0.840	0.131	0.850	1.059	94	513
1.250	-7.373	3.142	-1.285	27.568	0.177	0.564	-0.371	-0.033	0.619	0.838	0.130	0.848	1.050	95	515
1.429	-7.170	3.153	-1.347	28.415	0.213	0.521	-0.320	-0.010	0.594	0.832	0.126	0.842	1.030	95	517
1.481	-7.114	3.156	-1.365	28.640	0.223	0.506	-0.308	-0.004	0.589	0.831	0.125	0.840	1.026	95	517
1.600	-6.993	3.161	-1.402	29.109	0.242	0.473	-0.282	0.008	0.577	0.827	0.123	0.837	1.016	95	517
1.667	-6.929	3.164	-1.422	29.353	0.252	0.454	-0.269	0.015	0.572	0.826	0.122	0.835	1.012	95	517
1.818	-6.795	3.169	-1.464	29.861	0.272	0.411	-0.243	0.028	0.562	0.822	0.119	0.831	1.003	95	517
1.905	-6.725	3.172	-1.487	30.126	0.282	0.387	-0.230	0.034	0.558	0.821	0.118	0.829	0.999	95	517
2.000	-6.654	3.174	-1.510	30.398	0.292	0.362	-0.217	0.041	0.554	0.819	0.116	0.827	0.995	95	517
2.174	-6.539	3.179	-1.550	30.849	0.307	0.317	-0.197	0.052	0.548	0.816	0.113	0.824	0.989	95	517
2.381	-6.425	3.183	-1.592	31.320	0.321	0.269	-0.177	0.064	0.545	0.813	0.110	0.820	0.984	95	517
2.500	-6.370	3.185	-1.615	31.563	0.328	0.244	-0.168	0.070	0.544	0.811	0.108	0.818	0.982	95	517
2.632	-6.316	3.188	-1.638	31.810	0.334	0.218	-0.159	0.076	0.543	0.809	0.106	0.816	0.981	95	517
2.703	-6.291	3.189	-1.649	31.936	0.337	0.204	-0.154	0.079	0.543	0.809	0.105	0.815	0.980	95	517
2.857	-6.241	3.191	-1.673	32.190	0.343	0.178	-0.146	0.086	0.544	0.807	0.103	0.814	0.979	95	517
2.941	-6.218	3.193	-1.685	32.318	0.345	0.164	-0.142	0.089	0.545	0.806	0.102	0.813	0.978	95	517
3.125	-6.177	3.195	-1.710	32.578	0.349	0.137	-0.134	0.096	0.547	0.805	0.100	0.811	0.978	95	517
3.226	-6.158	3.197	-1.722	32.709	0.351	0.124	-0.131	0.099	0.548	0.804	0.098	0.810	0.978	95	517
3.448	-6.127	3.199	-1.748	32.972	0.354	0.097	-0.124	0.106	0.552	0.802	0.096	0.808	0.979	95	517
3.571	-6.115	3.201	-1.760	33.104	0.354	0.084	-0.122	0.110	0.555	0.802	0.094	0.807	0.979	95	517
3.846	-6.101	3.203	-1.786	33.367	0.355	0.060	-0.117	0.117	0.561	0.800	0.091	0.806	0.981	95	517
4.000	-6.099	3.205	-1.798	33.497	0.354	0.048	-0.115	0.121	0.564	0.800	0.090	0.805	0.983	95	517
4.348	-6.109	3.207	-1.823	33.754	0.351	0.027	-0.114	0.129	0.573	0.799	0.086	0.803	0.986	95	517
4.545	-6.122	3.209	-1.835	33.878	0.349	0.017	-0.113	0.133	0.577	0.798	0.084	0.803	0.989	95	517
5.000	-6.169	3.211	-1.858	34.117	0.343	0.001	-0.115	0.141	0.589	0.798	0.080	0.802	0.995	95	517
5.263	-6.204	3.212	-1.868	34.228	0.338	-0.005	-0.118	0.146	0.596	0.798	0.078	0.802	0.999	95	517
5.882	-6.306	3.214	-1.886	34.426	0.326	-0.013	-0.126	0.155	0.611	0.798	0.073	0.801	1.008	95	517
6.250	-6.375	3.215	-1.892	34.509	0.318	-0.014	-0.132	0.160	0.620	0.799	0.070	0.802	1.013	95	517
7.143	-6.562	3.214	-1.900	34.625	0.299	-0.011	-0.149	0.171	0.639	0.801	0.065	0.803	1.026	95	517
7.692	-6.684	3.213	-1.899	34.648	0.287	-0.007	-0.161	0.177	0.649	0.802	0.062	0.805	1.034	95	517
9.091	-7.005	3.207	-1.885	34.588	0.258	0.009	-0.195	0.190	0.670	0.808	0.055	0.809	1.051	95	517
10.000	-7.213	3.201	-1.868	34.481	0.242	0.019	-0.219	0.198	0.680	0.812	0.051	0.813	1.060	95	517
11.111	-7.460	3.191	-1.841	34.297	0.225	0.030	-0.248	0.206	0.689	0.817	0.047	0.818	1.070	95	515
11.765	-7.600	3.185	-1.823	34.168	0.216	0.035	-0.266	0.210	0.693	0.820	0.045	0.821	1.075	95	515
13.333	-7.918	3.167	-1.775	33.812	0.199	0.044	-0.308	0.220	0.696	0.828	0.041	0.829	1.083	95	515
14.286	-8.098	3.155	-1.743	33.570	0.191	0.046	-0.334	0.226	0.696	0.834	0.039	0.834	1.086	95	515
16.667	-8.501	3.121	-1.657	32.910	0.180	0.045	-0.397	0.239	0.685	0.847	0.036	0.847	1.090	95	515
18.182	-8.724	3.097	-1.599	32.461	0.178	0.041	-0.436	0.246	0.673	0.855	0.034	0.856	1.089	94	512
20.000	-8.961	3.066	-1.528	31.905	0.182	0.033	-0.481	0.255	0.654	0.866	0.032	0.866	1.085	94	511